Iwaki Akiyama

Editor

Acoustical Imaging

Volume 29

with CD-ROM

Acoustical Imaging

Volume 29

Acoustical Imaging

Recent Volumes in This Series:

Acoustical Imaging
Volume 29

Edited by

Iwaki Akiyama

Shonan Institute of Technology, Kanagawa, Japan

Springer

Editor
Iwaki Akiyama
Shonan Institute Technology
Faculty of Engineering
1-1-25 Tsujido-Nishikaigan
Fujisawa, Kanagawa-ken
251-8511 Japan

Printed on acid-free paper

9 8 7 6 5 4 3 2 1

springer.com

29th International Symposium on Acoustical Imaging

Chairman: Iwaki Akiyama

Executive Council

Walter Arnold, Germany
Noriyoshi Chubachi, Japan
Kenneth Erikson, USA
Joie P. Jones, USA

Hua Lee, USA
Roman Maev, Canada
Piero Tortoli, Italy

International Advisory Board

Iwaki Akiyama, Japan
Michael Andre, USA
Walter Arnold, Germany
Jeff Bamber, United Kingdom
Noriyoshi Chubachi, Japan
Kenneth Erikson, USA
Helmut Ermert, Germany
Woon S. Gan, Singapore
James Greenleaf, USA
Joie P. Jones, USA
Hiroshi Kanai, Japan
Pierre Khuri-Yakub, USA

Hua Lee, USA
Sidney Lees, USA
Vadim M.Levin, Russia
Roman Maev, Canada
William O'Brien, USA
Patrick Rafter, USA
Daniel Rouseff, USA
Bernhard Tittmann, USA
Piero Tortoli, Italy
A.F.W. van der Steen, Netherlands
Glen Wade, USA
Peter N.T. Wells, United Kingdom

Technical Program Committee

Walter Arnold
Nobuyuki Endoh
Hiroyuki Hachiya
Joie P. Jones
Tomoo Kamakura
Hiroshi Kanai
Junichi Kushibiki
Kohji Masuda
Kentaro Nakamura

Akihisa Ohya
Yoshifumi Saijo
Tsuyoshi Shiina
Piero Tortoli
Takao Tsuchiya
Shin-ichiro Umemura
Oliver B. Wright
Kazushi Yamanaka

Local Organizing Committee

Iwaki Akiyama	Toshiaki Nakamura
Kunihiro Chihara	Naotaka Nitta
Noriyoshi Chubachi	Gosuke Ohashi
Nobuyuki Endoh	Akihisa Ohya
Hiroyuki Hachiya	Yoshifumi Saijo
Kazuhiko Hamamoto	Yasutsugu Seo
Hideyuki Hasegawa	Tsuyoshi Shiina
Tutomu Hoshimiya	Chikayoshi Sumi
Hiroshi Inoue	Yasuhito Takeuchi
Takashi Itoh	Shin-ichiro Umemura
Tomoo Kamakura	Shin-ichi Yagi
Naohisa Kamiyama	Akira Yamada
Hiroshi Kanai	Yoshiki Yamakoshi
Nobuki Kudo	Katsuyuki Yamamoto
Junichi Kushibiki	Kazushi Yamanaka
Mami Matsukawa	Masahide Yoneyama
Kentaro Nakamura	Yoshiaki Watanabe

CONTENTS

PREFACE

The 29th International Symposium on Acoustical Imaging was held in Shonan Village, Kanagawa, Japan during April 15–18, 2007. Despite the unusually cold and rainy weather for Shonan Area in April, the symposium was a great success owing to lively discussions among enthusiastic speakers and audiences, which assured us the future prosperity of the field of Acoustical Imaging. There were more than 100 participants and 83 presentations were given by delegates from about ten countries, e.g. Japan, USA, Canada, Italy, England, and Germany. I would like to express my gratitude to the following six invited speakers, who presented appreciative speeches at the symposium: Prof. James F. Greenleaf, Prof. Roman G. Maev, Prof. Kazushi Yamanaka, Prof. F. Levent Degertekin, Dr. Shin'ichi Sakamoto and Dr. Chiaki Miyasaka. Like its predecessors in the series this Volume 29 contains an excellent collection of papers, including the six invited speeches, presented in nine major categories:

- Strain Imaging
- Biological and Medical Applications
- Acoustic Microscopy
- Non-Destructive Evaluation and Industrial Applications
- Components and Systems
- Geophysics and Underwater Imaging
- Physics and Mathematics
- Medical Image Analysis
- FDTD method and Other Numerical Simulations

The 29th International Symposium on Acoustical Imaging owes its success to so many people that it is difficult to list all the names. However, I would like to acknowledge particularly for assisting me in the organization of the symposium: Prof. Noriyoshi Chubachi, Prof. Junichi Kushibiki and Prof. Hiroshi Kanai, who helped to realise this symposium in Japan, Mrs. Michiko Ohse and Mrs. Ayako Kamimura, who performed the preparations and arrangements, Dr. Akihisa Ohya and Dr. Tadashi Yamaguchi, who gave full assistance during the symposium itself, Prof. Michael P. Andre, the chairman of AI28, who gave instructive advices in organizing the symposium, and Prof. Yohichi Suzuki, the former president of Acoustic Society of Japan, who kindly agreed to co-organizing the symposium. Thanks also to Prof. Yoshiaki Watanabe, for his valuable advices.

Iwaki Akiyama

STRAIN IMAGING

USE OF RADIATION FORCE TO MEASURE ARTERIAL PROPERTIES

J.F. Greenleaf, X. Zhang, C. Pislaru

Ultrasound Research Laboratory, Dept. of Physiology and Biomedical Engineering, Mayo Clinic College of Medicine, Rochester MN 55905, USA

Abstract: Pulse wave velocity (PWV) is widely used for estimating the stiffness of an artery. PWV is measured by the time of travel of the "foot" of the pressure wave over a known distance. This technique has a low time resolution and is an average measurement of artery stiffness between the two measuring sites. In this paper an external short pulse wave is generated noninvasively in the arterial wall by the radiation force of ultrasound. The impulse wave velocity in the artery is measured noninvasively with high time resolution over a short distance of a few millimeters.

Key words: Local arterial stiffness, Noninvasive, Ultrasound

1.   BACKGROUND

Cardiovascular disease (CVD) has been the number one killer in the United States according to recent statistics by the American Heart Association [1]. It has long been recognized that a high percentage of all cardiovascular disease is associated with the hardening of arteries or arteriosclerosis [2]. Increased stiffness of arteries has recently gained acceptance as a fundamental risk factor for cardiovascular and many other diseases [3]. Pulse Wave Velocity, or the velocity of the heart pulse, has been shown to have a great deal of variability and cannot be used with great precision [4].

   In a series of recent studies, we proposed producing a bending wave in the arterial wall using localized ultrasound radiation force and measuring the wave velocity along the arterial wall [5,6,7]. The wave velocity can be determined accurately over short distance in a few millimeters. In this paper,

a new imaging technique is further developed for measuring the wave velocity in arteries under the excitation of ultrasound. This technique measures wave velocity over a short distance of a few millimeters assessing the local stiffness of the artery for early arterial disease diagnosis.

2.   METHOD

The radiation force of ultrasound is used to noninvasively generate a localized force on an artery. The excitation of this force produces a bending wave propagating along the artery [5]. A confocal ultrasound transducer is used to generate a short impulse wave in an artery with ultrasound toneburst signals. For example, a 3 MHz toneburst signal of 900 cycles results in a 0.3 millisecond pulse. The focal depth of the transducer is 10 cm. The focal size of the ultrasound beam is about 0.7 mm in diameter. The center of the artery was placed at the focal plane of the transducer. The impulse response of the artery is the forced response to the pulse excitation. The artery can be pressurized at given pressure and the experiments were conducted in a water tank (Fig. 1).
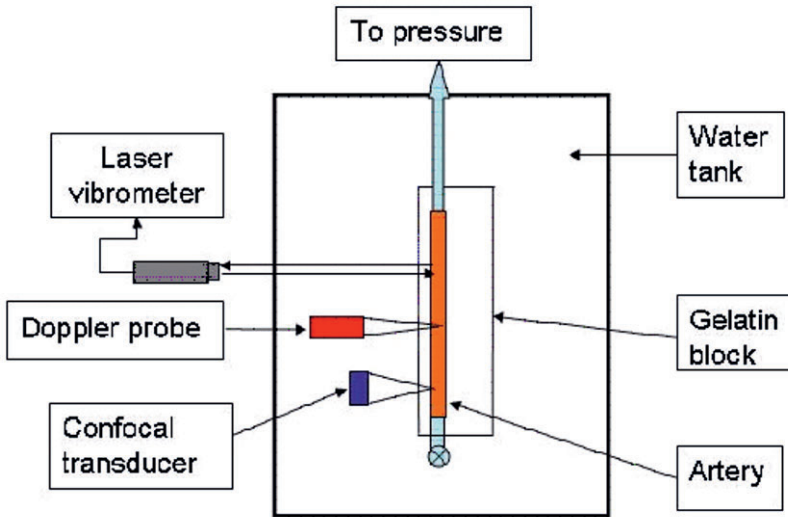
Figure 1. Schema of the experimental system The artery can be pressurized by internal saline through a connecting tube. A confocal ultrasound transducer remotely produces a localized force at the artery. The wave propagation in the artery is measured noncontact by a laser vibrometer system or a Doppler probe. The experiment is carried out in a water tank.

3.   RESULTS AND DISCUSSION

Figure 2 is a three-dimensional image of pulse wave propagation in a rubber tube embedded in tissue-mimicking gelatin phantom. The three coordinates of the image are respectively the time, distance, and wave amplitude. This image is the response of the tube to the pulse excitation of a 3 MHz ultrasound toneburst of 300 cycles generated at a point of the tube. The time and space resolutions of the image are 10 µs and 0.1 mm respectively. The signal amplifier gain was adjusted so that the wave amplitude signals were digitized between ±2048. To obtain this image, the laser detector was fixed and the force transducer was scanned along the tube at 0.1 mm intervals. For each position, the tube vibration velocity signal was sampled with the laser vibrometer at 100 k samples/s.

The wave velocity of the pulse can then be calculated from any two pulse shapes separated by a known distance. Any two pulse shapes in Fig. 2 can be used for measuring the pulse wave velocity. Although in Fig. 2 we have fine distance resolution, 0.1 mm, between two pulses, we do not necessarily need such fine resolution. If we measure in 2 mm and take the first and 21st pulses in Fig. 2, we can draw two pulse shapes as shown in Fig. 3. We can use a characteristic point in the pulse shape to measure the transit time, for example, the first positive peak or the first negative peak as a reference point.
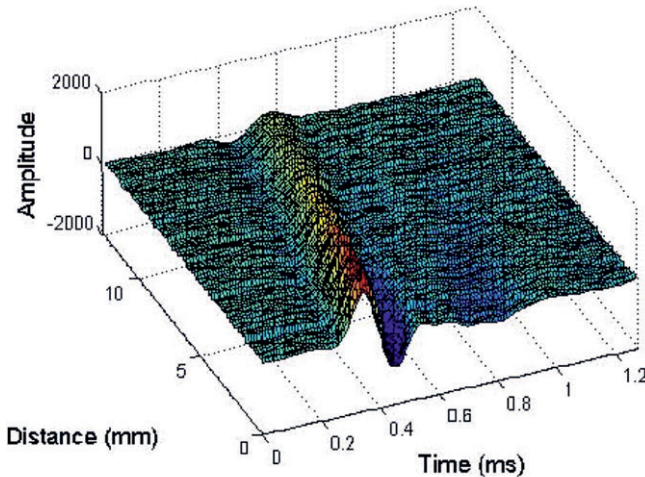
Figure 2. Graphs of pulse wave propagation in a rubber tube embedded in gelatin. The time resolution is 10 µs, the distance resolution is 0.1 mm, and the wave amplitude signals are digitized between ±2048; three-dimensional image.
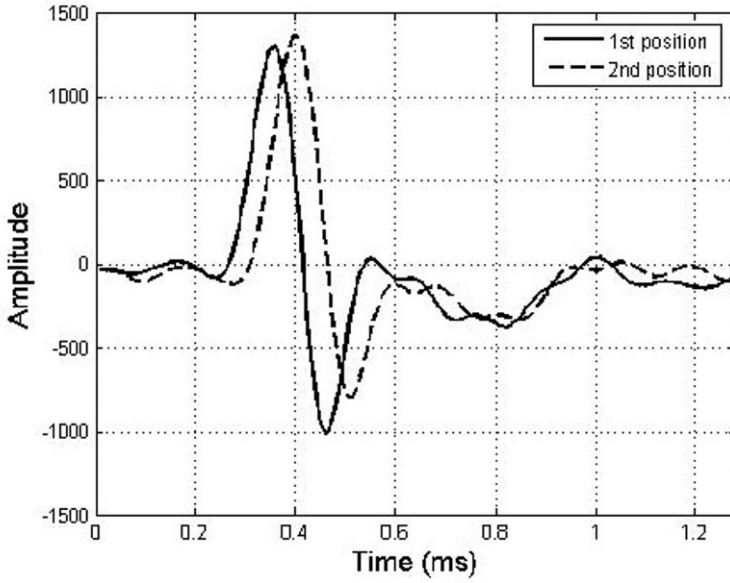
Figure 3. Two pulse shapes at two positions with 2 mm distance.
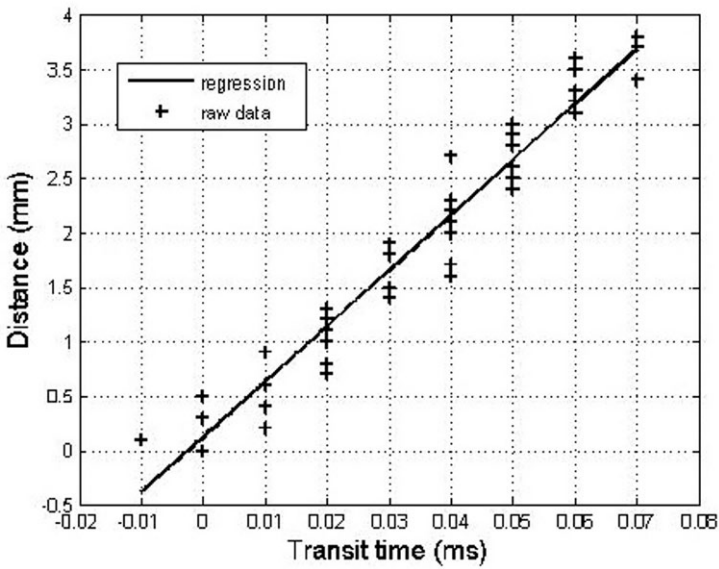
Figure 4. Regression equation is $\Delta y = 50.9058 \Delta t + 0.1248$ with a 95% confidence interval and the pulse wave velocity is $c_F = 50.9$ m/s.

A better way to measure the pulse wave velocity is to use all the data from the image. This can be done by determining the regression of the transit time Δt of the wave propagation and the distance Δy the wave takes. The time of the first peak of the wave at the initial position 0 mm is taken as reference, and the transit time of the wave at another position is measured by the time difference of its first peak with the reference time. The regression line can be obtained by "best fitting" a linear relationship of the transit time Δt and the distance Δy in the least mean squares (LMS) sense and its equation is $\widehat{\Delta y} = a\Delta t + b$, where   denotes the value of Δy on the regression for a given value of Δt.

The pulse wave velocity can be estimated by

$$c_p = \widehat{\Delta y} / \Delta t = a,$$ (1)

where   is the estimation of pulse wave velocity from the regression analysis that should be better than just using two curves in the image.

The regression analysis for the pulse wave in the tube embedded in gelatin is shown in Fig. 4. The regression equation, with the LMS of a 95% confidence interval, is $\Delta y = 50.9058\Delta t + 0.1248$ and the estimation of the pulse wave velocity is $c_F = 50.9$ m/s.

In vivo experiments of the impulse wave velocity on the femoral artery of pig were tested. A vibroacoustography (VA) image of the femoral artery of the pig is made from which the force transducer can be accurately positioned at the desired position on the femoral artery. Once the force transducer is positioned, the sensing Doppler transceiver is focused and placed over the artery such that its focal region is spaced approximately 15 mm downstream from the excitation point on the artery. The femoral artery was vibrated by localized ultrasound radiation force using a pulse of 1 ms duration ultrasound tone burst. The excitation was triggered by the ECG signal from the pig at the peak R-wave of the electrocardiograph QRS complex. The arterial wall vibration velocity resulting from the excitation was sensed by a 6 MHz Doppler transceiver operating in CW mode.

The excitation and the detection are both focused at the center of the artery cross section. Doppler signals from the artery were bandpass filtered (120–1000 Hz) to measure the artery vibration response. The vibration velocity signal was sampled at a rate of 100 kHz, amplified and output in voltage, as shown in Fig. 5. When the first measurement at 0 mm position is done, the force transducer is moved longitudinally along the artery 5 mm away for measuring the resulting vibration at the second position. The arterial wave velocity due to the pulse excitation can be estimated by finding the time delay of the waves at 0 mm and 5 mm. The time delay can be measured by identifying the time delay of the characteristic point on the wave curve. The time delay is measured 1.1 ms between the first maximum negative peaks of the two pulse curves, therefore, the pulse velocity is

calculated as 5 mm/1.1 ms = 4.5 m/s. The same value of pulse velocity can be measured if we measure the time delay using the first maximum positive peak of the pulse curve.

There are some advantages of the present technique over the classical "foot-to-foot" technique. One advantage is that the wave velocity can be measured locally in a few millimeters. Therefore, local arterial stiffness can be measured. In the "foot-to-foot" technique, the pulse wave velocity is measured over a relatively long distance. The measured length, for example the aorta pulse wave velocity measurement from carotid – femoral arteries, is typically a few hundred millimeters, therefore, it is difficult to evaluate the local arterial stiffness and its variation. Another advantage is that an external short pulse is used. The time resolution of our method can be of 10 μs that is several orders higher than that of blood pressure pulse. The blood pressure pulse is predominately a low frequency wave of a few Hz and its ability to differentiate the time change is typically in the range of a few tens of milliseconds. Higher time resolution helps to measure the local wave velocity and local arterial stiffness for early diagnosing artery disease.
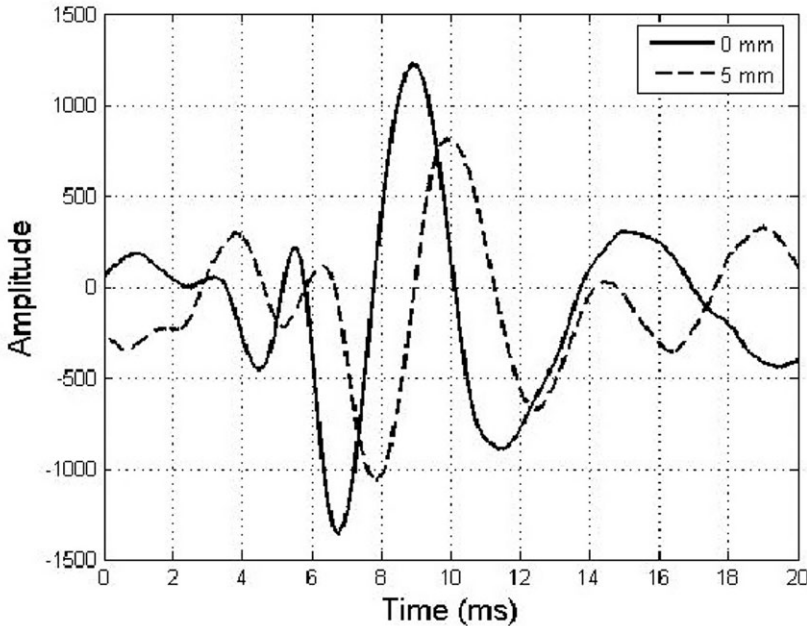
Figure 5. Two impulse wave shapes of the in vivo femoral artery at positions 0 mm and 5 mm under the ultrasound pulse excitation. The time delay of wave propagation can be measured accurately from the first maximum negative peak of two pulses. The pulse wave velocity is measured 4.5 m/s.

4. DISCUSSION

In this paper an external short pulse wave is generated noninvasively in the arterial wall by the radiation force of ultrasound. The impulse wave velocities are measured noninvasively for both an arterial rubber phantom and in vivo femoral artery of pig with high time resolution over a short distance of a few millimeters.

ACKNOWLEDGEMENTS

REFERENCES

1. American Heart Association, *Heart Disease and Stroke Statistics – 2003 Update*, Dallas, American Heart Association, 2003.
2. P. Hallock, "Arterial elasticity in man in relation to age as evaluated by the pulse wave velocity method," *Archives of Internal Medicine*, vol. 54, pp. 770–798, 1934.
3. M. F. O'Rourke, J. A. Staessen, C. Vlachopoulos, D. Duprez, and G. E. Plante, "Clinical application of arterial stiffness; definitions and reference values," *American Journal of Hypertension*, vol. 15, pp. 426–444, 2002.
4. W. W. Nichols and M. F. O'Rourke, *McDonald's Blood Flow in Arteries*, third edition, London, Edward Arnold, 1990.
5. X. Zhang, R. R. Kinnick, M. Fatemi, and J. F. Greenleaf, "Noninvasive method for estimation of complex elastic modulus of arterial vessels," *IEEE Transactions on Ultrasonics, Ferroelctricx, and Frequency Control*, vol. 52, pp. 642–652, 2005.
6. X. M. Zhang and J. F. Greenleaf, "Noninvasive generation and measurement of propagating waves in arterial walls", *The Journal of Acoustical Society of America*, Vol. 119, No. 2, pp. 1238–1243, 2006.
7. X. Zhang and J. F. Greenleaf, "Measurement of wave velocity in arterial walls with ultrasound transducers", *Ultrasound in Medicine and Biology*, Vol. 32, No. 11, pp. 1655–1660, 2006.

MICROSCOPIC MEASUREMENT OF THREE-DIMENSIONAL DISTRIBUTION OF TISSUE VISCOELASTICITY

T. Shiina, M. Yoshida, M. Yamakawa, N. Nitta

Graduate School of Systems and Information Engineering, University of Tsukuba, Tsukuba 305-8573, Japan; Institute for Human Science and Biomedical Engineering, National Institute of Advanced Industrial Science and Technology, Tsukuba, Ibaraki 305-8564, Japan

Abstract: According to recent development of practical system for tissue elasticity imaging, it is required to elucidate the quantitative relationship between diseases and parameters about tissue elasticity and viscosity to diagnose the stage of disease progression and differentiate malignant from benign precisely. From this viewpoint, we are investigating on development of a three-dimensional tissue viscoelasticity microscope for accumulating quantitative data on mechanical properties of tissues. In this study primary system was constituted and its basic performance was evaluated using tissue phantom.

Key words: Tissue characterization, Ultrasound microscope, Elastic modulus, Viscoelasticity

1.   INTRODUCTION

Ultrasonic tissue elasticity imaging has been investigated for the purpose of utilizing mechanical properties of tissues for diagnosis [1,2,3]. Recently, practical equipment for assessing tissue elasticity in the form of strain images has been developed and used for diagnosing diseases such as breast cancer [4,5]. To diagnose the stage of disease progression and differentiate malignant from benign precisely using parameters which represent tissue elasticity and viscosity, it is required to elucidate the quantitative relationship between these parameters and diseases. However, any database to refer such a kind of the relation has hardly been established yet.

For this purpose, some approaches to the microscopic measurement of tissue elasticity have been proposed [6]. These methods are aimed at attaining higher spatial resolution with high frequency ultrasound, consequently, thin slices of tissue must be used to prevent the attenuation of ultrasound. However, such thin slices are two-dimensional (2D) distributions, and the real mechanical properties of tissue are apt to change when the tissue is sliced thinly since the tissue microstructure is destroyed. To evaluate the mechanical properties of tissues under similar conditions to clinical use, it is important to measure the three-dimensional (3D) distribution of mechanical properties by using a relatively thick specimen to preserve the microstructure of tissues.

From the above viewpoint, we are investigating the development of a 3D tissue viscoelasticity microscope for accumulating quantitative data on the mechanical properties of tissues. In this study, the primary system was constructed and its basic performance was evaluated using a tissue phantom.

2.   PARAMETERS ON TISSUE VISCOELASTICITY

Among the various approaches for tissue elasticity imaging, the major approach is the static method, which utilizes the deformation of tissues induced by compression and relaxation and displays the strain distribution or percentage of deformation as a preliminary step. Its second step is the estimation of the elastic modulus by solving the constitutive equation from the strain distribution and boundary condition similar to stress distribution on the surface.

The static method has the advantages that the system is simple since no other additional devices than a probe is required, and it is easy to reconstruct elasticity images with high spatial resolution since strain is basically obtained by comparing RF signals of two frames. In addition, the data acquisition time is of the same order as that of conventional ultrasonography, which is suited to three-dimensional measurement. Therefore, a practical system for clinical use, based on static methods, has recently been developed by us in cooperation with medical-equipment makers [4,5]. Considering the process of elasticity imaging for clinical diagnosis, the microscopic measurement proposed in this study is based on static methods.

In terms of the elastic properties of tissues, Young's modulus is defined as the slope of the stress-strain curve as follows:

$$E(\varepsilon) = \frac{\partial \sigma(\varepsilon)}{\partial \varepsilon},$$ (1)

where E is Young's modulus, and σ and ε indicate axial stress and axial strain, respectively. It is well known that the stress-strain relationship of most soft tissue exhibits the exponential property [7]. By applying the exponential relationship of the stress-strain curve to Eq. (1), it is proven that Young's modulus-strain curve is also exponential, as shown by

$$E(\varepsilon) = E_0 \cdot e^{\beta \cdot \varepsilon}, \tag{2}$$

Parameter E_0 corresponds to Young's modulus of a linear elastic body under slight deformation, and parameter β quantifies the intensity of the elastic nonlinearity of soft tissue. By taking the logarithm of both sides of Eq. (2), the exponential curve is converted to a linear profile, as shown by Eq. (3). Therefore, parameters E_0 and β can be obtained by applying the least-squares method to the profile.

$$\log E(\varepsilon) = \log E_0 + \beta \cdot \varepsilon \tag{3}$$

In addition to the above elastic properties, considering the hysteresis loops of the stress-strain curves, we tried to extract a parameter of tissue viscoelasticity [8]. In general, the stress-strain curve in the relaxation process falls below that in the compression process because of strain energy dissipation, as illustrated in Fig. 1. The area of the hysteresis loop, H, reflects each tissue type. To discriminate between normal and pathological tissue, such as carcinoma, it is expected that the area of the hysteresis loop will play an important role in actual clinical diagnosis based on tissue viscoelasticity.
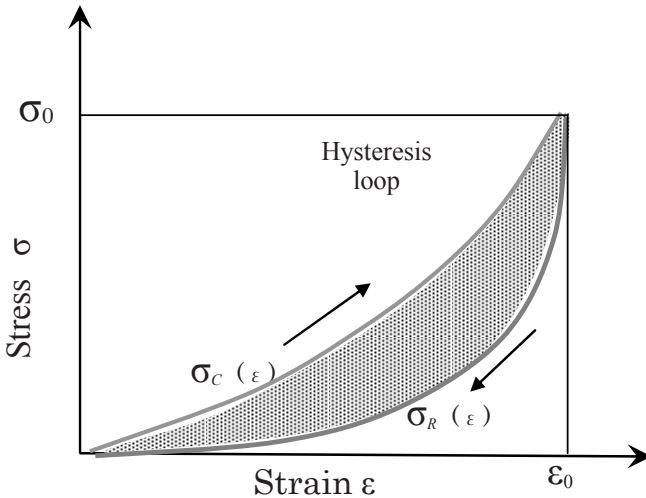
Figure 1. Typical hysteresis loop of stress-strain curves in soft tissue.

Since the area of the hysteresis loop is dependent on strain ε_0 at the turn-around point, at which the compression process switches to the unloading process, for quantitative assessment of the hysteresis property, we introduced the following hysteresis parameter HP,

$$HP = \frac{\int_0^{\varepsilon_0} \sigma_c(\varepsilon)d\varepsilon - \int_0^{\varepsilon_0} \sigma_R(\varepsilon)d\varepsilon}{\int_0^{\varepsilon_0} \sigma_c(\varepsilon)d\varepsilon}, \qquad (4)$$

where $\sigma_c(\varepsilon)$ and $\sigma_R(\varepsilon)$ are the stress-strain curves in the compression and relaxation processes, respectively. The parameter HP takes a value within 0 and 100%, and a large value of HP implies that viscosity is dominant. The processing details are described in the next section.

3.   MEASUREMENT SYSTEM

We constituted an experimental system as shown in Fig. 2. By considering the appropriate penetration depth and spatial resolution, a probe with a relatively low frequency, 20 MHz is used to image a thick sample, for example, more than 5 mm. A sample is located in the degassed water and compressed by a plate. A thin film is stretched on the hole which is opened at center of the plate. The water tank is located on the electric balance to measure the pressure during compression. First, volumetric data of echo signals from the tissue specimen is obtained by scanning the probe in the horizontal direction or the xy plane. Next, after the tissue specimen is compressed by the plate driven by a stepping motor, another set of volumetric data of echo signals is obtained by scanning the probe in the xy plane. At the same time, the applied pressure is also recorded by the electric balance. The three-dimensional distribution of axial strain is obtained from echo signals in adjacent frames using the combined autocorrelation method (CAM) that we developed for clinical equipment for real-time tissue elasticity imaging [3,4,5].

To obtain the elastic modulus using Eq. (1), we assumed that stress distribution is uniform within the specimen and the surface pressure mechanically measured with the sensor was assigned as the internal stress value. This approximation is reasonable since the area of the compression plate is sufficiently large compared with the thickness of the specimen. Finally, the stress-strain curve or hysteresis loop at each portion is obtained on the basis of the accumulated strain and the surface pressure during the compression and relaxation processes. Then HP is obtained using Eq. (4).
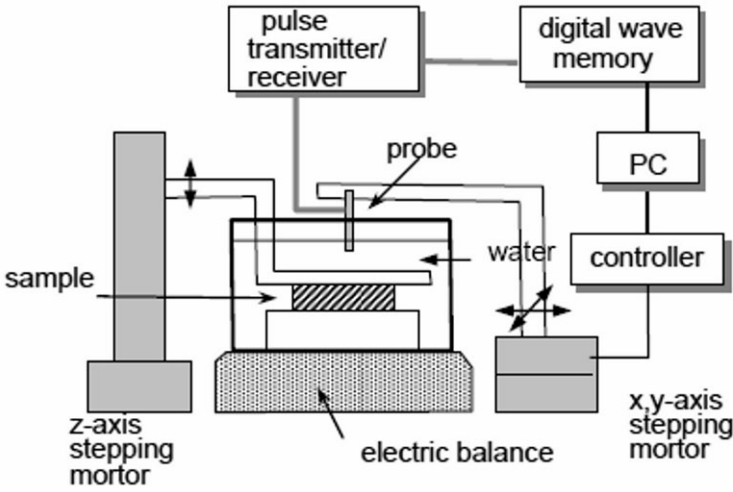
Figure 2. Measurement system.

4. RESULTS

Phantom was made of konnyaku and included a square column which was made of acrylamide and 2 mm on a side. Elastic modulus of konnyaku measured by mechanical method was about 35 kPa, whereas that of the inclusion was about 290 kPa. The sample was scanned at the interval of 0.1 mm in the lateral, x, and the elevational direction, y. Echo signals were sampled at the rate of 250 MHz. Figure 3 shows a result of measurement of three-dimensional distribution of elastic modulus and hysterisis parameter HP on the vertical cross section.

The inclusion is clearly imaged as a harder region and the value of elastic modulus (Young's modulus) was coincident with the value mechanically measured. In terms of *HP*, the inclusion is displayed as having a low value of *HP* which is coincident with the results of mechanical measurement. However, an artifact with shallow areas of konnyaku, which shows low *HP*, is also observed. This may be caused by the error in the strain estimation. It can be said that the spatial resolution is about 1 mm for this measurement system. In order to precisely evaluate spatial and contrast resolutions in comparison of the results of simulation analysis, a more appropriate phantom is required.
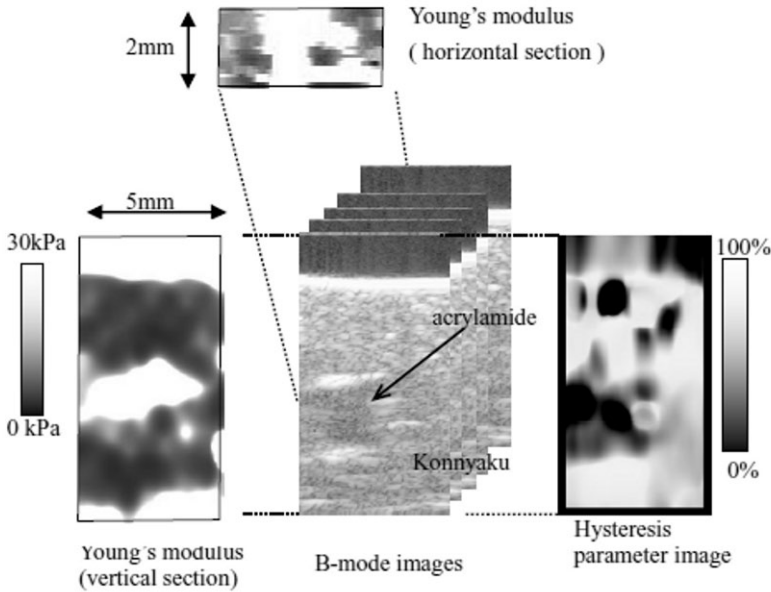
Figure 3. A result of phantom experiment.

5.   CONCLUSION

In this paper, we constituted an experimental system of a three-dimensional tissue elasticity microscope and verified its feasibility for measuring three-dimensional distribution of elastic modulus for relatively thick sample. The reconstructed image of the hysteresis parameter showed some coincidence with the real distribution. However, the results revealed that there was still room for improvement in the precision of strain estimation. Although the distribution of stress was assumed to be uniform in this study, we should calculate the stress distribution by the finite element method to confirm whether there is a significant difference in estimated parameters or not. Another important aspect is to determine the optimal specifications, for example, frequency, pulse waveform and material of compressing thin film, for a practical system.

ACKNOWLEDGEMENTS

REFERENCES

1. J. Ophir, I. Cespedes, H. Ponnekanti, Y. Yazdi and X. Li: Elastography: Ultrason. Imag 13 (1991) 111.
2. K. J. Parker, S. R. Huang, R. A. Musulin and R. M. Lerner: Ultrason. Med. Biol. 16 (1990) 241.
3. T. Shiina, N. Nitta, E. Ueno, J. C. Bamber: J. Med. Ultrason. 29 (2002) 119.
4. A. Itoh, E. Ueno, E. Tohno, H. Kamma, H. Takahashi, T. Shiina, M. Yamakawa, T. Matsumura: Radiology, 231 (2006) 341.
5. M. Yamakawa, N. Nitta, T. Shiina, T. Matsumura, S. Tamano, T. Mitake and E. Ueno: Jpn. J. Appl. Phys. 42 (2003) 3265.
6. N. A. Cohn, S. Y. Emelianov, M. A. Lubinski and M. O'Donnell: IEEE Trans. Ultrason. Ferroelect., Freq. Contr. 44 (1997) 1304.
7. Y. C. Fung: Biomechanics: Mechanical Properties of Living Tissues, 2nd ed. Springer-Verlag, New York (1993).
8. N. Nitta, T. Shiina and E. Ueno: Proc. of 2003 IEEE International Ultrasonics Symposium (2003) 1606.

STRAIN IMAGING FOR ARTERIAL WALL WITH TRANSLATIONAL MOTION COMPENSATION AND CENTER FREQUENCY ESTIMATION

H. Hasegawa, H. Kanai
Graduate School of Engineering, Tohoku University, Sendai 980-8579, Japan

Abstract: Atherosclerotic change of the arterial wall leads to a significant change in its elasticity. For assessment of elasticity, measurement of arterial wall deformation is required. For motion estimation, correlation techniques are widely used, and we have developed a phase-sensitive correlation-based method, namely, the *phased-tracking method*, to measure the regional strain of the arterial wall due to the heartbeat. Although phase-sensitive methods require less computation in comparison with the correlation between RF signals, the displacements estimated by such phase-sensitive methods are biased when the center frequency of RF echo varies. One of reasons for the change in the center frequency is the interference of echoes from scatterers within the wall. The artery-wall displacement includes both the component due to the radial translation of the arterial wall and that contributing to strain. In the case of the arterial wall, the displacement due to radial translation is larger than that contributing to strain by a factor of 10, and, thus, the error resulting from the translational motion often becomes larger than the small displacement contributing to strain. To reduce this error, in this study, a method is proposed in which the global translational motion is compensated before correlating echoes in two different frames to estimate the displacement distribution contributing to strain. Using this procedure, the significant error due to the large translational motion can be suppressed in comparison with the simultaneous estimation of the displacements due to translational motion and strain in the conventional methods. In this study, the accuracy improvement by the proposed method was validated using phantoms. The error from the theoretical strain profile and standard deviation in strain estimated by the proposed method was 12.0% and 14.1%, respectively, significantly smaller than that (23.7% and 46.2%) obtained by the conventional method.

1.   INTRODUCTION

We have developed a phase-sensitive correlation method, namely, *phased-tracking method*, for estimating the displacement distribution in the arterial wall for strain imaging [1]. In such methods, ultrasonic pulses with finite frequency bandwidths are used. Therefore, the apparent change in center frequency occurs due to the interference of echoes from scatterers in the wall. Under such a condition, the displacement estimates are biased because it is obtained using the phase change and center frequency of received RF echo. An autocorrelation-based method was proposed to compensate for this apparent change in center frequency [2]. However, the performance of this method is limited because the autocorrelation technique prefers the narrow band signals [3]. To reduce the influences of the change in center frequency, the large translational motion of the arterial wall should be compensated because the error due to the change in center freqeucy depends on the magnitude of the displacement (= phase change) and the translational motion of the arterial wall is much larger than strain. In this study, the displacement distribution of a phantom mimicking the artery was estimated using the autocorrelation technique with the translational motion compensation and error correction.

2.   METHODS

2.1   Displacement Estimation Using Conventional Autocorrelation Methods

The phases of echoes from a moving target, which is located at depth d in the initial frame, are different in two consecutive n-th and $(n+1)$-th frames. This phase shift, $\Delta\theta_d(n)$, depends on the displacement between these two frames of the target. Therefore, the instantaneous displacement $\Delta x_d(n)$ between these two consecutive frames is estimated as follows:

$$\Delta x_d(n) = \frac{c_0 \Delta\theta_d(n)}{4\pi f_{0e}}, \qquad (1)$$

where c_0 and f_{0e} are the speed of sound and the frequency used for displacement estimation, respectively. Phase shift $\Delta\theta_d(n)$ is estimated by the complex cross-correlation function $\gamma_{d,n}$ using the complex quadrature demodulated signals $z(d; n)$ of received RF echo as follows:

$$\Delta\theta_d(n) = \angle\gamma_{d,n} = \sum_{d \in R} z^*(d + x_d(n); n) \cdot z(d + x_d(n); n+1), \quad (2)$$

where * shows the complex conjugate. The accumulated displacement $x_d(n)$ is obtained by accumulating the instantaneous displacement with respect to time, and the displacement distribution is obtained by estimating the accumulated displacement $x_d(n)$ at each depth d which corresponds to the arterial radial direction. Finally, strain distribution is obtained by the spatial differentiation of displacements with respect to the arterial radial direction.

2.2 Translational Motion Compensation

As shown by Eq. (1), in conventional phase-sensitive autocorrelation method, the knowledge of center frequency is required to obtain the unbiased displacement estimates. The estimated displacement of the arterial wall Δx can be expressed by the sum of two components Δx_t and Δx_s due to the translational motion and contributing to strain as follows:

$$\Delta x = \Delta x_t + \Delta x_s = \frac{c_0}{4\pi f_{0e}}\Delta\theta_t + \frac{c_0}{4\pi f_{0e}}\Delta\theta_s, \quad (3)$$

where $\Delta\theta_t$ and $\Delta\theta_s$ are phase shifts of echoes caused by the translational motion and strain, respectively. The estimated displacement is biased when frequency f_{0e} used for estimation is different from the center frequency of RF echo. As an typical case, the translational motion of the arterial wall is larger than strain (change in thickness) by a factor of ten. Therefore, the error resulting from the translational motion is far greater than that from strain. This significant error can be reduced by removing the first term in the right-hand side of Eq. (3), which corresponds to the compensation of the translational motion. In this study, the translational motion is removed before estimating the phase shift of echoes due to strain as described below.

The translational motion of the wall is compensated by tracking the echo from the luminal interface using the conventional method because the echo from the luminal interface is dominant and is less influenced by the interference from other echoes from scatterers in the wall. In this study, *key*

frames are defined as the frames at which the estimated displacement of the luminal interface $\Delta x_i(n)$ is the integral multiple of the spacing of the sampled points ΔX. Figure 1(a) and 1(b) shows the RF echoes from the cylindrical phantom used in this study in two successive *key frames*. The region of interest (ROI) is manually assigned in the initial frame and, then, its position at each time is automatically determined by estimating the displacement of the luminal interface (the shallowest edge of the ROI). The displacement of the luminal interface between two successive *key frames* is just a spacing of sampled points, and the translational motion can be compensated by shifting the ROI by one point as shown in Fig. 1(c) and 1(d). After compensation, the phase shift of echoes between these two *key frames* is estimated at each depth d along the radial direction of the phantom. In this case, the estimated phase shift contains only the phase shift due to strain. Therefore, the error due to the translational motion can be reduced.
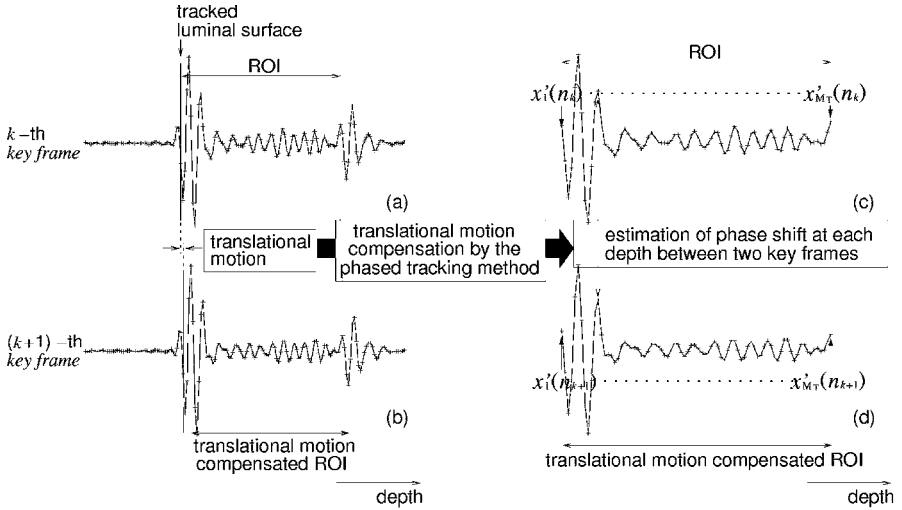
Figure 1. Displacement estimation with translational motion compensation.

2.3   Error Correcting Function

After compensation of translational motion, the displacement contributing to strain is estimated using the phase shift of RF echoes. In such a situation, a large error resulting from the translational motion is removed, but error due to the mismatch between the frequency used for estimation and the actual center frequency still remains in the estimation of the displacement contributing to strain even after the compensation of translational motion.

This error is much smaller than that in the case when the simultaneous estimation of displacements due to the translational motion and strain. However, in this study, an error correcting function is introduced to further reduce this small error in addition to the error due to the translational motion. The error correcting function $\beta_{d,k}$ in k-th *key frame* (n_k-th frame) is defined as follows:

$$\beta_{d,k} = \frac{\dfrac{c_0}{4\pi f_{0e}} \left| \angle \left(\gamma'_{d,k} \cdot \gamma^*_{d,k} \right) \right|}{\Delta X}, \tag{4}$$

$$\gamma'_{d,k} = \sum_{d \in R} z^*(d + x_l(n_k); n_k) \cdot z(d + x_l(n_k); n_{k+1}), \tag{5}$$

$$\gamma_{d,k} = \sum_{d \in R} z^*(d + x_l(n_k); n_k) \cdot z(d + x_l(n_{k+1}); n_{k+1}), \tag{6}$$

where ΔX is the spacing of sampled points. *Key frames* are assigned so as to be $|x_l(n_{k+1})-x_l(n_k)|=\Delta X$, and the signal $z(d+x_l(n_k); n_{k+1})$ in $\gamma_{d,k}$ is artificially displaced by a spacing of sampled points in comparison with $z(d+x_l(n_{k+1})$; $n_{k+1})$ in $\gamma'_{d,k}$. This artificial displacement can be expressed by angles of $\gamma_{d,k}$ and $\gamma'_{d,k}$, and the difference between angles of $\gamma'_{d,k}$ and $\gamma_{d,k}$, which can be shown by $|\angle(\gamma'_{d,k}\gamma^*_{d,k})|$, should be $4\pi f_0\Delta X/c_0$. However, the frequency used for displacement estimation f_{0e} is different from the actual center frequency f_0, and Eq. (4) shows the ratio of the artificial displacement estimated by phase shift to actual one. The error-corrected displacement $\Delta x_{s,d}(n_k)$ between n_k-th and n_{k+1}-th key frames contributing to strain can be obtained as follows:

$$\Delta x_{s,d}(n_k) = \frac{1}{\beta_{d,k}} \frac{c_0}{4\pi f_{0e}} \angle \gamma_{d,k}. \tag{7}$$

3.   BASIC EXPERIMENTAL RESULTS

In this study, a custom-made phantom containing 5% carbon powder (by weight) was scanned in its longitudinal direction with a 10-MHz linear array probe (Aloka SSD-6500, Tokyo). RF echoes were sampled at 40 MHz. As

shown in Fig. 2, the change in internal pressure was generated by a flow pump. The internal pressure was measured with a pressure transducer.
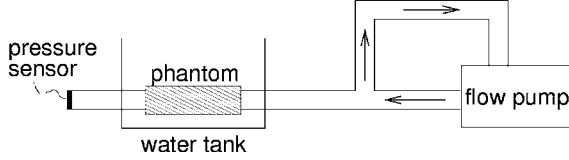
Figure 2. Experimental system.

Figure 3(a) shows the strain distribution along the ultrasonic beam (the radial direction of the phantom) estimated by the conventional autocorrelation method. Plots and vertical bars show means and standard deviations of 46 ultrasonic beams. The dashed line shows the theoretical strain profile [4], which is obtained by the measured internal pressure and elastic modulus (749 kPa) of the wall. The elastic modulus of the phantom was measured by the different pressure-diameter testing. Although mean values follow the theoretical strain profile, standard deviations of strains estimated by the conventional method are large. In Fig. 3(b), the center frequency estimation proposed in [2] was applied to the conventional method. However, the strain estimates are not improved so much. Figure 3(c) shows the strain distribution obtained by the proposed method. Strain estimates were improved significantly by translational motion compensation and error correction.
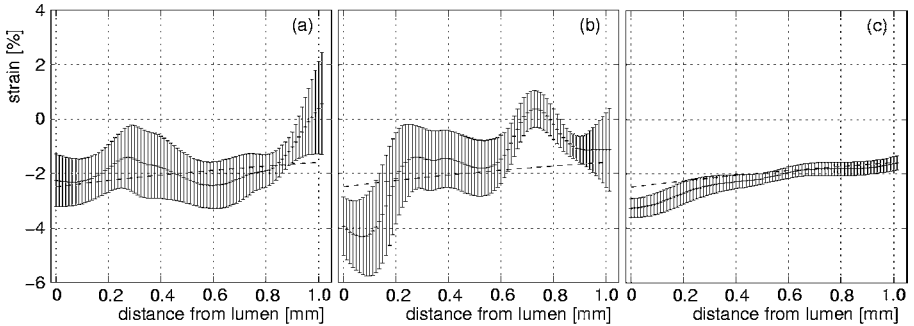
Figure 3. Estimated strain distribution. (**a**) Conventional method. (**b**) Conventional method with center frequency estimation [2]. (**c**) Proposed method with translational motion compensation and error correction.

4. CONCLUSIONS

This study addressed that the apparent change in center frequency due to the interference of echoes from scatterers leads significant error in the strain estimation. Through the basic experiments using a phantom mimicking the artery, it was shown that the proposed method with translational motion compensation and error correction reduces this error significantly.

REFERENCES

1. H. Kanai, M. Sato, N. Chubachi, and Y. Koiwa, Transcutaneous measurement and spectrum analysis of heart wall vibrations, *IEEE Trans. Ultrason. Ferroelect. Freq. Contr.* **43**, 791–810 (1996).
2. S. I. Rabben, S. Bjærum, V. Sørhus, and H. Torp, Ultrasound-based vessel wall tracking: an auto-correlation technique with RF center frequency estimation, *Ultrasound Med. Biol.* **28**, 507–517 (2002).
3. H. Hasegawa and H. Kanai, Improving accuracy in estimation of artery-wall displacement by referring to center frequency of RF echo, *IEEE Trans. Ultrason. Ferroelect. Freq. Contr.* **53**, 52–63 (2006).
4. S. P. Timoshenko and J. N. Goodier, *Theory of Elasticity*, 3rd ed., McGraw Hill, New York (1970).

NEAR-REAL-TIME 3D ULTRASONIC STRAIN IMAGING

G. Treece, J. Lindop, A. Gee, R. Prager

University of Cambridge, Department of Engineering, Trumpington Street, Cambridge CB2 1PZ, UK

Abstract: This paper describes a near-real-time system for acquiring and displaying 3D ultrasonic strain images using a mechanical sector transducer. For improved image quality and robustness, all signal processing is fully 3D, including 3D data windows, 3D least-squares fitting for the displacement-to-strain calculation, 3D strain normalization and full displacement tracking in the axial, lateral and elevational directions. Notwithstanding this thorough signal processing, 3D strain volumes are typically available for inspection within 20 seconds of performing the scan, with no need for special hardware. The speed is achieved by iterative phase-zero displacement tracking in the axial direction and novel methods for tracking in the lateral and elevational directions. Since the displacement tracking does not rely on the common (but brittle) zero-displacement assumption at the transducer face, high quality strain images are obtained reliably. The paper includes examples of in vitro strain images with full details of the acquisition and processing times.

Key words: 3D ultrasound, Strain imaging, Elastography, Real-time

1. INTRODUCTION

2D ultrasonic imaging of axial strain is emerging from the laboratory to feature in the latest generation of commercial medical scanners. Strain images are obtained by differentiating displacement maps, calculated by matching a large number of RF data windows in pre- and post-deformation scans. The resulting images allow qualitative assessment of tissue stiffness, which is often a clinically useful indicator of disease. Here, we extend the paradigm to the realm of 3D ultrasonic imaging with mechanical sector

transducers. 3D strain images are of potential clinical utility since they allow quantitative volume measurement and full 3D characterization of pathological entities. The only previously published work in this area [1] used 1D windows for both displacement and gradient estimation, did not track displacement in the elevational direction and nevertheless required several minutes of computation per volume. Here, we describe improved algorithms featuring true 3D signal processing, which nevertheless achieve near-real-time operation on standard hardware.

2.   METHOD

An overview of the entire process, from RF data acquisition to display of the 3D strain image, is provided in Fig. 1. To minimize estimation noise, we use 3D data windows which have approximately equal dimensions in the axial, lateral and elevational directions. For improved speed and superior image quality, axial displacement tracking is carried out not using exhaustive search (which can sometimes find spurious, false matches) but iterative phase-zero methods [2]. However, this requires each window's initial displacement estimate to be within half a wavelength of the correct axial shift. Traditionally, this is achieved by assuming zero shift at the transducer face and tracking the displacement estimates downwards in the axial direction. However, the zero shift assumption fails when the transducer is not in good contact with the skin over the entirety of the scanning aperture. Instead, we employ a novel tracking method that constructs a 3D displacement map plane-by-plane, as illustrated in Fig. 2. The first lateral-elevational plane is initialised with a lateral sawtooth displacement pattern of amplitude 4 wavelengths. It is positioned at a depth where an axial displacement of 4 wavelengths would correspond to an accumulated 5% strain. Assuming the average strain to this depth is in the range –5% to +5%, a section of the sawtooth will be within half a wavelength of the correct displacement, which is the convergence range for phase-zero displacement estimation. The next stage is to perform an axial phase-zero search at all windows in the lateral-elevational plane. Some of the resulting displacement estimates will be correct while the majority will converge to the wrong RF cycle. The alignments are then adjusted in the lateral and elevational directions by comparing each window with nearby windows on neighbouring A-lines and frames. We now have a dense map of 3D displacement estimates in one lateral-elevational plane (Fig. 2a), with a small number of correct entries arising from the sawtooth initialisation. These correct estimates are distinguished by greater correlation coefficients between the pre- and post-deformation windows.
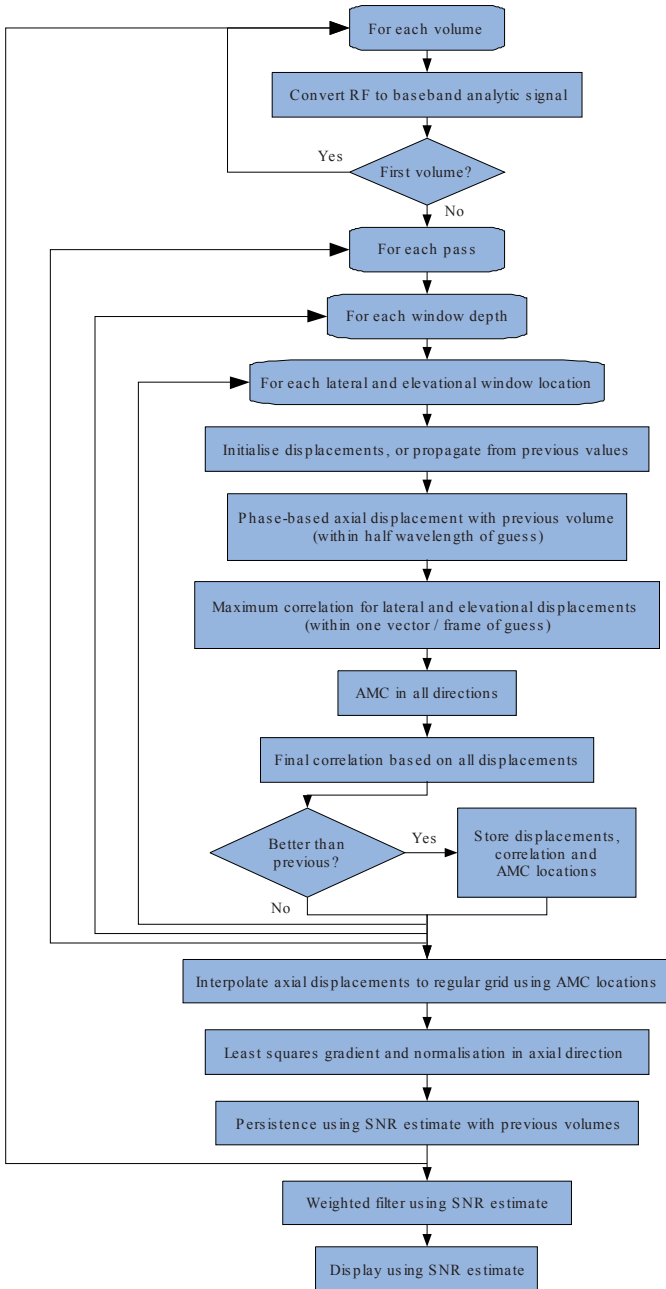
Figure 1. Overview of the 3D strain imaging algorithm (AMC is defined in the text).

This process is repeated at neighbouring planes in the up and down axial directions. However, this time each window's displacement is initialised not

by a "catch all" sawtooth pattern, but by searching a local 2D patch of windows in the previous plane for the highest pre- and post-deformation correlation coefficient. The small number of correct results in the first plane therefore seed a greater number of good displacement estimates in subsequent planes (Fig. 2b). The phase-zero search finds the correct peak in an ever growing number of windows, propagating outwards from the initial "lucky" hits in the sawtooth pattern. Within a few plane iterations, correct displacement tracking is well established at all windows. However, when the algorithm reaches the upper and lower axial extremities (Fig. 2c), there is still a small region around the starting plane with incorrect displacement estimates from the initial sawtooth initialisation. We therefore repeat the process, but this time reversing the direction of travel, sweeping the lateral-elevational planes from the extremities back to the centre. In this second pass, the phase-zero searches refine axial displacement estimates at the new elevational and lateral shifts, while the incorrect axial displacements near the starting plane are overwritten by correct values, distinguished by superior correlation coefficients, propagating from the extremities (Fig. 2d).
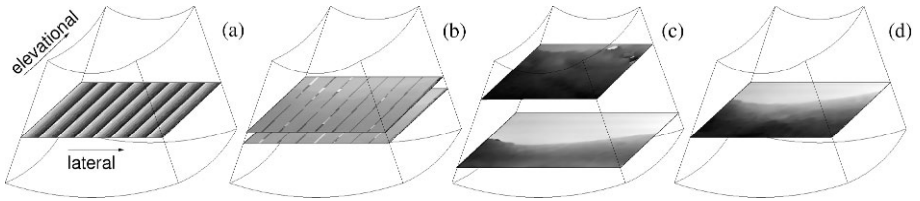
Figure 2. 3D displacement tracking.

The remaining part of the flow chart in Fig. 1, below the nested inner loops, describes how a dense strain image is constructed from the relatively sparse 3D displacement field. We have, for each 3D window, estimates of the axial, lateral and elevational displacement. These are represented as cylinders in Fig. 3, one for each window, and we need to interpolate them to the finer display grid, represented as circles in Fig. 3. We do not assume that the 3D displacement applies at each window's centre, since this results in the well-known amplitude-modulation artefact in the final strain image. Instead, we use an amplitude-modulation correction (AMC) technique [3] to estimate the location in each window where the 3D displacement is most valid (the arrows at the base of each cylinder in Fig. 3). In Fig. 3's 2D example, the displacements and lateral AMC locations are first moved to their correct axial locations using the axial AMC estimates. The values are then interpolated axially to populate the dense axial grid. The displacements are then moved to their correct lateral locations using the interpolated lateral AMC locations, before interpolating laterally to complete the grid.
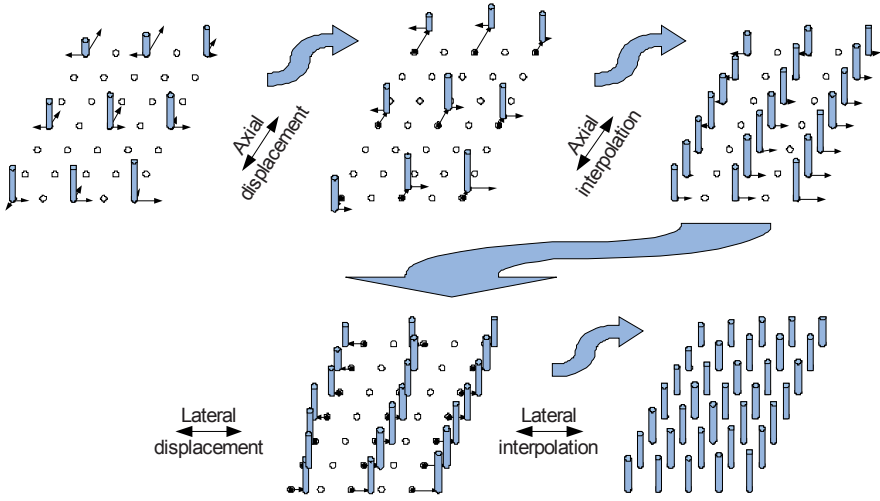
Figure 3. Interpolation to a regular 2D grid (the same principles apply in 3D).

Even though we have estimated displacements in the axial, lateral and elevational directions, we display only axial strain, since the sampling resolution in the lateral and elevational directions is not sufficient for high quality imaging. The axial strain is calculated using a 3D least-squares gradient operation over the entire 3D volume. The strain is then normalized by an estimate of the stress field, the aim being to produce strain images that reflect mechanical tissue properties and not local stress. The stress estimate is obtained by fitting the function a(1+by)(1+cx+dz) to the 3D strain field, where a-d are constants. We can thus allow for decaying stress with depth, and any variation in contact pressure across the transducer face.

If there are more than two data volumes, multiple strain volumes can be averaged using an elastographic SNR weighting derived from the correlation and the local strain. Finally, the normalized strain is displayed using an appropriate colour map: in this paper, we use a simple grey-scale varying from 0 (no strain) to 255 (normalized strain of 2). Alternative, polychromatic colour maps allow simultaneous display of strain (hue) and SNR (intensity), with regions of poor quality strain data (for example, below a blood vessel) de-emphasized in favour of regions with better elastographic signal content.

3. EXPERIMENTS AND RESULTS

The results in Fig. 4 were obtained using a GE RSP6-12 mechanical sector probe interfaced to a Dynamic Imaging Diasus ultrasound machine. Real-time

RF data acquisition and simultaneous control of the probe's stepper motor were managed by our freely available Stradwin software. The system is capable of RF data acquisition at a rate of approximately 7 volumes per second. The protocol for strain imaging was to record one volume, apply slightly greater probe pressure, then record a second volume, the entire acquisition process taking less than 2 s. The processing time on a 2.1 GHz CPU was then 17 s for the sphere phantoms (60 frames per volume) and 32 s for the olive phantom (120 frames per volume).

(a) 15mm diameter sphere
Axial tracking only

(b) 15mm diameter sphere
3D displacement tracking

(c) 5mm diameter sphere
3D displacement tracking

(d) Half olive in gelatine
3D displacement tracking
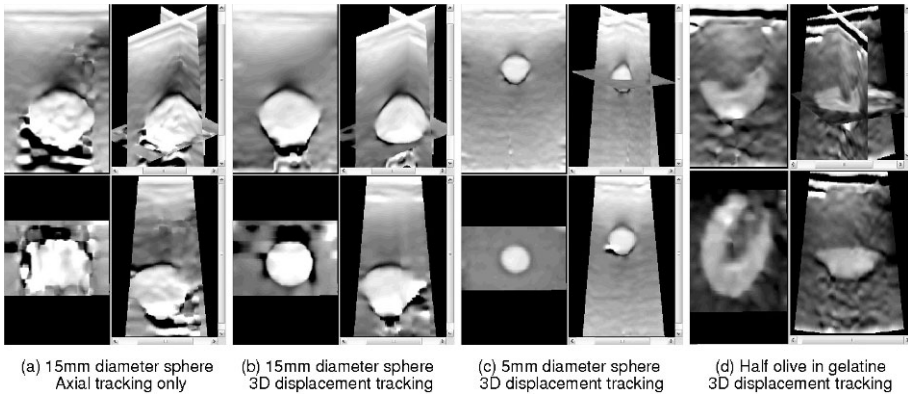
Figure 4. In vitro 3D strain volumes.

Each result in Fig. 4 shows typical axial-lateral, axial-elevational and lateral-elevational slices through the normalized 3D strain field, along with a composite 3D view showing the slices' relative locations. Note in Fig. 4(a) and Fig. 4(b) the need for full 3D displacement tracking: the axial strain field can be severely degraded if we track displacements in the axial direction only. Figure 4(c) shows excellent definition of a 5 mm diameter spherical inclusion in all three dimensions, while Fig. 4(d) illustrates good 3D geometrical characterization of half an olive embedded in gelatine.

REFERENCES

1. Lorenz, A., Pesavento, A., Pesavento, M., and Ermert, H., 1999, Three-dimensional strain imaging and related strain artefacts using an ultrasonic 3D abdominal probe. *Proc. IEEE Ultrason. Symp*. **2**:1657–1660.
2. Pesavento, A., Perrey, C., Krueger, M., and Ermert, H., 1999, A time efficient and accurate strain estimation concept for ultrasonic elastography using iterative phase zero estimation. *IEEE Trans. Ultrason. Ferr. Freq. Cont*. **46**(5):1057–1067.
3. Lindop, J., Treece, G., Gee, A., and Prager, R., 2007, Estimation of displacement location for enhanced strain imaging. *IEEE Trans. Ultrason. Ferr. Freq. Cont*. **54**(9):1751–1771.

DYNAMIC RESOLUTION SELECTION IN STRAIN IMAGING

J. Lindop, G. Treece, A. Gee, R. Prager

University of Cambridge, Department of Engineering, Trumpington Street, Cambridge CB2 1PZ, UK

Abstract: Ultrasonic strain imaging promises to be a valuable tool in medical diagnostics. Reliability and ease-of-use have become important considerations. These depend on the selection of appropriate imaging parameters. Here we undertake two tasks: (1) the tradeoff between resolution and estimation precision is examined closely, establishing quantitative models for the impacts of imaging parameters and data properties; and (2) these models are applied in a system for automatically selecting parameters responsive to data quality and required estimation precision. This yields more meaningful images when scan conditions vary. We apply the new scheme to simulation and *in vivo* data for validation. It reduces the complexity of the sonographer's task, producing reliable images even when the quality of the underlying data is inconsistent.

Key words: Strain imaging, Resolution, Tradeoff, Parameter selection, User interface

1.   INTRODUCTION

With Dynamic Resolution Selection [1] (DRS) we aim to steer imaging parameters automatically towards appropriate settings responsive to the underlying data quality. Thereby (1) DRS reduces the complexity presented to the sonographer – the controls are reduced to a single noise-rejection setting – and (2) parameters vary within each frame to produce reliable strain data even when the signal quality is inconsistent [2,3]. We outline DRS conceptually, and we implement a prototype for Weighted Phase Separation [4] with Amplitude Modulation Correction [5] and least squares strain. Simulations support development and validation, followed by an in vivo demonstration.

2.   DEVELOPMENT

Strain imaging requires at least two stages of signal processing: (A) displacement and (B) strain (i.e., gradient) estimation. This applies effectively even if the stages are not explicit in algorithm descriptions [6]. The parameters of both stages affect a precision/resolution tradeoff (see Fig. 1). In general, excessive estimation errors can be reduced by spatial averaging. Uncorrelated errors cancel out, but this leads to blurring of the final image.
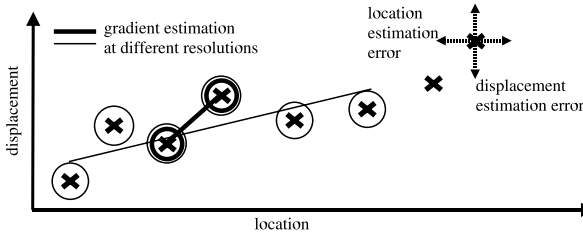
Figure 1. 1D illustration of the tradeoff in Stage B (strain estimation). The flow of displacement estimation error into strain error can be suppressed by sacrificing resolution.

Specifically, we consider least squares strain estimation – kernel length and width govern the tradeoff, and a similar tradeoff at Stage A is governed by the length and width of displacement estimation windows. Resolution can also be limited by window/kernel spacing, but this is not a tradeoff with precision, so we use dense window/kernel spacing and our results focus on the filtering effects of different window/kernel sizes.

Firstly, we test resolution. We record the contrast between alternating bands of 0% and 1% strain in simulated RF data [1]. This contrast crosses zero at the resolving limit, when windows/kernels are large (e.g., Fig. 2). We use square 2D windows/kernels, only quoting length (1 sample is 1/11 of the wavelength; axial length of 30 samples corresponds to lateral width of 1 A-line), and image borders are blocked-out where the stated parameters do not fit (the borders grow with increasing window/kernel size).
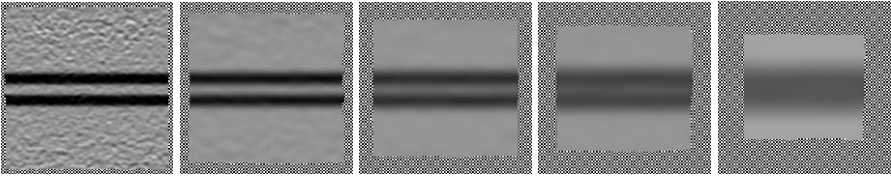
Figure 2. Strain resolution example. Window/kernel lengths from left to right: 75/90, 175/210, 275/330, 375/450 and 525/630 samples. These yield contrast of +0.781%, +0.492%, +0.229%, +0.060% and –0.036% respectively. On the right the structure is unresolved.

Using our simulation data we plot resolution contours in Fig. 3a, indicating that resolution depends primarily on either window or kernel size, whichever has the greater filtering effect. Hence the size ratio between windows and kernels should be fixed to maximise precision at any given resolution. Extreme window/kernel lengths at each resolution are plotted in Fig. 3b, indicating an appropriate size ratio of 1:1.2.
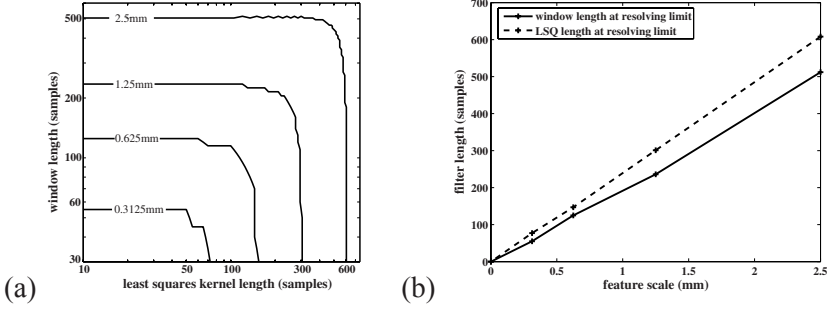
Figure 3. Resolution data: (**a**) contours of resolving limit and (**b**) extreme parameter values at each resolution indicate the appropriate size ratio between window and kernels.

Secondly, we consider displacement estimation precision. Typically displacement precision is proportional to window size, as indicated by Fig. 4 (albeit at very low strain).
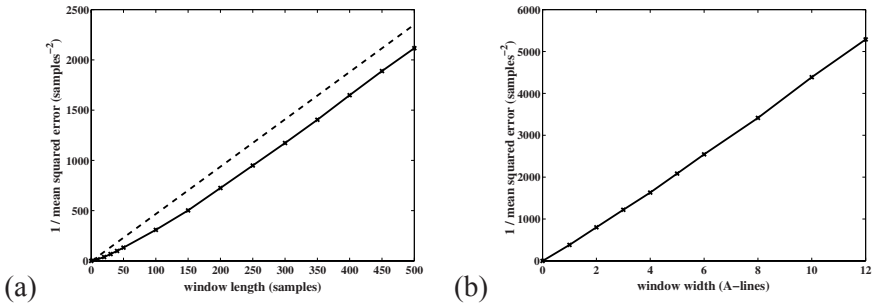
Figure 4. Simulations at 0.01% strain indicate displacement precision approximately proportional to (**a**) window length (width = 1 A-line) and (**b**) width (length = 120 samples).

Displacement precision is affected by noise and decorrelation, which are both accounted for in a modified signal-to-noise ratio, $SNR_s = \rho/(1-\rho)$, where ρ is the correlation coefficient of small windows. The linear relation in Fig. 4 must be scaled by SNR_s to adjust for changes in signal quality.

However, estimation precision sometimes drops with an increase in window length. We see this in Fig. 5, in which contours of SNR_e are plotted

over window/kernel length, where SNR_e(=strain/standard deviation of strain estimates) is a performance measure. The eventual drop in SNR_e with long windows is the result of within-window phase-wrapping. This affects almost all algorithms that do not warp the signals (it is not a particular feature of phase-based methods) [4,5,6]. In DRS we will avoid this behaviour by capping the window length at 500 samples/strain (%).
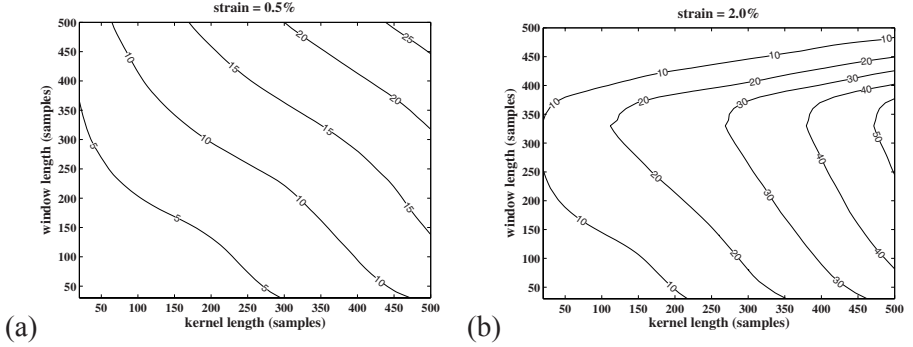
Figure 5. SNR_e contours at (**a**) 0.5% and (**b**) 2% strain.

Thirdly, we model the flow from displacement precision through to strain precision. Its reciprocal is least squares strain variance $\hat{\sigma}_{\hat{s}}^2$:

$$\hat{\sigma}_{\hat{s}}^2 = \frac{\sum_i \sum_j \hat{y}_i \hat{y}_j \hat{\sigma}_{\hat{d}_i \hat{d}_j}}{\left(\sum_k \hat{y}_k^2\right)^2} \approx K \sum_i \sum_j \left(\frac{\hat{y}_i \hat{y}_j \times \text{overlap}}{\text{win. size} \times \text{SNR}_s}\right) \bigg/ \left(\sum_k \hat{y}_k^2\right)^2,$$

where $\hat{y}_i$ is an axial location and $\hat{\sigma}_{\hat{d}_i \hat{d}_j}$ is the covariance between nearby displacement estimates. We mostly estimate cross-covariances using window overlap, but we also consider accounting only for auto-covariances.

Finally, we draw these concepts together to implement DRS. Each strain image is formed by: (1) coarse "pre-estimation" of strain and SNR_s using short windows and long kernels, followed by further spatial filtering; (2) "prediction" (using models discussed) of smallest DRS windows/kernels in the correct size ratio that yield SNR_e exceeding $minSNR_e$ (user-set target); (3) "strain estimation" for final image using DRS windows/kernels.

3.   VALIDATION

We use simulations to compare the predicted SNR_e after "pre-estimation" against the recorded SNR_e as window/kernel sizes are increased (see Fig. 6).
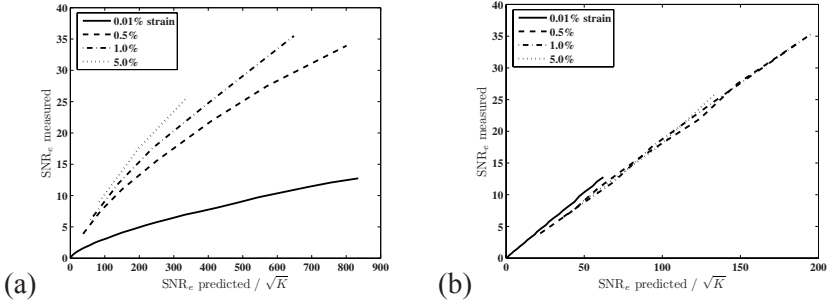
Figure 6. Recorded SNR_e against predicted SNR_e in simulations across a wide range of strains, where the SNR_e predictions (**a**) ignore and (**b**) account for cross-covariances.

Considering the displacement covariances in full yields good predictions, as in Fig. 6b, but we also need the scale from our equation, $\sqrt{K}$. Results in Fig. 7 indicate $\sqrt{K}$ varies depending on the source of noise, since the error autocorrelation length is different for motion decorrelation and white noise. Variation is < one order of magnitude, so later we use a mid-range value.
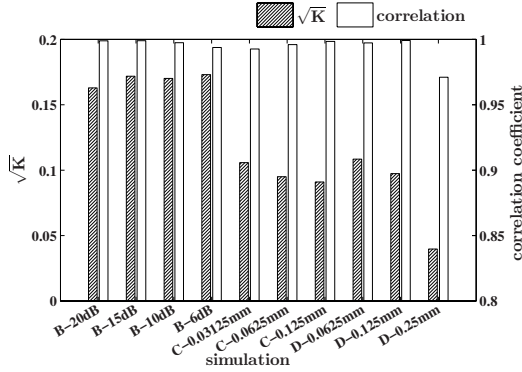
Figure 7. Estimates of $\sqrt{K}$ and correlation between predictions and measurements of SNR_e for different simulations (B: white noise, C: lateral and D: elevational motion). High correlations indicate good predictions, but $\sqrt{K}$ depends on the source of noise.

Finally, we demonstrate DRS in application to a simulation with variable noise (see Fig. 8) and an image from freehand *in vivo* scanning (see Fig. 9).

4. CONCLUSION

We outlined DRS, showed that it can be implemented, and illustrated the benefits that similar approaches may bring to future strain imaging systems.
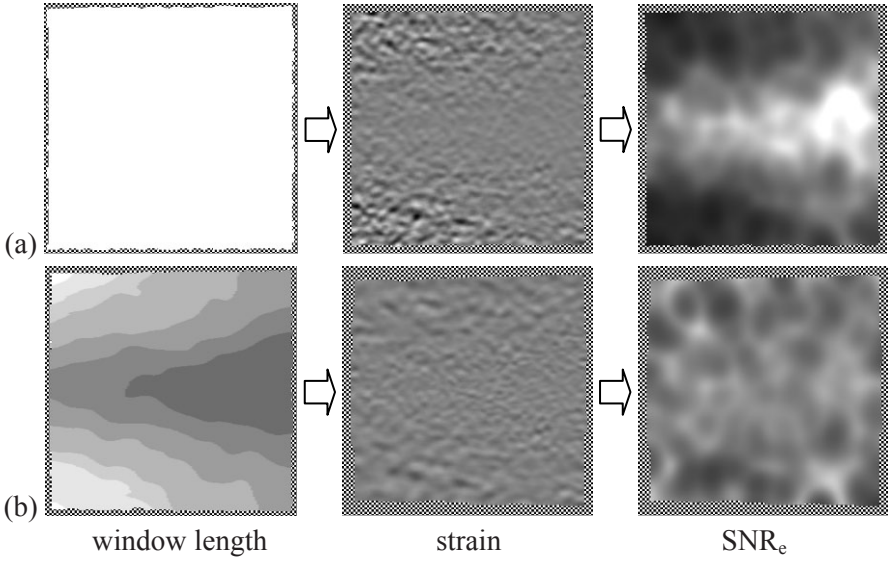
Figure 8. Simulation of variable noise and uniform strain with (**a**) fixed parameters and (**b**) DRS. Overall SNR_e is the same in both images, but local variation is misleading when parameters are fixed, while DRS offers uniform SNR_e and changes in resolution are visible.
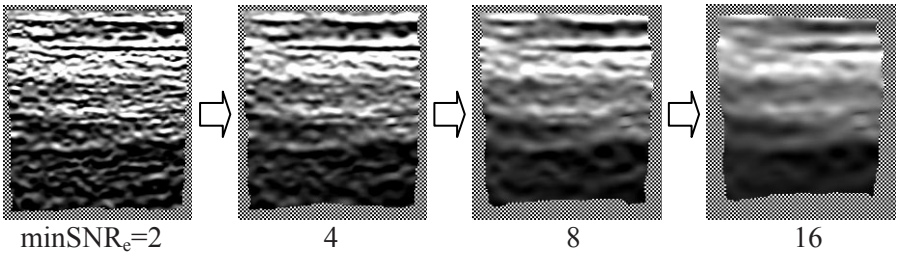
Figure 9. Biceps scan. Users influence the resolution/precision tradeoff in DRS strain imaging through a single control parameter, $minSNR_e$, which has intuitively appealing properties.

REFERENCES

1. J. E. Lindop, G. M. Treece, A. H. Gee, and R. W. Prager. CUED/F-INFENG/TR 566 (2006).
2. T. Varghese and J. Ophir. Ultrason. Med. Biol., 23 (1997) 1343.
3. F. Kallel, T. Vargese, J. Ophir, and M. Bilgen. Ultrason. Med. Biol., 23 (1997) 1357.
4. J. E. Lindop, G. M. Treece, A. H. Gee, and R. W. Prager. CUED/F-INFENG/TR 555 (2006).
5. J. E. Lindop, G. M. Treece, A. H. Gee, and R. W. Prager. CUED/F-INFENG/TR 550 (2006).
6. S. K. Alam, J. Ophir, and E. E. Konofagou. IEEE T. UFFC, 45 (1998) 461.

A NEW NON-INVASIVE ULTRASONIC METHOD FOR MEASUREMENTS OF LONGITUDINAL LENGTH ALTERATION OF THE ARTERIAL WALL – FIRST IN VIVO TRIAL

M. Cinthio[1,2], Å. R. Ahlgren[3], H.W. Persson[1], K. Lindström[1]

[1]*Dept. of Electrical Measurements, Lund Institute of Technology, Lund University, Lund, Sweden;* [2]*Dept. of Electronic Engineering, Graduate School of Engineering, Tohoku University, Sendai 980-8579, Japan;* [3]*Dept. of Clinical Sciences, Clinical Physiology and Nuclear Medicine Unit, Malmö University Hospital, Lund University, Malmö, Sweden*

Abstract: We have recently shown that there is a previous unknown longitudinal movement present in the arterial wall. We aim now to investigate whether the longitudinal movement causes length alteration of the arterial wall. The objective of this paper was to describe a new non-invasive ultrasonic technique that measures the length alteration of arteries in human in-vivo. Results indicate that a significant length alteration is present in the common carotid artery.

Key words: Carotid artery, Vascular mechanics, Arterial wall movements, Vascular ultrasound

1.   INTRODUCTION

In cardiovascular research the radial movement of the arterial wall, the diameter change, has been the subject of extensive research. In contrast to the radial movements, the longitudinal movements and the length reduction of the arterial wall have gained little attention. It has been assumed that the longitudinal movement of the arterial wall during the cardiac cycle is negligible when compared with the radial movement [1]. However, we [2–4] have recently questioned these results. Using a new high-resolution non-invasive ultrasonic

measurement technique in vivo in humans [3], we have clearly demonstrated that there is a distinct longitudinal movement of the arterial wall during the cardiac cycle of the same magnitude as the diameter change in central elastic arteries as well as in large muscular arteries [4]. We also demonstrate that the inner parts of the vessel wall, the intima-media complex, show a larger longitudinal movement than the outer part of the vessel wall, the adventitial region, introducing the presence of substantial shear strain, and thus shear stress within the vessel wall [4]. Furthermore, Tozzi et al. have recently reported a significant length reduction in the investigated common carotid artery on exposed vessel in pigs [5].

The aim is to investigate whether there is a length alteration of the arterial wall also in humans. The objective of this paper was to describe a new non-invasive ultrasonic technique that measures the length alteration of arteries in human *in vivo*. Furthermore, results from the first *in vivo* study are presented.

2.   MATERIAL & METHODS

The longitudinal length alteration of the arterial wall was measured using B-mode ultrasound using a commercial ultrasound system (HDI 5000, Philips Medical Systems, Bothell, WA, USA). The image data was transferred to a PC for post processing and visualized on the PC in HDILab (Philips Medical Systems, ATL Ultrasound, Bothell, WA, USA), a software designed for off-line cineloop analysis.

To measure the length alteration of the arterial wall the longitudinal movement of the intima-media complex was measured [3] at two positions simultaneously along the artery. The measurement was carried out by placing two region-of-interests at two different distinct echoes of inhomogeneities in the arterial wall. The chosen echoes were tracked and they must therefore be visible in all images during several cardiac cycles. The position of the echoes was recorded at end-diastole at each heartbeat, and the distance between them was registered as the origin distance. Thereafter the length alteration was estimated by quantifying the difference of longitudinal movement between the two echoes during the cardiac cycle (1).

$$Length\ Alteration = \left(Pos_{ROI_x} - Pos_{ROI_{x-end-diastole}} \right) - \left(Pos_{ROI_y} - Pos_{ROI_{y-end-diastole}} \right) \quad (1)$$

In this study the length alteration of the common carotid artery was measured on one healthy normotensive woman, 47 years old. The longitudinal movement was recorded at six positions over 15 mm long segment 2–3 cm proximal to the bifurcation during five consecutive cardiac

cycles. The longitudinal arterial length alteration was thereafter estimated between these positions in all different combinations. This gave all together 15 different measurements of the length alteration. The maximum length reduction and length expansion during the cardiac cycle was detection. Resulting data are presented as the mean value ± SD.

During the measurements the vessels were scanned in the longitudinal direction and oriented horizontally in the image. The transducer was in all instances placed in a fixative clamp to avoid introducing false movements by the operator. Care was taken to minimize the pressure of the transducer.

3.   RESULTS

Result from a measurement of the length alternation during five consecutive heartbeats is shown in Fig. 1. Both the maximum length reduction and the maximum length expansion seem to be larger as the distance between the measurement regions is increased, see Fig. 2. The mean distance between the origin positions in the 15 measurements was (5.74 mm (SD 3.64);
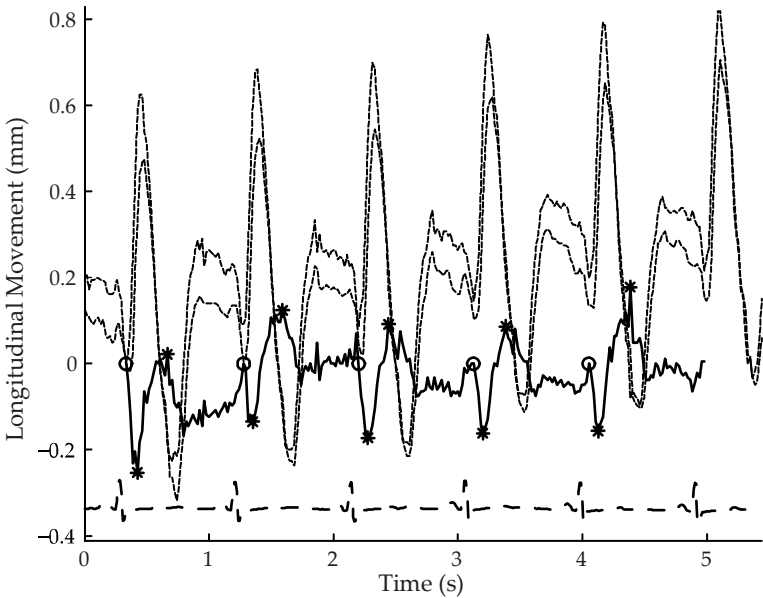
Figure 1. The longitudinal movement of the intima-media complex of the far wall (---) at two different measurement sites separated approximately 10 mm, as well as, the resulting arterial longitudinal length alteration (——) during five consecutive cardiac cycles in relation to the ECG in the common carotid artery of a 47-year-old female. The rings mark end-diastole and the stars mark the maximum length expansion and maximum length reduction during a cardiac cycle, respectively.

range 0.58–12.10 mm, Fig. 2). The maximum length reduction was (–130 μm (SD 59); range 33–242 μm, Fig. 2) and the maximum length expansion was (85 μm (SD 60); range 13–190 μm, Fig. 2). The beat-to-beat standard deviation between the five consecutive cardiac cycles for the length reduction was (29 μm (SD 12); range 7–51 μm, Fig. 2) and (36 μm (SD 15); range 16–65 μm, Fig. 2) for the length expansion.
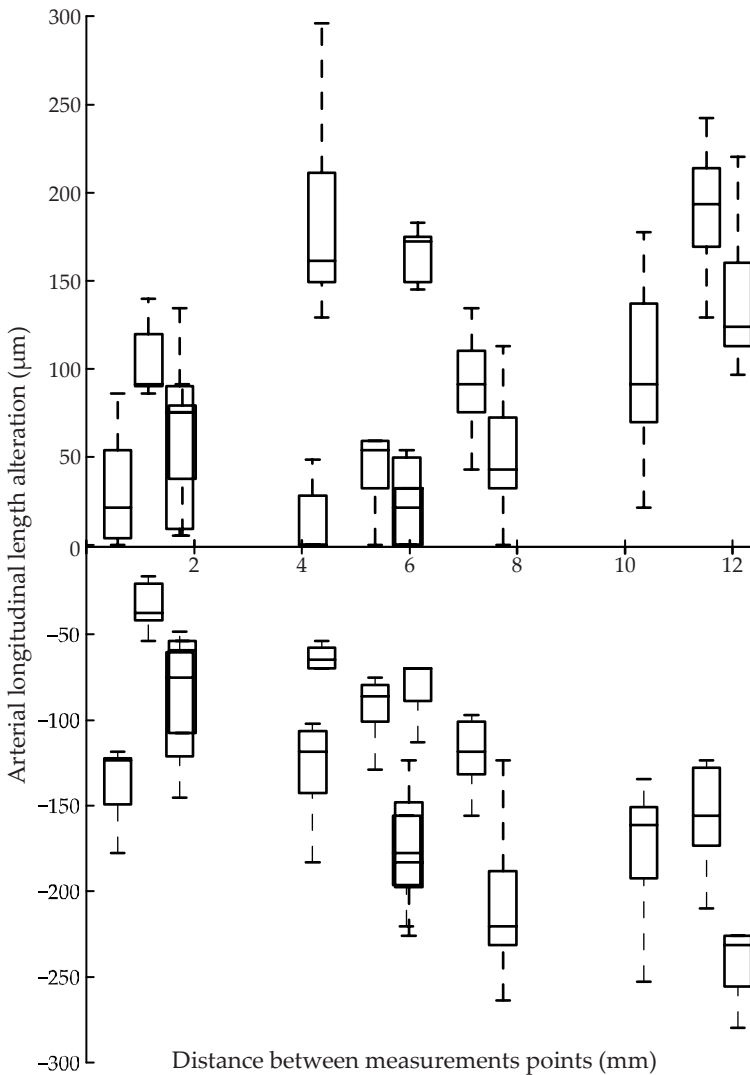
Figure 2. The maximum length expansion and length reduction versus the origin distance between measurement points at end-diastole. The boxes indicate the lower and upper quartiles and the median. The bar lines indicate the minimum and maximum values.

4.   CONCLUSIONS

This first *in vivo* study, using a new non-invasive ultrasonic measurement method to study the length alteration of the arterial wall, indicates that a significant length alteration is present in the common carotid artery during the cardiac cycle. Additional studies are needed to further explore this new phenomenon.

REFERENCES

1. W.W. Nichols and M.F. O'Rourke, *McDonald's Blood Flow in Arteries*, 4th ed. (Edward Arnold, London, 1998).
2. M. Persson, Å. Rydén Ahlgren, A. Eriksson, T. Jansson, H.W. Persson, and K. Lindström, *2002 IEEE Ultrason Sympo.* **2**, 1783 (2002).
3. M. Cinthio, Å. Rydén Ahlgren, T. Jansson, A. Eriksson, H.W. Persson, and K. Lindström, *IEEE Trans Ultrason Ferroelect Freq Contr.* **52** (8), 1300 (2005).
4. M. Cinthio, Å. Rydén Ahlgren, J. Bergkvist, T. Jansson, H. W. Persson, and K. Lindström, *Am J Physiol Heart Circ Physiol* **291**, H394 (2006).
5. P. Tozzi, D. Hayoz, C. Oedman, I. Mallabiabarrena, and L. K. von Segesser, *Am J Physiol Heart Circ Physiol* **280**, H2300 (2001).

EVALUATION OF TISSUE MOTION VECTOR MEASUREMENT SYSTEM UTILIZING SYNTHETIC-APERTURE ARRAY SIGNAL PROCESSING FOR REAL-TIME ELASTOGRAPHY

S. Yagi, A. Sanuga, K. Tamura, M. Sato

Graduate School of Information Science, Meisei University, Tokyo 198-8655, Japan; Medical System Engineering Department, Aloka Co. Ltd., Tokyo198-8577, Japan; R&D Department, Microsonic Co. Ltd., Tokyo113-0033, Japan

Abstract: Real-time elastography is a promising dynamic tool providing viscoelastic properties of living tissue in vivo by advanced evaluation of the spatio-temporal vector motion in tissue. This study experimentally verified the performance of our proposed measurement system for practical evaluation of two-dimensional motion vector dynamics followed by pulsed shear wave generation and its propagation across a phantom.

Key words: Real-time elastography, Synthetic aperture, Array signal processing, Virtual source generation, Spherical irradiation, Local phase difference, Cross-correlation, Successive echo frames

1.   INTRODUCTION

Quantitative real-time elastography, a dynamic version of static elastography, is a promising breakthrough for advanced diagnostic and therapeutic treatment in living soft tissue. The required key technologies were high-speed acquisition of successive echo frame data and a robust algorithm of distributed motion-vector evaluation. Our real-time imaging of shear-wave propagation across liver tissue in vivo caused by sequential

heartbeats [1,2,3] could be dynamically demonstrated by considering only beam-directional local tissue displacement at the same frame rate of ordinary B-mode imaging. To meet these requirements, our proposed measurement method [4,5] strategically combines multi-directional evaluation of local phase differences derived by shear-wave oriented change of local echo signal with Synthetic-Aperture (SA) array signal processing of successive echo frames. In addition, the irradiation and control of a spherical sound field for SA array signal processing are virtually realized by means of a point-focused beam forming using an appropriate aperture of the array transducer.

Numerical analysis [6] of our proposed measurement system experimentally verified the overall system performance for evaluating spatially distributed motion vectors in accuracy, variance and resolution by processing two static echo frames acquired from a slightly displaced tissue phantom that was free from inner strain. The dynamical changes of the spatio-temporal motion vector representing generation and traveling of a pulsed shear wave triggered by flushing water into an occluded rubber tube embedded in the phantom were clearly demonstrated by processing successive echo data acquired at 4000 fames/s when such data were synchronized with the alternate virtual source generation.

2.   EXPERIMENTAL SETUP

The combination of SA array signal processing coupled with directional virtual source generation and evaluation of local echo phase change using spatial cross-correlation between two successive echo frames is implemented through the practical system integration in the following experimental setup for two-dimensional motion vector evaluation.
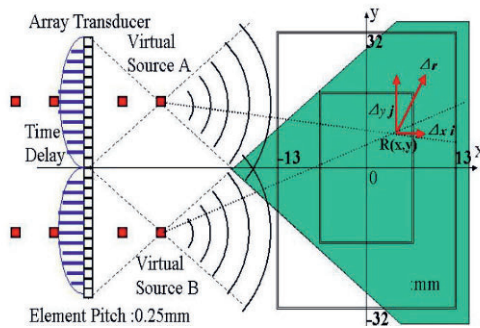
Figure 1. 2-Dimensional displacement vector measurement by means of alternate pulsed irradiation of two spherical virtual sources.

In order to calculate the components of a two-dimensional displacement vector, two directional sound fields must be alternately irradiated so as to overlap each other across the tissue medium. To practically realize these irradiated fields, two virtual sources of pulsed spherical waves are alternately generated by point-focused beam forming using the same array transducer for SA array signal processing, as shown in Fig. 1. For the experimental system setup, a customized linear array transducer having 256 elements with 0.25 mm lateral pitch and 13 mm elevational width is operated at a 3 MHz center frequency over a 2 MHz bandwidth. The program-controlled beam former can drive each transmission element individually with delayed bipolar pulses, and each receiving element is connected to an A-D converter (30 MHz, 12-bit) followed by a 256MB high-speed static memory, enabling over one minute of real-time data acquisition at a maximum rate of 1000 frames per second, when one frame is set to 256 channels of 4KB echo data. For further practical adoption, the orientations of two virtual sources are fixed to +/–16mm along the lateral (Y) coordinate and longitudinally adjusted to obtain the required overlapped area of their irradiation fields, in accordance with the numerical analysis of statistical variance in local vector evaluation [6], and with fixed elevational beam forming by an array transducer with a focal length of 50 mm in the X-Z plane.

3.   PHANTOM EXPERIMENTS

3.1   Static Motion Vector Evaluation

The integrated system performance was verified experimentally by determining the accuracy and spatial distribution of two-dimensional local displacement vectors across a tissue phantom. In this experiment, a 0.3-degree clockwise rotation of a 5% gelatin phantom including uniformly scattered starch particles is clearly visualized in each comparative gradient of the planar phase distribution across the overlapped irradiation area in the X-Y plane. These local phase evaluations are obtained by means of the ordinary cross-correlation method [4,5,6] between echo frames acquired before and after the phantom displacement, triggered by dual pulses of upper and lower virtual sources (A and B in Fig. 1). This phantom rotation demonstrates the smoothed distribution of the rotational motion vector around the center of rotation inside the overlapped area of alternate spherical irradiation (Fig. 2). The accurate distribution of evaluated rotational motion vectors can be clearly recognized in spite of the small movement of the phantom.
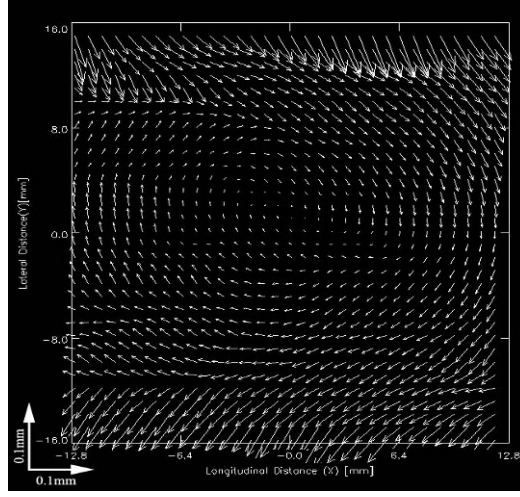
Figure 2. Distribution of experimentally obtained rotational vectors across a tissue phantom.

4.   DYNAMIC MOTION VECTOR EVALUATION

The advanced dynamic performance of the proposed measurement system was also experimentally verified by spatio-temporal motion vector imaging that successively demonstrates the generation and propagation of various pulsed shear waves across a tissue medium. In this experiment, shear waves were manually triggered by flushing water into a closed-end rubber tube 5 mm in diameter, which is embedded 50 mm from the array transducer in a tissue phantom and aligned perpendicular to the X-Y plane. The water injection is externally controlled by a syringe piston through a catheter tube connected to the rubber tube. The experimental phantom setup using an amorphophallus konjac block is depicted in the photograph of Fig. 3, and the details are schematically diagramed in Fig. 4. Two pairs of successive echo frames are used to evaluate two kinds of directional local phase differences and are sequentially nested inside one another by the two sets of alternate spherical irradiations from virtual sources A and B as illustrated in Fig. 4. Therefore, the two-directional phase differences are temporally interpolated to calculate the true motion vector.
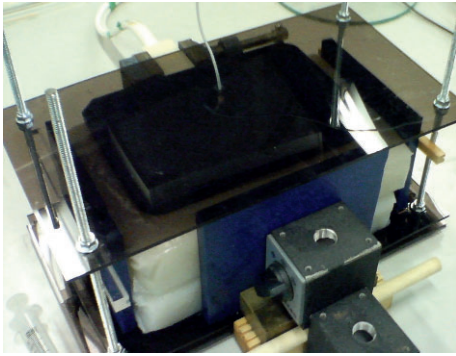
Figure 3. Tissue phantom for shear wave observation.
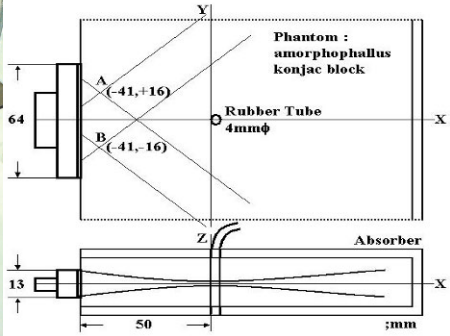
Figure 4. Phantom geometry.
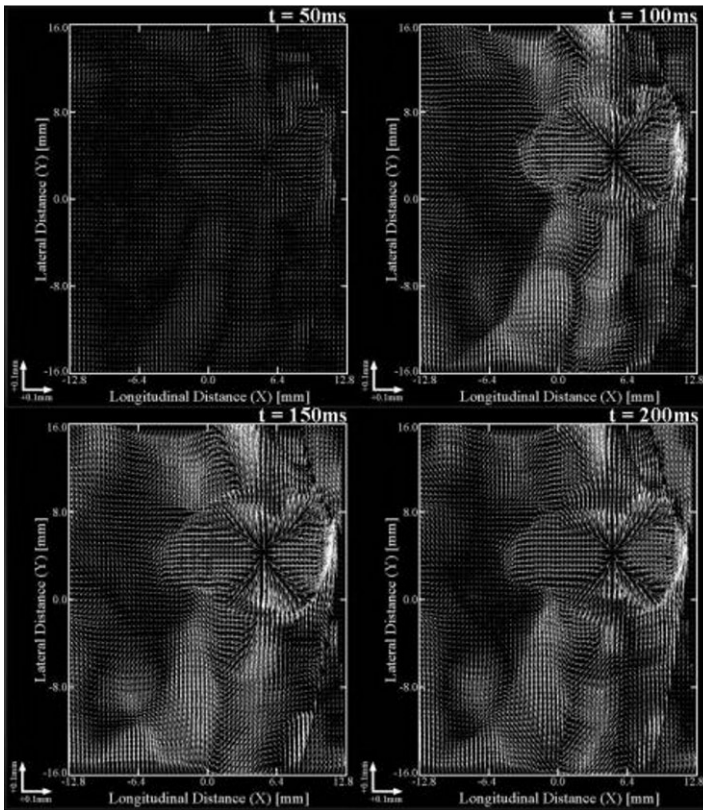
Figure 5. Dynamic motion of shear wave caused by pulsed dilatation of rubber tube at 50 ms Intervals.

Dynamic motion vectors calculated from successive echo data acquired at 4000 frames/s represent the generation and propagation of shear waves excited by pulsed dilatation of a rubber tube across a tissue phantom at 50 ms intervals in Fig. 5; each vector displacement during the 10 ms period is evaluated. The distributed local motion vector indicates the excellent spatial and temporal performance of the proposed measurement system.

5.   CONCLUSION

The proposed system integration for tissue local motion vector evaluation is a promising step toward ultrasonic real-time elastography as demonstrated by the revealed dynamic behavior of living tissue in vivo.

ACKNOWLEDGEMENTS

REFERENCES

1. H. Machida and S. Yagi: "Tissue Dynamic Imaging of Shear Wave Traveling across a Liver Tissue Stressed by Heart-beat Using Real-Time Displacement Tomography," Proc. Int. Conf. Acoust. 2004, pp. 907–908, 2004.
2. H. Machida, S. Yagi, Y. Kondo, Y. Murata and S. Akimoto: "Real-time monitoring of shear wave traveling in liver tissue in vivo," Jpn. J. Appl. Phys., vol. 42. no. 5B, 3241–3244, 2004.
3. S. Yagi, A. Sanuga, K. Kondo, K. Tamura and M. Sato: "Analysis of transient shear wave generation for real-time elastography," Proc. 2005 IEEE Ultrason. Symp., vol. 2, pp. 18–21, 2006.
4. S. Yagi and Y. Minochi: "High-precision real-time evaluation of tissue local motion vectors utilizing synthetic aperture array-signal processing," Proc. Int. Conf. Acoust. 2004, pp. 905–906, 2004.
5. Y. Minochi, S. Yagi and H. Nishiyama: "Estimation of local displacement vector in random medium utilizing synthetic aperture array signal processing," Jpn. J. Appl. Phys., vol. 42, no. 5B, pp. 3103–3106, 2004.
6. S. Yagi, A. Sanuga, T. Nishiyama, K. Tamura and M. Sato: "Evaluation of Tissue Motion Vector Distribution utilizing Synthetic Aperture Array-Signal Processing Triggered with Successive Virtual Source Generation," Proc. 2006 IEEE Ultrason. Symp., pp. 1205–1208, 2007.

ULTRASONIC IMAGING OF HEMODYNAMIC FORCE IN CAROTID BLOOD FLOW

N. Nitta, K. Homma

Institute for Human Science and Biomedecial Engineering, National Institute of Advanced Industrial Science and Technology (AIST), Tsukuba, 305-8564, Japan

Abstract: Hemodynamic forces including blood pressure and shear stress affect vulnerable plaque rupture in arteriosclerosis and biochemical activation of endothelium such as NO production. In this study, a method for estimating and imaging shear stress and pressure gradient distributions in blood vessel as the hemodynamic force based on viscosity estimation is presented. Feasibility of this method was investigated by applying to human carotid blood flow. Estimated results of shear stress and pressure gradient distributions coincide with the ideal distributions obtained by numerical simulation and flow-phantom experiment.

Key words: Hemodynamic force, Shear stress, Pressure gradient, Viscosity, Velocity vector, Navier-Stokes equations, Carotid blood flow.

1.   INTRODUCTION

Hemodynamic forces including blood pressure (or pressure gradient) and shear stress affect vulnerable plaque rupture in arteriosclerosis and biochemical activation of endothelium such as NO production. If these hemodynamic force distributions are estimated noninvasively, we can attain some useful information for prevention of vascular disease.

There are some methods for shear stress estimation. One is the computation-based method, which combines 3-D vascular reconstruction using X-ray CT, MRI, IVUS and CFD [1]. The other method is based on the measurement-based approach by MRI or ultrasound, in which the shear rate

is evaluated [2] or shear stress obtained by multiplying the shear rate by the predetermined viscosity measured by using blood sample [3]. On the other hand, a method for estimating the viscosity and pressure gradient have been proposed [4]. However, this method is based on 1-D problem using Stokes equation.

In this study, a novel method for estimating and imaging shear stress and pressure gradient distributions as hemodynamic force based on 2-D velocity vector distribution and viscosity estimations is presented. Feasibility of this method is investigated by applying to human carotid blood flow.

2.   METHOD

The method for estimating shear stress and pressure gradient in this study consists of three stages. First, 2-D velocity vector distribution is estimated by using Doppler-measured velocity component and incompressible condition. That is, lateral velocity component in 2-D velocity vector is obtained in this stage. Second, kinematic viscosity as viscosity is estimated by using the measured velocity vector distribution and Navier-Stokes equations. The kinematic viscosity is derived by differentiating 2-D Navier-Stokes equations with respect to spatial coordinates (x and y) and eliminating the pressure terms [5]. Therefore, kinematic viscosity is estimated by the only velocity vector distribution. Third, the shear stress and pressure gradient distributions are imaged. In this stage, shear stress is quantitatively estimated by velocity vector distribution, kinematic viscosity and Newton's law of viscosity [6]. Moreover, the pressure gradient is also quantitatively estimated by velocity vector distribution, kinematic viscosity and Navier-Stokes equations [7]. In this study, it is assumed that the density of blood is known and spatially-homogeneous.

3.   THEORETICAL FLOW ANALYSIS

Figure 1 shows the results of theoretical flow analysis in a duct with a step simulating an arteriosclerosis plaque. The kinematic viscosity is estimated by the only velocity vector components as shown in Fig. 1(a) and (b). Figure 1(c) shows the estimated kinematic viscosity in changing the true kinematic viscosity, and validates the feasibility of this method. Figure 1(d) to (g) show the shear stress and pressure gradient distribution in changing viscosity under the constant flow rate, and indicate the necessity of viscosity estimation because the magnitude of both shear stress and pressure gradient change due to viscosity.

(a) *x* component

(b) *y* component

(c) estimated kinematic viscosity

(d) Shear stress at 1.5 mm^2/s

(e) Shear stress at 5.0 mm^2/s

(f) Pressure gradient
at 1.5 mm^2/s

(g) Pressure gradient
at 5.0 mm^2/s
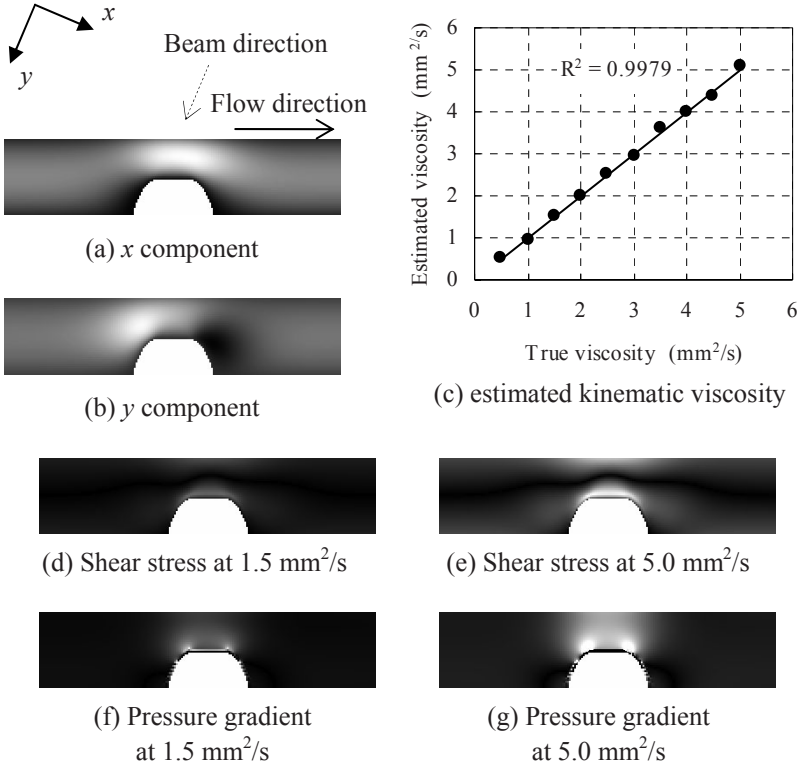
Figure 1. Shear stress and pressure gradient in changing viscosity
(simulation).

4. EXPERIMENT

Figure 2 shows the experimental results. Two types of fluid with scatterer were flowed at constant flow rate in a silicone tube with a step, in which one is water and another is water mixed by PVA. Fluid viscosity increases by mixing PVA. Figure 2(a) and (b) show the example of velocity vector components in water. Figure 2(c) shows the estimated kinematic viscosity in water and water mixed by PVA, based on the only velocity vector. These estimated values are significantly-distinguishable. Moreover, these estimated values coincided with the measured kinematic viscosity values by viscometer (water: 1.5 mm^2/s, water mixed by PVA: 6.4 mm^2/s). Figure 2(d)

to (g) show the shear stress and pressure gradient distribution in both fluids. The magnitude changes of shear stress and pressure gradient due to viscosity changes are reasonably observed by this method.
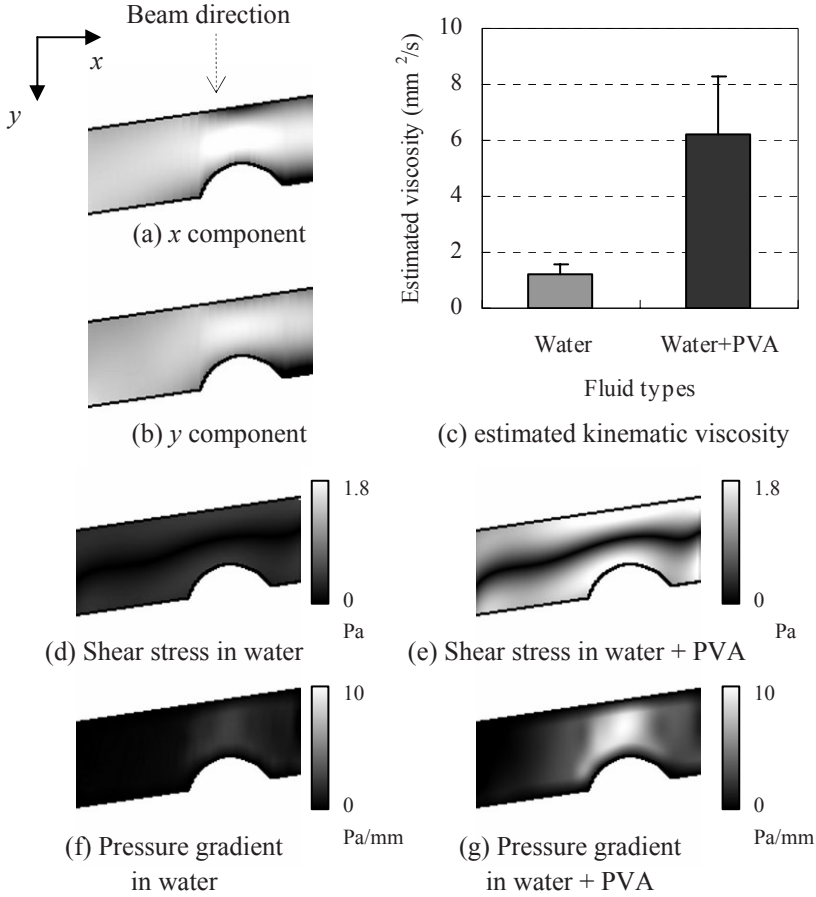
Figure 2. Shear stress and pressure gradient in changing viscosity (experiment).

5.   HEMODYNAMIC FORCE IMAGING IN CAROTID

Figure 3 shows the examples of shear stress and pressure gradient images at bifurcation part of carotid. A step-like structure is observed in Fig. 3(a) (arrowed line), as shown in the previous simulation and experiment. In

Fig. 3(b) and (c), both shear stress and pressure gradient around the step-like structure (arrowed line) are bigger than those in other areas.

Figure 3(d) and (e) show the profiles of shear stress and pressure gradient at each point of A, B and C. These profiles are normalized by mean values at the center point of the lumen (C in Fig. 3(a)) for comparison. Although these profiles exhibit cyclic patterns because of pulsation and non-Newtonian property of blood, both shear stress and pressure gradient become the biggest in the narrow lumen (A), second biggest in the wide lumen (B), and the smallest in the center (C). These tendencies coincide with the results of simulation and experiment.

(a) B mode   (b) Shear stress   (c) Pressure gradient

(d) Shear stress profiles   (e) Pressure gradient profiles
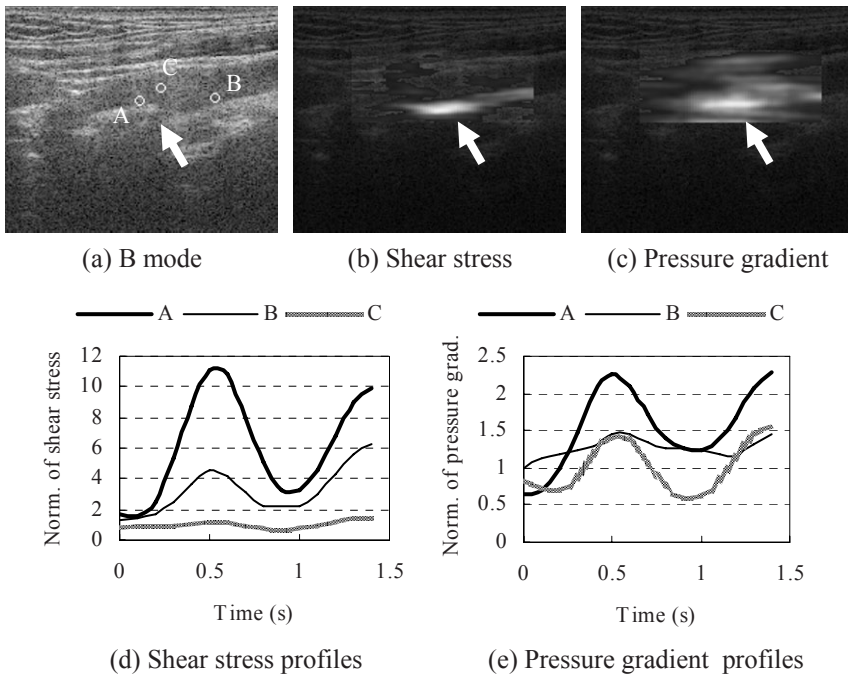
Figure 3. Shear stress and pressure gradient images at bifurcation part of carotid.

Figure 4 shows the examples of shear stress and pressure gradient images at straight part of carotid. While clear shear stress pattern is observed near posterior wall as indicated by arrowed line in Fig. 4(b), pressure gradient image does not exhibit significant pattern in Fig. 4(c). There might be little spatially-difference of pressure gradient in this case because the target is the straight part of carotid and has no stenosis.

Again, Fig. 4(d) and (e) show the profiles of shear stress and pressure gradient at each point of A, B and C. Near the wall of A and B, the same

levels of shear stress and pressure gradient were observed and these values are bigger than the value of the center C. These results are theoretically reasonable.

(a) B mode   (b) Shear stress   (c) Pressure gradient

(d) Shear stress profiles   (e) Pressure gradient profiles
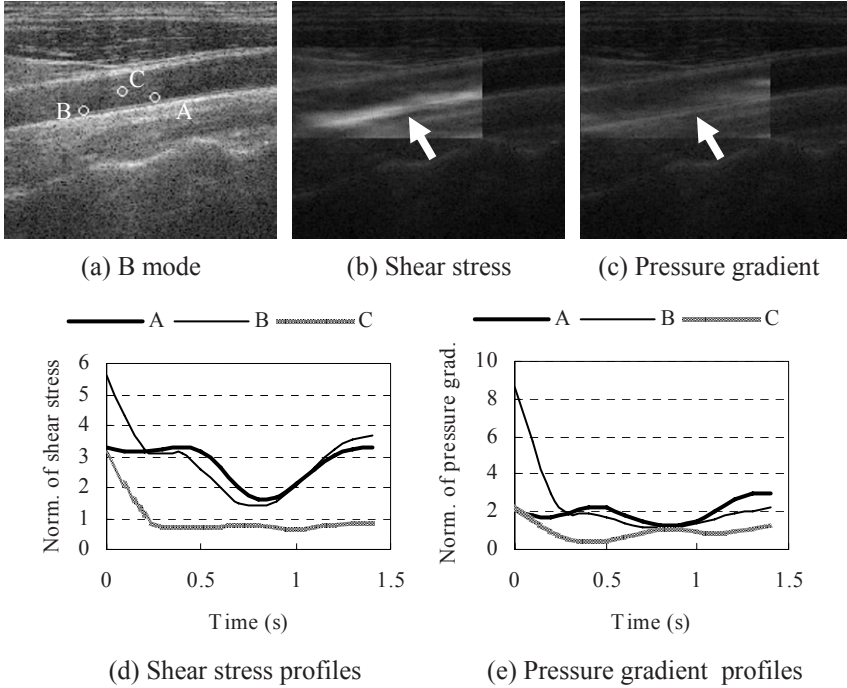
Figure 4. Shear stress and pressure gradient images at straight part of carotid.

6.   CONCLUSION

A method for estimating and imaging hemodynamic force was presented. Shear stress and pressure gradient imaging for carotid blood flow revealed the feasibility of this method. However, in both cases of carotid blood flow, shear stresses near the anterior wall were not appeared clearly. In future works, we are going to overcome this problem, improve the accuracy of estimation and establish clinical usefulness.

REFERENCES

1. R. Krams, J.J. Wentzel, J.A. Oomen: Arterioscler Thromb Vasc Biol. 17 (10): 2061–2065, 1997.
2. G. Bambi, T. Morganti, S. Ricci, F. Guidi, P. Tortoli: Proc. of 2004 IEEE Int Ultrason Symp. 592–595, 2004.
3. S.P. Wu, S. Ringgarrd, E.M. Pedersen: Mag Res Imag. 22 (3): 345–351, 2004.
4. C. C-Bacrie: Proc. of 1999 IEEE Int Ultrason Symp. 1489–1492, 1999.
5. N. Nitta, K. Homma: Jpn. J. Appl. Phys. 44 (2005) 4602.
6. N. Nitta, K. Homma: Trans. Jpn. Soc. Med. Biol. 44 (2006) 190.
7. N. Nitta, K. Homma, T. Shiina: Jpn. J. Appl. Phys. 45 (2006) 4740.

INCREASING ACCURACY OF TISSUE SHEAR MODULUS RECONSTRUCTION USING ULTRASONIC STRAIN TENSOR MEASUREMENT

Lateral Modulation and Regularization

C. Sumi

Faculty of Science and Technology, Sophia University, Tokyo, Japan

Abstract: Previously, we developed three displacement vector measurement methods, i.e., the multidimensional cross-spectrum phase gradient method (MCSPGM), the multidimensional autocorrelation method (MAM), and the multidimensional Doppler method (MDM). To increase the accuracies and stabilities of lateral and elevational displacement measurements, we also developed *spatially variant, displacement component-dependent regularization*. In particular, the regularization of only the lateral/elevational displacements is advantageous for the lateral unmodulated case. The demonstrated measurements of the displacement vector distributions in experiments using an inhomogeneous shear modulus agar phantom confirm that displacement-component-dependent regularization enables more stable shear modulus reconstruction. In this report, we also review our developed lateral modulation methods that use Parabolic functions, Hanning windows, and Gaussian functions in the apodization function and the optimized apodization function that realizes the designed point spread function (PSF). The modulations significantly increase the accuracy of the strain tensor measurement and shear modulus reconstruction (demonstrated using an agar phantom).

Key words: Shear modulus reconstruction, Displacement vector measurement, Strain tensor measurement, MAM, MDM, MCSPGM, Spatially variant regularization, Displacement-component-dependent regularization, Lateral modulation, Agar phantom

1.   INTRODUCTION

It is remarkable that the pathological state of human soft tissues highly correlates with their static and low-frequency mechanical properties, particularly, shear elasticity [1]. Many researchers, including us, have thus been developing strain or displacement-measurement-based shear modulus reconstruction methods [1] and using various ultrasonic strain or displacement measurement methods [e.g., Doppler method, autocorrelation method, cross-correlation method, sum-squared difference (SSD) method, multidimensional cross-spectrum phase gradient method (MCSPGM) [2,3], multidimensional autocorrelation method (MAM) [4,5], and multidimensional Doppler method (MDM) [4,5]].

In our case, we have been developing 1D, 2D and 3D shear modulus reconstruction techniques [4,6] as diagnostic tools for various in vivo tissues, e.g., breast and liver. In the 1D [7], 2D and 3D techniques, 1D, 2D and 3D models are used together with the 1D axial strain field, and the 2D and 3D strain tensor fields obtained by differentiating the measured 1D axial displacement field, and the 2D and 3D displacement vector fields (i.e., generated by extracorporeally applied pressure or vibration, or spontaneous heart motion). For such in vivo tissues [6], we confirmed that a suitable combination of simple, minimally invasive therapy techniques (e.g., chemotherapy, cryotherapy, and thermal therapy) with our shear modulus reconstruction techniques are expected to lead to an innovative, new clinical technique that will enable differential diagnosis followed by immediate treatment so that overall medical expenses will be substantially reduced. Furthermore, we have also proposed methods of reconstructing density and dealing with dynamic deformation generated by vibration or heart motion, although a typical density might be used (nearly 1.0×10^3 kg/m^3) [4]. In conjunction with this, we have also reported on visco-shear modulus reconstruction [4].

Here, we report our two developed methods for increasing the accuracy and stability of the strain-measurement-based shear modulus reconstruction, i.e., lateral modulation of echo data and spatially variant regularization.

2.   SHEAR MODULUS RECONSTRCUTION
METHODS

We have reported shear modulus reconstruction Method F [1,6] and Methods B[4] and C [4,8]. Method F requires a typical Poisson's ratio [6], whereas in Method C, the mean normal stress and Poisson's ratio remain unknown [4,8].

Like the 3D method, the 2D Method F using a 2D stress assumption yields accurate shear modulus reconstruction values. This 2D method is very useful because it enables the use of conventional 2D ultrasonic imaging equipment by employing displacement regularization as described later. Proper configurations of the reference shear modulus region (i.e., initial condition) and mechanical sources should be realized such that reference regions extend widely in the direction crossing the predominant tissue deformation. The relative shear modulus distribution is reconstructed by using a quasi-reference shear modulus (e.g., unity).

However, we proposed three novel methods, Methods A to C, that deal with the mean normal stress p approximated by the product of λ and the volume strain $\varepsilon_{\alpha\alpha}$ as an unknown [4,8] as reported by Plewes et al. [9] because reconstruction errors have also been confirmed to be due to the difference between the original value of the Poisson's ratio ν and the set value.

It is almost impossible for in vivo applications to realize the boundary conditions required by Plewes et al. [9] (i.e., shear modulus and mean normal stress) in Method C [4,8] that uses FDM. However, by using a quasi-reference point (Method C1) or a quasi-reference region (Method C2) of the mean normal stress p (an arbitrary finite value, e.g., zero) and the reference shear modulus μ (not the boundary condition but the initial condition as in Method F), only μ is reconstructed while p remains unknown (neither p nor ν is reconstructed). Thus, Method C enables us to deal with arbitrary soft tissues, including completely incompressible tissues (physically, complete incompressibility is impossible), nearly compressible tissues or compressible tissues, and tissues having an inhomogeneous Poisson's ratio. We can thus set the quasi-reference mean normal stress point *at an arbitrary point* in the ROI regardless of the mechanical source [8]. Solutions obtainable by iteration (e.g., the conjugate gradient method) require more iterations to obtain convergence because Method A, which also yields only shear modulus reconstruction, uses no reference p.

Method B[4] that uses FDM or FEM can be applied when using reference p as the initial condition (e.g., using a homogeneous reference material of μ and ν together with the measured volume strain). The mean normal stress p is thus reconstructed together with the shear modulus μ and the density ρ. If the tissues are compressible, Poisson's ratio ν can also be obtained. When using FEM, the sinc function can also used as a basis function.

Tables 1 and 2 present the uses of the references of μ, p and ρ for Methods A-C and F in static and dynamic deformation cases. Methods D uses neither reference of μ nor ρ, but Method E uses quasi-references of μ or ρ. Both Methods D and E yield relative reconstructions with no

geometrical artifact (however, the absolute values obtained are dependent on the initial estimates of the iterative solution or the quasi-reference values). Thus, both are effective, particularly for deeply situated tissues.

Table 1. For static deformation case, the setting of references for methods A-E of shear modulus and mean normal stress p. U, use; -, no use; Q, quasi-reference is used. Bracket in the case where the use in FEM is different from that in FDM.

Method	p	μ	E (μ)
A, F	-	U	Q
B	U	U	Q [-]
C	Q	U [-]	Q [-]
D	-	-	Q
	U	-	Q [-]
	Q	-	Q [-]

Legend
U   Use
-       No use
Q   Quasi-reference is used.

Table 2. For dynamic deformation case, the setting of references. See captions of Table 1.

Method	P	ρ	μ	E (ρ or μ)
A, F	-	-	U	Q [only μ]
B	U	-	U	Q [-]
C	Q	-	U [-]	Q [-]
A, F	-	U	-	Q [only ρ]
B	U	U	-	Q [-]
C	Q	U [-]	-	Q [-]
A, F	-	U	U	-
B	U	U	U	-
C	Q	U [-]	U[-]	-
D	-	-	-	Q
	U	-	-	Q [-]
	Q	-	-	Q [-]

3.   DISPLACEMENT VECTOR AND STRAIN TENSOR MEASUREMENTS – LATERAL MODULATIONS

We also developed the (multidimensional) rf-echo phase matching method [2,3,5,10], the lateral Gaussian envelope cosine modulation method (LGECMM) [4,5,11,12], and the multidirectional synthetic aperture method (MDSAM) [4,5,12] to increase the measurement accuracy of the displacement vector, particularly the accuracies of the lateral and elevational

displacement components, which are much less accurate than the axial displacement component due to inevitable contamination in echo data. The rf-echo phase-matching method [10] also enables freehand strain measurements (e.g., breast including large displacement) as well as coping with tissue lateral motion (e.g., liver motion). However, the rf-echo phase matching method alone cannot yield adequately accurate lateral and elevational displacement measurements. In conjunction with the use of MDSAM and LGECMM, the 2D and 3D techniques also require special 2D and 3D ultrasound (US) data acquisition systems [4–6].

LGECMM yields more accurate displacement vector measurement than MDSAM, as confirmed in references [5,12] by simulations and geometrical evaluations. The spectra are not band-limited when using Jensen's modulation method [13], i.e., ringing-expressed by sinc functions and cause aliasing. We have reported that LGECMM [11,4,5,12] can be used to realize band-limited, modulated spectra. If lateral modulation is performed during ultrasonic transmission as well, LGECMM can be applied more easily (i.e., electric voltage can be easily weighted using Gaussian functions). For our tissue shear modulus reconstruction, the modulation frequency of LGECMM is significantly increased compared with that in the reported application of lateral modulation to blood-flow measurement. Thus, conventional spherical focusing was used instead of axicon focusing. Moreover, we introduced compensation parameters because the designed lateral modulation frequency and lateral bandwidth cannot be realized due to the inappropriateness of Fraunhofer approximation [5]. However, for practical modulation, the transmitting apodization can by realized only by a classical synthetic aperture (SA, hereafter referred to as Method 1) or multiple transmitting modulations in the axial direction as a multiple transmitting focus. The use of plural simultaneously or successively transmitted crossed plane waves (Method 2) or scanned beams (Method 3) [5] will also be advantageous because such a classical SA is not robust against rapid tissue motion due to the weakness of the US transmitted from one element. If necessary, separate plural transducers will also be used (e.g., for heart). Reference [14] reports the 2D shear modulus reconstructions obtained on an agar phantom using LGECMM together with MCSPGM, MAM and MDM. Accurate reconstruction values of a stiff inclusion were obtained. Moreover, the same order of measurement accuracy of MCSPGM, MAM and MDM confirmed by simulations [4] was also obtained in the reconstructions, i.e., for a high-echo SNR, MAM and MCSPGM > MDM.

We also succeeded in breaking away from the Fraunhofer approximation by using parabolic functions (parabolic modulation method (PAM)) and Hanning windows (Hanning modulation method (HAM)) instead of Gaussian functions in the apodization function. [15,16] The uses of PAM and HAM enabled decreasing the effective

aperture size and increasing the echo SNR and lateral bandwidth without resulting in ringing in the spectra. For instance, Fig. 1 [16] depicts an agar phantom having a stiff circular cylindrical inclusion (relative shear modulus of the inclusion to that of the surrounding region, 3.29) that
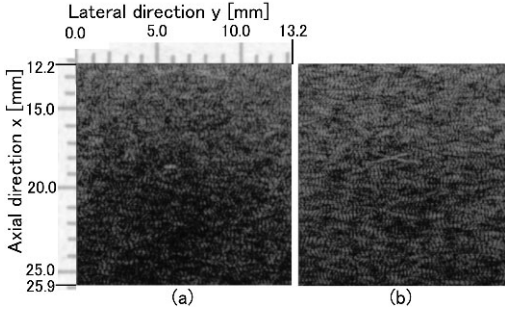
Figure 1. B-mode images (square detection) obtained on agar phantom using PAM (modulation freq., 3.75 MHz) with Methods (**a**) 1 and (**b**) 2. US freq. 7.5 MHz.
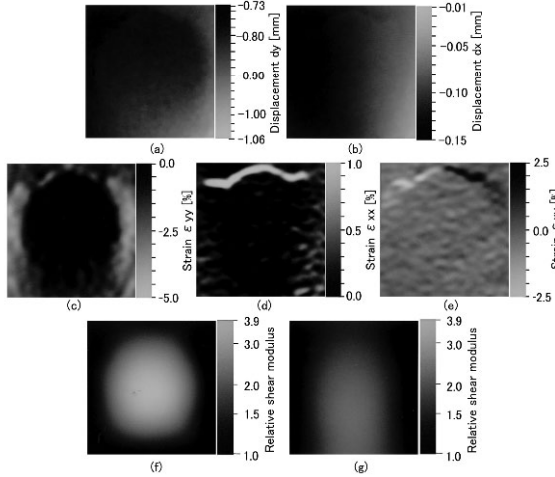
Figure 2. Agar phantom experiments using PAM with Method 1 (Fig. 1a, modulation freq., 3.75 MHz), MAM and Method F (2D stress assumption). (**a**) lateral and (**b**) axial displacements, (**c**) lateral, (**d**) axial and (**e**) shear strains, and (**f**) 2D and (**g**) lateral 1D (i.e., only using lateral strain) shear modulus reconstructions.

was compressed in a lateral direction [17], B-mode images (square detection) obtained using PAM with Methods (a) 1 and (b) 2 (modulation freq., 3.75 MHz vs US freq., 7.5 MHz). Figure 2 presents the measured (a) lateral and (b) axial

displacements [linear gray-scale images], (c) lateral, (d) axial and (e) shear strains [linear gray-scale images], and (f) 2D and lateral 1D shear modulus reconstructions [log gray-scale images] using the modulated echo data (1a), MAM and Method F under a 2D stress assumption. Table 3 lists their means and standard deviations (SDs) [central 5 mm side square region] obtained

Table 3. Means and SDs obtained on agar phantom experiments (see Figs. 1 and 2). SDs are in parentheses.

Method and modulation freq.	Strains			Shear moduli	
	Lateral	Axial	Shear	2D	1D
PAM –Method 1,	−0.20	0.01	0.07	3.28	1.95
3.75 MHz	(0.28)	(0.10)	(0.22)	(0.35)	(0.12)
	−0.27	0.05	0.06	–	–
7.5 MHz	(0.22)	(0.16)	(0.20)		
–Method 2,	−0.20	0.005	0.01	2.34	1.45
3.75 MHz	(0.72)	(0.28)	(0.66)	(0.18)	(0.05)
	−0.35	0.16	−0.05	–	–
7.5 MHz	(1.89)	(1.04)	(1.17)		
-Only at receiving,	−2.93	−0.28	−0.83	–	–
3.75 MHz	(5.72)	(2.14)	(4.64)		
LGECMM –Method 1	−0.22	0.01	0.06	3.14	1.85
3.75 MHz	(0.34)	(0.13)	(0.24)	(0.32)	(0.13)
	−0.26	0.08	0.06	–	–
7.5 MHz	(1.29)	(0.72)	(1.00)		
–Method 2	−0.21	0.002	0.03	2.60	1.94
3.75 MHz	(0.50)	(0.21)	(0.44)	(0.22)	(0.12)
	−0.34	0.13	−0.02	–	–
7.5 MHz	(1.59)	(0.96)	(1.02)		
-Only at receiving,	−2.06	−0.08	−0.37	–	–
3.75 MHz	(4.13)	(1.56)	(3.25)		
Unmodulated	−0.82	0.24	−0.03	–	–
	(0.24)	(0.12)	(0.22)		

using PAM and LGECMM with Methods 1 and 2 for the phantom. Note that the measurements and reconstructions obtained using Method 2 are less stable and less accurate than those using Method 1. The use of a current real-time beam former will improve the stabilities and accuracies owing to increased echo signal-to-noise ratio (SNR) because all the data were obtained using a monostatic SA. This will be reported elsewhere including the uses of a multistatic SA, multiple transmitting modulations and Method 3.

In order to measure displacement more accurately, we propose to determine an apodization function that realizes the designed point spread function (PSF) and spectra by optimization [15,16,18,19]. Weighted least squares estimation, singular value decomposition (SVD), and regularization are performed using a beam property of a US element obtained by a field

calculation. Such a beam property can also be obtained experimentally. Thus, the beam-forming parameters such as a US pulse shape and US element material and size can also be optimized. Figure 3 presents the apodization function estimated by such a field calculation for a designed 2D (x,y) Gaussian envelope PSF having the standard deviations $\sigma_x = \sigma_y = 0.8$ mm, US speed 1,500 m/s, US frequency 3.5 MHz, and modulation frequency $1/\lambda$ mm^{-1} (a preliminary result) [18]. The modeled linear transducer has an element width, an element height of 5.0 mm, and a distance between elements of 0.1 mm. From the viewpoint of echo SNR and spatial resolution, the concept can also be used for so-called US imaging [15,16,18,19], although even the B-mode image (Fig. 1a) obtained using PAM and Method 1 may be useful.
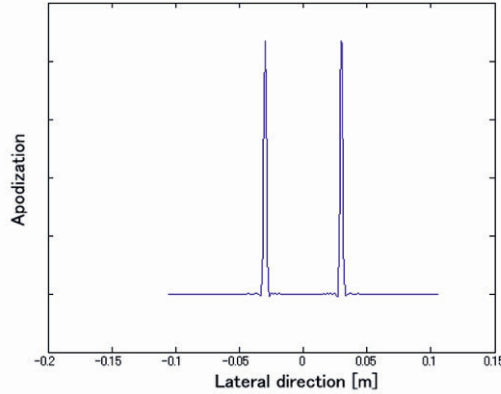
Figure 3. Estimated apodization function using SVD.

4. REGULARIZATION OF DISPLACEMENT VECTOR MEASUREMENT/SHEAR MODULUS RECONSTRCUTION

In addition, we previously reported the effectiveness of regularization for stabilizing displacement vector (strain tensor) measurement [12,20–23], particularly when not using special US systems, i.e., for decreasing the measurement instability due to contamination in echo data and tissue deformation and that of the shear modulus reconstruction [4,6,20–22,24]. Such regularization enables the incorporation of a priori knowledge that the

targets are spatially smooth. Regularization increases the accuracies of the measurement and reconstruction, and yields useful, unique results because the target distributions are those of low-frequency deformations and mechanical properties.

We proposed to properly set the regularization parameters for the regularization of the displacement measurement and the shear modulus reconstruction at each position (i.e., spatially variant regularization parameters) [4,6,20–22] because the measurement accuracies of the displacements and strains vary spatially. The regularization parameters were preliminarily set proportional to the reciprocal of the power of the correlation coefficient [20,21] because the measurement accuracies of the strains can also be evaluated using the correlation coefficient obtained after phase matching. We further proposed more effective methods of setting the regularization parameters for measurement and reconstruction, i.e., methods using the variances [20,22–24,12] of the displacement vector component and strain tensor component measurements. The variances [20,22,4] of the displacements and strains can be experimentally evaluated using plural field measurements or a single field measurement (e.g., when using the cross-correlation method, by using the Ziv-Zakai Lower Bound (ZZLB) and the coefficients of the differential filter used for the partial derivatives of displacements). Thus, the different regularization parameters are used for the displacement components (displacement-component-dependent regularization) [20,21,23,12].

Table 4. CNRs of 2D shear modulus reconstructions obtained on an agar phantom and mean shear moduli evaluated in the inclusion.

Strain Method	Nonregularized F (stress)	MA F (stress)	Regularized F (stress)	F (strain)	C
CNR	23.8	169.3	179.6	18.6	37.8
Mean	1.24	1.21	1.25	1.23	1.52

(a) (b) (c)
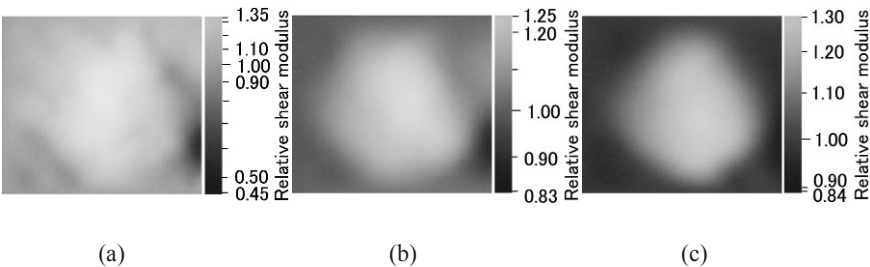
Figure 4. Shear modulus reconstructions obtained on agar phantom by Method F under a 2D stress assumption using (**a**) nonregularized, (**b**) moving-averaged and (**c**) properly regularized lateral displacements.

The 2D shear modulus reconstructions are obtained on an agar phantom having a stiff circular cylindrical inclusion (relative shear modulus, 2.06) from unmodulated echo data using MAM and Method F (2D stress assumption). Figure 4 presents log gray-scale images of the reconstructions obtained using (a) nonregularized, (b) moving-averaged and (c) properly regularized lateral displacements. Table 4 lists the contrast-to-noise ratios (CNRs) of the reconstructions and mean reconstructed shear moduli of the inclusion together with those obtained by Method F under a 2D strain assumption and Method C. As shown, the combination of the displacement-component-dependent regularization and Method F enabled more stable shear modulus reconstruction, although smoothing made the mean shear modulus of the inclusion inaccurate. Method F under a 2D strain assumption and Method C were not so effective for 2D reconstructions as confirmed by simulations [4,6].

REFERENCES

1. Sumi C. *et al.* 1995 *IEEE Trans. on BME* 42:193–202.
2. Sumi C. *et al.* 1995 *IEICE Trans. on Fundamental* E78-A: 1655–1664.
3. Sumi C. 1999 IEEE *Trans. on UFFC* 46:158–166.
4. Sumi C. 2006 *IEEE Trans. on UFFC* 53:2416–2434.
5. Sumi C. Displacement vector measurement using instantaneous ultrasound signal phase 2008 *IEEE Trans. on UFFC* 55:24–43.
6. Sumi C. 2005 *IEEE Trans. on UFFC* 52:1670–1689.
7. Sumi C., Matsuzawa H. Shear modulus reconstruction by ultrasonically measured strain ratio 2007 *J. Med. Ultrason.* 34:171–188.
8. Sumi C. Effective shear modulus reconstruction obtained with approximate mean normal stress remaining unknown 2007 *IEEE Trans. on UFFC* 54:2394–2402.
9. Plewes D. B. *et al.* 2000 *Phys. Med. Biol.* 45:1591–1610.
10. Sumi C. *et al.* 1995 *J. Med. Ultrason* 22(suppl I):44 (in Japanese).
11. Sumi C. Improvement of measurement accuracy of displacement vector by lateral modulation *Proc. of 2004 Autumn Meeting of Acoust. Soc. Jpn.* 1353–1354 (in Japanese).
12. Sumi C. *et al.* 2006 *5th Int. Conf. Ultrason. Meas. Imag. Tissue Elasticity* p. 30.
13. Jensen J. A. 1998 *IEEE Trans. on UFFC* 45:837–851.
14. Sumi C. Shear modulus reconstruction by strain tensor measurement using lateral modulation *Acoust. Sci. Tech.* (in press).
15. Sumi C. *et al.* Lateral Gaussian envelope cosine modulation method (LGECMM) (4th report) – A breakaway from Fraunhofer approximation *Proc. of 2006 Autumn Meeting of Acoust. Soc. of Jpn.* 1035–1036 (in Japanese).
16. Sumi C. *et al.* Effective lateral modulations with applications to shear modulus reconstruction using displacement vector measurement *IEEE Trans. on UFFC* (in press).

17. Sumi C. Ultrasonic axial strain measurement for lateral tissue deformation 2007 *Ultrasound in Med. Biol.* 33:1830–1837.
18. Sumi C. A case of apodization function using singular value decomposition: Determination of beamforming parameters by optimization 2008 *Acoust. Sci. Tech.* 29:185–187.
19. Sumi C. Beamforming for realizing designed point spread function 2007 *IEEE Int. Ultrason. symp.* 1557–1562.
20. Sumi C. Regularization for strain measurement and shear modulus reconstruction 2005 *4th Int. Conf. Ultrason. Meas. Imag. Tissue Elasticity* p. 114.
21. Sumi C. Spatially variant regularization for tissue strain measurement and shear modulus reconstruction 2007 *J. Med. Ultrason.* 34:125–131.
22. Sumi C., Sato K. 2007 *Acoust. Sci. Tech.* 28:352–356.
23. Sumi C., Sato K. Regularization for ultrasonic measurements of tissue displacement vector and strain tensor 2008 *IEEE Trans. on UFFC* 55:787–799.
24. Sumi C., Sato K. Regularization of tissue shear modulus reconstruction using strain variance 2008 *IEEE Trans. on UFFC* 55:297–307.

BIOLOGICAL AND MEDICAL APPLICATION

PRE-CLINICAL EXPERIENCE WITH FULL-WAVE INVERSE-SCATTERING FOR BREAST IMAGING
Sound Speed Sensitivity

M.P. André, C.H. Barker, N. Sekhon, J. Wiskin, D. Borup, K. Callahan

Dept. of Radiology, San Diego VA Healthcare System, 3350 La Jolla Village Dr., San Diego, California 92161, USA, Dept. of Radiology (9114), University of California, San Diego, California 92093, USA, Techniscan Medical Systems, Inc., 1011 Murray Holladay Rd., Salt Lake City, Utah 84117, USA

Abstract: A new transmission ultrasound CT breast scanner (Techniscan Medical Systems, Inc.) was installed for pre-clinical testing at UCSD Medical Center. The scanner utilizes a 3D inverse scattering method to produce whole-breast tomographic images with resolution approximately 1.5 mm in plane, 3.5 mm slice profile and slice spacing of 1 mm. Sound speed accuracy and sensitivity were found to be highly linear (R^2=0.99) over the wide range of 1370–1620 m/sec. Attenuation provided a wide image contrast and is able to localize and identify breast lesions. We present representative cases of human subjects enrolled in the pre-clinical study and describe future plans for the system.

Key words: Breast ultrasound, Ultrasound CT, Speed of sound, Attenuation, Inverse scattering

1.   INTRODUCTION

Conventional breast sonography is a notoriously challenging exam to perform. Quality of the results is highly dependent on the skill of the operator, the nature of the patient's breast tissue as well as technical features of the scanner. In order to obtain high resolution the field of view is very small, which complicates interpretation and localization of a mass. Laboratory and in vivo measurements have suggested that normal breast

tissue, benign lesions and cancerous lesions may be identified by their acoustic properties (particularly sound speed and attenuation).

Over the past 20 or more years transmission ultrasound computed tomographic (USCT) imaging of the breast has been applied to this problem by several researchers with varying degrees of success [1–4]. In general, these methods used two-dimensional linearization techniques to solve what is inherently a non-linear and three-dimensional problem. It is now clear that the range of tissue properties encountered in the breast is sufficiently large that linear approximations lead to severe artifacts and inadequate spatial resolution.

Figure 1. TMS USCT scanner.

Until recently the engineering technology and mathematical methods for full-wave inverse-scattering 3D tomography have been so complex that practical results in humans were not realized. Techniscan Medical Systems (TMS), Inc. (Salt Lake City, Utah), has developed a scanner (Fig. 1) for breast imaging that uses a multi-frequency non-linear 3D inverse-scattering algorithm [5,6].

The TMS system was installed at the University of California, San Diego (UCSD) to study clinical feasibility of using Ultrasound CT (USCT) to evaluate and detect breast masses. Performance of this pre-clinical prototype system especially with respect to sound speed measurements was examined for this report.

2.   METHODS

The TMS scanner is an automated system that performs a standardized scan of the whole breast nearly independent of operator expertise. Furthermore,

the images present a global view of both breasts in 3D. The patient lies prone with her breast pendant in a controlled 31°C water bath within the field of view of a transmitter and receiver array that rotate around 360° to collect 180 tomographic views of ultrasound wave data. The transmitter emits broad-band plane pulses (0.3–2 MHz) while the receiver array, comprised of 960 elements in 6 vertical rows, digitizes the time signal. A full data set consists of 50 or more overlapping levels of data, depending on breast size, are acquired 2 mm apart. An algorithm is utilized that simulates wave propagation in 3D and inverts for a fully 3D representation of sound speed and attenuation [6]. Unlike a 2D algorithm where one level of transmitted data is used, in the 3D inversion all levels of data are simultaneously inverted by the algorithm that propagates simulated 3D waves in a computational grid that extends above and below the data levels approximately 37 mm. The resulting image consists of voxels that are 0.8 mm by 0.8 mm in the horizontal, and 1 mm in the vertical direction.

The accuracy of sound speed measurements by USCT were tested with phantoms of known composition including solutions of CaCl, various oils and tissue-mimicking materials (CIRS, Waltham, MA). Solutions of CaCl ranging from 0.0 to 37.5% wt/vol, dilutions of isopropyl alcohol and various mineral oils were prepared in the laboratory to provide a range of sound speeds from 1370 ± 2.1 to 1620 ± 6.0 m/sec at 31°C. The materials were suspended in the USCT scanner water tank in thin-walled round 300 ml latex rubber containers and imaged at 31°C.

Under IRB approval, fifty-one patients with findings known on conventional breast sonography and mammography have been scanned to date in San Diego ranging in age from 20 to 78. Region-of-interest measurements were made in the sound speed and attentuation images for normal tissues and masses whose tissue types were known from other procedures (biopsy, aspiration, mammography, sonography, etc.).

3. RESULTS

3.1 Performance Measurements

Sound speed accuracy and linearity from the prepared solutions are shown in the plot in Fig. 2. Very high sound speed linearity was found ($R^2=0.992$) over the range of boundary values of the algorithm. Sound speed contrast sensitivity of the images was 3.5 m/sec. Speed of sound images were also computed at multiple temperatures ranging from 21 to 74°C. In the CaCl solutions, temperature changes were detectable under these conditions as speed of sound differences (SOS = 1.8·Temp + 1504) with a sensitivity of

2.1°C. In Fig. 2 the error bars (±SD) on the data points are smaller than the symbols.

In the current prototype, for the sound speed image the full-width half-maximum of the point spread function is approximately 1.5 mm in plane with ~3.5 mm slice sensitivity profile at 1.25 MHz. At present, the 3D algorithm is about 25% sharper than the 2D approach.
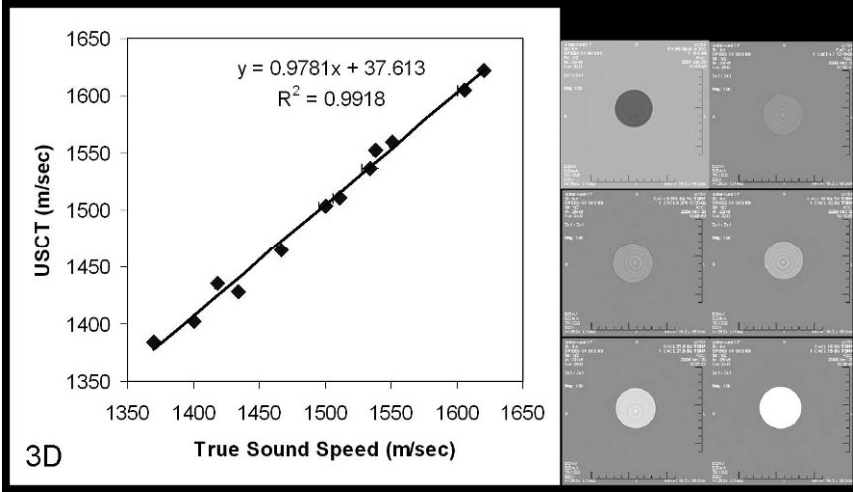
Figure 2. USCT sound speed sensitivity.
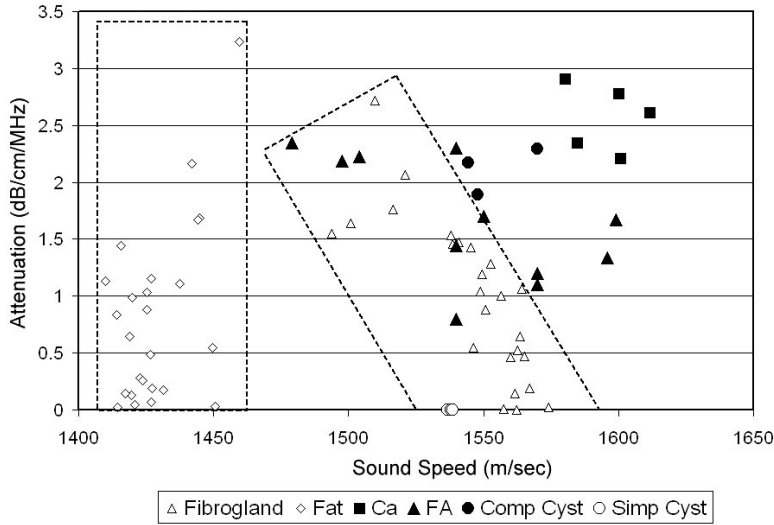
Figure 3. Sampling of acoustic properties of normal tissues and masses.

A sample of region of interest measurements from the sound speed and attenuation images for the research subjects is shown in Fig. 3 for normal structures and a variety of masses. These measurements are not yet complete but normal fatty and fibroglandular tissues (boxes) are well separated by speed and attenuation, while fibroadenomas (FA) and complex cysts show some overlap. Cancers (Ca) have both high speed and attenuation while simple cysts have very low attenuation comparable to water.

3.2   Case Presentations

For this study patients were recruited from women who were scheduled for a conventional diagnostic breast ultrasound exam. This generally included patients who had a screening mammogram requiring further diagnostic work-up or those with an abnormal physical examination that necessitated a diagnostic breast sonogram. Patients younger than 40 typically would not be screened with mammography, but several were enrolled in our study when clinical concern required an ultrasound evaluation. Patients received USCT scan prior to any biopsies.

Proprietary interactive 3D review software was developed by Techniscan to display volumetric USCT data in multi-planar format. Screen shots from the viewer are included below for the three sample cases (Figs. 4, 5, 6): a biopsy-proven malignant invasive tubular carcinoma, benign fibroadenoma and benign cyst. The upper row of images maps the speed of sound characteristics, while the lower row maps the attenuation of the breast tissue. The left-most images are coronal slices through the volume, the middle column are axial, and the right-hand images are saggital views. This image review software allows typical functions such as scrolling, window levelling, spatial and pixel value measurements. An extremely useful feature for the radiologists is a corellative feature that allows the operator to click on a point in any image and automatically register in 3D all three orthonormal views. For clarity in print, the three views are not displayed at identical scales.

3.2.1 Invasive Tubular Carcinoma

The patient is a 66 year old female with medical history significant only for hypertension and hypercholesterolemia. A suspicious mass was seen on her screening mammography and she was subsequently examined with conventional ultrasound, USCT, followed by needle biopsy. Pathology reported invasive tubular carcinoma. Note in Fig. 4 below that USCT images reveal a very bright area compared to any other structures including water in the speed of sound images (upper row), which corresponds to high speed throughout the lesion (approx 1610 m/s). The attenuation images (lower row) show a mass at the same location as the sound speed images with

values of 300 dB/m. The mass appears to have irregular shape with a bright (high attenuation) "halo" with a less attenuating center.
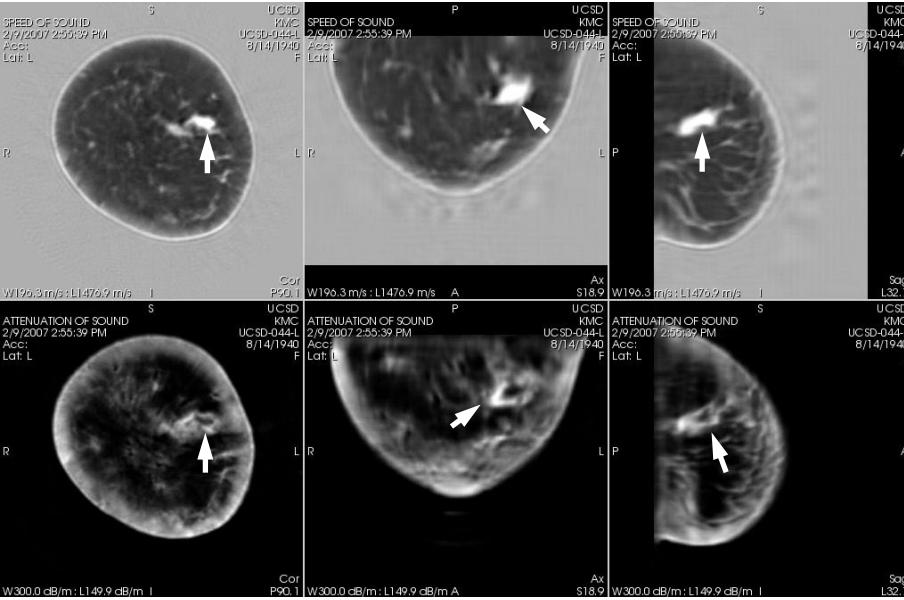
Figure 4. Invasive tubular carcinoma
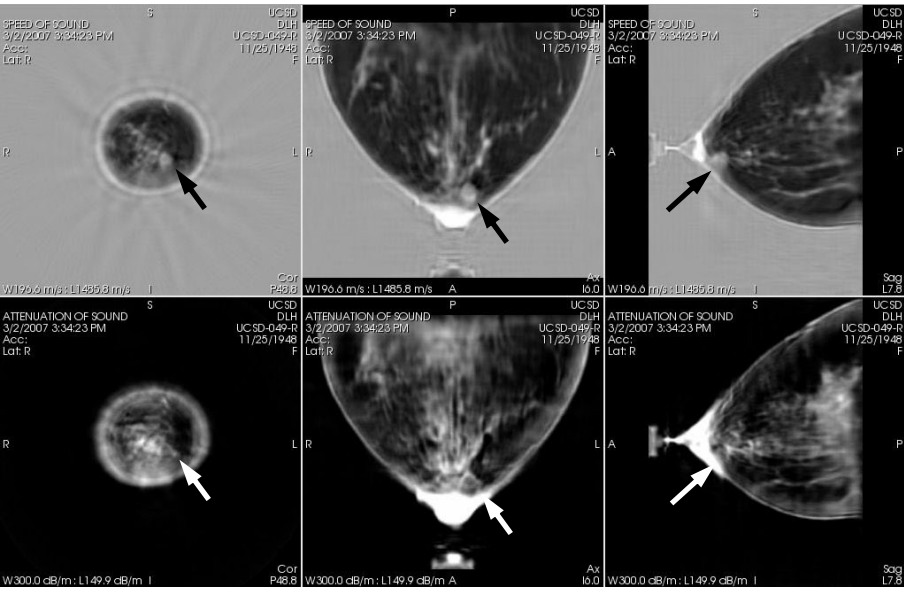
Figure 5. Fibroadenoma, 10 mm.

3.2.2 Fibroadenoma

The patient is a 58 year old female with no significant medical history concerning the breasts. The screening mammogram, follow-up diagnostic mammogram and sonogram all revealed a 10 mm, subareolar mass. USCT were performed prior to ultrasound-guided biopsy, which confirmed a fibroadenoma. The fibroadenoma is easily seen with USCT in the subareolar region (Fig. 5 above) as a well-circumscribed spherical 10 mm mass. The mass had both sound speed and attenuation values intermediate between fat and fibroglandular tissue (~1520 m/s and 130 dB/m, respectively).
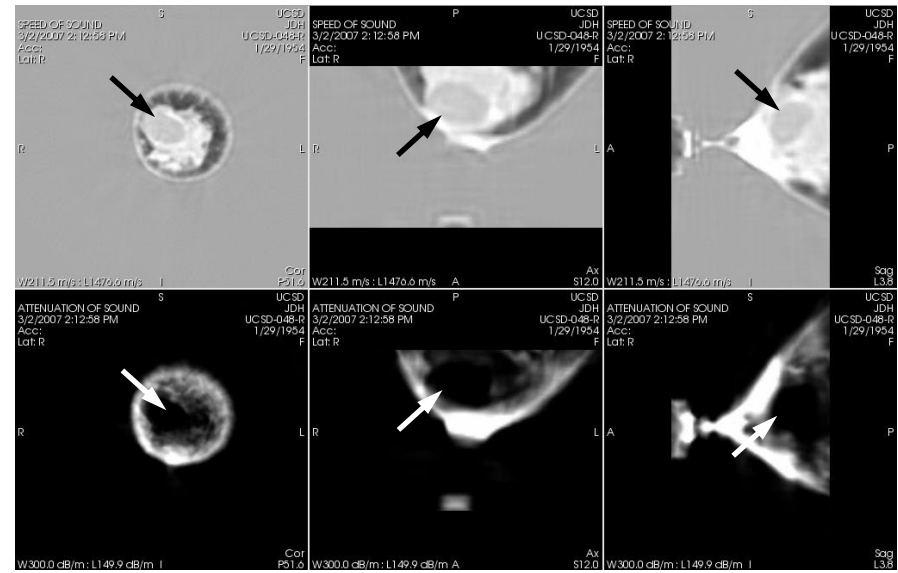
Figure 6. Fluid-filled simple cyst.

3.2.3 Simple Cyst

This patient is a 57 year-old female with history significant for profound nipple discharge of the left breast. The images in Fig. 6 above are of the right breast, which had a negative biopsy five years prior to our scan. The patient complained of a palpable abnormality on the right lasting for approximately one month. A mass was detected on mammography and was confirmed by sonogram to be cystic. USCT shows a large mass with sharp borders readily seen just posterior to the nipple. The sound speed values of the mass (upper row Fig. 6 above) are slightly higher (1540 m/s) than that of water (1510) while the attenuation images show a black void representing low attenuation values similar to that of water (0 dB/cm).

4.   CONCLUSIONS

This pre-clinical study of a prototype inverse-scattering transmission ultra-sound tomography system shows promise for breast imaging and characterization of tissue. We have shown examples where it was possible to readily distinguish breast masses on the basis of their intrinsic properties, attenuation and speed of sound. Image contrast and reproducibility are excellent and the current prototype scanner provides particularly clear images in patients with large fatty breasts.

Although it is incomplete, an overall assessment of the 51 patients scanned to date shows that the combined properties of sound speed and attenuation may provide a means to uniquely classify some tissues (Fig. 3). At this early stage of analysis there appears to be overlap between some types of solid masses and normal fibroglandular structures. This tissue characterization capability could be a worthy adjunct to the current methods of breast mass discrimination. Specifically, having the capability to better distinguish malignant from benign breast masses or to increase confidence in benign findings could give the radiologist a tool to decrease the dependence on breast biopsies.

Based on the experience gained with this study, a second generation scanner is currently under production that will implement a number of improvements. One modification will decrease the effective slice thickness while another will implement a high-resolution reflection tomography mode.

ACKNOWLEDGEMENTS

REFERENCES

1.   J.F. Greenleaf, S.A. Johnson, W.F. Samayoa, F.A. Duck: Acoustical Imaging (1975).
2.   M.P. André, H.S. Janée, G.P. Otto, et al.: Intl J Imaging Systems Technol 8 (1997) p. 137.
3.   N. Duric, P. Littrup, O. Rama, E. Holsapple: Acoustical Imaging 28 (1997) p. 173.
4.   V.Z. Marmarelis, J. Jeong, D.C. Shin, S. Do: Acoustical Imaging 28 (1997) p. 195.
5.   S.A. Johnson, T. Abbott, R. Bell, M. Berggren, et al.: Acoustical Imaging 28 (2007) p. 147.
6.   J. Wiskin, D.T. Borup, S.A. Johnson, M. Berggren, et al.: Acoustical Imaging 28 (2007) p. 183

HIGH-FREQUENCY PULSE-COMPRESSION ULTRASOUND IMAGING WITH AN ANNULAR ARRAY

J. Mamou, J.A. Ketterling, R.H. Silverman

F. L. Lizzi Center for Biomedical Engineering, Riverside Research Institute, 156 William St., New York, NY 10038, USA

Abstract: High-frequency ultrasound (HFU) allows fine-resolution imaging at the expense of limited depth-of-field (DOF) and shallow acoustic penetration depth. Coded-excitation imaging permits a significant increase in the signal-to-noise ratio (SNR) and therefore, the acoustic penetration depth. A 17-MHz, five-element annular array with a focal length of 31 mm and a total aperture of 10 mm was fabricated using a 25-µm thick piezopolymer membrane. An optimized 8-µs linear chirp spanning 6.5–32 MHz was used to excite the transducer. After data acquisition, the received signals were linearly filtered by a compression filter and synthetically focused. To compare the chirp-array imaging method with conventional impulse imaging in terms of resolution, a 25-µm wire was scanned and the -6-dB axial and lateral resolutions were computed at depths ranging from 20.5 to 40.5 mm. A tissue-mimicking phantom containing 10-µm glass beads was scanned, and backscattered signals were analyzed to evaluate SNR and penetration depth. Finally, ex-vivo ophthalmic images were formed and chirp-coded images showed features that were not visible in conventional impulse images.

Key words: Ultrasound, Chirp, High-frequency, Pulse-compression

1. INTRODUCTION

Ultrasound is currently utilized to visualize tissues at frequencies between 1 and 10 MHz. Operating at higher frequencies leads to images with finer resolution but at a cost of reduced penetration depth because of

frequency-dependent attenuation and a limited DOF because of the tightly focused, single-element transducers normally utilized for HFU imaging. In this study, we report a method combining pulse-compression and annular arrays to improve the DOF and penetration depth of HFU.

2.   METHODS

The annular array used in this study was described in detail elsewhere [1,2]. Briefly, the array consisted of a 25-μm thick copolymer membrane bonded to a single-sided, copper-clad polyimide film. The array had a radius of curvature of 31 mm and an aperture of 10 mm. After impedance matching, the nominal center frequency of each element was 17 MHz with a -6-dB fractional bandwidth of $\approx 35\%$.

In this study, pulse-compression imaging consisted of the design of a long-duration chirp and of a compression filter. A chirp is a coded signal that linearly spans a frequency bandwidth $B=f_2-f_1$, where f_1 and f_2 are the starting and ending frequencies, respectively. The long-duration chirp permits an increase in penetration depth. The compression filter is applied to the received echo signals to restore axial resolution [3]. Theoretically, a chirp of duration T leads to an SNR improvement equal to the time-bandwidth (TB) product of the chirp [3]. In this study, a 8-μs chirp spanning frequencies from 6.5 to 32 MHz was used.

The following imaging method was used: the chirp was input into an arbitrary waveform generator; then the annular array was scanned across the sample five times (generating a transmit pulse from a different element in each pass while receiving on all elements); the 25 pairs of transmit/receive pairs of radiofrequency (RF) signals were digitized at 200 MHz; then each RF signal was compressed; finally an image was constructed after a synthetic-focusing algorithm was applied to the RF signals [1]. The synthetic focusing algorithm allowed reconstructing an image in focus at every depth.

3. RESULTS

3.1 Resolution Study

To determine how our coded-excitation method affects image resolution, a 25-μm diameter tungsten wire was scanned at depths ranging from 20.5 mm to 40.5 mm using pulse-compression and a conventional impulse imaging method. The -6-dB axial and lateral resolutions revealed that the resolution was not degraded by pulse-compression imaging (Fig. 1).
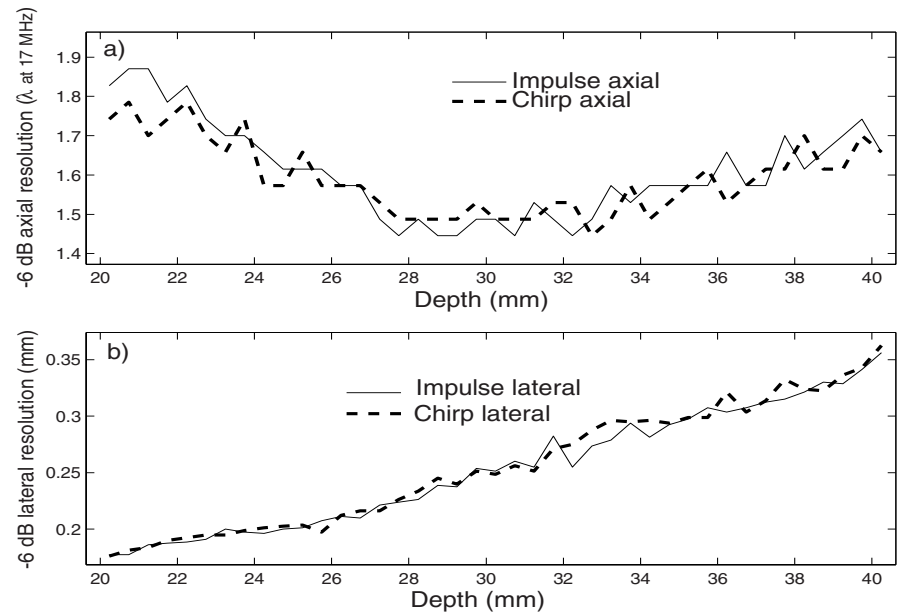
Figure 1. Axial (**a**) and lateral (**b**) -6-dB resolutions obtained as a function of depth using chirp and impulse excitation.

3.2   Penetration Depth Study
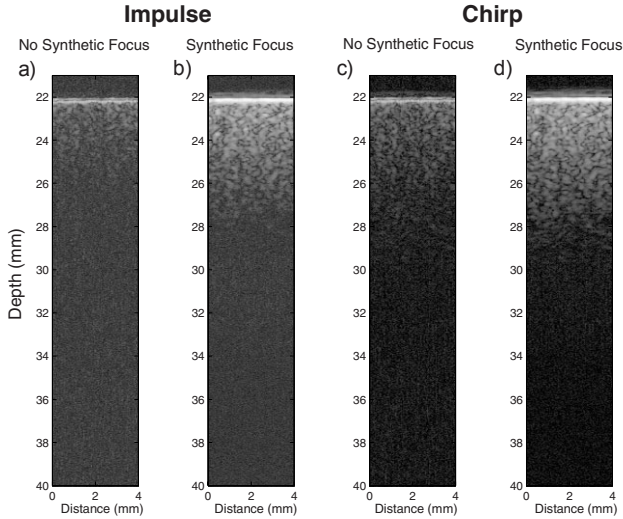
Figure 2. Images of a tissue mimicking phantom containing 10-μm glass beads with four different imaging methods (60 dB dynamic range).

Our second experiment investigated whether coded excitation increases SNR and penetration depth compared to what can be achieved with conventional-impulse imaging. For this experiment, a tissue-mimicking phantom containing 10-μm glass beads (8×10^6 beads/cm^3) was scanned using chirp and impulse excitation. Images were formed with and without synthetic focusing for each imaging method (Fig. 2). Synthetic focusing permitted deeper penetration into the phantom because backscatter from the glass beads can be observed deeper. Also, the coded excitation led to an increase in SNR independently of whether the synthetic focusing algorithm was used. To quantify these observations, we examined the average backscatter from each of the four images as a function of depth (Fig. 3). The four curves indicate that the average backscatter decreased with depth and reached a noise plateau. This plateau was used to define the SNR.

Table 1. SNRs and penetration depth of the phantom images.

Method	Dynamic focusing	SNR (dB)	Penetration depth (mm)
Impulse	No	30.3	29.1
Impulse	Yes	46.9	33.8
Chirp	No	39.4	31.6
Chirp	Yes	58.8	37.5

Table I displays the SNRs and penetration depths for each of the four imaging methods. As we observed qualitatively in Fig. 2, the SNR increased with synthetic focusing and coded excitation. The penetration depth (symbolized on Fig. 4 by the cross symbol) was the value at which the absolute value of the curve gradient dropped below a certain small threshold. Synthetic focusing and chirp coding each contributes individually to increasing the effective penetration depth. In particular, the maximum effective penetration depth is obtained when both methods are combined.
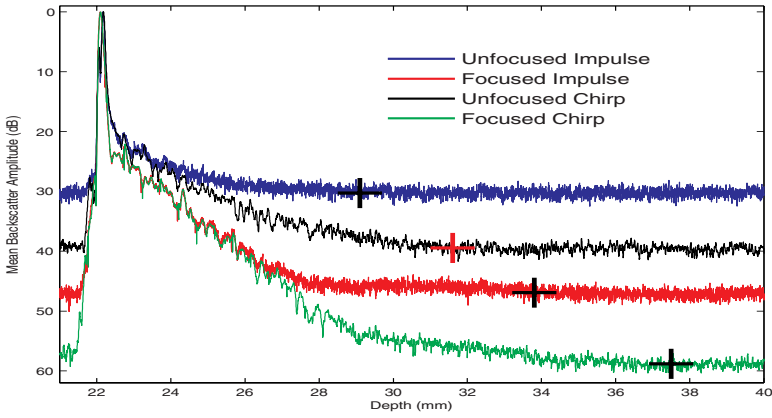
Figure 3. Mean average backscatter as a function of depth of the images of Fig. 2.

3.3   Ex-vivo Imaging Study

Three ultrasound images of a bovine eye are displayed in Fig. 4. Figure 4a represents the state of the art for ultrasound ophthalmologic imaging because without synthetic focusing, the annular array is equivalent to a single-element transducer. The anterior segment of the eye was in the defocused near-field in the images and this area was poorly resolved. As shown in Fig. 4b, synthetic focusing provides a dramatic improvement in image quality. This figure clearly shows that the anterior and posterior segments are in sharp focus. A detachment of the corneal epithelium, which is not visible in Fig. 4a was clearly observable in Fig. 4b. Similarly, the anterior chamber was more clearly visualized with synthetic focusing. Further improvement in image quality was observed in the chirp image (Fig. 4c); not only was the full globe in focus, but the increase in SNR allowed visualization of structures that previously were hidden by noise. The lens circumference was

fully visible, and scattering from the vitreous was apparent proximal to the retina. Figure 5c demonstrates the strength of combining annular array imaging with coded excitation.
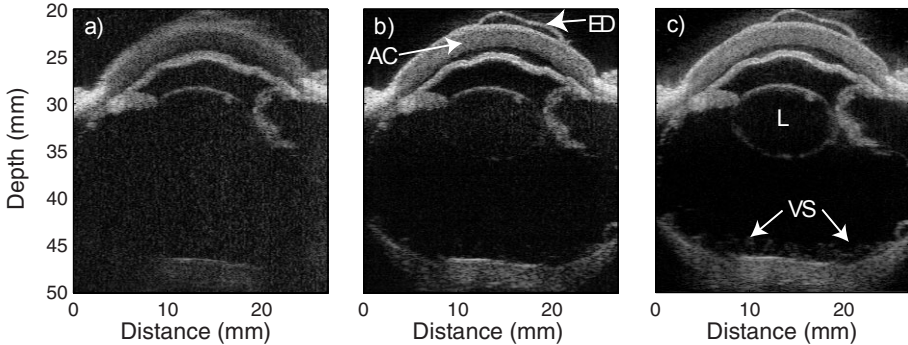
Figure 4. Images of a bovine eye. (**a**) Impulse without synthetic focusing 60 dB dynamic range. (**b**) Impulse with synthetic focusing (60 dB). (**c**) Chirp with synthetic focusing (75 dB). The anterior chamber (AC), an epithelial detachment(ED), the lens (L) and vitreous scattering (VS) are labeled.

ACKNOWLEDGEMENTS

REFERENCES

1. J. A. Ketterling, O. Aristizábal, D. H. Turnbull, and F. L. Lizzi, "Design and fabrication of a 40-mhz annular array transducer," IEEE Trans. Ultrason. Ferroelect. Freq. Contr., vol. 52, pp. 672–681, 2005.
2. J. A. Ketterling, S. Ramachandran, and O. Aristizábal, "Operational verification of a 40-mhz annular array transducer," IEEE Trans. Ultrason. Ferroelect. Freq. Contr., vol. 53, pp. 623–630, 2006.
3. T. Misaridis and J. A. Jensen, "Use of modulated excitation signals in medical ultrasound. part II: Design and performance for medical imaging applications," IEEE Trans Ultrason Ferroelectr Freq Control, vol. 52, pp. 192–207, 2005.

BLOOD FLOW IMAGING IN MATERNAL AND FETAL ARTERIES AND VEINS

S. Ricci, G. Urban, P. Vergani, M. J. Paidas, P. Tortoli

Dept. of Electronics and Telecommunications, University of Florence, Italy; Dept. of Obstetrics and Gynecology, Bicocca University, Monza, Italy; Dept. of Obstetrics, Gynecology & Reproductive Sciences, Yale University, New Haven, CT.

Abstract: Maternal and fetal blood circulation has been investigated for nearly a decade through ultrasound (US) techniques. Evaluation of the spectrogram related to a single sample volume has been proven valuable for the assessment of fetal well-being and for prediction of pregnancy complications. In this work, an alternative technique, called Multigate Spectral Doppler Analysis (MSDA), is proposed. In this approach, 128 sample volumes aligned along the same scan line are simultaneously investigated to detect the blood velocity profile with high resolution. Profiles obtained through MSDA reveal features not detectable with the standard US technique, thus representing a more accurate flow signature. Some preliminary illustrative results are reported here.

Key words: Fetal circulation, Maternal circulation, Blood velocity profiles, Ultrasound techniques

1.   INTRODUCTION

Investigation of blood flow in maternal and fetal vessels is made hard by concurring difficulties. On the maternal side, all vessels are characterized by noticeable tortuosity. The maternal blood, rich in O_2 and nutrients, is transferred by the umbilical vein to the fetus, where it flows in arteries and veins having small diameters and lengths. Deoxygenated blood is finally sent back to the placenta through the umbilical arteries, which are repeatedly twisted around the vein.

Despite the difficulties due to such a complex circulation, it is worth investigating blood flow in maternal and fetal vessels, because it can help to predict the outcome of pregnancies or to diagnose possible diseases [1].

Doppler ultrasound (US) has been widely used in this field [1,2]. In particular, spectral Doppler has been recommended as the most reliable technique [3]. In this case, a single sample volume (SV) is selected through the help of B-mode or color flow imaging, and the spectral contributions originated from this SV are analyzed in real-time. Proofs of correlation between abnormal umbilical flow waveforms and compromised fetal conditions have been given [3,4].

Notwithstanding some encouraging results, analyzing flow through a single SV yields problems of vessel identification and low reproducibility [5]. The conventional Doppler waveform shape is not always sufficient to indicate the type of flow within the vessel. For example, a preliminary off-line analysis of pulsed Doppler-generated flow-velocity waveforms has demonstrated that flow velocity profiles in the umbilical vein are not perfectly parabolic, as frequently assumed, and they modify along the cord [6].

A real-time velocity profile detection method, here referred to as Multigate Spectral Doppler Analysis (MSDA), has been recently proven valuable in hemodynamic studies of adult large arteries [7,8]. In this approach, 128 SVs aligned along the same scan line are simultaneously investigated. When the scan line intercepts one or more vessels, processing of the 128 Doppler signals produces a display showing the corresponding distribution of Doppler frequencies (spectral profile). In this study, the MSDA method has been applied to the investigation of maternal and fetal blood circulation in 120 patients. Some illustrative examples of analysis are presented, and the potentiality of the MSDA method to distinguish different flow configurations is discussed.

2.   MATERIALS AND METHOD

The experimental set up used in this study is based on a proprietary ultrasound research board (URB) [9] hosted in a PC and connected to modified echographic apparatus (Fig. 1). Two commercial echographs (MyLab25 by Esaote SpA, Italy, and SSD 1400 by Aloka Co. Ltd., Japan) have been adapted to supply beamformed echo-signals in two different labs.

The URB is a compact and programmable research platform equipped with state of the art analog and digital circuits. The beamformed received echo-signal is digitized in the URB by a 14 bit analog to digital converter (ADC) at 64 MSPS. This radio frequency (RF) data is phase-quadrature demodulated in a Field Programmable Gate Array (FPGA) from the Stratix family (Altera, San Jose, CA, USA). A digital signal processor (DSP) of the TMSC320C6x family (Texas Instruments, Austin, TX, USA), can access both RF and demodulated data to perform the specific processing in real

time. The URB also includes a 64 Mbyte SDRAM buffer suitable to gather several seconds of RF or demodulated data that can be downloaded to the host PC.
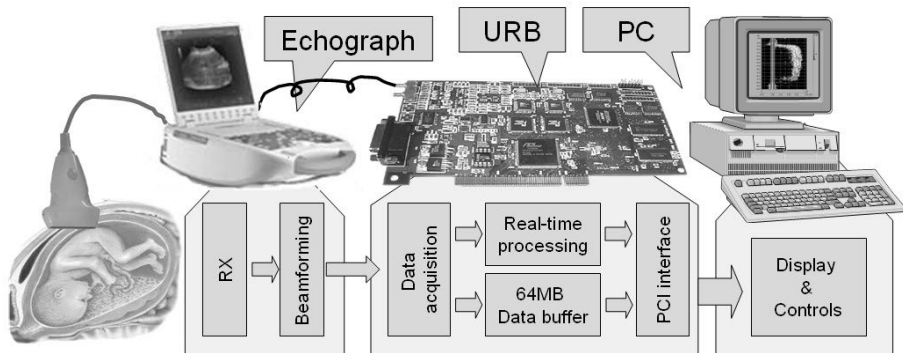
Figure 1. Experimental set up: A modified commercial US machine feeds the ultrasound research board (URB) with beamformed echoes. The URB processes in real time the data to produce velocity profiles displayed in the host PC.

3. PRELIMINARY RESULTS

The MSDA has been applied to the study of maternal and fetal blood circulation in 120 volunteers, after informed written consent was obtained. The study was made at New Haven Yale University Hospital (CT, USA) and at the San Gerardo Hospital (Monza, Milano-Bicocca University). For each session, depending on the fetus position, either an abdominal or a transvaginal probe, with frequency of 2.5 or 5 MHz, was used. The operator first used the US machine in B-mode and placed the scan line in the region of interest. The machine was then switched to Pulse Doppler Mode (PDM), so that the URB could produce the blood flow spectral profiles, whose real-time display helps for fine transducer positioning. Once the set-up was considered satisfactory, the raw Doppler data were acquired in the URB and downloaded to the PC hard-disk.

Investigated vessels included fetal aorta, fetal cerebral artery, umbilical cord, uterine vessels, hypogastric artery. Investigations covered gestation ages between the 6th to the 36th week. The analysis of the acquired data has confirmed the capability of MSDA of easily detecting the blood flow patterns in a variety of situations in which the standard Doppler approach frequently fails. A few examples are presented here.

Figure 2 reports some screenshots obtained by analyzing the umbilical cord in a 18-week gestation. Figure 2 (a) shows the B-mode image in which the cord is intercepted by the M-line at depths between 28 and 35 mm. The blood flow crossing the SV produces the sonogram reported in Fig. 2 (b) showing contemporaneous pulsatile and steady flow contributions. The echoes backscattered along the scan line were also elaborated according to MSDA to produce the spectral profile that clearly differentiates the pulsatile arterial flow from the nearly constant venous flow. Figure 2 (c) shows a screenshot of the velocity profile frozen at the systolic peak. The vertical and horizontal axes represent the depth and the Doppler frequency, respectively. One of the two umbilical arteries is visible at depths between 28 and 31 mm and features positive Doppler frequencies, while the vein is revealed between 31 and 35 mm and is characterized by negative frequencies. The two spectrograms on the right (d-e) are extracted from the SVs contributing to the spectral profile at about 29 and 33 mm depths, respectively.
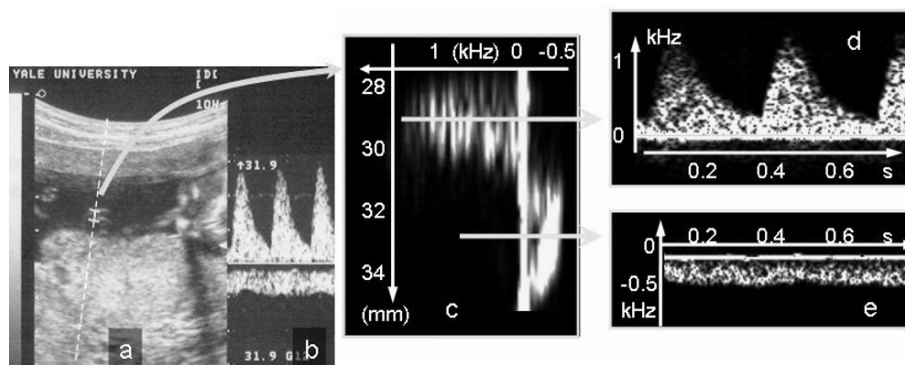
Figure 2. Umbilical cord investigated with standard US technique (**a,b**) and MSDA (**c,d,e**). In (**a**) the B-mode image shows the cord with the selected SV, (**b**) reports the resulting standard sonogram. In the velocity profile produced by MSDA (**c**) the contributions of one artery (**c**, *top*) and the vein (**c**, *bottom*) are clearly distinguished and their spectrograms are shown in (**d,e**) respectively.

Figure 3 shows some screenshots of a fetal aorta taken during the 33rd week of gestation. The aorta was identified in the B-mode display at an average depth of 45 mm and the M-mode scan line was placed to form a Doppler angle of about 60°. A convex array was here employed with 2.5 MHz frequency. Figure 3 (a) shows the sonogram with superimposed three vertical lines that point out the time instants at which the velocity profiles (b,c,d) have been obtained. The reported profile screenshots show how the blood flow changes during a cardiac cycle. During the systolic acceleration the profile assumes almost a "triangular" shape (b) that then develops in a

pseudo-laminar flow (c). The cardiac cycle terminates with the residual diastolic flow whose profile is visible in (d).
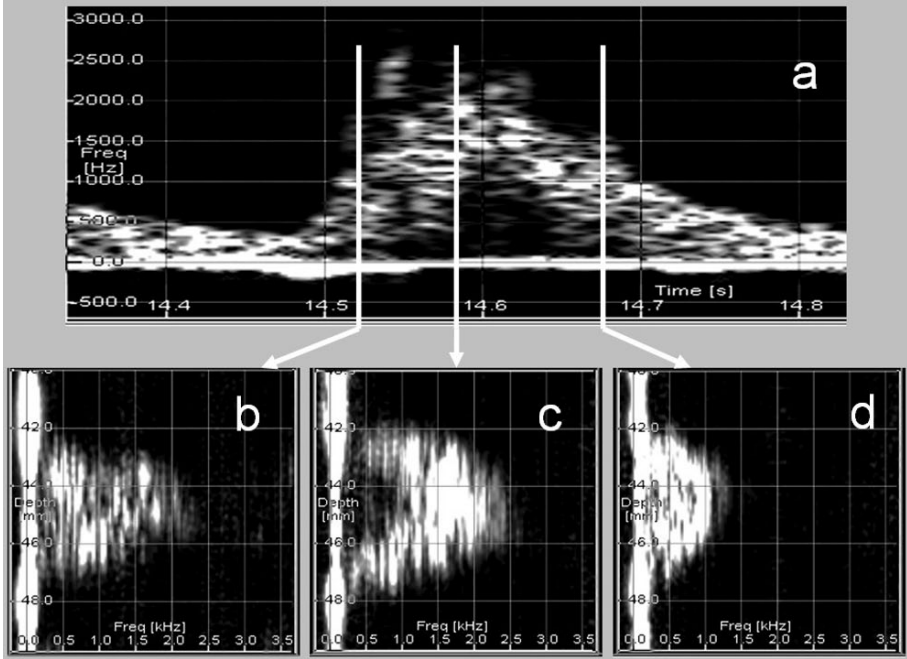
Figure 3. Fetal aorta during the 33rd week of gestation. Standard sonogram (a) and screenshots (a,b,c) of the velocity profile. Each screenshot was taken at the time instant highlighted by a corresponding line in the sonogram.

4. DISCUSSION

Standard Doppler US is widely used for investigating maternal and fetal circulation, and has already been proven valuable for detecting some pathological situations. MSDA adds the possibility of obtaining accurate velocity profiles that reveal features of the flow that the standard PDM fails to detect.

The analysis of the database acquired on 120 patients is currently in progress. This study is expected to provide normative profile data in healthy pregnancies and determine the relationship, if any, between the morphology of the flow, placentation abnormalities and fetal complications, such as fetal anemia. Further studies are planned to correlate the velocity profiles, in acquired or inherited thrombophilic conditions, and a variety of biomarkers (e.g. markers of thrombin generation, inflammation, implantation, angiogenesis/

vasculogenesis). MSDA could represent a method to improve the reliability of US in predicting pregnancy complications and in detecting pathological cases.

ACKNOWLEDGEMENTS

REFERENCES

1. D.E. FitzGerald and J. Drumm, Noninvasive measurement of human fetal circulation using ultrasound: a new method. *Br Med J* **2**, 1450–1451 (1977).
2. D. Maulik, Doppler Ultrasound velocimetry for fetal surveillance. *Clin Obstet Gynecol,* **38**(1), 91–111 (1995).
3. D. Arduini, G. Rizzo, M.R. Boccolini, C. Romanini and S. Mancuso, Functional assessment of uteroplacental and fetal circulations by means of color Doppler ultrasonography. *J Ultrasound Med*, **9**, 249–253 (1990).
4. B.J. Trudinger, W.B. Giles, C.M. Cook, A. Connelly and R.S. Thompson, Umbilical artery flow velocity waveforms in high risk pregnancy: Randomized, controlled trial. *Lancet*, **344**(8938), 188–190 (1987).
5. R.L. Thomas, T.C.C. Peng, G.S. Eglinton, D.M. Strobino and T.R. Johnson, Precision of umbilical artery Doppler studies: intraobserver, interobserver, and biologic variability of fetal Doppler velocimetry. *J Ultrasound Med* **10**, 201–204 (1991).
6. G. Pennati, M. Bellotti, C. De Gasperi and G. Rognoni, Spatial velocity profile changes along the cord in normal human fetuses: can these affect Doppler measurements of venous umbilical blood flow? *Ultrasound Obstet Gynecol* **23**, 131–137 (2004).
7. G. Bambi, F. Guidi, S. Ricci, P. Tortoli, M.R. Cirelli and L. Pedrini, Ultrasound blood flow imaging in carotid arteries before and after endarterectomy, *Acoustical Imaging*, Vol. 27, Edited by W. Arnold and S. Hirsekorn, Kluwer Academic/Plenum Publishers, Dordrecht & New York, 471–476 (2004).
8. P. Tortoli, G. Bambi, F. Guidi and R. Muchada, Toward a better quantitative measurement of aortic flow. *Ultras Med & Biol*, **28**(2), 249–257(2002).
9. S. Ricci, E. Boni, F. Guidi, T. Morganti and P. Tortoli, A Programmable Real-Time system for development and test of new ultrasound investigation methods. *IEEE Trans Ultrason Ferroelect Freq Contr*, Special Issue, **53**(10), 1813–1819, (2006).

CAROTID PLAQUE TISSUE DIFFERENTIATION BASED ON RADIOFREQUENCY ECHOGRAPHIC SIGNAL LOCAL SPECTRAL CONTENT (RULES: RADIOFREQUENCY ULTRASONIC LOCAL ESTIMATORS)

E. Biagi, S. Granchi, A. Luddi, L. Breschi, R. Facchini, A. Ricci, L. Masotti
Department of Electronics and Telecommunications, via S.Marta 3, 50139 Firenze, Italy

Abstract: An echographic method is proposed in order to detect and differentiate carotid vessel plaques. The method, based on spectral processing procedure for the radiofrequency echo signal, is named RULES (Radiofrequency Ultrasonic Local EStimators).

Key words: Tissue characterization, Carotid plaque, Spectral processing, Signal processing.

1.   INTRODUCTION

In echographic images, local organization of the microstructures, such as cells and micro vessels, give rise to a speckle effect. The speckle depends on the mechanical characteristics and spatial distribution of the microstructures. The multitude of the echo wavelets, generated from the tissue structural elements, interferes in constructive and destructive manners on the receiving transducer surface, according to their propagation path differences. These interferences and reflectivity variations in the time domain are responsible for spectral amplitude modulation in the frequency domain. As a consequence, the preservation of the entire band of the RF signal is essential to "read" this amplitude spectrum shape, in order to gain further information for tissue characterization and differentiation purposes.

In this scenario, we proposed the RULES [1] method to provide a detailed description of the RF signal spectral content for gaining local microstructure information about tissue.

RULES produces a final image where the different structural organization of an investigated tissue is recognized and represented by different chromatic codes over a conventional B-Mode image. In particular, in this work RULES has been devoted to differentiation of the different plaque components.

2.   INVESTIGATION METHOD

The RF signal contains information about ultrasound–tissue interaction and it is necessary to employ a processing method capable of extracting the information in a meaningful way. Biological tissue can be seen as a distribution of non-regularly located scatterers which generate non-stationary signals. Consequently, the spectral content of the transmitted signal is locally modified and a Time-Frequency Representation (TFR) is required.

The discrete form of the Wavelet Transform, and in particular the Discrete Wavelet Packets Transform (DWPT) with the third decomposition level without decimation was chosen.

The processing steps of RULES can be summarized as follows. Each RF signal is decomposed into eight bands, derived from the third decomposition level, and eight sets of DWPT coefficients are produced. RULES allows local tissue characterization because it considers for each time instant (i.e. depth in the tissue) the eight DWPT coefficients whose behavior in the frequency domain was interpolated by means of a 4th order polynomial. The polynomial coefficients a_0, a_1, a_2, a_3 and a_4 are used as Local EStimators (LES). The chosen order of the polynomial is a good compromise between the computational load and the fitting features. For each RF frame, five LES matrices are calculated. An appropriate-sized rectangular window is translated step by step over the five LES matrices, in order to extract the histograms of the LES. The next processing step leads to individuate those portions of the RF frame that exhibit similar histogram characteristics for the same Local EStimator (LES). In Fig. 1, the histograms of the five LES are shown for three different regions of an echographic image. It should be noted that the same LES gives different histograms for the three selected regions (region A, B and C of Fig. 1). The shape of the obtained histograms is a signature of the structural organization of the tissue. As a consequence, tissue regions which produce similar histograms can be considered acoustically homogeneous. Similarity criteria are formulated for LES histograms by evaluating the following statistical parameters: maximum

occurrence frequency, classes of values, standard deviation and shape indices (kurtosis and skewness). By defining "Configuration" as a particular set of value of these statistical parameters, several possible "Configurations" can be found to recognize different homogeneous regions, in the tissue under investigation. The histological analysis of the investigated tissue allows to give a biological meaning to the concept of "Configuration". In the RULES "learning phase" the "Configurations" are continuously improved till the matching with the histological analysis is reached. The last step of RULES method concerns the visualization of the results. For each recognized "Configuration" a chromatic or grey code was superimposed on the conventional B-Mode image. The different chromatic codes correspond to homogeneous areas with different histological significance.
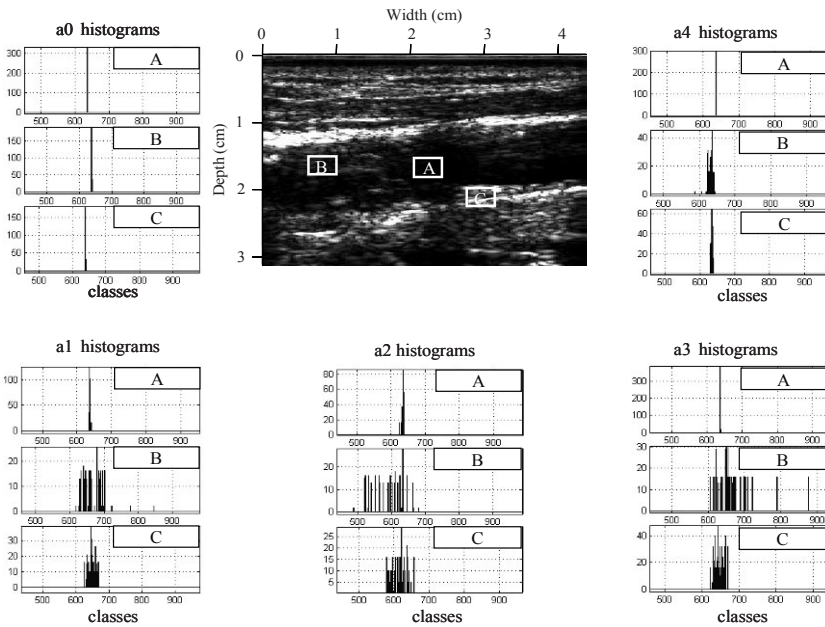
Figure 1. LES histograms referred to three different homogeneous areas in the carotid vessel (A, B and C).

3. EXPERIMENTAL SET UP

The experimental set-up is reported in Fig. 2. The dimensions of the window employed for the LES statistical analysis were fixed at 1 mm (depth) × 1.1 mm (width. The window was translated by 0.3 mm in depth and by 0.25 mm in width throughout the frame.

The RULES learning phase was performed by selecting 22 patients affected by different degrees of carotid stenosis requiring surgery. For each patient, two experimental phases were performed. The first consisted in in vivo acquisition before the surgical operation and the second, which constituted the learning phase, was performed in vitro on the removed carotid specimens immersed in a water tank. Histological maps were then produced on the removed specimens.
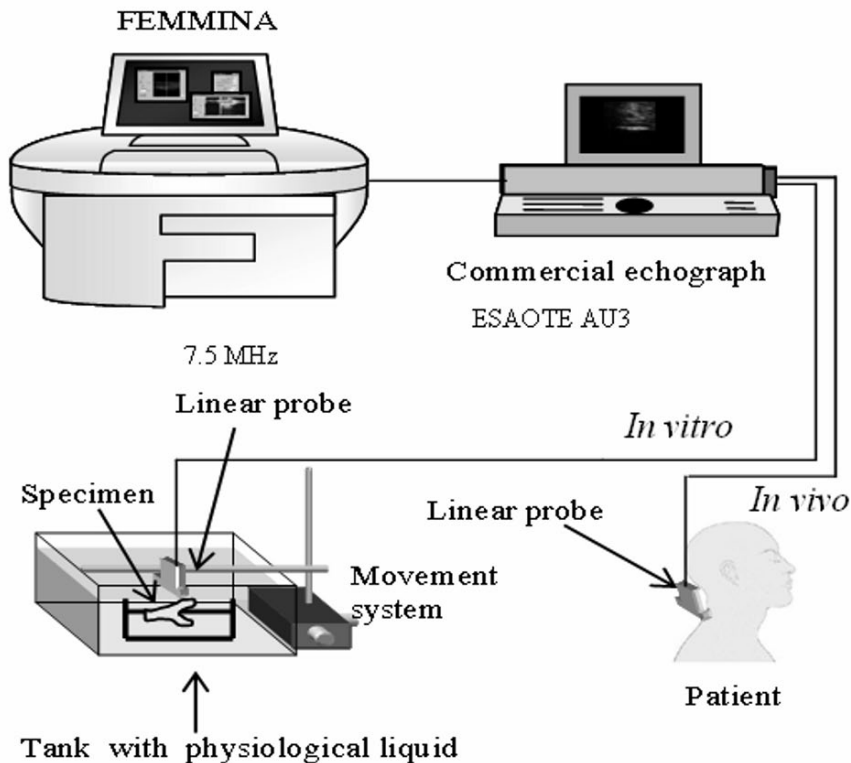
Figure 2. "In vitro" and "in vivo" acquisition setups: a FEMMINA [2] platform is connected to a commercial echograph. During "in vitro" acquisitions, the specimen was placed in a tank filled with normal saline and it was ultrasonically scanned.

A total number of 440 in vivo and 187 in vitro RF frames were produced.

The learning phase for carotid characterization was performed on 187 in vitro frames by comparing the results with the related 187 histological maps. Then, by comparing the homogeneous image portions thus produced with the corresponding zone of the histological maps, it was possible to drive the search for the most appropriate RULES "Configurations" for plaque

structure differentiation. The learning phase was closed when a good matching was found between RULES "Configuration" and histology results.

In particular, two typical sets of parameters defined as "Configuration L" and "Configuration C" were produced for lipids and calcification detection, respectively.

In a previous work, the authors had identify a specific RULES "Configuration", labeled "Configuration B", for detecting blood presence.

The conjunction of the three "Configurations" can furnish a complete carotid vessel characterization, where the information on plaque structure is enriched with indications regarding the residual lumen dimension. These three "Configurations" were then tested on the in vivo acquisitions previously collected and the results are discussed in the following section.
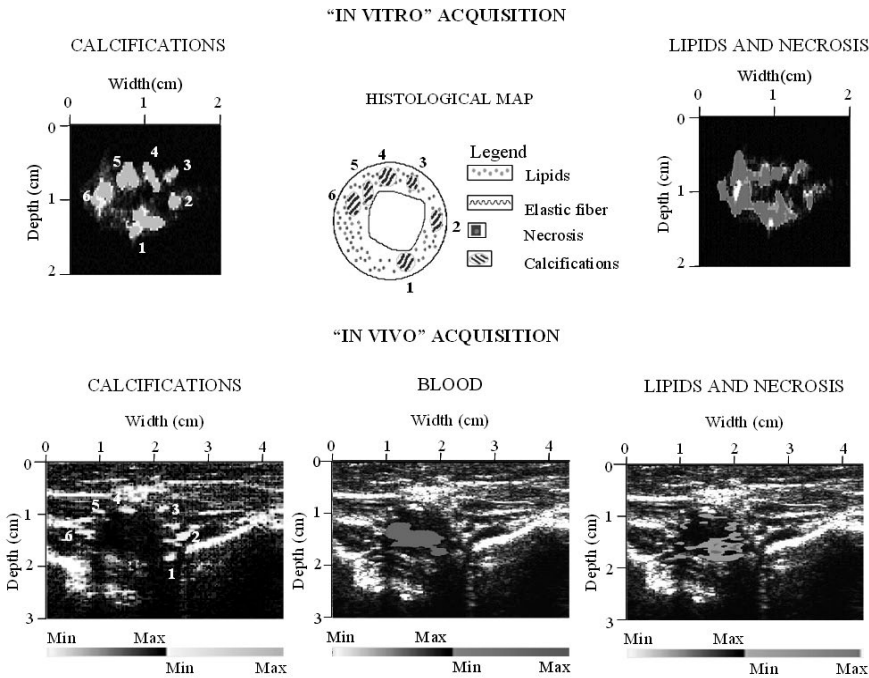
Figure 3. Carotid transversal section, acquired both in vitro and in vivo. The 3 different "Configurations" were represented with 3 different gray-scale levels over the B-Mode image.
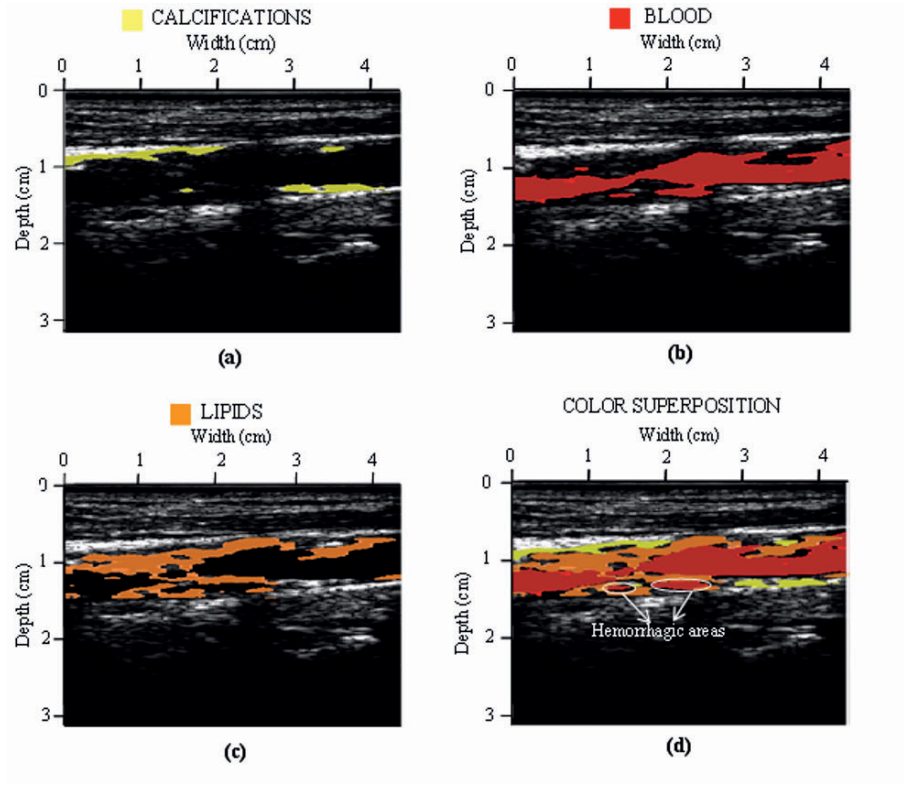
Figure 4. RULES images of an "in vivo" carotid longitudinal section.

4.   RESULTS

The learning phase is concluded when a good spatial matching between RULES "Configurations" and histological maps occurs. At the top of Fig. 3, an example of such a matching is shown. The final marked frames and the corresponding histological map are reported, for a single "in vitro" section. At the bottom of Fig. 3, the images obtained with the three "Configurations" are referred to the in vivo acquisition of the same patient. In this case, the frame of the acquired RF sequence spatially corresponding to the in vitro section is considered. In clinical application the physician could choose to operate with three distinct images for calcifications, blood and lipid as appears in Fig. 4 (a), (b) and (c) respectively, or select their composite visualization as in Fig. 4 (d).

5. CONCLUSION

It has been demonstrated that the three defined "Configurations" well classify all the 22 patients involved in the learning phase. Considering these results, RULES is currently under clinical test in the Department of Vascular Surgery of the University of Florence, in order to check for specificity and sensitivity.

REFERENCES

1. L. Masotti, E. Biagi, S. Granchi, and L. Breschi, Method and device for spectral analysis of an echographic signal, *U.S. Patent* **US 2003/0167003 A1**, (2003).
2. M. Scabia, E. Biagi, and L. Masotti, Hardware and software platform for real-time processing and visualization of echographic radiofrequency signals, *IEEE Trans. Ultrason. Ferroelect. Freq. Contr.* **49**, 1444–1452 (2002).

CROSS–SAMPLING MEASUREMENT OF VOCAL-FOLD VIBRATION USING ULTRASOUND

O. Oshiro, S. Kamei, Y. Masuda, Y. Kuroda, T. Kuroda

Graduate School of Engineering Science, Osaka University, 1 - 3 Machikaneyama, Toyonaka 560 - 8531, Japan

Abstract: This paper describes a measurement system for detecting the spatial distribution of vocal-fold vibration. In the proposed system, focused ultrasound pulses were transmitted in the same direction, and the distribution of the vocal-fold vibration could be obtained. Experimental results demonstrate that the vocal-fold vibration was in good agreement with the voice frequency. Furthermore, we succeeded in visualizing the spatial distribution of the vocal-fold vibration. Therefore, our proposed method has the potential to visualize the dynamics of the vocal fold.

Key words: Ultrasound, Vocal fold, Vibration distribution, Fourier transform, Voice frequency.

1.   INTRODUCTION

We speak, sing and communicate with friends using voice. Voice is produced with a vocal organ, the vocal fold, and voice frequency coincides with the vocal-fold vibration. Fourier analysis of voice reveals the voice frequency, but the spatial distribution of the vocal-fold vibration cannot be visualized.

Several methods have been developed to measure vocal-fold vibration. In the optical method, a camera synchronized with a light source captures the vibration [1]. However, this method is very invasive because both devices must be inserted into the throat. In contrast, the velocity of organ

movement [2] and blood flow [3] can be measured non-invasively with ultrasound. The velocity distribution can also be obtained.

Here, we propose a measurement system for detecting the spatial distribution of vocal-fold vibration using ultrasound. Moreover, this system non-invasively visualized the frequency characteristics of the vocal fold.

2.   MEASUREMENT SYSTEM

Figure 1 schematically illustrates the proposed measurement system. First, focused ultrasound pulses are transmitted in the same direction at a constant repetition time of 0.3 msec. The ultrasound signal was transmitted using a probe with a central frequency of 3.5 MHz that was connected to an ultrasound device (Hitachi Medical Echopal). Second, the reflected signals were amplified and digitized with an analog–to-digital board (Interface PCI 3161) at a sampling frequency of 40 MHz. Final, the digitized data were transferred to a PC (CPU clock 3 GHz, memory 2 GB) and analyzed with a Fourier transform. Simultaneously, voice was detected with a conventional microphone and digitized at a sampling frequency of 22 kHz.
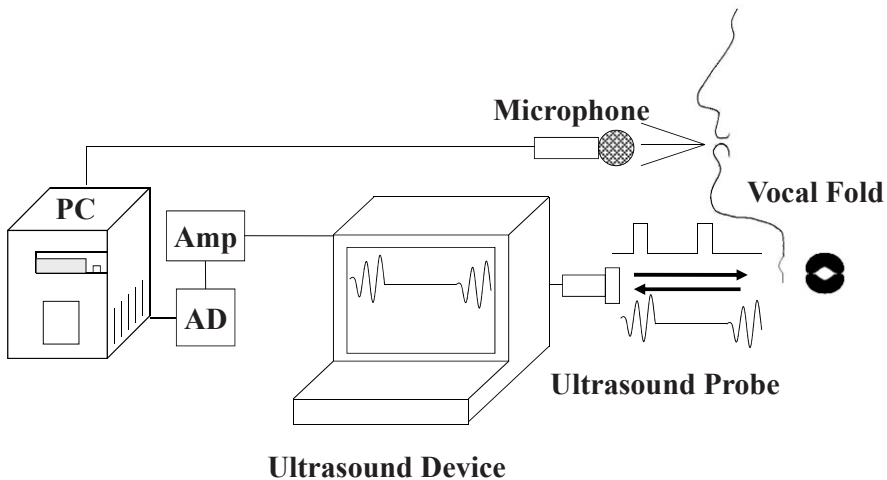
Figure 1. Schematic view of the proposed measurement system. The focused ultrasound pulses are transmitted at a constant repetition time. The reflected signals were then amplified, digitized and transferred to a PC. Simultaneously, the voice was detected with a conventional microphone.

3. METHOD AND RESULT

In this experiment, four subjects vocalized /a/ for a few seconds. Ultrasound pulses were transmitted 256 times at a repetition time of 0.3 msec from the frontal side of the neck surface, and sound pressures were sampled at 4076 points. Figure 2 depicts the reflected waveform featuring four epochs.
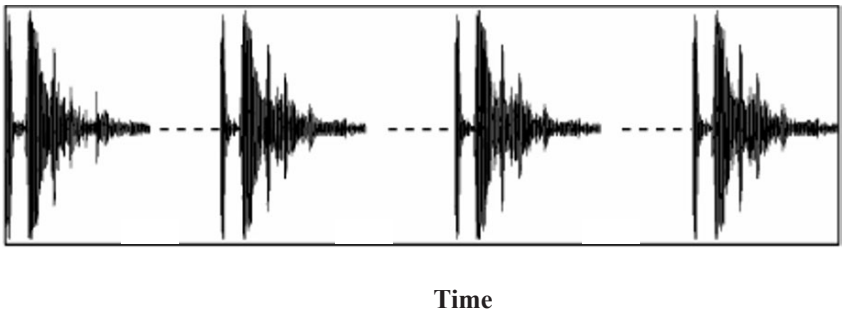
Time

Figure 2. Reflected waveform featuring four epochs. Ultrasound pulses were transmitted 256 times at a repetition time of 0.3 msec, and sound pressures were sampled at 4076 points.

(a)   (b)
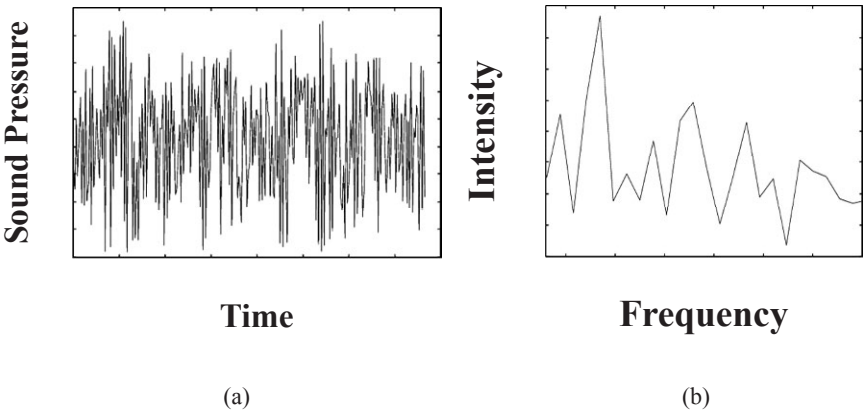
Figure 3. Waveforms (**a**) and frequency characteristic (**b**) from the sound pressures at the same latency. We regarded signal (**a**) as the vocal-fold vibration.

The sound pressures at the same latency from pulse transmission were under–sampled and collected. Figure 3 (a) plots the waveform from under-sampled data. We regarded the under-sampled signal as the vocal-fold vibration. The frequency of the vibration was obtained by Fourier

transformation of the signal. Figure 3 (b) plots the frequency characteristics and indicates the vocal-fold dynamics at a certain site. In this method, changing latency reveals vocal-fold dynamics at shallower or deeper points from the neck surface.
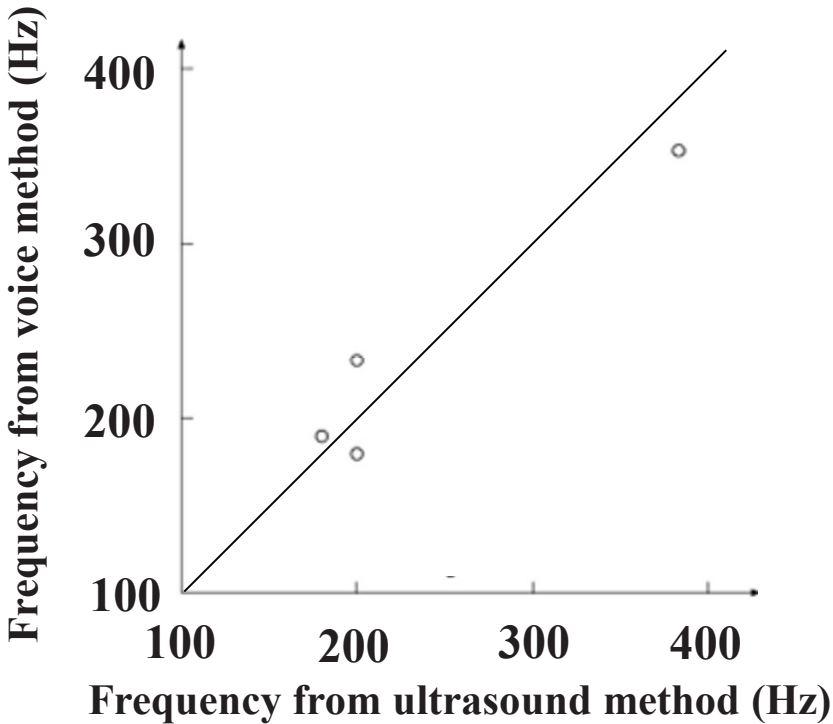
Figure 4. Relationship between two methods. The horizontal axis corresponds to the frequency with the maximum intensity in the ultrasound method; the vertical axis corresponds to the frequency with the maximum intensity in the voice method.

To analyze the frequency in the proposed method, we compared the vocal-fold vibration with voice frequency. Figure 4 diagrams the relationship between the two methods. The horizontal axis corresponds to the frequency with the maximum intensity in the ultrasound method; the vertical axis corresponds to the frequency with the maximum intensity in the voice method. Figure 4 indicates that the frequencies from the two methods are in good agreement.

Figure 5 illustrates the distribution of the vocal-fold vibration. The horizontal axis corresponds to the distance from the neck surface, and the vertical axis corresponds to the frequency of the vocal-fold vibration. The

frequency intensity was color–encoded; yellow indicates higher intensity and blue indicates lower intensity. The frequency distribution at shallower sites was obtained from the short latency; the distribution at deeper sites, from the long latency.

The higher frequency intensities were found inside the white ellipse in Fig. 5. The distance between each center was about 10 mm, which is consistent with the size of the vocal fold. These results demonstrate that our proposed method enables visualizing the spatial distribution of vocal-fold vibration.
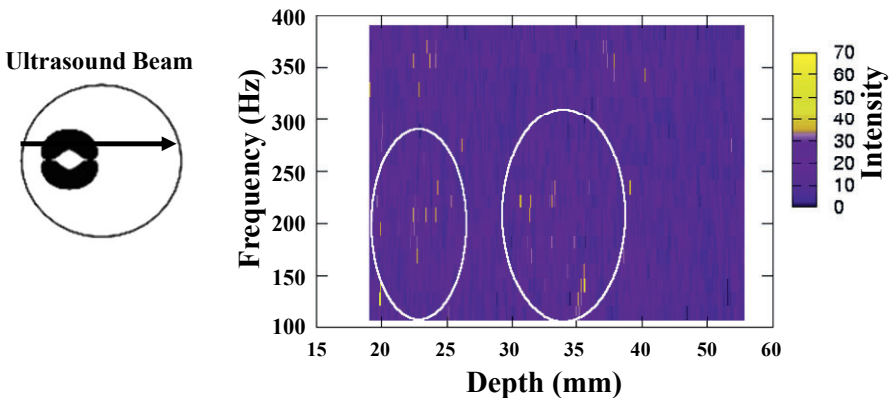
Figure 5. Distribution of vocal-fold vibration. The horizontal axis corresponds to the distance from the neck surface, and the vertical axis corresponds to the frequency of the vocal-fold vibration.

4. CONCLUSION

We constructed a measurement system to detect the spatial distribution of vocal-fold vibration using ultrasound. The transmission of focused ultrasound pulses and the variation of the latency from the transmission enabled us to obtain the distribution of the vocal-fold vibration. Experiment results demonstrate that the vocal-fold vibration was in good agreement with the voice frequency. We also succeeded in visualizing the spatial distribution of the vocal-fold vibration. Therefore, our proposed method has the potential to visualize the dynamics of the vocal fold.

REFERENCES

1. J. S. Lee, E. Kim, M. W. Sung, K. H. Kim, M. Y. Sung and K. S. Park; A method for assessing the regional vibratory pattern of vocal folds by analyzing the video recording of stroboscopy: Medical and Biological Engineering and Computing, 39, pp. 273–278 (2001).
2. S. C. Davies, A. L. Hill, R. B. Holmes, M. Halliwell and P. C. Jackson; Ultrasound quantization of respiratory organ motion in the upper abdomen: British Journal of Radiology, 67, pp. 1096–1102 (1994).
3. A. Kitabatake, T. Masuyama, M. Asao, J. Tanouchi, T. Morita, K. Ishihara, K. Fujii, H. Ito, M. Hori, M. Fukushima, M. Inoue, H. Abe and K. Chihara; Noninvasive estimation of the degree of aortic valve regurgitation using two – dimensional Doppler echo angiography: Journal of Cardiology, 14, pp. 101–102 (1984).

PRESSURE-DEPENDENT ATTENUATION OF ULTRASOUND CONTRAST AGENTS

N. Kudo, N. Hirao, K. Okada, K. Yamamoto

Graduate School of Information Science and Technology, Hokkaido University, Sapporo 060-0814, Japan; Division of Cardiovascular Disease, Sapporo-Kosei General Hospital, Sapporo 060-0033, Japan

Abstract: This paper describes a method for measuring extinction coefficients of a microbubble suspension at different probing pulse pressures. The experimental results demonstrated the usefulness of this method for evaluating acoustic properties of microbubbles of ultrasound contrast agents and also for finding the optimum exposure conditions of ultrasound.

Key words: Ultrasound contrast agent, Microbubbles, Pressure-dependent attenuation, Extinction coefficient, Absorption, Scattering

1. INTRODUCTION

Contrast echography using a microbubble suspension as a contrast agent now has an important role in diagnostic ultrasound. Many new agents have been developed in the past 10 years, and it is now widely recognized that the contrast agents have different acoustic properties and different optimal conditions of ultrasound exposure. To determine the optimal exposure conditions, it is important to understand the dynamics of microbubbles under exposure to pulsed ultrasound. Two methods have been used to evaluate characteristics of ultrasound contrast agents: direct optical observation of microbubble dynamics using a high-speed camera [1,2] and measurement of acoustic characteristics of a bubble suspension [3,4].

Differences in acoustic properties of ultrasound contrast agents are caused by differences in physical properties of microbubbles such as size

distribution of bubbles, elasticity of shell material, and nature of encapsulated gas. Basically, attenuation of typical biological tissues is not pressure-dependent in the pressure range of diagnostic ultrasound. However, attenuation caused by microbubble dynamics is strongly pressure dependent because bubbles have a wide range of motion, from small-amplitude linear oscillation to inertial cavitation. Therefore, evaluation of pressure-dependent attenuation yields much information about bubble behavior. High-speed optical observation is also useful to visualize pressure-dependent bubble dynamics [5]; however, the acoustic method described here has the advantage of enabling evaluation of the acoustic properties of a multibubble system that contains a huge number of microbubbles of different sizes [6,7].

This paper describes a method for measuring extinction coefficients of a microbubble suspension at different pressures and presents some experimental results.

2.   METHODS

The key parts of the experiment system used in this study are a small water bath and a wideband ultrasound transducer (Fig. 1). The water bath was made using a 20 mm-thick glass plate as the base plate, and the bath was filled with saline or a bubble suspension diluted with saline. A flat-faced transducer (V311-SU, Panametrics-NDT) was placed in the water bath with its immersed face parallel to the bottom plate. The transducer was driven by a Pulser/Receiver (5900PR, Panametrics-NDT) and transmitted wideband probing pulses of 10 MHz in center frequency. The transducer was also used to receive the pulses reflected from the bottom plate. The amplified signals from the Pulser/Receiver were fed to a digital oscilloscope and averaged in the time domain. The averaged signal was then transferred to a personal computer (PC), and the frequency spectrum was calculated using FFT. This procedure was repeated several times, and the frequency spectra were also averaged in the frequency domain.
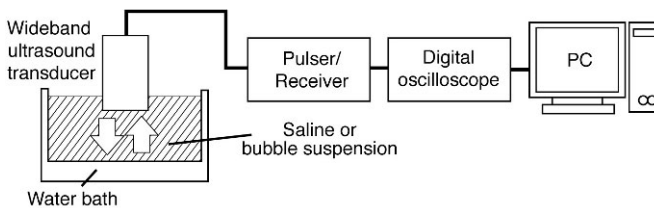
Figure 1. Experimental system.

Ultrasound propagating through a bubble suspension is attenuated by absorption and scattering of the ultrasound by the bubbles. The sum of absorption and scattering coefficients is called the extinction coefficient (Eq. 1). The frequency dependence of extinction coefficients (extinction coefficient curve) is calculated as the ratio of frequency spectra of probing pulses traveling through saline to that traveling through a bubble suspension (Eq. 2).

$$\mu_e(\omega) = \mu_a(\omega) + \mu_s(\omega) \qquad (1)$$

$$\mu_e(\omega) = \frac{P_{\text{Saline}}(\omega)}{P_{\text{Bubble suspension}}(\omega)} \qquad (2)$$

The above procedure was repeated at different pressure amplitudes of probing pulses, and pressure-dependent extinction coefficient curves were obtained. Most of the measurement procedures were automated by the PC, and the software was coded using LabVIEW. Figures 2(a) and (b) depict typical frequency spectra of probing pulses at four pressure amplitudes that propagated through saline (a) and that propagated through a microbubble suspension (b). Figure 2(c) plots extinction coefficient curves calculated as the ratio of the frequency spectra.

Two series of experiments were conducted in this study. In the first series, three types of microbubbles were used (plastic-shelled microbubbles and microbubbles of two types of ultrasound contrast agents (Levovist and Definity)). Concentrations of bubbles were fixed to 5×10^5 bubbles/ml. The stiffness of the plastic-shelled bubbles exceeded that of the agent bubbles. In the second series of experiments, bubbles of another ultrasound contrast agent, Imagent, were used, and extinction coefficients were evaluated at two different concentrations at which amplitudes of received pulses in the bubble suspension were 10% and 20% lower than that in saline.
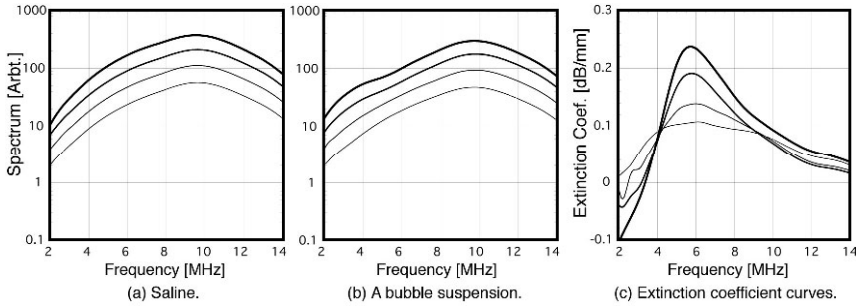
Figure 2. Typical frequency spectra of probing pulses and pressure-dependent extinction coefficient curves. (**a**) Frequency spectra of probing pulses propagating through saline and (**b**) frequency spectra of probing pulses propagating through a bubble suspension diluted with saline. (**c**) Extinction coefficient curves calculated as the ratio of (**a**) to (**b**).

3.   RESULTS

Figure 3 presents extinction coefficient curves measured in the first series of experiments using three types of microbubbles. In these measurements, pressure amplitudes of probing pulses were varied from 0.05 to 0.32 MPa.

For plastic-shelled microbubbles, the extinction coefficient curves were almost identical at all pressures of probing pulses, suggesting that the microbubbles were intact in this pressure range. For the ultrasound contrast agent bubbles, however, extinction coefficient curves exhibited pressure dependence. The rates of increase in extinction coefficient were large for Definity and small for Levovist. This means that the pressure amplitude required to activate microbubbles of Definity is lower than that required to activate microbubbles of Levovist.
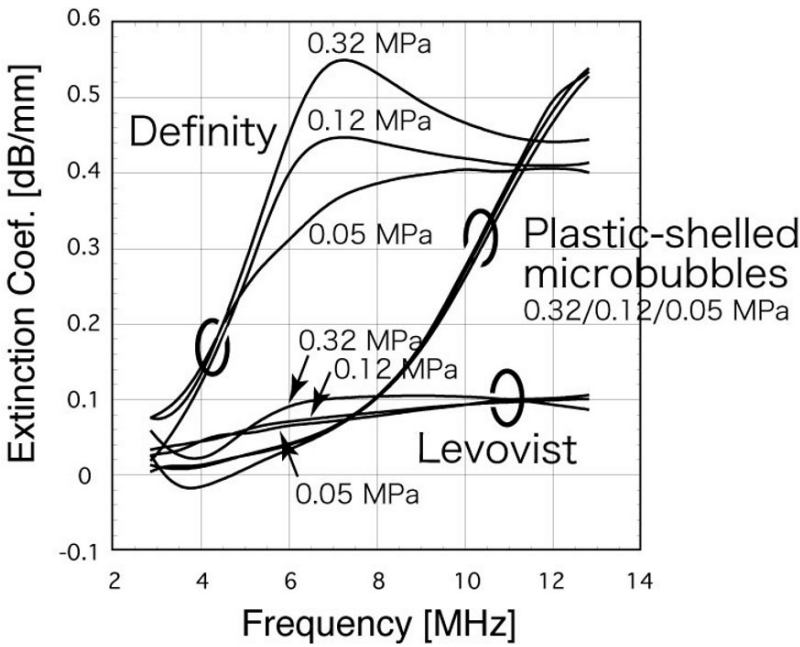
Figure 3. Pressure-dependent extinction coefficient curves of three types of microbubbles.

Figure 4 plots pressure-dependent extinction coefficient curves of Imagent microbubbles measured at two different concentrations of 10% and 20% attenuation. Pressure amplitudes of probing pulses were varied from 0.04 to 0.51 MPa in this series of experiments, and increases in extinction coefficients were clearly observed in the low-pressure range as well.

The extinction coefficient curves of Imagent had local maxima at about 4 MHz and 9 MHz. Pressure-dependent increases in the 4 MHz maxima exceeded those in 9 MHz maxima, and frequencies that produced the 4 MHz maxima shifted lower with increasing pressure of probing pulses. In these results, a reduced increase and subsequent decrease in the 4 MHz maxima were observed at higher probing pulse pressures (arrowheads, Fig. 4 (a) 0.32, 0.51 MPa and (b) 0.51 MPa). This tendency was clear, particularly for 10% attenuation (a), suggesting that Imagent bubbles collapsed when exposed to high-pressure pulses.
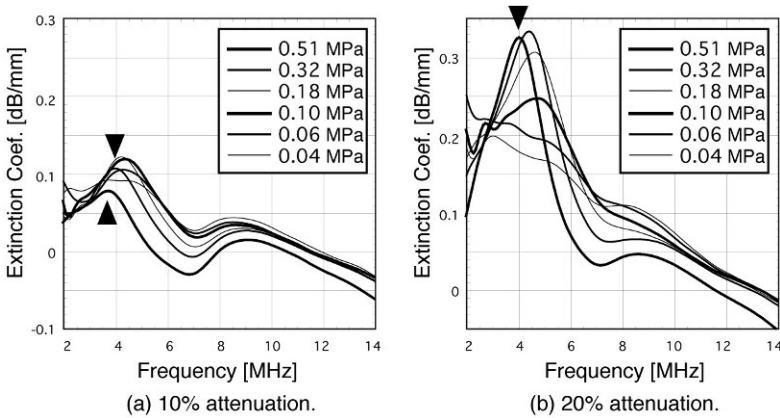
Figure 4. Pressure-dependent extinction coefficient curves of Imagent.

4.   DISCUSSION

A pressure-dependent increase in attenuation was observed only in suspensions of the ultrasound contrast agents that can oscillate at the pressure range used in the experiments, suggesting that bubble dynamics that causes heat production and secondary acoustic emission can be characterized by evaluating pressure-dependent attenuation. The difference found in the pressure amplitudes to activate Definity and Levovist microbubbles is consistent with clinical exposure conditions used for these contrast agents, demonstrating the usefulness of this method for finding the optimum exposure condition of ultrasound for an individual contrast agent.

The maxima of the extinction coefficient curves were observed at about 8 MHz for Definity and at about 9 MHz for Imagent. The frequencies that produce these maxima, which are obviously higher than the resonant frequencies of the microbubbles, are strongly affected by the center frequency of the probing pulse [7]. However, the presence of maxima of about 4 MHz (Fig. 4) demonstrates that the bubble resonant frequency and strength of bubble oscillation can be estimated by evaluating the pressure-dependent attenuation.

When evaluating pressure-dependent attenuation of a bubble suspension, the attenuation should be low because significant attenuation of a probing pulse during propagation causes bubbles to be activated by nonuniform pressure. However, low attenuation causes insufficient signal-to-noise ratio in the measurement results. Increasing the numbers of points averaged in time and expanding the frequency domain improve the signal-to-noise ratio,

but exposing bubbles to many high-pressure probing pulses will cause the bubbles to collapse. Compensation of the effect of bubble collapse is a subject of future investigation.

5.   CONCLUSION

Pressure-dependent extinction coefficient curves of microbubbles were measured, and it was demonstrated that information about bubble dynamics could be derived from the measurement results. This method is very simple and useful for evaluating acoustic properties of microbubbles and also for finding the optimum exposure conditions of ultrasound.

ACKNOWLEDGEMENTS

REFERENCES

1. N. de Jong, P.J. Frinking, A. Bouakaz, M. Goorden, T. Schourmans, X. Jingping, and F. Mastik, Optical imaging of contrast agent microbubbles in an ultrasound field with a 100-MHz camera. Ultrasound Med Biol, **26**(3), 487–492 (2000).
2. M. Postema, A. van Wamel, C.T. Lancée, and N. de Jong, Ultrasound-induced encapsulated microbubble phenomena. Ultrasound Med Biol, **30**(6), 827–840 **(2004)**.
3. N. de Jon, L. Hoff, T. Skotland, and N. Bom, Absorption and scatter of encapsulated gas filled microspheres: theoretical considerations and some measurements. *Ultrasonics* **30**(2), 95–103(1992).
4. N. de Jong and L. Hoff, Ultrasound scattering properties of Albunex microspheres. *Ultrasonics* **31**(3), 175–181(1993).
5. N. Kudo, K. Okada, and K. Yamamoto, Study on an evaluation method of shell characteristics of ultrasound contrast agent using a high-speed camera, 2003 IEEE Ultrasonics Symposium Proc., 1507–1510 (2003).
6. N. Kudo, N. Hirao, K. Okada, and K. Yamamoto, Studies on evaluation of shell parameters of microbubbles in ultrasound contrast agents using high-speed observation. IEICE Trans. **J89-A**(9), 746–753 (2006).
7. Q. Chen, J. Zagzebski, T. Wilson, and T. Stiles, Pressure-dependent attenuation in ultrasound contrast agents. Ultrasound Med. Biol. **28**(8), 1041–1051 (2002).

3-D ACOUSTIC IMAGING SYSTEM WITH A REFLECTOR AND A SMALL ARRAY

For medical diagnosis of heart diseases

H. Taki, T. Sato

Department of Communications and Computer Engineering, Graduate School of Informatics, Kyoto University, Kyoto 606-8501, Japan

Abstract: We propose an imaging system based on a hybrid method using a synthetic aperture technique for medical diagnosis of heart diseases. When the time resolution is 200 3-D images/s, the number of elements can be reduced to about 1/11 of a dense array of a digital beamforming imager having the same time and spatial resolutions.

Key words: Ultrasound, Hybrid method, Real-time, 3-D, Imaging, 2-D array, Reflector, Synthetic aperture, Digital beamforming, Phased array

1.   INTRODUCTION

We proposed a 3-D real-time acoustic imaging system based on a hybrid array-reflector configuration [1–3]. This system consists of a small 2-D element array, a reflector mirror, and an impedance matching fluid, as depicted in Fig. 1. The transmitted signal is radiated over the entire measurement field. Figure 2 schematically illustrates the system in the receive phase. The echo from a target is gathered by the reflector and then received by the array. The target images are reconstructed from the received signals using numerical back-projection. Since most of the echo reflected by the mirror is received on the array, the angular resolution and signal-to-noise ratio (SNR) of the proposed method are improved over those of a digital beamforming imager with a similarly sized 2-D array.

2.   IMPROVED SPATIAL RESOLUTION FROM MULTIPLE TRANSMIT AND RECEIVE EVENTS

In the proposed method, a 3-D image is acquired from a single transmit and receive event. When the measurement range is 0.16 m, the time resolution is 5000 3-D images/s. A lower time resolution is sufficient for medical diagnosis, and so the spatial resolution and SNR can be improved by using multiple transmit and receive events.
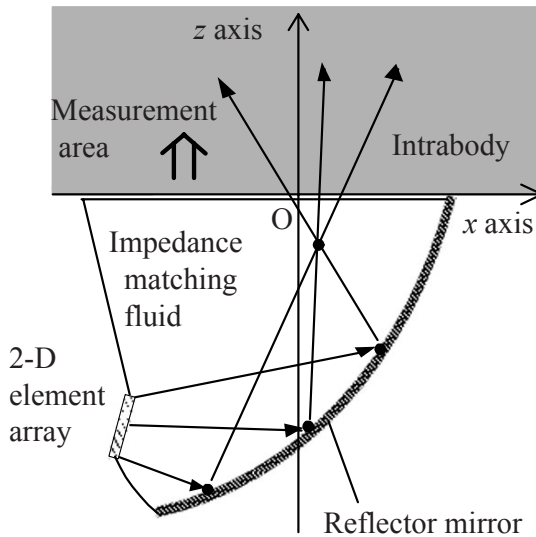
Figure 1. Schematic of the system in the receive phase.

As depicted in Fig. 2, the used area is defined as the region on the mirror where the echo from a target is reflected and reaches the array in the geometric optics. We also define an effective aperture as a section of the field between the target and the used area. Since the echo reflected at the used area is received on the array, the spatial resolution of the proposed imager is equivalent to that of a digital beamforming imager with an array the same size as the effective aperture.

For a wide transmit beam with high power, all elements of the array radiate ultrasound pulses at appropriate time delays for focusing by the reflector. The focal position can be changed by employing a different time delay. A 3-D image is then reconstructed from multiple transmit and receive

events with different focal positions. Utilizing a synthetic aperture technique [4], the coherent integration of multiple transmit and receive events equivalently enlarges the aperture size, thus improving the spatial resolution.
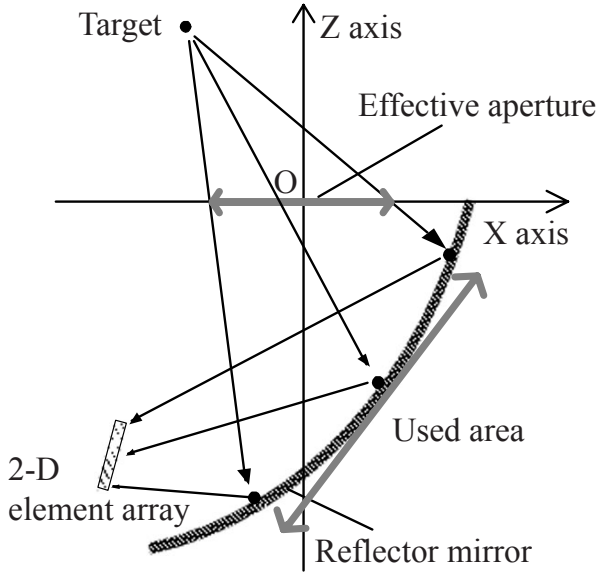
Figure 2. Schematic of the system in the transmit phase.

3. RESULTS AND DISCUSSION

Since a single transmit and receive event can make a 3-D image, the time resolution of the proposed imager is 5000 images/s when the measurement range is 0.16 m. A lower time resolution is sufficient for medical diagnosis of heart diseases. In this paper, we set the time resolution to 200 3-D images/s. The spatial resolution can thus be improved from 25 transmit and receive events using a synthetic aperture technique. Figure 3 presents an arrangement of the foci and the effective aperture in the x-y plane. Figure 4 depicts the aperture enlarged from the coherent integration of 25 transmit and receive events.

Figure 5 displays the spatial resolution of the proposed imager acquired from a single transmit and receive event and from 25 transmit and receive

events. This demonstrates the effectiveness of the synthetic aperture technique for improving lateral resolution.

We compare the spatial resolution of the proposed imager with that of digital beamforming imagers in Fig. 6. The spatial resolution of digital beamforming imagers is also improved by using 25 transmit and receive events. The x-z and y-z -3dB lateral resolutions of the proposed imager with a circular array of 0.016 m width for a 0.07 m depth are 0.99 λ and 0.93 λ. These resolutions are the same as those of a digital beamforming imager with a dense elliptic array 0.051 m long and 0.055 m wide. Since the elements are spaced at intervals of one-half of a wavelength on the array, the area of the array is proportional to the number of elements. Therefore, the number of elements can be reduced to about 1/11 of that in a digital beamforming imager having the same spatial resolution.
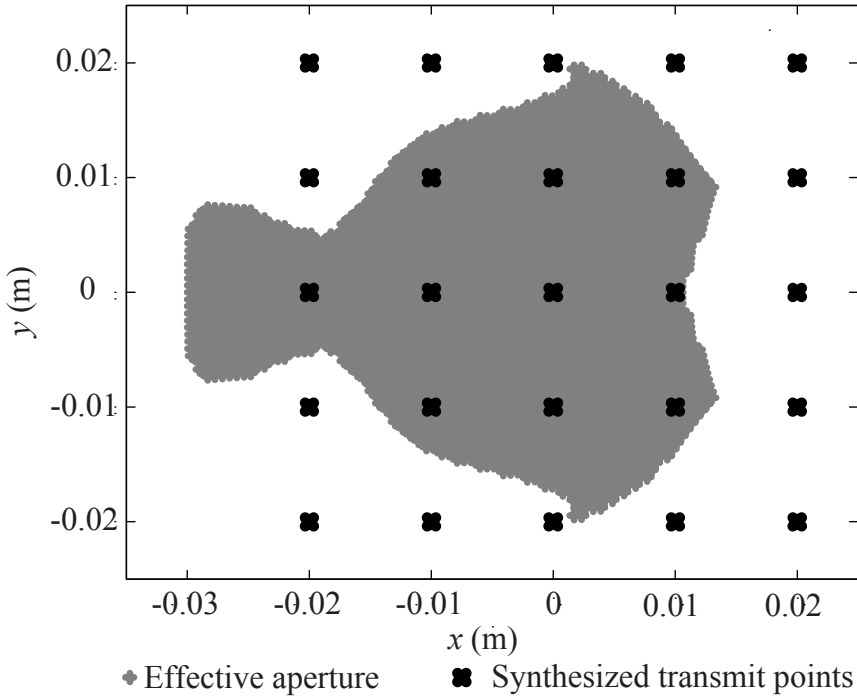
Figure 3. Arrangement of the foci and the effective aperture in the x-y plane.
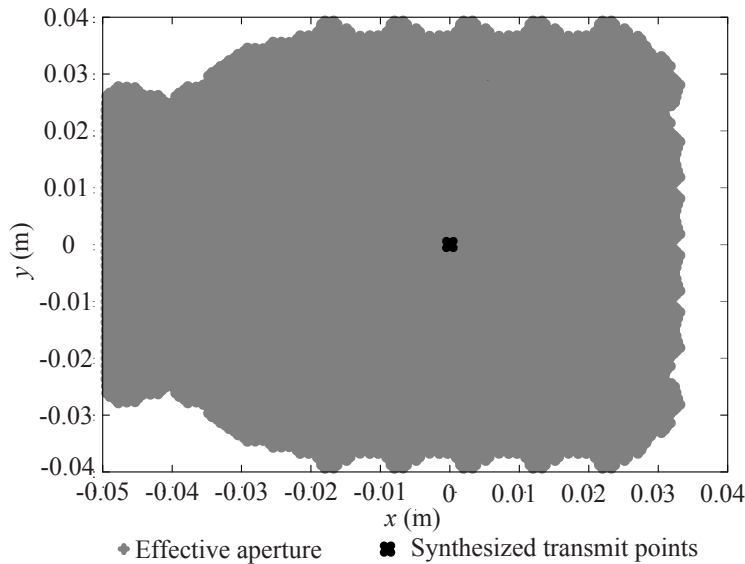
Figure 4. Synthesized aperture derived from 25 transmit and receive events in the x-y plane.
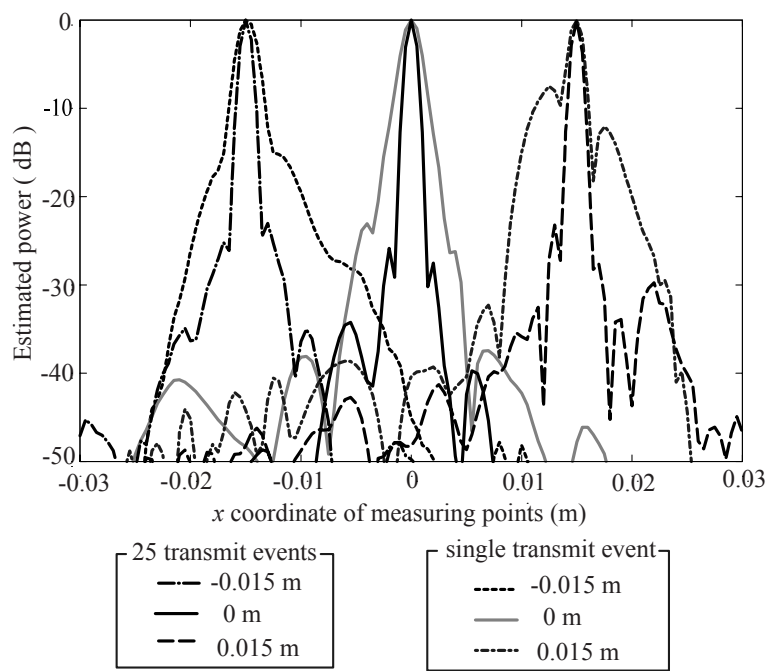
Figure 5. Lateral resolution of the proposed image acquired from 25 transmit and receive events in the x-z plane for a 0.07 m depth. A point target is placed at x = −0.015, 0, and 0.015 m in the x-z plane for a 0.07 m depth.
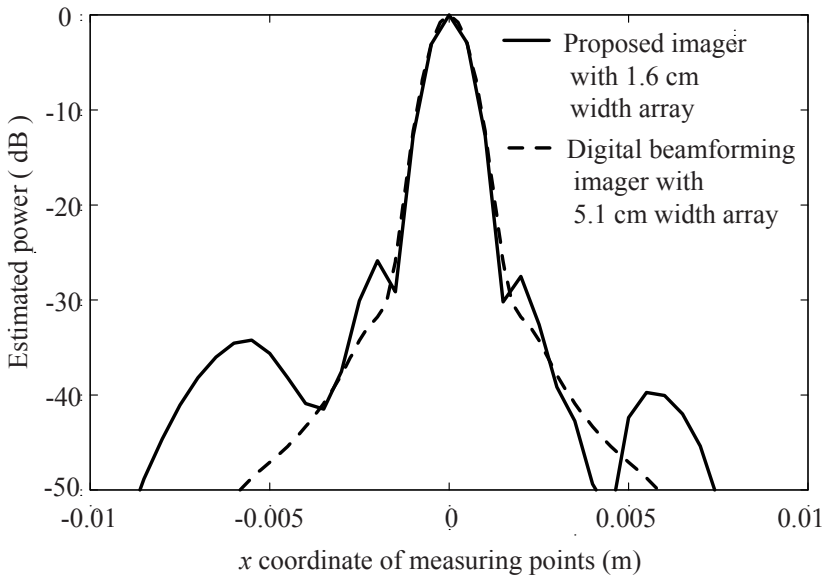
Figure 6. Lateral resolution of the proposed imager with a 0.016 m width array and digital beamforming imagers with 0.016 and 0.051 m width arrays. A point target exists at the center for a 0.07 m depth.

REFERENCES

1. H. Taki and T. Sato: Jpn. J. Med Ultrason **33** (2006) Suppl. S280 [in Japanese].
2. H. Taki and T. Sato: IEICE Tech. Rep. US106-109 (2006) [in Japanese].
3. H. Taki and T. Sato: accepted to J. Medical Ultrasonics.
4. G. R. Lockwood, J. R. Talman and S. S. Brunke: IEEE Trans. Ultrason. Ferroelec. Freq. Contr. **45** (1998) 980.

NEW METHOD FOR ULTRASOUND CONTRAST IMAGING USING FREQUENCY-MODULATED TRANSMISSION

H. Ohuchi, N. Kamiyama, T. Kawagishi, T. Imamura, T. Asanuma, H. Ishikura, S. Beppu

Toshiba Medical Systems Corp., Otawara, Tochigi 324-8550, Japan; School of Allied Health Sciences, Faculty of Medicine, Osaka University, Osaka 565-0871, Japan

Abstract: In diagnostic ultrasound imaging, microbubble-based contrast agents are currently used to enhance blood flow signals. The microbubbles in the blood vessels have various diameters and various resonant frequencies. Therefore, only some bubbles will be stimulated by a transmission pulse with a single frequency component. In this report, we propose a multiple-pulse transmission method with different frequencies to stimulate more microbubbles. We have confirmed both an increase in bubble echoes and the suppression of tissue echoes with this method. In phantom experiments, wideband bubble echoes were obtained using the proposed method, and the bubble-tissue ratio was improved by 8.3 dB as compared with the conventional second-harmonic method. In animal experiments, the tissue echoes were adequately suppressed as compared with conventional second-harmonic images.

Key words: Ultrasound contrast agent, Microbubble, Nonlinear, Frequency modulation.

1.   INTRODUCTION

In diagnostic ultrasound imaging, microbubble-based contrast agents are currently used to enhance blood flow signals. To detect the signals from the microbubbles, several second-harmonic imaging methods such as pulse inversion harmonics [1] are clinically available. In these methods, it is known that the second-harmonic signals are generated not only from the microbubbles

but also from the tissues due to nonlinear propagation, which reduces the contrast resolution of diagnostic images. Moreover, the microbubbles in the blood vessels have various diameters and various resonant frequencies. Therefore, only some bubbles will be stimulated by a transmission pulse with a single frequency component. To stimulate more microbubbles, a multiple-pulse transmission method with different frequencies is proposed. An increase in bubble echoes and the suppression of tissue echoes with this method were confirmed in this study.

2. PRINCIPLE

The definition of "frequency-modulation imaging (FMI)" is to modulate the behavior of the microbubbles by means of multiple-pulse transmission with different frequencies. Three types of pulses are transmitted in the same direction. The first and second pulses have different waveforms with different frequency components. The third transmission is the reversed waveform of the sum of the first and second pulses. (The specified waveforms are shown in the next section.) All three received signals are summed in the receiver unit, and the fundamental-frequency components are filtered. As a result of these procedures, linear echo signals due to scattering are canceled out, while the nonlinear signals, which are mainly generated from the microbubbles, are retained. It is therefore possible to extract the transient signals of the microbubbles.

3. NUMERICAL SIMULATION

The frequency spectra of the radiation sound pressure from the microbubbles in the FMI method were calculated numerically. A differential equation [2] based on the Rayleigh-Plesset equation that includes the shell parameters of the bubble was used:

$$\rho R \ddot{R} + \frac{3}{2}\rho(\dot{R})^2 = \left(P_0 + \frac{2\sigma}{R_0} + \frac{2\chi}{R_0}\right)\left(\frac{R_0}{R}\right)^{3\gamma}\left(1 - \frac{3\gamma}{c}\dot{R}\right) - \frac{4\mu}{c}\frac{\dot{R}}{R} - \frac{2\sigma}{R}\left(1 - \frac{1}{c}\dot{R}\right) \quad \cdots (1)$$

$$-\frac{2\chi}{R}\left(\frac{R_0}{R}\right)^2\left(1 - \frac{3}{c}\dot{R}\right) - 12\mu_{sh}\varepsilon\frac{\dot{R}}{R(R-\varepsilon)} - (P_0 + P_{driv}(t))$$

where R is the radius of the bubble, R_0 is the initial radius of the bubble, P_0 is the hydrostatic pressure, μ is the viscosity of the gas, μ_{sh} is the viscosity of the shell, ρ is the density of the liquid, χ is the elasticity

module of the lipid shell, γ is the polytropic gas exponent, σ is the interfacial tension coefficient, ε is the thickness of the lipid shell, and P_{driv} is the time-varying acoustic pressure. For this simulation, we set $R_0 = 2.0$ [μm], $P_0 = 101$ [kPa], $\mu = 0.001$ [Pa·s], $\varepsilon = 1.0$ [nm], $\mu_{sh} = 0.6$ [Pa·s], $\rho = 998$ [kg/m³], $\chi = 0$ [N/m], $\gamma = 1.07$, $\sigma = 0.051$ [N/m], and $P_{driv} = 200$ [kPa].

The calculation was performed with MATLAB using the fourth-order Runge-Kutta method. The transmission waveforms and their spectra are shown in Fig. 1. The transmission frequencies used were 1.5 MHz and 3.6 MHz. The waveform and spectrum from the microbubbles after summation of the three echoes are shown in Fig. 2. In these results, large nonlinear components were observed in the fundamental component.
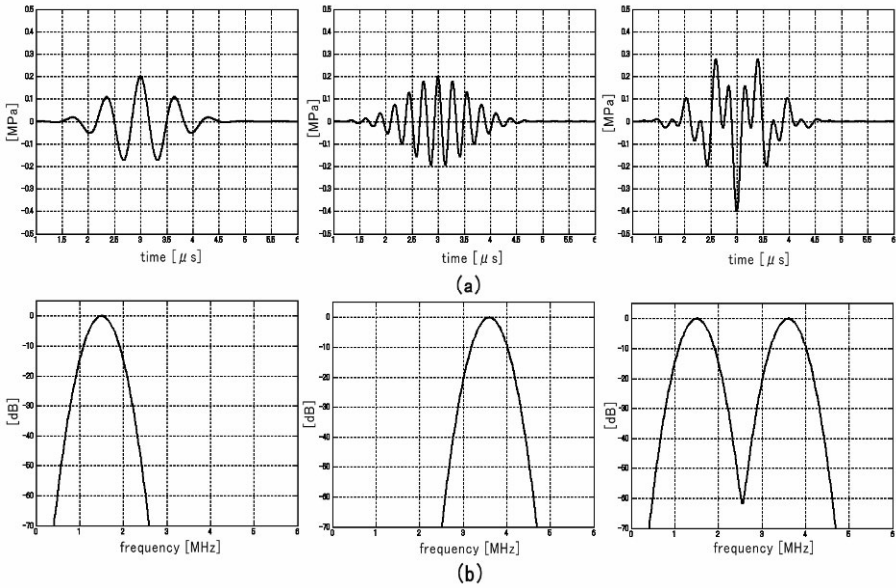
Figure 1. Transmission pulses: (**a**) waveforms of the three pulses and (**b**) their spectra.
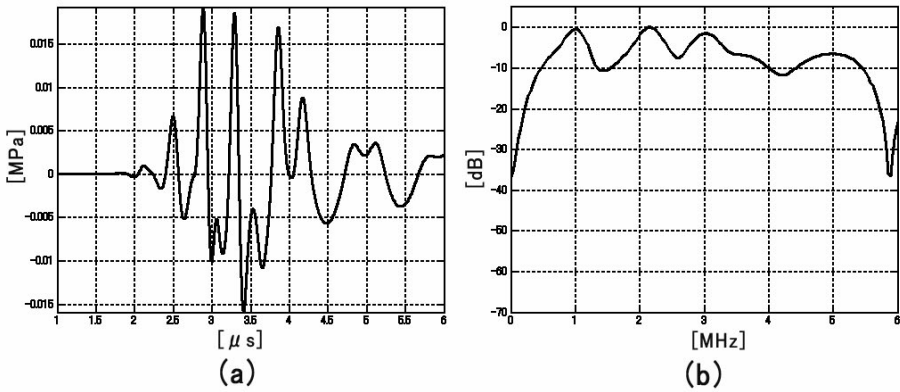
Figure 2. Echo from microbubbles after summation: (**a**) waveform and (**b**) frequency spectrum.

4.   PHANTOM EXPERIMENTS

The phantom used was an agar-graphite tissue-equivalent phantom. The ultrasound system and probe employed were an SSA-770A prototype (Aplio, Toshiba Medical Systems, Otawara, Tochigi, Japan) and a PST-25BT (sector type, 2.5-MHz center frequency), respectively. The contrast agent used was Definity^{TM} (Bristol-Myers, NY, USA). A narrow pool was made in the phantom filled with the contrast agent solution. The transmission frequencies were 1.4 MHz and 3.0 MHz, and the mechanical index was set to approximately 0.1.

Figure 3 shows a comparison of the bubble echoes for FMI and for single-frequency transmission. Using the FMI method, a wider range of frequency components of the bubble echoes can be obtained as compared with single-frequency transmission. Figure 4 shows a comparison of the echo levels from tissues for FMI and for conventional second-harmonic imaging. The amplitude of each transmission was adjusted so that the echo levels from the bubbles appeared equal. Quantifying the echo levels between the bubble and tissue regions showed that the bubble-tissue ratio was improved by 8.3 dB with the FMI method as compared with the second-harmonic method. This result suggests that the FMI method can reduce tissue echoes adequately.
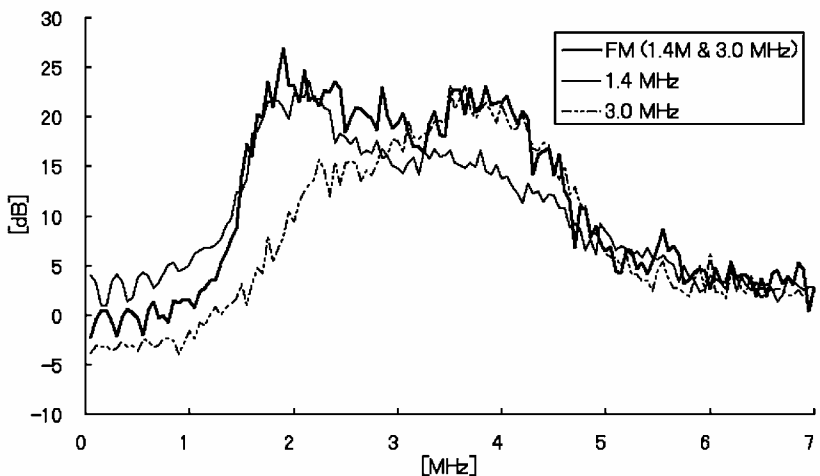
Figure 3. Comparison of bubble echoes between FMI and single-frequency transmission.

SHI   **FMI**
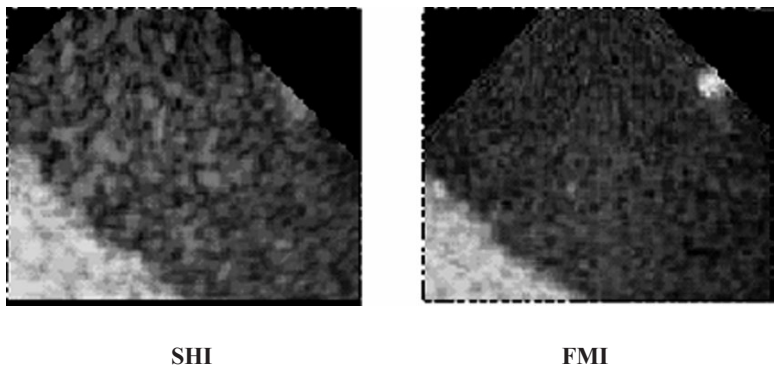
Figure 4. Comparison tissue echoes between FMI and second-harmonic imaging.

5.   ANIMAL EXPERIMENTS

An anesthetized dog was employed in these experiments. The ultrasound equipment and contrast agent were the same as used in the phantom experiments. The contrast agent was injected using an infusion pump to maintain a constant concentration in the blood. The transmission frequencies were 1.5 MHz and 3.6 MHz and the reception frequency was 2.6 MHz.

From the results of the image before injection of the contrast agent (Fig. 5a), tissue echoes from the myocardium were sufficiently suppressed. From

the results after injection (Fig. 5b), the myocardium was sufficiently enhanced by the microbubbles with high spatial resolution.
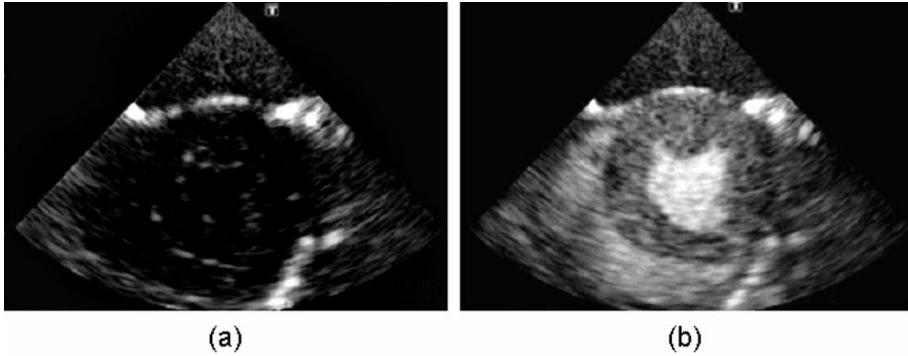
Figure 5. Myocardial contrast imaging of the dog using the proposed method: (**a**) without contrast agent, (**b**) with contrast agent.

6.   CONCLUSION

In the present study, we have confirmed that the FMI method can reduce tissue echoes and increase bubble echoes as compared with conventional second-harmonic imaging. The results suggest that this method can improve the diagnostic imaging of small blood flow such as myocardial perfusion.

REFERENCES

1. P.N. Burns et al., "Pulse inversion imaging of liver blood flow: Improved method for characterizing focal masses with microbubble contrast". Invest. Radiology, 35, 58–71 (2000).
2. K. Morgan, J. Allen, et al., "Experimental and theoretical evaluation of microbubble behavior: Effect of transmitted phase and bubble size", IEEE Trans. on UFFC, 47(6), 1494–1509 (2000).

ULTRASONIC DETECTION AND IMAGING OF BRACHYTHERAPY SEEDS BASED ON SINGULAR SPECTRUM ANALYSIS

J. Mamou, E. J. Feleppa

F. L. Lizzi Center for Biomedical Engineering, Riverside Research Institute, 156 William St., New York, NY 10038, USA

Abstract: A commonly used, effective method of treating localized prostate cancer is implantation of small radioactive seeds. The standard imaging modality for treatment-planning dosimetry and for guiding and monitoring seed implantation is transrectal ultrasound (TRUS). However, movement of the prostate during seed insertion can cause seed misplacement, hemorrhage, and clutter from calcifications and other hyperechogenic scattering objects, and the specularity of seeds themselves make detecting seeds and verifying proper dosimetry difficult in an intraoperative time frame. Radiation oncologists would find a real-time imaging system that is capable of providing accurate, post-insertion, seed-location information to be very valuable because the information would enable timely feedback for intraoperatively correcting deficiencies in the radiation dose. Therefore, a remaining challenge for TRUS-guided brachytherapy of prostate cancer is accurate detection and localization of the seeds upon their insertion.

Key words: Ultrasound, Brachytherapy seed, Singular spectrum

1.   INTRODUCTION

Implantation of seeds that contain a radioactive material into the prostate is becoming a commonly used means of treating gland-confined cancer. The standard imaging modality for treatment-planning dosimetry and seed-implantation guidance is transrectal ultrasound (TRUS). Radiation oncologists would find a real-time imaging system that is capable of

providing accurate, post-insertion, seed-location information to be very valuable because the information would enable intraoperatively correcting deficiencies in the radiation dose delivered to the gland. In our study, a new signal-processing method based on singular spectrum analysis (SSA) was investigated to detect and image seeds ultrasonically [1].

2.   METHODS
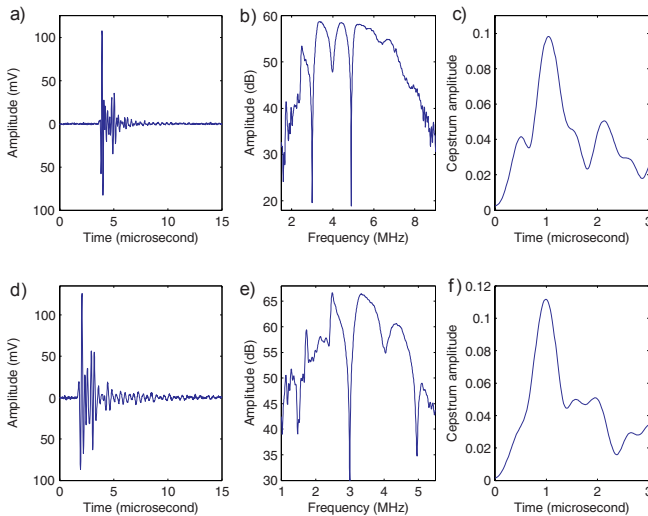
Figure 1. RF signals (**a**, **c**), log spectrum (**b**, **d**), and cepstrum (**c**, **f**) obtained from a seed with a 5-MHz transducer (*top*) and 3.5-MHz center-frequency transducer (*bottom*).

A non-radioactive titanium-shelled seed was inserted seed into an acoustically transparent gel pad. Following seed insertion, the gel pad was scanned using two, different, single-element, focused ultrasound transducers operating at center-frequencies of 3.5 and 5.0. Figure 1a and 1d show typical backscattered radiofrequency (RF) signals from the seed acquired with the 5-MHz and 3.5-MHz transducers, respectively. These signals show a first echo followed about 1 μs later by a second echo that is very similar in shape to the first echo. Figure 1b and 1e display the log power-spectra of the backscattered signals of Figs. 1a and 1d. The spectra contain periodic scallops that are about 1 MHz apart. Scallops in spectra indicate repetitions in the corresponding time signal. Figure 1c and 1f show the cepstra derived from the RF signals of Fig. 1a and 1d. These cepstra contain a single, very

clear peak near 1 µs, which indicates that repetitions exist in the original signal with a repetition period (i.e., time separation) of approximately 1 µs. Thus, a repetition frequency near 1 µs may be typical of (and possibly specific for) these seeds. Based on this observation, a signal-processing strategy based on SSA was developed to ultrasonically detect and image implanted radioactive seeds. This SSA-based strategy utilizes pairs of eigenvalues derived from the autocorrelation matrix of envelope-detected radiofrequency echo signals to identify seed-specific signal repetitions (i.e., the 1-µs repetition period). The power spectrum associated with a repetition signal is computed to derive a P-value indicative of the likelihood of the presence of a seed at the location of that repetitive signal. P-values throughout each scan plane then are color-coded and superimposed on the corresponding conventional grayscale ultrasound images. These new ultrasound images, termed P-mode images, potentially are usable by clinicians to locate seeds.

3. RESULTS

3.1 Simulations
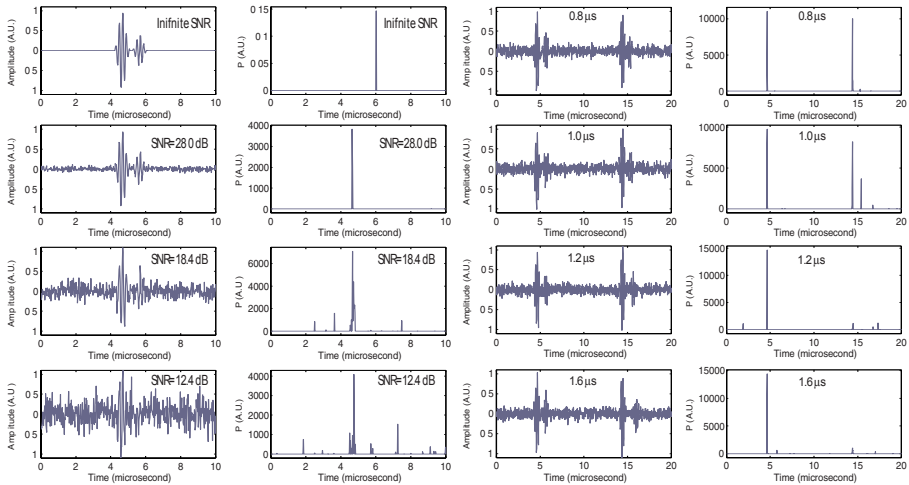
Figure 2. Evaluation of the SSA algorithm with simulations.

The SSA algorithm was first evaluated using simulations. The simulations consisted of running the algorithm on simulated RF signals containing repetitions of various repetition periods and levels of white noise. Figure 2 demonstrates that the algorithm is robust to noise and very selective to the chosen repetition frequency (here 1 μs).

3.2   Seed in a Gel Pad
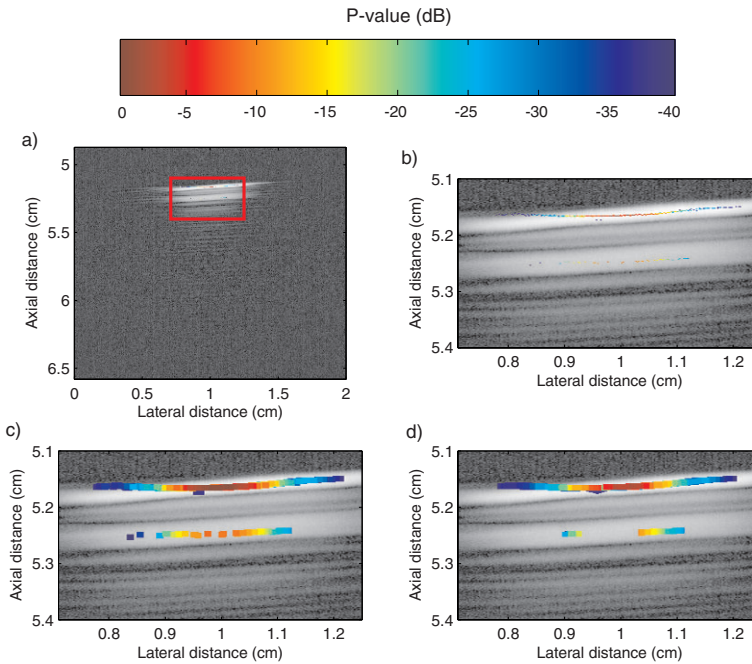
Figure 3. Images of a single seed in an acoustically transparent gel pad; (**a**) P-mode image of a seed in gel pad; (**b**) zoomed-in version of the red rectangle of (**a**); (**c**) dilated version of (**b**); and (**d**) median-filtered version of (**c**).

We evaluated the SSA method in the ideal case of a 5-MHz scan of a seed in an acoustically transparent gel pad. The reconstructed P-mode image is displayed in Fig. 3a. This image was reconstructed by retaining the P-values that fell within a 40-dB dynamic range. All of the P-values in the 40-dB dynamic range are very well localized in the red rectangle. No leakage of high P-values occurred outside the actual seed location. To improve the reconstructed P-mode image, we consecutively applied two non-linear image-processing steps: dilation (Fig. 3c) and median filtering (Fig. 3d). The

final P-mode image (Fig. 3d) shows excellent results; the seed is clearly visible and the SSA algorithm does not produce any false-positive indications.

3.3 Ex vivo Experiment
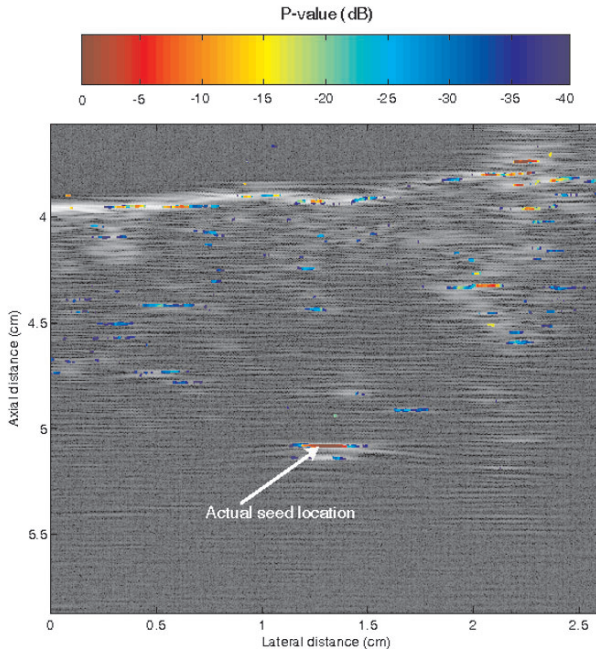
Figure 4. P-mode image obtained with a 3.5-MHz transducer of a seed inserted in beef.

A seed was implanted in a degassed piece of fresh beef; and several planes were scanned with the 3.5-MHz transducer and processed using our SSA algorithm. In this setting, the true location of the seed was well known because it was implanted into the piece of previously degassed beef with a needle. This experiment is meaningful because biological tissues are strong generators of speckle, and because the small, spatial variations of acoustical properties that exist in tissue create clutter and phase aberrations. Figure 4 shows a P-mode image obtained ex-vivo. In Fig. 4, the largest P-value is at the actual seed location, and we can state confidently that the seed is localized using our SSA methodology. However, in the same image, significant P-values are scattered along the water-meat interface. In

particular, a strong (about -3 dB) P-value is displayed at an axial distance of approximately 3.7 cm and a lateral distance of 2.25 cm. In the absence of prior knowledge, this component might be interpreted as a seed, and if so, would represent a false-positive. The only other possible false positive is located at an axial distance of 4.4 cm and a lateral distance of 2.1 cm. The P-values at that location are about −10 dB so that even though these values are significantly lower than those of the actual seed, this connected component possibly might be interpreted as a seed.

4.   CONCLUSIONS

The results of this study showed an encouraging potential of SSA for seed detection and imaging. The algorithm is fast and all the signal processing is conducted on envelope-detected signals. Simulations and basic experiments demonstrated the feasibility of the SSA method for clinical seed imaging applications. The algorithm is currently being evaluated for robustness with respect to seed angle.

ACKNOWLEDGEMENTS

REFERENCES

1. J. Mamou and E. J. Feleppa, "Singular Spectrum Analysis Applied to Ultrasonic Detection and Imaging of Brachytherapy Seeds," J Acoust Soc Am, vol. 121, pp. 1790–1801, 2007.

EVALUATION OF POST WALL FILTER FOR DOPPLER ULTRASOUND SYSTEMS

T. Baba

Toshiba Medical Systems Corporation, 1385, Shimoishigami, Otawara-Shi, Tochigi, Japan, 324-8550

Abstract: Recent advances in digital devices permit high-performance signal processing to be performed with ease. In conventional Doppler ultrasound examinations, the weak blood flow signals are separated from clutter signals, such as those from the cardiac valves and walls, using a time domain pre wall filter in order to avoid saturation of the subsequent frequency analyzer. At this time, due to the expanded dynamic range in signal processing, we have conducted investigations to determine whether it is possible to eliminate the pre wall filter and replace it with a post wall filter after the frequency analyzer. The results of these investigations showed that it is possible to obtain frequency characteristics equivalent to those obtained with a pre wall filter by compensating for the sampling function in frequency analysis processing and simplifying Doppler signal processing. Moreover, it was found that both blood inflow signals and mitral valve motion in the left ventricle can be observed without saturation, confirming the feasibility of real-time simultaneous display using a post wall filter.

Key words: Doppler ultrasound, FFT, Sampling function, Wall filter, Post filter, Mitral valve, Left ventricle.

1.   PROBLEM OF CONVENTIONAL SYSTEM

In a conventional system as shown in Fig. 1, the dynamic range in signal processing is narrow and the received signals are likely to exhibit saturation. The strong echoes received from structures such as the vascular walls and myocardium (clutter signals) therefore cannot be completely eliminated, and as a result, the blood flow detection sensitivity is reduced. The time domain pre wall filter was originally intended to limit the dynamic range of the frequency analyzer and the audio signal processor in subsequent stages [1,2].

Recently, however, signal saturation is less likely to occur because the input dynamic range of the digital beam former and the Doppler frequency analyzer has been expanded [3].
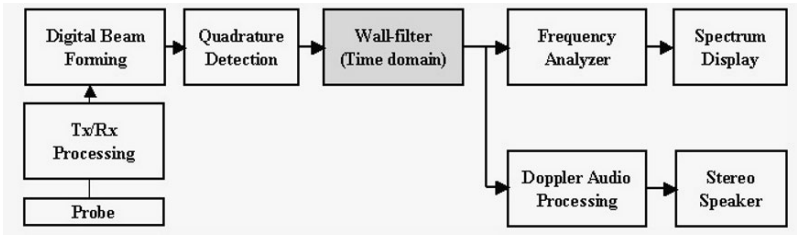
Figure 1. Signal processing in a conventional Doppler ultrasound system.

Figure 2 shows the Doppler shift signal and its spectrum for the left ventricle acquired without the wall filter. Figure 2 (a) shows the Doppler signal after quadrature detection. The broken line indicates the I component and the solid line indicates the Q component. Figure 2 (b) shows the spectra for sampling ranges [1] and [2] set in Fig. 2 (a). As can be seen in these spectra, there is power difference of 40 to 60 dB between the clutter component and the blood flow component.

(a) IQ signal sampled with RG set to 80 mm   (b) Spectra for sampling ranges [1] and [2]
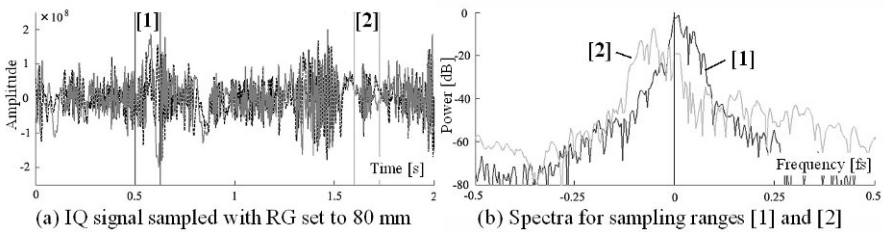
Figure 2. Doppler signal and spectra (without wall filter).

We investigated the possibility of replacing the time domain pre wall filter before frequency analysis with a post wall filter after frequency analysis. The post wall filter has two advantages. The first advantage of the post wall filter is that it reduces the computational load on the hardware. The second advantage of the post wall filter is that it reduces the transient response inherent to a time domain pre wall filter [4,5]. A time domain pre wall filter is a high-pass filter and is therefore inevitably associated with significant transient response due to changes in the conditions of the system or other factors. Figure 3 shows spectrum images of sine waves containing white noise. A large DC change was applied at time 0.35 s. Figure 3 (a) shows a response image of the pre wall filter and Fig. 3 (b) shows a response image of the post wall filter. Ringing is reduced in the post wall filter image, demonstrating that this filter is effective in reducing the transient response.
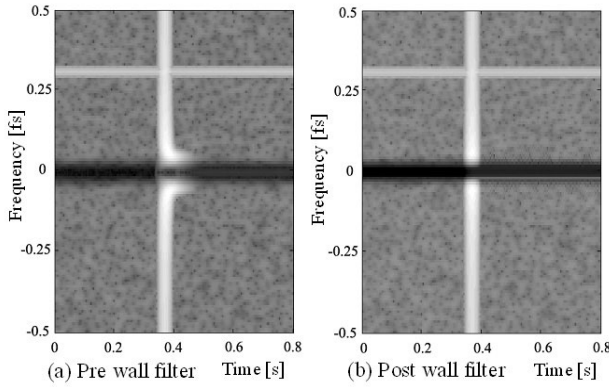
Figure 3. Comparison of transient response.

2. SIMULATION AND RESULTS

Figure 4 shows a block diagram of the simulation. The input signal was a chirp wave mixed with white noise. The number of FFT points was set to 128, a 4th-order Butterworth filter was used, and the filter cutoff frequency was set to 0.1. For comparison, an image obtained with a conventional pre wall filter was specified as SD (spectrum display) 1, an image obtained with a frequency domain post wall filter with ideal characteristics was specified as SD2, and an image obtained with a frequency domain post wall filter compensated for the sampling function was specified as SD3.
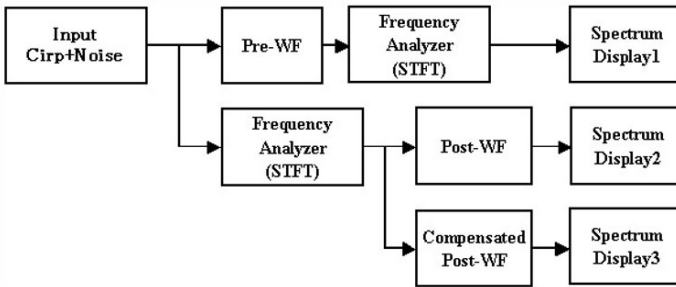
Figure 4. Block diagram of signal processing simulation.

SD2 shows steeper cutoff characteristics than SD1 because there is no spread of the spectrum in the cutoff region. This is because the influence of the sampling function was not taken into consideration. Spectrum images were obtained by short-time Fourier transform (STFT), and the effects of the STFT sampling function should therefore be taken into consideration [6–8]. In

order to achieve cutoff characteristics equivalent to SD1 with the post wall filter, convolution between the sampling function and the ideal cutoff characteristics in the frequency domain is required.

The images corresponding to SD1, SD2, and SD3 in Fig. 4 are shown in Fig. 5 (a), (b), and (c), respectively. The steeper cutoff characteristics shown in SD2 were uncomfortable to users familiar with the characteristics shown in SD1. SD3, compensated for the sampling function, shows cutoff characteristics similar to those shown in SD1.
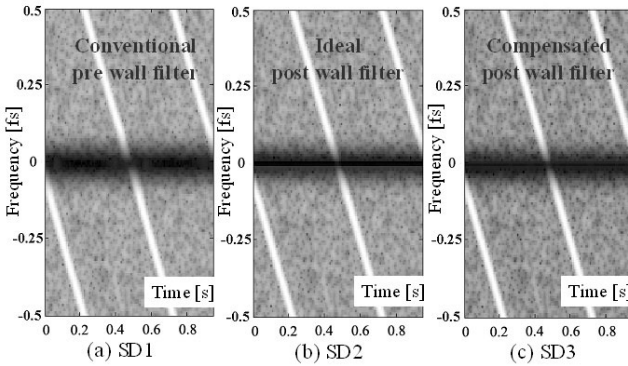
Figure 5. Comparison of STFT images.

The results of image quality simulation showed that a post wall filter compensated for the sampling function can provide cutoff characteristics similar to those of a pre wall filter. Based on these results, we replaced the pre wall filter with one with lower-order characteristics and succeeded in significantly reducing the computational load. A low-order pre wall filter was used rather than no pre wall filter in order to eliminate the DC component. This filter also has the advantage of reducing the internal word length due to its low transient response. With regard to the Doppler audio processing system, we developed a complex band-pass filter [9,10] with asymmetric band-pass characteristics in order to enhance its ability to eliminate the clutter component.

3.   PROSPECTS FOR NEW CLINICAL APPLICATIONS

As suggested in the previous section, it is expected that expanding the dynamic range of the ultrasound signal processing system should permit the simultaneous evaluation of the blood flow spectrum and valve clutter spectrum. Figure 6 shows a system for analyzing left-ventricular inflow and

the mitral valve. In this system, the valve clutter component is separated from the blood flow velocity component using two post wall filters with different characteristics, after which two spectrum images are generated. The system then performs conventional PWD (Pulse Wave Doppler) and TDI (Tissue Doppler Imaging) [11,12].
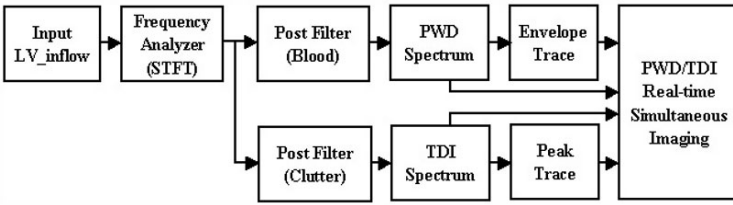
Figure 6. Feasibility study for new clinical application.

(a) PWD image and envelope trace

(b) TDI(PWDTDI) image and peak trace

(c) Simultaneous display
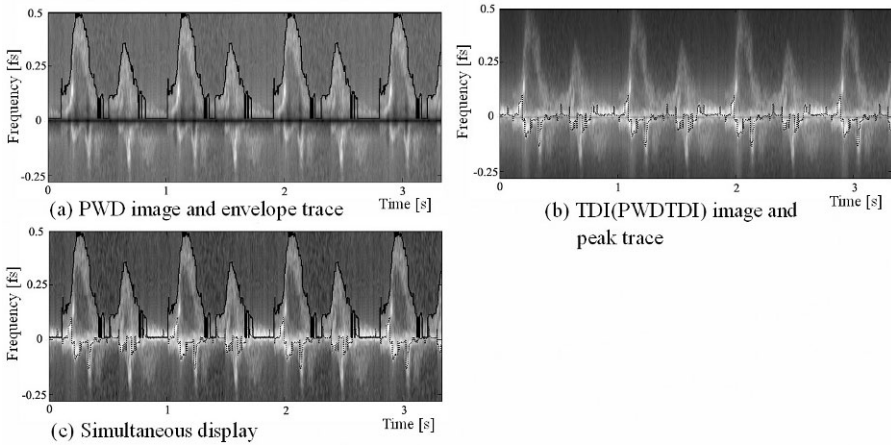
Figure 7. PWD/TDI simultaneous image.

Figure 7 (a) shows the blood flow spectrum separated using a high-pass filter with cutoff frequency 0.1 and its envelope trace. Figure 7 (b) shows the mitral valve spectrum separated using a low-pass filter with cutoff frequency 0.2 and its peak trace. Figure 7(c) shows the original spectrum on which the two trace waveforms are superimposed. Since the blood flow velocity and mitral valve clutter velocity can be measured at the same time, this method is expected to be useful for the evaluation of patients with cardiac hypertrophy etc. [13,14].

4.   SUMMARY

There have been significant advances in high-speed and high-dynamic-range signal processing technologies. Given this background, we investigated the use

of a frequency domain post wall filter rather than a time domain pre wall filter intended to limit the dynamic range of the frequency analyzer. The results showed that using a frequency domain post wall filter compensated for the sampling function can markedly reduce the computational load. In addition, this method is useful for obtaining left ventricular inflow data and mitral valve clutter data simultaneously without saturation. The blood flow component and the mitral valve clutter component are extracted separately from a spectrum containing both the blood flow spectrum and the valve clutter spectrum. These findings suggest that this method may open up new possibilities in ultrasound diagnosis.

REFERENCES

1. Jorgen Arendet Jensen, 1996, *Estimation of blood velocities using ultrasound: A signal processing approach,* Cambridge University Press, New York, pp. 111–114.
2. Steinar Bajarum, Hans Torp and Kjell Kristoffersen, Clutter filter design for ultrasound color flow imaging, *IEEE UFFC,* **49**(2), 204–216 (2002).
3. T. Baba, Investigation of auto gain control tecqunique in Doppler ultrasound system, *Proc. J. Acoust. Soc. Jpn.*, p. 54 (2006)
4. R. N. Bracewell, 2000, *The Fourier Transform and Its Applications,* McGraw-Hill Companies Inc., Boston, pp. 385–398.
5. V. Cappellini, A. G. Constantinides and P. Emiliani, 1978, *Didital Filters and Their Applications*, Academic Press Inc., London, pp. 161–185.
6. T. Baba, Investigation of time scale optimization for Doppler measurement, *Proc. J. Med Ultrasound Soc. Jpn.*, **2005**(4), pp. 29–34 (2005)
7. T. Araki, 1985, *The Communication System Theory and Reality*, Kogaku Tosho Co., Inc., Tokyo, pp. 78–83.
8. K. Maeda, A. Sano, H. Takaie and S. Hara, 2001, *Wavelet Transform and Its Application*, Asakura Publishing Co., Ltd., Tokyo, pp. 67–81.
9. T. Baba, The investigation of the direction split technique of the Doppler ultrasound: Comparison of six kinds of Doppler audio processing, *J. Soc. Signal Processing Applications and Technology of Japan*, **8**(2), 14–20 (2005).
10. T. Baba, Investigation of the audio direction separation in Doppler ultrasound system: Signal processing of Doppler audio for aliasing, *J. Acoust. Soc. of Jpn.,* **62**(3), 153–160 (2006).
11. Hiroshi Kanai and Yoshiro Koiwa, Myocardial Rapid Velocity Distribution, *Ultrasound in Med. & Biol.,* **27**(4), 481–498 (2001).
12. Cecilia Wallentin Guron, MD, Marianne Hartford, MD, PhD, Anita Persson, MSC, Johan Herlitz, MD, PhD, Dag Thelle, MD, PhD, and Kenneth Caidahl, MD, PhD, Timing of Regional Left Ventricular Lengthening by Pulsed Tissue Doppler, *J. Am. Soc. Echocardiography*, **17**(4), 307–312 (2004)
13. Jennifer Lisauskas, Jasvindar Singh, Michael Courtois and Sandor J. Kovacs, The Relation of the peak Doppler E-wave to peak mitral annulus velocity ratio to diastolic function, *Ultrasound in Med. & Biol.,* **27**(4), 499–507 (2001)
14. Christian Bruch, MD, Rainer Gradaus, MD, Stefan Gunia, MD, Gunter Breithardt, MD, FACC, and Thomas Wichter, MD, Doppler Tissue Analysis of Mitral Annular Velocities, *J. Am. Soc. Echocardiography*, **16**(10), 1031–1036 (2003)

COMBINING ULTRASONIC AND MAGNETIC-RESONANCE SPECTRAL METHODS FOR IMAGING PROSTATE CANCER

E. Feleppa, S. Dasgupta, S. Ramachandran, J. Ketterling, A. Kalisz, C. Porter, M. Lacrampe, C. Isacson, S. Haker, C. Tempany
Riverside Research Institute, New York, NY 10038; Virginia Mason Medical Center, Seattle, WA 98101; Brigham and Women's Hospital, Boston, MA 02115

Abstract: We aim to improve existing prostate tissue type imaging methods to better distinguish between cancerous and noncancerous prostate tissue. In doing so, we hope to increase the effectiveness of biopsy guidance, therapy targeting, and treatment monitoring. Spectral parameters obtained from radiofrequency (RF) ultrasonic (US) echo signals acquired from biopsy regions, along with the PSA level were used to train a neural network classifier. This method produced an ROC curve area of 0.84 compared to 0.64 obtained from Bmode, image-based classification. In order to further improve our prostate tissue typing methods, the integration of ultrasonic and magnetic resonance (MR) methods, to take advantage of the independent information provided by US and MR is being investigated. We are developing effective means of 3D spatial coregistration of US and MR data along with histological data used for validation.

Key words: Ultrasound spectra, Magnetic resonance spectra, Prostate cancer imaging, Spectral parameters

1.   INTRODUCTION

Prostate cancer is the second-leading cause of cancer death in men in the United States [1]. Many men are not accurately diagnosed due to the inability of existing transrectal ultrasound (TRUS) imaging to reveal cancerous prostate tissue reliably for biopsy targeting. As a result, prostate cancer often is detected only at an advanced stage, when the disease is difficult to treat.

We currently use artificial neural networks to classify prostate tissue into cancerous and noncancerous types based on the values of ultrasound spectral (USS) parameters and PSA level [2–4]. We aim to improve our existing prostate tissue typing methods by including in our classifier, independent prostate tissue properties sensed by magnetic resonance (MR) techniques such as the cholinetocitrate ratio detected by MR spectroscopy (MRS) [5–8].

The probes used for data acquisition deform the prostate differently in each imaging modality; furthermore, scan planes used in the two modalities are likely to differ in location and orientation. Successfully combining the independent parameters provided by USS and MRS requires accurate spatial coregistration of the data acquired by the two modalities.

2.   METHODS

An artificial neural network (ANN) classifier was trained using USS parameters computed from US radio frequency (RF) data acquired from 617 biopsy regions during prostate examinations of 64 patients. Biopsy-core histology spatially matched to US echosignals from the biopsy location was used as the gold standard for training the ANN. ROC analysis provided our assessment of ANN performance. A lookup table generated from the classifier returned cancer-likelihood scores for various combinations of USS-parameter and PSA values [2,3].

In order to assess the feasibility of spatially coregistering and combining USS, MRS, and histology information, we used a prostate phantom (CIRS Inc. Norfolk, VA) with 3 hypoechoic inclusions. We took two series of transverse scans, with 2 mm spacing between consecutive scan planes. The first scan series was performed with a Hitachi EUB525 scanner (Hitachi Medical Systems America, Inc., Twinsburg, OH) using a transrectal US probe to acquire echosignal data. The second scan series was performed with a 3T magnetic resonance (MR) imager (GE Healthcare, Waukesha, WI) using a standard clinical endorectal coil and balloon. In both cases, the extent to which the prostate phantom was deformed by the US and MR probes was comparable to deformations occurring in clinical prostate examinations; the prostate phantom was deformed less by the smaller US probe.

3D renderings of the prostate phantom were generated from the MR and US transverse scans using Amira 3D visualization and volume-modeling software (Mercury Computer Systems Inc., Chelmsford, MA). Amira was used to warp the MR rendering in 3D to correct for the greater phantom deformation caused by the endorectal coil and balloon compared to the US transrectal probe. The urethra and gland boundaries in the US volume rendering were used as a reference for coregistration. The positions of the

inclusions in the phantom before and after warping served as a measure of how well our warping methods were able to compensate for the distortions. We then applied our warping methods to 3D renderings generated from US, MR, and histology images acquired from a clinical prostatectomy case. Finally, coregistered MR and US images were generated by volumetric matching of MR images with US images using soft-tissue deformation models.

3. RESULTS

The ROCcurve area for US neural network based classification was 0.84 compared to the ROCcurve area of 0.64 for B-mode-based classification of the same biopsy sites. Our tissue-type images exposed cancerous regions that were not visible in conventional US images [4].

Figure 1 shows a 3D image of the prostate phantom made from transverse US and MR scans. The figure illustrates how the phantom prostate volume rendering generated from MR scans is flattened to a greater degree compared to the US rendering because of the larger endorectal probe used in MR imaging. Using the US image as the reference, the prostate with its inclusions and the urethra are correctly positioned relative to the gland boundaries in the MR rendering; however, they appear larger in the MR rendering because of the poorer spatial resolution of the MR data. In the MR renderings, the 1-cm inclusions appear to have a diameter of 1.3 cm and the 0.7-cm urethra appears to have a diameter of 1 cm.
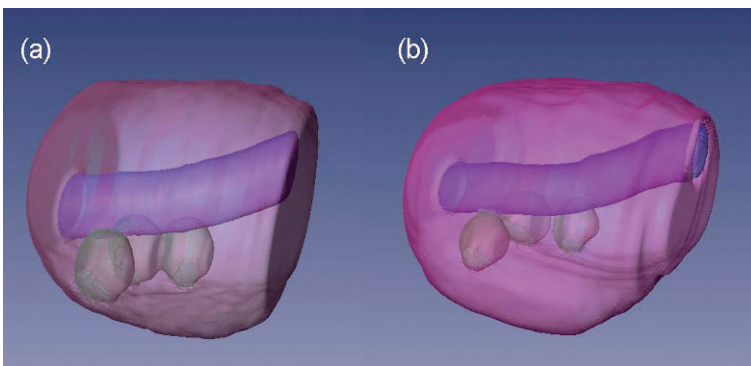
Figure 1. Prostate phantom with inclusions: (**a**) MR before warping, (**b**) US.

After applying the warping methods described previously, the inclusions in the phantom moved into the correct position (Fig. 2).
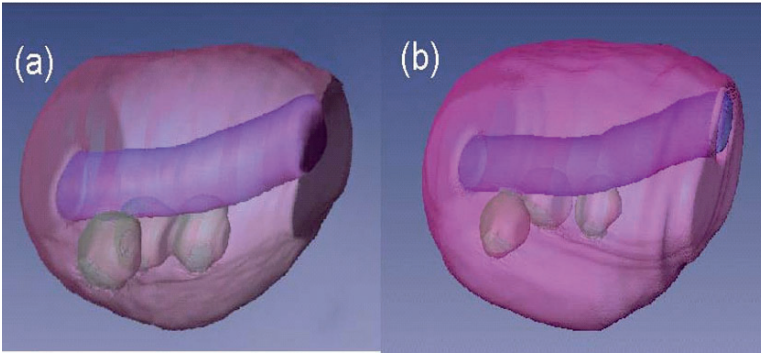
Figure 2. Prostate phantom with inclusions: (**a**) MR after warping, (**b**) US.

Figure 3 shows 3D renderings of the prostate generated from transverse US and MR scans and from histology images. As in the case of the prostate phantom, the large endorectal MR coil results in the severely flattened appearance of the prostate in the MR rendering compared to the US rendering. The 3D histology rendering is generated from transverse plane wholemount depictions reconstructed from separate quartermount thin sections of the surgically removed specimen. As a result of distortion during histological preparation and the reconstruction, the gland shape in the histological rendering is different from the shape in the US and MR 3D renderings. We compensated for these differences using the US image as a reference and warping the MR and histology data as in the phantom renderings (Fig. 4).
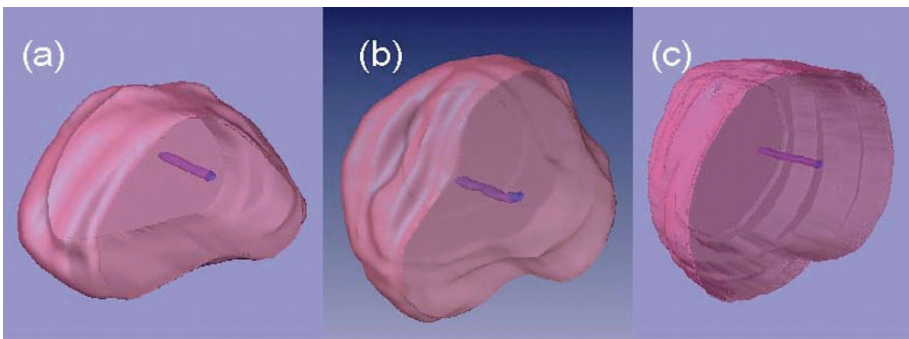
Figure 3. 3¬D volumes generated from unwarped data: (**a**) MR, (**b**) US, and (**c**) histology.
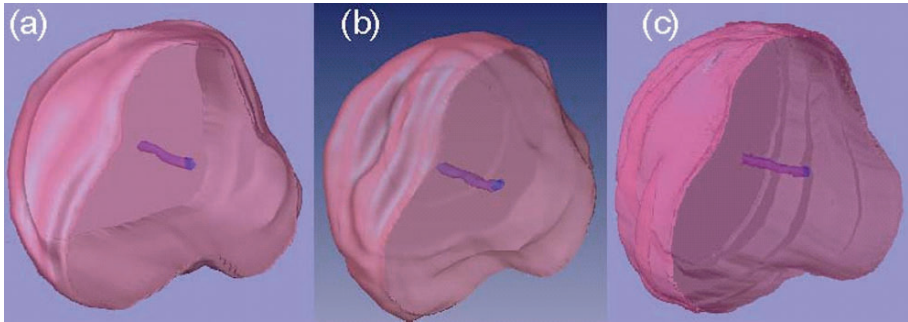
Figure 4. 3¬D renderings after deformation compensation of the volumes in Fig. 3: (**a**) MR, (**b**) US, and (**c**) histology.

Crosssections through the 3D US and MR volumes are shown in Fig. 5. After warping the MR volume, the corresponding planes from the two imaging modalities more closely resemble each other.

Figure 5. Cross¬section of 3¬D volumes from Fig. 4: (**a**) US, (**b**) MR before warp (**c**) MR after warp.

An example of MR to US prostate registration is shown in Fig. 6. The image in the top left of the figure shows a midgland axial slice through an US image volume taken at the start of a brachytherapy procedure at Brigham and Women's Hospital, and at top right is a slice through a T2-weighted MR image volume, at a similar spatial position, taken prior to therapy. The bottom image in the figure is created by volumetric registration using a novel 3D algorithm developed at Brigham and Women's; it shows a slice through a synthetic image volume of the 3D-US image data created by digitally excising the gland from the US volume and replacing it with the image data from the spatially matching slice from the registered MR volume [7,8]. Excellent agreement exists between the MR and US depictions of the boundary between the peripheral (PZ) and central zones and the location and extent of hyperplastic regions (BPH) in the central zone.
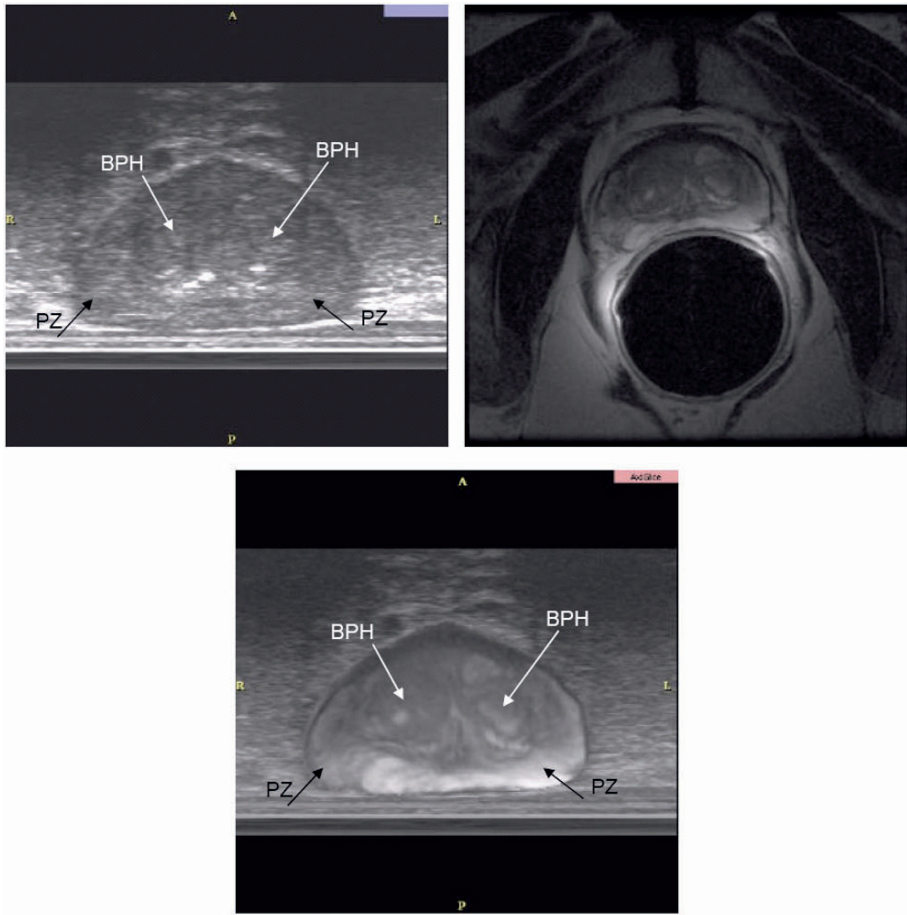
Figure 6. MR¬to¬US registration by volumetric registration to create a fused image.

4. CONCLUSION

We currently are able to warp 3D renderings of the prostate successfully to compensate for the different deformations introduced by the US and MR probes and, for the different orientations and locations of US and MR scan planes. Although not shown here, we similarly are able to compensate for artifactual distortions by histology-specimen preparation. Therefore we can produce accurately coregistered 3D data volumes acquired from US, MR, and histology to train our ANNs and validate our tissue-typing methods. Success in depicting cancerous regions in the prostate by combining USS

and MRS parameters will be invaluable for noninvasively diagnosing prostate cancer, for planning its treatment, and for monitoring its progression over time.

ACKNOWLEDGEMENTS

REFERENCES

1. Cancer Facts and Figures 2006 (American Cancer Society, 2007) 10
2. E. Feleppa, S. Dasgupta, S. Ramachandran, J. Ketterling, C. Porter, M. Lacrampe, D. Dail: Proc. IEEE Ultrason. Symp. (2006)
3. E. Feleppa, C. Porter, J. Ketterling, S. Dasgupta, S. Ramachandran, D. Sparks: Acoust. Imag. 28 (2006) 335
4. E. Feleppa, C. Porter, J. Ketterling, P. Lee, S. Dasgupta, S. Urban, A. Kalisz: Ultrason. Imag. 26 (2004)163
5. J. Kurhanewicz, D. Vigneron, R. Males: Rad. Clins. N. Am. (2000) 115
6. J. Kurhanewicz, D. Vigneron, H. Hrickak, P. Carroll, P. Narayan, S. Nelson: Radiol. 198 (1996) 795
7. S. Haker, S. Warfield, C. Tempany: Proc. Med. Image Computing and ComputerAssisted Intervention, LNCS 3216 (2004) 853.
8. S. Angenent, S. Haker, A. Tannenbaum, R. Kikinis: IEEE Trans on Med Imag. 18 (1999) 700

RADIO FREQUENCY SIGNAL ANALYSIS FOR TISSUE CHARACTERIZATION OF CORONARY ARTERY: IN VIVO INTRAVASCULAR ULTRASOUND STUDY

T. Iwamoto, Y. Saijo, A. Tanaka, E. S. Filho, S. Li, M. Yoshizawa
Graduate School of Engineering, Tohoku University, Sendai, 980-8579, Japan; Institute of Development, Aging and Cancer, Tohoku University, Sendai, 980-8575, Japan; Faculty of Symbiotic Systems Science, Fukushima University, Fukushima, 960-1296, Japan; Information Synergy Center, Tohoku University, Sendai, 980-8578, Japan

Abstract: Intravascular ultrasound (IVUS) is an important clinical tool that provides high resolution cross-sectional image of coronary artery. However, it is difficult to accurately classify plaque composition by conventional IVUS images. In the present study, we apply self-organizing map (SOM) of radiofrequency (RF) signal spectra for automatic plaque classification in IVUS diagnosis. IVUS data were acquired with a commercially available IVUS system with the central frequency of 40 MHz. We used double SOM classifier. The 1st classifier is supervised-SOM, learned four structures (blood, catheter, shadow, and outer lumen) based on spectral parameters. The 2nd classifier is unsupervised-SOM, used for classifying remained data, which were not classified the 1st classifier. We defined categories on the 2nd SOM by using K-means clustering method. Finally, color codes were assigned to the plaque component values, and the tissue color coded maps were reconstructed. Results suggest that the proposed technique is useful for automatic characterization of plaque components in IVUS image.

Key words: Intravascular ultrasound, Tissue characterization

1. BACKGROUND

Rupture of vulnerable atherosclerotic plaque is the cause of most acute coronary syndromes. Accurate in vivo identification of plaque components may allow the detection of vulnerable atheroma before rupture.

Intravascular ultrasound (IVUS) allows the visualization of cross-sections of coronary artery with atherosclerotic plaques in vivo [1,2]. In standard IVUS gray-scale echo-image, calcified plaque regions and dense fibrous components generally reflect ultrasound energy well and thus appear bright and homogeneous. In addition, we can get more detailed information by analysis of radio frequency (RF) ultrasound signals than by the visual interpretation of echo-image [3,4].

In this study, we analyzed the spectrum of IVUS signal through application of self-organizing map (SOM) aiming automatically plaque characterization. With the use of a combination of spectral parameters, classification schemes were developed for the analysis of IVUS data, and the RF spectral information were used to reconstruct color coded tissue maps.

2. METHOD

RF Signal data were acquired from 30 human left anterior descending (LAD) coronary arteries at PTCA (percutaneous transluminal coronary angioplasty). The average age was 72 ± 12 years.

2.1 Data Acquisition

IVUS data were acquired with an IVUS console "Clear View Ultra" (Boston Scientific Inc, USA) and 40 MHz, mechanically rotating IVUS catheter "Atlantis SR Plus" (Boston Scientific Inc, USA).

RF data were digitized and stored in a PC (Dell Precision Workstation 330, Dell Inc, USA) using an A/D board "GAGE compuscope 8500" (500Msamples/sec., with 8 bits of resolution, Gage Applied Inc, Montreal, Canada) for off-line analysis.

2.2 IVUS Data Analysis

IVUS RF signal from the ROIs selected by the expert medical doctor were processed in MATLAB 7.3.0 (The MathWorks Inc, USA) as follows. Initially, a band-pass filter (20 MHz–100 MHz) was applied to the IVUS RF signal data. Then each line in the ROI is scanned by a 128-points width

hamming window. The frequency spectrum is calculated in each windowed area using a mathematical autoregressive (AR) model. AR processes are known to be more appropriate for short data records, such as IVUS RF signals, than discrete Fourier transforms and have been shown to result in high resolution spectral estimates [4].

Further, the AR spectra were used to compute 10 spectral parameters for each ROI. These parameters were: fundamental frequency and power, second harmonic frequency and power, mid-band-fit [5], mean, standard variation and skewness of integrated backscatter, ROI position at line.

2.3   SOM

As classifier of IVUS RF data, we used the SOM classifier.

The SOM is a neural network based on unsupervised learning proposed by T. Kohonen [6,7]. It is a vector quantization method which places the prototype vectors on a regular low-dimensional grid in an ordered fashion. A SOM consists of neurons organized on a regular low-dimensional grid. Each neuron is a *d*-dimensional prototype vector where *d* is equal to the dimension of the input vectors. The neurons are connected to adjacent neurons by a neighborhood relation, which dictates the structure of the map.

For classifying IVUS RF data, we used dual-layer SOM classifier. The 1st layer of the classifier is supervised SOM to classify "structure regions". And the 2nd layer of the classifier is unsupervised SOM to cluster and classify "plaque regions" which was not classified by the 1st layer.

2.4   The 1st SOM Classifier Condition

The 1st SOM classifier is for classifying "structure regions", which is not plaque region. After using the 1st SOM classifier, unclassified regions were used by the 2nd SOM classifier.

2.4.1   Training Data and Test Data

ROIs for training data and test data for the 1st SOM classifier were selected from IVUS echo-images by an expert medical doctor. These IVUS echo-images were reconstructed from the RF data by software written by our group. Then four structure types (catheter, blood, shadow, outer lumen, and blood region) were defined and extracted 2500 windowed regions respectively. Seventy five percentage of these data were used as training data of the 1st SOM classifier. The rest of these data was used as test data of the 1st SOM classifier.

2.4.2   Training Settings

The SOM training settings were as follows.   Map size was 30×17 of hexagonal lattice. Training phase was 20,000 times. A batch training algorithm was used, the data set were presented to the SOM as a whole, and the new weight vectors were weighted averages of the data vectors.

   After training, the neurons of the 1st SOM were labeled in accordance with the representatives vectors of the training data. Each label was decided based on the major component of the group.

   Finally, the 1st SOM classifier was validated through classifying training data and test data to determine predictive accuracy, sensitivity, and specificity from widely accepted equations in biomedical literature [8].

   By using this classifier, "structure regions" of IVUS data were classified.

2.5   The 2nd SOM Classifier Condition

The 2nd SOM classifier is for clustering "plaque regions", which is not classified by the 1st SOM classifier. The 2nd SOM classifier was trained for clustering "plaque regions" and learned how to classify "plaque regions" into these clusters.

2.5.1   Training Data

As training data for the 2nd SOM classifier, the regions which were not classified by the 1st SOM classifier were used as "plaque regions". Structure regions in 10 echo-images were classified by the 1st SOM classifier. After that, 3000 windowed regions were collected from unclassified area in the echo-images classified by the 1st SOM classifier as "plaque regions"

2.5.2   Training Settings

The SOM training settings were as follows. Map size was 15×10 of hexagonal lattice. Training phase was 20,000 times. A batch training algorithm was used. After training, K-means clustering method [9] applied to the SOM.

2.6   Plaque Classification

The SOM classifier learned how to classify the artery component types by using spectral parameters. Frequency spectra of signals within the windowed area were calculated, and spectral shape parameters were derived. The plaque types were classified based on these parameters. The window was

then moved by one sample, and data were reanalyzed. Then, each sample was classified by the SOM classifiers and given a particular value corresponding to one of the cluster components. Color codes were assigned to the component values, and the tissue maps were reconstructed by our algorithm. These tissue maps were then checked by an expert medical doctor to assess the plaque characterization.

3.   RESULT

The 1st SOM classifier was applied on the training data and test data. For the training data, the average sensitivity and specificity of classified data were 86.8% and 76.1%, respectively. For the test data, the average sensitivity and specificity of classified data were 86.3% and 75.9%, respectively.

The 2nd SOM classifier successfully classified the training data into eight categories. And these segmented regions were assessed as fibrosis, calcification, blood, and shadow.

Color-coded images that classified whole echo-images by the SOM are showed in Fig. 1. Figure 1a is the original echo-images, Fig. 1b is the color-coded images by the 1st SOM classifier, and Fig. 1c is the color-coded images by the 2nd SOM classifier. In the Fig. 1b, the "N/A" regions mean the regions that were not classified by the 1st SOM classifier.

The SOM classified well the lumen fibrous and calcified regions, as shown in Fig. 1.
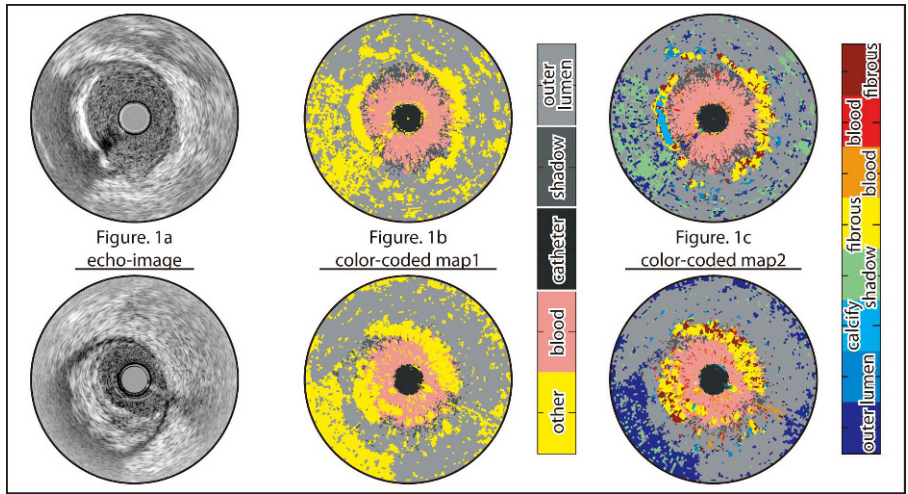
Figure 1. (**1a**) echo-images, (**1b**) color coded map generated by the 1st SOM classifier, (**1c**) color coded map generated by the 2nd SOM classifier.

4.   CONCLUSION

In this study, we classified IVUS RF data of coronary tissues using a SOM classifier based on multiple spectrum parameters. These results suggest that the proposed technique is useful for automatic characterization of plaque components in IVUS image. In future studies, with further data collection, we plan to develop statistically stable and robust classification rules for prediction of atherosclerotic plaque formation.

ACKNOWLEDGEMENTS

REFERENCES

1. Nissen SE, Gurley JC, Grines CL, et al., Intravascular ultrasound assessment of lumen size and wall morphology in normal subjects and patients with coronary artery disease. *Circulation*. **84**, 1087–1099 (1991).
2. Schoenhagen P, Ziada KM, Kapadia SR, et al., Extent and direction of arterial remodeling in stable versus unstable coronary syndromes. *Circulation*. **101**, 598–603 (2000).
3. Baldeweck T, Laugier P, Herment A, et al. Application of utoregressive spectral analysis for ultrasound attenuation estimation: interest in highly attenuating medium. *IEEE Trans. Ultrason. Ferroelectr. Freq. Control*. **42**, 99–110 (1995).
4. Anuja Nair, Barry D. kuban, Nancy Obuchowski and D. geoffrey Vince, Assessing spectral algorithms to predict atherosclerotic plaque composition with normalized and raw intravascular ultrasound data. *Ultrasound in Med. and Biol.*, **27**(10), 1319–1331 (2001).
5. Litti FL, Ultrasonic parametric imaging, *WCU 2003*, (Paris, September 7–10, 2003)
6. Kohonen T, Self-Organizing Map, 3rd Edition (Springer, 2004).
7. Kohonen T, New developments of learning vector quantization and the self-organizing map, SYNAPSE'92, Symposium on Neural Networks (Osaka June 24–26, 1992)
8. Metz CE, Basic principles of ROC analysis. *Semin Nucl Med*. **8**. 283–298 (1978).
9. Hartigan JA and Wong MA, A K-Means Clustering Algorithm, *Applied Statistics*, **28**, 100–108 (1979).

TISSUE THERMAL PROPERTY RECONSTRUCTION BY STOPPING HEATING AND PERFUSION

C. Sumi, T. Uchida, T. Ooba, K. Inoue
Department of Electrical and Electronics Engineering, Sophia University, Tokyo, JAPAN

Abstract: In this paper, we report robust noninvasive techniques for reconstructing the thermal properties of living tissues, such as thermal conductivity, thermal capacity and thermal diffusivity, for the diagnosis, monitoring and planning of thermal treatments such as high-intensity focus ultrasound (HIFU). Internal tissue temperature distributions can be measured using ultrasonic imaging or magnetic resonance imaging. Provided that the reference thermal properties of living tissues are given in the region of interest (ROI) as initial conditions, we can determine thermal property distributions by solving bioheat transfer equations as simultaneous first-order partial differential equations having temperature distributions as inhomogeneous coefficients. By using the reported technique, the perfusion by blood flow and thermal sources or sinks can also be reconstructed. However, in this study, we perform reconstruction after stopping heating and perfusion; only the thermal properties of living tissues can be reconstructed under such conditions. Simulations were conducted to verify the feasibility of the reconstruction. A minimally invasive thermal treatment will be realized by using our proposed reconstruction technique.

Key words: Thermal property reconstruction, Ultrasound, Temperature measurement, Thermal conductivity, Thermal capacity, Thermal diffusivity, Thermal source, Perfusion, Thermal treatment, HIFU, Minimally invasive treatment

1.   INTRODUCTION

We previously reported robust, noninvasive techniques of reconstructing the thermal properties of living tissue, including thermal conductivity, thermal capacity and thermal diffusivity, for the diagnosis, monitoring and planning

of thermal treatments such as a high-intensity focus ultrasound (HIFU) [1–4]. Internal tissue temperature distributions can be measured using ultrasonic imaging or magnetic resonance (MR) imaging (see refs. [5–7]). Provided that the reference thermal properties are given in the region of interest (ROI) as initial conditions, we can determine thermal property distributions by solving bioheat transfer equations as simultaneous first-order partial differential equations having temperature distributions as inhomogeneous coefficients. Using the method, the perfusion by blood flow and thermal sources or sinks can also be reconstructed. Perfusion is a measure for differentiating tumor progress. A novel regularized numerical solution for realizing useful, unique, stable reconstructions of thermal property distributions is also presented. The feasibility of the numerical solution was verified using tissue phantoms, i.e., simulated and ultrasonic agar phantoms.

   However, in this study, we perform the reconstruction after stopping heating and perfusion. Under such conditions, only thermal properties can be reconstructed without increasing the number of equations, i.e., the number of measured sequential independent temperature fields.

2.   RECONSTRUCTION TECHNIQUE

When the nonsteady temperature field T(t,x,y,z) is measured in a 3D ROI Ω whose thermal conductivity distribution $k(x,y,z)$, thermal capacity (product of density ρ (x,y,z) and specific heat $c(x,y,z)$) distribution, perfusion distribution P(t,x,y,z) by blood flow and heat source or sink distribution Q(t,x,y,z) are unknown, the following first-order partial differential equation (PDE) (i.e., bioheat transfer equation) holds for the unknown distributions [3,4].

$$\rho c \frac{dT}{dt} = \nabla T \cdot \nabla k + k \nabla^2 T + P + Q \qquad (1)$$

In Pennes' bioheat transfer equations, the perfusion term P(t,x,y,z) appears on the right-hand side of (1) as $w_b c_b (T - T_b)$. w_b, c_b and T_b are the flow rate, specific heat, and measured temperature of blood. However, in this study, we do not deal with such perfusion terms and assume that no heat source or sink exists in the ROI. That is, the ROI is set such that the heat source or sink exists outside it (although the heat source or sink can be locally eliminated from the ROI or evaluated as an inhomogeneity in thermal properties). Otherwise, as in this study, we deal with temperatures after stopping heating and perfusion. However, in (1), we expressed the perfusion

term as P(t,x,y,z) to enable us to also deal with large blood vessels. In [4], we addressed the reconstruction of perfusion and heat sources or sinks, and in [8], we reported some of the simulation results.

If the reference regions ω_l ($l = 1,…,N$) whose conductivity distributions $k_l(x, y, z)$ or capacity distributions $\rho c_l(x, y, z)$ are known are properly given in the ROI Ω [e.g., in homogeneous tissues such as parenchyma, fatty tissue, and bone [9]] as the initial conditions, i.e.,

$$k(x, y, z) = k_l(x, y, z) \text{ or } \rho c(x, y, z) = \rho c_l(x, y, z)$$
$$(x, y, z) \in \omega_l \ (l = 1,…, N), \tag{2}$$

the conductivity distribution, capacity distribution, and diffusivity distribution in $\Omega - \sum_{l=1}^{N} \omega_l$ can be determined from only two independent sets of measured sequential temperature distributions. Strictly speaking, the proper configurations of reference regions and heat sources or sinks can be realized by considering the characteristic curves [1,2] of PDEs (1). However, as indicated in [3,4], the temporal change in temperature is very slow, and so reference regions and sources or sinks can be configured in the same manner as that in a steady-state problem [1,2] such that reference regions widely extend in the direction crossing heat fluxes or that a reference region surrounds heat sources or sinks. In such proper configurations, the target distributions can be determined by solving the initial-value problem of two PDEs and the initial conditions.

However, note that the inverse problem becomes ill-posed due to the fact that the measured temperature data are always noise-contaminated. Moreover, improper configurations of reference regions and sources or sinks may occur (e.g., a short reference region). Our previously developed robust numerical approach [1,2] is then utilized in a novel way to uniquely and stably determine thermal property distributions [3,4]. Specifically, the targets are properly regularized using different regularization parameters.

Phantom and in vitro calf [6] experiments clarified that the accuracy is low for measuring a high temperature and large changes in temperature. Thus, stabilization by regularization must be performed thoroughly in such regions, particularly, the region of thermal sources or sinks and the neighboring area (i.e., spatially variant regularization). Moreover, heat capacity reconstruction must also be stabilized more thoroughly than thermal conductivity reconstruction because the thermal diffusivity of tissues is low. The bandwidth of the temporal derivative of temperature must be chosen

sufficiently narrow. Furthermore, the reference conductivity should be used rather than the reference capacity.

3.   SIMULATIONS

A cubic tissue phantom (50.0 mm sides; x, y and z = 0.0–50.0 mm) was simulated. It contained a spherical inclusion (dia. = 6.0 mm), which had a conductivity and a specific heat twofold those of the surrounding medium, i.e., 1.0 vs 0.5 W/(mK), and 8,400 vs 4,200 J/(Kkg) (typical values similar to those of water). The density was uniform at 1,000 kg/m^3. A cubic ROI (20.0 mm sides) was set at the center of the phantom with a spherical inclusion, as illustrated in Fig. 1a (z = 25 mm). The phantom has a uniform temperature of 36.0 °C. As depicted in Fig. 1a, a spherical heat source Q of 3 W (dia. = 6.0 mm) was set at t = 0 sec such that it overlaps the inclusion. The time series of the temperature distribution was calculated by the successive over-relaxation (SOR) method using a time step of 0.1 sec. Figure 1b plots the time courses of temperatures at the five positions depicted in Fig. 1a. The heating was stopped (t = 14.1 sec) when the highest temperature in the ROI exceeded 100 °C, and two sets of sequential temperatures (Table 1) were then used (i.e., 20 and 30, 60 and 70, 100 and 110, and 30 and 70). The cutoff frequency of the temporal differential filter used is 1.12 Hz.

   The means of the reconstructions evaluated in the central square region of 1.0 × 1.0 mm^2 in the inclusion are also listed in Table 1. As indicated, the thermal properties are accurately reconstructed. Because the temperature has not yet changed at t = 20 and 30 sec in the peripheral region of the ROI, the reconstructions are unstable in such a region (omitted). Figure 2 presents the reconstructions with instabilities obtained using temperatures around t = 60 and 70 sec. However, regularization effectively stabilized the reconstructions (omitted) together with reconstructions using white data as the temperature measurement noise (discussed next).

   Figure 3 (4) illustrates the reconstruction using the same (lower) cutoff frequencies of the temporal differential filter, i.e., 1.12 and 0.56 Hz [nonregularized (a) conductivity and (b) capacity; regularized (c) conductivity and (d) capacity]. As indicated, the regularization was effective when combined with the use of a proper cutoff frequency of the temporal differentiation of temperature. However, note that these processes made the values smaller than the originals. The means of the reconstructions in the inclusion are also listed in Table 1.

4.   CONCLUSIONS

The reconstruction proposed here enables the real-time planning of the conditions for thermal treatment, i.e., the next spatial position to be heated, the thermal source shape and the ultrasound intensity from the successful numerical estimation of thermal properties. A practical protocol for such treatment can be obtained, i.e., (0) with perfusion stopped or continuing, and by iteration of (1) heating, (2) stopping heating, (3) immediate reconstruction, and (4) the determination of the next heating. The reconstructions obtained using the temporal changes generated by stopping the perfusion were reported in [8] (omitted).

Table 1. Means of reconstructions in inclusion.

Times Sec	Conductivity W/(m K)	Capacity ($\times 10^6$) J/(m^3 K)	Diffusivity ($\times 10^{-7}$) m^2/s
Original	1.00	8.40	1.19
20 and 30 (1.02 Hz) –Nonregularized	0.78	6.30	1.24
60 and 70	1.06	8.71	1.22
with noise (1.02 Hz) -Nonregularized	0.71 (0.05)	6.94 (1.38)	1.05 (0.02)
-Regularized	0.75 (0.04)	7.06 (0.38)	1.06 (0.02)
(0.56 Hz) -Nonregularized	0.76 (0.06)	8.13 (0.92)	0.94 (0.05)
-Regularized	0.75 (0.04)	7.79 (0.63)	0.96 (0.03)
100 and 110	0.90	7.87	1.15
30 and 70	1.02	8.69	1.18
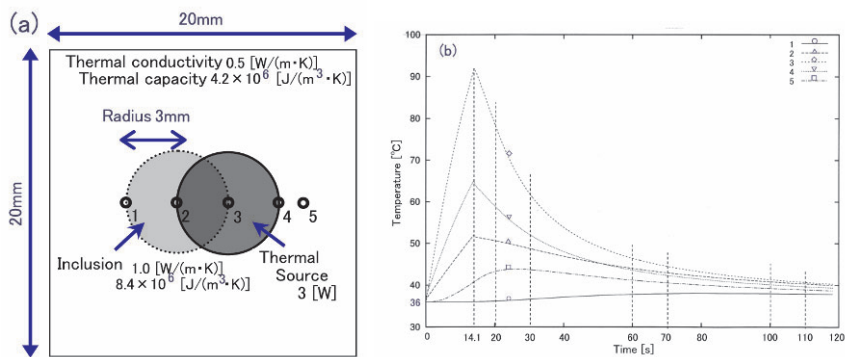
*Figure 1. (**a**) Central plane in ROI (z = 25 mm). (**b**) Time courses of temperatures at five positions depicted in (**a**).*
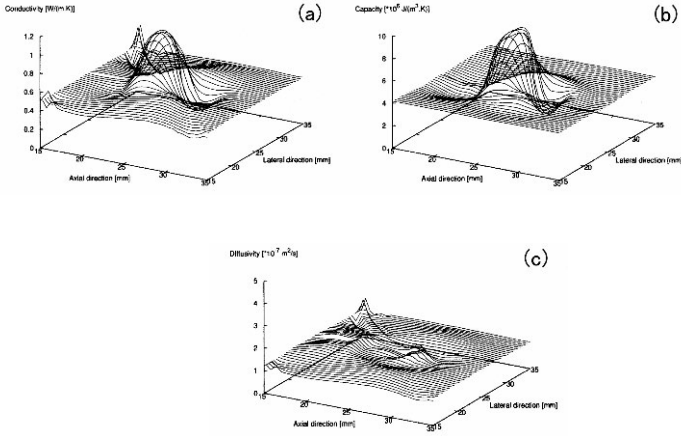
Figure 2. (**a**) Reconstructions of (**a**) thermal conductivity, (**b**) capacity and (**c**) diffusivity obtained using temperatures around t = 60 and 70 sec.
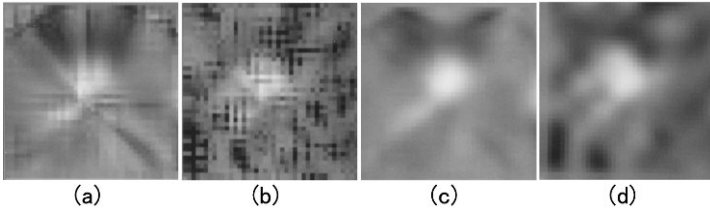
Figure 3. Nonregularized (**a**) conductivity and (**b**) capacity reconstructions, and regularized (**c**) and (**d**) reconstructions obtained using high cutoff frequency (1.12 Hz). Image range, conductivity (0.26–1.04 [W/(m K)]); capacity (1.76 to 10.39e6 [J/(K m^3)]).
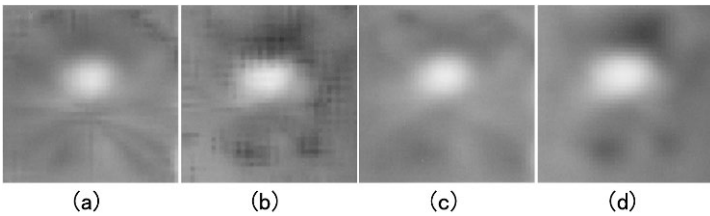
Figure 4. Reconstructions obtained using low cutoff frequency (0.56 Hz). (a)–(d) see Fig. 3.

The size of the region of reconstruction should not be too large for treating a local tumor due to low tissue diffusivity. However, a small thermal source must also be used. More specifically, large (small) thermal sources must be used to heat the center of a tumor (marginal regions). Furthermore, heating must be applied from a deep region to a shallow region. Thus, a

minimally invasive treatment will be realized by using our proposed reconstruction technique during thermal treatment. In the near future, the use of MR temperature measurement and the reconstructions of thermal sources or sinks and perfusion [8] will also be reported in detail elsewhere.

REFERENCES

1. Sumi C. 2001 Reconstruction of thermal conductivity distribution from measured temperature distributions. *Proc. 40th SICE Annual Conf. (Nagoya)*, p. 202B4 (in Japanese).
2. Sumi C. and Kuwabara J. 2006 Determination of thermal conductivity distribution from internal temperature distribution measurements. *Review of Scientific Instruments* **77**:064904.
3. Sumi C. and Yanagimura H. 2005 Reconstruction of thermal property distributions – Thermal conductivity, diffusivity, capacity. *Proc. 2005 IEEE Int. Ultrason. Symp. (CD-ROM)*, pp. 21–25.
4. Sumi C. and Yanagimura H. 2007 Reconstruction of thermal property distributions of tissue phantoms from temperature measurements – Thermal conductivity, thermal capacity and thermal diffusivity. *Physics in Medicine and Biology*, vol. 52, pp. 2845–2864, 2007.
5. Simon C., VanBaren P. and Ebbini E. 1998 Two-dimensional temperature estimation using diagnostic ultrasound. *IEEE Trans. Ultrason., Ferroelect., Freq. Contr.* **45**:1088–99.
6. Sumi C. and Yanagimura H. 2007 Spatial inhomogeneity of tissue thermal parameter of Ebbini's model and its dependency on temperature. *Jpn J Appl Phys* **46**: 4790–4792.
7. Rhoon G. and Wust P. 2005 Introduction: Non-invasive thermometry for thermotherapy. *Int. J. Hyperthermia* **21**:489–95.
8. Sumi C., Uchida T. and Minami A. 2007 Thermal property measurements based on ultrasonic temperature measurements (8th report). *Proc. of 2007 Autumn Meeting of Acoust. Soc. of Jpn.*
9. Chato J. C. 1985 Selected thermophysical properties of biological materials (Appendix 2) in Heat Transfer in Medicine and Biology Vol. II edited by Shitzer A. and Eberhart R. C. (New York and London: Plenum Press).

ACOUSTICAL MICROSCOPY

NEW GENERATION OF HIGH RESOLUTION ULTRASONIC IMAGING TECHNIQUE FOR ADVANCED MATERIAL CHARACTERIZATION: REVIEW

R.Gr. Maev

DaimlerChrysler/NSERC Industrial Research Chair in Applied Solid State Physics and Material Characterization, University of Windsor, Windsor, Ontario, Canada

Abstract: The role of non-destructive material characterization and NDT is changing at a rapid rate, continuing to evolve alongside the dramatic development of novel techniques based on the principles of high-resolution imaging. The modern use of advanced optical, thermal, ultrasonic, laser-ultrasound, acoustic emission, vibration, electro-magnetic, and X-ray techniques, etc., as well as refined measurement and signal/data processing devices, allows for continuous generation of on-line information. As a result real-time process monitoring can be achieved, leading to the more effective and efficient control of numerous processes, greatly improving manufacturing as a whole. Indeed, concurrent quality inspection has become an attainable reality. With the advent of new materials for use in various structures, joints, and parts, however, innovative applications of modern NDT imaging techniques are necessary to monitor as many stages of manufacturing as possible. Simply put, intelligent advance manufacturing is impossible without actively integrating modern non-destructive evaluation into the production system.

Key words: Ultrasonic imaging, High resolution, Material characterization.

1.   INTRODUCTION

Acoustical imaging is a well-known and powerful tool for studying the microstructure and properties of materials. It has attracted the efforts of numerous research groups throughout the world. In actuality, high-resolution acoustic imaging is a relatively new technique that has only recently been employed to evaluate the microstructure of condensed matter. The

suggestion to use of sound rather than light as a microscope was first put forth by a Russian scientist (Solokov, 1934) just before the Second World War. However, due to the limitations of existing technology, it was many years before high-resolution acoustic imaging was fully realized. The first acoustic microscopy prototype was fabricated in the United States (C. Quate, Stanford University) in 1974. Today the industrial application of acoustic microscopy continues to be a developing field of study [20].

The most popular quantitative technique in acoustic microscopy is the V(z) method [1,2], in which the acoustic velocity and attenuation of leaky surface acoustic waves, as well as a reflectance function, is determined from the output signal V of the transducer. This information is acquired as a function of the specimen displacement, z. In addition to the V(z) method, several techniques employing separate transmitting and receiving transducers have been recently developed for both the analysis of acoustic parameters and quantitative material characterization. For example, an ultrasonic micro-spectrometer with spherical-planar-pair lenses allows for the measurement of the reflection coefficient [3,4]. Here the angular spectrum of the reflected wave in such system is determined by the rotation of the lens system as a whole, relative to the specimen surface.

A two-transducer ultrasonic system is also used to obtain the resonant transmission coefficient [5], as well as for the determination of Lamb dispersion curves [6]. To gather the data necessary for reconstruction, two measurements were required: the voltage of the output transducer as a function of (1) the lateral displacement of the transducer on the specimen's surface and (2) the frequency of the probing electrical tone burst pulse. A two-dimensional recording of the wave (as scattered by the specimen) was proposed [7] for measuring elastic constants. In this method the transmitting transducer is focused at the surface of the specimen; the scan plane of the receiver is located far from the focus. Thus, the recorded spatial distribution represents the angular spectrum of the reflected or transmitted wave. The angular resolution of this method is determined by both the spatial resolution of the receiver and the distance between the scan plane and the focus. In previous articles we developed a new technique for measuring acoustical parameters called the A(z) method for the transmission mode [8,9]. A new V(x) method was introduced later for the reflection mode [10,11]. Both the A(z) and V(x) methods may include additional options, based on the air-coupling pair measurement technique for both the reflection and transmission modes.

2. HIGH HARMONIC MODE OF THE ACOUSTICAL MICROSCOPE

The signal of the second harmonic, generated by nonlinear reflection, is in most cases 30–50 dB weaker than the signal of fundamental frequency. Therefore, it is necessary to carefully select the experimental parameters. To maximize the spatial resolution of the acoustic microscope, a single, short pulse of sound is usually generated. The wide-band spectrum of such a pulse, however, contains strong components at double frequency. Also, the inherent bulk nonlinearity of the acoustical components of the microscope and object (and especially of the coupling liquid) produces uninteresting second harmonic waves which accompany those of the fundamental frequency. These waves will therefore contribute to the image at second harmonic – identical information to that already found in the linear picture [12]. In [13–15], this was demonstrated experimentally for the resolution of weak-reflecting inclusions using a scanning microscope with a 25 MHz acoustical focusing lens. A selective filter-amplifier with a basic frequency of 50 MHz and a bandwidth of 4 MHz was incorporated into the receiving branch (see Fig. 1).
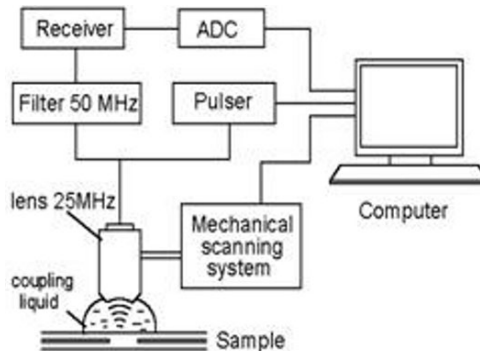
Figure 1. Schematic diagram of the scanning acoustical microscope as used for second harmonic imaging.

The sound wave was excited by applying a single pulse to the lens transducer with amplitude 120 V and duration 16 ns. Without taking any specific action to enhance the second harmonic, its level in the received signal stood at approximately 25 dB (measured during reflection from the surface of a steel plate in beam focus). By decreasing the receiver bandwidth, the tone burst of the second harmonic had a significantly longer

duration compared to that without frequency selection. This led to deterioration in spatial resolution for depths up to 0.5–0.7 mm.
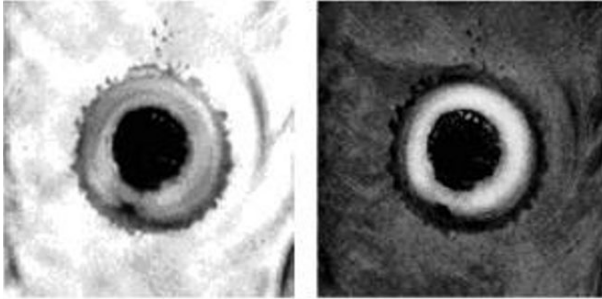
Figure 2. C-scans of spot weld, obtained on fundamental frequency (*left*) and on second harmonic (*right*). Size of scanned region is 12×12 mm.

The C-scan image was generated by the mechanical raster scanning of an area up to 40 × 40 mm along the surface with steps of 0.01–0.05 mm thickness. Figure 2 presents the scans of a specimen consisting of two galvanized steel sheets with a thickness of 2 mm, joined together by a resistance spot weld. To exclude any aberration due to non-planar surface conditions, the indentation from the weld electrode was removed by milling. The dark spot in the center of the pictures is the weld nugget. Sound can freely pass through this area; only some reflecting in-homogeneities are visible as light points.

The bright area outside the weld corresponds to the free internal surface of the upper sheet – an area with nearly 100% sound reflection. Between these regions lies a gray ring that corresponds to a zone with poor acoustical contact. It is known that within this zone melted zinc accumulates during the welding process (the so named "corona effect"), creating numerous connected stalactite-stalagmite type structures [14]. Such a micro rough connective layer is expected to be a very good source of contact acoustical nonlinearity. Since the thickness of this layer and its microstructures are much less than that of a wavelength, they contribute in an integral way. Indeed, the second harmonic picture shows this region as a bright white ring. The amplitude of the second harmonic in this region is at least ten times larger than that of the other regions.
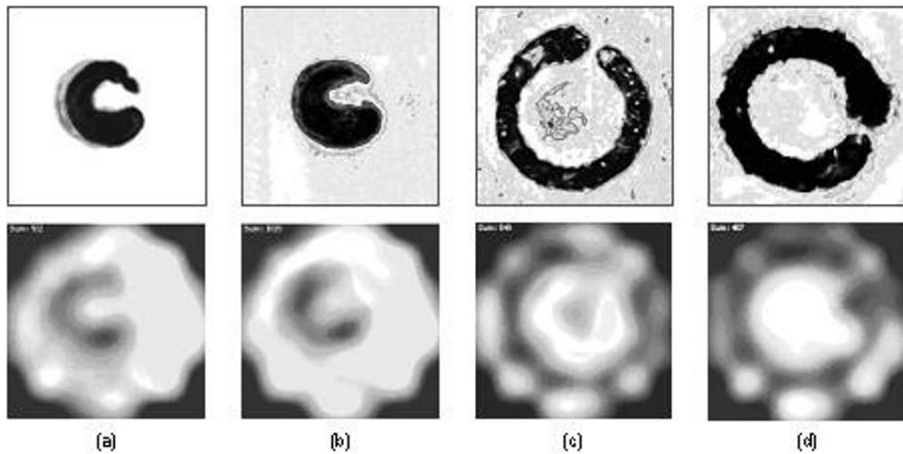
Figure 3. Acoustic imaging inspection of laser spot welds with a desktop scanning acoustic microscope and corresponding images obtained with the 52-element array: (**a**), (**b**) 0.75 mm thick steel plate approximately 3.0 mm. weld; (**c**), (**d**) 1.0 mm thick steel plate around 7.0 mm weld. Detectable imperfections: Insufficient length, Seam interruption, Lack of fusion, Pin hole existence.

3.   2D MATRIX TRANSDUCER

2D Matrix array transducers offer several enhanced capabilities in imaging and beam formation when compared to single transducer scanning systems. 2D-Matrix array transducer technology allows for fast data acquisition and imaging even when using motionless transducers. Advanced technologies such as micro-machining and IC manufacturing can produce matrices of thousands of elements less than 0.1 mm in size, in turn creating an acoustic analogue to the CCD camera [16]. The proper dimension of the elements in an array is of great importance; in order to achieve efficient beam forming, each must be approximately half a wavelength in size [17].

For matrices that do not use phased principles to build the acoustic beam, however, elements of this minute size are disadvantageous. Due to power dissipation restrictions, matrix transducers having such high densities can only operate in the pick-up mode. Moreover, acoustic wavelengths at megahertz frequencies are at least 103 times larger than that of light. Finally, imaging capability of a system is generally dependent on the penetration depth of the transducer. This penetration depth drops with the decreasing size of the element due to the beam divergence and the increasing electrical mismatch associated with 50 Ohm transmitters and receivers. Thus, there seems to be no reason to go down to the micron range resolution [16,17].

4.   HIGH RESOLUTION ULTRASONIC INSPECTION METHODS FOR JOINTS

Traditional methods of joint monitoring involve a combination of visual inspection, pry testing and destructive tests. For example, in the analysis of resistance spot welds a hammer and chisel is often used. The only truly effective non-destructive evaluation technique has been the ultrasonic pulsed-echo technique, based on the evaluation of ultrasonic echo patterns in a specimen [18]. Current ultrasound methods are to determine both the micromechanical parameters and the microstructure of bulk materials and various joints.

C-scans:

B-scans:
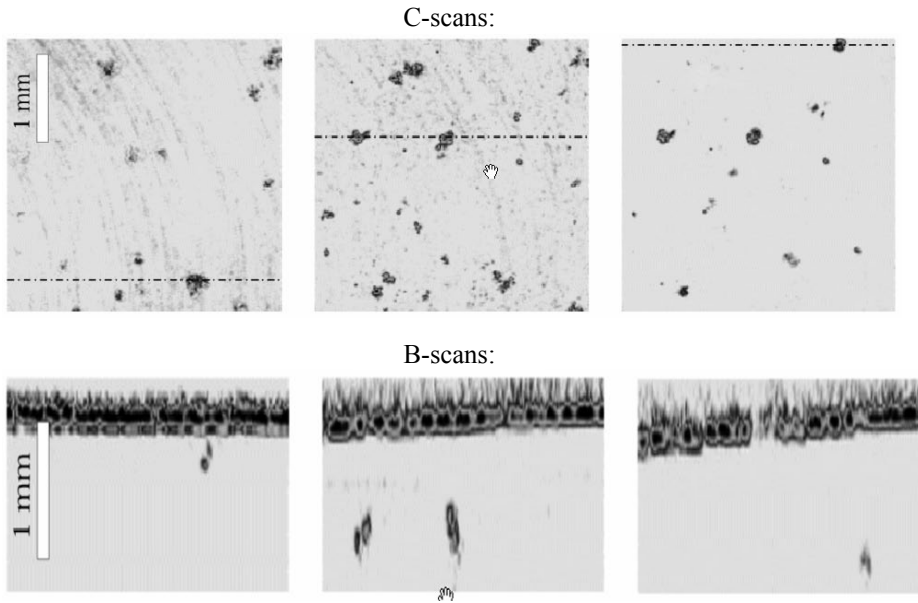
Figure 4. Acoustic images of various porosity in an aluminum casting.

Measure of weld diameter.	Detection of inclusions.
Corona effect.	Stick welds.
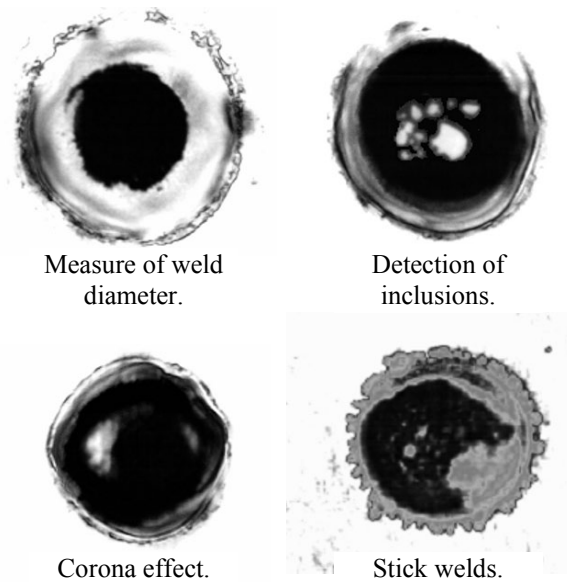
Figure 5. C-scan Images of the interface area (depth penetration 1 mm) from the spot welding.

One of the hottest NDT problems of today involves the high-resolution inspection of welding joints. Indeed, the problems associated with the evaluation of the multi-layered joints formed by spot (or diffusion) welding are currently under intense scrutiny. Acoustic imaging systems using short probe pulses have been shown to provide an effective way to visualize small-scale failures of various defects at different depths. Further, acoustic spot weld imaging techniques make it possible to inspect the internal structure of joints in spite of the curved outer surfaces of welding spots.

To illustrate the potential that high-resolution acoustic imaging holds, we used a wide-field short-pulse acoustic microscope (see Fig. 1). The method described above was utilized in the evaluation of the sub-surface microstructure of cast iron and aluminum castings (see Fig. 4), spot-welding and laser welding joints, etc. (see Fig. 3 and Fig. 5) The combination of the C- and B-scan images in one picture can reveal a 3D representation of the defect distribution inside the welding zone, which can be also very useful from a technological point of view.

In spite of the fact that the top surface of specimen was distributed by welding, high quality acoustic images of the nugget zone were obtained [18–20] (see Fig. 5). The C- and B-scan images contain well-shaped defects of joints and confirm the power of the method for NDT and QC of spot-weld

joints. Today we use SAM techniques as a routine certification procedure within the automotive industry (see Fig. 6).

The current results of this study show that high-resolution acoustic imaging techniques can be successfully applied to spot welding analysis. Certainly it is an effective inspection method by which one may detect internal defects of any kind. For this reason it is easily adapted for us in the quality control of manufacturing welds.

Acoustic imaging methods that are based on acoustic visualization and characterization are also extremely promising for the quality evaluation of laser welds and rivet joints (see Fig. 3). This technique can provide the total bulk reconstruction of the joint zone, including the topography of the top and bottom faces, the structure of the interface between the sheets, and any expulsions, voids, pores, cracks or other defects in the welding zone.
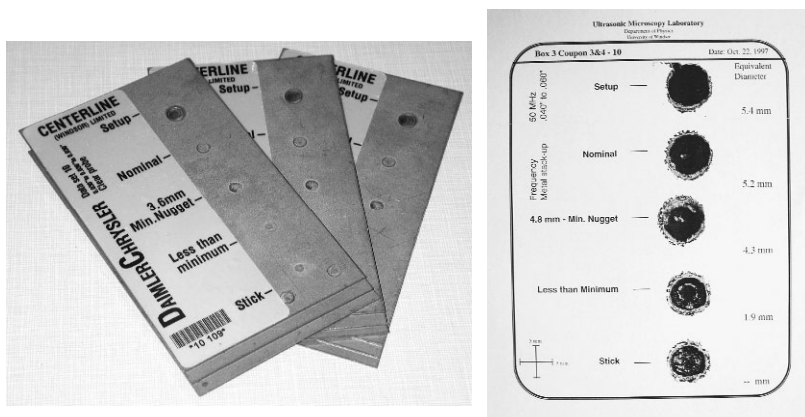
Figure 6. Certification of weld coupons.

5.   CONCLUSION

During the last few decades, the acoustic microscope has become a common instrument for investigating the internal structure of materials and for industrial non-destructive evaluation. At the same time, quantitative acoustic imaging research has found its place in material imaging and various fields of biomedical imaging. Further improvements in quantitative methods may be realized through the use of complimentary types of ultrasonic-media interactions and, accordingly, provide additional specific information about the object. The realization of these methods will constitute a considerable and exciting expansion in the applicability of the acoustic microscope.

Indeed, quantitative acoustical imaging techniques greatly enhance material characterization capabilities, making possible the effective imaging of various micro-inhomogeneities. This is crucial for the integrity of high-damage risk materials and products used in NDE aviation technology, automotive and nuclear power industries, and microelectronics as well. Such techniques have the potential to provide a reliable, rapid and cost effective method to visualize high contrast, small scale failures and defects at different depths within inspected objects.

ACKNOWLEDGEMENTS

REFERENCES

1. A. Briggs, Acoustic microscopy, Oxford, Clarendon Press, 1992.
2. R. Weglein and R. Wilson, "Characteristic material signature by acoustic microscopy", Electron. Lett., 14, 352–354, (1978).
3. N. Nakaso, K. Ohira, M. Yanaka Y. Tsukahara, "Measurement of acoustic reflection coefficients by an ultrasonic microspectrometer", IEEE Trans. Ultrason. Ferroelec. Freq. Contr., 41, 494–502, (1994).
4. N. Nakaso, Y. Tsukahara and N. Chubachi, "Evaluation of spatial resolution of spherical–planar–pair lenses for elasticity measurement with microscopic resolution", IEEE Trans. Ultrason. Ferroelec. Freq. Contr., 43, 422–427, (1996).
5. O. Lobkis, D. Chimenti, "Three–dimensional transducer voltage in anisotropic materials characterization", J. Acoust. Soc. Amer., 106, 36–45, (1999).
6. T. Kundu, A. Maji, T. Ghosh, and K. Maslov, "Detection of kissing bonds by Lamb waves", Ultrasonics, 35, 573–580, (1998).
7. R. Smith, D. Sinclair and H. Wickramasinghe, "Acoustic microscopy of elastic constants" Proceeding Ultrasonic Symp., 677–682, (1988).
8. R. Gr. Maev, "Scanning acoustic microscopy of polymeric and biological substances", Tutorial Archives of Acoustics, Poland, 13, N 1-2, 13–43, (1988).
9. R. Gr. Maev, V.M. Levin, "Principles of local sound velocity and attenuation measurements using transmission acoustic microscope", IEEE Trans.Ultrason.Ferroelec.Freq.Contr., 44, N6, 1224–1231, (1997).

10. R. Gr. Maev, S.A. Titov, "Measurement method based on scanning Doppler continuous wave acoustic microscope", Topics on Non-destructive Evaluation Series, 3, ASNT Publication, 343–350, (1998).

11. S. Titov and R. Maev, "V(X,T) acoustic microscopy method for leaky surface acoustic waves parameters measurements", Proc. IEEE Ultrason. Symp., 607–610, (2000).

12. Y. Lee and S. Cheng, "Measuring Lamb dispersion curves of a bi-layered plate and its application on material characterization of coating", IEEE Trans. Ultrason. Ferroelec. Freq. Contr., 48, 830–837, (2001).

13. Y. Zheng, R. Gr. Maev, I. Yu. Solodov, "Nonlinear acoustic applications for material characterization: Review", Canadian Journal of Physics, pp. 927–979, (1999).

14. R.Gr. Maev, New development in nonlinear inspection and materials evaluation based on quantitative ultrasonic technique foe vehicle quality control. Review. Non-destructive Characterization of Materials, Proceed. of 11th Intern. Symposium, Berlin, Germany, June, 2002, Springer Press, 2002.

15. R.G. Maev, Nonlinear Acoustic Imaging. Tutorial. Topics on Non-destructive Evaluation Series, v. 6, ASNT Publication, 2002.

16. A.A. Denisov, C.M. Shakarji, B.B. Lawford, R.Gr. Maev, J.M. Paille, "Spot Weld Analysis with 2D Ultrasonic Array", Journal of Research of the National Institute of Standards and Technology, 109, N.2, March-April (2004).

17. S. Titov, R. Maev, A. Bogachenkov, "Use of ultrasonic transducer array for measuring the velocity and attenuation of leaky acoustic waves", Technical Physics Letters, 30, No 10, (2004).

18. R. Gr. Maev, "Physical sciences and advanced vehicle technologies. Review.", Workshop of the Dunsmuir Workshop of Division of Industrial and Applied Physics, CAP, June 2001 (CD Proceeding), BC, Canada.

19. R. Gr. Maev, A. Ptchelintsev, A. A. Denissov, "Ultrasonic imaging with 2D matrix transducers", Acoustical Imaging, 25, 157162, (2000).

20. R.Gr. Maev , Development of Novel Principles and Methods of High Resolution Acoustic Imaging for Material Characterization, Review, J. Physics in Canada, V.62, N.2, pp. 91–98, (March/April 2006).

VISUALIZATION OF ACOUSTIC WAVES PROPAGATING WITHIN A SINGLE ANISOTROPIC CRYSTALLINE PLATE WITH A HYBRID ACOUSTIC IMAGING TECHNIQUE

C. Miyasaka, K.L. Telschow, J.T. Sadler, R.Gr. Maev

Department of Physics, University of Windsor, 401 Sunset Avenue, Windsor, ON, N9B 3P4, Canada; Idaho National Laboratory, Idaho Falls, ID 83415-2209, USA

Abstract: We present a hybrid acoustic imaging system to directly visualize acoustic waves propagating within a single anisotropic crystalline plate. A high frequency acoustic point focus lens was used to form a small point source within the plate. A laser interferometric system was used to visualize the acoustic wave propagation. Distinct amplitude patterns at each focal plane were experimentally visualized. The patterns are also theoretically calculated with an Angular Spectrum of Plane Waves method.

Key words: Laser based ultrasonics, Acoustic lens, Angular spectrum, Anisotropy

1.   INTRODUCTION

The mechanical scanning acoustic reflection microscope (hereinafter called simply "SAM") operating with frequencies substantially ranging from 0.1 to 2.0 GHz has proven to be a useful apparatus for characterizing of anisotropic materials on the scale of individual grains [1–3]. Note that the SAM is basically designed to visualize the surface and/or the subsurface of microstructure features of the material, but not directly the acoustic waves propagating within the material. However, observing a wave front traveling within the material would be significant for understanding physical phenomena, such as scattering from microstructure features [4–7]. In

addition, visualization of the acoustic wave front can help in measurement of elastic properties and improve quality evaluation of an acoustic lens.

In this article, we present a hybrid imaging system comprising laser based acoustic microscopy and scanning acoustic microscopy for directly visualizing wave front amplitudes of acoustic bulk and surface waves emanating from a focused source outside and inside a material sheet. A high frequency (~200 MHz) acoustic lens tightly focused compression waves onto the back surface of a thin silicon plate, crystalline plane (100) oriented with its normal to the plate surface, via a coupling medium (i.e., distilled water). A laser beam focused onto the front surface of the specimen via an optical objective lens included in the laser interferometric system detected the amplitudes of the bulk and surface acoustic waves at the front surface of the plate. Distinct symmetric amplitude patterns that altered in predictable ways, as the acoustic focal point moved toward the front surface of the plate, were observed. Predictions of the acoustic wave fields generated by the acoustic lens within the plate are being investigated with an Angular Spectrum of Plane Waves method for an anisotropic crystalline solid [8–10].

2.   THEORETICAL APPROACH

We adopt "Angular-Spectrum of Plane Waves" approach [10] to predict the acoustic wave amplitude at the surface of the silicon plate taking into account all the modes excited through. If the wave amplitude or stress distribution is known on any plane, then the corresponding wave amplitude or stress can be calculated on any other parallel plane through a summation of plane waves propagating form one plane to the other. Each plane wave component must be a solution to the appropriate wave equation for the medium through which it travels. Since the angular frequency and the parameters of the acoustic lens are known, the acoustic field focused on the back surface plane can be calculated. The summation must occur over all in-plane components of wave-number and include propagating as well as non-propagating wave-vectors. The main complication to this approach is that the Christoffel equation must be solved for the z-component of the wave-vector that satisfies for the frequency used and all the in-plane wave-vector components. In this way, the acoustic displacement amplitude on any plane in the water and inside or at the surface of the silicon plate can be calculated with reflectance and transmission functions.

3.   EXPERIMENT

Figure 1 illustrates a schematic diagram of the experimental measurement. The optoacoustic system comprises a computer for controlling all operations and data acquisition, a laser interferometric system based on the photorefractive effect, a detachable revolving nosepiece including optical objective lenses, and an inverted SAM including a receiver and/or transmitter, and a specimen holder allowing x-y-z motions.

An acoustic lens was used to form a point focus within the specimen. The point focus acoustic lens comprises a piezoelectric transducer (i.e., zinc oxide) and a buffer rod made of a single crystal of sapphire.   The piezoelectric transducer located on the top of the buffer rod was driven in the continuous wave mode at a single frequency. The excitation voltage at the transducer was approximately 5 volt peak-to-peak. The electrical signal was converted into an acoustic signal (i.e., ultrasonic plane wave) by the transducer. The shape of the transducer was substantially circular with a diameter of 1mm and a thickness of about 10 µm respectively. The maximum output from the transducer was measured at 185 MHz.   The ultrasonic plane wave traveled through the buffer rod to a spherical recess (hereinafter called simply the "lens") located at the bottom of the buffer rod. The lens contained a silicon-oxide layer to form an acoustic impedance matching layer (i.e., acoustic anti-reflection coating) for coupling into water. The diameter of the lens aperture was 843 µm, the aperture angle 120º, and the working distance was 310 µm.

A thin (100) silicon plate (thickness 75 µm) was used as a specimen. The back surface of the specimen was above the lens with its normal along the lens Z-axis.   The front and back surfaces of the specimen had been mechanically polished to provide a well characterized boundary. The ultrasonic beam was focused onto a predetermined interior or exterior plane of the specimen by controlling the standoff distance between the lens and the back surface.   A special filling apparatus was designed to keep the water coupling in place over periods of a week or more without refilling.   The water temperature was substantially kept at 23ºC.

The laser interferometer utilized a CW 532 nm Nd:YAG laser and a photorefractive interferometer based on Bismuth Silicon Oxide.   Data acquisition was synchronized to the source excitation so that complete determination was made of the ultrasonic normal displacement amplitude and phase spatially along the sample front surface plane. With a 20X optical objective, the field of view was about 300 µm, and the spatial resolution was on the order of 1–2 µm.
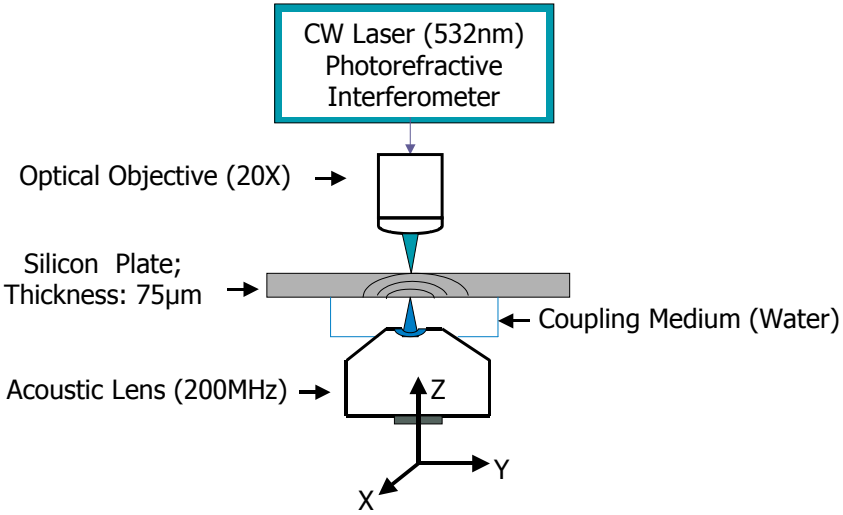
Figure 1. A schematic diagram of an optoacoustic system.

4. EXPERIMENTAL AND THEORETICAL RESULTS

Figure 2 shows the focusing geometry for the measurements, defining the standoff distance Z_F. This distance was varied to change the acoustic lens focal point from outside to inside the material plate. The zero point for Z_F is a location about 600 μm below the plate front surface, as shown. When Z_F = +200 μm, the focal point is calculated to be at the plate back surface. At each standoff distance, the ultrasonic displacement was recorded at the plate front surface by scanning the sample under the optical objective. Although the system employed can image the data without scanning, the low signal to noise level observed precluded imaging for the excitation levels employed.
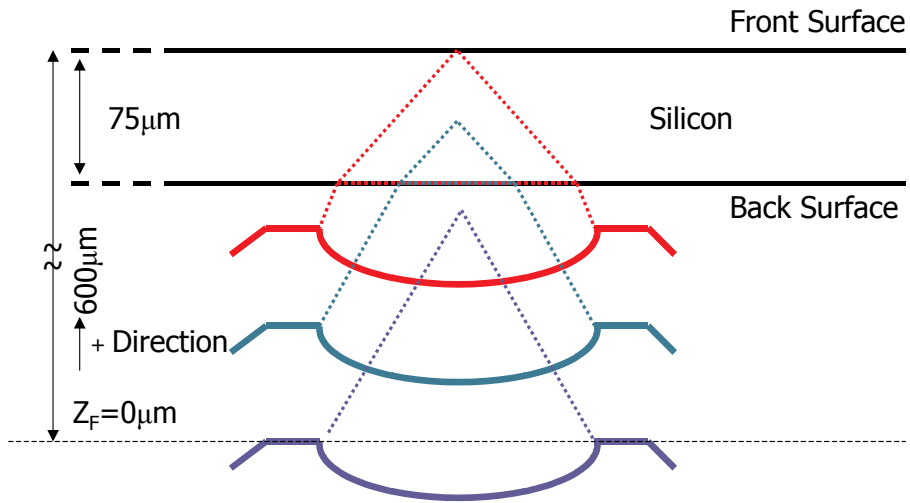
Figure 2. Focusing geometry showing the focal distance variable ZF that is varied from – 891 μm to +300 μm to produce focal points outside and inside the material plate. The origin ZF = 0 is 600 μm from the front surface of the silicon plate.

Figure 3(c) shows the images when the acoustic lens is substantially focused onto the back surface of the specimen. The focal beam spot (the circle at the center) having the maximum intensity is clearly observed. Figure 3(d) shows the phase velocities and wave slowness diagrams for Si(100) and illustrates the variety of wave propagations possible. Also shown is the slowness diagram for S_0 mode plate waves as a function of propagation direction along the plate surface. At the high frequency employed, the S_0, A_0 and Rayleigh modes all coincide. The images of the acoustic wavefronts have essentially the same symmetry properties as the wavenumber as a function of propagation direction, since the material is cubic. Comparison of the acoustic displacement amplitude with the wavenumber prediction for Si(100) shows this similarity in Fig. 3(d).

Figure 3(e) and 3(f) are the experimental and theoretical images when the acoustic lens is mechanically moved toward the front surface from the back surface plane, which would place the focal point above the front surface. Since the aperture angle of the lens is large, longitudinal, shear and surface acoustic waves are all generated when defocusing the lens toward the specimen. Also, since the excitation is continuous, plate wave modes are present due to multiple reflections from the surfaces. Figure 3(e) shows all wave amplitudes simultaneously; therefore, only through mathematical modeling can discrimination be accomplished between the various types of waves shown in the image.

5.   CONCLUSIONS

We presented a hybrid acoustic imaging technique to directly visualize amplitude of acoustic waves propagating within a thin silicon (100) plate as a complimented approach to the conventional SAM. The technique comprises a laser based acoustic microscopy and a mechanical scanning acoustic reflection microscopy. A high frequency acoustic point focus lens (~200 MHz) was used to form a small point source within the plate. Distinct symmetric amplitude patterns were observed as the acoustic focal point moved toward the front surface of the plate. We are planning to use a newly designed acoustic lens for generating large amplitude of ultrasonic waves with higher frequency to form their clearer visualization without mechanical scanning.

   We have also developed a mathematical model (i.e., a method of angular spectrum for a plane wave) to calculate an elastic wave field for prediction of acoustic behavior of isotropic and/or anisotropic materials. The computer simulation results based on the model have been compared to the experimental results and had good agreement.

ACKNOWLEDGEMENTS

(a) Experiment

(b) Theory

(c) Experiment

(d) Theory

(e) Experiment

(f) Theory
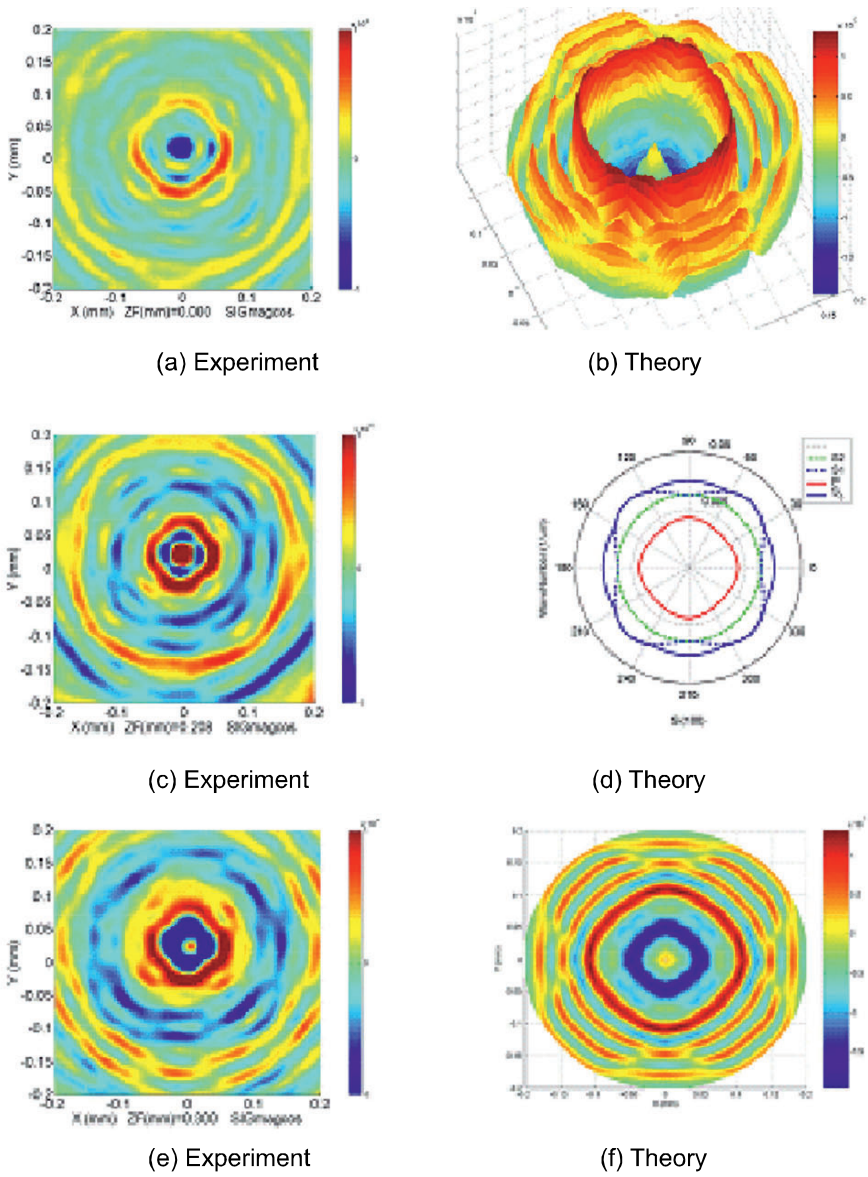
Figure 3. Images of the ultrasonic motion (magnitude x cosine (phase)) at the surface as the standoff distance ZF is changed as indicated.

REFERENCES

1 C. F. Quate, "Acoustic Microscopy," *Physics Today*, Vol. 38, pp. 34–42, (August 1985).

2 N. Chubachi, "Ultrasonic Micro-Spectroscopy via Rayleigh Waves," in *Rayleigh-Wave Theory and Application*, edited by E. A. Ash and E. G. S. Paige, Proceedings of an International Symposium Organized by the Rank Prize Funds at the Royal Institution, London 15-17 July, 1985, pp. 291–297.

3 J. Kushibiki, N. Chubachi, "Material Characterization by Line-Focus-Beam Acoustic Microscope," *IEEE Trans.* **SU-32**(2), pp. 189–212, (March 1985).

4 K. L. Telschow, "Full-Field Imaging of Gigahertz Film Bulk Acoustic Resonator Motion," *IEEE Trans.* **50**(10), pp. 1279–1285, (October 2003).

5 K. L. Telschow, V. A. Dearson, D. L. Cottle, and J. D. Larson III, "Full-Field Imaging of Acoustic Motion at Nanosecond Time and Micron Length Scale," in 2002 *IEEE Ultrasonics. Symposium,* pp. 601–604, (2002).

6 K. L. Telschow, V. A. Dearson, D. L. Cottle, and J. D. Larson III, "UHF Acoustic Microscopic Imaging of Resonator Motion," in 2000 *IEEE Ultrasonics. Symposium,* pp. 631–634, (2000).

7 K. L. Telschow, V. A. Dearson, R. S. Schley, and S. M. Watson, "Direct Imaging of Lam Waves in Plates using Photorefractive Dynamic Holography," *J. Acoust. Soc. Am.*, **106**(5)*, pp. 2578–2587, (1999).

8 M. F. Hamilton, Yuri A. Il'inskii, and E. A. Zabolotskaya, "Nonlinear Surface Acoustic Waves in Crystals," *J. Aoust. Soc. Am.* 105(2), pp. 639–651, (February 1999).

9 D. J. Vezzetti, "Propagation of Bounded Ultrasonic Beams in Anisotropic Media," *J. Aoust. Soc. Am.* **78**(3), pp. 1103–1108, (September 1985).

10 A. Atalar, "An Angular-Spectrum Approach to Contrast in Reflection Acoustic Microscopy," *J. Appl. Phys.*, **49**(10), pp. 5130–5139, (October 1978).

ULTRASONIC NANO-IMAGING SYSTEM FOR MEDICINE AND BIOLOGY

Y. Saijo, N. Hozumi, K. Kobayashi, N. Okada, Y. Hagiwara, H. Sasaki, E.d. S. Filho, T. Yambe
Department of Medical Engineering and Cardiology, Institute of Development, Aging and Cancer, Tohoku University, Sendai 980-8575, Japan; Aichi Institute of Technology, Toyota 470-0392, Japan; Honda Electronics Co. Ltd., Toyohashi 441-3193, Japan; Department of Orthopedic Surgery, Tohoku University, Graduate School of Medicine, Sendai 980-8575 Japan

Abstract: The ultrasonic nano-imaging system for medicine and biology that has two measurement modes was developed. The transmission mode realized non-contact high resolution imaging of cultured cells. This mode can be applied for assessment of biomechanics of the cells and thinly sliced tissues. The reflection mode visualized fine structures of the brain of rat. This mode can be applied for intra-operative pathological examination because it does not require slicing or staining.

Key words: Acoustic microscopy, Nano-imaging, Cell

1.   INTRODUCTION

We have been developing acoustic microscopy for medicine and biology for more than twenty years. Application of acoustic microscopy in medicine and biology has three major features and objectives. First, it is useful for intra-operative pathological examination because staining is not required. Second, it provides basic acoustic properties to assess the origin of lower frequency ultrasonic images. Third, it provides information on biomechanics at a microscopic level.

In the present study, an ultrasonic nano-imaging system that has two measurement modes, non-contact mode for cells and contact mode for tissues, is proposed.

2.   METHODS

2.1   Instruments

Figure 1 shows the block diagram of the ultrasonic nano-imaging system. An electric impulse was generated by a high speed switching semiconductor. The start of the pulse was within 400 ps, the pulse width was 2 ns, and the pulse voltage was 40 V. The frequency of the impulse covered up to 500 MHz. The electric pulse was input to a transducer with sapphire rod as an acoustic lens and with the central frequency of 300 MHz. The ultrasound spectrum of the reflected ultrasound was broad enough to cover 100–500 MHz.
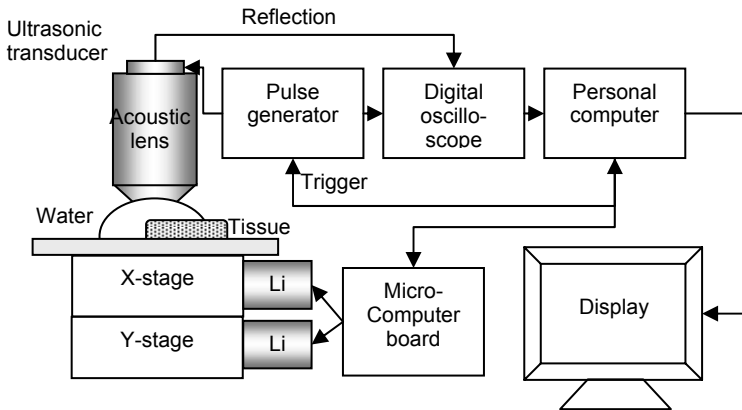
Figure 1. Block diagram of the ultrasonic nano-imaging system.

The reflections from the tissue was received by the transducer and were introduced into a Windows-based PC (Pentium D, 3.0 GHz, 2GB RAM, 250GB HDD) via a digital oscilloscope (Tektronix TDS7154B, Beaverton, USA). The frequency range was 1 GHz, and the sampling rate was 20 GS/s. Four values of the time taken for a pulse response at the same point were averaged in order to reduce random noise.

The transducer was mounted on an X-Y stage with a microcomputer board that was driven by the PC through RS232C. The Both X-scan and Y-scan were driven by linear servo motors.

The ultrasonic nano-imaging system has two different modes for observation. Figure 2 shows the schematic illustration. The left figure shows the transmission mode for precise imaging (classical acoustic microscopy). The ultrasound propagates through the thinly sliced specimen or cultured cells and reflects at the interface between the specimen and substrate. The right figure shows the reflection mode (acoustic impedance imaging). The ultrasound propagates through the thin plastic plate and reflects at the interface between plastic and tissue.
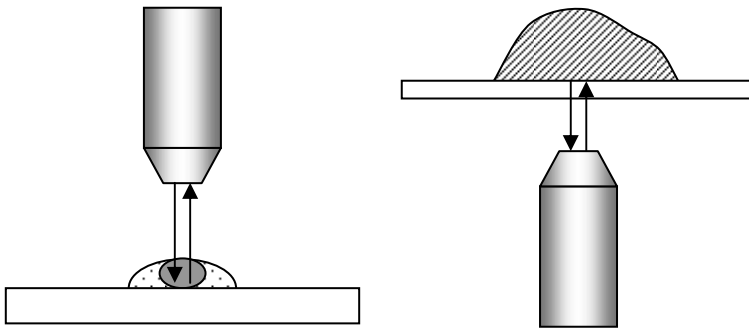
Figure 2. Schematic illustration of two measurement modes in ultrasonic nano-imaging system. *Left*: transmission mode, *right*: reflection mode.

2.2   Tissue preparation

2.2.1   Transmission Mode

Transmission mode is mainly used for visualization of thinly sliced tissues or monolayered cultured cells. In the present study, cultured fibroblast cells were observed by the transmission mode of the ultrasonic nano-imaging system. Fibroblasts were cultured on 35 mm diameter dishes with the Dulbecco's modified Eagle's medium and 10% heat-incubated bovine serum [1]. The incubator was maintained at 37°C and filled with 95% air and 5% CO_2. After 4 days of culture, cells were found to be in the confluent state by inverted microscopy.

2.2.2   Reflection Mode

Reflection mode can be applied for visualization of tissue surface without thinly slicing the biological tissue. Rats were dissected and removed their whole brain. A sagittal cross section was made to the brain by a rotor slicer. The specimen was rinsed and preserved in the phosphate buffer solution. For optical observation, some adjacent slices were subjected to immuno-histochemical staining against calbindin D-28k.

2.3   Signal Processing

2.3.1   Transmission Mode
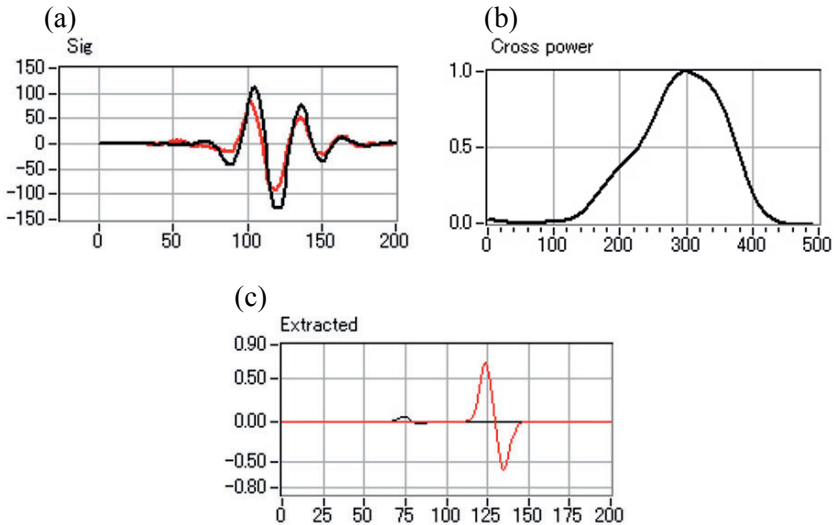
Figure 3. (**a**) The waveform at the tissue area (*red*) and that from substrate (*black*), (**b**) the power spectrum of the reflection at the tissue area, (**c**) reflection from the tissue surface (*black*) and the reflection from the substrate (*red*).

Reflected waveforms are shown in Fig. 3(a). The waveform at the tissue area is shown in black line and that from substrate is shown in red line. Both signals were captured on the same line in x-scanning. The power spectrum of the reflection at the tissue area is shown in Fig. 3(b). The spectrum covers the frequency up to 500 MHz. The reflection from the tissue area contains two components. One is from the tissue surface and another from the

interface between the tissue and substrate. Frequency domain analysis of the reflection enables the separation of two components. Figure 3(c) shows the response to a singlet. The left black wave is the reflection from the tissue surface and the right red wave is the reflection from the substrate. These signal processing enables the calculation of tissue thickness and speed of sound [2].

2.3.2 Reflection Mode

The target signal is compared with the reference signal and interpreted into acoustic impedance as

$$
Z_{target} = \frac{1 - \dfrac{S_{target}}{S_0}}{1 + \dfrac{S_{target}}{S_0}} Z_{sub} = \frac{1 - \dfrac{S_{target}}{S_{ref}} \cdot \dfrac{Z_{sub} - Z_{ref}}{Z_{sub} + Z_{ref}}}{1 + \dfrac{S_{target}}{S_{ref}} \cdot \dfrac{Z_{sub} - Z_{ref}}{Z_{sub} + Z_{ref}}} Z_{sub}
$$

where S_0 is the transmitted signal, S_{target} and S_{ref} are reflections from the target and reference, Z_{target}, Z_{ref} and Z_{sub} are the acoustic impedances of the target, reference and substrate, respectively [3].

3. RESULTS

Figure 4(a) shows the images obtained with the ultrasonic nano-imaging system. The left figure shows the cultured fibroblasts by transmission mode. The high intensity area at the central part of the cell corresponds to the nucleus and the high intensity area at the peripheral zone corresponds to the cytoskeleton. The division of the nucleus is clearly shown. Figure 4(b) shows the brain of rat by transmission mode. Four layers are visible; molecular layer (ML), Purkinje layer (PL), internal granular layer (IGL) and white matter (WM) in mature cerebellum.
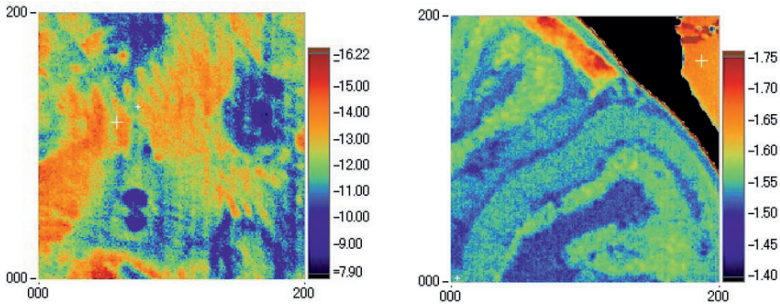
Figure 4. Images obtained with ultrasonic nano-imaging system. *Left*: cultured fibroblast, *right*: brain of rat.

4.   CONCLUSIONS

The ultrasonic nano-imaging system for medicine and biology that has two measurement modes was developed. The system can be applied for intra-operative pathological examination because it does not require slicing or staining.

ACKNOWLEDGMENTS

REFERENCES

1.   Saijo Y, Sasaki H, Sato M, Nitta S, Tanaka M. *Ultrasonics* 38 (2000) 396.
2.   Hozumi N, Yamashita R, Lee CK, Nagao M, Kobayashi K, Saijo Y, Tanaka M, Tanaka N, Ohtsuki S. *Ultrasonics* 42 (2004) 717.
3.   Hozumi N, Kimura A, Terauchi S, Nagao M, Yoshida S, Kobayashi K, Saijo Y. *Proc 2005 IEEE International Ultrasonics Symposium* 170.

ELASTIC CHANGES OF CAPSULE IN A RAT KNEE CONTRACTURE MODEL ASSESSED BY SCANNING ACOUSTIC MICROSCOPY

Y. Hagiwara, E. Chimoto, A. Ando, Y. Saijo, E. Itoi

Department of Orthopaedic Surgery, Tohoku University, Graduate School of Medicine, Sendai 980-8574, Japan; Department of Medical Engineering and Cardiology, Institute of Development, Aging and Cancer, Tohoku University, Sendai 980-8575, Japan

Abstract: Sound speed of a capsule in a rat knee contracture model was measured by scanning acoustic microscopy. There was no statistical significant difference in the anterior capsule compared with the control group. However, the sound speed of the posterior capsule was significantly greater compared with the control group after prolonged immobilization.

Key words: Immobility, Knee, Capsule, Sound speed, Contracture

1.   INTRODUCTION

Joint contracture is defined as a decrease in both active and passive ranges of motion after immobilization. It is often seen in daily examinations, but its pathogenesis has been unsolved. Disadvantages of limited motion of the joints include various degrees of limitation in the activities of daily living. Even by extensive rehabilitation or surgical treatment, however, it is difficult to regain the full ROM (ranges of motion) in an established joint contracture after a long period of immobilization [1,2]. Therefore, prevention of joint contracture is of prime importance for clinicians.

A fibrotic change of a capsule is suggested to be one of the main causes of joint contracture [3]. However, it is not known yet how the elasticity of the capsule is affected by immobilization. In our previous study, range of motion was severely restricted in extension in our model and was recovered

after release of the posterior capsule. This result indicated that the posterior capsule was one of the main causes of limitation in extension.

In the present study, we applied a scanning acoustic microscopy (SAM) to examine the elasticity of the capsule in the course of knee joint immobilization in a rat experimental model.

2.   MATERIALS AND METHODS

Animals: The protocol for this experiment was approved by the Animal Research Committee of Tohoku University. Adult male Sprague-Dawley rats (CLEA Japan Inc., Tokyo, Japan) weighing from 380 to 400 g were used. Their knee joints were immobilized at 150° in flexion with a plastic plate (POM-N, Senko Med. Co., Japan) and metal screws for various periods (1, 2, 4, 8 and 16 weeks) [4]. Sham operated animals had holes drilled in the femur and tibia and screws inserted but none of them were plated (Fig. 1). The surgery was performed under anesthesia with sodium pentobarbital (50 mg/kg) administered intraperitoneally. The animals were allowed unlimited activity and free access to water and food. Sixty rats were prepared (1, 2, 4, 8, and 16 weeks, 6 rats for each group at each time point). The immobilized animals and the sham operated animals made up the immobilized group and the control group, respectively.
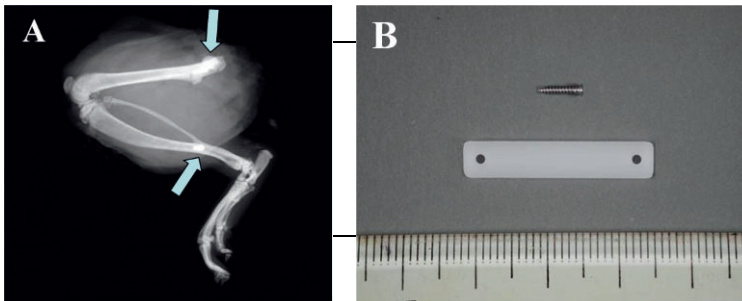
Figure 1. Method of a knee joint immobilization. **A**; Lateral X-ray picture of a rat knee. **B**; Plate and screw. Arrows indicated screws. The plate was not identified on X-ray picture because it was radiolucent.

Tissue Preparation: The rats were anesthetized and fixed with 4% paraformaldehyde in 0.1 M phosphate-buffer, pH 7.4 by perfusion through the aorta. The knee joints were resected and kept in the same fixative overnight at 4°C. To keep the morphology intact, the specimens were decalcified as a whole knee joints in 10% EDTA in 0.01 M phosphate-buffer,

pH 7.4 for 2 months at 4°C. After dehydration through a graded series of ethanol solution, the specimens were embedded in paraffin. The embedded tissue was cut into 5-μm sagittal sections from the medial to the lateral side of the joint. Standardized serial sections were kept in the medial midcondylar regions of the knee. The serial sections were prepared for hematoxylin-eosin stain to observe the histological appearance of the capsule after immobilization (Fig. 2).
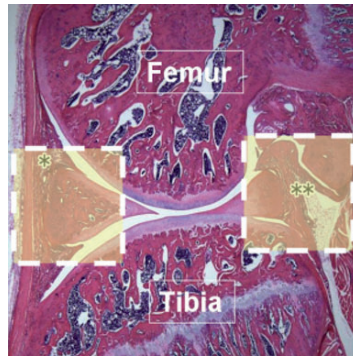
Figure 2. Microphotograph of a sagittal section in the medial midcondylar region of a rat knee. Squares indicate regions of analysis by scanning acoustic microscopy in the anterior(*) and posterior(**) capsules. (Original magnification $\times$ 10, hematoxylin-eosin stain).

2.1　　Scanning Acoustic Microscopy

Our SAM consists of five parts: (1) ultrasonic transducer, (2) pulse generator, (3) digital oscilloscope with PC, (4) microcomputer board and (5) display unit. A single pulsed ultrasound with 5 ns pulse width was emitted and received by the same transducer above the specimen. The aperture diameter of the transducer was 1.2 mm and the focal length was 1.5 mm. The central frequency was 80 MHz and the pulse repetition rate was 10 kHz. Considering the focal distance and the sectional area of the transducer, the diameter of the focal spot was estimated as 20 μm at 80 MHz. Distilled water was used as the coupling medium between the transducer and the specimen. The reflections from the tissue surface and from interface between the tissue and the glass were received by the transducer and were introduced into a digital oscilloscope (Tektronics TDS 5052, USA). The frequency range was 300 MHz and the sampling rate was 2.5 GS/s. Four pulse responses at the same point were averaged in the oscilloscope in order to reduce random noise.

The transducer was mounted on an X-Y stage with a microcomputer board that was driven by the computer installed in the digital oscilloscope through an RS-232C. The X-scan was driven by a linear servo-motor and the

Y-scan was driven by a stepping motor. Finally, two-dimensional distributions of the ultrasonic intensity, sound speed and thickness of the 2.4 by 2.4 mm specimen area were visualized with 300 by 300 pixels. The total scanning time was 121 s.

2.2   Signal Analysis

The reflected waveform comprises two reflections at the surface and the interface between the tissue and the glass. The thickness and sound speed were calculated by Fourier-transforming the waveform [5].

   Image analysis: A region of analysis by SAM was set in the anterior and posterior capsule in each section (Fig. 2). In the region, the sound speed of capsule was calculated with a gray scale SAM images. SAM images with a gradation color scale were also produced for clear visualization of the sound speed.

   Statistics: Statistical analysis among groups was performed using the Kruskal-Wallis test, with Bonferroni/Dunn post-hoc multiple comparisons. Differences between the experimental and control groups were compared at each time point by Mann-Whitney's U test. A *P* value less than 0.05 was considered statistically significant.

3.   RESULTS

Gradation color images: In the posterior capsule, the low sound speed area decreased and high sound speed areas gradually increased in the experimental group with time. The anterior capsule was similar in all the experimental and control groups irrespective of immobilization periods (Fig. 3).
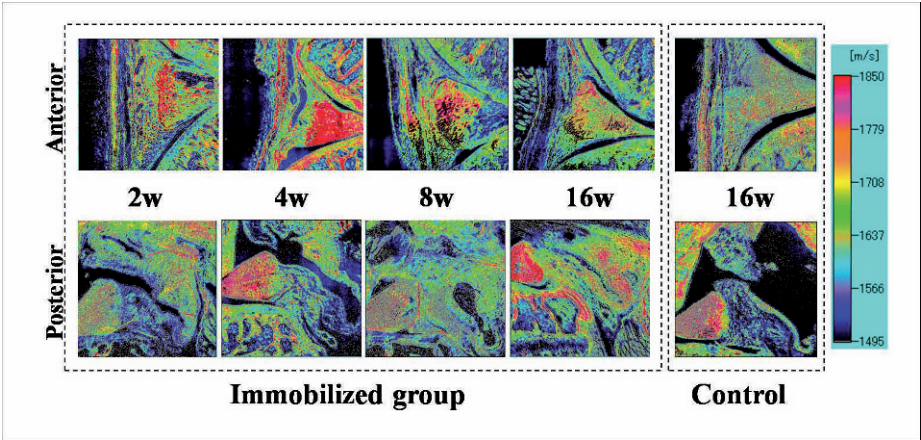
Figure 3. Gradation color images of scanning acoustic microscopy in the anterior and the posterior capsules.

Sound speed: In the posterior capsule, there was no statistical difference between the experimental and the control groups in 1-, 2- or 4-week immobilization. However, the sound speed in the experimental group was significantly higher than that in the control group in 8- and 16-week immobilization. There was no statistical difference in the anterior capsule in all the experimental and the control groups at any period of immobilization (Fig. 4).
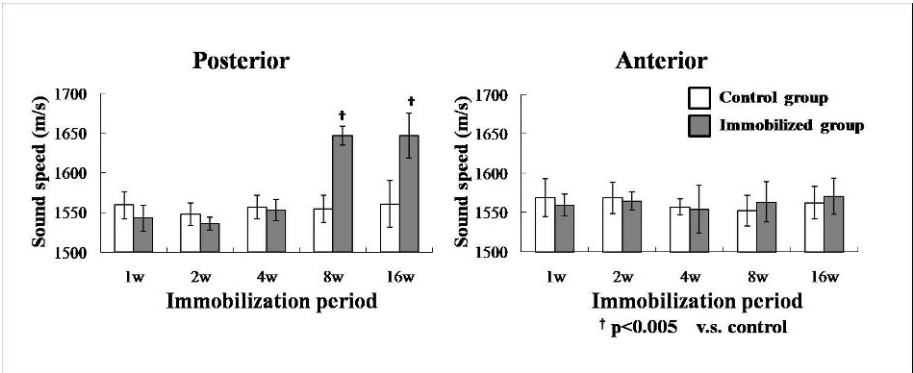
Figure 4. Sound speed changes of the anterior and the posterior capsules.

4. DISCUSSION

In a study using a canine shoulder contracture model, the intra-articular pressure rose higher by injection of Hypaque contrast medium and the filling

volume was smaller compared with the control group at a rupture of the capsule [6]. This study suggests that immobilization changes a mechanical property of the capsule, which may mostly contribute to production of joint contracture.

Connective tissue response after immobilization is important to understand the mechanism of the increased elasticity of the posterior capsule. Some suggestions concern changes in the biochemical composition of periarticular fibrous connective tissue (e.g. patellar tendon, ligament and joint capsule) after immobilization. The notable change was a reduction of water and glycosaminoglycans without decreased collagen mass [3,7–9]. These changes were expected to alter plasticity and pliability of connective tissue matrices and to reduce lubrication efficiency [8].

Difference in elasticity of the anterior and posterior capsules may be explained by the potential remnant mobility of the patella in the medial/lateral directions in the anterior part of the joint even after immobilization. Another possible explanation would be a difference in blood flow in the stretched side and compressed side of the joint. Whatever the reason, the structural changes occurred mainly in the posterior capsule.

5.   CONCLUSION

Elasticity of the posterior capsule increases in a rat knee contracture model after prolonged immobilization.

REFERENCES

1. Peacock EE. Ann Surg 164 (1966) 1.
2. Damron TA, Greenwald TA, Breed A. Clin Orthop 301 (1994) 249.
3. Woo SL, Matthews JV, Akeson WH, Amiel D. Convery FR Arthritis Rheum 18 (1975) 257.
4. Hagiwara Y, Saijo Y, Chimoto E, Akita H, Sasano Y, Matsumoto F, Kokubun S. Ups J Med Sci 111 (2006) 303.
5. Hozumi N, Yamashita R, Lee CK, Nagao M , Kobayashi K, Saijo Y, Tanaka M, Tanaka N, Ohtsuki S. Ultrasonics 42 (2004) 717.
6. Shollmeier G, Sarkar K, Fukuhara K, Uhtoff HK. Clin Orthop 323 (1996) 310.
7. Amiel D, Akeson WH, Harwood FL, Mechanic GL. Connect Tissue Res 8 (1980) 27.
8. Akeson WH, Woo SL, Amiel D, Coutts RD, Daniel D. Clin Orthop 93 (1973) 356.
9. Akeson WH, Amiel D, La Violette D. Exp Gerotol 3 (1968) 289.

A STUDY OF THE POTENTIAL TO DETECT CARIES LESIONS AT THE WHITE-SPOT STAGE USING V(Z) TECHNIQUE

E. Y. Bakulin, L. A. Denisova, R. Gr. Maev
Department of Physics, University of Windsor, Windsor, Ontario, Canada

Abstract: Current wide-spread methods of non-destructive methods of caries diagnostics, such as X-ray techniques, do not provide the possibility to efficiently detect enamel caries lesions at the beginning ("white-spot") stage, when the tooth tissue is only slightly altered and no loss of the tissue occurs. Therefore, it is of paramount importance to develop new, more sensitive methods of caries diagnostics. In this paper, certain aspects of the ultrasonic approach to the problem are discussed - in particular, detection of the enamel's surface caries at the white-spot stage with a focused ultrasonic sensor positioned in front of the caries lesion (without cross-sectioning the tooth). Theoretical model using V(z) approach for layered media was applied to perform computer simulations resulting in V(z) curves for the different parameters of carious tissue and the degree of degradation. The curves were analyzed and it was shown that, comparing to a short-pulse/echo technique, V(z) approach provides much better distinction between sound and carious enamel and even makes possible to evaluate the degree of demineralization.

Key words: White-spot caries, Ultrasound, v(z).

1.   INTRODUCTION

According to existing literature [1,2], current wide-spread methods of non-destructive methods of caries diagnostics, such as X-ray techniques, do not provide the possibility to efficiently detect caries lesions at the beginning stage, when the tooth tissue is only slightly altered (by its density, bio-composition and elastic properties) and no loss of the tissue occurs. Therefore, it is of paramount importance to develop new, more sensitive methods of caries diagnostics.

The white-spot stage of the caries development is the stage at which, under certain conditions, demineralization of the tooth's dentin or enamel surface starts. This is immediately followed by the attempt of an organism to compensate for possible danger to the tissue by depositing a thin layer of more dense and mineralized tissue on top of the degrading region. The thickness of this layer is typically in the range of 10–30 μm, and the reduction in density and sound speeds in the core of the lesion can reach more than 20% [3–5].

It should be noted that though the carious lesions have been studied in cross-sections of the tooth [4–8], the problem of the ultrasonic white-spot caries detection from the external surface of an un-cut tooth was not approached widely.

The goal of this work was to theoretically investigate aspects of the ultrasonic detection of the enamel's surface caries at the white-spot stage with a focused ultrasonic sensor positioned in front of the caries lesion (without cross-sectioning the tooth) using V(z) approach for layered media.

2.   THEORETICAL MODEL

In order to provide clear understanding of ultrasonic methods which could be used for the detection of such lesion in-vivo (with an ultrasonic sensor positioned in front of the caries lesion), a series of computer simulations was performed in this work. The lesion was modeled as follows. The densities of the enamel were taken as 3.3, 3.2 and 2.5–3.2 g/cm^3 for the white layer, the sound and the carious enamel, respectively. The longitudinal sound speeds were taken as 6200, 6000 and 6000–4600 m/s for the white layer, the sound and the carious enamel, respectively. The shear sound speeds were taken as 0.5 of the longitudinal speeds. The thickness of the white layer was varied between 0 and 25 μm. For carious enamel, all parameters were varied together (lower values for higher degree of caries). The reflected signal was modeled using V(z) approach [9] for layered media [10] as follows.

Integrated received reflected field on the piezoelement is:

$$V(\Delta z) = V_0 \int_0^\infty \left(u_1^+(r)\right)^2 \cdot P^2(r) \cdot R(r/f) \cdot \exp\left[-i(k_0 \Delta z / f^2)r^2\right] \cdot r dr, \tag{1}$$

where Δz – vertical displacement of the lens from the focal position, $u_1^+(r)$ - acoustic field at the back focal plane of the lens; $P(r) = \{1, r \leq r_{max}; 0, r > r_{max}\}$ – pupil function of the lens; $f \approx R_{lens}/(1- c_0/c_{lens})$ – focal distance of the lens with curvature radius R_{lens} (made from material with sound speed c_{lens}) in coupling liquid (water with sound speed c_0); $R(r/f) =$

$(Z_{in} - Z_0)/(Z_{in} + Z_0)$ – complex reflectance function of the object (tooth) with respect to the angle of incidence θ_0 where $r/f = \sin\theta_0$; $Z_0 = \rho_0 c_0/\cos\theta_0$ – input impedance of the immersion (water); $Z = Z((d, c_l, c_s, \rho)_{\text{white layer}}, (c_l, c_s, \rho)_{\text{carious enamel}}, \theta_0, \omega)$ – complex input impedance of system "hard white layer – underlying softer enamel"; d – thickness, c_l, c_s – longitudinal and shear speed, ρ – density of each medium.

Taking into account possible future applications in clinics, an ultrasonic focused transducer with working frequency of 100 MHz (wavelength in enamel $\sim$ 50–60 µm) and a half-aperture of 50° was considered here for the following reasons:

(a) beam spot size must be smaller than 0.5 mm,

(b) wavelength must be much larger than the size of pores (see Fig. 1),

(c) wavelength must be comparable with the white layer's thickness,

(d) pulse length (tone-burst in V(z) mode is $\sim$10 periods) must be smaller than the carious region,

(e) aperture angle must be large enough to excite Rayleigh waves in demineralized enamel ($\sin^{-1}(1500/2000) \approx 50^\circ$).

3.   RESULTS

In the first series of simulations, amplitudes of the reflected signal at the vertical position, corresponding to the maximum amplitude, were calculated for different thicknesses of the white layer with varying sound speed under the layer. The results obtained (see Fig. 1) indicate that using only the amplitude of the reflected signal, it is practically impossible to clearly
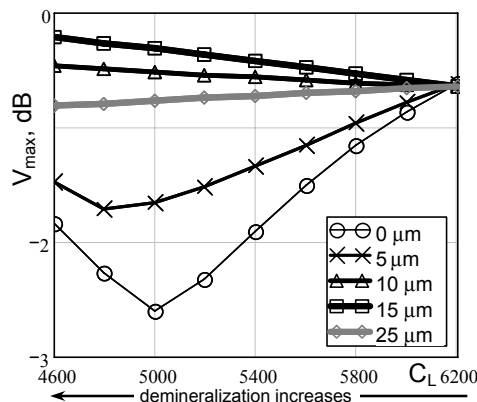
Figure 1. Reflected amplitude "at focus" vs. C_L in degrading enamel for different thickness of the white layer.

determine whether or not caries has developed (if the white layer is present) and the degree of enamel degradation under the layer – the amplitudes could be almost the same for very different combinations of parameters.

In the second series of simulations, dependencies of the amplitude and the phase of the reflected signal on the vertical position of the sensor (V(z) curves) were calculated (see Fig. 2).
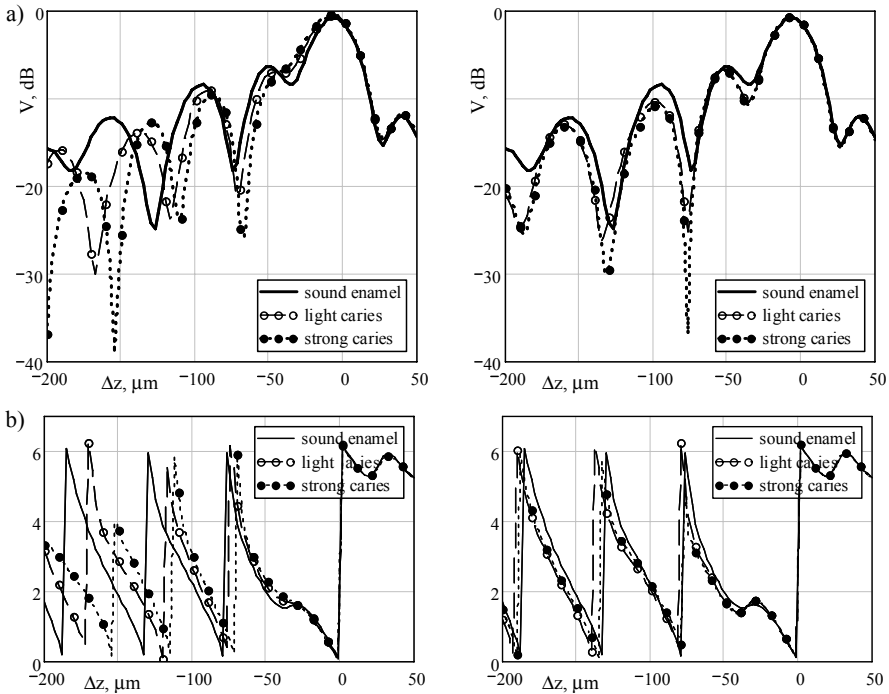
Figure 2. Amplitude (**a**) and phase (**b**) of the reflected signal for the sound enamel (*solid lines*), lightly developed lesion (*dashed lines*) and strongly developed lesion (*dotted lines*). Thickness of the white layer: *left graphs* – 10 μm, *right graphs* – 25 μm.

One can clearly see that in the case of thin white layer (10 μm, see Fig. 2 left graphs), even with the same values of the maximal amplitude and corresponding phase (at the focus), the shapes of V(z) curves are very different for the sound and carious enamel. This is caused by the decrease of the surface wave speed due to the demineralization. Therefore, in a real experiment, the degree of demineralization could be estimated as a value which is proportional to the shift of V(z) curves or, equivalently, to the change in the surface wave's speed (this speed can be calculated from V(z) curves using various techniques [11]).

However, in the case of thick white layer (25 µm, see Fig. 2 right graphs), the fastening effect of the dense white layer on the surface wave speed may overcome the slowing effect of the demineralization and the shift of the V(z) curves may be reversed. The next step of the research will be to overcome this difficulty,

4.   CONCLUSION

It has been shown that V(z) technique has higher potential for the detection of caries at the white-spot stage than traditional pulse-echo methods. The results of the computer simulations have shown, that using only the maximum amplitude of the reflected signal (i.e. in short pulse – echo approach), it is practically impossible to clearly determine whether or not caries has developed (if the white layer is present) and what is the degree of enamel degradation under the layer.

In the case of thin white caries layer, V(z) model provided good distinction between sound and carious enamel and even makes possible to evaluate the degree of demineralization and therefore has higher potential for the detection of caries at the white-spot stage than traditional pulse-echo methods.

In the case of thick white layer, the fastening effect of the dense white layer overcomes the effects caused by the underlying softer demineralized tissue and the shift of V(z) is reversed.

ACKNOWLEDGEMENTS

REFERENCES

1. A. Hall, J.M. Girkin: J. Dent. Res., 83 (2004), pp. 89–94.
2. G.K. Stookey, C. Gonzalez-Cabezas: J. Dent. Educ., 2001, 65(10), pp. 1001–1006.
3. A.I. Darling: Br. Dent. J., 101 (1956), pp. 289–297.
4. S.D. Peck, GAD Briggs: Adv. Dent. Res., 1 (1987), pp. 50–63.
5. R.Gr. Maev, L.A. Denisova, E. Yu. Maeva, A.A. Denisov: Ultrasound Med. Biol., 2002, 28(1), pp. 131–136.

6. S.R. Ghoraeb and T. Valle: Experimental evaluation of human teeth using noninvasive ultrasound: echodentograpgy. IEEE Trans. on UFFC, 2002; 49(10):1437–1443.

7. R. Wichard, J. Schlegel, R. Haak, J.F. Roulet and R.M. Schmitt: Dental diagnosis by high frequency ultrasound. In: Torboli P and Masotti L, eds. Acoustical Imaging Vol. 22. New York: Plenum Press, 1996; 329–334.

8. J.P. Zheng, E.Yu. Maeva, A.A. Denisov and R.G. Maev: Ultrasound imaging of human teeth using desktop scanning acoustic microscope. In: Hua Lee, ed. Acoustical Imaging Vol. 24. New York-London-Moscow: Kluwer Academic/Plenum Publishers, 2000; 165–171.

9. A. Atalar: J. Appl. Phys., 49 (1978), pp. 5130–5139.

10. L.M. Brekhovskikh: Waves in layered media, 2nd edition. Acad. Press, N.-Y., 1980.

11. G.A.D. Briggs, Acoustic microscopy, Oxford, Clarendon Press, 1992.

INVESTIGATION OF HUMAN NAIL MICROSTRUCTURE WITH ULTRASOUND

A.R. Maeva, E.Y. Bakulin, L.A. Denisova, R.Gr. Maev

Center for Imaging Research and Advanced Material Characterization, Faculty of Science, University of Windsor, Ontario, Canada

Abstract: Investigation of a human fingernail and the extraction of the data on its microstructure and elastic properties is important in three main aspects. First of all, various diseases of the nail can be differentiated more precisely; second of all, it is possible to non-invasively track during time the effects of a cosmetic product upon the nail; third of all, because various processes in the organism have a strong influence upon the nail plate growth, the monitoring of the nail morphology and its mechanical properties may be used as additional information for the diagnosis of a number of medical disorders, such as systemic sclerosis, psoriasis, chronic hand eczema, anemia etc. The aim of the present study was to carry out a detailed ultrasound investigation in the high-frequency range (25–50 MHz) of a human nail including micro-anatomical structure imaging and ultrasound velocity evaluation, using B-scans obtained with a scanning acoustic microscope. On the images, exact topology of the nail, nail matrix and the underlying bone have been revealed. Additionally, a certain type of inclined internal layering along the nails of some individuals has been found, which was not reported in previous ultrasonic studies of the nail.

Key words: Finger nail, Microstructure, Imaging, Ultrasound.

1.   INTRODUCTION

The development of new methods for the investigation of a human fingernail and the extraction of its data is important in three main aspects. First of all, various diseases of the nail can be differentiated more precisely and

therefore treatment efficiency can be improved; second of all, it is possible to non-invasively track during some period of time the positive and/or negative effects of a cosmetic product upon the elasticity and the structure of the nail and its surroundings; third of all, because various processes in the organism (such as blood circulation and metabolism) have a strong influence upon the nail plate growth, the monitoring of the nail morphology and its mechanical properties may be used as additional information for the exact diagnosis of a number of medical disorders, such as systemic sclerosis, psoriasis, chronic hand eczema, anemia etc [1]. In academic literature there are several papers showing the potential of ultrasound methods for the investigation of the human fingernails [2–6]. In our paper, a newer development of the ultrasonic micro-anatomical structure imaging of human nails is presented.

The aim of the present study was to carry out a detailed ultrasound investigation in the high-frequency range (25–50 MHz) of a human nail including micro-anatomical structure imaging and ultrasound velocity evaluation, using B-scans obtained with a scanning acoustic microscope.

2.   EXPERIMENTAL PROCEDURE

In the experimental series, the structure of the fingernail was investigated in vivo in several volunteers. The distal part of the palm was sunken into a plastic container filled with water and placed on the stage of the acoustic microscope "Tessonics AM-1103" (Tessonics Corp., Canada) working in short-pulse reflecting mode. The nail plate was then scanned horizontally by an acoustic lens and B-scans corresponding to the longitudinal and transversal sections of the finger were non-invasively obtained. Acoustic lenses with working frequencies of 25 and 50 MHz and a focal distances of 12.5 mm, providing a spatial resolution of about 80 and 50 μm, respectively, were used in the experiments. To provide a comparison with the previous studies, the sound speed in the fingernails was also determined by measuring the nail thickness at the dry end with a micrometer and by measuring the time-of-flight between the top and the bottom of the nail in different areas of the nail plate.

3.   RESULTS

In our experiments, new ultrasound B-scan data of live human finger-nails was obtained, revealing the fine structure of the nail plate, nail bed and nail matrix in-vivo (Fig. 1). In the B-scan in Fig. 1b a detailed microanatomy of

the nail matrix under the cuticle can be observed, nail plate thickness and condition can be evaluated, and the phalange bone is perceptible.

In some B-scans, several compartments or layers of the nail plate can be visualized in the B-scans in the proximal part of the nail plate. It is known [7] that three layers can be marked out by the nail thickness: the ventral, intermediate and dorsal ones, which differ slightly by their origin and biochemical composition.
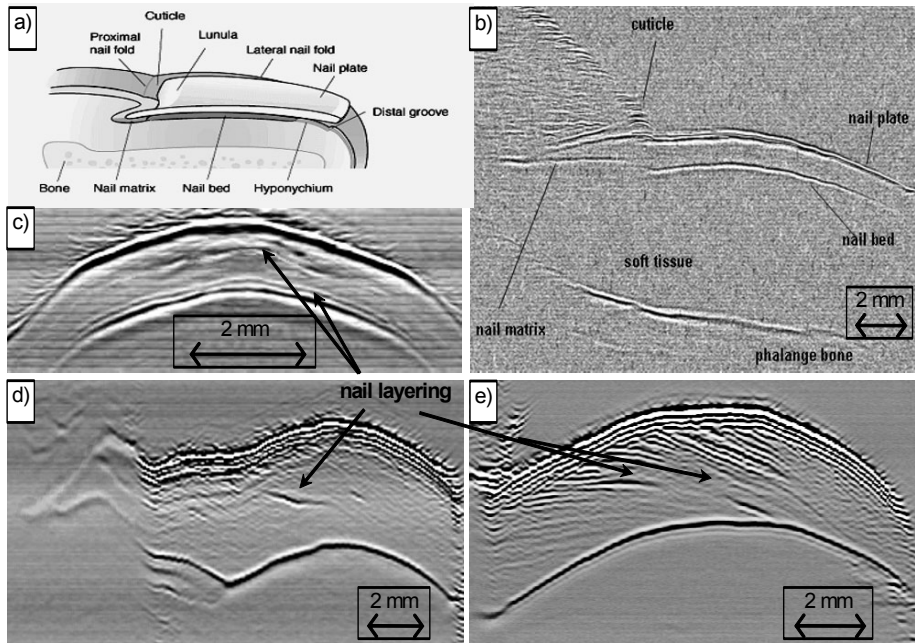
Figure 1. (**a**) - Principal scheme of a nail; (**b**) - Longitudinal B-scan (25 MHz); (**c**) – Transversal B-scan (25 MHz); (**d**) and (**e**) – Longitudinal B-scans (50 MHz).

Previously it was demonstrated [3] that the dorsal and medial plates can be differentiated (using non-focused 20 MHz probe) as smaller peaks between two strong reflections from the upper and the lower surfaces of the nail plate. A similar conclusion may be reached from our examples of the transversal B-scans (Fig. 1c). However, the use of higher-resolution focused transducer at 50 MHz enabled us to show that in certain cases such internal reflections are actually introduced by a different kind of irregularity. Examples of longitudinal B-scans (Fig. 1d,e) show the presence of possible delaminations or other layering in the nail plate, which do not represent typical horizontal structuring. Origins of the revealed nail layering are connected to biochemical composition and possibly reflect certain health conditions. Further studies with a larger number of individuals are planned.

4.   CONCLUSION

In this work, new ultrasound B-scan data of live human finger-nails were obtained using a scanning acoustic microscope working at a frequency of 50 MHz, revealing fine structure of the nail plate, nail bed and nail matrix in-vivo.

Certain type of inclined internal layering along the nails of some individuals has been found, which was not reported in previous ultrasonic studies of the nail.

Results clearly demonstrate that the scanning acoustic microscopy has high potential in the visualization of the fine nail elements and can be for the monitoring of their parameters and conditions in-vivo.

ACKNOWLEDGEMENTS

REFERENCES

1. R. Baran, R.P.R. Dawber, eds.: Diseases of the nails and their management, 2nd edition, (Oxford, Blackwell Scientific Publications, 1994).
2. A.Y. Finlay, H. Moseley, T.C. Duggan: British J. Dermatol., 117 (1987), 765–770.
3. G.B.E. Jemec, J. Serup: Archive Dermatol., 125 (1989), 643–646.
4. U. Wollina, M. Berger, K. Karte: Skin Research and Technology, 2001, 7, 60–64.
5. J. Serup, G.B.E. Jemec, eds., Handbook of non-invasive methods and the skin. (Boca Raton: CRC Press, 1995), 239–256.
6. T. Hirai, M. Fumiiri: Dermatol. Surg., 21 (1995), 158–161.
7. B.L. Lewis: A.M.A. Archives of Dermatology and Syphilology, 70 (1954), 732–747.

NON-DESTRUCTIVE EVALUATION AND INDUSTRIAL APPLICATION

ULTRASONIC ATOMIC FORCE MICROSCOPY OF SUBSURFACE DEFECTS

K. Yamanaka, K. Kobari, S. Ide, T. Tsuji

Dept. Material Processing, Graduate School of Engineering, Tohoku University, Sendai, 980-8579, Japan

Abstract: We show principle, implementation and remarkable applications of ultrasonic atomic force microscopy (UAFM) to evaluation of components with scientific and technological importance. In particular, carbon fiber in CFRP, domain of ferroelectric PZT and subsurface delamination of electrodes in microdevices are shown. We also show lateral modulation atomic force microscopy (LM-AFM) with application to a carbon nanotube composite and discuss its extension using combination with UAFM.

1.   INTRODUCTION

Atomic force microscope (AFM) [1] is an apparatus that uses a cantilever to measure nano-scale irregularities on the surface of a sample, utilizing the deflection of a cantilever supporting a tip due to the force acting between the sample surface and the tip. AFM have found intensive application in mechanics, electronics, and biotechnology. Methods have been proposed to measure the defect distribution and elasticity of a sample by detecting the vibration induced in the cantilever when the sample is vibrated at or higher frequency than its resonance frequencies [2,3]. They can measure the elasticity of stiff materials, which is not possible with the force modulation method [4] in which the sample is vibrated at a frequency about the same as or lower than the fundamental resonance frequency of the cantilever.

However, since the sample has to be bonded to an ultrasonic vibrator,
(1) Selection of optimum glues for each type of sample is time comsuming.
(2) Glues are a cause of sample contamination and cannot be used with LSI wafers and other samples requiring a high degree of cleanness.
(3) A large or irregularly shaped sample is hard to vibrate uniformly.
(4) Unwanted resonance peaks of the sample overlap cantilever resonances, degrading the precision.

These methods are therefore not ideal for inspecting samples requiring highest precision and in industrially important components such as large LSI wafers, magnetic heads and bearings and so on. We thus developed ultrasonic atomic force microscopy (UAFM) (Fig. 1) [5][6] for evaluation of defects at and in the vicinity of the sample surface and the measurement of sample elasticity, with high reproducibility, without requiring the sample to be bonded to a vibrator.

Adsorbed atoms and molecules on the surface as well as subsurface defects are also associated with friction and lateral contact stiffness (Fig. 1(d)). Friction force microscope (FFM) [7] was developed measuring the torsion of a cantilever due to the frictional force. However, FFM is sensitive also to curvature of the sample. We thus developed the lateral modulation AFM (LM-AFM) [8,9] where the sample or cantilever is vibrated transversely, thus inducing a torsional vibration on a cantilever. The phase and the amplitude of this torsion vibration are simultaneously measured using a lock-in amplifier. The LM-AFM has been applied to surface chemistry and tribology, etc. [10]. To evaluate lateral stiffness more precisely, lateral UAFM was extended to measure the torsional resonance [11,12]. A cantilever holder with two vibrators (`TR mode`) may be useful to efficiently excite the torsional resonance [13,14]. However, usual holders can be used without difficulty, because the cantilever shape is slightly asymmetric.

Here, we show principle, implementation and applications of UAFM. In particular, subsurface defect evaluation with scientific and technological importance is discussed. Also, we explain the need for shear force modulation modes initiated by LM-AFM and discuss its future development.

2.   PRINCIPLE OF UAFM

When the cantilever excited with higher order mode vibration is brought in contact with the sample, the sample is deformed depending on the vibrational mode of the cantilever. The physical properties of the sample can therefore be measured by measuring the cantilever vibration. In the present implementation of UAFM, the cantilever substrate is excited by using a piezoelectric vibrator driven by the output of the resonance frequency tracking circuit [15,16].

The low-frequency component of deflection signal of a soft cantilever is used to keep constant force and to precisely obtain the topography, as in the AFM, Fig. 1(a). When resonance cantilever vibration is excited, the sample is elastically deformed by the effective stiffening of cantilever due to inertia [Fig. 1(b)] [5,6], as demonstrated for the first time in the earlier method using nonlinear detection [2], as well as effective shortening of the cantilever due to formation of nodes [Fig. 1(c)].

The resonance frequency is calculated from the frequency equation both for UAFM [5, 12] and atomic force acoustic microscopy (AFAM) [17].

$$(k/3s_V)(\kappa L)^3(1+\cos \kappa L \cosh \kappa L) = \cos \kappa L \sinh \kappa L - \sin \kappa L \cosh \kappa L \quad (1)$$

where k is the cantilever stiffness, s_V is the (vertical) contact stiffness (slope of the force versus indentation depth relation), L is the cantilever length and $\kappa = \left[\omega^2 \rho A/(EI)\right]^{1/4}$ is the wave number of elastic wave on the cantilever in which ω is the angular frequency, ρ is the density, A is the area E is the elastic modulus and I is the moment of inertia of the cantilever, which depends on the width and the thickness of the cantilever. The cantilever stiffness k is given by $k = 3EI/L^3$ and in the case of rectangular section $k = Ewt^3/(4L^3)$ where w is the width and t is the thickness of cantilever. The contact stiffness in vertical direction s_V is usually approximated by the following equation $s_V = (3/2)aK$, where a is the contact radius and $K = (4/3)\left[(1-\nu_{Tip}^2)/E_{Tip} + (1-\nu^2)/E\right]^{-1}$ is the effective elasticity.

The contact stiffness is affected by defects as shown in (d). An open crack (A) reduces it until it is closed like (B). If the interface is welded (C), the contact stiffness is larger than frictionless cases (D) and (E).
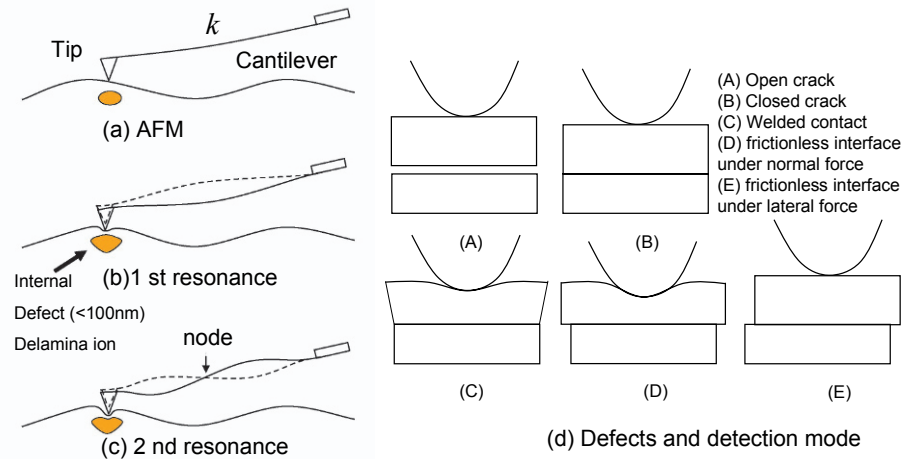
Figure 1. Principle of UAFM.

3.   IMPLEMENTATION OF UAFM

Figure 2 (a) shows UAFM with a phase-locked loop circuit [15], realizing resonance frequency mapping to quantitatively identify various areas with different mechanical property. Cantilever vibration is exited by a voltage-controlled oscillator (VCO). The VCO input voltage is adjusted to realize the resonance when the tip is in contact with a sample, and a frequency demodulator provides a DC voltage representing the resonance frequency. The resonance frequency is mapped in a memory during the raster scanning of the sample.
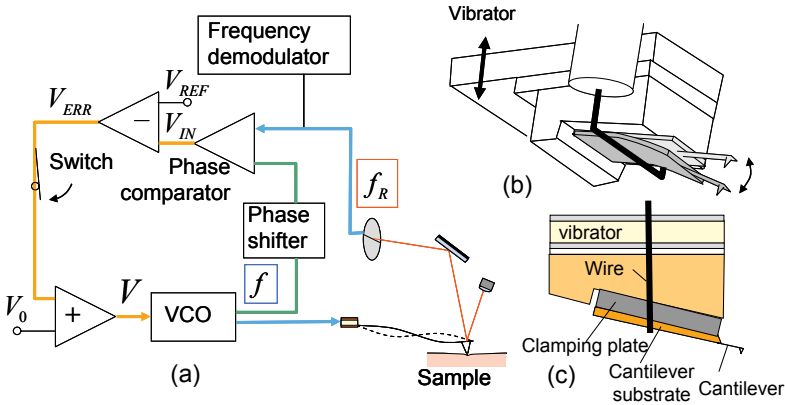
Figure 2. Implementation of UAFM (**a**) Frequency tracking system (**b**) Cause of spurious response; SR (**c**) Clamping plate for suppression of SR.

In dynamic-mode AFM, spurious response (SR) due to vibrations other than the cantilever vibration is detrimental when it overlaps the cantilever vibration spectra. In particular, it is the case when the quality (Q) factor, defined as the ratio of the resonance frequency and the width of the resonance peak, is not very high, such as in noncontact (NC)-mode AFM in liquid or contact resonance (CR)-mode AFM.

Figure 2 (b) shows a schematic illustration of a typical cantilever chip and cantilever holder in AFM. The holder transmits a vibration to the substrate of the cantilever chip upon driving the piezoelectric vibrator. When unnecessary vibration is generated on the substrate, it is overlapped with the vibration of the cantilever itself. As a result, the peaks of SR appear on the vibration spectrum of the cantilever, which cannot be explained by the vibration theory of the cantilever. However, a clamping plate attached to the cantilever substrate (c) is particularly useful for suppressing the SR [18], which is useful not only in UAFM but also in NC-AFM.

4. OBSERVATION OF NON-UNIFORM MATERIAL PROPERTIES IN COMPOSITES

As an application, we investigated a carbon fiber in a carbon fiber reinforced plastic (CFRP) [11]. The resonance frequency increased from 38.5 kHz at free resonance to 176 kHz for the carbon and 171 kHz for the epoxy. The Q factors were 180~200 for the carbon and 100~110 for the epoxy. Figure 3 (b) and (c) are the resonance frequency and Q factor images together with the topography in Fig. 4 (a). Surprisingly, we note a small but reproducible variation within the carbon area. In the frequency and Q factor profiles along the vertical dotted lines, the resonance frequency at the core was lower than that at the rim by 0.5~1 KHz. Similarly, the Q factor at the core was lower than that at the rim by 20~40. These differences have been interpreted by the manufacturer as difference in the degree of stabilization during heat treatment, which are important parameters for achieving high strength.
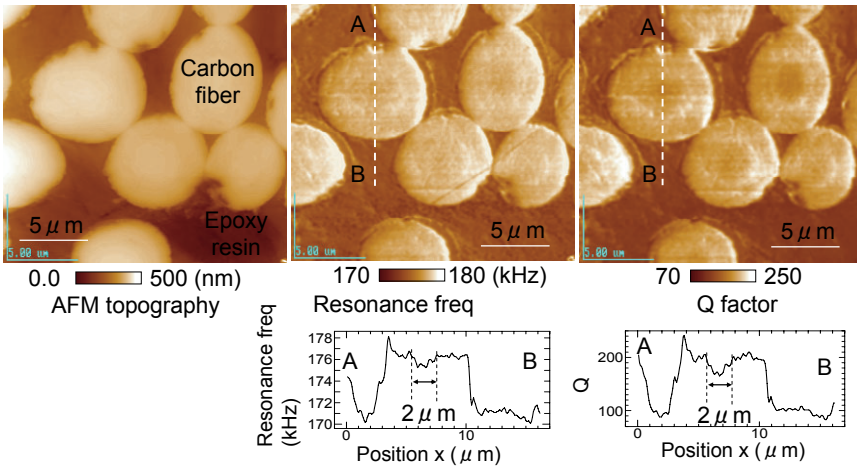
Figure 3. Non-uniform stiffness of carbon fibers in CFRP.

We also show the stiffness evaluation of the lead zinc titanate (PZT) ceramics used for actuators and ferroelectric memories [19,20].
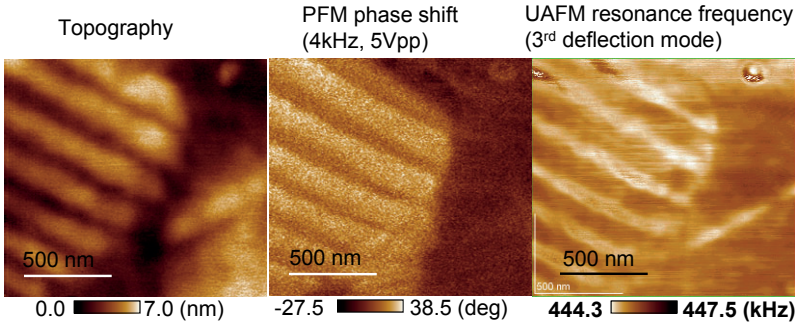
Figure 4. Domain structures of PZT.

Figure 4(a) is a topography, (b) is a PFM image showing the phase of the deflection vibration excxied by an AC voltage applied between the tip and the bottom electrode. The frequency and the amplitude of the AC voltage were 4 kHz and 5 Vp-p, respectively. There was a stripe pattern with a period of 250 nm representing differently oriented domains. Figure 4(c) shows a UAFM image representing the resonance frequency at the 3rd deflection mode. Darker color represents higher resonance frequency, indicating higher contact stiffness. As a result, it was demonstrated that the UAFM can evaluate the different elasticity due to the differently oriented domains of PZT. Such observation will be useful for evaluation of polarization fatigue in memory and actuators [19–21].

5.   DELAMINATION OF ELECTRODE

UAFM is particularly useful to evaluation of subsurface defects in microdevices [22,23]. We show evaluation of an chromium (Cr) electrode fabricated using the lift-off process with a thickness of 240 nm shown in Fig. 5 [24], with the topography of edge area shown in Fig. 6 (a).

In the UAFM resonance frequency image of Fig. 6 (b), darker area had lower resonance frequency, indicating lower contact stiffness. The low frequency region is probably due to delamination. To confirm it, spectra were measured at positions A, B, C and D. The peak frequency decreased from A to D, indicating decreased contact stiffness. Moreover, asymmetric shapes of spectrum B and C indicate the contact vibration of the gap, schematically shown by a motion between (A) and (B) in Fig. 1(d).
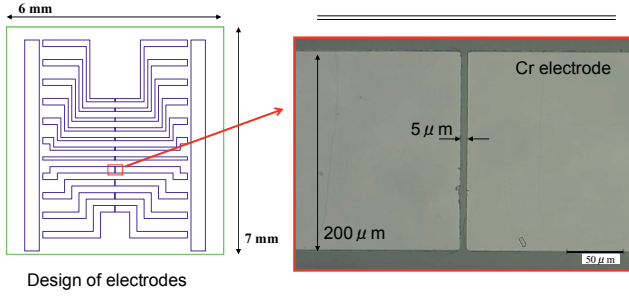
Figure 5. Cr electrode deposited on a substrate.
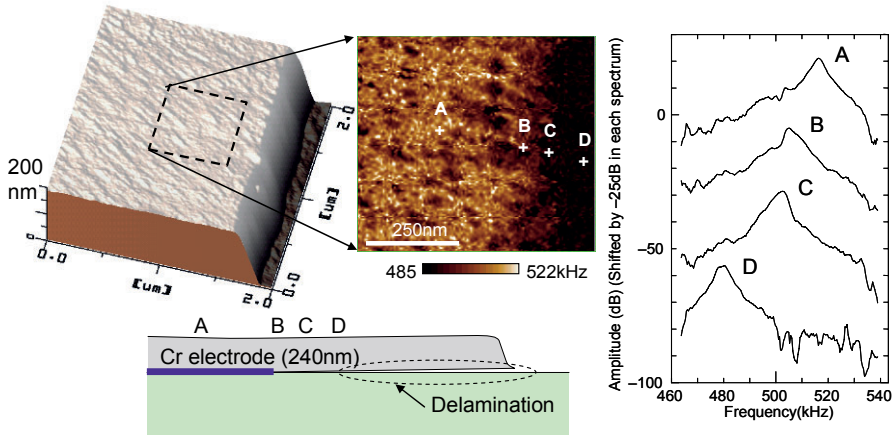
Figure 6. Observation of subsurface delamination of Cr electrode (**a**) Topography (**b**) UAFM frequency image and (**c**) spectra taken at points A to D.

6. LATERAL STIFFNESS AND FRICTION EVALUATION

When an ordinary FFM is used, it is difficult to precisely measure friction force because of curvature of the surface. The LM-AFM solved this problem. As shown in Fig. 7, a flat area with high friction leads to a small static angle θ and a large vibration amplitude $\Delta\theta$ of cantilever torsion when the sample is laterally vibrated. A tilted area with low friction leads to a large θ and small $\Delta\theta$. Figure 8 shows carbon nanotube (CNT) emerged on a polystyrene (PS) matrix in a PS-CNT composite, a promising light strong conductive material. FFM image of Fig. 8 (b) shows geometrical artifact of PS due to

the large tilt θ. LM-FFM image of Fig. 8 (c) shows only CNT with lower friction or lateral contact stiffness. This feature of LM-AFM is useful for precise evaluation of magnetic recording instruments, lubricant on a medium, and contamination of engineering surfaces which are not necessarily atomically flat.

For precise evaluation of lateral contact stiffness, it is needed to suppress sliding of the tip. In LM-AFM, it has been achieved by monitoring the phase signal of torsion vibration [8].
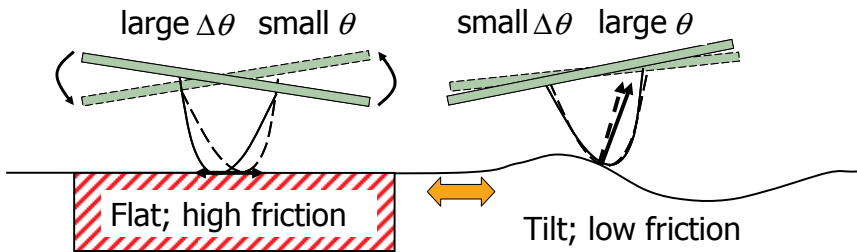
Figure 7. Principle of LM-AFM.

(a) Topography (0~18.9nm)   (b) FFM   (c) LM-AFM
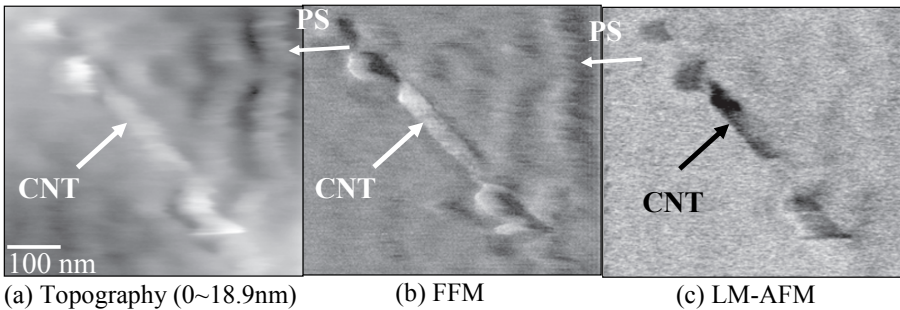
Figure 8. Observation of carbon nanotube (CNT) on polystyrene (PS).

For detection of closed buried interface, evaluation of the contact stiffness is useful. If the interface has low friction, the contact stiffness will be smaller than at a welded interface (cf. (C) and (D) of Fig. 1 (d)). The reversible motion of subsurface edge dislocation [23] may be due to a similar effect, since the extra-half plane has very low friction. LM-AFM, lateral UAFM or TR mode that causes sliding such as shown in (E) of Fig. 1(d) may have lager sensitivity to evaluation of such an interface.

REFERENCES

1. G. Binnig, C. F. Quate and Ch. Gerber, Phys. Rev. Lett. 12, 930, (1986)
2. K. Yamanaka, H. Ogiso and O. Kolosov: Appl. Phys. Lett. 64, 178 (1994).
3. U. Rabe and W. Arnold: Ann. Physik 3,589 (1994).
4. M. Radmacher, R. W. Tillmann, and H. E. Gaub: Biophys. J. 64, 735 (1993).
5. K. Yamanaka and S. Nakano, Jpn. J. Appl. Phys., 35 (1996) 3787.
6. K. Yamanaka, United States Patent 6,006,593, December 28, 1999.
7. Mate, McClelland, Erlandsson and Chiang, Phys. Rev. Lett., Vol. 58, No. 17, 26 Oct. 1987, pp. 1942-1945.
8. K. Yamanaka and E. Tomita, Jpn. J. Appl. Phys. 34 (1995) 2879.
9. K. Yamanaka and E. Tomita, United States Patent 5,804,708, September 8, 1998.
10.   G. Haugstad, Tribology Letters, 19 (2005) 49
11. K. Yamanaka and S. Nakano, Appl. Phys. A, 66 (1998) 313.
12. K. Yamanaka, A. Noguchi, T. Tsuji, T. Koike and T. Goto, Surf. Interface. Anal., 27 (1999) 600.
13. M. Reinstädtler, T. Kasai, U. Rabe, B. Bhushan, and W. Arnold, J. Phys. D. 38 (2005) R269.
14. Y. Song and B. Bhushan: J. Appl. Phys. 99 (2006) 094911.
15. K. Yamanaka, Y. Maruyama, T. Tsuji and K. Nakamoto, Appl. Phys. Lett., 78 (2001) 1939.
16. K. Yamanaka and K. Nakamoto, United States Patent 6,983,644, January 10, 2006.
17. U. Rabe, K. Janser, and W. Arnold, Rev. Sci. Instrum., 67(1996) 3281.
18. K. Yamanaka, Japanese Patent 2006-184079.
19. T. Tsuji, H. Ogiso, J. Akedo, S. Saito, K. Fukuda, and K. Yamanaka, Jpn. J. Appl. Phys., 43 (2004) 2907.
20. T.Tsuji, S. Saito, K. Fukuda, K. Yamanaka, H. Ogiso, J. Akedo and K. Kawakami, Appl. Phys. Lett., 87(2005) 071909.
21. Seishiro Ide, Kentaro Kobari, Toshihiro Tsuji, Kazushi Yamanaka, Jpn. J. Appl. Phys, (2007) in press.
22. K. Yamanaka and Y. Enomoto, J. Appl. Phys. 53 (1982) 846.
23. T. Tsuji and K. Yamanaka, Nanotechnology, 12 (2001) 301.
24. Kentaro Kobari, Seishiro Ide, Toshihiro Tsuji and Kazushi Yamanaka, Proc. Japanese Society of Applied Physics, Spring Meeting (2007) 465.

QUANTITATIVE MATERIAL CHARACTERIZATION AND IMAGING AT NANOSCALE USING A NEW AFM PROBE

F.L. Degertekin, M. Balantekin, A.G. Onaran
G.W. Woodruff School of Mechanical Engineering, Georgia Institute of Technology, Atlanta, Ga 30332

Abstract: The structure of an Atomic force microscope (AFM) probe that integrates fast electrostatic actuation and highly sensitive optical interferometric detection of tip motion is described. The use of this so-called FIRAT probe for quantitative material characterization with high spatial resolution is demonstrated through contact and adhesion modeling. Time resolved interaction forces between the AFM tip and the sample surface is used to map material properties of several samples including silicon, polymer and carbon nanotubes. Non-resonant tapping mode operation of the FIRAT probe has also been demonstrated for use with existing commercial AFM systems.

Key words: Atomic force microscopy, Material characterization.

1.   INTRODUCTION

Since its invention, the atomic force microscope (AFM) [1] has been widely used in the field of material characterization [2]. Several cantilever-based methods have been developed to measure the surface mechanical properties with high lateral resolution provided by the AFM. The nanoindentation technique [3] is suitable for single-point, static measurements, but the modeling can be complicated due to tip rotation with applied force. The force modulation method measures only the sample stiffness. Ultrasonic AFM or acoustic AFM performed by vibrating either the AFM cantilever or the sample at ultrasonic frequencies, may require large static forces that can be destructive, and tip wear can cause the results not to be always

reproducible [4,5]. Pulsed force mode operation of the AFM provides quantitative information with a slow speed due to high quality factor of the commercial cantilevers [6]. Techniques have also been developed to obtain material property information from the regular tapping mode AFM imaging data. Monitoring the phase of the output signal often gives high-contrast images, but the interpretation of the results may not be easy [7]. More recently higher-harmonic imaging techniques have been developed where the signals generated at the harmonics of the tapping oscillation frequency are monitored [8]. These methods use the advantage of low impact force of the tapping-mode operation, but the whole spectrum of the interaction force is not captured and an inversion from the harmonics needs to be performed to obtain the temporal signals.

In this paper, the operation of a recently introduced AFM probe structure called Force-sensing Integrated Readout and Active Tip (FIRAT) is reviewed and described [9,10]. This probe is capable of acquiring time resolved interaction force (TRIF) signals and has the tip normal to the sample during imaging, resulting in a simpler analysis. The outline of the quantitative property inversion is provided along with sample data and images. Non-resonant tapping mode imaging with the FIRAT probe is also described.
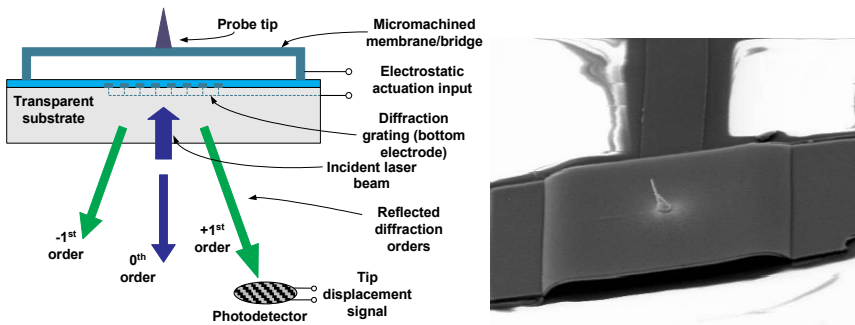
Figure 1. Left: Schematic cross section of a FIRAT probe showing the mechanical structure, optical detection and electrostatic actuation details. *Right*: The SEM of a FIRAT probe using a clamped beam structure. The aluminum beam is 60 μm×40 μm and it is 0.8 μm thick.

2. THE FIRAT PROBE STRUCTURE FOR AFM

The FIRAT probe, schematically shown in Fig. 1 (left), consists of a sharp tip placed on a micromachined membrane or beam structure built on a transparent substrate. The optical diffraction grating enables one to measure
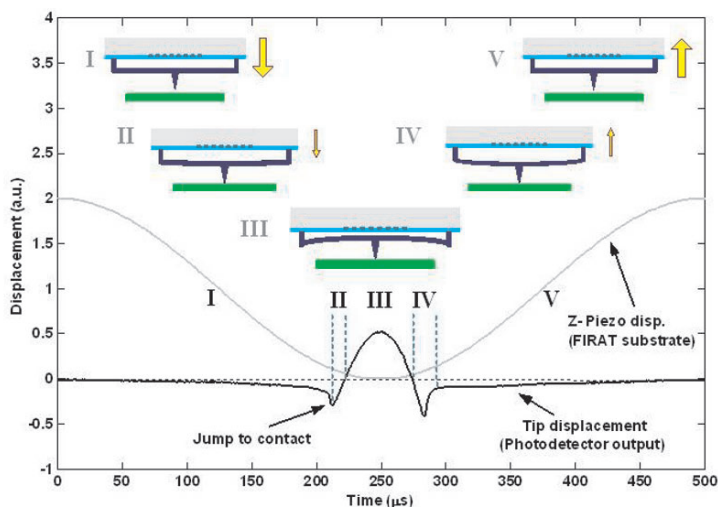
Figure 2. One cycle of TRIF mode imaging showing the substrate displacement and measured time resolved force signal on the tip. The shape of the FIRAT probe structure at different phases is also shown schematically. Figure reproduced from [10].

the displacement of the mechanical structure with interferometric sensitivity by detecting reflected diffraction orders. The optimal sensitivity is obtained by the built-in electrostatic actuator, which is formed by the rigid grating electrode and the electrically conductive flexible membrane/beam. A scanning electron micrograph (SEM) of a FIRAT probe with a clamped-clamped beam structure made of aluminum on quartz substrate is shown on the right side of Fig. 1. Details of the fabrications process is described elsewhere [11]. The dynamics of the probe can be adjusted by the dimensions of the structure and the thickness of the air gap between the beam and the quartz substrate. Devices with spring constants in the 40–300N/m range with resonance frequency of 1MHz and quality factor of 1–16 have been fabricated. These parameters are suitable for both material characterization and fast imaging applications.

3.   TIME RESOLVED INTERACTION FORCE (TRIF) MODE OPERATION

The TRIF-mode imaging with the FIRAT probe is similar to the widely used tapping-mode operation in which the sharp AFM tip encounters contact force only a fraction of the oscillation period. In the tapping-mode, the cantilever is driven at close to its resonance frequency and the oscillation amplitude is kept constant during the scan. In the TRIF-mode, on the other

hand, the substrate holding the FIRAT probe is driven below the first resonance frequency of the membrane and the RMS value of the measured tip displacement is kept constant. Figure 2 summarizes the TRIF-mode operation. At each cycle, the mechanical structure is deflected due to interaction forces. By multiplying the displacement with the effective stiffness of the membrane, the time-domain interaction force is obtained.
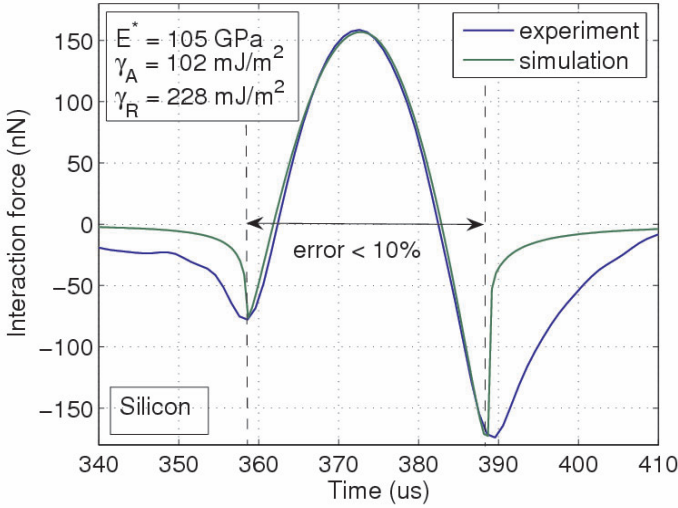
Figure 3. Comparison of experimental and simulated TRIF signals for silicon.

Once the time-domain interaction force is obtained, the sample properties can be extracted quantitatively using a suitable model. For example, to invert adhesive and elastic properties of surface one can use the Burnham-Colton-Pollock (BCP) contact mechanics [11] or the Derjaguin-Muller-Toporov (DMT) model [12]. The model requires the knowledge of tip material properties as well as the tip dimensions (radius of curvature) and the tip oscillation amplitude, and the spring constant of the FIRAT structure. In this particular case, the tip material (tungsten), tip dimensions (R=50 nm) and the spring constant (350 N/m) are known or directly measured and the oscillation amplitude is estimated by using a reference material, which in this case is silicon. The FIRAT tip is oscillated at 2 kHz and it comes in contact with the sample in the middle of each period. Given this information, one can simulate the shape of the TRIF signal and minimize the error between the simulated and measured force data between jump to contact and

snap back points, i.e. part of the curve between the dashed lines in Fig. 3. The error, ε, is defined as

$$\varepsilon = \frac{\int \left| F_{simulated} - F_{experimental} \right|}{\int \left| F_{experimental} \right|} \times 100\% \quad (1)$$

Figure 3 shows the simulated and measured TRIF signals for silicon substrate. In this case assuming an oscillation amplitude of 76 nm, ε is below 10% and we obtain the effective tip-sample elasticity and surface energies of the silicon sample to be E^*=117 GPa, γ_A=112 mJ/m^2, and γ_R =251 mJ/m^2. Here E^* is the effective Young's modulus given in terms of Poisson ratios ν and Young's moduli E of the tip and sample as

$$E^* = \frac{4}{3} \left[\frac{1 - \nu_{tip}^2}{E_{tip}} + \frac{1 - \nu_{sample}^2}{E_{sample}} \right]^{-1} \quad (2)$$

and γ_A and γ_R are the surface energies advancing (jump in to contact) and receding (adhesion) phases. Once the tip and experimental parameters are known, similar properties of other samples can be quantitatively inverted. Figure 4 shows a TRIF signal inversion example where the sample is diethylene glycol dimethacrylate (DEGDMA) sample. The simulation result is obtained with the sample parameters of E^*=24 GPa, γ_A=132 mJ/m^2, and γ_R =238 mJ/m^2. This set of parameters results in ε=8.6%. The extracted properties of this polymer are E^*=23 GPa, γ_A=141 mJ/m^2, and γ_R =269 mJ/m^2, which is in reasonable agreement with the expected bulk values.

By extending the model to account for other tip-sample forces, one can extract other sample properties. The extracted material properties can be mapped along with topography. An example of this type of simultaneous topography and surface property imaging is depicted in Fig. 5 where topography and surface energy images of a carbon nanotube (CNT) bundle over a silicon substrate surface are shown. Figure 5 (a) shows the topography and Fig. 5 (b) shows the surface energy in the receding phase. The bright regions in surface energy image correspond to the silicon substrate revealing that silicon is more adhesive than CNT.
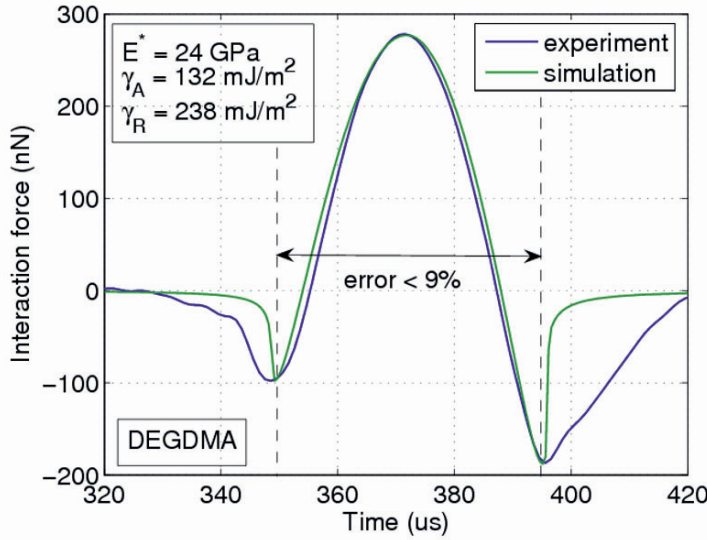
Figure 4. Comparison of experimental and simulation results for a DEGDMA sample.
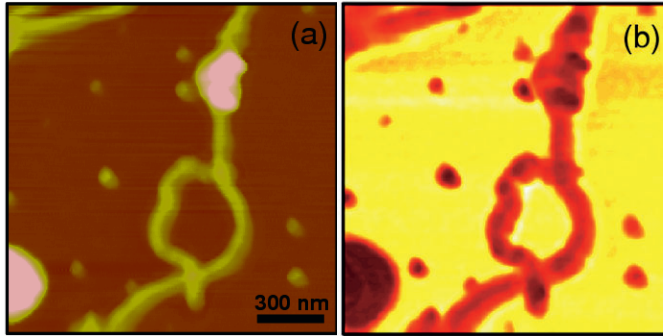
Figure 5. 1.5 μm × 1.5 μm image of carbon nanotube over silicon substrate. (**a**) Topography and (**b**) Surface energy in the receding phase which is related to adhesion. Image full contrast corresponds to 50 nm in (**a**) and 380 mJ/m^2 in (**b**).

4.   NON-RESONANT TAPPING MODE IMAGING

Another operational mode of the FIRAT probe is non-resonant tapping mode. In this mode, the probe is actuated electrostatically at a low frequency compared to its fundamental resonance and tapped on the surface for imaging similar to regular tapping mode imaging. The displacement of the

probe during imaging is then compared to its free air displacement measured with the same actuation but away from the surface. The difference between these two waveforms gives the time resolved interaction forces. Note that by moving the FIRAT membrane in a fast control loop where the interaction force during each tap is kept constant, one can perform fast topographic imaging as well as material property mapping with this mode.
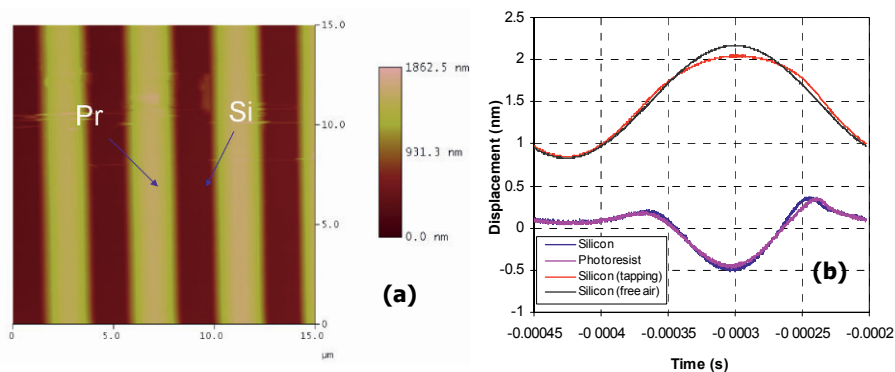
Figure 6. (**a**) 15 μm ×15 μm image of a photoresist on silicon sample. (**b**) Waveforms of probe displacement and interaction forces while the tip is tapped on silicon and photoresist surfaces.

The topographic image of a patterned photoresist layer on silicon sample with 4 μm periodicity acquired with this mode is given in Fig. 6-(a). In Fig. 6 (b)**,** the top waveforms show the displacement of the probe while it is tapping on a silicon sample and while it is being vibrated freely in air at 4 kHz. The bottom plots show the interaction force waveforms calculated from the free air and tapping signals on silicon and photoresist regions. For visual clarity the bottom plots are multiplied by a factor of 20. As expected the photoresist sample exerts a broader force pulse with a lower peak value, very similar to TRIF mode. By performing inversion as shown in Figs. 3 and 4, one can calculate and map certain material properties at each pixel of the image.

5. CONCLUSION

The FIRAT probe for AFM integrates fast electrostatic actuation and highly sensitive optical interferometric detection of tip motion in a probe for AFM imaging. This combination, in addition to the lack of tip rotation during surface contact, makes this probe suitable for fast topographic imaging with simultaneous quantitative material characterization with high spatial

resolution. TRIF mode and non-resonant tapping mode operation of the FIRAT probe has been developed for use with existing commercial AFM systems and has been demonstrated on silicon and polymer samples indicating unique capabilities of this novel AFM probe structure.

ACKNOWLEDGEMENTS

REFERENCES

1. G. Binnig, C. F. Quate, and C. Gerber, Atomic force microscope, *Phys. Rev. Lett.* **56**, 930 (1986).
2. M. E. Greene, C. R. Kinser, D. E. Kramer, L. S. C. Pingree, and M. C. Hersam, Application of scanning probe microscopy to the characterization and fabrication of hybrid nanomaterials, *Microscopy Res. and Tech.* **64**, 415 (2004).
3. N. A. Burnham and R. J. Colton, Measuring the nanomechanical properties and surface forces of materials using an atomic force microscope, *J. Vac. Sci. Technol.* **A 7**, 2906 (1989).
4. U. Rabe, K. Janser, and W. Arnold, Vibrations of free and surface-coupled atomic force microscope cantilevers: Theory and experiment, *Rev. Sci. Instrum.* **67**, 3281 (1996).
5. K. Yamanaka and S. Nakano, Ultrasonic atomic force microscope with overtone excitation of cantilever, *Jpn. J. Appl. Phys.*, *Part 1* **35**, 3787 (1996).
6. H. U. Krotil, T. Stifter, H. Waschipky, K. Weishaupt, S. Hild, and O. Marti, Pulsed force mode: a new method for the investigation of surface properties, *Surf. Interf. Anal.* **27**, 336 (1999).
7. M. Balantekin and A. Atalar, Power dissipation analysis in tapping-mode atomic force microscopy, *Phys. Rev. B* **67,** 193404 (2003).
8. O. Sahin, G. Yaralioglu, R. Grow, S. F. Zappe, A. Atalar, C. F. Quate, and O. Solgaard, High-resolution imaging of elastic properties using harmonic cantilevers, *Sens. Actuators A* **114**, 183 (2004).
9. F. L. Degertekin, A. G. Onaran, M. Balantekin, W. Lee, N. A. Hall, and C. F. Quate, Sensor for direct measurement of interaction forces in probe microscopy, *Appl. Phys. Lett.* **87**, 213109 (2005).
10. A. G. Onaran, M. Balantekin, W. Lee, W. L. Hughes, B. A. Buchine, R. O. Guldiken, Z. Parlak, C. F. Quate, and F. L. Degertekin, A new atomic force microscope probe with force sensing integrated readout and active tip, *Rev. Sci. Instrum.* **77**, 23501 (2006).
11. B. Bhushan ed. *Handbook of Micro/Nanotribology*, (CRC, Boca Raton, Florida, 1999).
12. N. A. Burnham, R. J. Colton, and H. M. Pollock, *Nanotechnology* **4**, 64 (1993).

NON-DESTRUCTIVE TESTING OF DIE-CASTING COMPONENTS OF NON-FERROUS METALS FOR SURFACE-NEAR POROSITY BY HIGH-FREQUENCY ULRASOUND

S. Hirsekorn[1], U. Rabe[1], D. Bruche[1], N. Grov[2], T. Kinzler[2], W. Arnold[2]

[1]Fraunhofer Institute for Non-Destructive Testing (IZFP), D-66123 Saarbrücken, Germany;
[2]ae light metal casting gmbh & co kg, D-36179 Bebra, Germany

Abstract: We have developed a high-frequency acoustical imaging system to detect porosity and single pores in the surface-near range (0.5–2 mm depth) in die-casting components. The scanning system employing a robot allows one to inspect components with curved surfaces.

Key words: High-frequency acoustical imaging, Inspection of die-cast component, Porosity

1.   INTRODUCTION

A large part of die-casting products made of aluminum, copper, magnesium and zinc base alloys, are used in car manufacturing. Many of these products are safety-related that must not fail and therefore have to be tested non-destructively. For cost-effective optimization of the production process also non-destructive testing (ndt) of the castings is required. Due to the manufacturing process die-casting components show inner volume porosity [1]. They may have effects on their strength, tightness, and surface structure [2]. A procedure for detecting and characterizing pores in die-casting components has been developed, employing high-frequency ultrasonic back-scattering signals to examine surface-near zones of 2 mm depth.

Generally, the scattering of ultrasound at the grain and phase boundaries in polycrystalline multiphase and/or porous materials causes attenuation and dispersive sound velocities. These effects, as well as the scattered wave

amplitudes, can be used for material characterization and also for the detection and evaluation of defects. Scattering and diffusion theory, and the pertaining applications correlate ultrasonic scattering parameters with characteristic materials quantities [3–13]. A considerable part of the ultrasonic scattering theory, as well as the ndt applications and nd-testing systems, were developed in the IZFP [3,6,8,9], for example to monitor hydrogen embrittlement of pipeline steels [14] and the case-hardening depth of steels [15].

For the detection and evaluation of different defects (pores) just below the surface to approximately 2 mm depth in die-casting components of complicated form, only the evaluation of ultrasonic backscattering is promising. Due to the geometry of the components no suitable sound paths are available for the measurement of sound velocities and scattering coefficients. Ultrasound-backscattering measurements were carried out on die-casting components of different forms and materials (aluminum, magnesium and zinc alloys), which were provided by industrial partners. Because of the complicated form of the components to be investigated, the use of a robot scanning system was required. Before testing a component, this system first learns its geometry. In a second step the surface of the component is scanned with a given pre-determined distance. A PC integrated in the measuring set-up and equipped with the adequate software permitted the one- two- or three-dimensional visualization of the recorded ultrasonic data [16,17]. For the quantitative evaluation of the scattering indications and the determination of detection limits an evaluation of the ultrasonic scattering theory is necessary. Interpretation and evaluation of the ultrasonic backscattering signals are validated by comparing X-ray images and metallographic micrographs.

2.   DESCRIPTION OF THE TESTING SYSTEM

In polycrystalline and multiphase and/or porous materials ultrasound is scattered at the grain as well as at the phase boundaries, so that the scattering waves emanating from the pores in the die-casting components superposes with the grain scattering, the so-called "grain noise". Figure 1a shows in a schematic way ultrasonic backscattering at pores and grain boundaries using a focusing probe. Porosity or single pores can only be detected when their scattering signals do not vanish within the background signal of the grain noise.

In Fig. 1b the robot-controlled high-frequency ultrasonic test system is shown schematically. Figure 2 shows photos of the system before and during measurement. The die-casting component to be tested is immersed in a water-tank with the water serving as the coupling medium. The probe is

fixed at the end of the robot arm. Due to the complex form of the components, their outer geometry is first recorded and learnt. Then by scanning over the test area and evaluating the time-of-flight of the entrance echoes [16], one is able to scan the surface of the component at a constant distance during the ultrasonic backscattering measurements. For perpendicular sound incidence the back-scattered ultrasonic time signals, i.e. the A-scans are recorded as a function of position in the test area. From these data B-scans and C-scan were formed.

The measurements were carried out with the ultrasonic test system HIS2 (bandwidth up to 200 MHz) using the focusing probe IAP-F50.2.0.5 of Krautkrämer Cologne, Germany (now GE Inspection Technologies) having a nominal frequency of $f = 50$ MHz and a focal length 1_{sc} of 12.7 mm in water. The length of the focus tube is $1_{sc}' \approx 5$ mm (-6 dB points). The diameter of the focal spot is $d_{sc} = 0.12$ mm and when focusing in the inspected component, d_{sc} changes little[18]. However, 1_{sc} as well as $1_{sc}'$ change with the ratio of the longitudinal ultrasonic velocities in the die-casting component and in water and hence $1_{sc}'$ decreases to ≈ 1.3 mm. Due to the frequency dependent attenuation in the inspected component and in water the received frequency is ≈ 30 MHz, and as a result $1_{sc}'$ increases again to $1_{sc}' \approx 2$ mm. With a probe distance of 8 mm to the surface of the component under test, the focal area is ≈ 0.5 to 2 mm below the surface. For the scanning of the die-casting components the precision robot μ-KROS 316 (manufactured by Bodenseegerätewerke, Germany) having six regulated axes, an operational range of 515 mm and a static repetitive accuracy of 5 μm[16] was used.

(a)   (b)
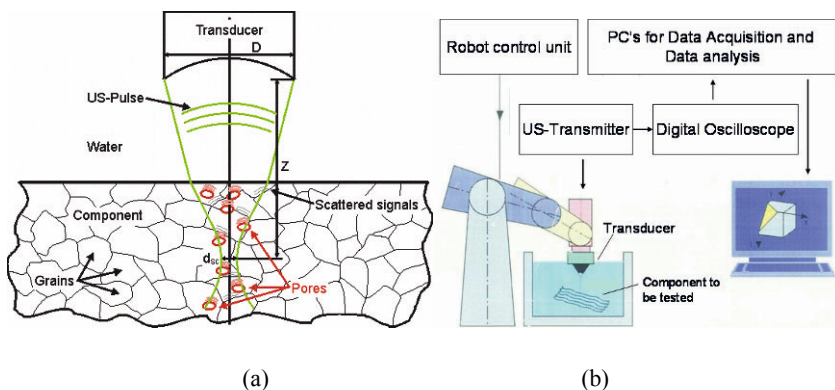
Figure 1. Schematic representation of (**a**) ultrasonic back-scattering at pores and grain boundaries using a focusing probe (Z = focal length, dSC = focus diameter, D = probe diameter) and of (**b**) the robot-controlled high-frequency ultrasonic testing system.
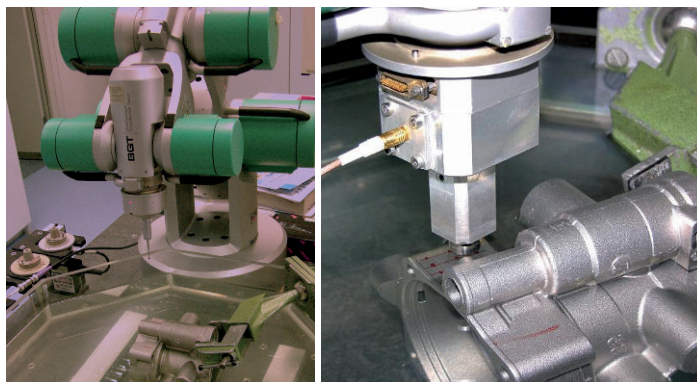
(a)   (b)

Figure 2. Photos of the robot-controlled high-frequency ultrasonic test system with a die-casting component in the water tank. Before starting the scanning procedure (**a**) the scanned surface of the component is determined by a mechanical feeler pin. To this end the robot is moved by hand and the surface is touched briefly by the feeler. The tools of mechanical feelers, optical feelers and ultrasonic probes which are automatically selected and stored by the robot, can also be seen in (**a**); (**b**) shows the test system during the scanning of the test area.

3.   RESULTS

In the following an example of our investigations on die-casting components provided by the industrial partners of the project is presented and discussed. Figure 3 shows a photograph of an aluminum die-casting component (AlSi10Mg, longitudinal sound velocity 6730 m/s) with the ultrasonic test area marked, the corresponding X-ray transmission image of this area and a metallographic micrograph from a depth of 1 mm of the area marked in the X-ray image. The X-ray image shows 4 holes made for marking (Fig. 3b). The porosity was determined from the micrograph to be 0.1%. The pore diameters are clearly below 100 μm (Fig. 3c). Figure 4 shows an A-scan and a B-scan of these components. The indication seen in the A-scan originates from a depth of 1 mm at x = 5.4 mm and y = 14.2 mm. When comparing this to the micrograph, one can conclude that the ultrasonic indications are caused by scattering at pores. Figure 5 shows two C-scans of the component from a depth of 0.55 and 1 mm, respectively. In both C-scans indications originating from pores can clearly be recognized.

4. EVALUATION OF THE SCATTERING DATA

Generally, in polycrystalline and multiphase and/or porous materials, ultrasound is scattered at grain and phase boundaries, so that the scattering waves emanating from the pores are superimposed by grain scattering which is deterministic, dependent on the point of insonification, the frequency and the transducer characteristics. Porosity or the individual pores can only be detected when their scattering signals are large enough in comparison to the grain noise. As limit of detectability, it is assumed that the amplitude of the scattering signal of the pores is equal to the amplitude of the grain noise signal. From the ultrasonic scattering theories the grain scattering as well as the scattering signal of a single defect or of a defect agglomeration can be calculated, when the structural and the elastic single-crystal data of the matrix material, and also of the defect are known. The scattering coefficients for grain and pore scattering are well known in the Rayleigh regime [4–7], i.e. $d/\lambda << 1$. As a result one obtains the ratio of pore scattering to grain scattering:

$$\frac{\alpha_{SL_{pores}}}{\alpha_{SL_{grain}}} = \frac{3}{4}5^3 \frac{S_P}{S_K}V_P\left(\frac{d_P}{d_K}\right)^3 \tag{1}$$

Here, S_K and S_P are the scattering factors for grain and pore scattering and d_K and d_P are the grain and pore diameter, respectively. V_P is the porosity (volume fraction of the pores). The derivation of the scattering coefficients of Eq. (1) was based on an isotropic grain orientation distribution [6,9]. As said above the criterion for the limit of the detectability of pores is

$$\frac{\alpha_{SL_{pores}}}{\alpha_{SL_{grain}}} \approx 1 \tag{2}$$

Equations (1) and (2) were evaluated numerically for aluminum, magnesium and zinc die-castings. In order to obtain complete data sets, we used data from the literature [19,20]. Included are also evaluations of the investigations on die-casting components that have not been discussed in this article but are described in a forthcoming article [21].
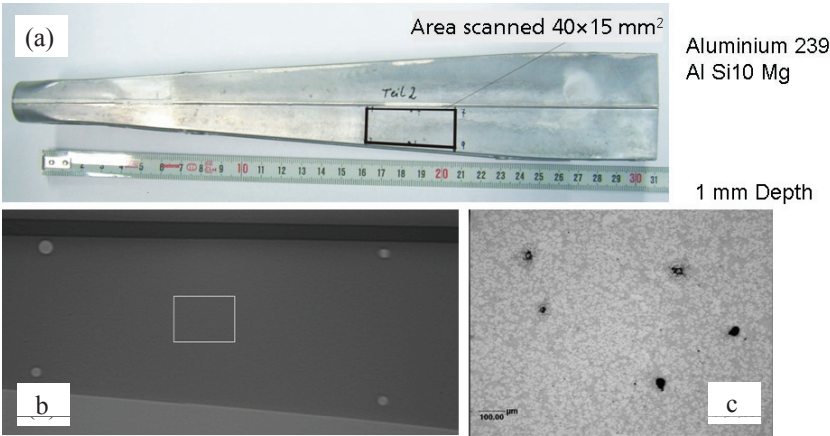
Figure 3. (**a**) Photography of a component of aluminum die-casting (AlSi10Mg) indicating the ultrasonic the testing area; (**b**) X-ray transmission image of this area, and (**c**) the metallographic micrograph from 1 mm depth corresponding to the insert in the X-ray image, porosity 0.1%.
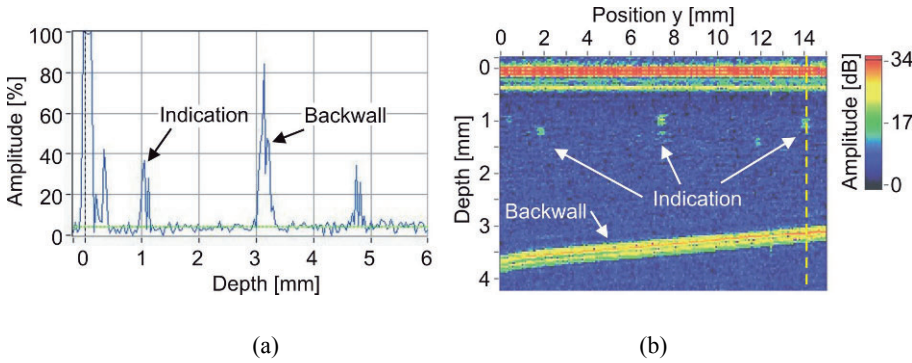
Figure 4. A- and B-scan of the aluminum die-casting component shown in Fig. 3 taken by the ultrasonic instrument HIS 2. The dashed line in the B-scan shows the position of the A-scan. At a depth of 1 mm one can see several indications (marked by arrows).
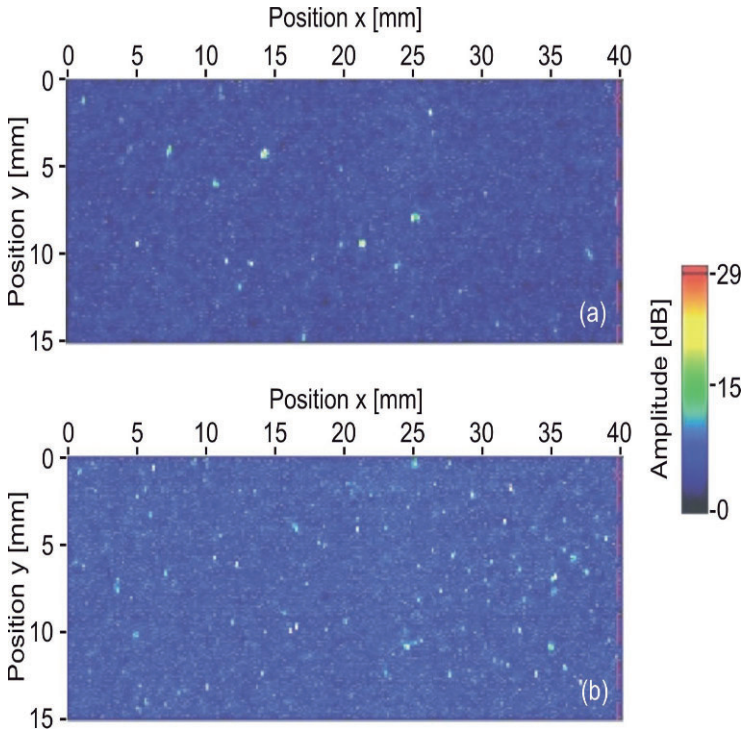
Figure 5. C-scans of the aluminum die-casting component displayed in Fig. 3 at a depth of (**a**) 0.5 and (**b**) 1 mm, respectively. The indications are caused by pores.

As magnesium and zinc do not show a cubic, but a hexagonal elastic anisotropy, the quantities were averaged accordingly. Figure 6a shows as a result the smallest detectable, relative pore size (ratio of pore to grain diameter) as a function of porosity in the range of 0.1 to 5.1%. In aluminum and magnesium die-castings pores can be detected that are smaller than the grains. The detection limit in zinc is at significantly larger pores, because of its high single crystal anisotropy and the corresponding enhance grain scattering in this material.

Numerical evaluations for aluminum die-casting with different grain sizes determined from micrographs yielding absolute values for the smallest detectable pore sizes are presented in Fig. 6b. In all cases pores of diameters down to the μm range are detectable already at a porosity of only 0.1%. A comparison of ultrasonic measurements with metallographic micrographs has already shown in the preceding section that porosities of 0.1% and pores of 30 μm diameter can be detected.

There are two possibilities for calibrating the ultrasonic back-scattering signals in order to determine absolute values for the porosity or pore size: (i) Computing the grain scattering based on the grain size and the elastic and

anisotropy constants of the matrix material or (ii) determining the insonified intensity as a function of depth which requires reference measurements on samples with flat-bottom holes at different depths.

As already pointed out above, one has to pay attention to the fact that the amplitudes of the ultrasonic signals depend on the pore size and the porosity, i.e. that these quantities are not independent from one another and that the given equations are valid for the Rayleigh range, i.e. $d/\lambda \ll 1$. Furthermore, the porosity determined from ultrasonic data relates for each measuring point
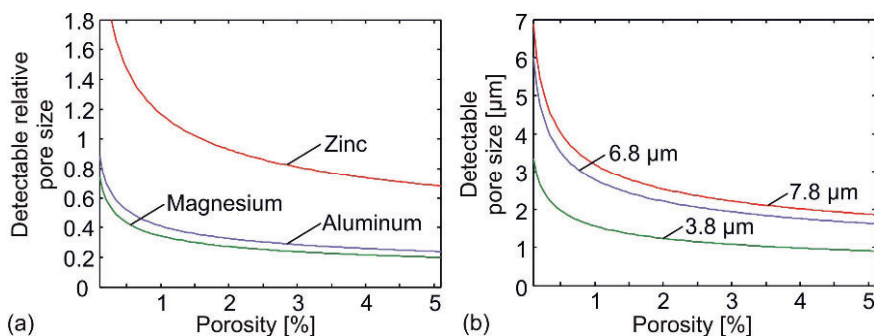
Figure 6. (**a**) Detectable relative pore size (dP/dK) as a function of porosity in the range of 0.1–5.1%. As criterion of detectability it is assumed that the pore scattering has to be equal or larger than the grain scattering; (**b**) Detectable pore size in aluminum die-casting as a function of porosity for different grain diameters.

to the volume covered by the ultrasonic ray, which varies with the transducer and the position of its focus. In the measurements described above and the employed transducers, the registered volume is very small (in the mm^3 range). An advantage of the present set-up is that pores of linear dimensions in the sub mm-range can be imaged directly and that the detection of pores in the μm range is possible due to their impedance contrast.

5.   SUMMARY

With the measurements and theoretical estimations pointed out above we have shown that ultrasonic back-scattering is suited to detect porosity and single pores in the surface-near range (0.5–2 mm depth) in die-casting components. For the range directly below the surface down to a depth of 0.5 mm the technique discussed here has to be further developed for example by using oblique insonification with separate transmitting and receiving transducers, so that scattering signals from pores are not masked by the entrance echo.

ACKNOWLEDGEMENTS

REFERENCES

1. VDG-Note "Volumendefizite von Gußstücken aus Nichteisenmetallen", Guideline P 201 of the Verein Deutscher Gießereifachleute (VDG), Düsseldorf, Germany, April 2002.
2. G. Schindelbacher, "Einfluß unterschiedlicher Porosität auf die mechanischen Eigenschaften der Legierung GD-AlSi9Cu3", *Gießerei-Praxis*, **19**, 381–392 (1993).
3. K. Goebbels, "Structured Analysis by Scattered Ultrasonic Radiation", in *"Research Techniques in NDT"*, Vol. IV, Ed. R.S. Sharpe, Academic Press, 87–157 (1980).
4. E.P. Papadakis, "Scattering in Polycrystalline Media", in *"Methods in Experimental Physics"*, edited by P.D. Edmonds, (Academic Press, New York, 1981) Vol. IXX, pp. 237–298.
5. C.M. Sayers and R.L. Smith, "The Propagation of Ultrasound in Porous Media", *Ultrasonics* **20**, 201–205 (1982).
6. S. Hirsekorn, "The Scattering of Ultrasonic-Waves by Polycrystals", *J. Acoust. Soc. Am*. **72**, 1021–1031 (1982); …"2. Shear Waves", **73**, 1160–1163 (1983).
7. F.E. Stanke, G.S. Kino, "A Unified Theory for Elastic Wave-Propagation in Polycrystalline Materials", *J. Acoust. Soc*. Am. **75**, 665–681 (1984).
8. C.B. Guo, P. Höller and K. Goebbels, "Scattering of ultrasonic waves in anisotropic polycrystalline metals", *Acustica* **59**, 112–120 (1985).
9. S. Hirsekorn, "The Scattering of Ultrasonic-Waves in Polycrystalline Materials with Texture", *J. Acoust. Soc. Am*. **77**, 832–843 (1985); "Directional Dependence of Ultrasonic Propagation in Textured Polycrystals", **79**, 1269–1279 (1986); "The Scattering of Ultrasonic-Waves by Multiphase Polycrystals", **83**, 1231–1242 (1988).
10. D. Nicoletti and D. Kasper, "Ultrasonic attenuation based on the Roney generalized theory and multiple power-law grain-size distributions", *IEEE Trans. UFFC*. **41**, 144–149 (1994).
11. J.A. Turner and R.L. Weaver, "Radiative-Transfer and Multiple-Scattering of Diffuse Ultrasound in Polycrystalline Media", *J. Acoust. Soc. Am*. **96**, 3675–3683 (1994).
12. P. Anugonda, J.S. Wiehn, and J.A. Turner, "Diffusion of Ultrasound in Concrete", *Ultrasonics* **39**, 429–435 (2001).
13. J.A. Turner and P. Anugonda, "Scattering of elastic waves in heterogeneous media with local isotropy", *J. Acoust. Soc. Am*. **109**, 1787–1795 (2001).
14. S. Hirsekorn, P.W. van Andel, and U. Netzelmann, "Ultrasonic Methods to Detect and Evaluate Damage in Steel", *Nondestr. Test. & Eval*. **15**, 373–393 (2000).
15. W. Theiner, R. Kern, and M. Stroh, "Process-Integrated Nondestructive Testing of Ground and Case Hardened Parts", Proc. 8th Eur. Con. Non-Destructive Testing, Barcelona, (2002), Code MC-4.1.

16. R. Herzer, O. Frick, C. Keferstein, and W. Arnold, "Self-tracking ultrasonic inspection", *Industrial Robot*, **22**, 25–27 (1995).
17. U. Netzelmann, R. Herzer, H. Stolz, and W. Arnold, "Volume acquisition and visualization of high-frequency ultrasound data", Proc. 19th Int. Symp. Acoustical Imaging, edited by H. Ermert and H.-P. Harjes (Plenum Press, New York 1992) Vol. IXX, pp. 553–557.
18. R.S. Gilmore, K.C. Tam, J.D. Young, and D.R. Howard, "Acoustic Microscopy from 10 MHz to 100 MHz for industrial applications", *Phil. Trans. R. Soc. London*, **A320**, 215–235 (1986).
19. G. Simmons and H. Wang, "Single Crystal Elastic Constants and Calculated Aggregate Properties: A Handbook", The M.I.T. Press, Cambridge, Massachusetts, 1971.
20. "Druckguss aus NE-Metallen", Technical Guidelines of the "Verband Deutscher Druckgießereien", Düsseldorf, March 2001.
21. S. Hirsekorn, U. Rabe, D. Bruche, N. Grov, T. Kinzler, J. Maurer, and W. Arnold, "Prüfung von Druckgusskomponenten aus Nicht-Eisen-Metallen auf oberflächenahe Porosität mittels Hochfrequenzultraschall", Materialprüfung, **50**, 206–215 (2008).

DETECTION OF HARMONIC COMPONENTS GENERATED FROM CREPT METAL ROD USING A DOUBLE-LAYERED PIEZOELECTRIC TRANSDUCER SYSTEM

M. Fukuda, M. Nishihira, K. Imano

Department of Electrical and Electronic Engineering, Faculty of Engineering and Resouce Science, Akita University, 1-1 Tegata Gakuen-machi, Akita 010-8502, Japan.

Abstract: Second harmonic components generated from plastic deformed metal rods are detected in real time by using a double-layered piezoelectric transducer (DLPT). The DLPT is comprised of two transducers with resonance frequencies of f_0; its resonance frequency is equal to $f_0/2$ when the transducers are connected in parallel and f_0 when the transducers are connected in series. The performance of the DLPT used in this ultrasonic system is evaluated. Samples of plastic deformed metal rods are prepared by tensile test equipment. The relative amplitude of the second harmonic component increased by approximately 25 dB in the metal rods after the tensile tests compared to before the tensile tests. A variation of second harmonic components generated by plastic deformed metal rods is distinctly measured by our system.

Key words: Double-layered piezoelectric transducer, Second harmonic component, Plastic deformed metal rod, Tensile test, Pulse echo

1. INTRODUCTION

Ultrasonic waves have been widely used in the nondestructive evaluation (NDE) of several materials including metal materials. Recently, harmonic ultrasonic waves have been tended to employ as new testing tool of the materials.

When metal materials are loaded with external force, dislocation, voids, closed cracks and open cracks are generated in metal material. The non-linearity of elasticity in metal materials is also remarkable [1]. It is possible that these

phenomena become one cause of generation of non-linear propagation of sound. Thus, the amplitude of second harmonic components generated by transmitting finite amplitude ultrasonic waves in these materials is considered to be varied. Detection of the variation of second harmonic components can play the important role in early discovering of the defects in metal materials. However, the sound pressure of these second harmonic components is very small, so a highly sensitive detecting system is needed to identify them. Several studies on detecting second harmonic components have been carried out [2–4].

A real time detection system for detecting second harmonic components has recently been constructed by the authors [5]. This system comprised a double-layered piezoelectric transducer (DLPT) made from two $PbTiO_3$ transducers, each of which had the same characteristics (resonance frequency f_0). The two transducers were stacked on top of each other and oriented with opposing directions of polarization. The resonance frequency of the DLPT was $f_0/2$ when the two transducers are connected in parallel, but remained as f_0 when the transducers are connected in series [6]. By switching the electrical connection of the DLPT, it was possible to improve the sensitivity of the received second harmonic component by approximately 40 dB, as compared with those obtained using conventional systems [5].

This paper examines the effective detection of second harmonic components generated by plastic deformed metal materials using DLPT.

2.   DOUBLE-LAYERED PIEZOELECTRIC TRANSDUCER

To detect the second harmonic pulse waves, a transducer which can transmit finite amplitude ultrasonic waves and sensitively receive second harmonic components is required. For achieving a simple test, the pulse echo method for detecting second harmonic components is desirable. The double-layered piezoelectric transducer (DLPT) was composed of two thickness-mode piezoceramic disks, each with the same characteristics (resonance frequency f_0 = 500 kHz) where the two disks were stacked and bonded to each other in the opposite direction of the polarization. The DLPT can be electrically connected either in parallel or in series [5,6]. The resonance frequency changes to 250 kHz ($f_0/2$) when connected in parallel, but remains as 500 kHz (f_0) when connected in series. An effective fundamental components of ultrasonic pulse wave transmission (250 kHz) was obtained if the DLPT was electrically connected in parallel, while an efficient second-harmonic components reception (500 kHz) was obtained if the DLPT was connected in series.

Because of the capacity and dead time of the switch, switching from a transmitting circuit for supplying large signals to a receiving circuit is not easy in a conventional pulse echo device. To perform a system for detecting second harmonic components, an ordinary electronic switch is used [5]. The switch is inserted between the electrode of backside and the ground on the parallel connection side. When the switch is turned on, the DLPT will be connected in parallel (250 kHz),

and when the switch is turned off, the DLPT will be connected in series (500 kHz). This configuration is able to avoid overloading the electronic switch and the receiving circuit.

3.   EXPERIMENTAL METHODS

In three metal rod samples (the No. 10 test piece of JIS 2201, SS400), tensile load using the tensile test equipment were applied. Maximum tensile load of all samples was 7300 kgf. Tensile loads of unloading and maximum strains were given to each three samples, as shown in Table 1; sample A was a metal rod before the tensile test, and then sample B, C and D became plastic deformation and had the necking center of them.

Table 1. Tensile loads of unloading and maximum strains for samples.

	Tensile load of unloading (kgf)	Maximum strain (%)
Sample A	—	0
Sample B	7000	28.8
Sample C	6000	37.1
Sample D	5000	44.1

A DLPT for second harmonic detection was manufactured from two $PbTiO_3$ (PT) thickness-mode piezoceramic plane disks, each having the same characteristics (resonance frequency = 500 kHz, diameter = 15 mm). These disks were stacked and bonded together using electroconductive silver paint such that their respective polarizations were oriented in opposing directions [7].

Our system used the pulse inversion method, which is the only means of extracting second harmonic components [8–10]. In the pulse inversion method, two pulse waves having opposite phases are transmitted alternately, and are time-averaged to cancel out the fundamental and odd-harmonic components of the waves. This method has recently been introduced into harmonic imaging in medical diagnostic equipment. It can also be applied to the detection of second harmonic components generated from plastic deformed materials.   The exciting voltage waveform for this pulse inversion was set in an arbitrary waveform generator. The exciting voltage waveform was designed with 20 cycles of 250 kHz burst sine (burst duration time: 80 μs). After an appropriate interval *T*, the next inverted exciting signal was applied to the DLPT. The interval of each signal was determined to be 2 ms. Pulse inversion was automatically carried out by averaging every *T*. Hereafter, we referred to this as pulse-inversion-averaging (PIA).
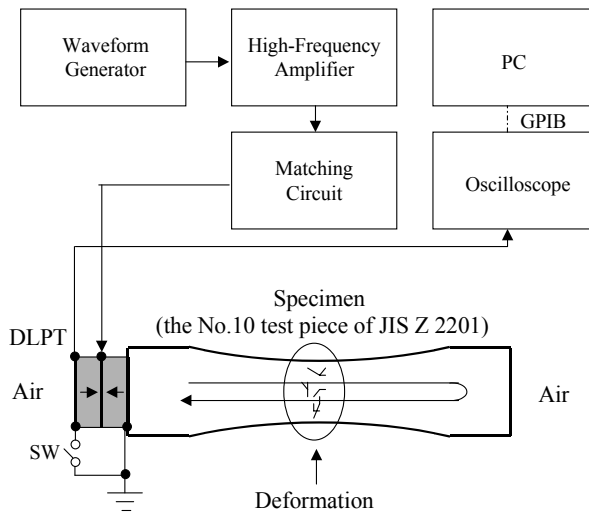
Figure 1. Experimental setup.

The system for detecting second harmonic components using the DLPT is shown in Fig. 1. The transmitting waves were generated using an arbitrary waveform generator (HP, 33120), and their amplitudes were amplified to 150 V with a high-frequency power amplifier (Thamway, T145-4716A-AK), which was electrically matched to the DLPT by an electrical impedance matching circuit (Thamway, T020-4734A). The switch was turned on to connect in parallel for transmitting a 250 kHz ultrasonic pulse wave. Ultrasonic pulses of 250 kHz were transmitted in the metal rod. While the ultrasonic pulse waves propagated in the metal rod, the second harmonic wave component (500 kHz) was generated by the nonlinear effect from the plastic deformed part of metal rod. Before the reflected pulse waves reached the DLPT transducer, the switch was turned off to change the connection to series for the efficient reception of the second harmonic waves. The received pulse waveform and its spectrum were displayed on an oscilloscope (Agilent, Infiniium 54845A), and the second harmonic component could be observed in real time using an FFT function of the oscilloscope. Finally, the received pulse waveforms were digitized and fed into a personal computer via a general purpose interface bus (GPIB).

4.   RESULTS AND DISCUSSION

The results of sample A are shown in Fig. 2. Figure 2(a) and 2(b) are a received waveform and its spectrum before pulse-inversion-averaging (PIA). Second harmonic components could hardly be detected because of the dominant fundamental component. Figure 2(c) and 2(d) are the received waveform and its spectrum after PIA. Submerged second harmonic components were extracted. The

difference A_{dif} in the amplitude between the fundamental (Fig. 2(b)) and second harmonic components (Fig. 2(d)) was approximately 60 dB.
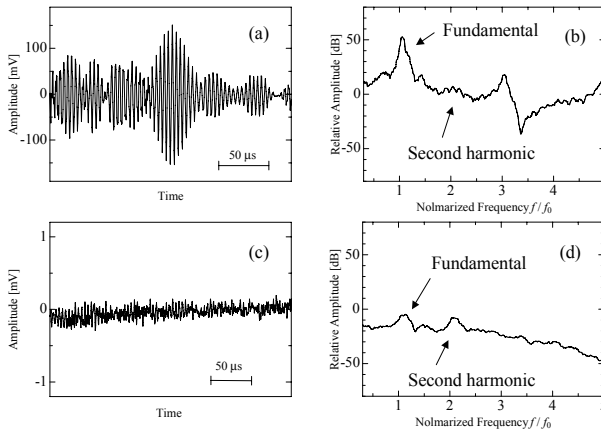
Figure 2. Results of Sample A. (**a**) Received waveform before PIA. (**b**) Spectrum of (**a**). (**c**) Received waveform after PIA. (**d**) Spectrum of (**c**).
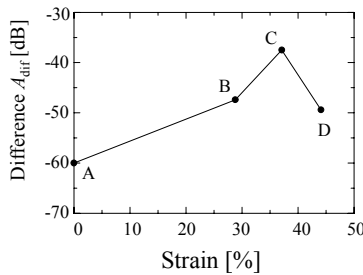
Figure 3. Relation of strain and amplitude difference between fundamental and second harmonic components.

These differences A_{dif} were also measured for other samples (B, C and D), and the results are shown in Fig. 3. The relative amplitude of the second harmonic component increased with the maximum strain up to 37.1% (sample C), but the amplitude decreased for sample D. The difference in amplitude A_{dif} of sample C was approximately 35 dB; i.e. the second-harmonic component in sample C increased by approximately 25 dB compared to sample A. We will hereafter discuss the reason that the amplitude decreases for sample D.

   The sensitivity of detection of second harmonic components was enhanced in our system, enabling us to determine accurately whether the metal rods were deformed by the tensile tests.

5.   CONCLUSIONS

The second harmonic components from the metal rod were successfully detected by our system using the DLPT. The second harmonic component in the received waves was improved by approximately 25 dB (with a sample of a maximum strain 37.1%) compared with the sample before the strain was applied. Our system was clearly able to detect variations in second harmonic components as the metal rods were deformed. In the future, the anatomical observation of cross section of plastic deformed metal rod will be executed to identify the source of harmonic wave.

REFERENCES

1. Cho-onpa Binran Henshuuiinkai eds.: *Chouonpa-Binran* (Ultrasonics) (Maruzen, Tokyo, 1999) pp. 216 [in Japanese].
2. K. Nakamura, K. Fukazawa, K. Yamada and S. Saito, Broadband ultrasonic transducers using a LiNbO$_3$ plate with a ferroelectric inversion layer, *IEEE Trans. Ultrason. Ferroelectr. & Freq. Control* **50**(11), 1558–1562 (2003).
3. H. Adachi, K. Wakabayashi, M. Nishio, H. Mizuno and T. Kamakura, Improvement of spatial resolution for third harmonic detection using a separately arranged transmitting/ receiving ultrasonic transducer, *Jpn. J. Appl. Phys.* **42**(1), 305–310 (2003).
4. I. Akiyama, A. Ohya and S. Saito, Speckle noise reduction by superposing many higher harmonic images, *Jpn. J. Appl. Phys.* **44**(6B), 4631–4636 (2005).
5. M. Fukuda, M. Nishihira and K. Imano, Real Time extraction system using double-layered piezoelectric transducer for second-harmonic ultrasonic pulse waves, *Jpn. J. Appl. Phys.* **45**(5B), 4556–4559 (2006).
6. H. Yamada and M. Onoe, Double frequency ultrasonic search unit, *Hihakai-Kensa* **20**(11), 605–608 (1971)[in Japanese].
7. M. Fukuda, M. Nishihira and K. Imano, Application of a Double-Layered Piezoelectric Transducer in the Generation of Short Ultrasonic Pulses, *Jpn. J. Appl. Phys.* **43**(5B), 3131–3133 (2004).
8. P. N. Burns, D. H. Simpson and M. A. Averkiou, NONLINEAR IMAGING, *Ultrasound in Med. & Biol.* **26**(1), S19–S22 (2000).
9. D. H. Simpson, C. T. Chin and P. N. Burns, Pulse Inversion Doppler: A New Method for Detecting Nonlinear Echoes from Microbubble Contrast Agents, *IEEE Trans. Ultrason. Ferroelectr. & Freq. Control* **46**(2), 372–382 (1999).
10. F. C. Simm, Phase Inversion Wideband Non-linear Imaging: Application to Tissue Harmonic Imaging, *J. Med. Ultrason.* **26**(4), 285 (1999).

OBSERVATION OF TWO-DIMENSIONAL SPATIAL DISTRIBUTION OF PLANE CRACK TIPS WITH LOW-POWER PULSED LASER

H. Fujii, T. Miyake, M. Matsukawa

Faculty of Engineering, Doshisha University, 1-3 Tatara-miyakotani, Kyotanabe, Kyoto, 610-0321, Japan

Abstract: We propose a simple and comparatively high spatial resolution method to nondestructively detect small plane cracks in solid materials. In this method, we used two techniques, a two-layered self-made transducer and low-power laser pulses. The two-layered transducer has two roles, it transmits low-frequency, high-amplitude longitudinal waves from a PZT transducer and it is a wideband receiver made of PVDF film. The low-frequency excitation causes the fluctuation of cracks. Combining these techniques, we succeeded in detecting plane crack tips and presenting them as two-dimensional images.

Key words: Plane crack tips, Low-power pulsed laser, Two-layered transducer, Two-dimensional mapping

1.   INTRODUCTION

The nonlinear approach is a recent means of detecting micro cracks in solid materials [1–3]. However, this approach has comparatively poor spatial resolution. The obtained data only indicates the existence of cracks in a large area of the wave propagation path. In practical nondestructive testing, therefore, we can learn the existence of micro cracks, but face difficulties deciding the actual position of the cracks. One idea to solve this problem is to use transducer arrays like an ultrasonic diagnostic system [4].

In this study, we propose a simple method to detect small cracks with comparatively high spatial resolution. This method combines two different

techniques. One is the use of short ultrasonic waves generated by the thermoelastic effect of low-power laser pulses. The thermoelastic effect at the sample surface enables repetitive excitation of a short ultrasonic wave pulse. The other is a two-layered transducer [5,6]. In this study, the two-layered transducer has two roles. One is to transmit low-frequency, high-amplitude wave, which cause the micro crack to fluctuate. The other is to receive the ultrasonic wave in a wide frequency range.

The combination of these two techniques yields interesting information about invisible plane crack tips using a simple measurement system. As we scan the measurement points by changing the focusing point of the low-power pulsed laser at the sample surface, we can obtain a two-dimensional image of the plane crack tips.

2.   SAMPLE AND EXPREMENTAL PROCEDURE

The initial sample in this study is 10 mm-wide, 15 mm-long polymethyl-methacrylate (PMMA). An initial crack was artificially formed from one point of the side surface. A 5 mm-thick sample was cut near the crack. The sample surface was then polished carefully. A PVDF film (40 μm, Kureha chemical industry) was attached to one sample surface. An aluminum film was evaporated on the other side of the PVDF film as an electrode. A PZT transducer (Fuji ceramics) was glued to this electrode. The structure of the two-layered transducer and sample is illustrated in Fig. 1(a). The PZT transducer transmits comparatively low-frequency longitudinal waves at 500 kHz. The PVDF transducer receives the low-frequency waves and the short ultrasonic pulse waves generated by the low-power laser pulses.

An aluminum film was evaporated onto a glass plate. The glass plate was attached to the other side of the sample surface. The attached glass plate modifies the sample surface and helps to induce longitudinal waves in the normal direction of the sample surface [7,8].

This surface was irradiated with laser pulses (1047 nm, 80 μJ, pulse width 5 ns, Spectra Physics R2-VS5-104Q) with a repetition time of 1 ms. The laser pulses hit the evaporated aluminum film through the glass plate. A short ultrasonic pulse wave was induced by a laser pulse at the evaporated aluminum film and passed through the crack in the sample. The laser pulse was focused and irradiated different points of the sample surface. The energy of laser pulses is so small that the thermoelastic effect does not degrade the sample surface. The diameter of focused laser beam was 0.6 mm. The interval of the measured points on the sample surface was 0.5 mm. The square area in Fig. 1(b) is the laser-irradiated region on the sample surface.

(a) Structure of the sample and
two-layered transducer

(b) Laser irradiated region
on the sample surface
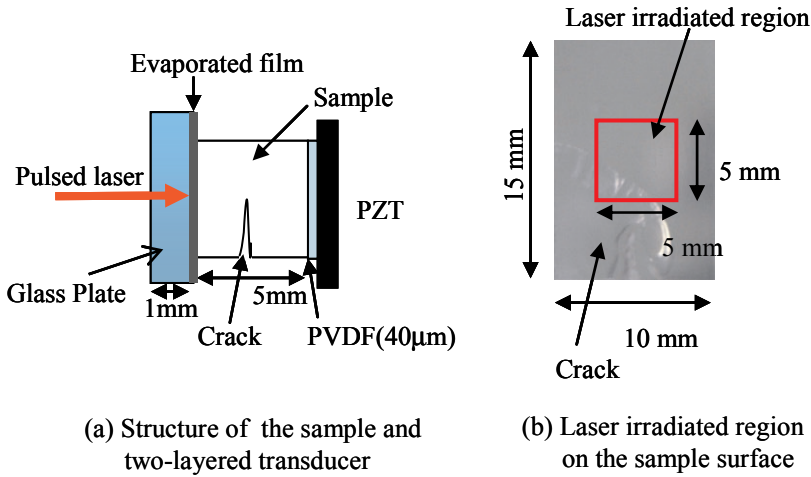
Figure 1. Sample and two-layered transducer.

3. EXPERIMENTS

The experimental system is depicted in Fig. 2. During the measurement, the PZT transducer transmitted 100 cycles of a sinusoidal longitudinal wave. The frequency of the radiated waves from the PZT transducer was 500 kHz. The repetition time of this low-frequency wave was 1 ms. The low-frequency wave causes fluctuation of the micro crack. The irradiation timing of the laser pulse was synchronized with the low-frequency component. By changing the irradiation timing of laser pulses, we can observe two types of induced longitudinal pulse waves, which passed through the crack at the negative or positive cycle of low-frequency waves. The wave received by the PVDF transducer was amplified by a preamplifier (NF electronic instruments BX-31) and observed by oscilloscope (Agilent Technologies 54852A). The signal-to-noise ratio was improved by averaging.
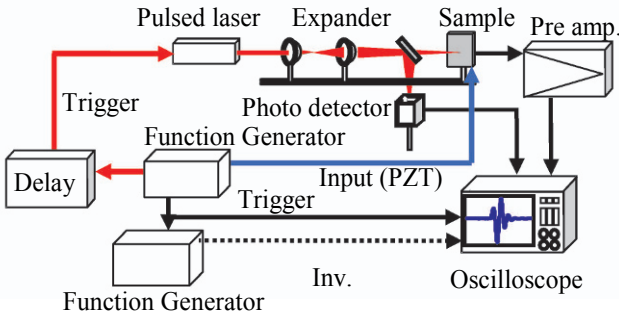
Figure 2. Experimental system.
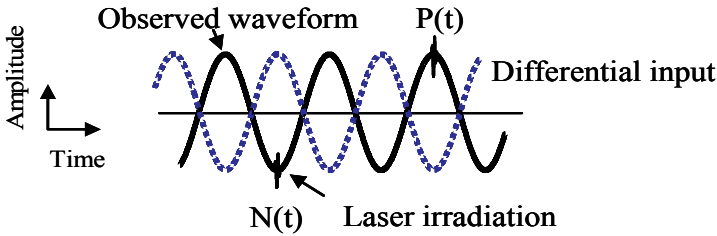
Figure 3. Image of laser-irradiation timing and low-frequency excitation.

Figure 3 illustrates the observed elastic wave. The laser-induced pulse waves were set to be observed at the time of maximum or minimum amplitude of the low-frequency component, to reflect the different status of micro cracks. The low-frequency component was eliminated by differential amplification using waves of reversed phase.

4.   RESULTS AND DISCUSSIONS

The PVDF transducer receives both low-frequency and laser-induced longitudinal pulse waves. We then delete the low-frequency waves and compare the pulse waves observed at positive (P) or negative (N) peaks of low-frequency components. The frequency spectrum at the positive peak wave (P(f)) was next normalized by that of the negative peak wave (N(f)) to extract the effect of low-frequency fluctuation. As a result, characteristic peaks appeared in the normalized spectrum. A typical spectrum is plotted in Fig. 4. Several characteristic peaks in this spectrum could not be observed

before normalization. The two-dimensional images of cracks were next obtained by two-dimensional mapping of the peak amplitudes in Fig. 4.
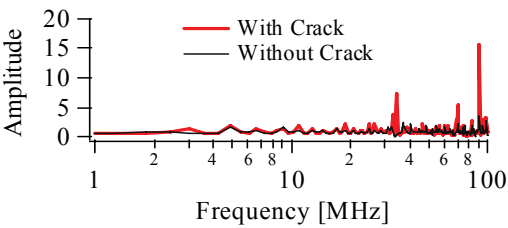
Figure 4. Normalized frequency spectrum.

Figure 5 presents the two-dimensional mapping of normalized spectrum amplitudes at different frequencies, (a) 13 MHz and (b) 35 MHz. As the frequency increased, the images moved in the expected direction of crack tips in the sample. The comparatively large tip image seems to result from the directivity of the laser-induced elastic wave. The HWHM of the directivity is expected to be around 35 degrees, which will possibly enlarge the tip image.

(a) 13 MHz   (b) 35 MHz
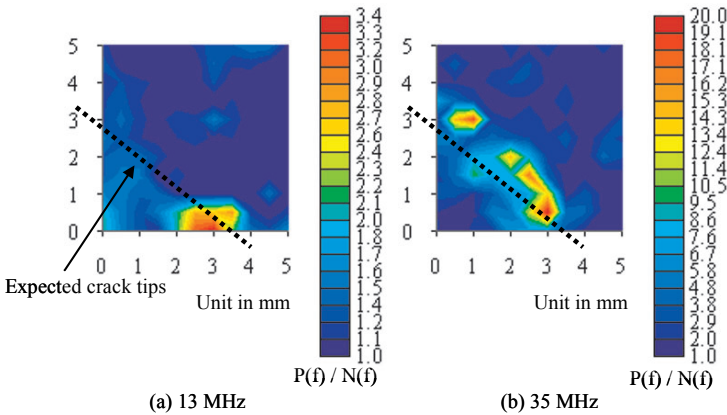
Figure 5. Spatial distribution of normalized spectrum.

Figure 6 depicts the spatial distribution of the peak amplitude of the induced wave pulse at the positive peak of the low-frequency component. We can see gradual changes of amplitude. However, it seems difficult to extract the clear points of crack tips, as indicated in Fig. 6.
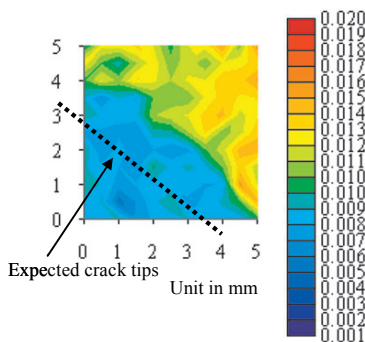
Figure 6. Spatial distribution of amplitude of the induced pulse wave.

5. CONCLUSION

We succeeded in measuring the two-dimensional spatial distribution of micro cracks by combining two different techniques, a two-layered transducer and low-power laser pulses. The obtained images represented the position of plane crack tips.

This simple measurement system enables easy detection of small plane crack tips and can be applied to various nondestructive evaluations.

REFERENCES

1. O. Buck, W. L. Morris and J. M. Richardson, "Acoustic harmonic generation at unbonded interfaces fatigue cracks", Appl. Phys. Lett. Vol. 33, pp. 371–373, 1978.
2. I. Yu. Solodov, N. Krohn and G. Busse, "CAN: an example of nonclassical acoustic nonlinearity in solids", Ultrasonics Vol. 40, pp. 621–625, 2002.
3. K. Yamanaka, T. Mihara and T. Tsuji, "Evaluation of nanoscale cracks by low pass filter effect in nonlinear ultrasound", Proc. IEEE Ultrasonics Symp., 4J-1, 2003.
4. Y. Ohara, R. Saeki, T. Ogata, T. Mihara and K. Yamanaka, "Evaluation of closed cracks by nonlinear ultrasonic phased array", Proc. Symp. Ultrason. Electron. Vol. 26, pp. 319–320, 2006.
5. I. Akiyama, A. Ohya and S. Saito, "Speckle noise reduction by superposing many higher harmonic images", Jpn. J. Appl. Phys. Vol. 44, pp. 4631–4636, 2005.
6. M. Fukuda, M. Nishihara and K. Imano, "Real time extraction system using double-layered piezoelectric transducer for second-harmonic ultrasonic pulse waves", Jpn. J. Appl. Phys. Vol. 45, pp. 4556–4559, 2006.
7. R. J. von Gutfeld and R. L. Melcher, "20-MHz acoustic waves from pulsed thermoelastic expansions of constrained surfaces", Appl. Phys. Lett. Vol. 30, pp. 257–259, 1977.
8. D. A. Hutchins, R. J. Dewhurst and S. B. Palmer, "Laser generated ultrasound at modified metal surfaces", Ultrasonics Vol. 19, pp. 103–108, 1981.

RECONSTRUCTION OF THE ULTRASONIC IMAGE BY THE COMBINATION OF GENETIC PROGRAMMING AND CONSTRUCTIVE SOLID GEOMETRY

M. Yamagiwa, F. Sugimoto, M. Yoneyama

Department of Information and Computer Science, Faculty of Engineering, Toyo University, 2100 Kujirai, Saitama 350-8585, Japan

Abstract: We propose a method for improving the highly-degraded images obtained by ultrasonic imaging system. To reconstruct 3-dimensional images from highly-degraded acoustic images, strongly typed genetic programming including constructive solid geometry which is an expression method of 3-dimensional object is used as post processor. In the tree structure of genetic programming, the temporally node is established in order to enable the individual change of type and position information of the primitive. By the experimental results, it is possible to specify type and position of the primitive from the 2-dimensional ultrasonic wave image

Key words: Visual system in extreme situations, Ultrasonic imaging system, Strongly typed genetic programming, Constructive solid geometry

1.   INTRODUCTION

This work assumes the vision system of a robot working in extreme situations in which the imaging by the optical means is impossible. This paper proposes a new reconstruction method of the object's image which does not require the learning about the object shape. The real point spread function of the ultrasonic imaging system can be decided by estimating the unknown parameters of the theoretical expression of point spread function. Applying this point spread function to the reconstructed image obtained by the Constructive solid geometry method combining with the Genetic programming, degraded image is obtained. This degraded image is compared with the measured ultrasonic image, and the difference between them is used

as the control signal. The tree structure of the genetic programming is controlled so as to minimize the difference signal. The conceptual scheme of this work is shown in Fig. 1.
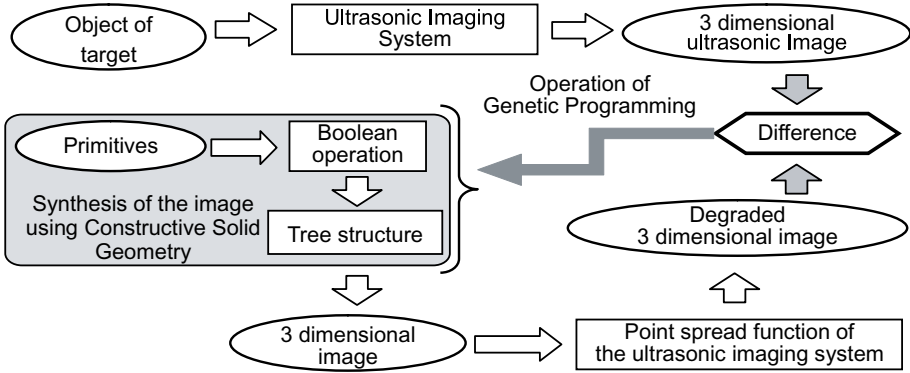
Figure 1. The conceptual scheme of this work.

2.   ULTRASONIC IMAGING SYSTEM

2.1   Ultrasonic Imaging Method [1–4]

The concept of ultrasonic imaging system is shown in Fig. 2.
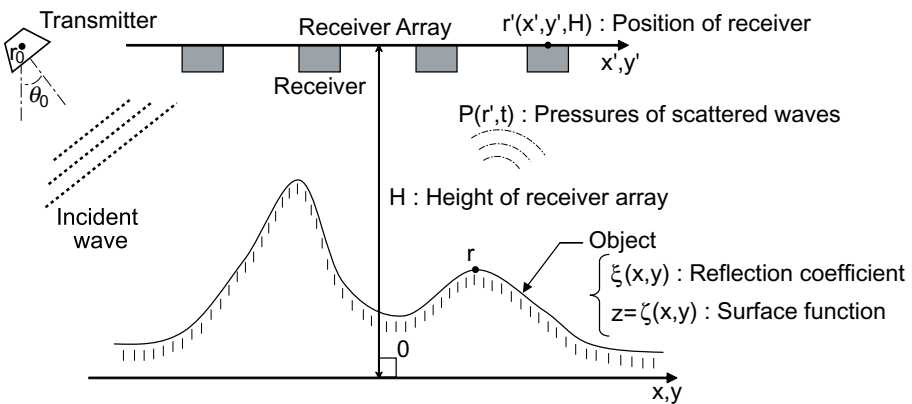
Figure 2. The relative positions of object, receiver array, and transmitter.

At t=0, the transmitter illuminates the object with an incident wave. The sound pressure of the incident wave is shown in Eq. (1).

$$P_{in}(r,t) = \Theta(ct - |r - r_0|) \cdot \exp(jk_{in} \cdot (r - r_0) - j\omega t)$$
$$k_{in} = (k\sin\theta_0, 0, -k\cos\theta_0) \tag{1}$$

In Eq. (1), c is the velocity of sound, r_0 is the position of transmitter, $r(x,y,z)$ is the surface point of the object, θ_0 is illuminating angle, k is the wave number vector, and Θ is the unit step function. $f(x,y,z)$ as the 3-dimensional image of the object is approximately obtained by calculating the inverse Fourier transform of the sound pressure of the scattered wave from the object, it follows in Eq. (2) [1].

$$f(x,y,z) = \xi(x,y)Q\{\varsigma(x,y) - z\}$$
$$= \frac{kz^2}{\pi}\left|\iint Q(r',z) \cdot \exp\left\{j\frac{k}{r'}(xx' + yy')\right\}dx'dy'\right| \tag{2}$$

In Eq. (2),

$$Q(r',t) = \frac{P\{r', (r' + r_0 - 2z\cos\theta_0/c)\} \times (H + z\cos\theta_0)}{\{(x' - r'\sin\theta_0)^2 + y'^2 + (H + r'\cos\theta_0)^2\} \cdot r'^3} \times \frac{1}{\exp(jkr')}$$

2.2 Ultrasonic Imaging System

The specification of the ultrasonic imaging system shows in Table 1.

Table 1. The specification of the ultrasonic imaging system.

The name of parameter	Value
Frequency of ultrasonic wave	40 kHz
Number of receiver	16×16 (256)
Size of receiver array	375×375 mm
Distance between the receiver array and floor	400 mm
Position interval of receiver	25 mm
Measurement number of wavelength in scattered wave	12

The ultrasonic transmitter illuminates a 3-dimensional object with ultrasonic wave, and the scattered wave from the object is divided in 12 wavelengths. Then, 12 images are calculated by Eq. (2) in each wavelength. The shape on the height is obtained by integrating the 12 images. The example of an object used for the imaging and 3-dimensional image obtained by the ultrasonic imaging system are shown in Fig. 3.

(a) The photograph of
example object

(b) The image obtained by the
ultrasonic imaging system
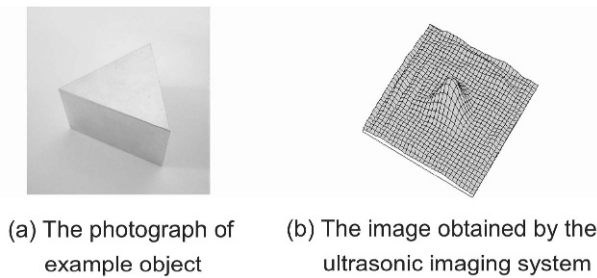
Figure 3. The example of object used for the imaging and 3-dimensional image obtained
by the ultrasonic imaging system.

3.   THE POINT SPREAD FUNCTION OF THE ULTRASONIC IMAGING SYSTEM

The theoretical point spread function (PSF) of the ultrasonic imaging system is possible to indicate by Eq. (3).

$$h(x,y) = a \cdot \frac{\sin \pi bx}{\pi bx} \cdot \frac{\sin \pi by}{\pi by} \tag{3}$$

Where, a is the amplitude parameter, b is the periodic parameter. The parameters a and b are unknown parameters. The parameter a and b are estimated using the genetic algorithm so as the minimize the difference between the theoretical response of an impulse object and the measured response. The results of estimation are a=0.819363 and b=0.068262.

4.   CONSTRUCTIVE SOLID GEOMETRY

Constructive solid geometry (CSG) is a technique used in solid modeling. CSG allows creating a complex object by using Boolean operation to combine some simple objects called primitive. It is possible to express the operation in the tree structure. Four kinds of primitives (square, circle, upward-triangle and downward-triangle) are used in this work, and the photograph of primitives and 2 dimensional images made from primitives are shown in Fig. 4.
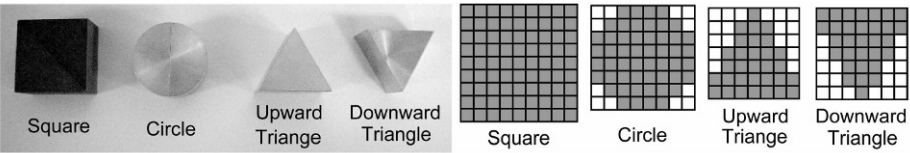
Figure 4. The photograph and 2 dimensional images of primitives.

5. DEFINITIONS OF THE DATA TYPE IN STRONGLY TYPED GENETIC PROGRAMMING

Strongly Typed Genetic Programming is an extension of the basic genetic programming approach [5]. The advantage which introduces the data type in genetic programming is improvement of the search efficiency of genetic programming by establishing the constraint in formed tree structure.

Strongly typed genetic programming has the termination nodes and the non-termination nodes. In this work, the non-termination node includes the Boolean operation, primitive temporally node (P-temp) and coordinates temporally node (C-temp). By the existence of primitive temporally node, the crossover of primitive is possible, while the coordinates is maintained. And the crossover of x and y coordinates (C-info (:1~32)) is possible at the same time by the coordinates temporally node. The sample of the tree growth by the definition of the data types are shown in Fig. 5.
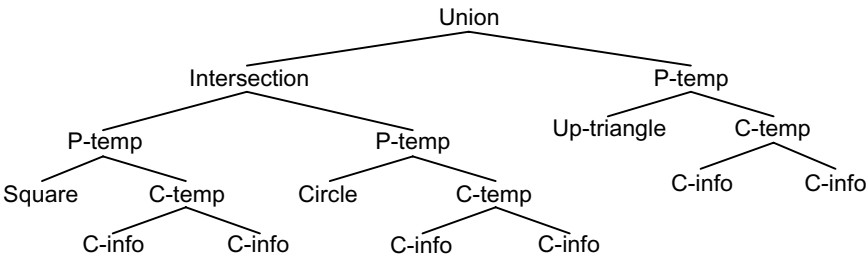
Figure 5. The example of tree growth.

6. EXPERIMENTS

By using the 2-dimensional images shown in Fig. 4 and the trees grown by genetic programming, the object images are reconstructed. The synthesized images are made by the procedure shown in Fig. 1. In the experiment, the object is limited to two primitives. As a result of the experiment, shape and

position of the object are rightly reconstructed. In the case of the primitive placing on the random position, one example of the results of the experiments is shown in Fig. 6.
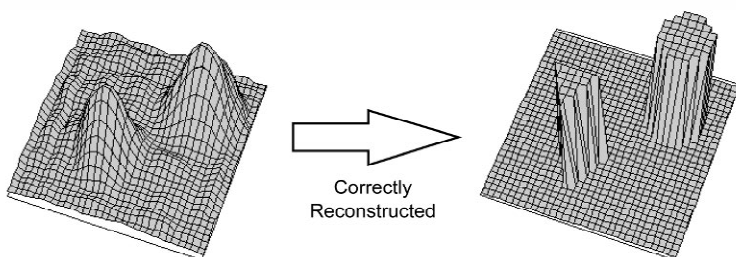
Figure 6. The image obtained by the ultrasonic imaging system and the reconstructed image.

7.   CONCLUSION

To reconstruct images from highly-degraded acoustic images, strongly typed genetic programming including constructive solid geometry was used as post processor. In the reconstruction of the ultrasonic image using genetic programming, the images of the primitives can be reconstructed at accurate position correctly. In the future, the images which are combined by more many primitives will be used in the reconstruction. Moreover, the reconstruction using genetic programming will adapt to the 3-dimensional image.

REFERENCES

1. S. Watanabe, and M. Yoneyama, "Ultrasonic robot eyes using neural networks", IEEE Trans. UFFC, Vol. 37, no. 3, pp. 141–147, 1990.
2. S. Watanabe and M. Yoneyama, "An ultrasonic visual sensor for three-dimensional object recognition using neural networks," IEEE Trans. Robot Autom, Vol. 8, no. 4, pp. 40–49, 1992.
3. S. Watanabe and M. Yoneyama, "A nonlinear ultrasonic imaging method based on the modified information criterion," Acoustical Imaging, Vol. 22, pp. 549–554, 1996.
4. M. Yamagiwa and M. Yoneyama, "Restoration for ultrasonic 3-dimensional image using Boltzmann machines," Proc. Int. Symp. Image and Analysis, pp. 946–951, 2003.
5. Montana, D. J., "Strongly typed genetic programming," Evolutionary Computation, Vol. 3, no. 2, pp. 199–230, 1995.

SOURCE LOCALIZATION BY SIMULATION OF TIME REVERSAL WAVE AND ITS RESOLUTION IMPROVEMENT WITH DECONVOLUTION TECHNIQUE

N. Wakatsuki, K. Mizutani

Graduate School of Systems and Information Engineering, University of Tsukuba, Tsukuba 305-8573, Japan

Abstract: We propose a source localization method based on a simulation of the time reversal wave. The fundamental principle has already been proposed. In this paper, the principle is applied to the sound field surrounded by reflective boundaries. The resolution is limited due to the length of the driving signal in ordinary way. However, the resolution can be improved by deconvolution technique if the waveform of the sound source is known. The proposed method can possibly be applied to acoustical flaw detection. In this paper, the source localization is only simulated numerically. We are planning experimental verifications in the future.

Key words: Source localization, Time reversal wave, Transmission line matrix, Fourier self-deconvolution, Resolution improvement

1.   INTRODUCTION

There are many applications of sound source localization such as ultrasonic flaw detection, acoustical underground inspection and so on. The source localizing methods includes beam scanning, acoustical holography and beam forming, in which transducer arrays are utilized. The waves transmitted from their sources spread outward by ordinary, however, time reversal waves [1], which are also called as phase-conjugate waves, concentrate toward the locations of the original sources by themselves. Thus, the sound source is

visualized by tracking the time reversal waves [2]. The time reversal wave is formed by following procedure; the waves which reach a boundary are stored, time reversed and transmitted from the same boundary after the sound field becomes stationary. Time reversal waves can be generated using phase-conjugate mirrors or transducer arrays. The source localization is achieved by simulating the time reversal wave in computers instead of actual generation. If there are anomalies such as flaws in the sound field, their locations become secondary sources. So the anomalies can be localized by similar procedure. This is expected to be used for anomaly detection such as ultrasonic flaw detection of plates.

If the source is impulse, high resolution is achieved in the visualized source image. However, the source waveform is expanded due to the property of the source. This fact degrades the visualized image. If the source waveform is known, the image resolution can be improved by applying Fourier self-deconvolution [3] to the waves on the boundaries, which are the source of the time reversal waves.

In this paper, the simulations of source localization and anomaly detection in a two-dimensional sound field are demonstrated. In addition, the resolution improvement by applying Fourier self-deconvolution method is confirmed.

2.   PRINCIPLE

2.1   Simulation of Time Reversal Wave

Figure 1 shows a two-dimensional sound field considered here. Several sound paths are illustrated by dashed arrows. The waves generated at a sound source are possibly reflected several times on the boundaries and then received at a sensor array, and finally absorbed in an absorbing zone behind the array. The waveforms of signals received by the sensor array are all stored. After the system becomes stationary, the waveforms are time reversed and then inputted from the array in a numerical simulation of the time reversal waves. The waves will concentrate toward the source point in the simulation, so the source is localized. A transmission-line matrix (TLM) model is utilized for the numerical simulation, in which wave propagations are modeled by pulses propagating in an orthogonal grid of transmission lines. The propagation process of waves is similar to the explanation of the Huygens' Principle. The wave propagation is simulated by tracing the pulses in the TLM model step by step. In this sense, this method has the same scheme as finite difference time domain (FD-TD) method. While the

medium in which sound waves propagate is indicated as an elastic plate in Fig. 1, the waves are modeled as scalar waves. This modeling may give a scalar approximation of elastic waves.
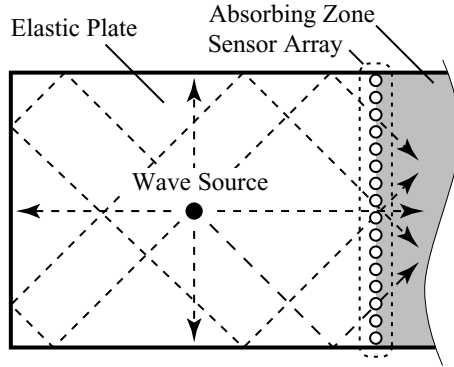
Figure 1. Principle of source localization.

2.2 Resolution Improvement by Fourier Self-Deconvolution

In linear time-invariant systems, an observed signal $x(t)$ is represented by a convolution integral of a driving signal $s(t)$ and an impulse response $h(t)$ of the system. While the information of the field including the source location is in $h(t)$, the source is localized from the observed signal, $x(t)$. So the resultant source image degrades unless $s(t)$ is an impulse. If the waveform $s(t)$ is known, the impulse response $h(t)$ is estimated from an observed signal $x(t)$ by using Fourier self-deconvolution,

$$H(\omega) = \frac{X(\omega)}{S(\omega)}, \tag{1}$$

where $S(\omega)$, $X(\omega)$ and $H(\omega)$ are Fourier transforms of $s(t)$, $x(t)$ and $h(t)$, respectively. The estimated system impulse response $\tilde{h}(t)$ is obtained by inverse Fourier transform of $H(\omega)$. If the waveform of $s(t)$ is limited, the division by $S(\omega)$ may emphasize measurement noise especially in higher frequencies. Thus, an appropriate low pass filter must be applied to estimated signal in real situations. By applying deconvolutions by the waveform of the sound source to all signals received at the sensor array, the resolution of the image will be improved.

3.   NUMERICAL SIMULATION

3.1   Source Localization

The proposed method of the source localization is evaluated using numerical simulations. A two-dimensional sound field is assumed as shown in Fig. 2. The field is divided into 400×280 TLM elements. A wave source is located at (200 Δl, 140 Δl), which is the center of the field. The waveform of the source is assumed as an impulse response of a single resonance system with dumping as shown in Fig. 3. The waveform will approximate the impulse response of typical transducers. The responses on all of 280 TLM elements on the absorbing boundary are used as input signals in subsequent time reversal simulation. There are no reflective objects here, while one is illustrated in Fig. 2. This will be considered in the following simulation.

Visualized sound source images with and without the deconvolution are shown as gray scale in Fig. 4. Although the location of the source can be recognized in both images, surrounding parts of the source fluctuates in Fig. 4(a) due to the source waveform.

Whereas with the deconvolution, the image becomes clear and the fluctuation vanishes as shown in Fig. 4b. Even with the deconvolution, radial artifacts appear around the source because the signals received at the array are truncated before the field becomes completely stationary.
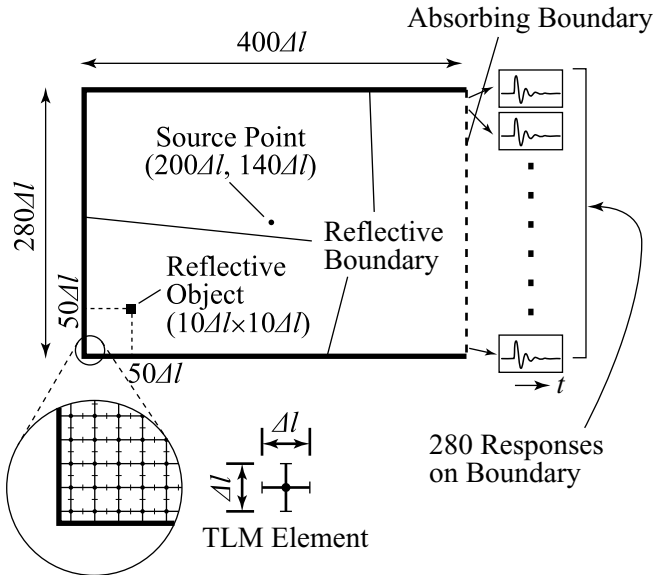
Figure 2. Configuration of the simulation.
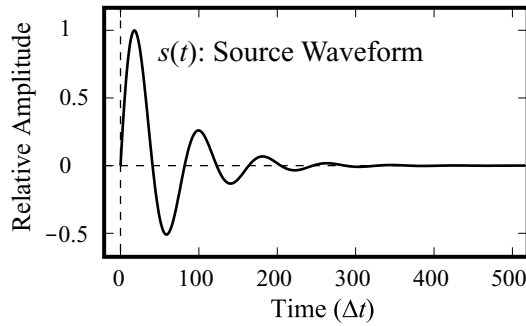
Figure 3. Assumed impulse response of the system.

(a) Without deconvolution.   (b) With deconvolution.
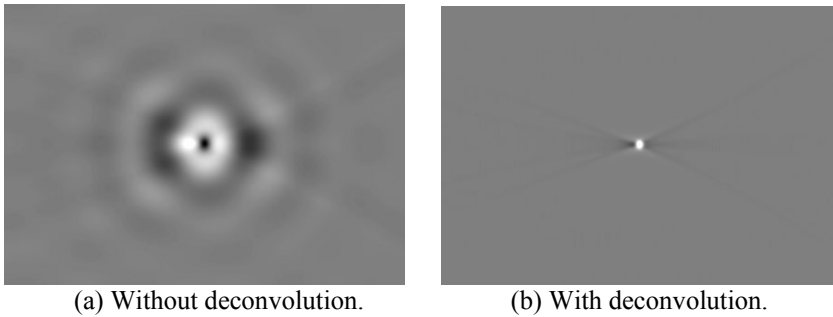
Figure 4. Reconstructed images of sound source.

3.2 Anomaly Detection

A reflective object in the sound field behaves as a secondary sound source when the wave is scattered by the object. Thus, time reversal waves will concentrate toward the object location as well as the primary source. If the object is small, however, the reflected waves are so weak compared with the primary wave that they can hardly be observed. Therefore, the reference fields, in which there are no reflective objects, are simulated as well as actual fields. The image of the anomaly will be emphasized by calculating the difference of both fields. This technique can be utilized for ultrasonic flaw detection and so on.

A reflective rectangular object is taken as an anomaly whose size is 10 Δl × 10 Δl. Its center is located on (50 Δl, 50 Δl). The images in Fig. 5 indicate the root mean square values of the difference fields accumulated during the time reversal process. The location of the anomaly can be discriminated, however, the image is blurred and many artifacts appear due to the source

waveform that is not an impulse in Fig. 5a. By applying Fourier self deconvolution, the artifacts are reduced and the resolution of the image is improved. As the result, the shape becomes able to be discriminated as shown in Fig. 5b. Even with the deconvolution, minor artifacts are still left due to the same reason as in the previous source localization. In addition, multiple reflections between the object and reflective boundaries also contribute the occurrence of the artifacts.

(a) Without deconvolution.   (b) With deconvolution.
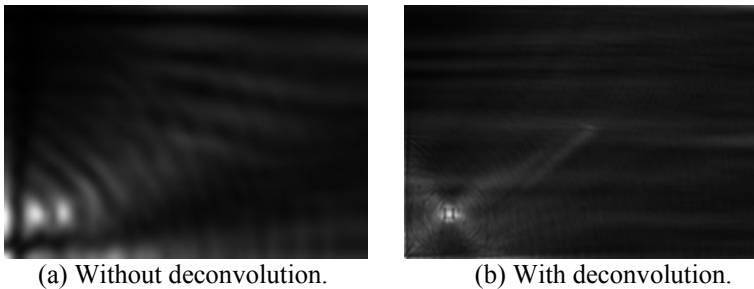
Figure 5. Anomaly detection.

4.   CONCLUSIONS

A sound source in a rectangular field was localized from time reversal waves simulated with TLM modeling. A transducer array was located on a single absorbing boundary, while other boundaries were reflective. The resolution of a reconstructed image was improved by applying the deconvolution with the impulse response to the received signals. A reflective object in the sound field was also localized by calculating the difference from a reference field, in which no reflective objects exist. The image of the object is also improved by applying the deconvolution. This method is expected to be utilized for various nondestructive inspections such as ultrasonic flaw detection. Experimental confirmation is planned for future work.

REFERENCES

1. M. Fink: IEEE Trans. Ultrason. Ferroelec. Freq. Contr. **39** (1992) 555.
2. Y. Kagawa, T. Tsuchiya, K. Fujioka and M. Takeuchi: J. Sound Vib. **255** (1999) 61.
3. J. K. Kauppinen, D. J. Moffatt, H. H. Mantsch and D. G. Cameron: Appl. Spectrosc. **35** (1981) 271.

COMPONENTS AND SYSTEMS

NONLINEAR MULTIBEAM ULTRASONIC IMAGING
Simultaneous Transmission of Ultrasonic Waves of Two Frequencies

I. Akiyama, N. Yoshizumi, A. Ohya, S. Saito

Department of Electric and Electronic Engineering, Shonan Institute of Technology, Fujisawa 251-8511, Japan; Graduate School of Systems and Information Engineering, University of Tsukuba, Tsukuba 305-8573, Japan; School of Marine Science and Technology, Tokai University, Sizuoka 424-8610, Japan

Abstract: Studies were conducted on multi-frequency ultrasonic imaging to employ simultaneous transmission of 2 and 8 MHz pulses, where the secondary waves generated through nonlinear ultrasound propagation is utilized. Multi-frequency images are constructed by using various frequency components extracted from echo signals. Annular PZT transducers are used as transmitters while a PVDF piezo-film bonded on the surface of the PZT transducers is provided as a receiver. A commercially available mechanical sector scanner equipped with these transducers is employed in experiments of imaging the phantom and pork sample. Using the present imaging system, images are successfully obtained by secondary waves as well as the primary waves. Superposing those images reduces image speckle.

Key words: Annular transducer, PVDF piezo-film, Phantom imaging, Secondary waves

1.   INTRODUCTION

The authors are broadening the frequency band of imaging systems and reducing the speckle by utilizing multi-frequency echoes in order to improve the picture quality of ultrasonic echographs. A bi-layered transducer where a broad-band PVDF piezofilm is bonded on the vibrating surface of a PZT transducer has been prototyped for detecting harmonics above the second order that are induced by acoustic nonlinearity in water [1–4]. Signal processing

to reduce the speckle utilizing those multiple-frequency signals [5] has also been proposed and experimentally confirmed [5]. In addition, real-time data acquisition and image formation have been conducted with this transducer installed on a commercially available mechanical sector diagnostic system [6].

This imaging method uses low-amplitude, higher-harmonic components generated due to the nonlinearity in the medium, so the S/N ratios can be insufficient in attenuating medium such as biological tissues, particularly for harmonics above the third order. To avoid relying on the nonlinear generation of harmonics above the third order, ultrasound with a triple frequency can be simultaneously radiated as a primary signal. However, the difference frequency then coincides with that of the second harmonic generated by the lower primary, and the triple frequency radiation is not always effective. As a more effective technique, this paper examines simultaneously transmitting ultrasound with a quadruple frequency with two annular PZT transducers. When a primary ultrasound beam of 2 and 8 MHz is emanated from this transducer, five different ultrasonic beams are assumed to be generated in total, together with nonlinearly generated secondary waves of 4, 6 and 10 MHz. Consequently, three different ultrasound beams of the secondary waves can be effectively generated through nonlinear propagation in spite of simultaneous transmission similar to the aforementioned triple frequency ultrasound.

Thus, an annular PZT transducer is prototyped to enable simultaneous transmission of 2 and 8 MHz waves. A PVDF piezofilm is attached to the surface, and the annular transducer is installed on a mechanical sector ultrasonic diagnostic system. An imaging experiment for the phantom and pork sample immersed in water is conducted using this system to examine the feasibility of the present method.

2.   SIMULTANEOUS TRANSMISSION OF TWO-FREQUENCY ULTRASOUND

2.1   Annular PZT Transducer

Simultaneous transmission of ultrasonic pulses with two different center frequencies induces harmonic components with double, sum and difference frequencies due to the nonlinear effect in the medium that results in forming various ultrasonic images. When 2 and 8 MHz are selected as the frequencies, the frequencies of secondary waves are 4, 6 and 10 MHz. Since these frequency components are generated as secondary waves, the echoes can be received with rather high S/N ratios compared with harmonics above

the third order. For this reason, an annular PZT transducer is prototyped for simultaneously transmitting 2 and 8 MHz waves. An 8 MHz transducer is set inside, and a 2 MHz one is set outside. The properties of each transducer are listed in Table 1.

Table 1. Transducer characteristics

	Inner transducer diameter: 7 mm	Outer transducer diameter: 17 mm, Bore: 9 mm
Resonance Frequency [MHz]	8.1	2.2
Focal Distance [mm]	45	45
Fractional Bandwidth [%]	52	39
Capacitance [pF]	440	1400
Impedance [Ω]	34	74

2.2   Two-Frequency Transmission and Secondary Wave Generation

A PVDF piezofilm is conventionally bonded to receive the broadband echo signal induced by the simultaneous transmission of 2 and 8 MHz waves with an annular PZT transducer. Figure 1 depicts the mechanical sector ultrasonic probe for this transducer. When this probe emanates an ultrasound wave in water, the generation of primary and secondary waves is confirmed. An analog signal to drive the PZT transducers is obtained with a D/A converter card (Gage, CG8150). The envelope of the superposition of a 5-cycle, 2 MHz signal and a 20-cycle, 8 MHz signal is shaped with the Hanning window as illustrated in Figs. 2a, b. This voltage is applied to the PZT transducers through a 50 dB power amplifier (ENI, 2100L).

The waveform and its spectrum observed near the focus are shown in Figs. 2c, d. High intensity peaks are found at the primary frequencies of 2 and 8 MHz. Other peaks are also found at the secondary wave frequencies of 4, 6 and 10 MHz.

The profiles of 2 to 10 MHz ultrasonic beams are then examined. The ultrasound waves are detected with a hydrophone (Force Institute) moving in 1 mm steps in the radial direction and 5 mm steps in the axial direction. The spectrum of the observed 100 MS/s waveform is computed through the FFT after 256 cycles are averaged on an 8-bit digital oscilloscope (LeCroy, 9370CL). The maximum value near each frequency is plotted on the contour map of Fig. 3 as the intensity of the harmonic component.

Figure 1. Mechanical sector ultrasonic probe equipped with a two-layered transducer and a PVDF piezofilm bonded on an annular transducer.
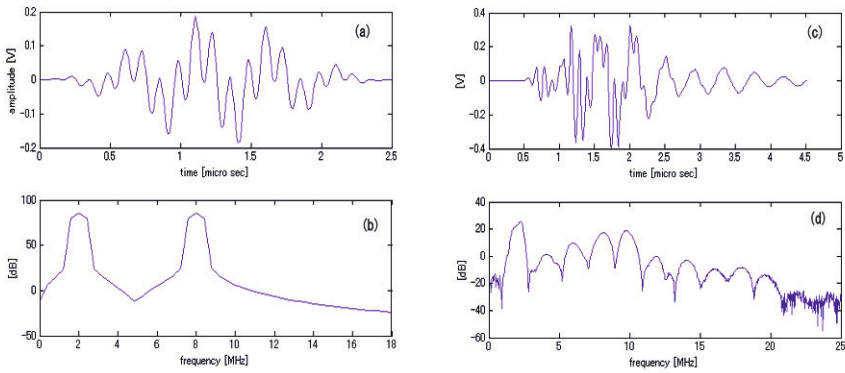
Figure 2. Input signal to PZT transducer; (**a**) Waveform, (**b**) Spectrum. Waveform (**c**) and its spectrum (**d**) of the pressure observed near the focus.

2.3   **Mechanical Sector Diagnostic System**

The imaging experiment is conducted using a commercially available mechanical sector ultrasonic diagnostic system (Aloka, SSD1000) equipped with the prototype ultrasonic probe. The input signal is supplied to the PZT transducer as described in the previous section. After amplification, the analog signal is received with the PVDF and downloaded as a 14-bit signal with a 100 MHz sampling frequency using an A/D card (Gage, CS14200). The block diagram of this system is illustrated in Fig. 4.
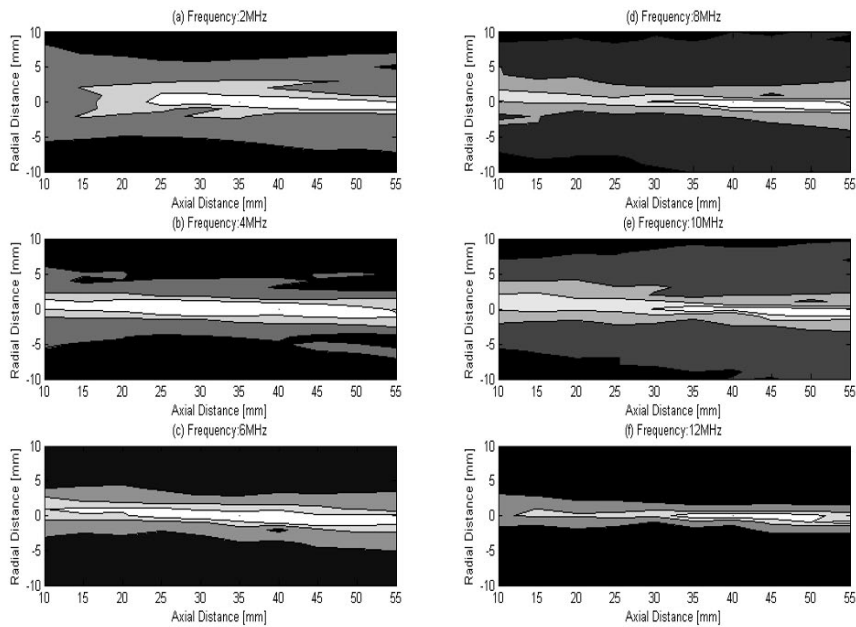
Figure 3. Beam profile of each frequency component for simultaneous transmission of 2 and 8 MHz signals. Contours indicate the levels of –5, –10, –20, –40 and –60 dB relative to each maximum amplitude.
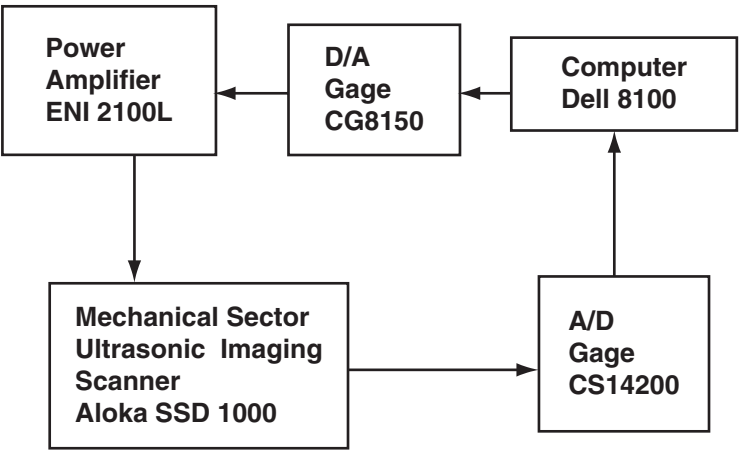
Figure 4. Block diagram of the experimental system.

3.   IMAGING EXPERIMENT

3.1   Phantom Experiment

The imaging experiment is conducted with a gel phantom immersed in a water tank. Figure 5 presents images generated from signals separated with a band-pass filter with 2 MHz bandwidth whose center frequency is set at 2, 4, 6, 8 or 10 MHz. It is seen that the speckle pattern smoothes more at higher frequency. After orthogonal detection, all the output signals multiplied together are presented in Fig. 5f in a logarithmically compressed display. A smooth image with reduced speckle is obtained. This image is equivalent to the superposition of all the images of Figs. 5a–e. The improvement of SNR is evaluated in Table 2, which lists the SNR derived from each image. Compared with the average of 22 dB, the SNR is improved by about 5.5 dB. The superposition of five uncorrelated images should yield a 7.0 dB improvement, but this improvement is slightly lower. This means that the images are slightly correlated.

3.2   In Vitro Imaging Experiment

An imaging experiment was conducted with a pork sample in water. Figure 6 presents the result of superposing the image of the components of 2, 4, 6, 8 and 10 MHz. The boundary between the muscle and fat layers is clearly recognized in Fig. 6 by virtue of the speckle reduction effect.

4.   CONCLUSION

An ultrasonic imaging system that simultaneously transmits 2 and 8 MHz waves was investigated. An annular PZT transducer was prototyped as a transmitter, and a PVDF piezofilm was bonded on the PZT transducer surface for a receiver. An imaging experiment for a phantom and pork sample was conducted using the above transducer installed on a commercially available mechanical sector diagnostic system. The beam profile of the transmitted ultrasound will be further improved by incorporating a composite transducer instead of an annular one.

ACKNOWLEDGEMENTS
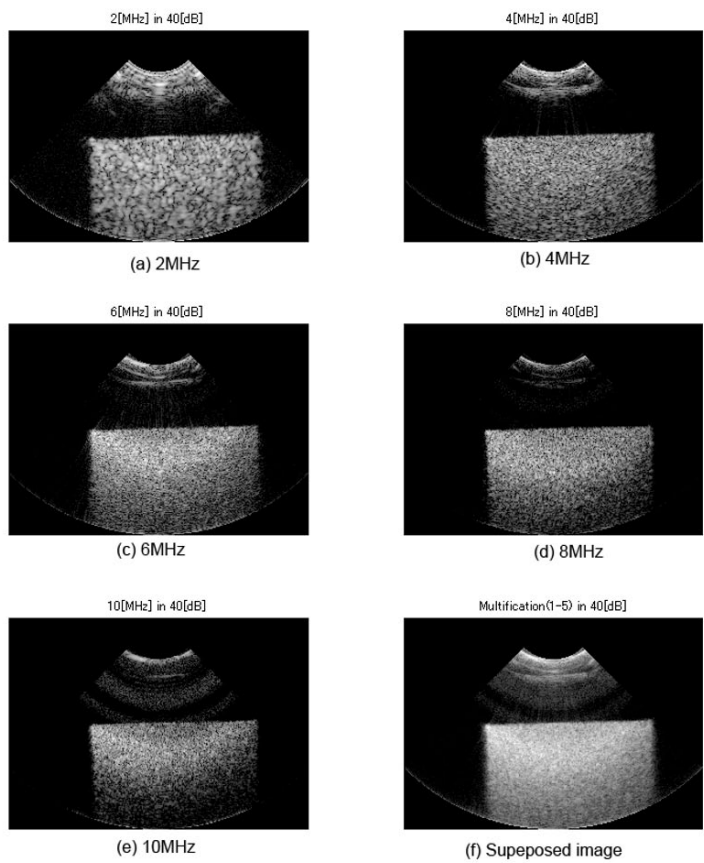
Figure 5. Images generated by passing the received signal through a 2 MHz width band-pass filter with a center frequency of (**a**) 2, (**b**) 4, (**c**) 6, (**d**) 8, and (**e**) 10 MHz. (**f**) Superposed image from 2 to 10 MHz image. Each image has been logarithmically compressed within a dynamic range of 40 dB.

Table 2. Comparison of SNR between harmonic images and superposed image.

2 MHz	4 MHz	6 MHz	8 MHz	10 MHz	Superposed image
21.8 dB	22.0 dB	21.5 dB	22.7 dB	22.0 dB	27.5 dB
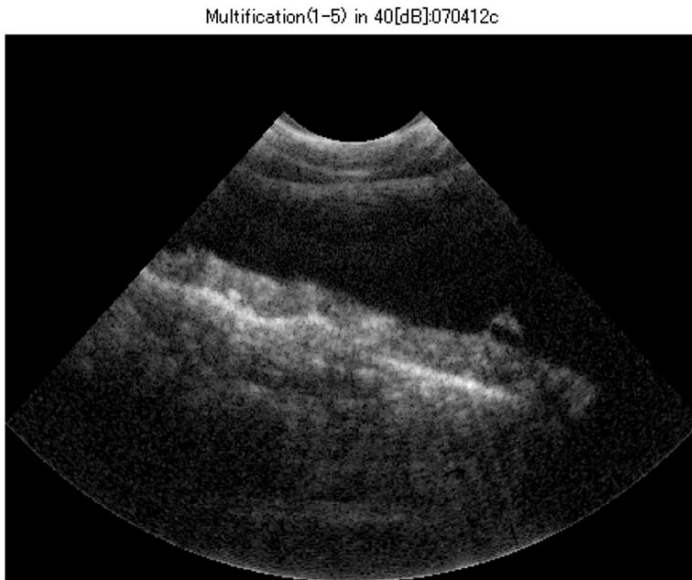
Figure 6. Logarithmically compressed superposed images of pork sample with a dynamic range of 40 dB.

REFERENCES

1. Akiyama I, Yamamoto H, Ohashi G and Saito S: Ultra broadband ultrasonic imaging. – Harmonic generation and detection by bi-layer type probe – Technical Report of IEICE, US2003-107, 2004 [in Japanese].
2. Akiyama I and Ohya A: Development of ultra broadband ultrasonic imaging system – Prototype of mechanical sector equipment – Technical Report of IEICE, US2005-3, 2005 [in Japanese].
3. Akiyama I, Yamamoto H, Ohashi G, et al.: Speckle reduction by summation of higher order harmonic images. Acoustical Imaging Vol. 27, 27: 651–7, 2004.
4. Akiyama I, Saito S and Ohya A: Speckle noise reduction by superposing many higher harmonic images. Jpn J Appl Phys 44: 4631–6, 2005.
5. Akiyama I, Saito S and Ohya A.: Development of an ultra-broadband ultrasonic imaging system: Prototype mechanical sector device, J Med Ultrasonics Vol. 33(2): 71–76, 2006.
6. Akiyama I, Ohya A and Saito S: Ultra-broadband ultrasonic imaging using bi-layer structure probe, Acoustical Imaging, Springer, Dordrecht, Vol. 28, pp. 101–109, 2007.

DYNAMIC-RECEIVE FOCUSING WITH HIGH-FREQUENCY ANNULAR ARRAYS

J.A. Ketterling, J. Mamou, R.H. Silverman
Riverside Research Institute, Frederic L. Lizzi Center for Biomedical Engineering, New York, NY 10038, USA; Weill Medical College of Cornell University, New York, NY, 10021, USA

Abstract: High-frequency ultrasound is commonly employed for ophthalmic and small-animal imaging because of the fine-resolution images it affords. Annular arrays allow improved depth of field and lateral resolution versus commonly used single-element, focused transducers. The best image quality from an annular array is achieved by using synthetic transmit-to-receive focusing while utilizing data from all transmit-to-receive element combinations. However, annular arrays must be laterally scanned to form an image and this requires one pass for each of the array elements when implementing full synthetic transmit-to-receive focusing. A dynamic-receive focusing approach permits a single pass, although at a sacrifice of depth of field and lateral resolution. A five-element, 20-MHz annular array is examined to determine the acoustic beam properties for synthetic and dynamic-receive focusing. A spatial impulse response model is used to simulate the acoustic beam properties for each focusing case and then data acquired from a human eye-bank eye are processed to demonstrate the effect of each approach on image quality.

Key words: Annular array, High-frequency ultrasound, Beamforming, Ophthalmic imaging

1.   INTRODUCTION

Current high-frequency ultrasound (HFU, > 20 MHz) transducers are single-element, focused devices that have excellent lateral resolution within their typically limited –6-dB axial depth of field (DOF). Array transducers, successfully implemented at lower frequencies, are the natural approach to improving HFU DOF while maintaining a fine lateral resolution. HFU linear arrays have proven to be very difficult to fabricate and are still in the

prototype phase [1]. We have demonstrated that excellent HFU images can be obtained using an annular-array transducer fabricated with a piezopolymer film [2,3]. The annular-array approach is appealing because it requires relatively few elements, and the elements have a surface area similar to current single-element devices.

Our initial image-formation approach was to digitize all of the transmit-to-receive pair echo data and then to post process the data with a synthetic-focusing algorithm [4]. However, we were required to laterally scan the transducer across a sample 5 times in order to obtain all of the transmit-to-receive data. As we move towards a real-time implementation of the annular array, a single-pass approach is more ideal. Here, we evaluate a single-pass, dynamic-receive-focusing beamforming approach to image formation.

2.   METHODS

2.1   Annular Array

The methods of fabricating and instrumenting the annular array were described previously [4,5]. For these studies, we utilized a five-ring, 17-MHz annular array. The array had a total aperture of 10 mm and a geometric focus of 31 mm. Insertion losses were 17, 25, 28, 31, and 30 dB, and the –6-dB fractional bandwidths were 28, 25, 34, 35, and 31% from the center to outer annulus, respectively.

An automated scanning system permitted a single element to be pulsed and then the received radio-frequency echo data to be simultaneously digitized from all five elements [4]. Using this system, we scanned a human eye-bank eye and acquired data for all 25 transmit-to-receive element pairs. These data were then post processed to demonstrate different beamforming strategies.

2.2   Simulations

A spatial impulse response (SIR) method was employed to model the acoustic field of the annular array [4,6]. The SIR, $\mathbf{h}(\mathbf{r},t)$, was calculated at a point in space $\mathbf{r}$ for a transmit, $\mathbf{h}_t(\mathbf{r},t)$, and a receive element, $\mathbf{h}_r(\mathbf{r},t)$. The voltage at the receive element of the transducer was then proportional to the convolution $\partial^2 \upsilon(t)/\partial t^2 * \mathbf{h}_t(\mathbf{r},t) * \mathbf{h}_r(\mathbf{r},t)$, where $\upsilon(t)$ is the surface velocity of the transducer. Beam simulations were performed by calculating the transmit-to-receive voltages for all 25 array element combinations at a position $\mathbf{r}$ and

then processing the resulting data with synthetic-focusing or dynamic-receive-focusing algorithms [4].

Focusing was achieved by applying digital delays to each transmit-to-receive signal and then summing the 25 signals. Lateral and axial acoustic beam profiles were calculated by finding the peak signal amplitude of the focused data over a range of **r** values. For dynamic focusing, a single transmit focal zone and a series of receive focal zones were utilized. For synthetic focusing simulations, a composite beam simulation was calculated by merging data from a series of axial transmit-to-receive focal zones. A fixed-focus case was also calculated by summing the 25 pairs of transmit-to-receive data with no delay corrections.

3.   RESULTS

3.1   Simulations

The theoretical simulations of axial beam profiles and –6-dB lateral beam widths are shown in Fig. 1 for the three cases: fixed focusing (FF, all elements treated as one), dynamic-receive focusing (DR, single transmit focal zone and 41 receive focal zones), and full transmit-to-receive synthetic focusing (SF, 41 transmit-to-receive focal zones). The axial beam simulations (Fig. 1a) showed that the DR case had an improved DOF versus the FF case, but the SF case was far superior to DR and FF. The –6-dB axial DOFs spanned 18 mm for SF (19–37 mm), 5.5 mm for DR (28–33.5 mm), and 4 mm for FF (29–33 mm).

The lateral beam-width simulations showed that the FF case had its best resolution at the geometric focus and this resolution deteriorated very quickly when moving away from the geometric focus (Fig. 1b). The DR case slightly improved upon the FF case in the DOF region and showed a strong improvement outside of the –6-dB axial DOF. However, outside the DOF the relative axial signal amplitude was small. Of the three simulations, the SF case had by far the best overall lateral resolution over the DOF.

One means of improving axial DOF and lateral resolution for the DR case is to transmit at multiple depths and then merge the receive focus data into a series of focal zones. Figure 2 shows DR examples for transmit foci at 23, 27, 31, and 35 mm. The DOF was observed to increase as the transmit focus increased, which is consistent with an effective increase of F-number. Figure 2 also shows that SF remains the preferred beam-forming strategy to achieve the best axial DOF and lateral resolution. DR approaches SF as the number of transmit foci increase, but the advantage of DR as a rapid

beamforming strategy diminishes as the number of transmit foci increase. For 5 or more transmit foci, SF is the more advantageous approach.
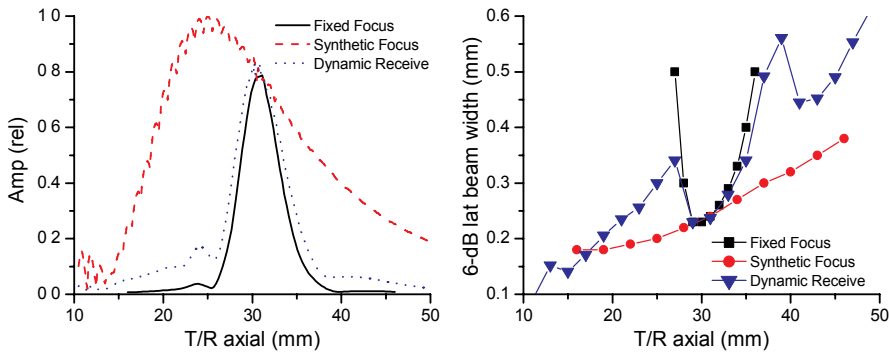
Figure 1. Simulations for the 20-MHz array of (**a**) axial beam profiles and (**b**) –6-dB lateral beam widths. The plots show the cases of fixed, dynamic-receive, and full synthetic focusing.
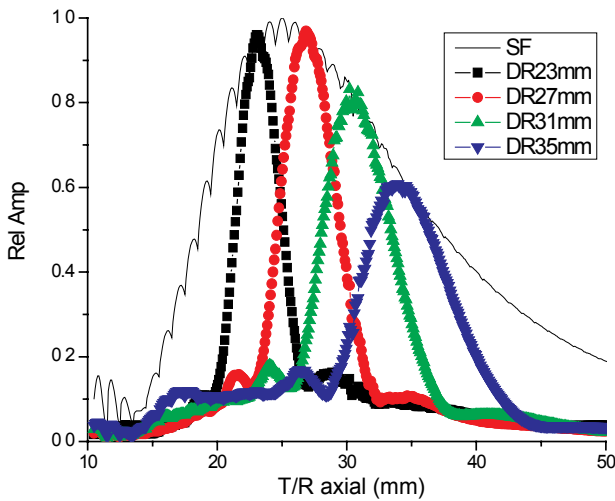
Figure 2. Axial beam simulations of several DR cases compared to the SF case. The four DR cases represent transmit foci at 23, 27, 31, and 35 mm with 41 receive focal zones. The DR cases overlap the SF case at the transmit foci.

3.2   *Ex Vivo* Scans

To demonstrate the different beamforming strategies in practical terms, a human eye-bank eye was scanned. Data from all transmit-to-receive pairs were acquired at a sampling rate of 200 MHz (8-bit samples). Each scan line

had 7500 points, 271 scan lines were acquired, and the scan lines were separated by 100 μm. The data were then post processed using each beamforming strategy. The FF case (Fig. 3a) simulated a single-element transducer and represented the lowest image quality, as expected from the simulation results. The DR case (Fig. 3b) showed a moderate improvement in image quality versus the FF case and the background noise was reduced. The best image quality was from the SF case with 41 focal zones (Fig. 3c). For this case, the whole globe was resolved, the noise was low, and the anterior and posterior features were clearly revealed. The image quality of the *ex vivo* results mirror what was found from the theoretical simulations.
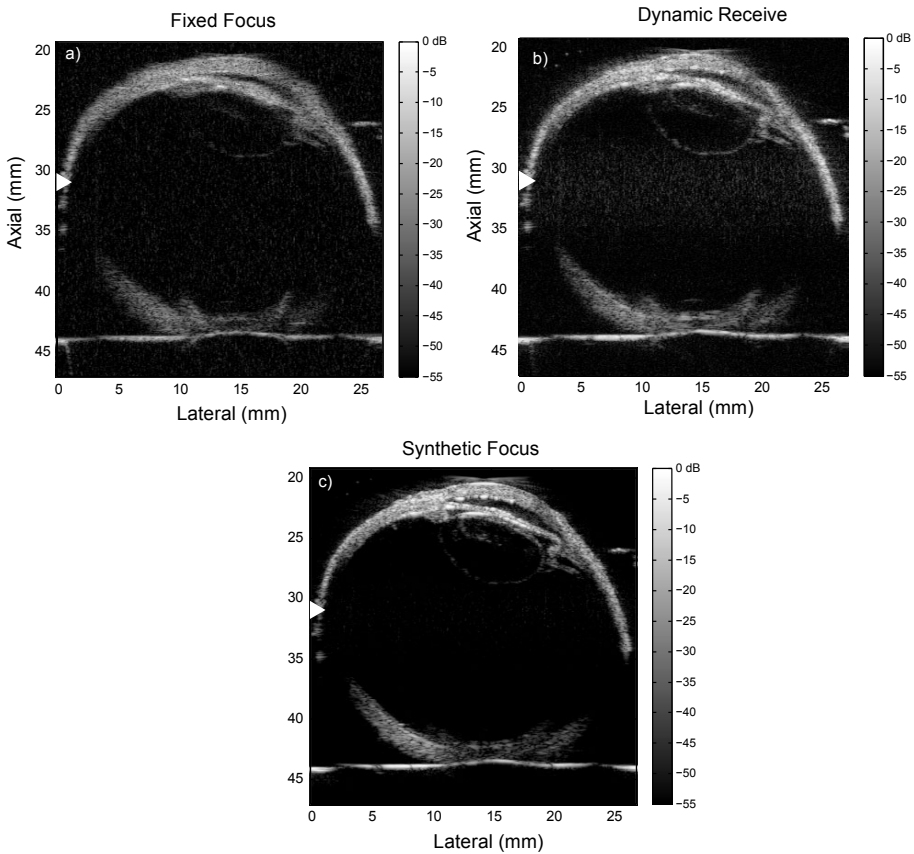
Figure 3. Ex vivo scans of a human eye-bank eye showing the case of (**a**) fixed focusing, (**b**) dynamic-receive focusing with transmit focus at 31 mm and 41 receive focal zones, and (**c**) synthetic focusing with 41 focal zones. The white triangle indicates the location of the geometric focus.

4.   CONCLUSIONS

Numerical beam simulations were performed for a five-ring, 17-MHz annular array using three beamforming strategies: fixed focusing, dynamic-receive focusing, and synthetic focusing. The results showed that synthetic focusing resulted in the best image quality in terms of DOF and lateral resolution. Dynamic-receive focusing led to a moderate improvement in DOF and lateral resolution compared to fixed focusing. When the imaging strategies were applied to data from a human eye-bank eye, the images showed a similar trend to the simulations: synthetic focusing led to the best image quality and dynamic-receive focusing improved upon fixed focusing. We conclude that dynamic-receive focusing is a viable means to speed up data acquisition and image processing while improving image quality, but synthetic focusing will lead to the best ultimate image quality.

ACKNOWLEDGEMENTS

REFERENCES

1. J. M. Cannata, J. A. Williams, Q. Zhou, T. A. Ritter and K. K. Shung, "Development of a 35-MHz Piezo-Composite ultrasound array for medical imaging," *IEEE Trans. Ultrason. Ferroelect. Freq. Contr.* **53**, 224–236 (2006).
2. R. H. Silverman, J. A. Ketterling and D. J. Coleman, "High-frequency ultrasonic imaging of the anterior segment using an annular array transducer," *Ophthalmology* **114**, 816–822 (2007).
3. O. Aristizábal, J. A. Ketterling and D. H. Turnbull, "40-MHz annular array imaging of mouse embryos," *Ultrasound Med. Biol.* **32**, 1631–1637 (2006).
4. J. A. Ketterling, S. Ramachandran and O. Aristizábal, "Operational verification of a 40-MHz annular array transducer," *IEEE Trans. Ultrason. Ferroelect. Freq. Contr.* **53**, 623–630 (2006).
5. J. A. Ketterling, O. Aristizábal, D. H. Turnbull, and F. L. Lizzi, "Design and fabrication of a 40-MHz annular array transducer," *IEEE Trans. Ultrason. Ferroelect. Freq. Contr.* **52**, 672–681 (2005).
6. M. Arditi, F. S. Foster and J. W. Hunt, "Transient fields of concave annular arrays," *Ultrason. Imaging* **3**, 37–61 (1981).

FULLY FIBER OPTIC ULTRASONIC PROBES FOR VIRTUAL BIOPSY

E. Biagi, S. Cerbai, P. Gambacciani, L. Masotti
Laboratory of Ultrasound and Non Destructive Testing, Department of Electronics and Telecommunications, University of Florence, Via S. Marta 3, 50139 Florence, Italy

Abstract: The proposed probe consists of two optical fibers: one generating ultrasounds by opto-acoustic conversion, the second one, based on acousto-optic effect, used to detect ultrasounds. The intrinsic high frequency and wide bandwidth associated both to the opto-acoustic source and to the interferometric acousto-optic element could open a way towards a "virtual biopsy". "Virtual biopsy" is perspective to provide the physicians the possibility of studying the nature and health condition of small portions of living tissue "in situ" by using ultrasounds[1].

Key words: Opto-acoustic, Acousto-optic, Fiber optic transducer, Virtual biopsy, Ultrasound

1.   INTRODUCTION

The present state of art for opto-acoustic and acousto-optic device technology lets us foresee the possibility of realizing a miniaturized transducer able to treat wide band ultrasounds. The idea is to use Thermo-elastic Ultrasound Generation (TUG) [2–6], in conjunction with fiber-based interferometric receiver [7].

Our group proposed the design and realization of an ultrasonic source based on opto-acoustic effect in 1996, with a metal layer over the fiber optic tip as absorbing target [2,3]. In 2001 we improved the opto-acoustic conversion by replacing the metal absorbing target with a graphite one [5,6]. Two years later, in 2003, we proposed a complete opto-acoustic and acousto-optic setup for a fully fiber optic ultrasonic probe [6,7]. Today we present our technological achievements in the development of the all fiber optic

probe and the first images of simple test objects, obtained with a complete opto-acoustic setup.

The transmitting element, depicted on the left in Fig. 1, is constituted by a fiber optic on whose tip an absorbing layer is deposed; TUG takes place when the laser pulse hits this absorbing thin layer and the induced thermal expansion generates a mechanical shock wave. In order to improve the efficiency of TUG in thin films, it appears reasonable to replace the metallic film with a layer exhibiting higher optical absorption, lower reflectivity and good thermal properties. The innovation that we have introduced in this field made it possible to increase the opto-acoustic conversion efficiency of about two order of magnitude. Layers made with crystalline graphite or by using graphite powder mixed with epoxy resin are proposed and demonstrated to be suited for generating large-bandwidth ultrasonic pulses with high efficiency [4,5].
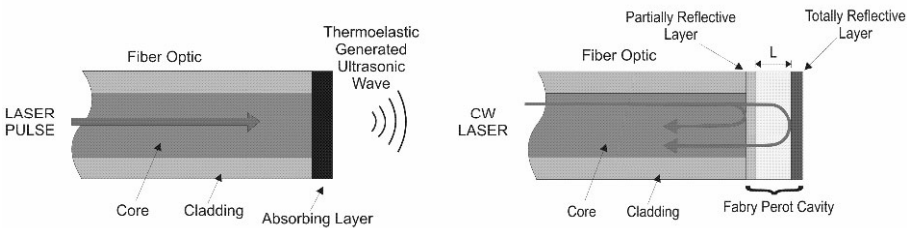
Figure 1. On the *left*: fiber optic ultrasonic source based on opto-acoustic conversion. On the *right*: fiber optic ultrasonic receiver based on acousto-optic conversion.
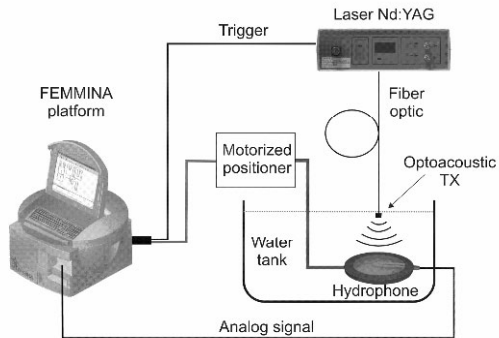
Figure 2. Experimental setup for TUG. The characterization of the opto-acoustic source is performed by means of a PVDF membrane hydrophone (Marconi 699/1/00002/200). A FEMMINA system is used both to acquire data and to manage hardware control and synchronization.

The receiving element is constituted by an extrinsic fiber hydrophone, based on a Fabry-Perot interferometer, as depicted on the right in Fig. 1. A continuous wave laser beam is launched inside a fiber. The device works as follows: a pressure wave, impinging over the interferometer, modulates its thickness. This change in thickness produces a modification in the interferometer reflectance, defined as the ratio between the reflected and incident light power, and thus induces a change in the light intensity detected by a photodiode.

2.   OPTO-ACOUSTIC SOURCE

Large bandwidth ultrasound generation is obtained by means of TUG generation, that takes place when a laser pulse hits the optical absorbing layer deposed over the fiber tip [2–6].

In Fig. 2, a typical setup used for opto-acoustic ultrasound generation is shown. A FEMMINA (Fast Echographic Multi parameters Multi Image Novel Apparatus) system [8] is used both to acquire data and to manage hardware control and synchronization. FEMMINA is a hardware/software platform devoted to acquire, analyze and visualize, in real time, data produced at the same time from different sources or algorithms. A large bandwidth and high frequency analog board, inserted in FEMMINA hardware, is used to acquire the signal received by a PVDF membrane ultrasonic hydrophone (Marconi 699/1/00002/200). A second digital board in FEMMINA is used to produce synchronization between laser pulse triggering, transducer motion control and analog acquisition.

A Q-switch 1064 nm Nd:YAG laser (LaserTech LCS-DTL-122QT) is used to feed an optic fiber on whose tip an adsorbing layer, based on a mixture of graphite powder and epoxy resin, is deposed.

Different graphite powder concentrations and absorbing layer thicknesses were tested [5]; the results are shown in Fig. 3. These results highlight that an efficient source of ultrasound can be obtained by coupling a fiber optic to a low-power pulsed laser, if a graphite or graphite compound layer capable of absorbing laser light is mounted at the fiber end [5,7]. The highest efficiency can he obtained by using a layer with small thickness and high graphite concentration.
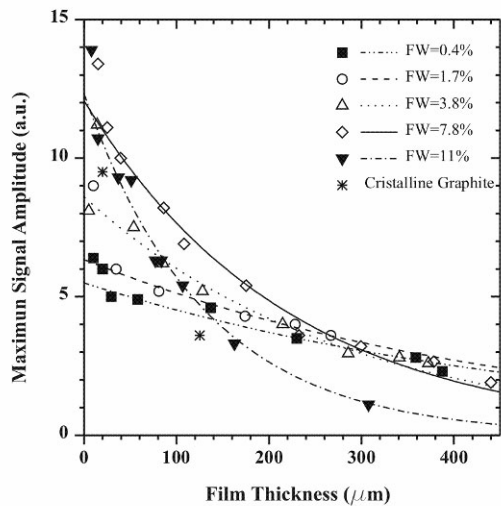
Figure 3. Peak-to-peak maximum amplitude of radio frequency signal versus sample thickness (μm) detected for different graphite powder concentration (FW, Fractional Weight) and for two crystalline graphite samples. For each FW value, the curves are plotted following an exponential decaying law.
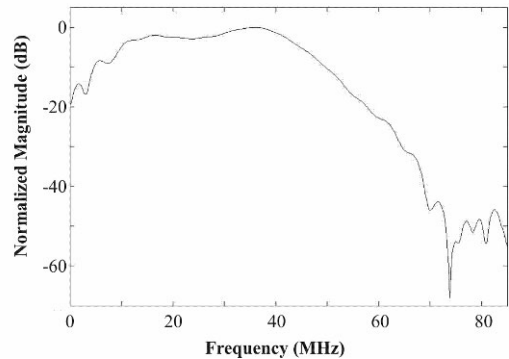
Figure 4. High frequency portion of normalized spectra for ultrasonic signals obtained with samples having FW=3.8% and different thickness.

In Fig. 4 a frequency spectrum of the generated ultrasound is shown, obtained by using an absorbing layer thickness of about 20 μm deposed over the tip of a 600 μm core quartz fiber, a laser pulse energy of 13 μJ and 8 ns laser pulse duration. The energy of the pulse at the tip of the fiber is estimated to be about 10 μJ. Pressure pulses with amplitude up to 150 kPa and bandwidth extending over 50 MHz have been generated.

3.   ACOUSTO-OPTIC RECEIVER

Large bandwidth ultrasound detection is performed by means of an interferometer on the tip of a fiber optic. Ultrasound impinges on the cavity of the interferometer, varying its thickness and modifying the cavity optical response. The interferometric cavity, placed on the tip of a monomodal fiber optic, is constituted by two metallic mirrors (respectively with reflectance of 30% and 95%), separated by a 23 µm polymer spacer. In Fig. 5 the spectrum received by the interferometric transducer is compared to the one received by a PVDF hydrophone (Marconi 699/1/00002/200). The experimental setup is composed by a 20 MHz Panametric probe as ultrasonic source both for fiber receiver and for the hydrophone. A 0.5 mW CW tunable laser (Santec TSL-210H) and a photodiode are employed to detect the cavity thickness variation. As it can be observed, the spectra of the two received signals are pretty similar.
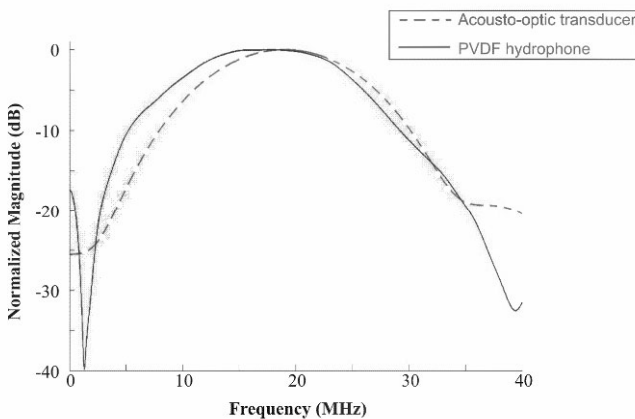
Figure 5. Experimental comparison between the spectra collected by interferometric receiver and a PVDF membrane hydrophone by using a single element 20 MHz ultrasonic probe as transmitting element for both the receivers.

4.   CONCLUSIONS

By concluding, we report the first image obtained with the proposed fiber optic ultrasonic probe. On the left of Fig. 6, the employed experimental setup is reported; the transmitting and receiving fiber optic elements operate in a classical echo technique. The test object is constituted by a 50 euro cents coin. The image reported on the right of Fig. 6 is obtained by time of flight technique elaboration; the test object was fixed on the three axis positioner arm.
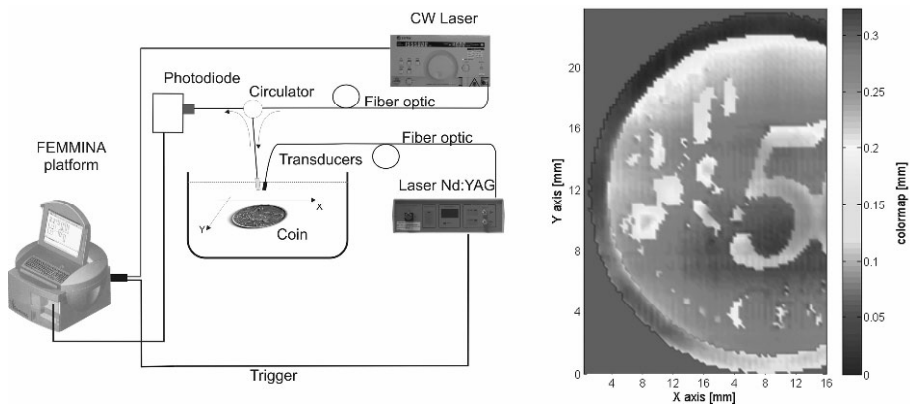
Figure 6. On the *left*: experimental setup for producing images by employing the proposed fully fiber optic ultrasonic transducer. On the *right*: ultrasonic image of a 50 euro cents coin.

REFERENCES

1. E. Biagi, L. Breschi, S. Granchi, and L. Masotti, Method and device for spectral analysis of an echographic signal, *U.S. Patent* **10/383674**, (2003).
2. E. Biagi, S. Fontani, F. Francini, L. Masotti, and M. Pieraccini, Photoacoustic generation all-fiber optic transducers, *Proc of Ultrasonic Symp.* **2**, 921–924 (1996).
3. E. Biagi, M. Brenci, S. Fontani, and L. Masotti, Photoacoustic generation: optical fiber ultrasonic sources for NDE and clinical diagnosis, *Optical Review* **4**, 481–483 (1997).
4. D. Menichelli and E. Biagi, Optoacoustic sources: practical Green function-base model for thin film laser-ultrasound generation, *J. Opt. A: Pure Appl. Opt.* **3**, S23–S29 (2001).
5. E. Biagi, F. Margheri, and D. Menichelli, Efficient laser-ultrasound generation by using heavily absorbing films as targets, *IEEE Trans. Ultrason. Ferroelect. Freq. Contr.* **48**(6), 1669–1680 (2001).
6. L. Masotti, E. Biagi, F. Margheri, and D. Menichelli, Opto-acoustic generator of ultrasound waves from laser energy supplied via optical fiber, *U.S. Patent* **6,519,376 B2**, (2003).
7. A. Acquafresca, E. Biagi, L. Masotti, and D. Menichelli, Towards virtual biopsy through an all fiber optic ultrasonic miniaturized transducer: a proposal, *IEEE Trans. Ultrason. Ferroelect. Freq. Contr.* **50**(10), 1325–1335 (2003)
8. L. Masotti, E. Biagi, M. Scabia, A. Acquafresca, R. Facchini, A. Ricci, and D. Bini, FEMMINA Real-Time Radio-Frequency Echo-Signal Equipment for Testing Novel Investigation Method, *IEEE Trans. Ultrason. Ferroelect. Freq. Contr.* **53**(10), 1783–1795 (2006).

HIGH RESOLUTION ULTRASONIC METHOD FOR 3D FINGERPRINT REPRESENTATION IN BIOMETRICS

R.Gr. Maev, E.Y. Bakulin, E.Y. Maeva, F.M. Severin
Center for Imaging Research and Advanced Material Characterization, Faculty of Science, University of Windsor, Windsor, Ontario, Canada

Abstract: Biometrics is an important field which studies different possible ways of personal identification. Among a number of existing biometric techniques fingerprint recognition stands alone – because very large database of fingerprints has already been acquired. Also, fingerprints are an important evidence that can be collected at a crime scene. Therefore, of all automated biometric techniques, especially in the field of law enforcement, fingerprint identification seems to be the most promising. Ultrasonic method of fingerprint imaging was originally introduced over a decade as the mapping of the reflection coefficient at the interface between the finger and a covering plate and has shown very good reliability and free from imperfections of previous two methods. This work introduces a newer development of the ultrasonic fingerprint imaging, focusing on the imaging of the *internal* structures of fingerprints (including sweat pores) with raw acoustic resolution of about 500 dpi (0.05 mm) using a scanning acoustic microscope to obtain images and acoustic data in the form of 3D data array. C-scans from different depths inside the fingerprint area of fingers of several volunteers were obtained and showed good contrast of ridges-and-valleys patterns and practically exact correspondence to the standard ink-and-paper prints of the same areas. Important feature reveled on the acoustic images was the clear appearance of the sweat pores, which could provide additional means of identification.

Key words: Fingerprint, Biometrics, Ultrasound, Acoustic imaging

1.   INTRODUCTION

Biometrics is currently a rapidly evolving scientific and applied discipline [1], which studies different possible ways of personal identification by

means of certain unique biological characteristics of each individual. Such identification is very important in various situations requiring restricted access to certain areas, information, personal data, and in case of some medical emergencies. A number of automated biometric techniques have been developed [2], including fingerprint, hand shape, eye and facial recognition, thermographic imaging, etc. All these techniques differ in the recognizable parameters, enrollability, usability, accuracy and cost. Among others, fingerprint recognition stands alone – because very large database of fingerprints has already been acquired (for historical reasons). Also, fingerprints are usually the main evidence left at a crime scene and can be used to track down criminals. Therefore, of all automated biometric techniques, especially in the field of law enforcement, fingerprint identification seems to be the most promising.

By now, there exist three main methods of fingerprint acquisition. The first is the old ink-and-paper method, which is slow, inconvenient and is subject to frequently happening imperfections in the process. The second is the optical method, in which ridges and valleys are recognized by the change of critical angle of refraction between the glass-skin (ridges) and the glass-air (valleys) interfaces [3]. Its main and significant drawback is that it is very sensitive to the surface contaminations, such as stain, dirt, oil, or skin wornness. The third, and the most recently developed, is the ultrasonic method [4–6]. Originally it was introduced as the mapping of the reflection coefficient at the interface between the finger and a plate and has shown very good reliability and free from imperfections of previous two methods.

In this paper, a newer development of the ultrasonic fingerprint imaging is introduced, focusing on the imaging of the *internal* structures of fingerprints (including sweat pores) with raw acoustic resolution of about 500 dpi (50 μm) using a scanning acoustic microscope to obtain images and acoustic data in the form of 3D data array.

2.   MATERIALS AND METHODS

The experimental setup is shown in Fig. 1. A special adjustable fixture for holding fingers in place was made, which incorporates a bed for a finger and a polystyrene cover plate (thickness 2.5 mm). Fingers of volunteers were placed in the fixture with the polystyrene plate pressed onto the top of the finger, and the fixture was submerged in water to provide coupling with acoustic lens. Acoustic gel was used between the plate and finger for better acoustic contact.
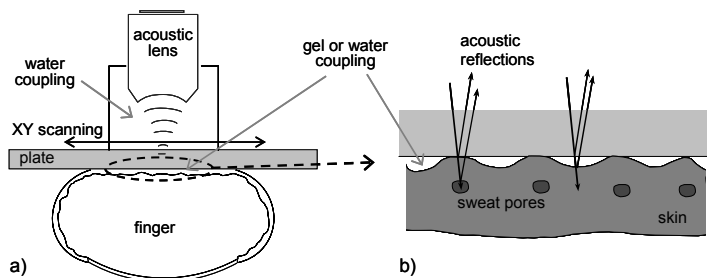
Figure 1. Schematic representation of the experimental setup: (**a**) positioning of a finger and acoustic lens; (**b**) principal structure of skin in the fingerprint area and corresponding acoustic reflections.

To acquire acoustic images (B- and C-scans), two scanning acoustic microscopes were used: "Tessonics AM-1103" (Tessonics Corp., Birmingham, MI, USA) and "Sonix HS-1000" (Sonix Inc., Springfield, VA, USA), both working in short-pulse mode and using a narrow-aperture focused ultrasonic transducers with water coupling.

To test the image resolution in relation to the ultrasonic frequency, these acoustic microscopes were used in conjunction with several acoustic lenses in the range of working frequencies from 25 to 100 MHz. Series of scans of a fingerprint were performed using the acoustic microscopes and different acoustic lenses (various frequencies from 15 MHz up to 100 MHz with different apertures) and it was found that the requirements for raw image resolution (~500 dpi – to be comparable with standard ink-and-paper fingerprint images) are satisfied with the lenses with working frequencies of 50 MHz or higher. However, no significant improvements in the image quality were found – probably due to the fact that higher working frequency of the lens results in higher attenuation and higher sensitivity to the finger's surface irregularities. Thus, it was concluded that the use of 50 MHz lens would be the most reasonable. For this reason, all further experimentation was continued using the 50 MHz acoustic lens.

In the main series of experiments, acoustic scans of several fingerprints of several volunteers (three males of 19, 27, 44 yrs. and two females of 19 and 38 yrs.) were performed with acoustic microscopes "Tessonics" and "Sonix" and data cubes were collected with the following parameters: frequency – 50 MHz (raw acoustic resolution about 50 µm, or 500 dpi); scanning step – 20 or 25 µm (corresponding pixel resolution of 1250 or 1000 dpi); field of scanning – 10×5 mm or 10×10 mm; depth of scanning (time length of A-scans, or penetration inside the skin) – about 0.5–1 µs (approx. 0.4–0.8 mm); lens was focused at the sweat pores.

The software of the used SAMs allows acquisition of 3-dimensional data array of reflected acoustic signal during scanning – A-scans are saved at

each point of XY plane. The internal software of the "Tessonics" SAM and the external application of the "Sonix" SAM allow well-adjustable manipulation of the saved 3D data array of acoustic data. This technique allowed us to only once obtain a scan and then vary the C-scan gate position and width to visualize acoustic reflections from any appropriate depth inside the skin. Also, B-scans and A-scans can be recreated from any position using such data array, giving the total control over visualization options.

For comparison purposes, fingerprints of all fingers scanned with acoustic microscopes were also acquired using a standard ink-and-paper method.

3.   RESULTS

Examples of raw acoustic images of a fingerprint, obtained in the manner described above are shown in Fig. 2. One can clearly see the valleys on the C-scan from under the plate (Fig. 2a). Such image can be inverted to create an image of ridges similar to ones obtained using previously mentioned fingerprint techniques, therefore providing direct connection and comparison with existing databases.

By setting the C-scan gate deeper inside the skin, distribution of the sweat pores (which are located along the ridges) can be easily visualized (Fig. 2b). Given that this distribution should be unique for each individual, this provides additional means of personal identification which is not affected by any changes (accidental or intentional) of the fingers' surface conditions.
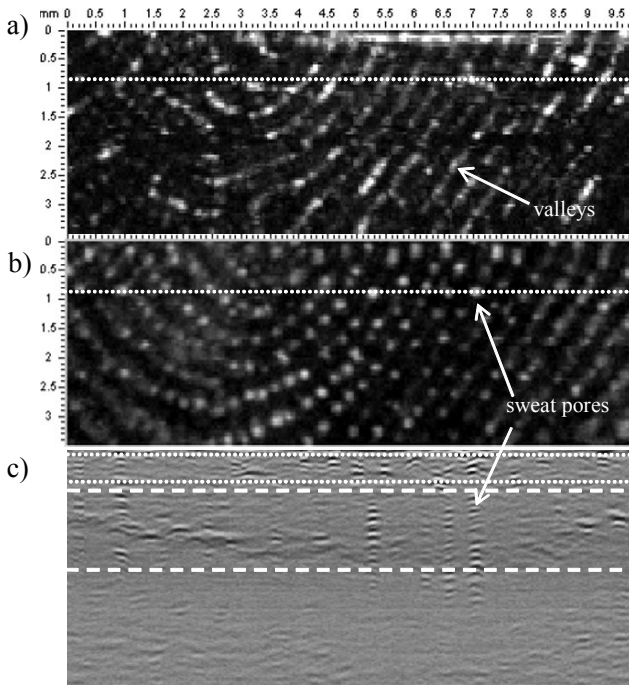
Figure 2. Raw acoustic images of a fingerprint area (50 MHz): (**a**) C-scan with time gate set just under the plate to visualize the valleys (time gate shown by *dotted lines* in B-scan); (**b**) C-scan deeper in side the skin, Showing reflections from the wet pores (time gate shown by *dashed lines* in B-scan); (**c**) B-scan (position shown by *dotted lines* on C-scans).

All acoustic images of fingerprints were compared to the ink-and-paper prints and very good correspondence was found practically in all cases. An example of such comparison is given in Fig. 3.

It is clearly seen that the groove lines on the C-scan exactly repeat the ones on the paper print. Therefore, possibly with aid of some image processing software, internal acoustic images of fingerprints can be used for biometric purposes just as easy as ink-and-paper prints.

Very important additional feature of these internal acoustic images is that they contain information about the distribution of the sweat pores, which can be extracted from the internal acoustic images and is not affected by the conditions on the surface of the finger (such as dirt, grease, scratches, etc.).
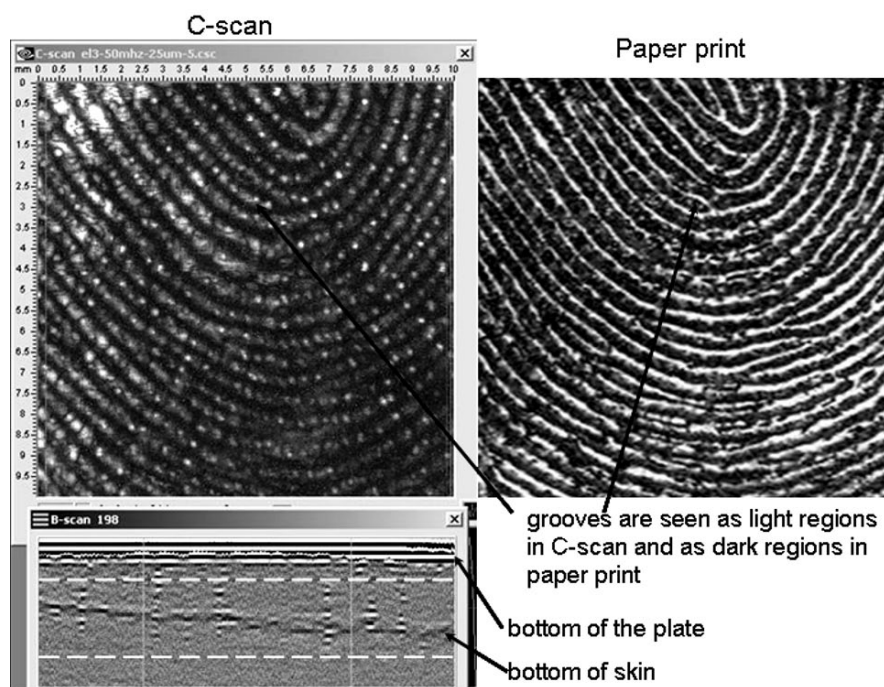
Figure 3. Comparison between acoustic (*left*) and ink-and-paper (*right*) images of the same area of the same finger. Position and width of C-scan gate are displayed by *horizontal dashed lines* on the B-scan. Lateral dimensions are shown along C-scan in mm.

4.   CONCLUSION

In this work, ultrasonic method of internal fingerprint imaging has been successfully applied using a scanning acoustic microscope working at a frequency of 50 MHz. High-resolution 3D data arrays and acoustic images of internal structures of fingerprints were obtained (acoustical resolution of 500 dpi and scanning pixel resolution of 1000 dpi) and compared with ink-and-paper prints.

Acoustic images obtained from inside the skin reveal high contrast of "groves and valleys" patterns, which are equivalent to ink-and-paper images and therefore can be connected to the existing databases. Also, the sweat pores are clearly seen in acoustic images, which provides additional valuable data for identification purposes. No sensitivity of the method to the surface contamination (such as paint, oil, dirt, etc.) has been found.

The results clearly show the advantages of the internal acoustic imaging of the fingerprints over surface-only fingerprint imaging techniques for the biometric identification purposes.

ACKNOWLEDGEMENTS

REFERENCES

1. Biometric Boom, IEEE Spectrum Magazine, March 2004, p. 13.
2. K. Millard, "Developments on Automatic Fingerprint Recognition", Proc. Int. Carnahan Conference on Security Technology, (1983), pp. 173–178.
3. C.M. Paralusz, "Internal Reflection Spectroscopy", ASTM Standardization News, February 1985, pp. 42–46.
4. J.K. Schneider, "Surface Feature Mapping Using High Resolution C-Scan Ultrasonography", Ph.D. Dissertation, State University of New York at Buffalo, Electrical and Computer Engineering Dept., 1990.
5. R.M. Schmitt, W.G. Scott, R.D. Irving, et al., IEEE Ultrasonics Symposium, 2004 pp. 680–688.
6. www.ultra-scan.com.

OPTOACOUSTIC IMAGING

M. Frenz, M. Jaeger, A. Gertsch, M. Kitz, D. Schweizer
Institute of Applied Physics, University of Bern, Switzerland; Fukuda Denshi Switzerland AG, Basel

Abstract: A medical ultrasound system was combined with a pulsed laser source to allow optoacoustic imaging. Whereas ultrasound imaging is based on reflection and scattering of an incident acoustic pulse at internal structures, optoacoustics probes optical properties and therefore provides much higher contrast and complementary information. Targeting structures to a depth of a few centimeters, optoacoustics supplies superior contrast and higher spatial resolution compared to conventional ultrasound. The two complementary methods combined in one single device are ideally suited for medical diagnostics.

Key words: Ultrasound, Laser-induced ultrasonography, Medical diagnostics, Doppler

1.   INTRODUCTION

The medical need for high quality diagnostic images has motivated research on biomedical optoacoustic imaging, a technique which combines the merits and most compelling features of ultrasound and optics. Optical techniques have by virtue of pronounced differences in optical properties high contrast in common. The intrinsic optical contrast of blood and surrounding tissue, for example, is very high in the visible or near infrared range [1]. Pure optical methods are, however, limited by scattering to either millimeter imaging depths (optical coherence tomography) or to poor resolution in the centimeter range for deeper imaging (optical tomography). Apart from providing magnitudes higher contrast, optical methods have the advantage of probing wavelength dependent features, such as blood oxygenation allowing functional imaging [2].

Optoacoustics, as hybrid method provides the optical contrast without the handicap of poor resolution [3]. The image contrast is given by light

absorbing chromophores either endogenous such as oxy- or deoxy-hemo-globin or exogenous e.g. dyes, nanoparticles or quantum dots [4]. The image resolution, as well as the maximum imaging depth, depends on the band-width of the pressure transducer used within the reach of diffuse photons. As the ultrasound frequency and bandwidth is increased, the spatial resolution improves at the expense of maximum imaging depth.

The laser-induced ultrasound transients propagate to the tissue surface and are detected by an acoustic transducer. One-dimensional optoacoustic signals contain quantitative information on optical tissue properties [5]. The time delay between laser pulse and detected pressure transient, its amplitude and temporal profile provide information about location, strength and spatial dimension of the acoustic source. Since most parts of the human body are not accessible from two sides (forward mode), laser illumination and acoustic sensing is done from the same surface (backward mode) [6–8].

Optoacoustic techniques have already been used to visualize breast cancer due to an increased angiogenesis. The increased blood content supplying its aggressive growth provides a native contrast for optoacoustic imaging [9,10]. Detection of early stage tumors in the sub-millimeter range when angiogenesis is not yet established makes a labeling with antibody-gold nanoparticle conjugates necessary. The use of gold nanoparticles together with antibodies makes optoacoustic imaging highly sensitive and selective. In addition, the selectively bound particles can be used for thermal therapy [11,12].

For real-time imaging both, the data recording using an ultrasound trans-ducer as well as the image reconstruction must be fast [13,14]. Besides piezoelectric ultrasound transducers, optical transducers, which measure the pressure-induced changes of index of refraction, are used. This can be realized by either using a Fabry Perot, a prism or a pressure transducer based on Schlieren imaging techniques [15–19].

To move optoacoustic imaging closer to the clinic, we combine opto-acoustic imaging with conventional ultrasound to simultaneously provide complementary information obtained from both techniques [17].

2.   INITIAL PRESSURE DISTRIBUTION

Irradiation of tissue with pulsed laser light gives rise to heat deposition, when part of the optical energy gets absorbed by a tissue structure. If the laser excitation fulfills the condition of stress confinement, a local pressure rise $p_o(\vec{x})$ is generated (thermoelastic effect).

The local value $p_0(\vec{x})$ [Pa] of this pressure at a position $\vec{x}$ is determined by the local absorbed energy density $u(\vec{x})$ [J/cm^3]. The relation between

absorbed energy density and pressure amplitude is linear for moderate densities u and is generally written as [20–22]:

$$p_o(\vec{x}) = \Gamma \cdot u(\vec{x}) \tag{1}$$

Γ [Pa cm^3/J] denotes the Grüneisenparameter, which depends on thermodynamic tissue properties, and on temperature (for water: at 20°C: Γ=0.12 Pa cm^3/J; at 37°C: Γ=0.19 Pa cm^3/J).

$$\Gamma = \frac{\beta}{\kappa \rho c_V} = \frac{\beta v_{sound}^2}{c_P} \quad \text{with} \quad \kappa = \frac{c_P}{c_V \cdot \rho \cdot v_{sound}^2} \tag{2}$$

β denotes the thermal coefficient of volume expansion [°C^{-1}], ρ = density [kg/m^3] and c_v and c_p = specific heat capacity [J/kg°C] at constant volume and pressure, respectively, v_{sound} denotes the speed of sound and κ = isothermal compressibility [Pa^{-1}].

The local density of heat deposition $u(\vec{x})$ is determined by the local laser fluence $H(\vec{x})$ [J/cm^2] and by the local absorption coefficient $\mu_{abs}(\vec{x})$ [cm^{-1}]:

$$u(\vec{x}) = \mu_{abs}(\vec{x}) \cdot H(\vec{x}) \tag{3}$$

Whereas optical properties are often assumed constant, the fluence is a strongly varying function of position, determined by both optical scattering and absorption. Models for light propagation are used in order to estimate H, or directly the product of H and μ_{abs}.

In an acoustically homogeneous medium, the scalar wave equation can be written as:

$$\Delta p(\vec{x},t) - \frac{1}{v_{sound}^2}\frac{d^2}{dt^2}p(\vec{x},t) = 0 \quad \text{with} \quad p(\vec{x},t=0) = p_o(\vec{x}) \tag{4}$$

The solution of the wave equation to the initial value is derived from a Poisson integral [21]:

$$p(\vec{x},t) = \frac{1}{4\pi v_{sound}^2} \cdot \frac{d}{dt} \int_{|\mathbf{x}-\mathbf{x'}|=ct} d\sigma \frac{p_0(\vec{x}')}{t} \tag{5}$$

The temporal profile of the pressure $p(\vec{x}, t)$ [Pa] detected at the surface by a linear ultrasound transducer leads to a signal $s(t)$ at the output of the acoustic transducer.

$$s(t) = \int_{-\infty}^{t} dt' \, p(\vec{\mathbf{x}}, t') \cdot h(t - t') \qquad (6)$$

$h(t)$ is the impulse response of the transducer to a Dirac delta impulse. The integral in Eq. (6) expresses that the signal output at a time t depends not only on the pressure input at time t, but also on the pressure measured at times $t' < t$.

3.   IMAGE RECONSTRUCTION

Detection of optoacoustic transients can be looked at as a transformation, where the originally generated spatial pressure distribution $p_0(\vec{x})$ is transformed to the signal $S(n_r, n_t)$, sampled at various points (indexed n_r) and at various times (indexed n_t). In the case of a linear array transducer, the element positions may be considered located on a Cartesian grid at positions $\vec{x}' = (n_r \cdot \Delta x, 0, 0)$, with the element pitch Δx. Considering linear sound propagation (in the case of small pressure amplitudes), the formation of the signal S can be described as a linear transformation $\mathbf{M}$ in terms of matrix multiplication:

$$S = \mathbf{M} \cdot P \qquad (7)$$

Thereby, P is a quantity correlated to p_0, but whereas p_0 is continuous and three-dimensional, P is sampled on a discrete 2D grid. The aim of reconstruction is to bring the resulting image J as close as possible to P. This is mathematically expressed by an approximate inverse $\mathbf{Minv}$. The formation of the image J corresponds to:

$$J = \mathbf{Minv} \cdot S = \mathbf{Minv} \cdot \mathbf{M} \cdot P \cong \mathbf{I} \cdot P = P \qquad (8)$$

The most frequently used methods to reconstruct optoacoustic images from acquired signals are backprojection and Fast Fourier transformation (FFT) [14,23–28]. In FFT, both the signal formation Eq. (7) and the inverse problem Eq. (8) are expressed in the frequency domain, and Eq. (8) is solved under regularizing constraints. The result is an algorithm where the

amplitudes $J_{\mathbf{k}}$ of an image Fourier component are interpolated from the amplitudes $S_{\mathbf{k}*}$ of the signal Fourier components using:

$$P_{\mathbf{k}=(k_x,k_z)} \equiv \frac{k_z}{k_t} \cdot \sum_{k_t^*} \left[\frac{1-\exp\left[-i\left(k_t - k_t^*\right)T\right]}{i\left(k_t - k_t^*\right)T} \cdot S_{\mathbf{k}*=(k_x,k_y,k_t^*)} \right]$$

$$k_t = -v_{sound} \cdot \sqrt{k_x^2 + k_y^2 + k_z^2}$$

(9)

(T: length [s] of acquisition time interval; **k**: wave vector in the image frequency domain; **k***: wave vector in the signal frequency domain)

A truncated version of the sum in Eq. (9), including only the most significant weights, is used in practice. In that way, the calculation time is governed by the FFT, which is $o(N \log_2 N)$. Such Fourier algorithm is very fast, compared to backprojection algorithms, which are at least $o(N^{4/3})$. Because of the limited length of a linear array transducer, **M** can not be exactly inverted and J is only an approximate reconstruction of P, leading to image artifacts.

4. MATERIALS AND METHODS

All ultrasound images were taken with a Sigma 5000 IMAGIC medical ultrasound system (Fukuda Denshi Switzerland AG, Basel). The Sigma 5000 includes B-Mode imaging and color Doppler mode. We used a 128 element array transducer with a total width of 38.4 mm and pitch of 0.3 mm. The transducer had a –6dB bandwidth of 5.25–9.75 MHz (central frequency of 7.5 MHz). The Sigma 5000 allows time gain compensation (TGC) and dynamic focusing with a digital beam-forming stage during recording of the ultrasonic signals. The soft- and hardware of the Sigma 5000 was adapted to alternately obtain ultrasound and optoacoustic images.

The optoacoustic excitation was performed with a Nd:YAG laser at $\lambda = 1064$ nm and a repetition rate of 10 Hz. The laser pulses ($\tau = 15$ ns) were coupled into a single fiber bundle, which was split into two arms with profile converters to homogeneously irradiate an area of 20×5 mm on both sides of the pressure transducer. The laser pulse energy was chosen to comply with the laser safety limits for maximum permissible skin exposure of 20 mJ/cm^2.

To validate the experimental setup we imaged a human finger tip using conventional US-Doppler and optoacoustic imaging.

5.   RESULTS AND DISCUSSION

Figure 1 shows two pictures of an A scan of a human finger tip taken with the Doppler US and the optoacoustic system. Due to their small size the blood capillaries can not be imaged by the Doppler ultrasound mode, only the echo signal from the bone is predominant. In contrast, the optoacoustic image shows the small blood vessels with high contrast. This clearly reveals the complementary information given by the two techniques.
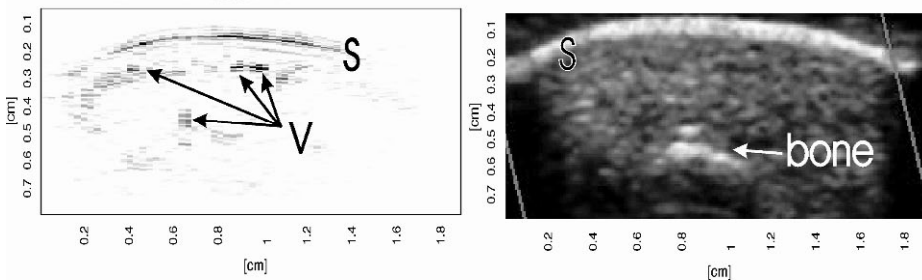
Figure 1. In-vivo optoacoustic image (*left*) and ultrasound image (*right*) of a human finger tip (palm towards transducer, s = skin surface). About 1 mm below the skin dorsal digital arteries or veins (v) are visible. These vessels can not be seen on the corresponding Doppler ultrasound image. The complete optoacoustic image was acquired in real-time with one single laser pulse.

The two imaging methods target on different imaging depths and tissue structures. The main advantages of the optoacoustic imaging are enhanced visibility of small blood vessels and functional imaging based on optical absorption. In optoacoustics, the strong optical absorption of the blood itself generates the ultrasound waves. In addition, exogenous optical contrast agents, such as selectively binding antibodies conjugated with absorbing nano-particles can be used to further enhance for example the contrast of cancerous tissue [29]. Optoacoustic imaging is a safe method, when irradiation is kept below the maximum permissible exposure level for skin. The combined ultrasound and optoacoustic imaging technique provides an optimum complementary set of information ideally suited for medical diagnostics.

6.   CONCLUSION

Optoacoustic imaging provides high contrast functional imaging on a conventional ultrasound device. Targeting on the centimeter range, opto-acoustic imaging is predestined to extend the capabilities of conventional ultrasound devices for small blood vessel monitoring. The combination of

the two complementary methods in one single device could create a new generation of high contrast online imaging diagnostic tools.

ACKNOWLEDGEMENTS

REFERENCES

1. A. J. Welch and M. J. C. van Germert, Optical-thermal response of laser-irradiated tissue, Plenum Press, New York and London, 1995.
2. M. Wolf, M. A. Franceschini, L. A. Opaunescu, V. Toronov, A. Michalos, U. Wolf, E. Gratton and S. Fantini, Absolute frequency-domain pulse oxymetry of brain: Methodology and measurements, Advances in Experimental Medicine and Biology 530 (2003), 61–74.
3. M. Xu and L. V. Wang, Photoacoustic imaging in biomedicine, Review of Scientific Instruments 77 (2006), no. 4, 41101–41122.
4. J. A. Copland, M. Eghtedari, V. L. Popov, N. Kotov, N. Mamedova, M. Motamedi and A. A. Oraevsky, Bioconjugated gold nanoparticles as a molecular based contrast agent: Implications for imaging of deep tumors using optoacoustic tomography, Molecular Imaging & Biology 6 (2004), no. 5, 341–349.
5. K. P. Kostli, M. Frenz, H. P. Weber, G. Paltauf and H. Schmidt-Kloiber, Optoacoustic infrared spectroscopy of soft tissue, Journal of Applied Physics 88 (2000), no. 3, 1632–1637.
6. V. G. Andreev, A. E. Ponomarev, P. M. Henrichs, M. Motamedi, E. Orihuela, E. Eyzaguirre and A. A. Oraevsky, Detection of prostate cancer with opto-acoustic tomography, Proceedings of the SPIE 4960 (2003), 45–57.
7. A. A. Karabutov, E. V. Savateeva, N. B. Podymova and A. A. Oraevsky, Backward mode detection of laser-induced wide-band ultrasonic transients with optoacoustic transducer, Journal of Applied Physics 87 (2000), no. 4, 2003–2014.
8. M. C. Pilatou, N. J. Voogd, F. F. M. de Mul, W. Steenbergen and L. N. A. van Adrichem, Analysis of three-dimensional photoacoustic imaging of a vascular tree in vitro, Review of Scientific Instruments 74 (2003), no. 10, 4495–4499.
9. S. Manohar, A. Kharine, J. C. G. van Hespen, W. Steenbergen and T. G. van Leeuwen, The twente photoacoustic mammoscope: System overview and performance, Physics in Medicine and Biology 50 (2005), no. 11, 2543–2557.
10. F. Yuncai, Photoacoustic ultrasonography and its potential application in mammography, Medical Physics 24 (1997), no. 10, 1647.
11. M. Eghtedari, J. A. Copland, N. A. Kotov, A. A. Oraevsky and M. Motamedi, Optoacoustic imaging of nanoparticle labeled breast cancer cells: A molecular based approach for imaging of deep tumors, Lasers in Surgery and Medicine (2004), 52–52.
12. N. L. Swanson and B. D. Billard, Optimization of extinction from surface plasmon resonances of gold nanoparticles, Nanotechnology 14 (2003), no. 3, 353–357.

13. K. P. Kostli, D. Frauchiger, J. J. Niederhauser, G. Paltauf, H. P. Weber and M. Frenz, Optoacoustic imaging using a three-dimensional reconstruction algorithm, IEEE Journal of Selected Topics in Quantum Electronics 7 (2002), no. 6, 918–923.

14. K. P. Köstli, M. Frenz, H. Bebie and H. P. Weber, Temporal backward projection of optoacoustic pressure transients using fourier transform methods, Physics in Medicine and Biology 46 (2001), no. 7, 1863 – 1872.

15. P. C. Beard, Two-dimensional ultrasound receive array using an angle-tuned Fabry-Perot polymer film sensor for transducer field characterization and transmission ultrasound imaging, IEEE Transactions on Ultrasonics, Ferroelectrics and Frequency Control 52 (2005), no. 6, 1002–1012.

16. J. J. Niederhauser, D. Frauchiger, H. P. Weber and M. Frenz, Real-time optoacoustic imaging using a schlieren transducer, Applied Physics Letters 81 (2002), no. 4, 571–573.

17. J. J. Niederhauser, M. Jaeger, R. Lemor, P. Weber and M. Frenz, Combined ultrasound and optoacoustic system for real-time high-contrast vascular imaging in vivo, IEEE Transactions on Medical Imaging 24 (2005), no. 4, 436–440.

18. G. Paltauf, H. Schmidt-Kloiber, K. P. Kostli and M. Frenz, Optical method for two-dimensional ultrasonic detection, Applied Physics Letters 75 (1999), no. 8, 1048–1050.

19. J. J. Niederhauser, M. Jaeger and M. Frenz, Real-time three-dimensional optoacoustic imaging using an acoustic lens system, Applied Physics Letters 85 (2004), no. 5, 846–848.

20. H. M. Lai and K. Young, Theory of the pulsed optoacoustic technique, Journal of the Acoustical Society of America 72 (1982), no. 6, 2000–2007.

21. G. Paltauf, H. Schmidt-Kloiber and M. Frenz, Photoacoustic waves excited in liquids by fiber-transmitted laser pulses, Journal of Acoustical Society of America 104 (1998), 890–897.

22. M. W. Sigrist and F. K. Kneubuhl, Laser-generated stress waves in liquids, Journal of the Acoustical Society of America 64 (1978), no. 6, 1652–1663.

23. K. P. Kostli and P. C. Beard, Two-dimensional photoacoustic imaging by use of fourier-transform image reconstruction and a detector with an anisotropic response, Applied Optics 42 (2003), no. 10, 1899–1908.

24. M. Xu and L. V. Wang, Time-domain reconstruction for thermoacoustic tomography in a spherical geometry, IEEE Transactions on Medical Imaging 21 (2002), no. 7, 814–822.

25. M. Xu and L. V. Wang, Universal back-projection algorithm for photoacoustic computed tomography, Physical Review E 71 (2005), no. 1, 16706.

26. M. Xu, X. Yuan and L. V. Wang, Time-domain reconstruction algorithms and numerical simulations for thermoacoustic tomography in various geometries, IEEE Transactions on Biomedical Engineering 50 (2003), no. 9, 1086–1099.

27. Y. Xu, Reconstructions in limited-view thermoacoustic tomography, Medical Physics 31 (2004), no. 4, 724–733.

28. X. Yuan, F. Dazi and L. V. Wang, Exact frequency-domain reconstruction for thermoacoustic tomography. I. Planar geometry, IEEE Transactions on Medical Imaging 21 (2002), no. 7, 823–828.

29. M. A. Eghtedari, J. A. Copland, V. L. Popov, N. A. Kotov, M. Motamedi and A. A. Oraevsky, Bioconjugated gold nanoparticles as a contrast agent for detection of small tumors, Proceedings of the SPIE The International Society for Optical Engineering 4960 (2003), 76–85.

NEW IMAGING METHOD BY USING ULTRASOUND VELOCITY CHANGE CAUSED BY OPTICAL ABSORPTION

H. Horinaka, T. Matsunaka, N. Nakamura, T. Mukaiyama, S. Kawakami, M. Kawasaki, K. Wada

Department of Engineering, Osaka Prefecture University, Sakai, 599-8531, Japan

Abstract: We measured optical absorption images of phantoms using our new method that detects ultrasonic velocity change caused by light illumination. The electric scan function of the remodeled diagnostic ultrasonic equipment quickly constructed the ultrasonic velocity change images. The spectroscopic information of phantoms was also obtained from the dependence of ultrasonic velocity change image on the wavelength of the tunable laser used for illumination. It was suggested that our method had the potential to monitor biomarkers used in drug-delivery systems.

Key words: Ultrasonic velocity, Tomography, Spectroscopic information, Diagnosis

1. INTRODUCTION

Optical tomography using near-infrared light is theoretically capable of imaging not only soft tissue information but also metabolic information of a living body using a spectroscopic method. However, it is very difficult to construct an optical image of regions deep within the human body because near-infrared light is severely scattered inside soft tissue.

We previously proposed a new tomography method for medical diagnosis based on the interaction between light and ultrasonic signals. References [1–3] Depth profiles of optical absorption were constructed by detecting ultrasonic velocity changes due to thermal agitation in a light-scattering medium with remodeled commercial diagnostic ultrasonic equipment [4].

To demonstrate the feasibility as a practical system for medical diagnosis using ultrasonic velocity change imaging, we attempted to determine the image distribution of optical absorption material and nanoparticles contained in the phantom.
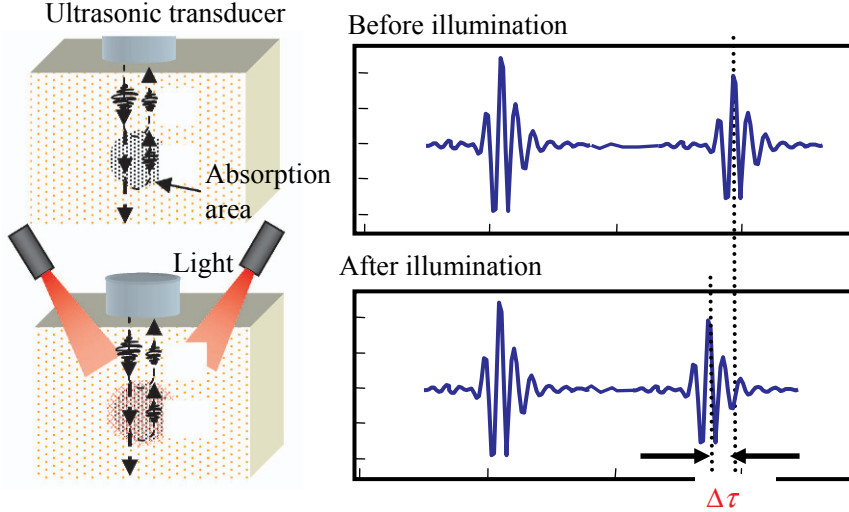
Figure 1. Ultrasonic velocity change due to light absorption.

2. PRINCIPLE OF NEW IMAGING BY DETECTING ULTRASONIC VELOCITY CHANGE

The ultrasonic pulses emitted from the linear array transducer are reflected from acoustic boundaries in the phantom. A normal B-mode image is constructed from the amplitude of echo pulses of every ultrasonic beam. When the light illuminates the phantom, the echo pulses reflected at the boundaries of the optical absorption region shift owing to the local temperature increase (Fig. 1). The propagation time of the echo pulse from the boundary and its change are denoted by τ and $\Delta\tau$. The temperature change ΔT caused by light absorption is represented by

$$\Delta T = K(T) v \frac{\Delta \tau}{\tau}, \tag{1}$$

where $K(T)$ is the compensation factor for ambient temperature T and v is the ultrasonic velocity at T. As τ, v and $K(T)$ are not changed directly by light illumination, the local temperature increase ΔT is determined from $\Delta\tau$. The

temperature change image is constructed from the time difference $\Delta\tau$ of the echo pulse. The optical absorption distribution is estimated from the temperature change image.

3.   EXPERIMENTAL SET-UP

The experimental set-up for ultrasound velocity change tomography is illustrated in Fig. 2. The signal processing board was attached to the remodeled diagnostic ultrasound equipment. The light is guided by the optical fiber or the mirror around the array transducer to illuminate the phantom. The echo pulses and their waveform data that pass through the array transducer connected to the equipment were stored in a personal computer before and after light illumination. The center frequency of the ultrasonic transducer was 13 MHz. An image frame consisted of 346 ultrasonic beams, and the frame frequency was 34 Hz.

Figure 3 depicts the procedure for calculating the ultrasonic velocity change image from the RF echo signal. The waveforms of echo pulses were interpolated to increase sampling points. The waveforms of echo pulses were divided into appropriate areas with the width of the transmitted pulse. The cross-correlation between the corresponding areas of the waveform data was calculated to obtain the time difference $\Delta\tau$ of the echo pulses before and after light illumination.
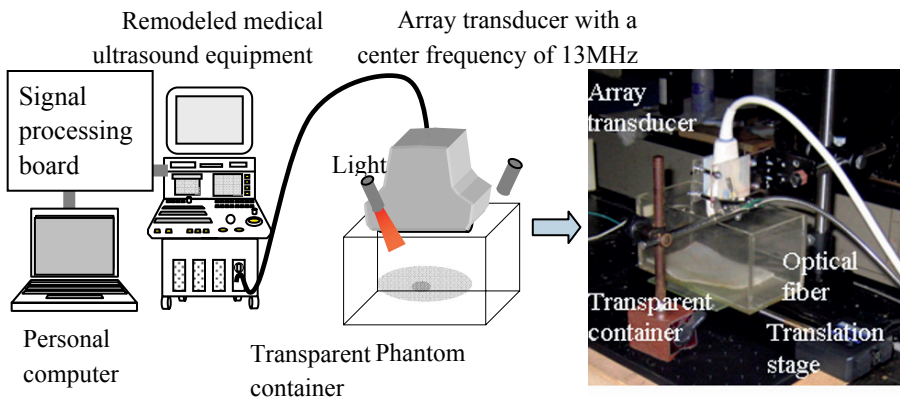
Figure 2. Experimental set-up of new imaging method.
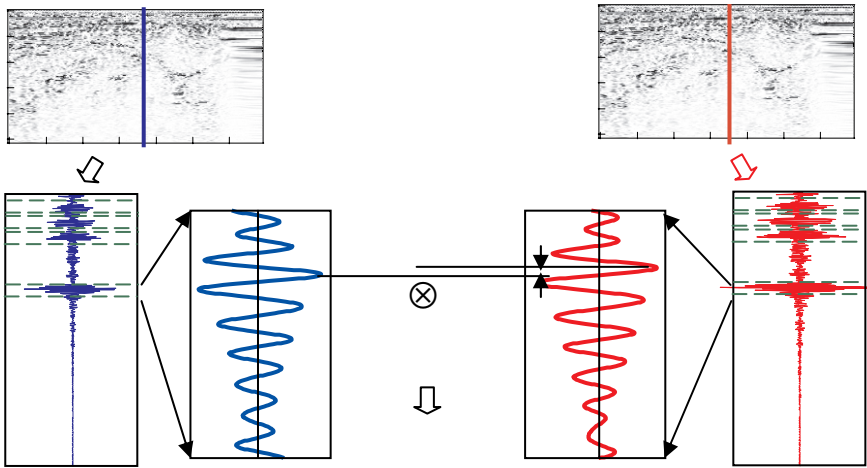
Figure 3. Procedure of calculating ultrasonic velocity change image from RF echo signal.

4.   CONSTRUCTION OF ULTRASONIC VELOCITY CHANGE IMAGE

4.1   Ultrasonic Velocity Change Images vs. Various Exposure Times

Agar dyed with black ink was prepared as an absorber. It was inserted into the white agar including the scattering medium of (Intralipid 10%) as depicted in Fig. 4(a). The light-scattering coefficient of the agar was adjusted to match the reported equivalent scattering coefficient of a living organism. The optical absorption region cannot be observed from the outside. Figure 4(b) presents the normal B-mode image of the phantom. The normal B-mode image does not indicate the position of the agar dyed with black ink. The ultrasonic velocity change image of the optical absorption region in the phantom was constructed under light with a wavelength of 532 nm (SHG of Nd:YVO$_4$ laser). Figure 4(c) depicts the ultrasonic velocity change images corresponding to light exposure times. The local temperature, which was estimated from the ultrasonic velocity change, increases with light exposure time. The ultrasonic velocity change images clearly reveal the temperature distribution that corresponds to the optical absorption region in Fig. 4(a).

(a) Phantom

(b) Normal B-mode image

(c) Ultrasonic velocity change images corresponding to light exposure times
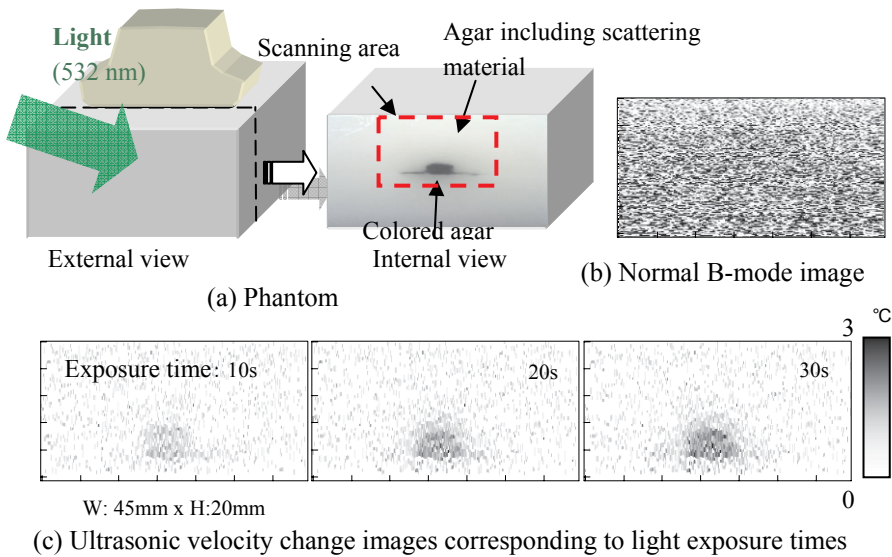
Figure 4. Images vs. light exposure times.

4.2 Dependence of Image Construction on Wavelength of Irradiated Light

Ternary compound semiconductor $AgGaSe_2$ exhibits impurity absorption at wavelengths exceeding the fundamental band-edge (680 nm). The agar including $AgGaSe_2$ particles was used as an absorber. It was inserted into the agar including the scattering medium Intralipid 10% as shown in Fig. 5(a). The absorption coefficient α spectrum of the absorber is represented in Fig. 5(b) by open circles. The ultrasonic velocity images were constructed at various wavelengths of light from a cw Ti:sapphire laser using the experimental set-up of Fig. 1. The ultrasonic velocity change images are presented in Fig. 5(c). Numbers of contours in Fig. 5(c) denote the temperature change due to light illumination. The temperature change at the center of the absorber was plotted as a function of wavelength of irradiated light (closed circles in Fig. 5(b)). The measured temperature change ΔT (closed circles) increase corresponds to the absorption coefficient α (open circles) of the absorber. The spectroscopic information of the phantom could be acquired by selecting the wavelength of the irradiated light.

(a) Phantom

(b) Absorption coefficient α spectrum and ΔT determined from ultrasonic velocity change

(c) Ultrasonic velocity change images (exposure time 40 s)
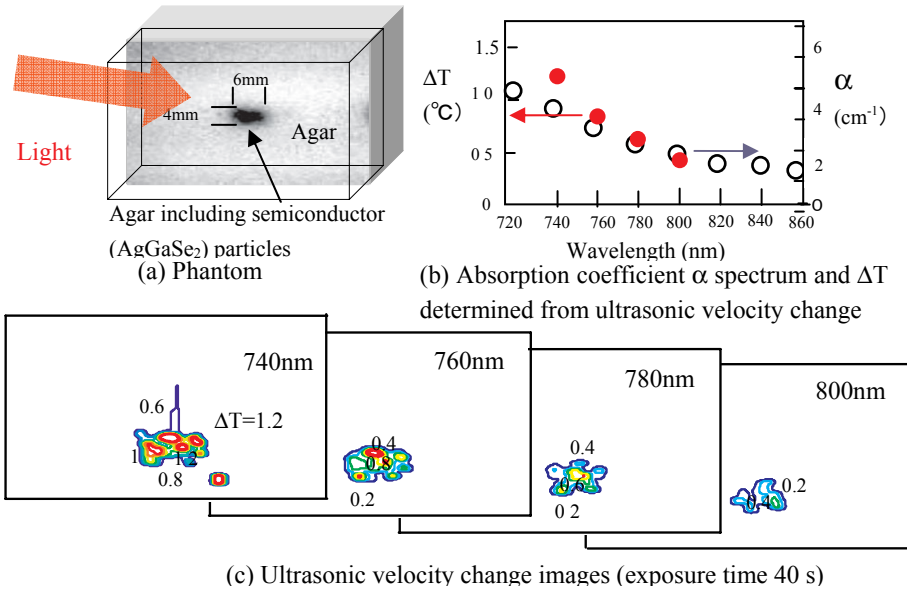
Figure 5. Experiment results of spectroscopic information.

4.3　　Image of Gold Nanoparticle in Tissue Mimics Phantoms

Gold nanoparticles are used as biomarkers in drug delivery systems. They exhibit a characteristic optical absorption spectra due to localized plasmon resonance. Gold nanoparticles deep in biological tissue must be monitored for medical diagnosis and treatment. We prepared an absorber made of agar containing 20 nm-diameter gold nanoparticles and a light-scattering medium (Intralipids) and cut it into a rectangular block. We inserted this absorber into the agar including "Intralipid 10%" as illustrated in Fig. 6(a). The gold nanoparticles exhibited an absorption peak around 520 nm, so light with a wavelength of 532 nm (SHG of Nd:YVO$_4$ laser) was used to illuminate the phantom. The ultrasonic velocity change due to light illumination was obtained, and an image of the gold nanoparticle distribution was constructed. The ultrasonic velocity change image reflected in the location of gold nanoparticles in the agar was obtained (Fig. 6(c)).

Agar including scattering medium

(a) Phantom (cross-section) (b) Normal B-mode (c) Ultrasonic velocity change
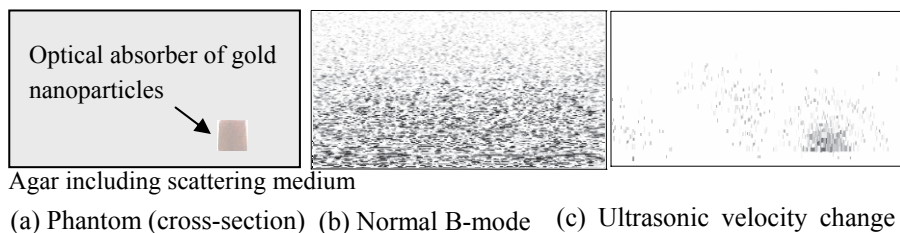
Figure 6. Normal B-mode image and ultrasonic velocity change image of nanoparticles in scattering medium.

5.   CONCLUSION

The ultrasonic velocity change image and the optical absorption distribution were obtained by the remodeled ultrasonic diagnostic equipment with an electric scan. The optical absorption spectrum information of the phantom were also obtained by this new imaging method and irradiated light with different wavelengths. It was possible to reveal the region in which gold nanoparticles were distributed in the tissue mimicking the phantom by detecting the ultrasonic velocity change owing light illumination. Experiment results suggested that our new imaging method could be applied in a practical monitor of biomarkers for medical diagnosis and treatment.

REFERENCES

1. H. Horinaka, K. Wada, A. Okasaka, Y. Cho, T. Matsunaka and S. Saimi: Proc. 2000 IEEE Ultrasonic Symp. (Puerto Rico, 2000), 1709.
2. H. Horinaka, T. Matsunaka, T. Iwade, T. Masumura, T. Kobayashi, T. Kiuchi, K. Wada and Y. Cho, Jpn. J. Appl. Phys. 41, 2002, 3555.
3. H. Horinaka, T. Iwade, Y. Kanetaka, F. Ogushi, T. Matsuyama, K. Wada, T. Matsunaka and Y. Cho: Jpn. J. Appl. Phys. 42, 2003, 3287.
4. H. Horinaka, T. Matsunaka, T. Ura, T. Mukaiyama, N. Nakamura and K. Wada: Proc. 2006 IEEE Ultrasonic Symp. (Vancouver, 2006), 2060.

RANGE MEASUREMENT USING ULTRASOUND FMCW WAVE

M. Kunita, T. Miki, I. Arai
University of Electro-Communications, Tokyo, Japan; Aloka CO., LTD., Tokyo, Japan

Abstract: The authors have proposed an ultrasound FMCW range-measuring system for diagnosis. In the proposed system, a transmitter and receiver operate at very low voltage. It is desirable to compose a simple transmitter and receiver and to protect the human body against damage caused by ultrasound power. The system results analyzed using saw-tooth and isosceles modulation waveform agreed with experiment results derived using delay lines.

Key words: Ultrasound diagnosis, FMCW, Range measurement

1. PRINCIPLE OF ULTRASOUND FMCW RANGE MEASUREMENT

Figure 1 illustrates the configuration of the ultrasound diagnosis FMCW system for range measurement.

The transmitted ultrasound signal $v_T(t)$ is given by Eq. (1) [1, 2].

$$v_T(t) = \sin[\omega_0 t + \Delta\omega F(t)] \tag{1}$$

Here, ω_0 is the ultrasound carrier frequency and $\triangle\omega$ is the frequency deviation. *F(t)* describes the instantaneous phase variation. Its time derivative corresponds to the instantaneous variation of frequency $f_i(t)$. The reflected signal from human tissue is given by Eq. (2) where attenuation is assumed to be α during two-way propagation from the transmitter to a reflection point.

$$v_R(t) = \alpha \sin[(\omega_0 + \omega_d)t + \phi_0 + \Delta\omega F(t - \tau)] \tag{2}$$

Here, ω_d is the Doppler frequency, ϕ_0 is the carrier phase difference between transmitter and receiver, and τ is the delay time between transmitting and receiving signals. Multiplication of $v_T(t)$ by $v_R(t)$ generates the baseband signal $v_D(t)$ [3].

$$v_D(t) = \alpha/2 \cdot \cos(\omega_d t + \phi_0) \cos\{\Delta\omega[F(t) - F(t-\tau)]\} + \sin(\omega_d t + \phi_o)\sin\{\Delta\omega[F(t) - F(t-\tau)]\} \quad (3)$$

Time delay τ can be estimated by the frequency difference, which is proportional to τ.

For a sawtooth modulation signal, $v_T(t)$ and $f_i(t)$ are presented in Fig. 2(A) and (B). Phase factors of $F(t)$ and $F(t-\tau)$ are compared in Fig. 2(C) and suggest that the phase difference $[F(t) - F(t-\tau)]$ in Fig. 2(D) has different time dependences for the two time intervals $\Phi_1(t)$ and $\Phi_2(t)$. Cosine and sine terms of the phase factor in Eq. (3) are expanded into a Fourier series as follows [4]. ω_m is the modulation angular frequency, $\omega_m = 2\pi/T_m$.
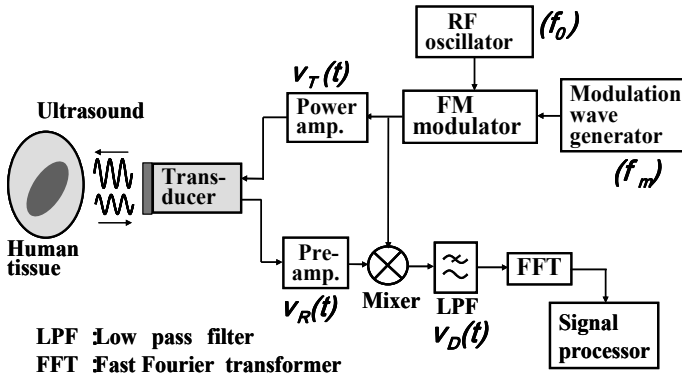
Figure 1. Construction of ultrasound FMCW range-measurement system.
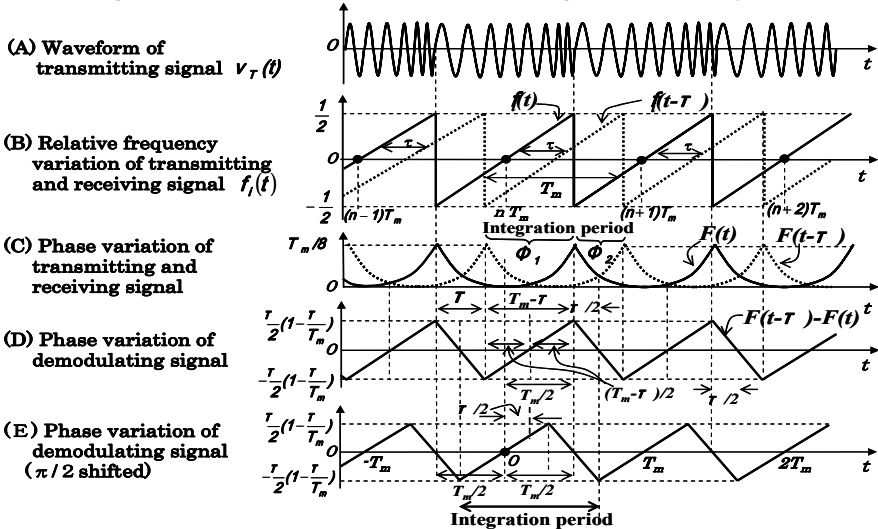
Figure 2. Instantaneous phase and frequency change in transmitting and receiving signal with sawtooth waveform.

$$\cos\Delta\omega[F(t)-F(t-\tau)]=\frac{a_0}{2}+\sum_{n=1}^{\infty}a_n\cos(n\omega_m t), \quad a_n=\frac{T_m}{4}\int_0^{T_m/2}\cos\{\Delta\omega[F(t)-F(t-\tau)]\}\cos(n\omega_m t)dt \quad (4)$$

$$\sin\Delta\omega[F(t)-F(t-\tau)]=\sum_{n=1}^{\infty}b_n\sin(n\omega_m t), \quad b_n=\frac{4}{T_m}\int_0^{T_m/2}\sin\{\Delta\omega[F(t)-F(t-\tau)]\}\sin(n\omega_m t)dt \quad (5)$$

The baseband signal $v_D(t)$ is expressed by Eq. (6).

$$v_D(t)=\frac{\sin[\Delta\omega\tau(T_m-\tau)/2T_m]}{\Delta\omega\tau(T_m-\tau)/2T_m}\cos(\omega_d t+\phi_0)+\Delta\omega\sum_{n=1}^{\infty}\left[\frac{\sin[(T_m-\tau)(\Delta\omega\tau+2n\pi)/2T_m]}{(\Delta\omega\tau+2n\pi)[\Delta\omega(T_m-\tau)-2n\pi]/2T_m}\cos(\omega_d t+\phi_0+n\omega_m t)\right.$$

$$\left.+\frac{\sin[(T_m-\tau)(\Delta\omega\tau-2n\pi)/2T_m]}{(\Delta\omega\tau-2n\pi)[\Delta\omega(T_m-\tau)+2n\pi]/2T_m}\cos(\omega_d t+\phi_0-n\omega_m t)\right] \quad (6)$$

In the isosceles sawtooth modulation signal, $v_T(t)$ and $f_i(t)$ are shown in Fig. 3(A) and (B). Phase difference $[F(t)-F(t-\tau)]$ exhibits different time dependences for the four time intervals Φ_1, Φ_2, Φ_3 and Φ_4 expressed in Fig. 3(C). Cosine and sine terms of the phase factor in Eq. (3) are expanded into a Fourier series using a similar manipulation of the sawtooth signal. $v_D(t)$ is expressed for $\tau \ll T_m$ by Eq. (7).

$$v_D(t)=\frac{\alpha}{4}\cdot\frac{\sin\frac{\Delta\omega\tau}{2}}{\frac{\Delta\omega\tau}{2}}\cos(\omega_d t+\phi_0)+\frac{\alpha}{4}\cos[(n\omega_m+\omega_d)t+\phi_0]\sum_{n=1}^{\infty}\left[\frac{\sin\frac{\Delta\omega\tau+n\pi}{2}}{\frac{\Delta\omega\tau+n\pi}{2}}+(-1)^n\frac{\sin\frac{\Delta\omega\tau-n\pi}{2}}{\frac{\Delta\omega\tau-n\pi}{2}}\right]$$

$$+\frac{\alpha}{4}\cdot\cos[(n\omega_m-\omega_d)-\phi_0]\sum_{n=1}^{\infty}\left[\frac{\sin\frac{\Delta\omega\tau-n\pi}{2}}{\frac{\Delta\omega\tau-n\pi}{2}}+(-1)^n\frac{\sin\frac{\Delta\omega\tau+n\pi}{2}}{\frac{\Delta\omega\tau+n\pi}{2}}\right] \quad (7)$$
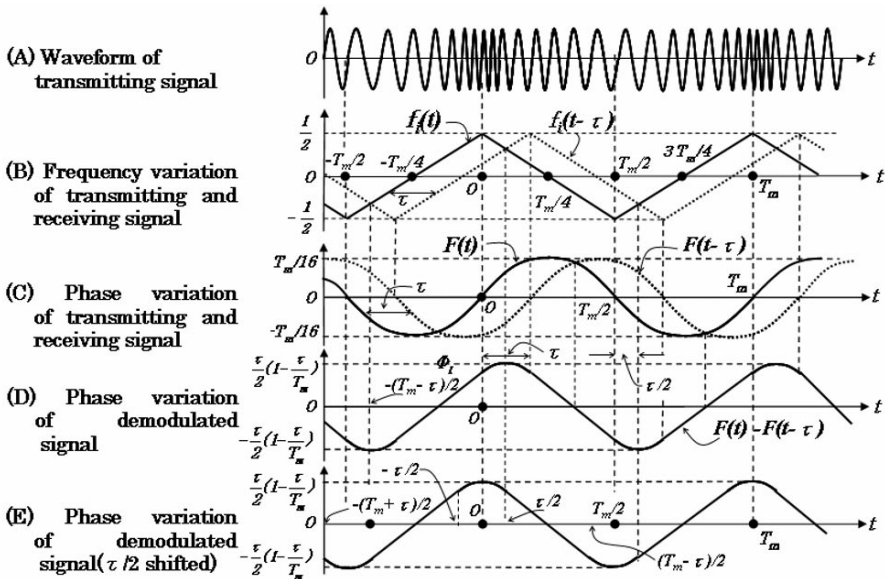
Figure 3. Instantaneous phase and frequency change in transmitting and receiving signal with isosceles sawtooth waveform.

2.   DISTANCE-DEPENDENCE SPECTRUM
OF THE BASEBAND SIGNAL

The maximum value of the voltage amplitude spectrum occurs at the harmonic where the following relations hold:

$$\tau_{\max s} = \frac{2n\pi}{\Delta\omega} = \frac{n}{\Delta f}\text{(sawtooth)}, \quad \tau_{\max i} = \frac{n\pi}{\Delta\omega} = \frac{n}{2\Delta f} \quad \text{(isosceles sawtooth)} \quad (8)$$

where $\tau_{\max s}$ and $\tau_{\max i}$ are the delays at which the n-th harmonics have their maximum values. Figure 4 illustrates the relation between delay time and the frequency spectrum in the baseband signal. The solid line marked $\tau_{\max s}$ in Fig. 4(A) indicates that, for a delay equal to an integer multiple of $1/\Delta f$, all harmonics are zero except for one that satisfies Eq. (8). The solid line marked $\tau_{\max i}$ in Fig. 4(B) demonstrates that, for a delay equal to an even integer multiple of $1/2\Delta f$, all harmonic are zero except the one that satisfies Eq. (8).   Equation (8) also shows that the depth l of the reflection point is determined from the number of the harmonic corresponding to the maximum of the measured frequency spectrum.
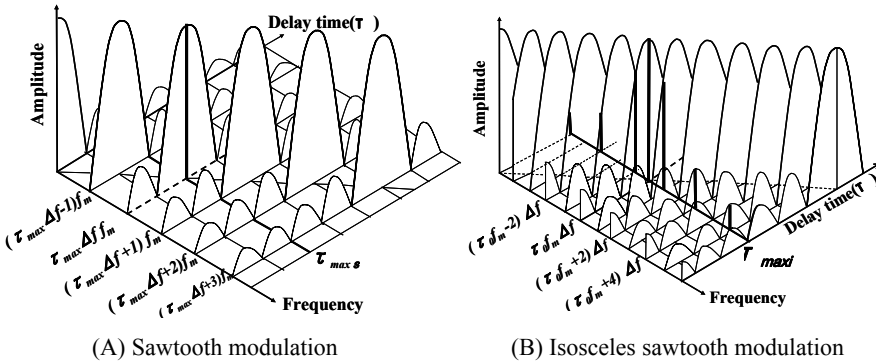
(A) Sawtooth modulation   (B) Isosceles sawtooth modulation
Figure 4. Relation between delay time and baseband frequency spectrum.

3.   EXPERIMENTAL RESULTS

In the experiment, an electrical delay line was used instead of an ultrasound phantom to avoid ambiguity caused by unexpected reflections.

Figure 5 illustrates the received baseband signal at the mixer output for an isosceles sawtooth modulation signal. As shown in the figure, the spectrum has a maximum at the second and the fourth harmonics. These

results suggest that the harmonic number at the spectrum peak increases linearly with an increase in the distance from the reflection point.
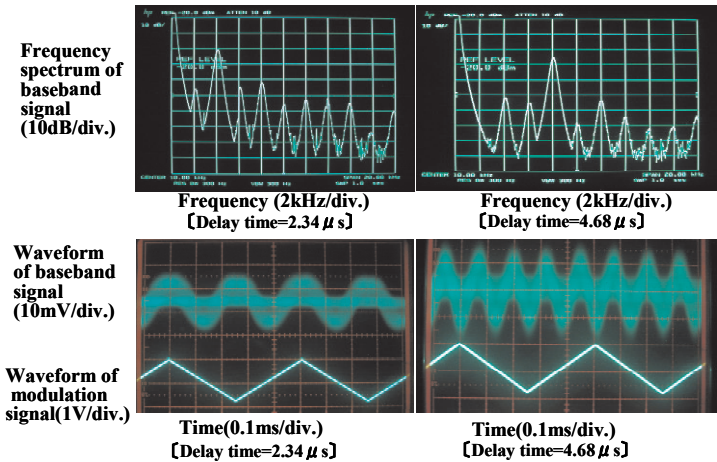
Figure 5. Frequency spectrum in baseband signal (isosceles modulation signal).

Figure 6. Relation between delay time and frequency spectrum in baseband signal (isosceles modulation signal, parameter: frequency deviation $\varDelta f$).

(A) Sawtooth baseband signal   (B) Isosceles sawtooth modulation signal

Figure 7. Relation between harmonics and delay time in baseband signal.
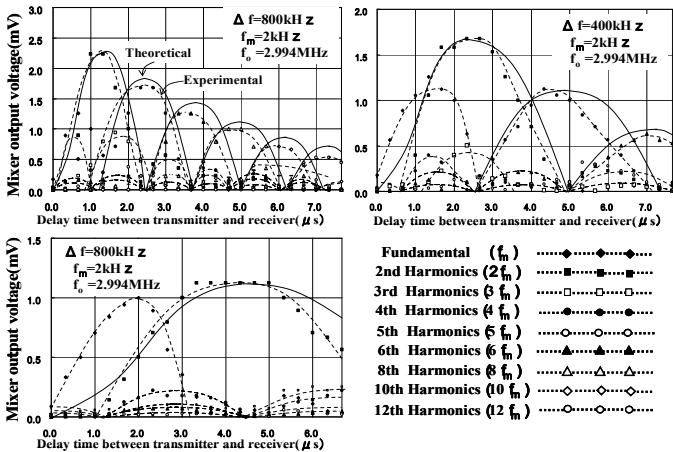
Figure 6 presents the measured and calculated harmonics spectrum in the baseband signal. Solid lines represent the calculated amplitudes of the harmonics, and dashed lines, the measured harmonics results.

These figures reveal that the spectral peak shifts toward higher harmonics with an increase in the delay time. Figure 7 depicts the relation between delay time and harmonic frequency at the spectral peak. The solid line indicates the calculated values, and the black circles represent the measured data. These figures confirm the tendency predicted theoretically by Eqs. (6) and (7). The harmonic number increases proportionally to the increase in the delay time in the sawtooth and isosceles sawtooth modulation signals. Since depth in the tissue is directly calculated from the delay time, coincidence of measured and calculated values indicates that the depth is obtained by measuring the baseband frequency spectrum.

4.   CONCLUSION

An FMCW ultrasound range-measuring system was proposed for measuring the position of human tissue. The demodulated signal is theoretically estimated, and the analyzed result enables us to calculate the frequency spectrum and range resolution in the system. The sawtooth and isosceles sawtooth modulation waveforms offer advantages in that the ultrasound measuring system can measure ranges from multiple reflection points simultaneously.

Experiments using an electrical delay line were performed to verify the validity of the analysis results. The agreement between the measured and calculated frequency spectrum indicates the validity of the analysis.

REFERENCES

1. Kunita M, Noda M. *Chouonpa FMCW Doppura keisoku shisutemu niyoru kuratta teigen kouka* (Clutter reduction in ultrasound FMCW Doppler measurement system). IEICE Trans Fundam Electron Commun Comput Sci (Japan. Ed.) 2004;J87-A:1272–1283.(In Japanese)
2. Stein S, Jones JJ. *Gendai no Tsuhshin kaisen Riron* (Modern communication principles). Morikita Shuppan (McGraw-Hill), 1962; pp. 160–162. (In Japanese)
3. Komarov IV, Smolskey SM. Fundamentals of short range FM radar. Artech House, 2003; pp. 17–22
4. Brigham EO. *Kousoku Furie Henkan*. Kagakugijutu Shauppansha (Prentice Hall), 1978, p 85. (in Japanese)

DIRECT VISUALIZATION OF HIGH-INTENSITY FOCUSED ULTRASONIC FIELD USING LIGHT-EMITTING DIODES AND PIEZOELECTRIC ELEMENTS

K. Nakamura, H. Ogura, T. Sugimoto

Precision and Intelligence Laboratory, Tokyo Institute of Technology, R2-26,4259 Nagatsuta, Midori-ku, Yokohama 226-8503, Japan; Faculty of Engineering, Toin University of Yokohama, 1614 Kurogane-cho, Aoba-ku, Yokohama 225-8502, Japan

Abstract: This paper presents a tool with a light-emitting diode (LED) connected to a piezoelectric ceramic element for directly visualizing an intense ultrasonic field. The piezoelectric element generates electric voltage proportional to the ultrasonic pressure applied to the element; the LED is then turned on by the voltage. The sound pressure is directly observed as light intensity of the LED by human eyes. This paper first explains the basic structure of the sensor device. Several methods to utilize the sensor are then presented. Second, visualization of a focused field excited by a concave transducer working at 500kHz is demonstrated using an array version of the proposed sensor.

Key words: Visualization, LED, Piezoelectric ceramics, PZT, Focused ultrasonic field, Array, Concave transducer

1.   INTRODUCTION

Among the various methods to visualize the distribution of an ultrasonic field in water, a mechanically scanned or arrayed hydrophone is the most common. However, a mechanical scanning system is basically an off-line method, where the output signal from the hydrophone is recorded on a PC through an A/D converting unit and then displayed on a screen. The array system is capable of real-time measurements in principle, but it requires the same number of high-speed A/D converters as the channels of measuring

points. The results are displayed on a PC screen at a remote location. Some of optical techniques such as the Schlieren method provide real-time imaging of a two-dimensional sound field. However, they need a bulky optical setup and cannot always be applied to all arrangements of ultrasonic transducers and water tanks. An intense sound field can also be visualized using chemical luminescence. However, the chemical method is not stable for long-term observation.

In this study, the authors investigate a new device consisting of a light-emitting diode (LED) and a piezoelectric ceramic element [1]. It has a simple structure and operation principle. The LED's light intensity is proportional to the strength of sound pressure applied to the piezoelectric element since the LED is directly fed by the voltage generated across the electrodes of the piezoelectric element. This device is suitable for being integrated into an array and enables us to observe the sound field distribution directly using our naked eyes. First, we explain the configuration and working principle of the present sensor device. Second, imaging of a high-intensity focused ultrasonic field is demonstrated using an arrayed version of the proposed method.

2. CONFIGURATION AND OPERATION PRINCIPLE

Figure 1 illustrates the basic structure of the sensor device to be considered in this study. A cubic piezoelectric element of 2 mm × 2 mm × 2 mm was used in our experiments as the piezoelectric generator that was polarized along one of the three axes and had a pair of parallel electrodes. The piezoelectric ceramics utilized here is PZT, and the material for the electrode is nickel. A visible red LED is connected to the PZT's electrodes with short wires. The LED is biased by a DC voltage source via a 1-kΩ resistor, and the voltage is adjusted to just below the LED threshold voltage.
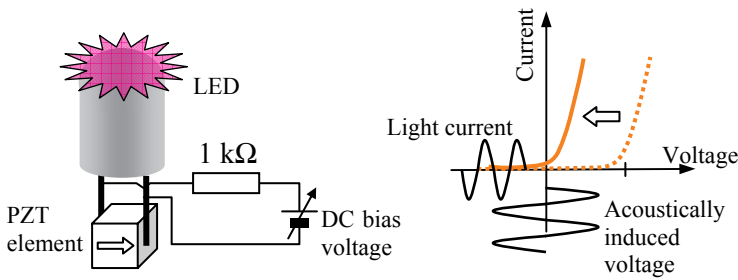
Figure 1. Configuration and working principle of sensor device.

A dynamic voltage is induced across the PZT electrodes in proportion to the sound pressure level and the piezoelectric constant of the piezoelectric material. Rectified waveforms are obtained as intensity modulation in the LED's brightness since the LED is a directional device. If the sensor device is mechanically scanned and observed using a video camera as shown in Fig. 2, we can record the spatial distribution of sound intensity as the brightness. If the emitted light is guided using an optical fiber to a photo diode, quantitative measurements and the observation of the waveform are possible. In such a setup, the sensor acts as a hydrophone with optical intensity output. Long-distance transmission and high immunity to electromagnetic noise are both expected due to transmitting an optical signal through a fiber cable. The DC bias voltage should be chosen high enough to avoid distortion of the waveform.
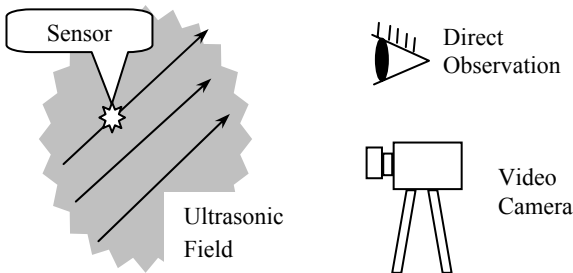
Figure 2. Mechanical scanning of the single sensor and observation.

Arranging many sensor devices in a two-dimensional array enables real-time, direct observation of the sound field distribution with the naked eye or a digital camera as illustrated in Fig. 3. In this study, we made a two-dimensional array for imaging a high-intensity ultrasonic field.
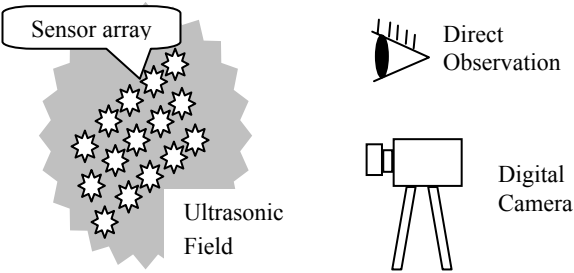
Figure 3. Real-time direct observation of sound field using the array configuration.

3.   EXPERIMENTAL SETUP

Figure 4 illustrates the experimental setup in which a concave PZT transducer with a diameter of 100 mm and radius of curvature of 100 mm is immersed at the bottom of a water vessel and is radiating ultrasound of 530 kHz in the vertical direction. The focal point is located around 10 mm beneath the water surface.
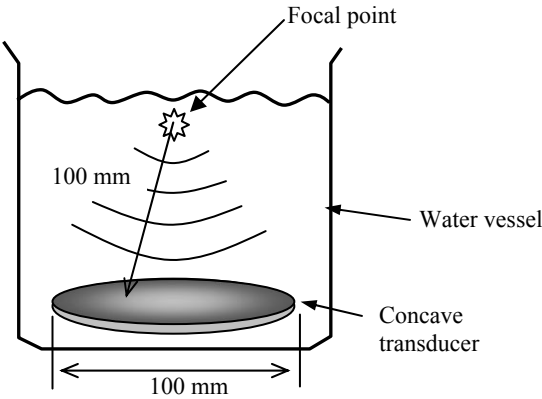
Figure 4. Ultrasonic focused field to be measured using the proposed method.
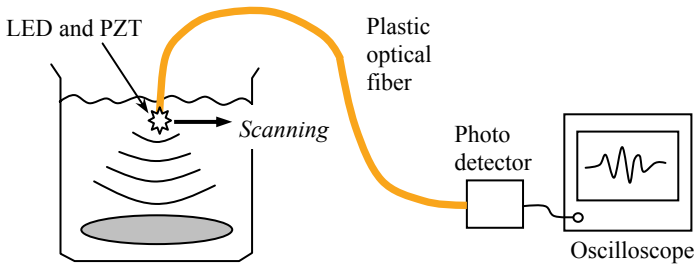
Figure 5. Setup for measuring the sound-pressure distribution near the focal point of a concave transducer. The output is guided to the photo diode using a fiber cable.

The sound pressure distribution near the focus was measured using the setup shown in Fig. 5 before the sound field imaging experiments using an array sensor. The output light is guided to a photo diode using a PMMA-based plastic optical fiber (core diameter 0.98 mm; cladding diameter 1 mm). DC bias was not applied, since the sound pressure was high. We calibrated the pressure sensitivity by comparing it with a conventional piezoelectric hydrophone with known sensitivity. The single sensor with fiber output was mechanically scanned in the horizontal direction across the focal point. The output amplitude of the photo diode is plotted in Fig. 6 with the theoretical curve. The focal spot diameter for –3dB is approximately 2 mm.
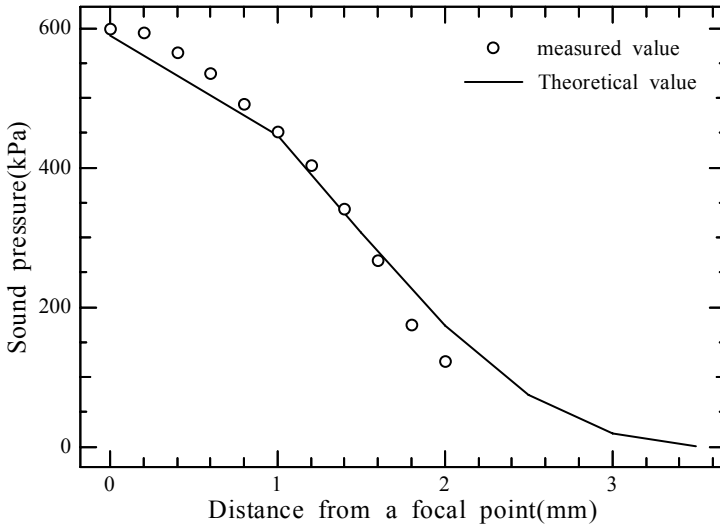
Figure 6. Sound pressure measured across the focal point along the horizontal axis.

4. OBSERVATION OF SOUND FIELD DISTRIBUTION USING ARRAY SENSOR

A two-dimensional array with 6 × 7 sensors was fabricated on a printed circuit board. Sensor spacing was 10 mm in both x and y directions. Figure 7 is a photo of the array sensor. The sensor was scanned by hand around the focal point with its aperture parallel to the aperture of the concave transducer located at the bottom of a water vessel. Light emission from the array was recorded by a digital video camera during the observation. Some of the pictures of the video file were selected and presented in Fig. 8. The position of the acoustic focus is clearly visualized as can been seen in the photos. The distance between the sensor and the transducer was not maintained perfectly constant, so the diameter of the bright region changes. Furthermore, the dynamic range of the digital video camera is limited, so the brightness is saturated in some of the pictures.
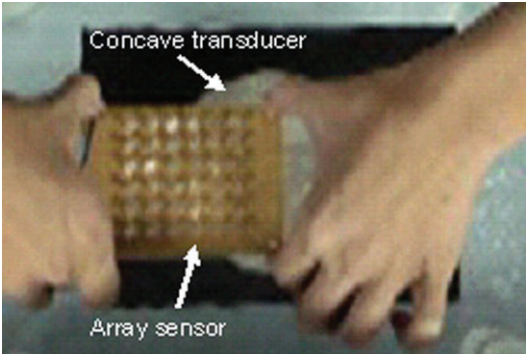
Figure 7. Observation of the focused fields using a 6 x 7 array.
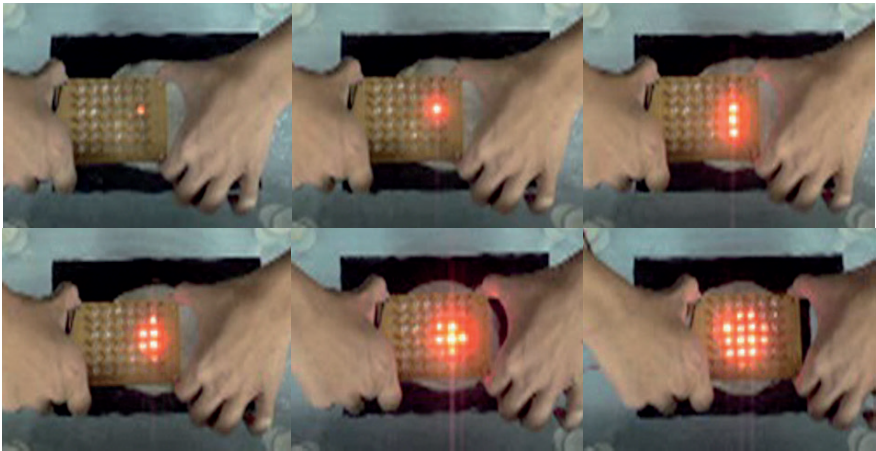
Figure 8. Photos from the video file observing the focused field.

5. CONCLUSION

A new method of visualizing an intense ultrasonic field using an LED and a PZT element was applied to integrate an array sensor. The focused field of the concave transducer was successfully observed. The method can be applied for examining and testing a high-intensity focused field and an ultrasonic cleaner.

REFERENCE

1. K. Nakamura and T. Sugimoto, Measurements of ultrasonic field using a piezoelectric-ceramics and a light emitting diode, *Trans IEICE*, **J86-C**(12), 1331–1336 (2003).

SENSOR SIGNAL PROCESSING FOR ULTRASONIC SENSORS USING DELTA–SIGMA MODULATED SINGLE-BIT DIGITAL SIGNAL

S. Hirata, M.K. Kurosawa, T. Katagiri

Department of Information Processing, Tokyo Institute of Technology, Yokohama, 226-8502, Japan; Sutekina Inc., Komagane, 399-4117, Japan

Abstract: Ultrasonic distance measurement is based on determining the time of flight of ultrasonic wave. The pulse compression technique that obtains the cross-correlation function between the received signal and the reference signal is used to improve the resolution of distance measurement. The cross-correlation method requires high-cost digital signal processing. This paper presents a cross-correlation method using a delta–sigma modulated single-bit digital signal. Sensor signal processing composed of the cross-correlation between two single-bit signals and a post-moving average filter is proposed and enables reducing the cost of digital signal processing.

Key words: Ultrasonic distance measurement, Pulse compression technique, Delta–sigma modulation, Cross-correlation, Moving average filter

1.   INTRODUCTION

Distance measurement employing ultrasonic sensors is used in autonomous mobile robot research. Its advantages include the use in hardware construction and reduced system size and cost.

Ultrasonic distance measurement is based on determining the time of flight (TOF) of an ultrasonic wave to a target. Distance to a target can be calculated from the TOF and the acoustic velocity. The resolution of distance measurement depends on the resolution of the TOF measurement, which is related to the clock frequency of the measurement system.

In a noisy environment, it is difficult to determine the TOF and measure the distance at high resolution. The pulse compression technique, in which the received signal is correlated with the reference signal, is used to improve the resolution of distance measurement in a noisy environment. To use the pulse compression technique, the transmitted signals should be frequency modulated (FM) or be modulated by pseudo-random sequences that have a high autocorrelation.

Sensor signal processing methods for distance measurement using the pulse compression technique require cross-correlation between the received signal and the reference signal. Calculating the cross-correlation requires huge numbers of multiplications and accumulations, necessitating high-cost digital signal processing. Therefore, it is difficult to calculate the cross-correlation for real-time measurement with the limited computational capacity of autonomous mobile robots.

This paper proposes a sensor signal processing method using a delta-sigma modulated single-bit digital signal. Multiplication and accumulation of two single-bit signals are replaced with logical-operations EXOR and NOT. Cross-correlation of single-bit signals using EXOR and NOT can reduce the calculation cost of digital signal processing.

The cross-correlation function obtained by the proposed method was examined by computer simulation.

2.   SENSOR SIGNAL PROCESSING

The proposed sensor signal processing method is composed of the cross-correlation between two single-bit signals and a post-moving average filter, as illustrated in Fig. 1.

The transmitted signal is converted into a single-bit signal $h(i)$ by a comparator as a reference signal, and a received signal that includes the transmitted signal is converted into a single-bit signal $x(i+t)$ by a delta-sigma modulator. The received signal $x(i+t)$ is correlated with the reference signal $h(i)$, and Eq. (1) of the cross-correlation function is expressed as

$$C(t) = \frac{1}{N}\sum_{i=1}^{N} h(i) \cdot x(i+t).$$
(1)
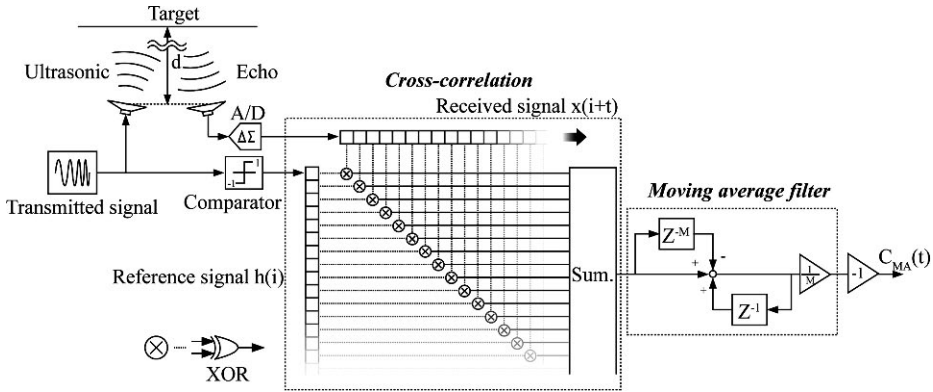
Figure 1. Proposed sensor signal processing method composed of the cross-correlation between two single-bit signals and a post-moving average filter.

The calculation is repeated with every new sample. The time at the peak of the cross-correlation function indicates the TOF of the ultrasonic wave.

Multiplications in cross-correlation between two single-bit signals are replaced with logical-operations EXOR and NOT. The proposed method enables reducing the calculation cost by employing these logical operations.

The cross-correlation of two single-bit signals contains high-frequency noise. The noise is quantized error of the received signal that the delta-sigma modulator shifts into the high-frequency band. This noise decreases the SNR of the obtained cross-correlation function.

A moving average filter is used to reduce the noise and improve the SNR of the cross-correlation function. Equation (2) represents the cross-correlation function filtered by the moving average filter before the cross-correlation operation.

$$C_{MA}(t) = \frac{1}{N}\sum_{i=1}^{N} h(i) \cdot \left\{ \frac{1}{M}\sum_{k=1}^{M} x(i+t+k-1) \right\} \tag{2}$$

This method increases the calculation cost. Equation (3), representing the cross-correlation function filtered by the moving average filter after the cross-correlation operation, is derived by transformation of Eq. (2).

$$C_{MA}(t) \quad = \quad \frac{1}{N}\sum_{i=1}^{N}h(i)\cdot\left\{\frac{1}{M}\sum_{k=1}^{M}x(i+t+k-1)\right\}$$

$$= \quad \frac{1}{M}\sum_{k=1}^{M}\frac{1}{N}\sum_{i=1}^{N}h(i)\cdot x(i+t+k-1) \tag{3}$$

$$= \quad \frac{1}{M}\sum_{k=1}^{M}C(t+k-1)$$

This method can reduce the cross-correlation function noise without increasing the calculation cost.

3.　　SIMULATION RESULT

The cross-correlation function using the proposed method was evaluated in a computer simulation. In the simulation, a chirp signal from 45[kHz] down to 35[kHz] with a duration 5[msec] was transmitted. The sampling frequency was 2[MHz], and the distance to the target was 2[m], so the TOF was 5.8[msec]. Attenuation of the ultrasonic wave in the air was 2.11[dB/m].

The transmitted signal was converted into a single signal by the comparator, and the received signal was converted into a single signal by a second-order delta-sigma modulator. The length of second-order moving average filter was 11.

The obtained cross-correlation function doesn't contain high-frequency noise (Fig. 2). The *X*-axis of the figure is the time, and the *Y*-axis of the cross-correlation function is normalized by the auto-correlation function. The time at the peak of the cross-correlation function represents the TOF.
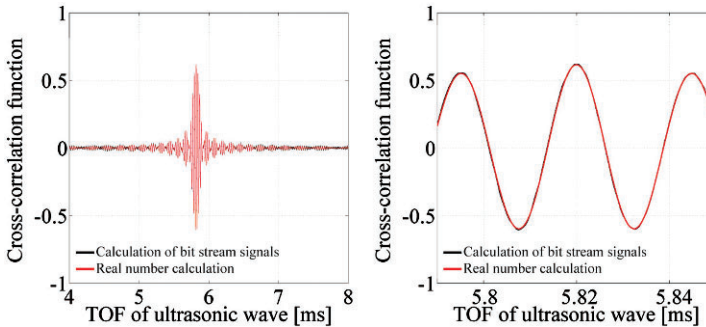
Figure 2. Cross-correlation function obtained by proposed method.

4. SNR AND ACCURACY OF CROSS-CORRELATION FUNCTION

The optimal length of the second-order moving average filter was determined from the SNR of the cross-correlation function. Figure 3 presents the simulation result of the SNR. The *X*-axis of the figure represents the length of the moving average filter, and the *Y*-axis is the SNR. The optimal length depends on the sampling frequency of the delta-sigma modulator.

The SNR at the optimal length increases with the sampling frequency. In the proposed method, increasing the sampling frequency effectively improves the SNR.
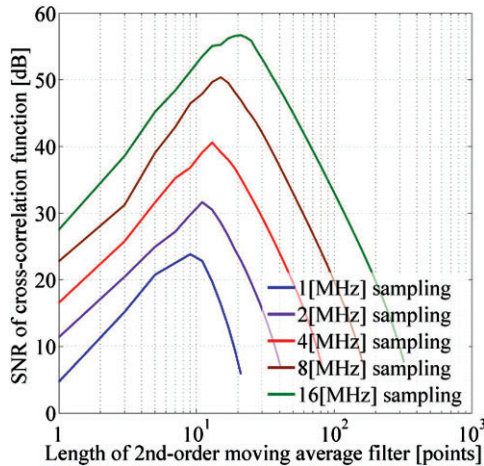
Figure 3. SNR of cross-correlation function with 2nd-order moving average filter.

The measured TOF is the time at the peak of the cross-correlation function. Figure 4 illustrates the simulation results for error distribution of the measured TOF. The simulation was conducted 1000 times, and the sampling frequency was 2[MHz]. The *X*-axis of the figure represents the error of the measured TOF, and the *Y*-axis, the probability.

The cross-correlation function from single-bit signals contains high-frequency noise. The noise increases the error distribution of the measured TOF. The moving average filter narrows the error distribution of the measured TOF by reducing the noise. The filter thus improves the accuracy of the measured TOF.
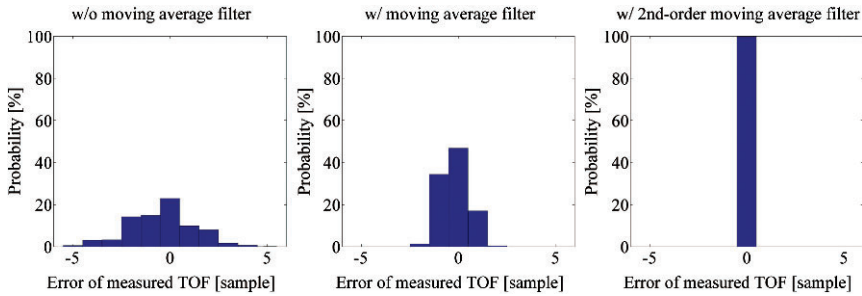
Figure 4. Error distribution of measured TOF.

5.   CONCLUSION

This paper proposes sensor signal processing using a delta-sigma modulated single-bit digital signal for real-time distance measurement by autonomous mobile robots using ultrasonic sensors.

The proposed sensor signal processing method is composed of the cross-correlation between two single-bit signals and a post-moving average filter that reduces the high-frequency error of delta-sigma modulated single-bit digital signal. The calculation cost of digital signal processing for cross-correlation is reduced without decreasing the SNR and accuracy of the cross-correlation function.

REFERENCES

1. Y. Nagashima, and S. Yuta, Ultrasonic sensing for a mobile robot to recognize an environment – Measuring the normal direction of walls, Proc. IEEE/RSJ International Conference on Intelligent Robots and Systems, Raleigh, NC, U.S.A, vol. 2, pp. 805–812, July, (1992).
2. K. W. Jorg, and M. Berg, Sophisticated mobile robot sonar sensing with pseudo-random codes, Robotics and Autonomous Systems vol. 25, no. 3, pp. 241–251, November, (1998).
3. J. Klahold, J. Rautenberg, and U. Ruckert, Continuous sonar sensing for mobile mini-robots, Proceedings of the 2002 IEEE International Conference on Robotics and Automation, Washington, DC, U.S.A, vol. 1, pp. 323–328, May, (2002).
4. S. R. Norsworthy, R. Schreier, and G. C. Temes, Book Delta-Sigma Data Converters Theory, Design, and Simulation (IEEE Press, Piscataway,1997).
5. F. Maloberti, Non conventional signal processing by the use of sigma delta technique: a tutorial introduction, Proceeding of the IEEE International Symposium on Circuits and Systems, San Diego, CA, U.S.A, vol. 6, pp. 2645–2648, May, (1992).

A METHOD OF INDOOR TARGET DETECTION USING M-SEQUENCE ACOUSTIC SIGNAL

T. Yamaguchi, K. Nishihara, H. Matsuo, Y. Wang, M. Hashimoto, H. Hachiya

Graduate school of Advanced Integrated Science, Chiba University, 1-33 Yayoi-cho, Inage-ku, Chiba, 263-8522, Japan; Graduate School of Science and Technology, Chiba University Japan; Matsushita Electric Industrial Co., Ltd.; Research Center for Frontier Medical Eng., Chiba University, Japan

Abstract: Acoustic sensing in air is a promising technology for fast and accurate characterization of objects. Nevertheless, it is difficult to clearly identify acoustic signals from small objects because of environmental noise and scattering from the object surface. Therefore, it is necessary to establish a sensing system that is able to measure objects in air. In this study, we localized small objects by using an M-sequence signal and phase information of received signals in a noisy indoor environment. The M-sequence signal was able to improve the SN ratio and to stably measure the reflected waves that cannot be detected by using a conventional impulse. The arrival direction information was used to extract reflected signals of targets from unwanted signals from the floor or ceiling. Using an M-sequence signal and the arrival direction information, the positions of small objects were detected in the indoor environment.

Key words: Acoustic sensing, M-sequence signal, Arrival direction, Acoustic imaging

1.   INTRODUCTION

Acoustic sensing systems operating in air have been proposed by many researchers as an effective method for acquiring information about an object such as its distance, shape and surface configuration, and environmental information such as temperature or wind velocity [1–4]. Nevertheless, it is difficult to identify acoustic signals of small objects clearly in an indoor

environment because of strong multiple reflections of walls, scattering of the object surface, and background noise. It is necessary to establish a sensing system capable of measuring in an indoor environment. It is especially important to improve the SN ratio in the measurement system because this ratio is one of the main factors determining the sensing accuracy. In this paper, we detected positions of small objects by using an M-sequence signal [5,6] in a noisy indoor environment. We tried to extract reflected signals of targets from unwanted signals from the floor or ceiling by using the arrival direction of the received signals acquired from phase information of multiple microphones.

2.   EXPERIMENT METHOD

2.1   Measurement Environment

In this study, we used a phase-modulated M-sequence signal for measurement. A 25 kHz signal is transmitted from a card speaker (Panasonic, WM-R57A). The degree of the M-sequence is 10, and there are three cycles per digit. The sequence is repeated three times during each transmission to eliminate the possible influence of sequence truncation. In the measurement that uses M-sequence signal, signal to noise ratio becomes high in a result of the correlation processing of the received signal and the transmitted discrete M-sequence signal. Theoretically, the SN ratio should be improved 30 dB using an M-sequence of degree 10 compared with a conventional impulse. The characteristics of the transmitted signal are summarized in Table 1.

These parameters were decided by considering the acoustic attenuation in the medium, the spatial resolution, and the card speaker characteristics [7]. The signal received by microphones (B&K, Type4939) is amplified and filtered by a high-pass filter with a cutoff frequency of 10 kHz, then digitized at a sampling rate of 250 kHz. Figure 1(a) presents the configuration of an experiment in an indoor space. The targets are five stainless-steel pipes 13 mm in diameter, and they are located between 1 and 2 m from the microphones and allocated in the measurement space shown in Fig. 1(a). All experiments were performed at stable room temperatures. Distance is calculated by using the speed of sound and the travel time. An approximate speed of sound, c (m/s) can be calculated as

Table 1. Characteristics of the transmitted signal.

carrier frequency f_0	25 kHz
digital length	3 cycles of 25 kHz = 0.12 ms
sequence length L	1023 digits (122.76 ms)
transmission length	3 (sequence periods = 368.28 ms)

$$c = 331.5 + 0.6 \times T_c \tag{1}$$

where T_c is the temperature in degrees Celsius.

2.2 Estimating Arrival Directions

It is possible to estimate the arrival direction of signals by using the travel time difference and/or the phase difference of the signals received at two microphones. Figure 1(b) illustrates the configuration of receivers for measuring the arrival direction. The arrival direction can be measured more precisely by using phase information. An arrival direction $\theta(t)$ can be calculated by using

$$\theta(t) = \arcsin \frac{\lambda}{2\pi d} \Delta\phi(t) \tag{2}$$

where λ is the wavelength, d is the spacing of two microphones, and $\Delta\phi(t)$ is the phase difference of the two received signals [8]. We used two microphones arranged vertically, and the distance between the two microphones was 7 mm.

(a) Configuration of objects   (b) Arrival direction of acoustic signals
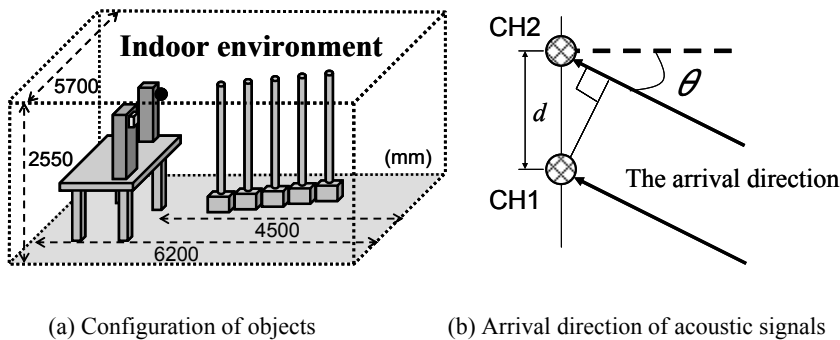
Figure 1. Measurement environment.

3.   RESULTS AND DISCUSSION

3.1   Estimating Arrival Directions

Figure 2 presents the result of measuring and estimating the arrival direction. Signals reflected from a target are shown in Fig. 2(a,b). The estimated arrival direction is shown in Fig. 2(c). The signal reflected from a target is recognized at 128.8 ms. The direction of arrival of sound from a target is estimated to be 0 deg, which means that the sound comes from a horizontal direction. The M-sequence signal facilitates both detecting the small objects and measuring the arrival direction.
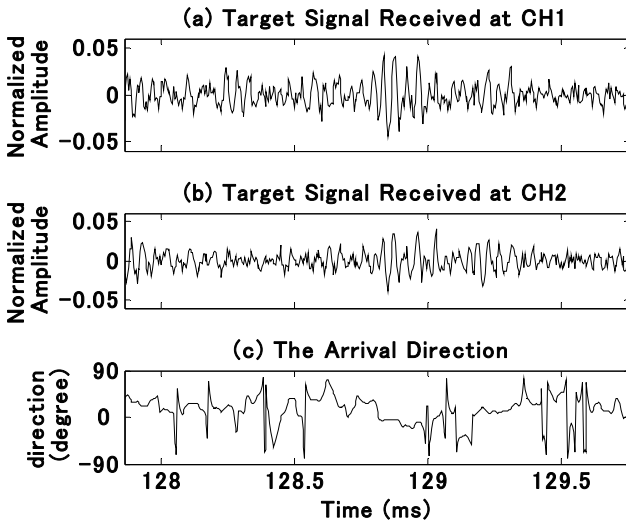
Figure 2. Measuring the arrival direction.

3.2   Acoustic Imaging Using M-Sequence Signal

For accurate validation, we made an image of the circumference of space by applying a simple acoustic imaging method for impulse sound [9]. To make the image, we captured reflected signals while moving the microphone horizontally in 10 mm increments from 0 to 300 mm.

Figure 3(a) depicts the acoustic images of targets by using signals acquired while moving a microphone horizontally every 10 mm from 0 to 300 mm. The origin of the imaging area agrees at the initial position of the moving receiver. A range of 2000 mm ($x = -1000$ to 1000 mm) × 2000 mm ($y = 400$–2400 mm) is imaged in this figure. This measurement configuration is equivalent to a one-dimensional array, in which the vertical

directivity of each element is broad. In the acoustic image, reflections from the ceiling and the floor around (–200, 1400) are also included as well as five targets located from (0, 1000) to (250, 2000) with equal spacing. The small objects were localized by using an M-sequence signal. Because reflections from the ceiling and the floor are strong, the image intensity of targets is relatively weak.

3.3   Imaging of the Selected Directional Response

Removing signals of the ceiling and/or floor in Fig. 3(a) requires resolution in the vertical direction. Three-dimensional space can be imaged by using a two-dimensional array, but the system becomes complicated and is a problem in practical use. The signals from the ceiling and/or the floor arrive at the microphone from a vertical direction, which differs from the direction of targets. We used the arrival angle in the vertical direction to remove the images of the ceiling and/or the floor.

It was confirmed that the arrival direction of the received signal can be acquired by using two microphones, and so we made an acoustic image by using two microphones arranged vertically. Two vertically configured microphones were moved horizontally in 10 mm increments from 0 to 300 mm. We can calculate the arrival direction of reflected sound from a pair of correlated results of two received M-sequence signals, as shown in Fig. 3.

Figures 3(b–d) present images constructed by considering the vertical arrival direction. Figure 3(b) shows the generated image using signals arriving from –30 degrees to 30 degrees in the vertical direction. The signals from the targets are emphasized by suppressing the signal from the ceiling and/or the floor.

Figure 3(c) shows an image produced using signals that come from less than –30 degrees in the vertical direction. Figure 3(d) shows the image using signals that come from greater than a 30-degree vertical direction. Comparison with the real environment confirmed that white dots around (–200, 1400) in Fig. 3(c) were signals reflected from the ceiling and that the responses in Fig. 3(d) were the floor and the aliasing image of the ceiling.

Using an M-sequence signal and the arrival direction information, the positions of small objects could be detected in an indoor environment.

4.   CONCLUSIONS

In this study, we presented results of target detecting small objects by using an M-sequence signal and phase information of the received signals in a noisy indoor environment. By using an M-sequence signal, it was we were

able to measure the reflected waves, which stably that could not be detected by using a conventional impulsive signal. We could precisely acquire the arrival direction of sound in the vertical direction precisely by using the phase information measured by multiple microphones. Small targets could be detected in the images which were generated from the extracted signals without unwanted signals.

(a) original

(b) $-30° \leqq \theta \leqq 30°$

(c) $30° < \theta$

(d) $\theta < -30°$
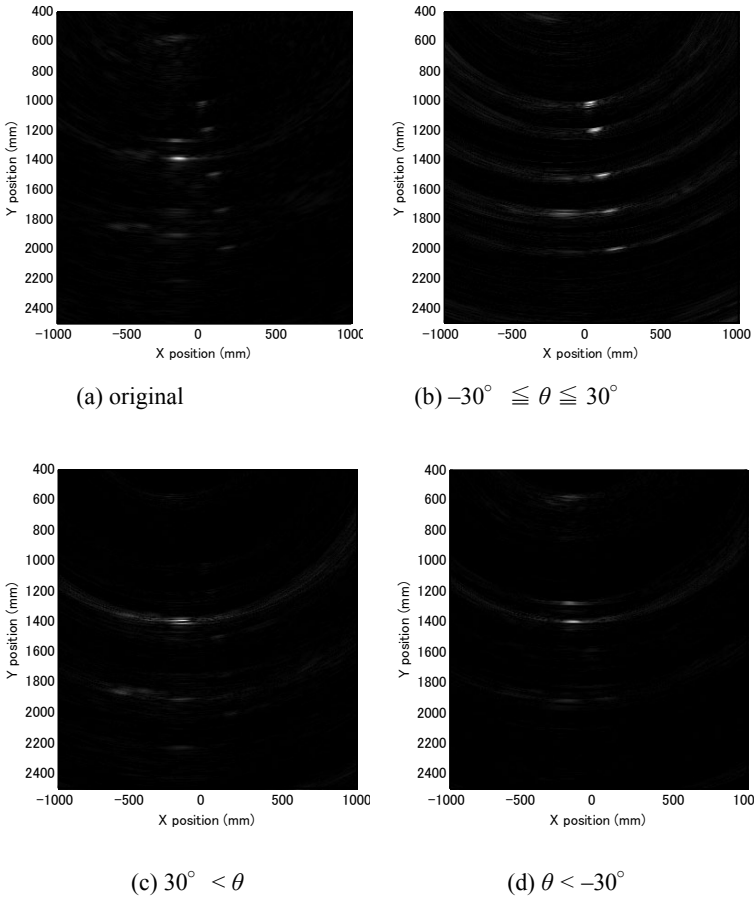
Figure 3. Acoustic image of indoor environment.

REFERENCES

1. K. Mizutani, S. Kawabe and H. Masuyama: Jpn. J. Appl. Phys. **45** 4516–4520 (2006).
2. D. D. Sukmana and I. Ihara: Jpn. J. Appl. Phys. **45**, 4534–4540 (2006).
3. K. Sasaki, M. Nishihira and K. Imano: Jpn. J. Appl. Phys. **45** 4560–4564 (2006).
4. J. A. Jiménez, M. Mazo, J. Ureña, E. Santiso et al.: IEEE Trans. Robot. **21**, 909–924 (2005).
5. T. Nakamura, I. Nakano, K. Metzger1 et al.: Jpn. J. Appl. Phys. **39**, 3193–3194 (2000).

6. Y. Wang, H. Hachiya, T. Nakamura and H. Fujimori: Jpn. J. Appl. Phys. **44,** 4729–4733 (2005).
7. K. Nishihara, T, Yamaguchi and H. Hachiya: Proc. 27th Symp Ultrasonic Electronics, 387–389 (2006)
8. Y. Wang, H. Hachiya, T. Nakamura and H. Fujimori: Jpn. J. Appl. Phys. **42**, 3206–3211 (2003).
9. M. Okujima, N. Endoh and T. Murotani: J. Acoust. Soc. Jpn. **33**, 515–523 (1977).

GEOPHYSICS AND UNDERWATER IMAGING

COMPARISON OF SOME ASPHERICAL CURVED SURFACES OF A SINGLE BICONCAVE ACOUSTIC LENS SYSTEM FOR AMBIENT NOISE IMAGING

K. Mori, H. Ogasawara, T. Nakamura

Department of Earth and Ocean Sciences, National Defense Academy of Japan, 1-10-20 Hashirimizu, Yokosuka, Kanagawa 239-8686, Japan

Abstract: Ambient Noise Imaging (ANI) is a revolutionary method for detecting silent objects using the ocean's background noise. In this study, a sound field focused by an acoustic lens system constructed with a single biconcave lens was analyzed using the 2-D Finite Difference Time Domain (FDTD) method in order to design an ANI system. The −3dB areas and relative pressure level at image points were surveyed using lenses with some aspherical curved surfaces, such as popular aspherical lenses (elliptical, parabolic, and hyperbolic) and an aplanatic lens. The analysis results indicate that the effects of both spherical and coma aberrations were corrected by the aplanatic lens.

Key words: Ambient noise imaging, Biconcave acoustic lens, Aspherical lens, Aplanatic lens, Spherical and coma aberrations, FDTD method

1.   INTRODUCTION

Much attention has been paid to a new approach for detecting silent target objects through the use of ocean ambient noise. This concept is called "Ambient Noise Imaging (ANI) [1–3]". Since an acoustic lens system does not require a large receiver array or a complex signal processing unit for forming a two-dimensional beam, such a system can be minimized, thus reducing ANI system costs. The authors analyzed the sound field focused by an acoustic lens system comprised of a single spherical biconcave lens using

the Finite Difference Time Domain (FDTD) method for designing an ANI system. In our previous study, we performed an analysis to determine the size of the lens aperture. At an aperture and radius of curvature of 2.0 m, −3 dB areas, which have less than the maximum pressure at the image point, do not practically overlap with each other at all incident angles. Therefore, a lens with an aperture size of 2.0 m has sufficient resolution to realize an ANI system; for example, the beam width is 1 deg at 60 kHz [4,5].

This study compares some aspherical curved surfaces of a single biconcave acoustic lens as part of the design process of an ANI system. Here, the effects of spherical and coma aberrations are surveyed by observing the −3 dB areas and the relative pressure levels of image points obtained using the 2-D FDTD method.

2.   POPULAR ASPHERICAL LENSES

This study employs the 2-D FDTD method developed by Iijima et al. [6] The analysis domain and the surface curves of a popular aspherical biconcave lens are depicted in Fig. 1. The analysis domain is the area bounded by the absorption layer (Fig. 1(a) in gray). The straight-line source (dotted line) at the bottom radiates a plane wave whose waveform is a Gaussian-windowed sine wave of 5 cycles at 60 kHz. The acoustic lens, which has an aperture and radius of curvature of 2.0 m and a center thickness of 25 mm, is arranged above the source, perpendicular to the y-axis. The material of the lens is acrylic resin. The sound pressure fields are obtained by changing the angle of incidence $\theta = 0,1,\cdots,15$ deg using the 2-D FDTD method. The details of the analytical conditions are the same as those of our previous studies [4,5]. Popular aspherical curved surfaces are defined as follows:

$$y = y_0 + \frac{sh^2}{1 + \sqrt{1 - (K+1)s^2h^2}}, \quad h^2 = (y - y_0),$$

where $s=1/R$ is the reciprocal of the radius of curvature R, and (x_0, y_0) is the origin. Here, each curve, which is spherical at $K=0$, elliptical at $K=-0.5$, parabolic at $K=-1$, and hyperbolic at $K=-2$, as shown in Fig. 1(b), where R is 2.0 m. The analytical results of spherical and popular aspherical lenses are presented in Fig. 2. We can see that the neighboring −3 dB areas of the spherical lens do not overlap, as depicted in Fig. 2(a) and (b). Therefore, a lens with an aperture size of 2.0 m provides sufficient resolution. As compared with Fig. 2(b), the −3 dB areas at small angles of incidence (<4 deg) are narrow, and the gaps between each −3 dB area at each adjacent

angle of incidence are wide, as seen in Fig. 2(c–e). This demonstrates that popular aspherical lenses correct the spherical aberration. However, the −3 dB areas at large angles of incidence (>10 deg) are wider than that of the spherical lens, and there are many overlaps, as illustrated in Fig. 2(c–e). It is suggested that the coma aberration has an undesirable effect on popular aspherical lenses. The relative pressure level at the image point is presented in Fig. 2(f). We can see that the pressure levels of popular aspherical lenses at small angles of incidence (<4 deg) are greater than that of the spherical lens but that the levels at large angles of incidence (>6 deg) are small. Again, it is suggested that popular aspherical lenses improve convergence by correcting the spherical aberration at small angles of incidence. However, the levels at large angles of incidence are reduced by the coma aberration.

3.   APLANATIC LENS

An absolutely aplanatic lens must satisfy the following three conditions. First, both surfaces of the lens are aspherical. Second, the lens must satisfy "the principle of equal optical path" in order to completely concentrate rays of normal incidence. The principle of equal optical path means that the optical paths of all rays are equal when they originate at the same source, even if they refract at any surface. In the present case, this includes any optical paths equal to the central optical path because all rays are focused at the same point. Third, "Abbe's sine-condition" must be satisfied for all points of incidence. A coma aberration is removed in a paraxial area when Abbe's sine-condition is satisfied without a spherical aberration.

(a) Analysis domain
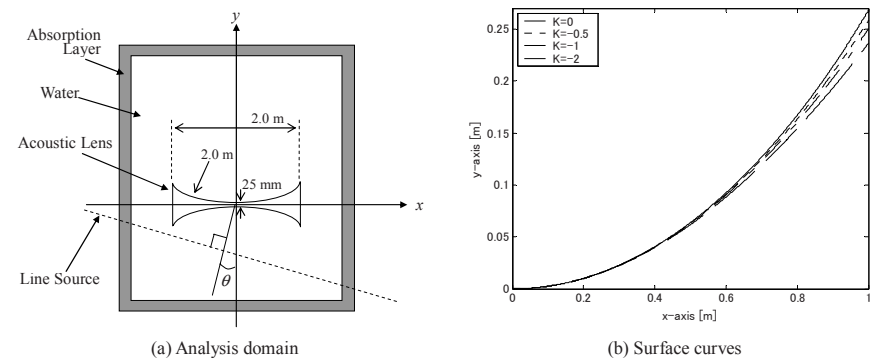
(b) Surface curves

Figure 1. Analysis domain and surface curves of popular aspherical biconcave lens.

(a) −3 dB area for the entire analysis domain of spherical lens (*K*=0)

(b) Magnification of the image point area of spherical lens ('*': image point, gray color zone: −3 dB area)

(c) Elliptical lens (*K*=−0 5)

(d) Parabolic lens (*K*=−1)

(e) Hyperbolic lens (*K*=−2)

(f) Relative pressure level at image point
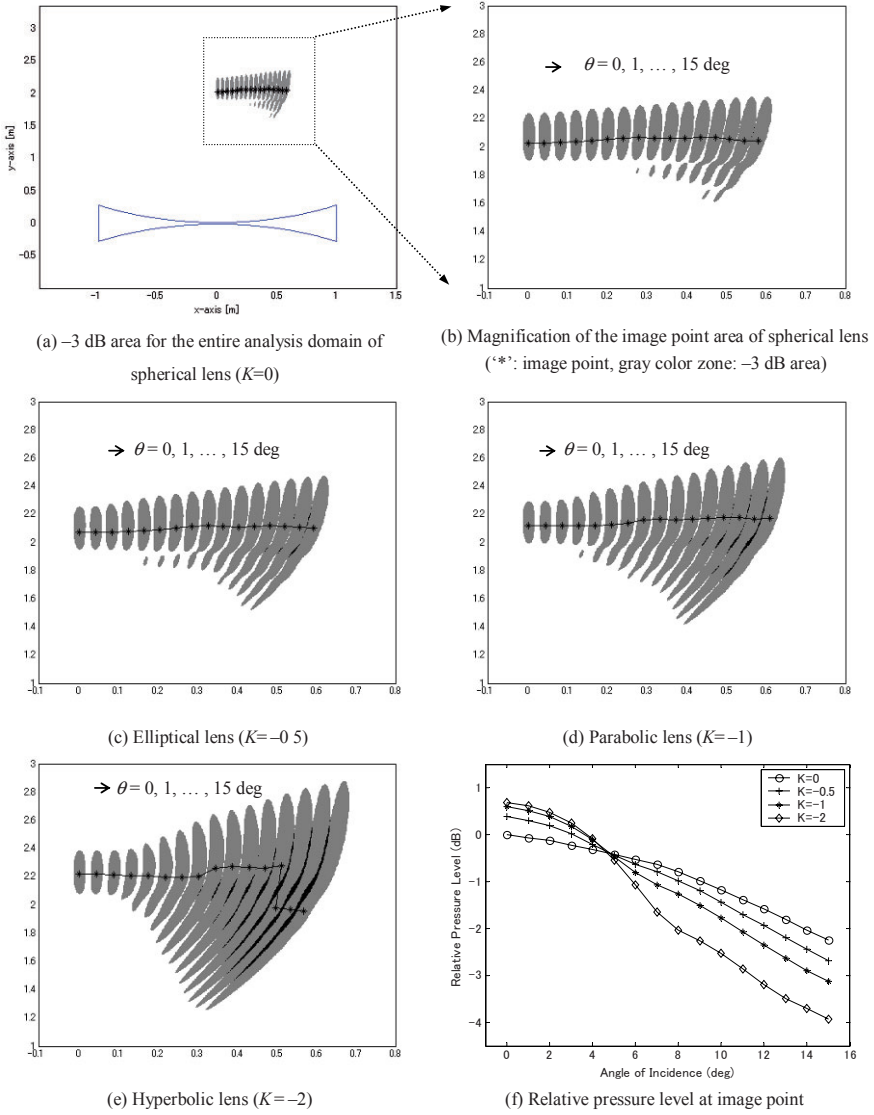
Figure 2. −3 dB area and relative pressure level at image point using popular aspherical lenses.

Yoshida [7] developed a numerical method for designing aplanatic lenses that satisfy the above three conditions for optical convex lenses. Sato et al. applied this method to design an acoustic aplanatic lens. They evaluated the convergence characteristics of the biconcave and biconvex aplanatic acoustic lenses analyzed using the ray path and the sound pressure distribution

obtained by the 2-D FDTD method [8]. The present study also uses this method to design the aplanatic lens for the ANI system.

The results of the analysis of the aplanatic lens are plotted in Fig. 3. The lens's shape is illustrated in Fig. 3(a). Here, the aperture is 2.0 m and the focal length is also 2.0 m. We can see that the neighboring −3 dB areas of the aplanatic lens do not overlap, as shown in Fig. 3(b). Additionally, as compared with Fig. 2(b–e), the −3 dB areas at all incident angles are narrow, and the gaps between each −3 dB area at each adjacent incident angle are wide, as shown in Fig. 3(b). This suggests that the aplanatic lens corrects both the spherical and coma aberrations. The relative pressure level at the image point is plotted in Fig. 3(c). We can see that the pressure levels of the aplanatic lens at all angles of incidence are greater than those of the spherical lens. In addition, the level of the aplanatic lens at 15 deg is down to only 1 dB as compared with approximately 2 dB of the spherical lens. Again, the aplanatic lens improves the convergences by correcting the spherical and coma aberrations at all angles of incidence.

(a) lens shape

(b) −3 dB area

(c) Relative pressure level at image point
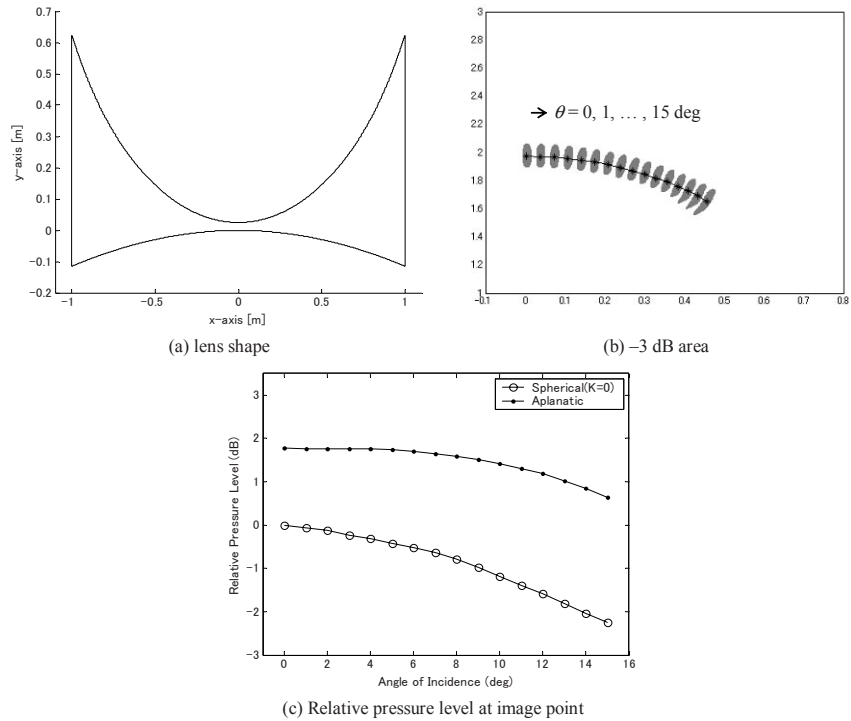
Figure 3. −3 dB area and relative pressure level at image point of aplanatic lens.

4. CONCLUSION

This study compared some aspherical curved surfaces of a single biconcave acoustic lens in the design of an ANI system. In popular aspherical lenses, the results demonstrated that the convergence characteristics are improved by correcting the spherical aberration at only small angles of incidence. However, the results at large angles of incidence were not improved; rather, they were worsened by the coma aberration. In contrast, the results of using the aplanatic lens, in which both spherical and coma aberrations are corrected, were better than those employing popular aspherical lenses. We conclude that the aplanatic lens is a strong candidate for use in an ANI system.

ACKNOWLEDGEMENTS

REFERENCES

1. M. J. Buckingham, B. V. Verkhout and S. A. L. Glegg, Imaging the Ocean with Ambient Noise, *Nature* **356**, 327–329 (1992).
2. C. L. Epifanio, J. R. Potter, G. B. Deane, M. L. Readhead and M. J. Buckingham, Imaging in the Ocean with Ambient Noise: the ORB Experiments, *J. Acoust. Soc. Am.* **106**(6), 3211–3225 (1999).
3. P. Venugopalan, M. A. Chitre, E. T. Tan, J. Potter, K. T. Beng, S. B. Ruiz and S. P. Tan, Ambient Noise Imaging – First Deployments of ROMANIS and Preliminary Data Analysis, *Proc. Oceans 2003 Marine Technology and Ocean Science Conf., San Diego, USA, Sept. 22–26*, CD-ROM (2003).
4. K. Mori, A. Miyazaki, H. Ogasawara, T. Yokoyama and T. Nakamura, FDTD Analysis of Underwater Acoustic Lens System for Ambient Noise Imaging, *Jpn. J. Appl. Phys.*, **45**(5B), 4834–4841 (2006).
5. K. Mori, A. Miyazaki, H. Ogasawara, T. Yokoyama and T. Nakamura, Numerical Analysis of an Underwater Acoustic Lens System for Ambient Noise Imaging using Finite Difference Time Domain Method, *IEEE Oceans '06 Asia Pacific Conf. Proc., Singapore, May 16–19*, CD-ROM (2006).
6. F. Iijima, T. Tsuchiya and N. Endoh, Analysis of Characteristics of Underwater Sound Propagation in the Ocean by a Finite Difference Time Domain Method, *Jpn. J. Appl. Phys.*, **39**(5B), 3200–3204 (2000).
7. S. Yoshida, Calculations Concerning Aspheric Aplanatic Lens with Exceptionally Large Aperture Ration. III, *Bull. Res. Inst. Sci. Meas., Tohoku University*, **6**(3), 123–144 (1958). (in Japanese).
8. Y. Sato, A. Miyazaki, K. Mori and T. Nakamura, Design of an Absolutely Aplanatic Acoustic Lens, *Jpn. J. Appl. Phys.*, **46**(7B), 4982–4989 (2007).

UNDERGROUND IMAGING USING SHEAR WAVES

Resolution improvement using pulse-compression processing

H. Kawasaki, T. Sugimoto

Department of Electronics and Information Engineering, Toin University of Yokohama, 1614, Kurogane-cho, Aoba-ku, Yokohama 225-8502, Japan

Abstract: A method using shear waves has been proposed to detect buried relics and ruins at shallow depths. Pulse-compression processing is examined for improving the underground imaging resolution. Both down-chirp signals (600–300 Hz) and 1 kHz burst signals can be generated using a super-magnetostriction vibrator as a sound source. First, pulse compression is simulated in the lab to confirm the resolution of underground images. Exploration experiments were then conducted at Heijyo-kyo in ancient Nara. The underground images are obtained from these experiments. We confirmed the effectiveness of the pulse-compression method for improving resolution.

Key words: Shear wave, Super-magnetostriction vibrator, Pulse compression, Chirp wave

1.   INTRODUCTION

An electrical method using a metal detector and an electromagnetic method using a ground-penetrating radar (GPR) have been widely used to detect buried relics. However, in marshes or swamps where the moisture content is high, electric and electromagnetic signals are strongly attenuated by the presence of water and electrolytes. In order to overcome this problem, a method using shear waves [1,2] has been proposed to find buried objects through underground imaging.

In our past research, a hammer method, in which a sound source is hit directly by a hammer, was used for making underground images. Although this method is easy to use, improving the underground image's resolution is difficult because the frequency and the waveform cannot be changed

arbitrarily. However, a super-magnetostriction vibrator [3] can change the frequency and the waveform easily at low frequencies (0–3 kHz). This characteristic is beneficial in our experiment. Therefore, we employ a super-magnetostriction vibrator as a sound source instead of a hammer. Two methods are considered for improving the resolution of underground images using this vibrator, using high frequency and using pulse compression. Pulse compression [4] is widely applied for radar and modulation signals such as M-sequence; FSK and chirp signals are used for pulse compression. We employ chirp signals applied by a Hanning window function for smooth movement of the vibrator.

We first simulated pulse compression in the lab to confirm the resolution of underground images. An exploration experiment was then conducted at Heijyo-kyo in ancient Nara. The underground images are made by stacking reflected scattered waves [1].

2. SIMULATION EXPERIMENT

2.1 Experimental Set-up
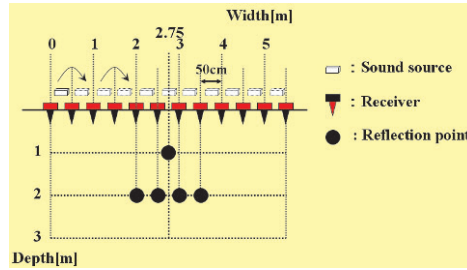
Figure 1. Simulation set-up for underground imaging.

Twelve receivers are arranged in line at 50 cm intervals on the ground. A sound source is moved between adjacent receivers (Fig. 1). To obtain a single image resolution, the reflection point is set at 1 m depth. Four reflection points are also set at 2 m depth at 50 cm intervals for comparison.

Two types of output signals are used in this simulation, an ordinary burst signal with a frequency of 1 kHz at 10 cycles and a down-chirp signal that oscillates from 600 to 300 Hz (duration 100 ms). A Hanning window function is applied to the output signal.

The propagation signals are assumed to be shear waves, and the speed of sound is assumed to be 140 m/s. The virtual reflection point is decided and the propagation distance is calculated. Delay time is calculated from the propagation distance. Gain was inversely proportional to the square of the propagation distance in consideration of damping. The computational simulation is shown in Eq. (1) and Fig. 2.

$$S_r(t) = S_{out}\left(t - \frac{d1 + d2}{v}\right) \times \frac{1}{(d1 + d2)^2} \qquad (1)$$

Here, *Sr* is defined as the received signals, S_{out} represents output signals, *v* is the speed of sound, *t* is time, *d*1 is distance from a sound source to a reflection point, and *d*2 is the distance from a reflection point to a receiver.
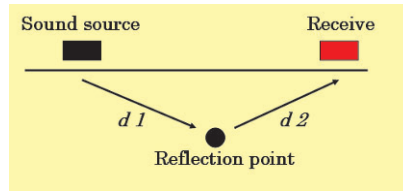
Figure 2. Simulation method.

2.2   Simulation Results

Two simulated images were made. One image is made by 1 kHz received signals, and the other, by pulse-compression processing. A simulation image produced by the hammer method is made for comparison. A frequency of 200 Hz at 5 cycles is used in the hammer method. Simulated images are presented in Fig. 3.
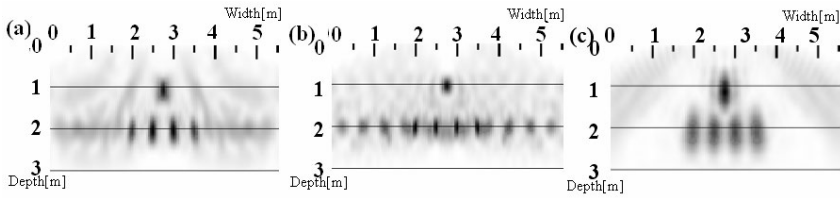
Figure 3. Images made by simulated signals. (**a**) Simulation by pulse-compression processing. (**b**) Simulation by 1 kHz at 10 cycles. (**c**) Simulation by 200 Hz at 5 cycles. (The hammer method is assumed.)

As illustrated in Fig. 3, the image produced by pulse compression and the image produced by 1 kHz signals have much better resolution than the image produced by the hammer method (Fig. 3(c)). However, feather-shaped lines appear on both sides of the reflection point on the line 1 m in depth in Fig. 3(a) and (b). On the 2 m line in Fig. 3(a) and (b), the feather-shaped lines accumulate and look like virtual images that appear near the assumed points. The image produced by 1 kHz signals seems to be more influenced by feather-shaped virtual images than the image produced by pulse compression.

Similar feather-shaped lines also appear in the image produced by the hammer method, but they are outside of the frame because of the broad wavelength. The feather-shaped lines are due to the method of stacking the reflected scattered waves.

3.   EXPLORATION EXPERIMENT

3.1   Experimental Set-up

To confirm the underground image's resolution, exploration experiments were conducted at Heijyo-kyo in ancient Nara. The experiment setup is the same as in the simulation experiment. A super-magnetostriction vibrator (Moritex Corp, AA140J013-MS1) is used as a sound source, and twelve geophones are used for receivers. The output signals were the same as in the simulation experiment.

First, the output signals are generated from the super-magnetostriction vibrator. Next, the phase of the output signals is reversed and the received waves are reversed again. Finally, in order to emphasize the shear waves, the

waveform of the received signal and the waveform of the reversed received output signal are added. Underground images are produced by using a stacking method of the reflected scattered waves. Generated sound waves are recorded simultaneously in a digital seismograph (Oyo Corp, McSEIS-SX, MODEL-1125R).

3.2   Signal Processing

The waveform of the received chirp signal is depicted in Fig. 4(a), and that of the received 1 kHz signals is depicted in Fig. 4(d).   The received waveforms are filtered because there is much electric noise in low frequencies. The chirp signal is filtered by a 300–600 Hz band-pass filter as illustrated in Fig. 4(b). The 1 kHz signal is filtered by a 800–1200 Hz band-pass filter as depicted in Fig. 4(e). The original output waveforms are overlapped in the filtered waveforms. To separate the overlapped original waveforms, the correlation function is applied for pulse compression. The resultant waveform is presented in Fig. 4(c); the pulse duration is compressed, and the overlapped signals are separated.
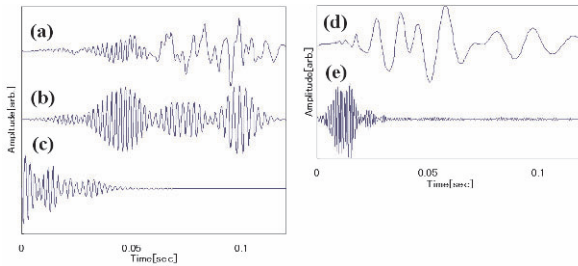
Figure 4. Examples signals after signal processing. (**a**) Received chirp signal. (**b**) Filtered chirp signal. (**c**) Waveform produced by pulse compression. (**d**) Received 1 kHz signal. (**e**) Filtered 1 kHz signal.

3.3　　Experiment Result
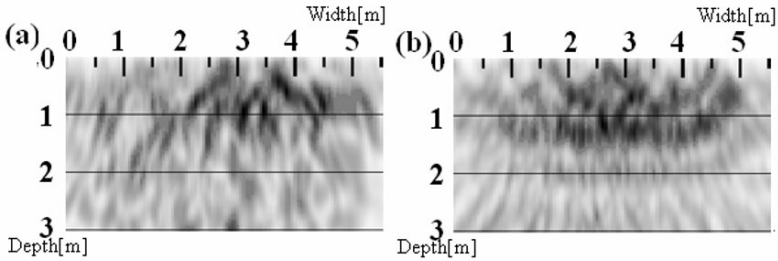
Figure 5. Example of underground images. (**a**) Underground image produced by pulse compression. (**b**) Underground image produced by received 1 kHz.

We produced two underground images in the exploration experiment, one by pulse compression and the other by received 1 kHz burst signals. These images are presented in Fig. 5. The speed of the shear wave is assumed to be 140 m/s.

Strong signals appear at almost the same positions in Fig. 5(a) and (b). The 1 kHz signals produce more strong signals the underground image than the pulse-compression method. It seems that feather-shaped virtual images in Fig. 3 influence the image produced by 1 kHz signals more than the image produced by pulse compression.

4.　　CONCLUSIONS

The simulation result clarified that the 600–300 Hz down-chirp signals using the pulse-compression method had almost the same resolution as 1 kHz, 10-cycle burst signals. However, it is necessary to solve the problem of virtual images in the resultant images. We think that our stacking method causes this problem.

By using a super-magnetostriction vibrator as a sound source, we confirmed that chirp and 1 kHz signals could be transmitted in shallow underground areas. In the exploration experiment in Heijyo-kyo, ancient Nara, strong signals appear at the same positions in the images produced by pulse compression and the images produced by 1 kHz at 10 cycles.

From these result, it seems that the images produced by pulse compression have almost the same resolution as the image produced by 1 kHz signals in those experiments. We confirmed the validity of the pulse-compression method for resolution improvement of underground images.

This time, we could not verify our experiment results by seeing what had actually been buried, because an excavation of the site has not yet been conducted. Therefore, the next experiment will be scheduled at a site where the buried object and position has already been revealed.

ACKNOWLEDGEMENTS

REFERENCES

1. T. Sugimoto and M. Okujima, Jpn J. Appl. Phys. Vol. 35, pp. 3105–3108 (1996).
2. T. Sugimoto, H. Saitou and M. Okujima, Archaeological Prospection Vol. 7, No. 4, pp. 249–261 (2000).
3. M. Moriya and T. Sugimoto, Jpn J. Appl. Phys. Vol. 41, pp. 3501–3502 (2002).
4. Earth Remote Sensing Data Analysis Center (ERSDAC), SAR processing algorithm description(2005, in Japanese).

HIGH-SPEED VORTEX WIND VELOCITY IMAGING BY ACOUSTIC TOMOGRAPHY

H. Li, T. Ueki, K. Hayashi, A. Yamada

Graduate School of Bio Applications & Systems Eng., Tokyo University of Agriculture & Technology, Koganei, 184-85-88, Japan

Abstract: A technique for monitoring strong vortex wind fields is highly desired due to the rapid development of global warming. Vortex wind velocity imaging using an acoustic travel time tomography technique was developed to meet this need. The method can be implemented with a small number of parallel facing pairs of acoustic transmitters/receivers from just a single illumination view direction, so that high-speed data acquisition compatible with instantaneous wind-flow imaging was accomplished. A test using an indoor wind velocity tomography system demonstrated that vortex wind velocity profiles generated by an electric fan could be instantaneously reconstructed with satisfactory quantitative precision.

Key words: Wind velocity tomography, Acoustic imaging of vortex air flow, Acoustic travel time tomography, Monitoring of strong wind field

1.   INTRODUCTION

With the escalation of the global warming, local strong wind disasters like tornados have been increasing yearly [1]. Hence, development of remote sensing techniques to measure the spatial and temporal wind distribution, including vortex wind flow, is much in demand. An acoustic tomographic imaging technique [2,3,4] can reconstruct two-dimensional wind velocity vector distributions based on the acoustic travel time observation data around the target medium. Since the technique is based on remotely measured data around the medium, it is not necessary to place the sensors in atmospheric medium. This characteristic is helpful when the method has to

be used in inaccessible regions, which is often the case for outdoor monitoring sites. The realization of the technique is, therefore, expected to satisfy the above need. The method presented by Norton [2] promises the quantitative reconstruction of the vortex wind field. It is based on the combination of the two-dimensional approximation of the flow field and its Helmholtz decomposition into the vortex and vortex-free component. However, we encounter a problem when applying the method to outdoor wind-flow monitoring, due to the necessity of a great number of densely arranged transducers to pick up the violent variations of the vortex field.

This paper presents a novel acoustic tomographic method [5] capable of quantitative wind velocity reconstruction as well as high-speed data acquisition. The technique assumes that the wind field consists of a single vortex component, so as to enable image reconstruction from a set of single-view observation data. To verify the validity of the method, an indoor wind velocity tomography system was fabricated with a parallel arrangement of facing pairs of transmitters and receivers along opposite sides of a square target region. It will be demonstrated that vortex wind velocity profiles generated by the wind source (fan) can be instantaneously reconstructed with satisfactory quantitative precision.

2. FORMULATION OF ACOUSTIC WIND VELOCITY TOMOGRAPHY

Let us denote the wind velocity vector field in the (x, y) two-dimensional plane as $\mathbf{v}(x, y)$ and the sound velocity scalar field as $c(x, y)$. We assume here that the absolute value of $\mathbf{v}(x, y)$ and the sound speed variation $\Delta c(x, y)$ $(=c(x, y)-c_0)$ are much smaller than the average sound velocity c_0 in the medium: i.e., $|\mathbf{v}(x, y)|, |\Delta c(x, y)| \ll c_0$. We collect travel time t_{ab} between transmitter a and receiver b. We also collect travel time t_{ba} in the opposite direction between transmitter b and receiver a. The travel time difference T_{ab} between t_{ab} and t_{ba} is then related with the wind velocity field of the medium $\mathbf{v}(x, y)$ according to the following equation:

$$T_{ab} = t_{ab} - t_{ba} \approx -\frac{2}{c_0^2} \int_a^b \mathbf{v} \cdot \mathbf{n}\, dl \, , \tag{1}$$

where dl is the line element on a straight-line path and $\mathbf{n}$ is its unit vector. Equation 1 represents the path-integral equation with respect to vector field $\mathbf{v}$. To reduce it to a simpler conventional scalar field equation, we decompose the vector field $\mathbf{v}$ into the sum of scalar potential Φ (irrotational

component) and vector potential $\mathbf{\Psi}$ (solenoidal component) as $\mathbf{v} = \nabla\Phi + \nabla\times\mathbf{\Psi}$. Here, we consider the case when the wind-speed profile is varied only in the (x, y) two-dimensional plane. On that basis, vector potential $\mathbf{\Psi}$ is considered having only z-component Ψ, i.e., $\mathbf{\Psi} = \Psi\hat{\mathbf{z}}$. As a result, Eq. (1) can be rewritten as,

$$T_{ab} \approx -\frac{2}{c_0^2}\int_a^b \nabla\times\mathbf{\Psi}(x,y)\cdot\mathbf{n}\,dl \ . \tag{2}$$

Equation (2) means that travel time T_{ab} contributes only vortex components $\mathbf{\Psi}$ and is represented by straight line path integral of $\nabla\times\mathbf{\Psi}$. Based on the formula described by Eq. (2), we consider a tomographic problem for the solution of the two-dimensional flow vector $\mathbf{v}(x,y)$ $(=\nabla\times\mathbf{\Psi})$ by obtaining the travel time data T_{ab} along various paths around the medium.

Equation (2) can be solved by applying the Fourier central slice theorem for the vector field, which is a straightforward extension of that for the conventional scalar field [2]. To show this, we denote the parallel beam set of the travel time data as $T_\theta(\rho)$ along the coordinate ρ at rotational angle θ. A one-dimensional Fourier transform of travel time $T_\theta(\rho)$ with respect to ρ, which is denoted by $T_\theta(k)$, is then related to the two-dimensional Fourier transform of the vector potential $\Psi(u,v)$ as

$$\Psi(u = k\cos\theta, v = k\sin\theta) = -\frac{c_0 T_\theta(k)}{2ik} \ , \tag{3}$$

where u and v are spatial frequencies with respect to x and y coordinates, respectively.
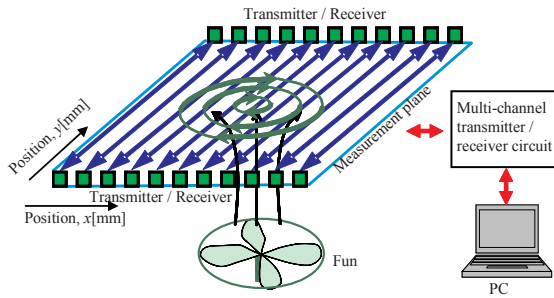
Figure 1. Experimental setup of wind velocity tomography system.

If rotational symmetry is assumed for the wind velocity fields, $T_\theta(\rho)$ becomes constant with respect to θ. Therefore, data $\Psi(u,v)$ is obtained over

the entire Fourier plane from a specified single rotational data $T_\theta(\rho)$. Vector potential $\Psi(x, y)$ is calculated by performing the two-dimensional inverse Fourier transform of the data thus obtained. Finally, objective vortex wind velocity $\mathbf{v}(x, y)$ can be obtained from the rotation operation $\mathbf{v}(x, y) = \nabla \times \Psi(x, y)$.

3.   EXPERIMENT EXAMINATION

3.1   Experimental Setup

We fabricated the acoustic wind velocity measurement system depicted in Fig. 1. Eleven bi-directional transmitter-receiver pairs (Murata: MA40B8 R/S, center frequency 40 kHz) were aligned at intervals of 40mm along opposite sides of a square region (400×400 mm). Pulsed sine signals with a frequency 40 kHz were sent from the transmitters, and transmitted signals were received at the opposite side by facing receivers. Rectified received signals were fed into the comparators to generate the received timing pulses. Time intervals between the sent and received pulses were measured with multi-channel counter circuits with a clock frequency of 10 MHz. To eliminate detection errors and reduce noise, data were measured 30 times at each point. Counted values are transferred to the personal computer (PC). Measurement time to acquire the data for one frame image (for 11-point data acquisition) was 3 s. After the tomographic calculations, wind velocity distributions were displayed on the monitor screen in real time. An electric fan with an aperture diameter of 190 mm was placed facing upward immediately underneath the horizontal measurement plane as a vortex wind source. Wind source velocities were calibrated by a hot-wire anemometer (Fuso Rika: AM-4204) in advance.

3.2   Examination Results

Dependencies of measured travel time $T(x)$ as a function of observation line coordinate x are plotted in Fig. 2. The predetermined wind source velocity, measured by the hot-wire anemometer, was chosen as a parameter. The results reveal the anti-symmetric dependencies with respect to x, having zero at the center $x=0$ and opposite signed peaks at the left and right symmetric positions. This confirms that the circular vortex air flows are formed in the horizontal measurement plane. The measured travel times at 11 discrete coordinate points, as demonstrated in Fig. 2, were interpolated
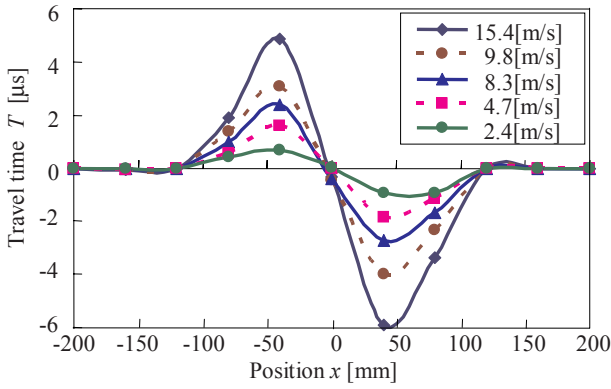
Figure 2. Measured travel time along observation axis transmitted through the vortex wind.
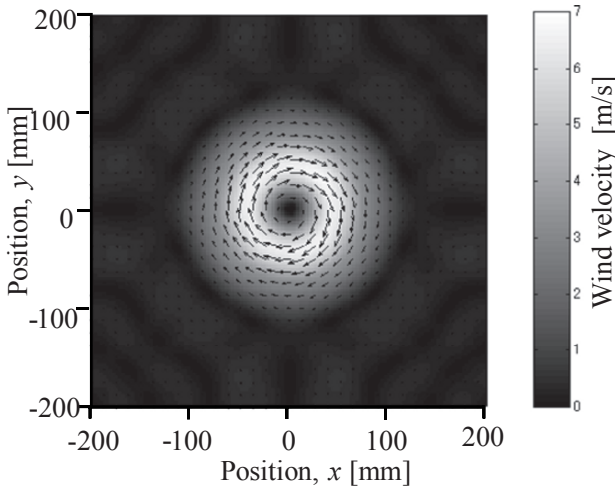
Figure 3. Reconstructed wind velocity vector profile generated by the vortex wind source.

to obtain the data at a continuous position. The reconstruction calculation was made according to the procedure described in Section 2. As a result, the wind velocity distribution $\mathbf{v}(x, y)$ was finally obtained as depicted in Fig. 3. We can see that the size of the wind source and the reconstructed vortex wind velocity field are in good agreement with the prediction. To demonstrate the quantitative precision of the present method, similar reconstructions were made by changing the wind source velocity. Figure 4 plots the reconstructed results of the maximum wind velocity as a function of the predetermined wind source velocity. We can see that the
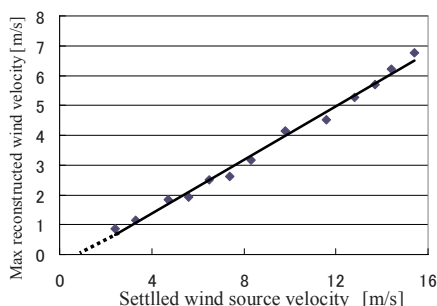
Figure 4. Maximum reconstructed wind velocity as a function of the predetermined source wind velocity.

proportionality between the reconstructed wind velocity peak and predetermined wind velocity is very good, verifying the quantitative precision of the reconstructed wind velocity.

4.   CONCLUSION

A method of imaging the vortex wind velocity profile using acoustic tomography has been presented. Tests with an indoor tomography system demonstrated that vortex air velocity fields could be reconstructed with a high-speed frame rate of 3 s while maintaining satisfactory quantitative precision of the reconstructed vortex wind velocities.

REFERENCES

1.   P.J. Webster, G.J. Holland, J.A. Curry, H.-R. Chang, "Changes in tropical cyclone number, duration, and intensity in a warming environment," Science, vol. 309, pp. 1844–1846, 2005.
2.   S.J. Norton, "Tomographic reconstruction of 2-D vector field: application of flow imaging," Geophys. J., vol. 97, pp. 161–168, 1988.
3.   D.K. Wilson, "An Overview of acoustic travel-time tomography in the atmosphere and its potential applications," ACUSTICA, vol. 87, pp. 721–730, 2001.
4.   P. Beckord, G. HoEfelmann, H.O. Luck, D. Franken, "Temperature and velocity flow fields measurements using ultrasonic computer tomography," Heat and Mass Transfer, vol. 33, pp. 395–403, 1998.
5.   H. Li, K. Hayashi, T. Ueki, A. Yamada, "Imaging of atmosphere wind velocity distribution by acoustic tomography," Meet. J. Acoustic. Soc. Jpn., CD-ROM, 1-8-2, pp. 23, Autumn, 2006.

PHYSICS AND MATHEMATICS

OPTICAL OBSERVATION OF TWO COLLAPSING BUBBLES ADHERING TO A QUARTZ WALL

Influences of bubble-bubble interaction on collapse behavior

K. Yoshida, S. Nakatani, Y. Watanabe

Faculty of Engineering, Doshisha University, 1-3 Tatara-miyakotani, Kyotanabe, Kyoto, 610-0321, Japan

Abstract: The collapse behavior of two bubbles adhering to quartz glass was optically observed to examine the influences of an interactive force called the secondary Bjerknes force on the collapse behavior of bubbles. It was demonstrated that the interactive force deformed bubbles asymmetrically. These deformations induced flow generation and splits of the bubble. Additionally, it was experimentally confirmed that the interactive force acted as an attractive force or a repulsive force. The deformation process of bubbles largely depended on whether an attractive force acted or a repulsive force acted. Moreover, both conditions of an attractive force acting and a repulsive force acting were examined. It was shown that an attractive force acted when the initial radii of two bubbles were larger or smaller than the resonant radius of a free bubble. When one initial radius of the two bubbles was smaller than the resonant radius and the other was larger, a repulsive force acted.

Key words: Ultrasound, Micro bubble, Asymmetrical collapse, Optical observation

1. INTRODUCTION

Bubble collapse phenomena induced by ultrasound irradiation have been applied widely in various fields such as ultrasonic cleaning and ultrasonic therapy technique [1]. One of the most important issues for these applications

is to determine the influences of interaction between bubbles on the bubble behavior. In the theory of bubble dynamics, an attractive force acts between bubbles when two bubbles vibrate in phase. In contrast, a repulsive force acts between bubbles when the phase relationship between two bubbles is opposite. This interactive force is called the secondary Bjerknes force [2] and causes various complex phenomena such as bubble aggregation [3]. Moreover, bubble behavior when an attractive force acts will be largely different from that when a repulsive force acts. However, it is not clear how the interactive force influences the collapsing bubble behavior because there are few reports of experiments on the interaction between bubbles.

Focusing on the interactive force, collapse behavior of two bubbles adhering to a quartz wall under ultrasound irradiation was observed optically. In this paper, collapse behavior occurring under different two conditions is discussed. One condition is when an attractive force acts; the other is when a repulsive force acts. Also, radial conditions of two bubbles for which an attractive force or a repulsive force act are examined.

2.   IMAGING SYSTEM
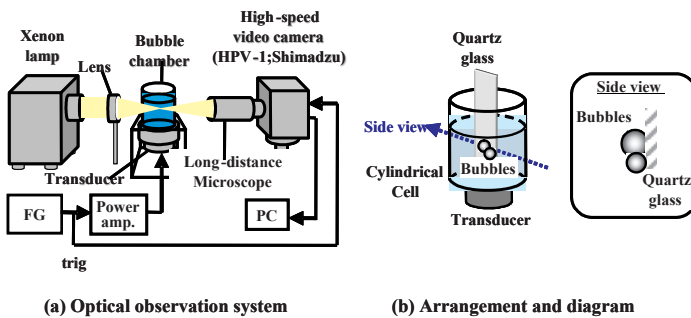
Figure 1. Observation system.

Figure 1 depicts the system for imaging bubble behavior. The Xenon lights used for a back light, the bubble chamber, and the high-speed video camera were arranged linearly. The bubble chamber consists of an acrylic cylindrical cell with a bolted Langevine transducer. A quartz glass was set in the bubble chamber, and two bubbles adhered to the quartz glass. The quartz glass was used to fix the bubbles. Figure 1(b) presents the arrangement of the bubbles, the quartz glass and the bubble chamber. In the condition shown in Fig. 1(b), the bubble behavior under ultrasound irradiation was observed using the shadow graph method. The maximum recording rate of the high-speed video

camera is 1,000,000 frames/sec. Bubble behavior was observed from the side face of the bubble. Figure 1(b) also illustrates diagrams of the images observed from the side view.

The electronic input to the transducer is a 10-cycle sinusoidal signal with a frequency of 27 kHz. Figure 2 plots the time profile of irradiated sound pressure measured with a needle hydrophone. In Fig. 2, the pressure amplitude at about the tenth wave is maximum due to the transition response of the transducer. In this observation, the amplitude of sound pressure at the tenth wave is set to be about 150 kPa.
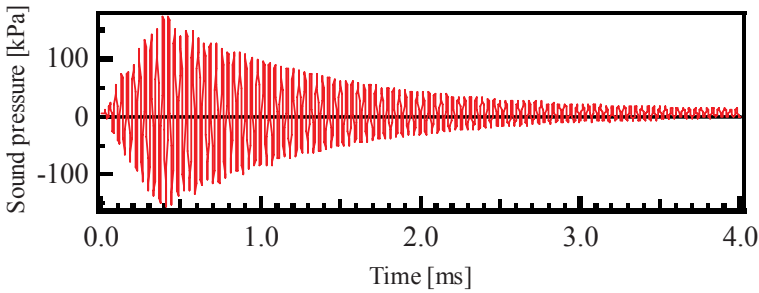
Figure 2. Temporal profile of irradiated sound pressure.

3.   COLLAPSE BEHAVIOR

This section discusses the collapse behavior of two bubbles focusing on the interactive force. The following two observation results were obtained.

Figure 3 displays the observation results when a repulsive force acts between the two bubbles. The initial radius of the larger bubble R_{ol} is 280 μm, and that of the smaller bubble R_{os} is 97 μm. The distance D from the center of a bubble to the other bubble is 491 μm. Figure 3(a) presents the observed images of bubble behavior. The observation timing of the image is overlaid on each image, and the input timing of the electrical signal to the transducer is referred to as 0 sec. Figure 3(b) depicts the temporal profile of S/S_o. S is the shadow area of the bubble in the image, and S_o is the initial area. S/S_o is used to roughly estimate the volume vibration of bubbles. Figure 3(b) confirmed that the relationship of the vibration phase between two bubbles is almost opposite. This opposite-phase vibration indicates that a repulsive force is acting between the bubbles. Figure 3(a) clearly demonstrates that the smaller bubble moves away from the larger bubble. This movement of the smaller bubble clearly indicates that a repulsive force

is acting. We next examine how a repulsive force influences collapse behavior. At 150 µs, the bubble surfaces near the other bubble were deformed locally. This deformation is probably induced by a repulsive force. The smaller bubble was then deformed while vibrating violently. At 246 µs, the extreme deformation caused a split of the smaller bubble. Focusing on the larger bubble behavior, it was observed at 226 µs that the surface on the deformed portion waved. From 226 µs to 314 µs, the waving surface propagated on the bubble surface. This waving surface caused flow generation and the split phenomenon. The flow was clearly observed at 282 µs. Images observed from 226 µs to 282 µs revealed that a flow into the bubble is generated when the bubble wall contracts locally. At 314 µs, the flow finally penetrated the larger bubble. The bubble split is observed at 314 µs, and a very small bubble was emitted near the deformed portion.

(a) Bubble behaviors　　　　　　　　(b) Temporal profile of S/S_o
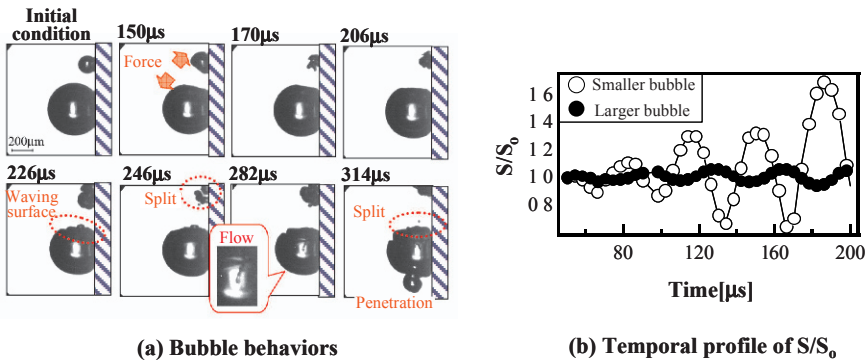
Figure 3. Collapse behavior induced by repulsive force.

Figure 4 depicts the observation results when an attractive force acts between two bubbles. Figure 4(a) presents the observed images of bubble behavior, and Fig. 4(b), the temporal profile of S/S_o. R_{ol}, R_o and D are 235 µm, 231 µm and 525 µm. Figure 4(b) demonstrates that two bubbles vibrate in phase in synchronization with the driving ultrasound, indicating that an attractive force acts between the bubbles. This attractive force makes the bubbles move together. This behavior was clearly observed in Fig. 4(a). From 196 µs to 268 µs, the top portion of each bubble gradually moved toward the other bubble. At 340 µs, the opposite bubble surfaces waved. This waving surface propagated on the bubble surface and generated flow into the bubble. The propagation was observed from 340 µs to 460 µs, and the flow into the bubble was observed at 428 µs.

Comparing these two observation results clearly demonstrates that the bubble deformation process largely depends on whether an attractive force acts or a repulsive force acts.

(a) Bubble behaviors

(b) Temporal profile of S/S$_o$
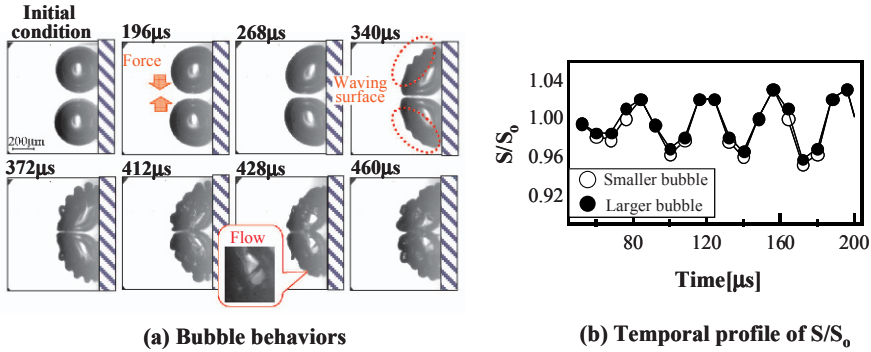
Figure 4. Collapse behavior induced by attractive force.

4. DEPENDENCE OF INTERACTIVE FORCE TYPE ON RADIAL CONDITIONS

The above section confirmed experimentally that the relationship of vibration phases between two bubbles determines whether an attractive force or a repulsive force acts. This section discusses whether the type of interactive force acting between bubbles depends on bubble sizes. In the linear vibration theory of a free bubble, the bubble vibration phase changes drastically at the resonant bubble radius R_{res}. The phase difference between a bubble larger than R_{res} and one smaller than R_{res} is π. It is thus expected that an attractive force will act if the radii of both bubbles are smaller or larger than R_{res}. If the radius of one bubble is smaller than R_{res} and that of the other is larger than R_{res}, a repulsive force will act. The collapse behavior of two bubbles with various bubble radii was observed to examine whether the type of interactive force depends on radii of the two bubbles.

Figure 5 illustrates the dependence of interactive force on initial radii of two bubbles. The vertical axis represents R_{os}/R_{res}, and the horizontal axis, R_{ol}/R_{res}. The blue plots (red plots) represent an attractive force (a repulsive force) acting between bubbles. The black plots represent conditions in which the type of interactive force cannot be identified. Figure 5 demonstrates that these experiment results agree well with the abovementioned theoretical prediction. Namely, an attractive force acts when the radii of R_{ol} and R_{os} are both greater than or smaller than R_{res} (blue region). When R_{ol} is greater than R_{res} and R_{os} is smaller than R_{res} (red region), a repulsive force acts.
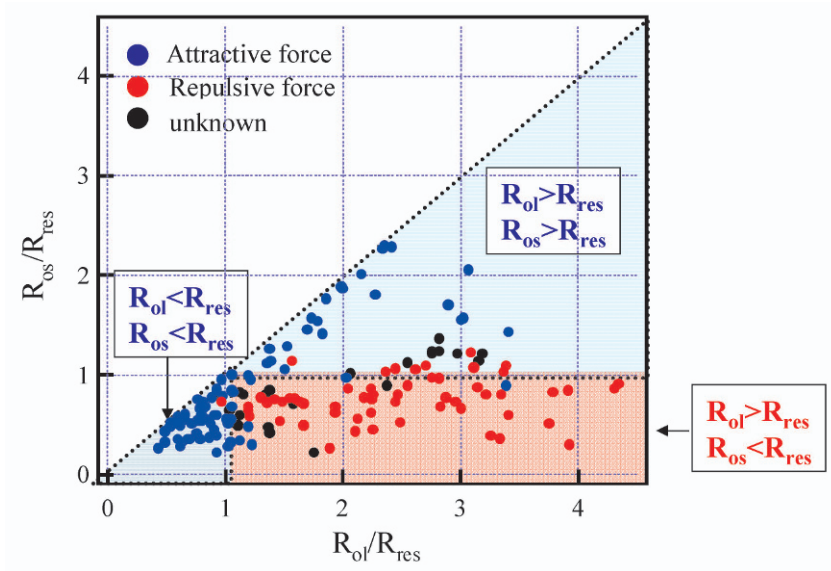
Figure 5. Dependence of interactive force on radii of two bubbles.

5.   SUMMARY

The collapse behavior of two bubbles adhering to a quartz glass was observed to examine the influences of interactive force on the collapse behavior. An interactive force deformed bubbles asymmetrically. These deformations generated flows and splits of the bubble. The interactive force could be attractive or repulsive. The deformation of bubbles largely depended on whether an attractive force acted or a repulsive force acted. Cases of an attractive force acting and a repulsive force acting were examined. It was shown that an attractive force acted when both bubble initial radii were greater than or smaller than the bubble resonant radius. When one initial radius was smaller than the resonant radius and the other was larger, a repulsive force acted.

REFERENCES

1. K. Tachibana and S. Tachibana: Jpn. J. Appl. Phys. **38** (1999), 3014.
2. T. G. Leighton, The Acoustic Bubble, Academic Press, 1997, pp. 356–366
3. Y. Yamakoshi, Y. Kurita and N. Masuda, Jpn. J. Appl. Phys, **40** (2001), 3852–3855.

OPTICAL OBSERVATION OF A COLLAPSING BUBBLE ADHERING TO A PIEZOELECTRIC TRANSDUCER SURFACE UNDER ULTRASOUND FIELD

K. Yoshida, S. Nakatani, Y. Watanabe

Faculty of Engineering, Doshisha University, 1-3 Tatara-miyakotani, Kyotanabe, Kyoto, 610-0321, Japan

Abstract: The detailed behavior of a single bubble adhering to a solid surface was optically observed using an ultra-high-speed camera (1,000,000 frames/sec) in order to clarify the mechanical effect of micro-bubbles. The changing pressure between the bubble and the surface was simultaneously observed by a thin piezoelectric transducer on the surface. When the bubble collapsed, we confirmed the radiation of a micro-jet from the bubble, which was followed by a counter jet. An impulse positive pressure applied to the surface was also observed synchronously with the collapse. This pressure seems to come from the jet flow or the violent vibration of the bubble.

Key words: Micro-jet, Micro-bubble, Ultra-high-speed camera, Piezoelectric transducer

1.   INTRODUCTION

A high-pressure sound wave generates micro-bubbles in a liquid. The micro-bubbles vibrate synchronously with the sound wave. For spherically symmetric vibration, the bubble can be a secondary sound source radiating shock waves. However, non-spherical vibration occurs when the bubble is near a solid surface. For example, a bubble adhering to the solid surface is deformed into a toroidal shape, which will be followed by water flow called a micro-jet [1]. These jets impact a small area on the solid surface. The mechanical effect due to these jets and shock-waves adversely affect hydraulic equipment, such as through vibration and erosion. However, these

mechanical effects are also used effectively in several fields, such as ultrasonic cleaning and gene therapy. The rapid, microscopic and complex behavior of bubbles in the sound field is still not fully understood. However, a more detailed understanding seems to open various applications in many fields.

In this study, therefore, the bubble behavior and mechanical effect in the sound field were observed simultaneously to clarify this generation mechanism. For this purpose, the motions of a single bubble adhering to a solid surface were optically observed by means of a high-speed video camera. The mechanical effect is determined by measuring a single bubble adhering to the surface of a thin piezoelectric sensor. We investigated various bubble motions by changing the initial bubble size.

2. EXPERIMENTAL SYSTEM

Figure 1(a) illustrates the observation system of the bubble collapse phenomenon. The high-speed video camera, bubble chamber, optical lens and xenon lamp are arranged linearly. The focal point of the high-speed video camera and the light from a xenon lamp are identical. We then observed the bubble behavior using the shadow graph method. The recording rate of this high-speed video camera was 250,000 fps. Figure 1(b) depicts the structure of the bubble chamber and the bubble position. This chamber is composed of an acrylic cylindrical container and a transducer. The bolt-on Langevin transducer was fixed at the bottom to generate sound waves.

(a) Optical observation system   (b) Arrangement and diameter

Figure 1. Observation system.

Figure 2 presents the waveform of the irradiated ultrasound. The maximum amplitude was 150 kPa and the frequency was 27 kHz. The solid surface for bubble adhesion was located at the maximum pressure position of the standing wave. Here, the adhesion surface is set vertically to the sound

propagation axis as indicated in Fig. 1(b). The adhesion surface was coated by a thin PVDF film transducer to measure the mechanical effect of the bubble. A single bubble with a radius of 30 to 120 µm is put on this film. In this condition, the bubble behavior and the waveforms detected from the transducer are simultaneously observed during ultrasound irradiation.

Figure 2. Temporal profile of irradiated pressure.

3.   EXPERIMENT RESULT

The collapsing behavior of bubbles strongly depended on the initial radius. The collapsing behavior of a bubble with a radius of less than 66 µm differed greatly from that of a bubble with a larger radius. In this study, the collapsing phenomena of a bubble with a radius of 66 µm or more is defined as "Pattern 1," and that of a bubble with a radius of less than 66 µm is defined as "Pattern 2." The collapsing phenomena are described in detail in the following sections.

3.1   Pattern 1 Collapse Phenomenon

The initial bubble radius was 71 µm, and the adhering bubble was assumed to be completely spherical. In this case, we observed a waveform with high-frequency impulse components in addition to the sinusoidal sound signal irradiated by the PVDF transducer. These impulse components seem to come from the mechanical effect caused by the bubble motion. For more detailed investigation, the differences of the waveforms with or without the bubble are plotted as a red line in Fig. 3(a). Here, the blue line is S/S_0. S is the

observed change in area of the bubble image, and S_0 is that of the initial image. S/S_0 was used to investigate the temporal vibration change of the bubble. The numbers in this figure correspond to each figure shown Fig. 3(b). It is clear that positive impulse signals are generated whenever the bubble motion changes from contraction to expansion. The images of the remarkable bubble motion observed before or after generation of the impulse signal are shown in Fig. 3(b). A typical sequence before the collapse is as follows.

1) Initial bubble before ultrasound irradiation (Fig. 3(b-0)). The central white part in the bubble represents the light transmitted directly from the lamp.
2) Small amplitude vibration and first contraction deforming into flat shape (Fig. 3(b-1)).
3) Generation of a micro-jet in the center of the bubble when the impulse signal was observed (Fig. 3(b-2)).
4) Second horizontal contraction keeping ring shape and vertical expansion (Fig. 3(b-3) and (b-4)).
5) Generation of a counter-jet in the direction vertical to the film, when the second impulse signal was observed (Fig. 3(b-5)).
6) Final collapse.

(a) The pressure signal caused by the bubble and the displacement of volume vibration.

(b) Images of remarkable bubble motion.
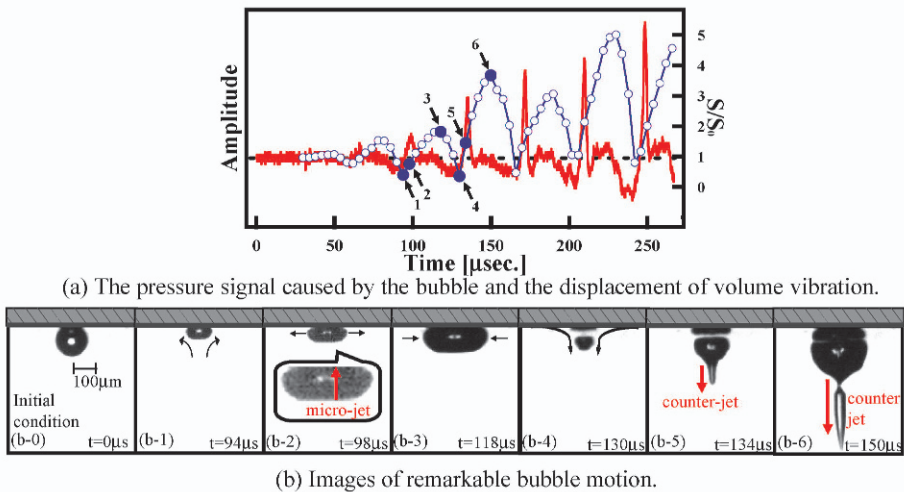
Figure 3. Typical Pattern 1 collapse phenomenon (Initial radius: 71 µm)

3.2 Pattern 2 Collapse Phenomenon

Figure 4(a) illustrates the pressure signal and S/S_0. The initial bubble radius was 64 μm. The numbers in this figure correspond to the images in Fig. 4(b). The positive impulse waveforms are generated when the bubble motion changed to the expanding phase like Pattern 1. However, the amplitudes of the impulse waveforms and S/S_0 were comparatively smaller than those of Pattern 1. This bubble behavior of Pattern 2 is depicted in Fig. 4(b). A typical sequence before the collapse is as follows.

1) Initial bubble before ultrasound irradiation (Fig. 4(b-0)).
2) Small amplitude vibration and first contraction exhibiting two parts with different radii (Fig. 4(b-1)).
3) Expansion in the horizontal direction, when the impulse signal was observed (Fig. 4(b-2))
4) Second horizontal contraction and separation into two parts. (Fig. 4(b-3), (b-4) and (b-5)).
5) Final separation into two parts and second expansion (Fig. 4(b-6))
6) Final collapse.

(a) The pressure signal caused by the bubble and the displacement of volume vibration.

(b) Images of remarkable bubble motion.
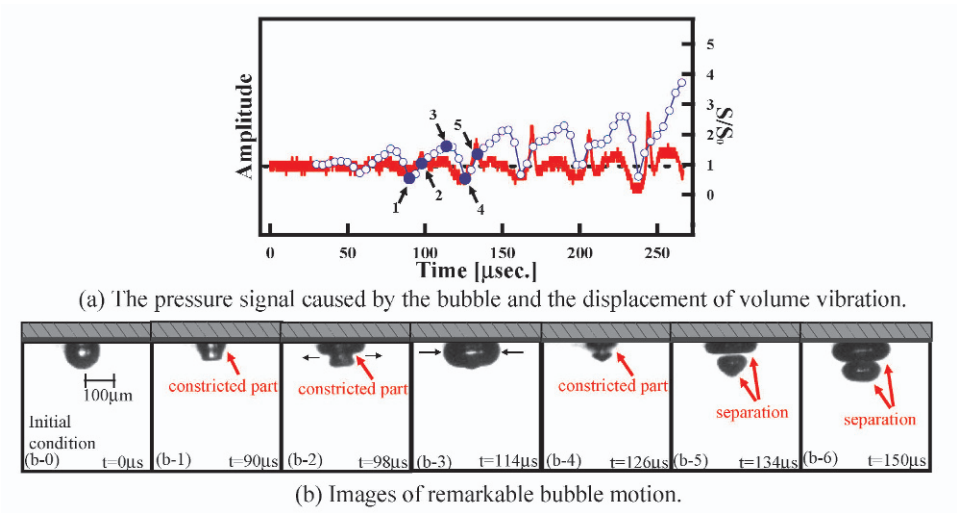
Figure 4. Typical Pattern 2 collapse phenomenon (Initial radius: 64 μm)

3.3   Influence of Bubble Size on Mechanical Effect

This section investigates the relationship between bubble motion and the strength of the mechanical effect. Figure 5 illustrates the relation between the initial bubble radius and the relative amplitude of the second impulse waveform at the time of collapse. The red plot indicates the bubble motion of the counter-jet (Pattern 1); the blue plot indicates that of separation (Pattern 2). The broken line represents the resonance radius of the free bubble at the frequency of the irradiated signal. This figure demonstrates that the amplitude of the impulse waveforms increased greatly in Pattern 1. There are two causes of the exponential increase. One is the hydrodynamic effect. Pattern 1 has violent jet motion. It was thought that this high-velocity fluid would impact the film. The other cause is shock-wave. The impulse waveform was generated whenever the bubble began to expand. It is thought that a shock-wave is generated and acted on the adhesion surface. The pressure amplitude of the shock-wave generated in Pattern 1 might be greater than that in Pattern 2 because the vibration amplitude (S/S_0) of Pattern 1 exceeds that of Pattern 2. It seems that this result was observed in both of these signals.
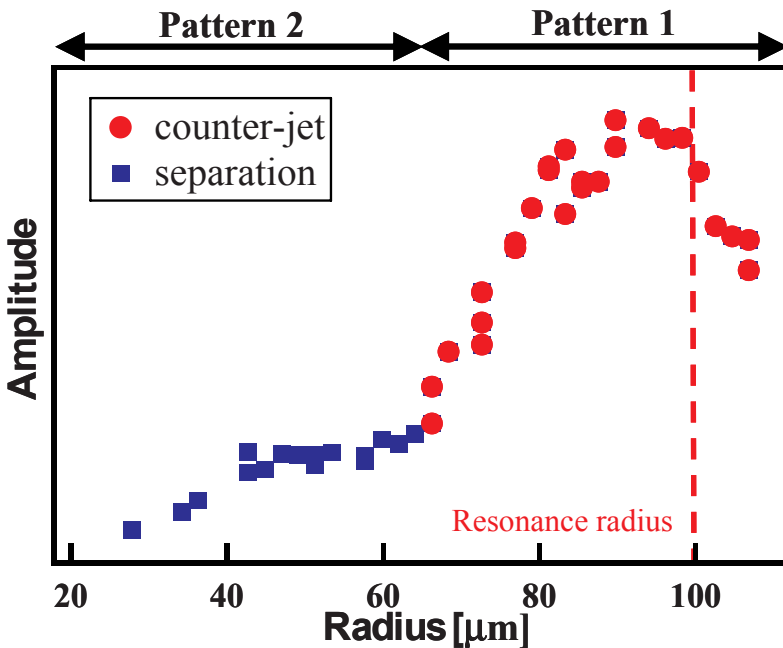
Figure 5. Relationship between the relative amplitude and the bubble radius.

4.   SUMMARY

The collapse phenomenon of a bubble adhering to a solid surface under ultrasound irradiation was experimentally investigated. The influence of bubble size on the mechanical effect was observed. Bubble motion was optically observed by using an ultra-high-speed camera. The pressure from the bubble to the surface was observed using a PVDF film transducer. Consequently, the collapsing patterns were divided into two types, depending on the bubble radius. In either case, an impulse pressure waveform was observed when the bubble motion changed from contraction to expansion. The amplitude of the impulse waveform differed between patterns.

REFERENCE

1.   T. G. Leighton, "The Acoustic Bubble," Academic Press, London, 1994.

VISCO-ELASTIC MODELS FOR SOFT TISSUES

S. Leeman, J. Jones

Hanmmersmith Hospital, Ducane Road, London, UK, Department of Radiological Sciences, University of California Irvine, Irvine, USA

Abstract: The simplest, and much utilized (despite its numerous shortcomings), model for soft tissue is based on the assumption of a linear elastic medium, although there is substantial evidence to suggest that soft tissue is, in fact, visco-elastic in nature. Here we discuss the simple and direct inclusion of visco-elastic concepts into descriptions of soft tissue. The two most elementary linear visco-elastic mechanical models (Maxwell and Kelvin-Voigt) are discussed. The wave equations for pressure propagation in these media are derived and their absorption and velocity dispersion characteristics are examined. One interesting feature is that explicit pulsed wave solutions may be derived in some cases. Another finding is that absorptive behavior may be characterized in a relative efficient manner, without recourse to the usual frequency-dependent description. The extent to which these media can be regarded as suitable for tissue modeling purposes is investigated. The incorporation of scattering into these models may be effected in the usual manner, except that scattering by absorption fluctuations is also predicted.

Key words: Visco-elasticity, Kelvin-Voigt model, Maxwell model, Absorption scattering

1.   INTRODUCTION

Much of the conceptual basis for medical ultrasound hinges upon the notion that soft tissues may be modeled as elastic media, with density and compressibility fluctuations. The latter generate scattering interactions upon which modern medical ultrasound pulse-echo imaging is reliant. However, soft tissues are manifestly also absorptive, and this feature is generally incorporated into the conventional model in a phenomenological, sometimes rather *ad hoc*, and not always satisfactory, manner. The aim of this ongoing

study is to utilize a known characteristic (visco-elasticity) of soft tissues in order to devise a realistic but simple model, and to explore some of the features predicted, primarily via the associated wave equation for longitudinal (pressure) waves.

2. THE CANONICAL TISSUE MODEL

Three basic assumptions give rise to what may be regarded as the simplest approach towards building a description of the propagation of (longitudinal) pressure waves in a (uniform) tissue medium. All equations are presented in their simplest, linear forms. A force law, describing the forces operating on a tissue element in a pressure field, is adopted. Neglecting complications such as viscous forces, etc., then, within the framework of Newton's second law, the following relationship holds

$$(\partial p/\partial x) = -\rho_0(\partial u/\partial t), \tag{1}$$

where $p(x,t)$ is the acoustic pressure, $u(x,t)$ is the particle velocity, and ρ_0 is the density of the unperturbed (i.e., in the absence of the pressure field) medium, assumed constant. Conservation of mass leads to the following continuity equation

$$(\partial \rho/\partial t) = -\rho_0(\partial u/\partial x), \tag{2}$$

with $\rho(x,t)$ denoting perturbation in density caused by the pressure wave.

The mechanical nature of the medium is embodied in the so-called constitutive equation. In this context, the simplest approach is to assume an elastic (spring-like) medium, i.e., one in which strain is proportional to stress. This may be written as

$$\rho(x,t) = \rho_0\kappa_0 p(x,t), \tag{3}$$

with κ_0 denoting the compressibility of the medium (also assumed constant). Note the association of strain with ρ and stress with p. At this level of approximation, all temperature effects are neglected.

Combining the above three equations leads to the well known wave equation describing the behavior of (longitudinal) pressure waves in an elastic medium

$$(\partial^2 p/\partial x^2) - (1/C^2)(\partial^2 p/\partial t^2) = 0, \tag{4}$$

where $C^2 = (1/\rho_0\kappa_0)$.

Note that this model is a linear one, exhibits no scattering (which may, however, be easily introduced by allowing density and compressibility to fluctuate), and is non-absorptive (a major flaw). The parameter C turns out to be the speed-of-sound which is dispersion free, in accord with observations in soft tissues in the diagnostic frequency range.

The limitations of such a simple model are well known. Below, we seek a more appropriate linear model for static uniform media (no scattering) that will incorporate absorption. This will be done by modifying only the constitutive equation to accommodate the visco-elastic nature of soft tissues [1]. The force law and continuity equation will be adopted without change. As before, temperature effects will be neglected.

3.   VISCO-ELASTIC MEDIA

The mechanical properties of visco-elastic media may be represented symbolically as combinations of two basic mechanical elements: an elastic element ("spring") and a viscous element ("dashpot") [1]. For the spring, stress is proportional to strain, $p \propto \rho$, while the dashpot has stress proportional to rate of strain, $p \propto (\partial\rho/\partial t)$. Only the very simplest models are considered below.

3.1   Kelvin-Voigt Medium

In this case, mechanical behavior is modeled as equivalent to a spring and dashpot in parallel. The constitutive equation becomes

$$\rho_0\kappa_0 p = \rho + A(\partial\rho/\partial t), \tag{5}$$

with A some constant characterizing the visco-elastic nature of the medium. This constant is chosen so that the constitutive equation reverts to that for an elastic medium when A vanishes. The constitutive equation is combined with the force law and continuity equation to give the wave equation

$$(\partial^2 p/\partial x^2) - (1/C^2)(\partial^2 p/\partial t^2) + A(\partial^3 p/\partial t\partial x^2) = 0. \tag{6}$$

Note that A has the dimensions of time. It is, in fact, the relaxation time for this medium. C has the same definition as before and has the dimensions of velocity; however, as we will see below, it no longer has the straightforward interpretation as being the speed of sound.

3.2   **Maxwell Medium**

Here mechanical behavior is modeled as being equivalent to a spring and dashpot in series. The constitutive equation becomes

$$(\partial\rho/\partial t) = \rho_0\kappa_0(\partial p/\partial t) + Bp, \qquad (7)$$

where B is a constant. Combining the force law with the above continuity equation gives the wave equation

$$(\partial^2 p/\partial x^2) - (1/C^2)(\partial^2 p/\partial t^2) - B(\partial p/\partial t) = 0. \qquad (8)$$

The relaxation time for the medium is given by $(1/BC^2)$.

Interestingly, this above wave equation was conjectured originally as a phenomenological construct [2,3] and is formally identical to the famous "telegraphers equation" used for investing communications via trans-Atlantic cable.

Absorption and velocity dispersions in visco-elastic media may be established by the following stratagem. Substitute a trial function of the form

$$p_{TR}(x,t) = \exp(-\alpha x) \bullet \exp[i(kx - \omega t)], \qquad (9)$$

which is a mono-frequency traveling plane wave modified by a loss factor into one of the above equations in order to establish whether it is indeed a solution. Note that the loss factor represents the effect of absorption on a uniform medium. Solutions will be found provided that there are certain constraints on α. These constraints may be expressed as a prescribed dependence of α on the frequency ω, with $\omega = 2\pi f$, provided that the dependence of k on ω has first been established. Note that for an elastic medium the trial solution does not satisfy the wave equation unless $\alpha = 0$ (so that it supports only lossless solutions, as is well known) and $\omega = Ck$, leading to phase velocity, $V(\omega) = \omega/k = C$. It is the phase velocity that is usually referred to as the speed-of-sound of the medium. However, as will be shown below, C will not have such a simple interpretation for visco-elastic media, even though it is a constant characterizing the medium.

4.   **THE KELVIN-VOIGT MEDIUM**

As expected for a visco-elastic medium, both the absorption and the phase velocity depend on frequency:

$$\alpha(\omega) = (\omega/C\sqrt{2})\{[(1 + A^2\omega^2)^{1/2} - 1] / [1 + A^2\omega^2]\}^{1/2}, \qquad (10)$$

$$V(\omega) = (C\sqrt{2})\{[1 + A^2\omega^2] / [(1 + A^2\omega^2)^{1/2} + 1]\}^{1/2}. \qquad (11)$$

Of interest, is the limiting case when $\omega A \ll 1$. Here,

$$\alpha(\omega) \sim \omega^2$$
$$V(\omega) \to C$$

In this limit, the Kelvin-Voigt medium exhibits "classical" absorption, with a phase velocity that is acceptable for soft tissues. But, from a tissue model point of view, the absorption rise is too steep in this frequency range. At higher frequencies ($\omega A \gg 1$) the absorption behavior is acceptable, but the phase velocity is overly dispersive when ω is large. Moreover, the wave equation does not look to be too simple to solve explicitly (if at all), so the model will be tentatively disregarded at this stage, even though it clearly merits further investigation.

5.   THE MAXWELL MEDIUM

Here,

$$\alpha(\omega) = [\omega / (C\sqrt{2})]\{[1 + (B^2C^4/\omega^2)]^{1/2} - 1\}^{1/2}, \qquad (12)$$

$$V(\omega) = [2\alpha(\omega)]/B. \qquad (13)$$

Note that $\alpha(\omega) \sim (\omega)^{1/2}$ for small ω ($\ll BC^2$) and $\to [(1/2)BC]$ for large ω ($\gg BC^2$). Also $V(\omega) \sim (\omega)^{1/2}$ for small ω and $\to C$ for large ω. Given that it is the attenuation (absorption + scattering) that is usually measured, and is roughly linear with frequency in the diagnostic frequency range, the behavior of $\alpha(\omega)$ is acceptable. Indeed, there are results that substantiate the (limited) suitability of the Maxwell model even for attenuation measurements in human muscle [4].

The phase velocity behavior is also acceptable for at least part of the frequency range (the dispersive behavior of the speed of sound in soft tissues at very low frequencies is not really actually established). Thus, the Maxwell model should not be regarded as necessarily being inconsistent with soft tissue data.

Given also that the wave equation may be explicitly solved for pulsed waves in Maxwell media, it may be concluded that the Maxwell model should be seriously considered as a first approximation in the quest for realistic (i.e., incorporating absorption) soft tissue models. It is noteworthy that, once a particular model has been ascertained, the entire frequency dependence of the absorption coefficient is efficiently determined by the specification of a small number of model parameters. Thus, for a Maxwell medium, C and B are sufficient to fix the absorption and velocity dispersion over the entire frequency range – rovided, of course, that the model itself is valid!

6.   PULSES IN UNIFORM MAXWELL MEDIA

The wave equation may be solved explicitly for a plane, circular, apodized transducer transmitting into a Maxwell medium [3]. The pulse exhibits the usual direct-/edge- wave components, albeit modified by absorption. Of interest, is the direct wave (DW) component, given in cylindrical polar coordinates (h, θ, z) by

$$P_{DW}(h, z; t) = D(h)\exp(-\beta z)\delta(t - z/C). \qquad (14)$$

Where D is the apodization function and $\beta = BC/2$. For simplicity, axial symmetry and impulsive excitation have been assumed.

It is noteworthy that the direct wave component is absorbed in a frequency independent way, exhibiting the maximum absorption attainable in this medium. The direct wave, which (in this configuration) marks the first arrival of the pulse at any point along the beam axis, travels with a constant speed C. Thus, the signal velocity in this dispersive medium is independent of frequency, and is equal to the maximal value of the phase velocity. These results, although obtained with the Maxwell model, are likely to hold generally for visco-elastic media and suggest that three sound speeds have to be distinguished when measuring transient fields in such media. (1) Phase velocity, given by ω/k, which is frequency dependent in Maxwell media; (2) Group velocity, given by $\partial\omega/\partial k$, which is likewise frequency dependent in Maxwell media; and (3) Signal velocity, which marks the speed of arrival of the first wave disturbance at a location, and which is frequency independent in Maxwell media. Clearly, all empirical studies need to pay close attention to identifying which particular sound speed is, in fact, being measured.

7. SCATTERING

Scattering by static structures may be introduced, as with the canonical model, by assuming non-constant medium parameters [5]. Thus, a varying density $\rho_0(x)$ incorporates scattering by density fluctuations and a varying compressibility $\kappa_0(x)$ incorporates scattering by compressibility fluctuations. But visco-elastic media have additional parameters characterizing, essentially, the absorptive behavior. In the case of the Maxwell medium, allowing B to vary as B(x) introduces scattering by absorption fluctuations. Such scattering *may* turn out to be very weak, in which case it would not be easily detectable, but it is surely an appropriate subject for future study. On the other hand, the existence of absorption scattering is suggested also by theoretical studies on how absorption modifies reflectivity properties of impedance mismatches [6,7]. The characteristics of absorption scattering will depend on the choice of the visco-elastic model. Although measurements of such scattering are not easy in practice, they will no doubt aid in establishing the appropriateness of a particular model.

8. CONCLUSIONS

Even relatively straightforward visco-elastic models are seen to provide a fertile basis for devising realistic (uniform) soft tissue models, incorporating absorption. In particular, the Maxwell medium is suggested to be a good starting point for further development. Scattering may be introduced in the usual way, and a new form of scattering, by absorption fluctuations, has been predicted. It has been suggested that closer attention be paid to identifying the particular sound speed (phase velocity, group velocity, or signal velocity) that is being measured in a given experiment, since it has been seen that not all of these velocities have identical values or dispersion characteristics, even in dispersive media.

REFERENCES

1. Y. C. Fung, Biomechanics: Mechanical Properties of Living Tissue, 2nd ed., Springer-Verlag (1993).
2. S. Leeman, "Ultrasound Pulse Propagation in Dispersive Media," *Physics in Medicine and Biology*, *25*, 481 (1980).
3. L. Hutchins, S. Leeman, & J. P. Jones, "Bounded Pulse Propagation," in *Acoustical Imaging*, 10, P. Alais & A. Metherell (eds), Plenum Press, 427 (1981).
4. S. Leeman & A. Peyman, "The Maxwell Model as a Soft Tissue Descriptor," in *Acoustical Imaging*, *25*, M. Halliwell & P. N. T. Wells (eds), Kluwer/ Plenum, 357 (2000).
5. P. M. Morse & K. U. Ingard, *Theoretical Acoustics*, McGraw-Hill, 400 (1968).

6. S. Leeman, R. Leeks, & P. Sutton, "Information Processing in Medical Imaging," in *Les Colloques de I'INSERM, 88*, R. Di Paola & E. Kahn (eds), INSERM, 35, (1979).

7. E. Nolan, *Reflection of Acoustic Waves From a Discontinuity in Absorption*, MS Thesis, University of California Irvine (1988).

EIGENVALUE IMAGING OF A0-MODE LAMB WAVE FIELD BASED ON SPATIO-TEMPORAL GRADIENT ANALYSIS

K. Teramoto, A. Uekihara

Graduate School of Advanced Systems Control Engineering, Saga University, Saga-shi, Japan

Abstract: The eigenvalue imaging based on the spatio-temporal gradient analysis is proposed in this paper. The third largest eigenvalue of a covariance matrix defined over the 4-dimensional vector space which is spanned by following components: (1) a vertical (z-directional) displacement, (2) its vertical particle velocity, (3) x-directional and (4) y-directional out-of-plane strains has an ability to classify the Lamb-wave field. Focusing the rank of the covariance matrix, we can find following facts: (1) rank=2: when no-reflected wave exists over the Lamb-wave field, or even when reflected waves exist only on the collinearly with an incident waves, (2) rank=3: in other cases. In this study, the eigenvalue imaging based on the spatio-temporal gradient analysis is discussed and the physical meanings of the eigenvalue imaging are investigated by numerical and acoustical experiments.

Key words: Lamb wave, Non-destructive testing, Spatio-temporal gradient analysis, Array signal processing

1.   INTRODUCTION

Lamb waves play important roles in NDE fields [1,2]. Being placed on the surface of a homogeneous defect-free plate, a source signal excites several kinds of waves: (a) pressure and shear waves propagating in the plate, (b) a Rayleigh wave that is confined to the surface of the plate, and (c) symmetric and anti-symmetric Lamb waves traveling along the plate. In contrast to these former waves, the velocity of each mode of Lamb wave varies with frequency. Consequently the detected ultrasound signal is very complicated, causing

difficulties in signal interpretation. It is important, therefore, to establish the signal detection criterion independent of local wave numbers. In this study, the eigenvalue imaging is proposed which has an ability to classify the Lamb wave field through the rank of the covariance matrix defined over the 4-dimensional vector space which is spanned by following components: (1) a vertical (z-directional) displacement, (2) its vertical particle velocity, (3) x-directional and (4) y-directional out-of-plane strains. Focusing the rank of the covariance matrix, we can find following facts: (1) rank=2: when no-defect exists over the Lamb wave field, or even when defects exist only on the collinearly with a pair of acoustic transmitter and receiver, (2) rank=3: in other cases. In this study, the computational process in the crack detection based on the spatio-temporal gradient analysis is discussed and the physical meanings of the third eigenvalue are investigated through several numerical experiments and acoustical experiments.

2.   PROBLEM FORMULATION

2.1   Spatio-Temporal Gradient Description

Assuming single plane wave propagating on the surface, the zeroth-order anti-symmetric mode Lamb wave field can be approximated at a point, (x, y) on the surface as follows:

$$f(x,y,t) = w(t - \frac{x\cos\theta + y\sin\theta}{v(\omega_0)}). \tag{1}$$

Here, $w(t)$, $v(\omega_0)$ and ω_0 denote the transmitted signal, the phase velocity of A0-mode Lamb-wave and center frequency respectively. On the same location, the vertical component of the particle velocity can be obtained by differentiating Eq. (1) for time as:

$$\frac{\partial}{\partial t} f(x,y,t) = \dot{w}(t - \frac{x\cos\theta + y\sin\theta}{v(\omega_0)}). \tag{2}$$

Here, $w(t)$ is the time-differential of $w(t)$. Orthogonal pair of out-of-plane shearing strains is derived by spatial differentiation as follows:

$$\nabla f(x,y,t) = -\begin{pmatrix} \cos\theta \\ \sin\theta \end{pmatrix} \frac{1}{v(\omega_0)} \dot{w}(t - \frac{x\cos\theta + y\sin\theta}{v(\omega_0)}). \tag{3}$$

Thus, it is clear from Eq. (3) that the orthogonal pair of out-of-plane strains are linearly dependent on the corresponding vertical-particle velocities, Eq. (2), when unique plane wave exists on the plate.

2.2 Spatio-Temporal Gradient Analysis

Reducing the disturbance caused by the noise and fluctuation of signal intensity, the covariance matrix of the spatio-temporal gradient vector is adopted. The four dimensional spatio-temporal gradient vector is defined as follows [3]:

$$\boldsymbol{f} = (\partial f/\partial x \; \partial f/\partial y \; \partial f/\partial t \; f)^{\mathrm{T}} \tag{4}$$

The covariance matrix is derived by the correlation among the each components of $\boldsymbol{f}$ as:

$$\boldsymbol{\Phi} = \lim_{T\to\infty} \frac{1}{T} \int_0^T \boldsymbol{f}\boldsymbol{f}^{\mathrm{T}} = \begin{pmatrix} \phi_{xx} & \phi_{xy} & \phi_{xt} & \phi_x \\ \phi_{yx} & \phi_{yy} & \phi_{yt} & \phi_y \\ \phi_{tx} & \phi_{ty} & \phi_{tt} & \phi_t \\ \phi_x & \phi_y & \phi_t & \phi \end{pmatrix} \tag{5}$$

In general case, a vertical displacement, f, and its time differential, $\partial f/\partial t$ are mutually independent. Based on Eq. (3), the rank of $\boldsymbol{\Phi}$ is degenerated to 2, when unique plane Lamb-wave exists on the perfect or defect-free plate.

2.3 An Overlap of Incident and Reflected Wave Fronts

If a reflected wave front exists on the surface, the rank of $\boldsymbol{\Phi}$ increases to 3. When single reflected wave front is assumed, Lamb-wave field is excited by the sum of the incident wave front and the reflected wave front as follows:

$$f(x,y,t) = w(t - \frac{x\cos\theta + y\sin\theta}{v(\omega_0)}) + A_r w(t - \frac{x\cos\varphi + y\sin\varphi}{v(\omega_0)} + D) \tag{6}$$

Here, A_r and φ are the amplitude of the reflected plane wave, the direction of the reflected wave propagation respectively. As the same way in Eq. (3), the particle velocity and corresponding pair of out-of-plane strains are obtained as follows:

$$\nabla f = \begin{pmatrix} -\dfrac{\cos\theta}{v(\omega_0)} & \dfrac{\cos\varphi}{v(\omega_0)} \\ -\dfrac{\sin\theta}{v(\omega_0)} & \dfrac{\sin\varphi}{v(\omega_0)} \end{pmatrix} \begin{pmatrix} \dot{w}(t - \dfrac{x\cos\theta + y\sin\theta}{v(\omega_0)}) \\ A_r\dot{w}(t - \dfrac{x\cos\varphi + y\sin\varphi}{v(\omega_0)} + D) \end{pmatrix} \tag{7}$$

On the basis of Eq. (7), $\partial f/\partial x$ and $\partial f/\partial y$ become linearly independent except the case that the reflected wave and incident one propagate in the same direction, $\theta = \pm\varphi$. The maximum rank of $\boldsymbol{\Phi}$ is limited to 3 owing to the linear advection.

Based on the above consideration, we can summarize the relation between the rank of $\boldsymbol{\Phi}$ and reflected plane waves as follows:

1. No reflected wave front: Rank($\boldsymbol{\Phi}$)=2,
2. Both an incident wave and its reflected wave front propagating in the same direction: Rank($\boldsymbol{\Phi}$)=2,
3. Otherwise: Rank($\boldsymbol{\Phi}$)=3.

3.   ACOUSTIC EXPERIMENTS

We have implemented and tested the proposed eigenvalue imaging method in the Proof-Of-Concept (POC) model.

3.1   Proof-Of-Concept Model

Figure 1 shows the block diagram of the POC-model [4]. Omni-directional transmitter which is located at the center of the disc vibrates the specimen with 500 kHz-monocycle pulse. Each receiving transducer detects the vertical displacement at the adjacent four points as, $f_{i(=1,2,3,4)}(x,y,t)$.

3.2   Spatio-Temporal Gradient Analysis

Figure 2(1) shows the vertical displacement at the point P1 (shown in Fig. 1) after normalization. In (2), two curves plots of the 3rd largest eigenvalue of $\boldsymbol{\Phi}$ and the minimum one which are normalized by the maximum eigenvalue. In this experiment, no evidence of the scattered wave is appeared in
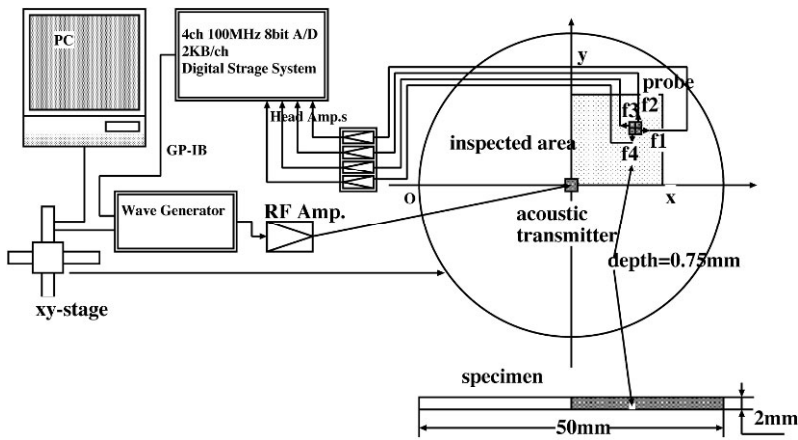
Figure 1. Block diagram of the proof of concept model.
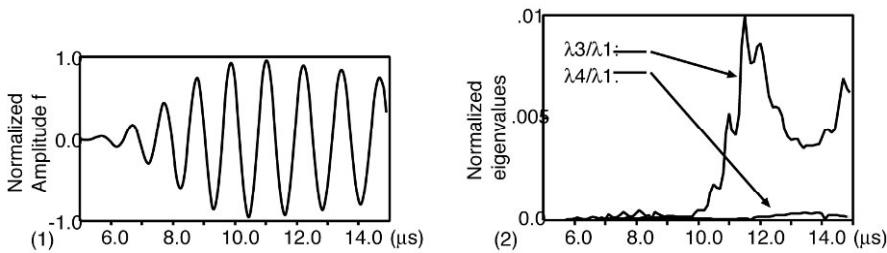
Figure 2. An example of observed signals: (1) normal displacement, (2) normalized eigenvalues: λ_3 / λ_1, and λ_4 / λ_1. The arrival time of the scattered wave front: 10.0 μs.
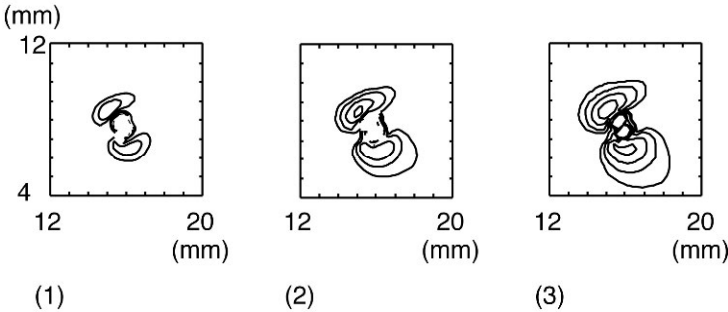
Figure 3. Wave frontal images obtained by the third largest eigenvalues (1) at 13 μs, (2) at 15 μs, (3) at 17 μs after irradiation.

Fig. 2(1), because the scattered Lamb wave is weak. The third eigenvalue, whereas, increases at 10 μs after irradiation in Fig. 2(2). The behavior indicates the arrival of another independent wave front which is scattered by the defect in the specimen. Fig. 3(1)(2) and (3) show the reconstructed wave fronts of the scattered signal at 13, 15, and 17 μs after the signal irradiation respectively.

4.   CONCLUDING REMARKS

This paper proposes the eigenvalue imaging to be independent of frequency and phase velocity, and presents simple digital signal processing algorithm characterizing the wave field where incident and scattered waves overlap each other. For detecting the defects, spatio-temporal gradient analysis based on the linear dependency among the vertical displacement, the vertical particle velocity, and a pair of shear strains is used. By analyzing the covariance matrix of the spatio-temporal gradient vector, it is found that the third largest eigenvalue becomes zero only when the surface is perfect, without defect or any fault. The several experiments with the POC-model were conducted with following conclusions.

- The eigenvalue imaging aims to detect the existence of defects.
- The reflected wave fronts from defects are discriminated from the rest of the wave field.

ACKNOWLEDGEMENTS

REFERENCES

1.   G. Burnett, J. Candy, "Using Signal Processing Techniques to Improve Element Modeling," J. Acoust. Soc. Am., 106(4), 2215 (1999)
2.   A. Bernard, M. J. S. Lowe, M. Deschamps, "Guided Waves Energy Velocity in Absorbing and Nonabsorbing Plate," J. Acoust. Soc. Am., 110(1), 186–196 (2001)
3.   S. Ando, H. Shinoda, et. al., "A Three-Dimensional Sound Localization Sensor System Based on the Spatio-Temporal Gradient Method," 29(5), 520–528 (1993)
4.   K. Teramoto, K. Tsuruta, "Spatio-Temporal Gradient Analysis for Detecting Defects," IEICE Trans. Fundamentals, E87–A(8), 2037–2004 (2004)

VECTOR THEORY OF ULTRASONIC IMAGING

W. S. Gan

Acoustical Technologies Singapore Pte. Ltd., 209-210, Innovation Centre, NTU, 16 Nanyang Drive, Singapore 637722, Singapore

Abstract: So far, works on ultrasonic diffraction imaging are based on scalar theory of sound wave. This is not correct as sound has vector nature. But when sound propagates in solids, its vector nature has to be considered as polarization occurs and transverse wave as well as longitudinal wave will appear. Vector theory is especially needed when the obstacle size is smaller than the wavelength. We use the Smythe-Kirchhoff approach for the vector theory of diffraction. We derive the image formation theory based on the vector diffraction theory. The effect of polarization on acoustical imaging is discussed.

Key words: Vector theory, Polarization, Transverse wave, Longitudinal wave, Smythe-Kirchhoff approximation, Azimuthal dependence, Image information theory, Angular spectrum, Evanescent waves

1.   INTRODUCTION

So far works on ultrasonic diffraction imaging are based on scalar theory of sound waves. This is not correct as sound has vector nature. When sound propagates in solids, its vector nature has to be considered as polarization occurs and both transverse wave and longitudinal wave will occur. Vector theory is especially needed when the obstacle size is smaller than the wavelength. This will produce better information on the objects details and better image resolution. Vector theory also provides a study on the effect of polarization on acoustical imaging.

2.   DERIVATION OF THE VECTOR ACOUSTIC
    WAVE EQUATION FOR SOLIDS

We will start with the vectorial Kirchhoff approximation. The acoustic
stress field $\vec{T}$ is analogous to the electric field $\vec{E}$. We begin with the
solution for the scalar wave function ψ :

$$\psi(\vec{x}) = \oint_S [\psi(\vec{x}')\vec{n}'\cdot\nabla'G(\vec{x},\vec{x}') - G(\vec{x},\vec{x}')\vec{n}'\cdot\nabla'\psi(\vec{x}')]da' \tag{1}$$

where $(\vec{n}')$ is an inwardly directed normal to the surface S. We then use
Eq. (1) for each rectangular component of $\vec{E}$ and write the obvious vectorial
equivalent:

$$\vec{E}(\vec{x}) = \oint_S [\vec{E}(\vec{n}'\cdot\nabla'G) - G(\vec{n}'\cdot\nabla')\vec{E}]da' \tag{2}$$

Equation (2) can be rewritten in this form:

$$O = \oint_S [2\vec{E}(\vec{n}'\cdot\nabla'G) - \vec{n}'\cdot\nabla'(G\vec{E})]da'$$

The divergence theorem can be used to convert the second term into a
volume integral, thus yielding

$$O = \oint_S 2\vec{E}(\vec{n}'\cdot\nabla'G)da' + \int_V \nabla'^2(G\vec{E})d^3x'$$

The following vector Kirchhoff integral relation can be obtained:

$$\vec{E}(x) = \oint_S [i\omega(\vec{n}\times\vec{\beta})G + (\vec{n}\times\vec{E})\times\nabla'G + (\vec{n}'\cdot\vec{E})\nabla'G]da' \tag{3}$$

For the acoustic fields, $\vec{E}$ is equivalent to $\vec{T}$ and $\vec{H}$ is equivalent to $\vec{V}$,
the velocity field and

$$\vec{T}(x) = \oint_S [i\omega(\vec{n}'\times\vec{V})G + (\vec{n}'\times\vec{T})\times\nabla'G + (\vec{n}'\cdot\vec{T})\nabla'G]da' \tag{4}$$

3. PRACTICAL EXAMPLE OF THE APPLICATION OF THE VECTOR DIFFRACTION FORMULA

The generalized Kirchhoff integral for Neumann boundary condition is

$$\psi(\vec{x}) = -\int_{S_1} \frac{\partial \psi}{\partial n'}(\vec{x}') G_N(\vec{x}, \vec{x}') da' \tag{5}$$

The vector relation for Eq. (5) is

$$\vec{T}_{diff}(\vec{x}) = \frac{1}{2\pi} \nabla \times \int_{apertures} (n \times \vec{T}) \frac{e^{iKR}}{R} da' \tag{6}$$

for the acoustic case. The first example is diffraction by a circular aperture [1]. We consider Fraunhofer diffraction, Eq. (7) reduces in this limit to

$$\vec{T}(\vec{x}) = \frac{ie^{iKr}}{2\pi r} \vec{K}' \times \int_{S_1} \vec{n} \times \vec{T}(\vec{x}') e^{-iKR} da' \tag{7}$$

We consider a plane wave incident at an angle α on a thin, perfectly elastic screen with a circular hole of radius a in it.
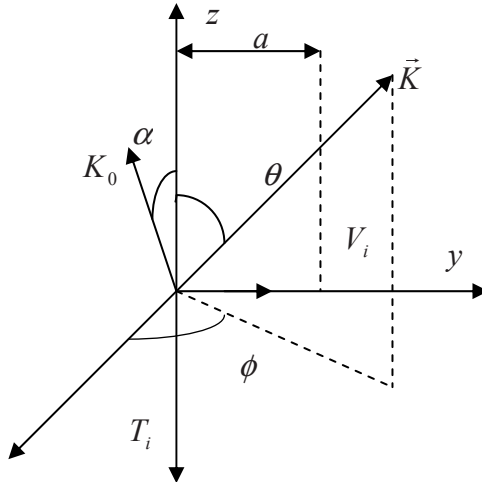
Figure 1. Diffraction by a circular hole of radius a.

Figure 1 shows an appropriate system of coordinates. The screen lies in the *x-y* plane with the opening centred at the origin. The incident wave's stress field, written out explicitly in rectangular components, is

$$\vec{T}_i = \vec{T}_0 \left(S_1 \cos\alpha - S_3 \sin\alpha \right) e^{-iK(z\cos\alpha + x\sin\alpha)} \tag{8}$$

where S = stiffness.

In calculating, the diffraction field with Eq. (7) we will make the customary approximation that the exact field in the surface integral may be replaced by the incident field.

Introducing plane polar coordinates for the integration over the opening, we have

$$\vec{T}(\vec{x}) = \frac{ie^{iKrT_0\cos\alpha}}{2\pi r} \left(\vec{K} \times \vec{S}_2 \right) \int_0^a \rho d\rho \int_0^{2\pi} d\beta e^{ik\rho[\sin\alpha\cos\beta - \sin\theta\cos(\alpha-\beta)]} \tag{9}$$

where θ, ϕ are spherical angles of $\vec{k}$. The resulting stress field is

$$\vec{T}(\vec{x}) = \frac{ie^{iKr}}{r} a^2 T_0 \cos\alpha \left(\vec{K} \times \vec{S}_2 \right) \frac{J_1(Ka\xi)}{Ka\xi} \tag{10}$$

The time averaged diffracted power per unit solid angle is

$$\frac{dP}{d\Omega} = P_i \cos\alpha \frac{(Ka)^2}{4\pi} \left(\cos^2\theta + \cos^2\phi\sin^2\theta \right) \left| \frac{2J_1(Ka\xi)}{Ka\xi} \right|^2 \tag{11}$$

where

$$P_i = \left(\frac{T_0^2}{2z_0} \right) \pi a^2 \cos\alpha, \tag{12}$$

is the total power normally incident on the aperture.

The power radiated per unit solid angle in the scalar Kirchhoff approximation is

$$\frac{dP}{d\Omega} = P_i \frac{(Ka)^2}{4\pi} \cos\alpha \left(\frac{\cos\alpha + \cos\theta}{2\cos\alpha} \right) \left| \frac{2J_1(Ka\xi)}{Ka\xi} \right|^2 \tag{13}$$

If we compare the vector result Eq. (11) with Eq. (13), we find that the scalar result has no azimuthal dependence, whereas the vector expression does. The azimuthal variation comes from the polarization properties of the field.

4.   DERIVATION OF IMAGE FORMATION THEORY

We shall use the angular spectrum approach [2]. Here, the various spatial Fourier components can be identified as plane waves traveling in different directions. The field amplitude of any other point can be calculated by adding the contributions of these plane waves, taking due account of the phase shifts they have undergone in propagating to the point in question.

Let the complex field across that plane be represented by $\vec{T}(x, y, 0)$; our ultimate objective is to calculate the consequent field $\vec{T}(x, y, z)$ that appears at a second point P_0 with coordinate (x, y, z).

Across the *xy* plane, the function $\vec{T}$ has a two-dimensional Fourier transform given by

$$\vec{A}_0(f_x, f_y) = \int\int_{-\infty}^{\infty} T(x, y, 0)\exp\left[- j2\pi(f_x x + f_y y)\right]dxdy \tag{14}$$

The function

$$\vec{A}_0\left(\frac{\alpha}{\lambda}, \frac{\beta}{\lambda}\right) = \int\int_{-\infty}^{\infty} \vec{T}(x, y, 0)\exp\left[- j2\pi\left(\frac{\alpha}{\lambda}x + \frac{\beta}{\lambda}y\right)\right]dxdy \tag{15}$$

is called the angular spectrum of the disturbance, $\vec{T}(x, y, 0)$.

$$\vec{T}(x, y, z) = \int\int_{-\infty}^{\infty} \vec{A}\left(\frac{\alpha}{\lambda}, \frac{\beta}{\lambda}, z\right)\exp\left[j2\pi\left(\frac{\alpha}{\lambda}x + \frac{\beta}{\lambda}y\right)\right]d\frac{\alpha}{\lambda}d\frac{\beta}{\lambda} \tag{16}$$

The $\vec{T}(x)$ determined by vectorial approach is given by Eq. (10). We now extend $\vec{T}(x)$ to $\vec{T}(x, y, z)$ to take account of the effect of propagation.

It is also to be noted that the vectorial approach is the proper approach for treating the existence of evanescent waves in the angular spectrum.

5.   DISCUSSION ON THE EFFECT OF POLARIZATION ON ACOUSTICAL IMAGING

We have seen from Eq. (11) the azimuthal variation due to the polarization properties of the acoustic field. For normal incidence, $\alpha = 0$ and $Ka \gg 1$, the polarization dependence is unimportant, the diffraction is confined to very small angles in the forward direction and all scalar and vector approximations reduce to the same expression. For $Ka = \pi$, there is a considerable disagreement between the vector and scalar approximations. It is to be noted that scalar approximation only gives information on the diffracted acoustic field in a particular component direction if the rectangular coordinates is used.

6.   CONCLUSION

So far, we have followed the Kirchhoff vector approximation in our work. It would be very useful to follow the exact calculations. There is reason to believe that the vector Kirchhoff result is close to the exact theory, even though the approximation breaks down seriously for $Ka \leq 1$. The vector approximation and exact calculation [3] for a rectangular opening yield results in good agreement even down to $Ka \sim 1$.

REFERENCES

1. J. D. Jackson, *Classical Electrodynamic* (John Wiley & Sons, New York, 1999), pp. 490.
2. J. W. Goodman, *Introduction to Fourier Optics* (McGraw-Hill, New York, 1968), pp. 48.
3. P. M. Morse and P. J. Rubenstein, The diffraction of waves by ribbons and by slits, *Phys. Rev.* **54**, 895–898 (1938).

GAUGE INVARIANCE APPROACH TO ACOUSTIC FIELDS

W. S. Gan

Acoustical Technologies Singapore Pte. Ltd. 209-210, Innovation Centre, NTU, 16 Nanyang Drive, Singapore 637722, Singapore

Abstract: We extend the gauge invariance property of the Maxwell's equations to the acoustic field equations. We solve the inhomogeneous wave equation for the scalar and vector potentials and obtain the velocity field and the stress field in terms of these potentials. Gauge invariance has symmetry property. We obtain the gauge form for the acoustic scalar potential and the vector potential and demonstrate their invariant property. We apply gauge invariance to negative refraction. Acoustic field equations also possess left hand and right hand symmetry and this gives rise to negative refraction. Here we extend negative refraction to anisotropic materials.

Key words: Gauge invariance, Velocity field, Stress field, Vector potential, Scalar potential, Symmetry, Christoffel equation, Negative refraction, Anisotropic materials

1.   INTRODUCTION

We extend the gauge invariance property of the Maxwell's equation to the acoustic field equations. Gauge invariance which includes symmetries is a basic property of field theory. In extending gauge invariance approach to acoustic fields, it will be a more sophisticated approach than the vector theory of acoustic fields and it will include also the characteristic of the vector theory. We apply gauge invariance to negative refraction and interpret the inhomogeneous wave equation in terms of gauge invariance. This will provide more understanding of the acoustic fields and throw lights on new potential applications. This paper is the first application of gauge invariance to acoustic fields.

2.   GAUGE INVARIANCE FORMULATION OF THE INHOMOGENEOUS WAVE EQUATION

We first derive the acoustic Lorentz gauge condition. For electromagnetic waves, the Lorentz gauge condition gives rise to the equation of continuity. The Lorentz gauge condition is given as

$$\nabla \cdot \vec{A} + \frac{1}{c^2} \frac{\partial \phi}{\partial t} = 0 \tag{1}$$

where $\vec{A}$ = vector potential and ϕ = scalar potential.

By substituting in the retarded potential for $\vec{A}$ and ϕ, we have

$$\nabla \cdot \frac{\mu_0}{4\pi} \int \frac{j(x'_\alpha)}{r(x_\alpha, x'_\alpha)} dV' + \frac{1}{c^2} \frac{\partial}{\partial t} \left(\frac{1}{4\pi\varepsilon_0} \right) \int \frac{\rho(x'_\alpha)}{r(x_\alpha, x'_\alpha)} = 0 \tag{2}$$

where j = current density, μ = permittivity, ε = permittivity, ρ = charge density, V = volume, r = radial distance.

This can be simplified to

$$\nabla \cdot j + \frac{\partial \rho}{\partial t} = 0 \tag{3}$$

which is the equation of continuity.

On the other hand the acoustic equation of continuity is

$$\nabla (\rho V) + \frac{\partial \rho}{\partial t} = 0 \tag{4}$$

with just replacing j by ρV which is correct with charge density being analogous to the mass density.

So we can use

$$\nabla \cdot \vec{A} + \frac{1}{c^2} \frac{\partial \phi}{\partial t} = 0$$

as the acoustic Lorentz gauge condition where c = sound velocity.

From the electromagnetic theory, the electric field $\vec{E}$ and the magnetic field $\vec{B}$ are expressed in terms of potential functions as:

$$\vec{E} = -\nabla\phi - \frac{\partial\vec{A}}{\partial t} \tag{5}$$

and

$$\vec{B} = \nabla\times\vec{A} \tag{6}$$

where ϕ = scalar potential and $\vec{A}$ = vector potential. These potentials are invariant under gauge transformation. We will use the analogy of $\vec{E}$ as $\vec{T}$ the acoustic stress field.

The usual acoustical wave equations are expressed in terms of wave functions ϕ or $\vec{A}$. This gives only partial aspects of the acoustic fields $\vec{V}$ and $\vec{T}$.

From Eq. (5) we can write

$$\vec{T} = -\nabla\phi - \frac{\partial\vec{A}}{\partial t} \tag{7}$$

From Maxwell's equation

$$\nabla\cdot\vec{E} = 4\pi\rho \tag{8}$$

For the acoustic field

$$\nabla\cdot\vec{T} = 4\pi\rho \tag{9}$$

Substituting Eq. (7) into Eq. (9), we have

$$\nabla\cdot(-\nabla\phi - \frac{\partial\vec{A}}{\partial t}) = 4\pi\rho$$

But Lorentz gauge condition:

$$\nabla\cdot\vec{A} = -\frac{1}{c^2}\frac{\partial\phi}{\partial t}$$

thus

$$-\nabla^2\phi+\frac{1}{c^2}\frac{\partial^2\phi}{\partial t^2}=4\pi\rho \tag{10}$$

which is an inhomogeneous wave equation in ϕ and ρ = field density.

We can also express the velocity field in terms of the scalar potential and vector potential as

$$\vec{V}=\nabla\phi+\nabla\times\vec{A} \tag{11}$$

The Christoffel equation for an isotropic medium with plane wave solutions and harmonic time variation [1] can be written as

$$c_{11}\nabla(\nabla\cdot\vec{V})-c_{44}\nabla\times\nabla\times\vec{V}=\rho\frac{\partial^2\vec{V}}{\partial t^2} \tag{12}$$

Substitution of Eq. (11) into Eq. (12) gives

$$\nabla(c_{11}\nabla^2\phi-\rho\frac{\partial^2}{\partial t^2}\phi)-\nabla\times(c_{44}\nabla\times\nabla\times\vec{A}+\rho\frac{\partial^2\vec{A}}{\partial t^2})=0 \tag{13}$$

For the second term, the quantity in brackets is set equal to the gradient of an arbitrary function f.

The vector potential A can thus be taken as a solution to the vector wave equation

$$\nabla^2\vec{A}-\frac{1}{V_s^2}\frac{\partial^2\vec{A}}{\partial t^2}=0 \tag{14}$$

The first term in Eq. (13) is made zero by simply requiring that the scalar potential ϕ satisfy the scalar equation

$$\nabla^2\phi-\frac{1}{V_l^2}\frac{\partial^2\phi}{\partial t^2}=0 \tag{15}$$

So we have obtained homogeneous wave equation in A and ϕ.

This shows that the acoustic fields $\vec{T}$ and $\vec{V}$ can be expressed in terms of the solutions of the homogeneous wave equations A and ϕ. A and ϕ in turn are only partial aspects of $\vec{V}$ and $\vec{T}$.

The Lorentz gauge condition has the advantage of introducing complete symmetry between the scalar and vector potentials i.e. it makes both potentials satisfy the same wave equation as that obeyed by the fields. Equations (14) and (15) are a symmetrical set of equations.

By using the analogy of momentum density $\vec{P}$ as equivalent to $\vec{B}$, we have

$$\vec{T} = -\nabla \phi - \frac{\partial \vec{A}}{\partial t} \tag{16}$$

and

$$\vec{P} = \nabla \times \vec{A} \tag{17}$$

Equations (16) and (17), are unchanged by transformation of the type [2]

$$A' = A - \nabla \phi \tag{18}$$

$$\phi' = \phi + \frac{\partial \phi}{\partial t} \tag{19}$$

These transformations are usually known as gauge transformations, and a physical law that is invariant under such a transformation is said to be gauge invariant.

3.   APPLICATION OF GAUGE INVARIANCE APPROACH OF ACOUSTIC FIELDS TO NEGATIVE REFRACTION

Veselago [2] derived the negative refraction theory from the consideration of negative permittivity and negative permeability, and is limited only to isotropic materials. In this paper, we extend his theory to acoustic wave and to anisotropic materials. We apply gauge invariance here. It is well known that an important property of gauge invariance is symmetry.

In an anisotropic material, the compliance and stiffness possess rotational symmetry. Compliance and stiffness together describe the intrinsic elastic properties of the medium. When rotating in the clockwise direction, it gives rise to left handed phenomenon such as negative refraction. When rotating in anticlockwise direction, it gives rise to the right handed phenomenon such as

positive refraction. Due to rotational symmetry, both the right handed phenomenon and the left handed phenomenon satisfy the acoustic field equations. According to parity conservation, acoustic law at the deepest level, there is no differentiation of right handed and left handed treatment. The performance of an object and that of its mirror image will satisfy the same law of physics. The negative refraction in fact is a mirror image of the positive refraction. So from the consideration of parity conservation or mirror symmetry, both negative refraction and positive refraction satisfy the physical laws of acoustics.

$$\vec{T} = c\vec{S} \tag{20}$$

where c = compliance.

Since compliance has rotational symmetry, it follows that $\vec{T}$ will also have rotational symmetry.

The acoustic Poynting vector is given as

$$\vec{P} = \frac{-\vec{V}^* \cdot \vec{T}}{2} \tag{21}$$

It follows that $\vec{P}$ will also have rotational symmetry.

4.   CONCLUSION

Gauge invariance or gauge field theory is a more sophisticated treatment of acoustic fields than vector theory. It gives a more accurate solution for the velocity field and the stress field than those obtained from the inhomogeneous wave equations. The symmetry argument also explains the phenomenon of negative refraction for the anisotropic case. It also gives the difference between the stress field and the velocity field which previously all treat them as wave functions. It provides better understanding of the stress field and the velocity field.

REFERENCES

1. B.A. Auld, Acoustic Fields and Waves in Solids, Vol. II, pp. 66 (1990). Robert Kriger Publishing Co.
2. V.G. Veselago, "The electrodynamics of substances with simultaneous negative values of ε and μ", Soviet Ohysics USPEKHI, 10, 509–514 (1968).

MEDICAL IMAGE ANALYSIS

REPRODUCIBILITY OF IMAGE ANALYSIS FOR BREAST ULTRASOUND COMPUTER-AIDED DIAGNOSIS

M. Galperin, M.P. Andre, C.H. Barker, L.K. Olson, M. O'Boyle, K. Richman, L. Mantrawadi

Almen Laboratories, Inc., Vista, California 92084, USA; Dept. of Radiology, San Diego VA Healthcare System, San Diego, California 92161, USA; Dept. of Radiology, University of California, San Diego, California 92093, USA

Abstract: We employ a Case-Based Reasoning approach to analyze breast masses in ultrasound and to classify them for level of suspicion for cancer following the ACR BI-RADS® protocol. Our computer-aided imaging system (Breast Companion®, BC) measures numeric features of the mass, determines Relative Similarity (RS) between the mass of interest and images in a database of masses with known findings and outcomes, then retrieves and displays the images of the most similar known masses instantaneously for the radiologist to review during interpretation. This study tested BC for reproducibility of performance in comparison to that of three radiologists under a variety of operating conditions. The long-term goal is to standardize diagnosis, reduce radiologist variability and reduce false positives.

Key words: Computer-aided diagnosis, Breast cancer, Ultrasound, Sonography, ROC analysis, Relative similarity

1.   INTRODUCTION

The breast ultrasound (US) exam is widely recognized to be one of the more difficult imaging procedures to perform and interpret. The American College of Radiology developed the (Breast Imaging Reporting and Data System) scheme to standardize scanning, interpretation and reporting. Acceptance and utilization of BI-RADS® increasing but it has proven difficult to teach

the method, the quality of breast ultrasound is still regarded as highly operator dependent and many published reports show radiologists are uncomfortable with the number of benign and malignant masses that overlap in appearance. As a result, even with combined information from mammography and ultrasound it is often the case that each radiologist will apply a different threshold for deciding to biopsy a suspicious mass.

Over several years, we have developed, tested and validated a sophisticated computer-aided system for analyzing breast ultrasound [1–5]. This system (Breast Companion®, BC, Almen Laboratories, Inc.) provides extensive tools to define and segment breast masses, computes numeric features of the mass, compares the mass using Relative Similarity (RS) to images in a database of masses with known findings and outcomes (Reference Template Database), then retrieves and displays almost instantaneously a cluster of the most similar cases. BC uses case-based reasoning analysis (computerized lesion assessment, CLA) derived from measurement of the following categories of lesion parameters: margins, shape, echogenicity, echo texture, orientation, and posterior acoustic attenuation pattern. BC requires no classifier training, its graphic user interface. An entirely new user interface was developed for BC that incorporates a medical reporting system in conformance with the BI-RADS® sonography protocol. It tailored for the diagnostic breast ultrasound examination with the goal to help standardize interpretation and reporting plus to potentially reduce radiologist variability

The purpose of this study was to examine some factors that may impact the reproducibility of results from the developed CAD in future clinical use. ROC analysis (Analyze-It®) was the performance measure to estimate variability in comparison to the intra- and inter-reader variability of three radiologists. Specifically, the following issues were addressed in this study: (1) BC performance compared to that of three radiologists reading three sets of similar or identical cases, (2) radiologists' reproducibility and (3) BC reproducibility of performance with three independent datasets having increasing number of test cases (152, 291, 595) compared to a constant Reference Template Database (331 templates).

2.   METHODS AND MATERIALS

BI-RADS® requires the radiologist to assign an assessment value of 0–6 to an image, where, 0 is equivocal (requires more information), 1 is "no finding," 2 is "definitely benign," 3 is "probably benign," 4 is "probably malignant," 5 is "definitely malignant," and 6 is a known cancer.

The procedural steps for BC analysis of a mass identified on breast sonography are:

1) Radiologist reviews all images in the study and then selects image view(s) to be assessed.

2) Radiologist pre-processes image using standard set of tools such as windowing, enhancing, smoothing, etc.

3) Radiologist guides automatic or manual segmentation of the suspicious mass. BC measures image features of the defined mass.

4) Radiologist selects BI-RADS® reporting descriptors of the mass from the report chart and records overall BI-RADS® Assessment of the lesion.

5) BC retrieves and displays the most similar masses from the Reference Template Database.

6) Based on all information including the retrieved similar cases with known findings, the radiologist decides whether to have BC compute an independent assessment, CLA (Fig. 1).

7) Radiologist completes intermediate report that contains impressions, BI-RADS® Assessment and optionally results of BC CLA that represents the highest assessed BI-RADS® Category for a view selected by the radiologist.

Relative Similarity (RS) of the unknown mass is determined as follows [2]. The combinations of measured features of the mass from step (3) above may be represented by an N-dimensional vector $\mathbf{P}$ used to calculate the "Relative Similarity," $\mathbf{R}$, of one lesion to another. A new case with an unknown finding is compared directly to the database of stored images and a measure of $\mathbf{R}$ is computed for different lesions with confirmed findings. Similarity is calculated for a particular lesion $\mathbf{P}_{it}$ (the index of this "lesion in question" object) compared to the other lesions, $\mathbf{P}_k$ (k=1,…L). Image pre-processing reduces speckle, increases contrast, enhances edge gradient, and reduces shading effects to facilitate segmentation of the borders of the mass but all measurements are made on the unprocessed image. Segmentation involves a sequence of multi-level thresholding, radial gradient and region growing. The process is successful with all patient cases but the radiologist may choose to guide or edit the segmentation of more difficult masses. Our system requires that the radiologist always be "in the loop" throughout the process to ensure accuracy of lesion border definition. The process is open ("white box") and the reasons for a particular CLA assessment may be displayed. Retrieval of the most similar cases for the radiologist to review during interpretation is nearly instantaneous. BC provides a numeric 2–5 score for CLA on a continuous scale therefore in this study performance of the CAD was examined for a variety of conditions using ROC analysis [6].

Figure 1 shows a screen image of BC for a complex cyst compared to other images in the Reference Template Database. The mass is dark, with some internal echoes consistent with a cyst but with irregular indistinct margins more consistent with a solid mass and higher suspicion for cancer. Seven cases are automatically retrieved and displayed (with contours) on the right listed in rank order of Relative Similarity. In this case, all seven of the "similar" masses were benign and a low CLA score of 2.3 was calculated.
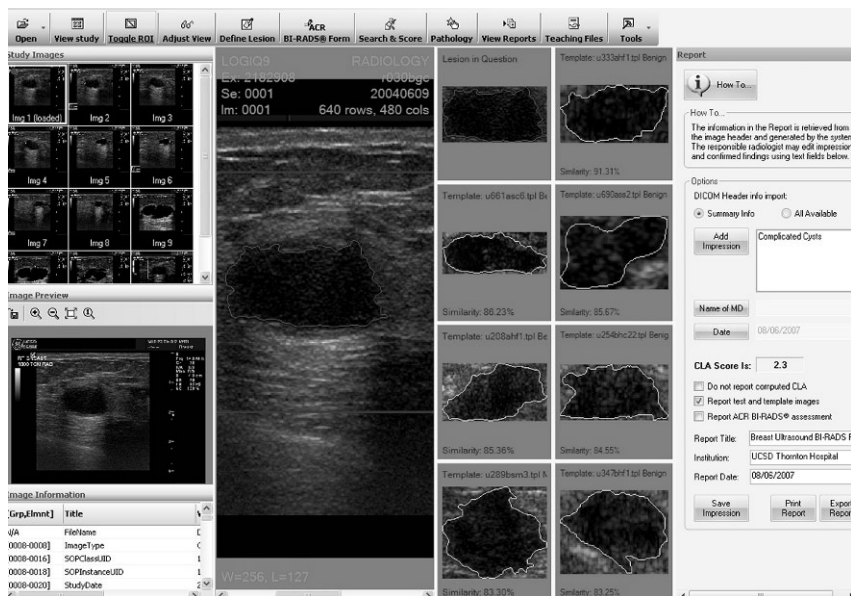
Figure 1. Complex cyst (*left* image) is compared to other images in the Reference Template Database.

Under IRB approval four different sets of breast sonography data were developed by retrieving cases chronologically from the medical center PACS and computerized medical records systems. When a suitable case was found where truth was confirmed (two-year benign follow up or biopsy), all ultrasound images of the study were examined to ensure they were free of graphic overlays or markers, had at least two views of each mass, had minimal artifacts, had conclusive pathology results, etc., in accordance with our acceptance criteria. Included cases were made anonymous and added with all its images to the Research PACS archive. The cases were assigned a sequential code number in the order of retrieval following our research protocol. Although arduous, our data mining methods are now highly refined and offer a very high yield of cases suitable for our research protocol.

The sizes of the three data sets read by the radiologists were: Set 1 (112 cases), Set 2 (215) and Set 3 (331). All three data sets contain non-overlapping

cases and had the following average mix of cases: 30% simple cyst, 18% complicated cysts, 30% solid benign and 22% malignant. A fourth independent data set (Set 4, 595 cases) was recently assembled with a statistically identical mix of cases. The radiologists' interpretation of these cases is not yet complete but performance of BC was measured with this new data set using the Reference Template Database (331 templates). For comparison we used a cohort of 152 cases assembled in a similar manner during our previous validation study in 2003–04 [4,5]. The new Set 4 of 595 cases was sampled to provide a smaller set of cases (291) with the same mix of findings. The age range was comparable for all data sets, 21–90 years old. The age distribution and mix of findings in these research databases correspond to the 5-year average population of cases in our Breast Imaging Service so they are presumed to be representative samples.

3. RESULTS

For three datasets (N=112, 215, 331) area under the ROC curve, A_Z, for the three radiologists varied from 0.90±0.03 to 0.83±0.03, while inter- and intra-reader ROC Areas were consistent within each data set but were not significantly different (Table 1). In Data Set 3 with 331 lesions, weighted kappa for the radiologists varied from 0.43 to 0.53 suggesting a "moderate" level of agreement. The standard deviation for A_Z was consistently ±0.02 to ±0.03 regardless of the size of the data set. BC was in an early form of development when Set 1 was tested, but by the time Set 3 was analyzed, extensive optimization of BC was completed. The stand-alone performance of BC was significantly higher than the three radiologists on the same Data Set 3.

Table 1. Radiologist ROC performance

	Set 1 (112) A_Z	Set 2 (215) A_Z	Set 3 (331) A_Z
BC	0.91 ± 0.02	–	0.98 ± 0.03
Rad1	0.90 ± 0.03	0.86 ± 0.03	0.87 ± 0.02
Rad2	0.87 ± 0.03	0.85 ± 0.03	0.83 ± 0.03
Rad3	–	0.87 ± 0.02	0.87 ± 0.02

Table 2. Breast companion ROC performance

	152 Cases A_Z	291 Cases A_Z	595 Cases A_Z
BC	0.958 ± 0.02	0.965 ± 0.02	0.982 ± 0.02

When the size of the data set of test cases was increased from 152 to 595 (Table 2) areas under the ROC curve, A_Z, for Breast Companion increased from 0.96 to 0.98 with a consistent standard deviation of ±0.02. Clearly the absolute number of benign cases was larger in the larger data sets but cancer prevalence remained constant at 21% ± 0.01.

4.   CONCLUSIONS

It remains to be seen how much variation for Ultrasound CAD will be acceptable in practice but the variability of the radiologists themselves offer a potential standard. The radiologists have not completed analysis of Set 4 (595) so direct comparison to BC is planned in a future study. Nonetheless, A_Z of BC for Set 3 and all three Data Sets in Table 2 are significantly higher that those of the three radiologists in Table 1. It appears BC's performance is consistent and stable with the highly suspicious cases (BI-RADS® Categories 4 and 5) and improves with the benign component because of very high accuracy of CLA on low-suspicion-level lesions (BI-RADS® Categories 2 and 3).

Results here suggest we may be able to study impact on radiologist reading performance by having them interpret the set of 595 cases with and without using BC (95% power). The goal will be to estimate potential reduction in the number of False Positives without a statistically significant increase in False Negatives. Much additional analysis needs to be done including evaluating effects of the size of the Reference Template Database on the reading performance and accuracy of CLA computations in general.

ACKNOWLEDGEMENTS

REFERENCES

1. MP Andre, M Galperin, G Contro, N Omid, L Olson: Acoustical Imaging 28 (2007) p. 267.
2. MP Andre, M Galperin, G Contro, N Omid, et al.: Acoustical Imaging 28 (2007) p. 341.
3. MP Andre, M Galperin, LK Olson, et al.: SPIE Medical Imaging 4322 (2001) p. 507.
4. M Galperin: SPIE Medical Imaging 5034 (2003).
5. MP André, M Galperin, LK Olson, et al.: Acoustical Imaging 26 (2002) p. 453.
6. JA Hanley, BJ McNeil: Radiology 148 (1983) p. 839.

WAVELET RESTORATION OF THREE-DIMENSIONAL MEDICAL PULSE-ECHO ULTRASOUND DATASETS IN AN EM FRAMEWORK

J. Ng, H. Gomersall, R. Prager, N. Kingsbury, G. Treece, A. Gee
Department of Engineering, University of Cambridge, Trumpington Street, Cambridge CB2 1PZ, United Kingdom

Abstract: The application of pulse-echo ultrasound to the non-invasive imaging of soft biological tissues is now well established in modern clinical practice. In spite of this, however, the quality of pulse-echo ultrasound images remains poor because of inherent blurring and low image resolution, and there exists significant scope for the development of restoration algorithms to address this problem. Like other similar inverse problems, the performance of a particular restoration algorithm is highly contingent on the appropriateness of its underlying image model. The modelling of piecewise smooth natural images has been well studied in mainstream image processing, and it is known that the sparsifying properties of the wavelet transform are especially useful to provide simple but effective image models, leading to computationally efficient wavelet shrinkage methods for denoising. In a previous publication, we showed how wavelet-based models of natural images could be used in the context of pulse-echo ultrasound for image restoration; in particular, we proposed a simple model for the acoustic reflectivity functions of typical soft biological tissues that was able to account for their different behaviours on macroscopic and microscopic scales. We demonstrated how this model could be used in an expectation-maximisation (EM) restoration algorithm that simply alternated between Wiener filtering and wavelet shrinkage. Our previous results for two-dimensional images showed excellent performance compared to other methods based on less sophisticated image models, and in this paper, we extend our algorithm to the restoration of three-dimensional datasets to correct also for out-of-plane blurring.

Key words: Restoration, Deconvolution, Wavelet, Expectation-maximisation, EM, Speckle

1.   INTRODUCTION

The objective of pulse-echo ultrasound imaging is to acquire a profile of the distribution of acoustic inhomogeneities (which are assumed, reasonably, to be strongly correlated with structural features) within a region of soft tissue. This is achieved by transmitting short-duration radio-frequency (RF) pressure pulses into the soft tissue and recording backscattered echoes which are then envelope-detected to construct an image of the anatomy. Because soft tissues typically contain dense concentrations of scatterers which are small compared to these pressure pulses, the rudimentary images constructed in this way are usually blurred, and acoustic interference between these scatterers gives rise to a pseudo-random texture known as *speckle*. Although speckle obscures significant image features and degrades the resolvability of structures, it also contains important textural information that is useful to clinicians for tissue identification. Therefore, in designing a suitable restoration algorithm, we seek to improve the resolution of the image while also retaining the textural information present in the speckle.

Under the standard assumptions of linear wave propagation and weak scattering [1,2], we may apply the Born approximation and express the relationship between the acoustic reflectivity function of the soft tissue and the backscattered RF echoes linearly. To sample the RF echoes more sparsely, we demodulate them to baseband and deal with complex-valued quantities. With these considerations, we may write $\mathbf{y} = H\mathbf{x} + \mathbf{n}$, where $\mathbf{y}$ is an $N \times 1$ vector of lexicographically arranged samples of the demodulated baseband image, $\mathbf{x}$ is a similar $N \times 1$ vector of samples of the acoustic reflectivity function, H is the $N \times N$ blurring matrix and $\mathbf{n}$ is an $N \times 1$ noise vector that accounts for measurement error. We assume $\mathbf{n}$ to be white and to obey a multivariate complex Gaussian distribution as defined in [3] with zero mean and covariance matrix $E(\mathbf{n}\mathbf{n}^{\mathrm{H}}) = 2\sigma_n^2 I_N$, i.e.

$$p(\mathbf{n} \,|\sigma_n) = \frac{1}{(2\pi\sigma_n^2)^N} \exp\left(-\frac{\|\mathbf{n}\|^2}{2\sigma_n^2}\right).$$

In this setting, the problem of image restoration is to estimate $\mathbf{x}$ given *a priori* knowledge of $\mathbf{y}$, H and σ_n^2. Since the blurring matrix H is usually singular or at least highly ill-conditioned, direct inversion of H is not viable and regularising constraints are usually imposed to confine our estimate of $\mathbf{x}$ to a predefined functional subspace. In a Bayesian context, this corresponds to maximum *a posteriori* (MAP) estimation: treating $\mathbf{x}$ and $\mathbf{y}$ as random vectors, and recognising that $\mathbf{x}$ and σ_n are independent, Bayes's rule yields $p(\mathbf{x}\,|\,\mathbf{y}, \sigma_n) \propto p(\mathbf{y}\,|\,\mathbf{x}, \sigma_n)\,p(\mathbf{x})$; substituting $\mathbf{n} = \mathbf{y} - H\mathbf{x}$ into

the probability density function of **n** and taking logarithms, our MAP estimate $\hat{\mathbf{x}}$ may thus be written as

$$\hat{\mathbf{x}} = \arg\,\min_{\mathbf{x}}\, \left[\frac{1}{2\sigma_n^2}\, \|\mathbf{y} - H\mathbf{x}\|^2 - \ln p(\mathbf{x}) \right].$$

Previously proposed choices for $p(\mathbf{x})$ include the Gaussian distribution, leading to Wiener filtering [4,5], and the Laplacian distribution [6].

2.   IMAGE RESTORATION

The problem with such simple priors as the Gaussian distribution or the Laplacian distribution is that neither of them account explicitly for the different behaviours of the reflectivity function on different scales. If we examine a typical ultrasound image, we observe two things.

Firstly, on a microscopic scale and within a homogeneous region of tissue, the speckle pattern behaves in a pseudo-random way and the degree of sample-to-sample correlation depends on the size of the pulse-echo blurring kernel. Therefore, in the absence of any blurring, we would expect to see very little sample-to-sample correlation, suggesting that, at a microscopic scale, the reflectivity function behaves like a random field of identically distributed, uncorrelated random variables.

Secondly, on a macroscopic scale, the locally averaged amplitude of speckle varies piecewise smoothly, changing slowly in regions of homogeneous tissue but changing sharply at structural boundaries. This behaviour is characteristic of natural images and suggests that, at a macroscopic scale, it is acceptable to treat the reflectivity function as a natural image and, like other natural images, we expect it to be well sparsified in the wavelet domain [7]. The locally averaged amplitude of the speckle is a measure of the scattering strength or *echogenicity* of the image.

Previously, we observed that both these behaviours could be simultaneously accommodated by modelling the reflectivity function as the product of a piecewise smooth echogenicity map and a random field [8]. Formally, we write $\mathbf{x} = S\mathbf{w}$, where S is a diagonal matrix containing samples of the echogenicity map (which is real-valued and positive), and $\mathbf{w}$ is a vector of identically distributed, uncorrelated, complex-valued random variables, each of which have zero mean and unit variance. In the absence of any further information about $\mathbf{w}$, we assume that each of its samples obeys a multivariate complex Gaussian distribution.

2.1   Expectation-Maximisation (EM)

To exploit this simple model of the reflectivity function, we use expectation-maximisation (EM) to develop an iterative restoration algorithm [9]. Given an inference problem where we seek the MAP estimate of a set of parameters Θ from observed data U, and given a model that contains unobservable nuisance parameters J, let $\widehat{\Theta}_k$ be the estimate of Θ at the kth iteration. The EM algorithm iteratively updates $\widehat{\Theta}_k$ by computing the following two quantities,

$$Q\left(\Theta \mid \widehat{\Theta}_k\right) = \int p\left(J \mid U, \widehat{\Theta}_k\right) \ln p\left(U, J \mid \Theta\right) dJ,$$

$$\widehat{\Theta}_{k+1} = \arg\max_{\Theta}\left[Q\left(\Theta \mid \widehat{\Theta}_k\right) + \ln p\left(\Theta\right)\right],$$

respectively in the E-step and the M-step of each iteration. For our restoration problem, we assign $U = y$, $\Theta = S$ and $J = x$.

2.2   E-Step: Wiener Filtering

With this particular assignment of variables, we find that

$$p\left(x \mid y, \widehat{S}_k\right) \propto \exp\left[-(x - m_k)^{\mathrm{H}} C_k^{-1}(x - m_k)\right],$$

$$m_k = \mathrm{E}\left(x \mid y, \widehat{S}_k\right) = \left(H^{\mathrm{H}}H \mid \widehat{\sigma}_n^2 \widehat{S}_k^{-2}\right)^{-1} H^{\mathrm{H}}y,$$

$$C_k \equiv \mathrm{Var}\left(x \mid y, \widehat{S}_k^{-2}\right) = 2\widehat{\sigma}_n^2\left(H^{\mathrm{H}}H + \widehat{\sigma}_n^2 \widehat{S}_k^{-2}\right)^{-1}.$$

The mean vector m_k represents the minimum mean squared error estimate of x and it is thus our best estimate of the reflectivity function at the kth iteration. Its computation is identical to applying a Wiener filter to y.

2.3   M-Step: Wavelet Shrinkage

Let $s_i = (S)_i$, $\sigma_{i,k}^2 = (C_k)_{ii}$ and $m_{i,k} = (m_k)_i$. In our case, the optimisation problem in the M-step reduces to

$$\widehat{S}_{k+1} = \arg\min_{S}\left[\sum_{i=1}^{N}\left(2\ln s_i + \frac{|m_{i,k}|^2 + \sigma_{i,k}^2}{2s_i^2}\right) - \ln p\left(S\right)\right].$$

It can be shown [8] that this minimisation problem corresponds to removing multiplicative noise from $\sqrt{\left|m_{i,k}\right|^2 + \sigma^2_{i,k}}$, and since the diagonal elements of S represent a piecewise smooth image, we are able to compute $\hat{S}_{k+1}$ very efficiently by taking logarithms (to turn the multiplicative noise into additive noise) and applying wavelet shrinkage. This corresponds to specifying the prior $p(S)$ in terms of the wavelet coefficients of the logarithm of the echogenicity map; the form of the prior depends on the exact shrinkage rule used. Because the wavelet transform sparsifies a natural image and compresses its energy into a small number of large wavelet coefficients, small coefficients are likely to correspond to noise, and wavelet shrinkage exploits this by attenuating small wavelet coefficients.

3. RESULTS

In Fig. 1, we present a set of simulation results for a three-dimensional dataset made up of four spherical regions with different echogenicities embedded in a homogeneous background, and we compare our algorithm with previously proposed methods. The reflectivity estimate from our EM algorithm achieves the best improvement in signal-to-noise ratio (ISNR) and qualitatively, it exhibits high resolution and good visual quality. The echogenicity map is also shown, and it is encouraging to see that it is substantially free of speckle as expected. In Fig. 2, we demonstrate the performance of our EM algorithm on an *in vitro* dataset, acquired by rectilinearly scanning a phantom containing spherical inclusions embedded in a homogeneous background. Our reflectivity estimate shows significantly better contrast and more sharply defined edges than the original dataset.

REFERENCES

1 Ng, J., Prager, R., Kingsbury, N., Treece, G and Gee, A., 2006, Modeling ultrasound imaging as a linear, shift-variant system, *IEEE Trans Ultrason Ferroelect Freq Contr*, **53**(3):550–568.
2 Jensen, J. A., 1991, A model for the propagation and scattering of ultrasound in tissue, *J Acoust Soc Am*, **89**:182–190.
3 Kay, S. M., 1993, *Fundamentals of Statistical Signal Processing: Estimation Theory*, vol. 1 of Signal Processing, Prentice Hall.
4 Taxt, T. and Strand, J., 2001, Two-dimensional noise-robust blind deconvolution of ultrasound images, *IEEE Trans Ultrason Ferroelect Freq Contr*, **48**(4):861–866.

5 Taxt, T., 2001, Three-dimensional blind deconvolution of ultrasound images, *IEEE Trans Ultrason Ferroelect Freq Contr*, **48**(4):867–871.
6 Michailovich, O. and Adam, D., 2005, A novel approach to the 2-D blind deconvolution problem in medical ultrasound, *IEEE Trans Ultrason Ferroelect Freq Contr*, **24**(1):86–104.
7 Mallat, S., 1999, *A Wavelet Tour of Signal Processing*, Academic Press.
8 Ng, J., Prager, R., Kingsbury, N., Treece, G. and Gee, A., 2007, Wavelet restoration of medical pulse-echo ultrasound images in an EM framework, *IEEE Trans Ultrason Ferroelect Freq Contr*, **54**:550–568.
9 Dellaert, F., 2002, The expectation-maximization algorithm, Technical Report GIT-GVU-02-20, Georgia Institute of Technology.
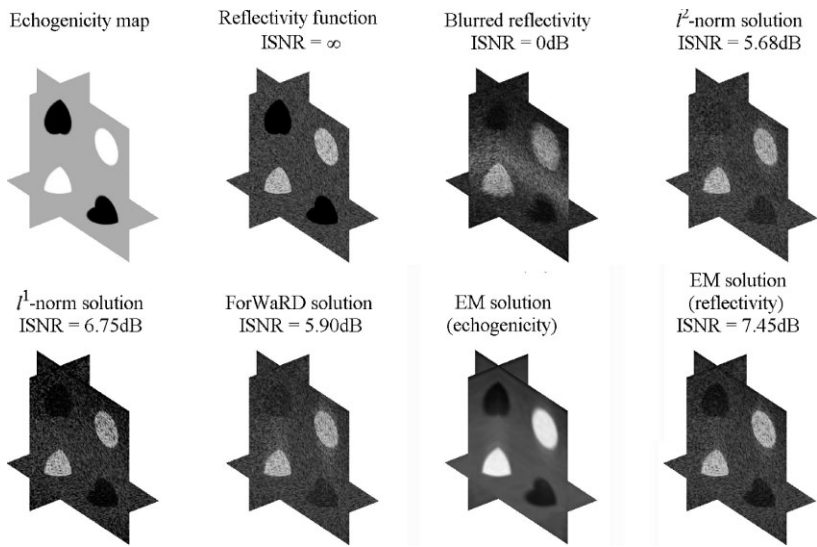
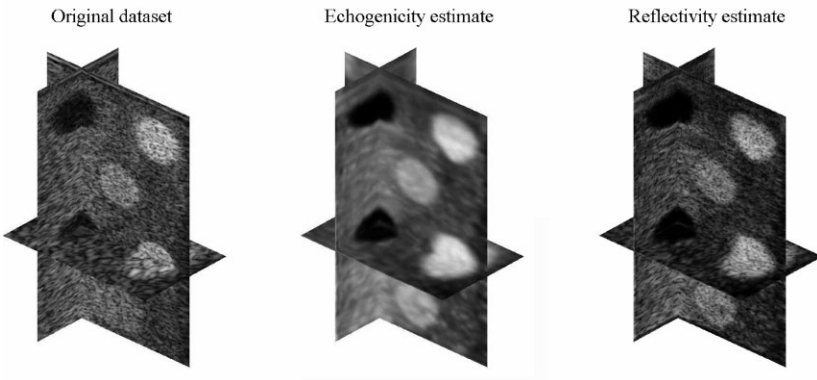*Figure 1.* Three-dimensional simulation results.

Figure 2. Three-dimensional *in vitro* results.

SYNTHETIC APERTURE FOCUSING OF ECHOGRAPHIC IMAGES BY MEANS OF PULSE COMPRESSION

E. Biagi, L. Masotti, L. Pampaloni, M. Scabia
Laboratorio Ultrasuoni e Controlli Non Distruttivi, Università di Firenze, Italy

Abstract: A novel technique for focusing echographic images inspired by Synthetic Aperture Radar focusing algorithms is presented. Pulse compression both in depth and lateral directions is used. Problems arising from the different geometry of the echographic case with respect to radars are solved through a remapping in the frequency domain. Experimental results demonstrating the improvement in resolution are shown.

Key words: Lateral matched filter, Plastic wire phantom, Tissue mimicking phantom

1.   INTRODUCTION

Synthetic Aperture Radars (SAR) employ a focusing technique that is much different than those used in echography by commercial scanners, in order to achieve focusing of B-Mode images.

An echographic image is typically focused by transmitting and receiving, for each line of sight, a short pulse through a certain "sub-aperture" of an array probe; the contribution of each element of this sub-aperture is processed with a delay calculated according to the geometric law for focusing at the desired depth; this process is repeated for all transmission foci.

On the other hand, SAR focusing is achieved by applying a phase equalization filter across the image in both dimensions (i.e. range and azimuth). This is obtained by transmitting a *chirp* excitation signal, and performing pulse compression along both image dimensions.

Applying Synthetic Aperture Focusing Techniques (SAFT) to ultrasonic imaging is an interesting and exciting prospect. This concept is not novel, and although not yet implemented in commercial systems, several authors in the past years worked either with chirp signals to increase ultrasound penetration in tissue [3,4] or with synthetic aperture techniques to achieve better lateral resolution. In order to apply SAFT to ultrasound it's necessary to operate on an unfocused received Radio-Frequency (RF) image, similar to the one received by a SAR before its matched filter. This kind of ultrasonic image can be obtained by performing the scan using a single transducer element of the linear array probe, instead of a sub-aperture. In order to compensate for the lower energy transmitted with this kind of scan, a chirp transmit signal can be used. The main difficulty in applying SAR focusing to echographic images lies in the different geometry of the SAR case compared to the ultrasonic case. This is due both to the different orders of magnitude of physical quantities (such as, for example, frequency and speed of propagation in the medium) and to the region investigated through ultrasound being much nearer to the probe, with respect to the probe width, compared to the distance of a SAR from its observed scene relatively to the scan length.

In this work we propose a technique that overcomes these limitations and applies Synthetic Aperture Focusing to echographic images. The method that we propose, labelled ICARUS (Imaging pulse Compression Algorithm through Remapping of UltraSound), operates a remapping of the RF ultrasonic image in the frequency domain in order to correctly perform the SAR focusing also in the echographic case.

2.   THEORETICAL ANALYSIS AND SIMULATED RESULTS

The application of SAR focusing to the typical geometries of echographic images was performed by simulating the unfocussed Radio-Frequency (RF) ultrasonic beam using the Field II ultrasound simulation tool [5].

For all simulations presented in this work we used the parameters of the LA523 linear array probe (Esaote S.p.a., Florence) that was employed to obtain the experimental results obtained in the next section. This probe features 192 elements spaced with a 0.245 mm pitch, with central frequency 7.5 MHz and –6 dB bandwidth 5.5 MHz. This is the same probe that was used to perform experimental characterization, described in the next section.

Let's consider the case of two point scatterers at different depths, 1.5 cm and 3 cm and lateral position 0.78 cm and 1.57 cm; a linear array ultrasonic probe is used for insonifying those scatterers by exciting each probe element

at a time with a chirp signal and for receiving the backscattered ultrasonic signal with the same element. This produces a completely unfocused RF ultrasonic image (Fig. 1) obtained with a scanning technique similar to the one employed in SAR.
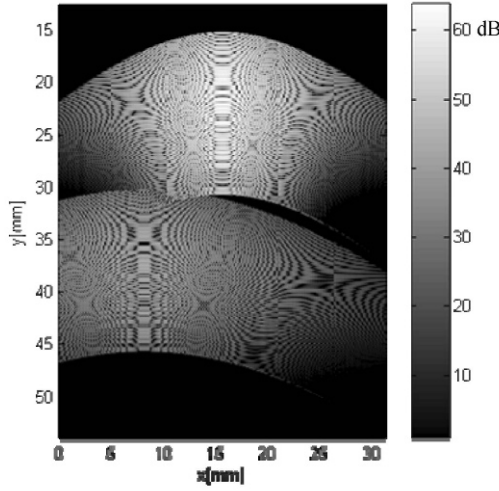

Figure 1. Simulated received (unfocused) RF image, obtained using x_0=15.6 mm, r=30 mm, f_t=7.5 MHz, k=3.15×10^4 rad/m, B=5 MHz, T=20 μs, b=1.40×10^6 rad/m^2. The depth envelope $p(\cdot,\cdot)$ is a rectangle while the lateral envelope $a(\cdot,\cdot)$ is a gaussian function.
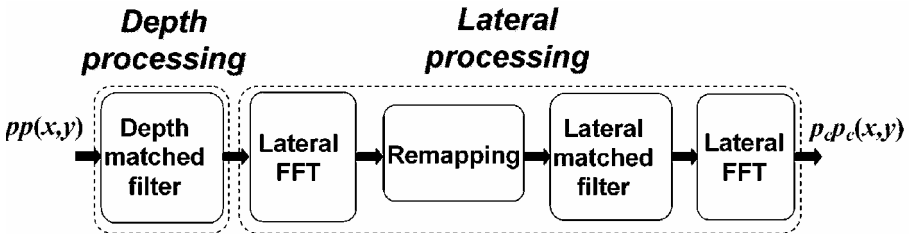
Figure 2. Block diagram of the ICARUS algorithm.

As shown in Fig. 2, ICARUS consists of two blocks: first, we have a depth (*y* coordinate) processing and then a lateral (*x* coordinate) processing. Depth processing consists of coherent demodulation and matched filtering of each vertical track. Lateral processing consists of matched filtering of each lateral track after remapping in the (ω_x, *y*) domain, where ω_x is the lateral spatial frequency. This remapping in the (ω_x, *y*) domain is the core of our algorithm and it is necessary because the unfocused received images are strongly affected by curvature. The echoes of different scatterers can be cross-coupled in the 2D spatial domain (*x, y*); however in the frequency-spatial

domain (ω_x, y) these same echoes are separated. Therefore in this domain we can compensate the curvature of the echo of each scatterer and then apply the matched filter in the lateral direction. It is possible to use a lateral matched filtering because the received RF frame presents a frequency modulation in the lateral direction as well, due to the different distances between the scatterer and the various elements of the array probe. The final result is shown in Fig. 3, where it is possible to observe how two different scatterers were focused through ICARUS.
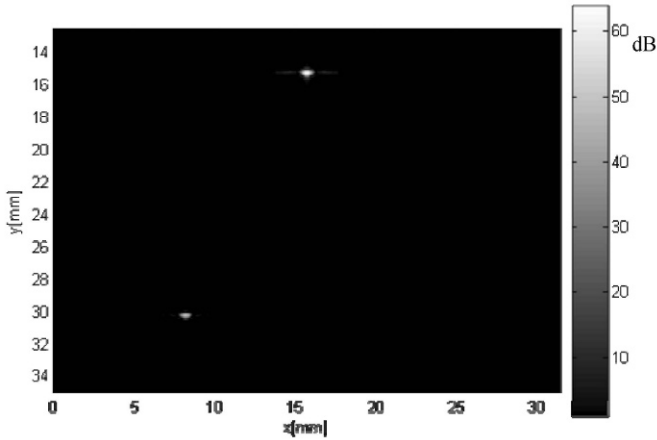
Figure 3. ICARUS focused version of image of 1.

Theoretical analysis of ICARUS [2] allowed us to identify some advantages of this method when compared to traditional focusing: (1) resolution throughout the image is uniform, due to the fact that axial resolution is dependent on bandwidth, while lateral resolution is dependent on angular dimension of the radiation pattern of the transducer. Both of these resolutions are independent from the actual position of the scatterer. This theoretical result is valid in the ideal case of a propagation medium without frequency selective attenuation. However, the resolution-loss along depth is much lower in ICARUS focusing than in traditional echographic focusing, where it is also caused by the geometry involved in the delay-and-add method and not only by frequency-selective attenuation. (2) Resolution is improved with respect to traditional focusing techniques due to the use of matched filters in both vertical and lateral directions.

3.   EXPERIMENTAL RESULTS

A first set of results was obtained on a test object consisting of two plastic wires with diameter 0.06 mm immersed in a water tank.
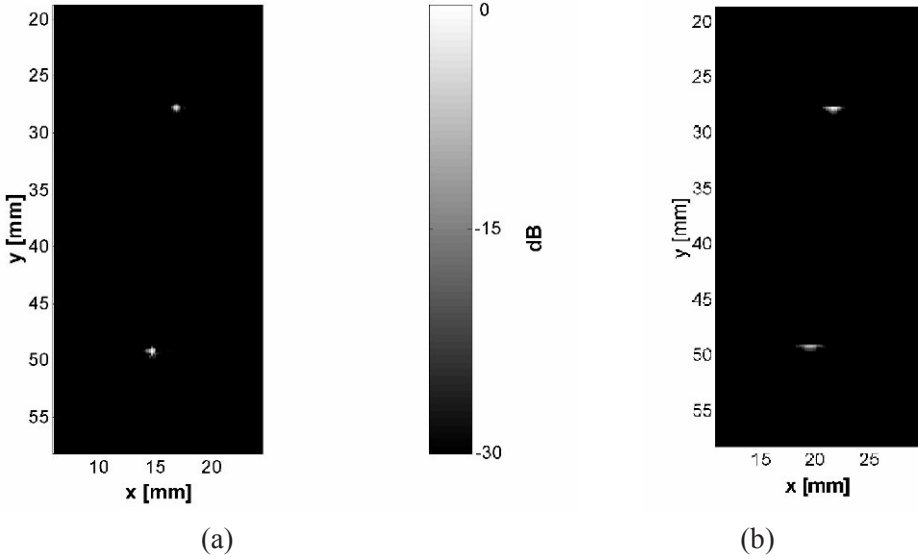
Figure 4. (**a**) ICARUS focused image of two plastic wires (φ 0.06 mm) immersed in a water tank; (**b**) traditionally focused image of the same phantom.

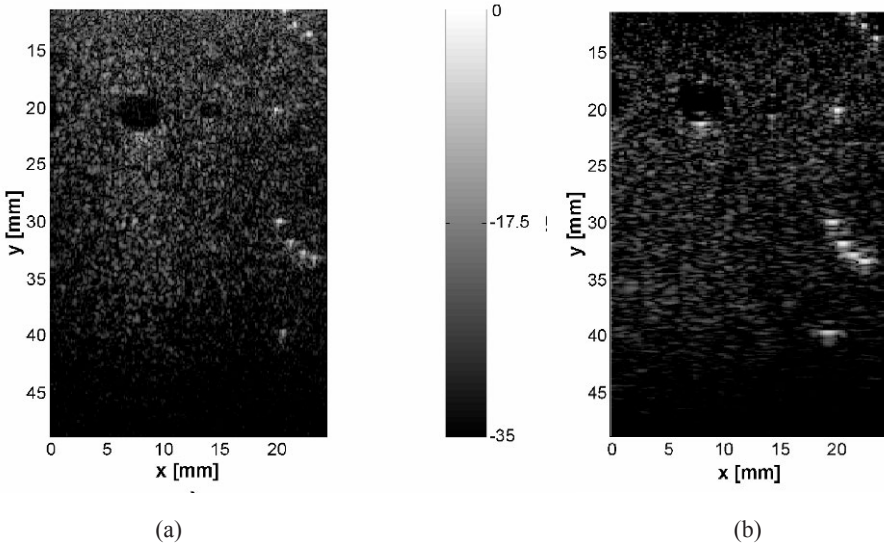Figure 5. (**a**) ICARUS focused image of RMI 414b phantom; (**b**) traditionally focused image of the same phantom.

The experimental setup that we used for validating the ICARUS technique was based on the FEMMINA (Fast Echographic Multi-parametric Multi-Image Novel Apparatus) platform [3], used to acquire and to process the RF signals in order to produce the ICARUS focused images in real-time.

FEMMINA was connected to the front-end of a commercial digital echograph (Megas, Esaote S.p.A., Florence) equipped with a 7.5 MHz central frequency, 192 elements linear array probe (prototype LA523, Esaote S.p.A., Florence).

In Fig. 4a we show the result of the application of ICARUS to this plastic wires phantom. The relative resolutions for the upper wire are: in depth 0.2 mm; in the lateral direction, 0.24 mm. Figure 4b shows the same test object imaged using traditional focusing. Resolutions in this case were 0.2 mm in depth, and 0.4 mm laterally. It is possible to observe how ICARUS resolution tends to remain more uniform along depth than in the traditionally focused image.

A second set of measurements was performed on a tissue mimicking phantom (model 414b, Radiation Measurements Inc., Middleton, WI). If we compare the two images of Figs. 5a, b we can see that ICARUS achieves a better resolution over the whole image, which appears sharper and presents details otherwise masked. ICARUS is also capable of resolving the tissue-mimicking speckle much more clearly.

4.   CONCLUSIONS

This paper describes a novel echographic focusing technique inspired by SAR algorithms. Because of the different geometry, SAR algorithms can not be directly applied to the ultrasonic case. We developed a method called ICARUS based on pulse compression of linearly frequency modulated signals that, through a remapping in the frequency domain, permits an improvement in resolution of echographic images in both depth and lateral directions. Experimental results demonstrated the validity of our method in improving resolution of echographic images.

REFERENCES

1. M. Pollakowski and H. Ermert, "Chirp Signal Matching and Signal Power Optimization in Pulse-Echo Mode Ultrasonic Nondestructive Testing", IEEE Trans. Ultrason. Ferroelec. Freq. Contr., vol. 41, no. 3, September 1992, pp. 655–659.
2. E. Biagi, L. Masotti, M. Scabia, I. Rossi, and N. Dreoni, "ICARUS. Metodo di focalizzazione di un'immagine ecografica e relativo sistema ecografico". Italian Patent n° FI2002A000228, 2003.
3. M. Scabia, E. Biagi, and L. Masotti, "Hardware and software platform for real-time processing and visualization of echographic radiofrequency signals". IEEE Trans. Ultrason. Ferroelec. Freq. Contr., vol. 49, no. 10, October 2002, pp. 1444–1452.

4. E. Biagi, N. Dreoni, L. Masotti, M. Scabia, "ICARUS: Imaging pulse Compression Algorithm through Remapping of UltraSound", IEEE Trans. Ultrason. Ferroelec. Freq. Contr. vol. 52, no. 2, February 2005, pp. 261–279.

5. J.A. Jensen, *Field: A Program for Simulating Ultrasound Systems*, Paper presented at the 10th Nordic-Baltic Conference on Biomedical Imaging Published in Medical & Biological Engineering & Computing, pp. 351–353, Vol. 34, Suppl. 1, Part 1, 1996.

ML ESTIMATION FOR ACOUSTICAL IMAGE DEBLURRING

A. Palladini, N. Testoni, L. De Marchi, N. Speciale
ARCES/DEIS – University of Bologna, Viale Risorgimento 2, 40136, Bologna, Italy

Abstract: In this paper we present a deconvolution technique for ultrasound images based on a maximum likelihood estimation procedure. In our approach the blur effect is estimated through homomorphic techniques either from the transducer response, measured with an experimental setting, or from the *in-vivo* scans. The ultrasonic signal envelope is then considered as a discrete sequence affected by a known intersymbol interference and additive white Gaussian noise and processed with a reduced complexity Viterbi algorithm, which is an optimum solution for the estimation of discrete sequences affected by both noise and intersymbol interference.

Key words: Ultrasound images, Images deblurring, ML estimation, Viterbi Algorithm

1.   INTRODUCTION

Ultrasounds (US) are a cost effective, mobile, noninvasive, harmless, and suitably accurate imaging technique. The main drawback is that signal resolution is limited by the transducer finite bandwidth and by the non-negligible width of the transmitted acoustic beam. Image restoration techniques, such as deconvolution, can be employed to improve the resolution of US images and their diagnostic significance.

Two approaches are the most common when dealing with US image deconvolution. The first incorporates the Point Spread Function (PSF) estimation procedure within the deconvolution algorithm. This approach often leads to the development of computationally heavy algorithms, usually far from satisfying the real-time signal processing constraints distinctive of the US biomedical investigation environment.

In the second approach, PSF and true image estimation are two disjoint procedures. Within this approach, these procedures can be implemented by relatively simple algorithms, often suitable for real-time implementation.

Generally speaking, as the PSF is a band-limited function and due to the presence of noise, image restoration is an ill-posed problem. To obtain a stable algorithm, delivering a unique solution, additional constraints must be imposed. Designing a method which exhibits the most suitable compromise among computational complexity, reliability and portability for biomedical real-time imaging applications is still an open challenge. Good reviews of the existing approaches are in Kundur [1] and Michailovich [2].

As the blurring effect can also be thought as an Intersymbol Interference (ISI) on the acquired radio frequency (RF) signal, in the present work we describe a de-blurring procedure, based on Viterbi algorithm (VA) [3], which is an optimum solution for the Maximum Likelihood (ML) estimation of discrete-value sequences in presence of ISI and memoryless noise.

2.   THE PROPOSED ALGORITHM

In order to develop an effective, stable and fast deconvolution method, suitable for real-time biomedical imaging applications, we estimate the PSF and the true image separately. Moreover, as done by Abeyratne [4], we reduce the deconvolution to a 1-D problem by processing each scan line separately, assuming the following discrete time model for the received image line:

$$z_k = y_k + n_k = \sum_{i=1}^{L} x_{k-i} h_i + n_k \tag{1}$$

where x_k are the true image coefficients, h_i are the PSF coefficients and n_k are Gaussian, zero-mean, noise samples. A 1-D deconvolution procedure is preferable for real-time processing: each scan line is processed during the signal acquisition step, avoiding the storage of the whole image.

For the estimation of the PSF, we adopted the homomorphic, Wavelet based, procedure presented by Adam[2], which assumes the model described by Eq. (1). According to this work, we estimated the pulse in the RF domain using a Wavelet analysis of the RF-sequence spectrum: doing this, we were able to avoid the problems associated with cepstrum-based techniques while still being capable of processing short data segments, with good noise tolerance[2].

The estimation was performed on two different experimental setups. In the former, the pulse was estimated by processing the whole imaging system

PSF measured by illuminating a metal wire in a water-filled tank. In the latter, *in-vivo* RF signal were sourced to extract the PSF.

To obtain a stable and computationally efficient image restoration algorithm, we choose a ML regularization approach. By modeling the true image coefficients x_k as a random process with uniform distribution over a finite alphabet of size M, the distorted signal sample y_k can be thought as a realization of a discrete-time Markov process with $J=M^{L-1}$ states.

The ML estimation of a Markov process state sequence y from the observation of a noisy sequence z can be computed in a recursive manner through a Viterbi Algorithm (VA) built over the trellis diagram[3] associated to the process. The drawback of this approach is that, even for moderately small values of M and L, the VA becomes impractical, as the computational and memory requirements for the estimation of a sequence of length K are proportional to $K \cdot M^{L-1}$.

In the proposed approach, we introduced a Modified Viterbi Algorithm (MVA) associating the trellis-diagram states to the distorted and noise-free signal symbols x, reducing the trellis to a full connected M-state diagram, where each state at step k is connected to all the states at step $k+1$. The resulting computational cost is proportional to $K \cdot M \cdot (M+L)$ and therefore suitable for real-time biomedical implementations.

Finally, to deal with the nonuniform statistic of US image amplitude, we adopted a nonuniform quantization alphabet defined through Lloyd-Max rules applied over the observed signal. This also allows for a quantization levels reduction, with a consequent computational cost reduction.

3.   APPLICATION TO BIOMEDICAL US IMAGES

In order to verify the effectiveness of the proposed algorithm as a de-blurring technique for biomedical images, we tested it on an US RF-signal database which comprises both synthetic phantom (CIRS Model 047) and *in-vivo* Trans-Rectal US (TRUS) acquisitions of prostatic glands (264 frames), all obtained with a commercial US equipment (MYLAB90 Esaote S.p.a.).

After the processing of the signal envelope, de-blurring performances were evaluated in terms of enhancement in both image resolution and quality. To quantify resolution improvement, we measured the lateral and axial resolution gain at –6dB (RG-L/A) [4]; conversely, Peak Signal to Noise Ratio (PSNR) and Quality Index (QI) were used to compute the dissimilarity between the original and processed image, in terms of loss of correlation, luminance and contrast distortion [5]; finally we measured image contrast enhancement on phantoms by means of the Contrast Gain (CG) [6].

All the images from the dataset were processed with our proposed de-blurring algorithm driven by the pulse estimated following the two proposed procedures. We find that image processing based on the PSF estimated directly from the *in-vivo* frames provides better performance with respect to the considered evaluation metrics. This is due to the system response aberration caused by tissue intrinsic sound speed propagation constant inhomogeneities, which can be accounted only by estimating the pulse form the *in-vivo* frames.

The results obtained with the pulse estimated from the *in-vivo* and phantom images are shown in Table 1; the best results in each column are written in bold. As it can be clearly seen, the proposed algorithm provides a good resolution increase in both axial and lateral direction for both *in-vivo* and phantom acquisitions, with better performance on the *in-vivo* frames.

Finally, we compared algorithm performance to other US deconvolution algorithms present in literature, FWRD [7] and WLSD [8], both applied on signal envelope. As it is clearly shown by the results in Table 1, our proposed algorithm outperforms both FWRD and WLSD with respect to all the proposed metrics. Figure 1 compares the visual quality of images processed with the proposed approach (Fig. 1b, d) to the original B-Mode images (Figure 1a, c): as it can be seen, the resolution and the contrast in the processed images are much better than in the original.

4.   CONCLUSIONS

A de-blurring technique for US images, based on two disjoint procedures for PSF estimation and image de-blurring was presented. Point spread function estimation is based on a 1-D homomorphic procedure. Ultrasound image de-blurring is performed by means of a ML estimation procedure. A novel, efficient implementation of the ML estimation procedure is proposed, based on a reduced complexity Viterbi algorithm.

Experimental results on both *in-vivo* and phantom US images show the effectiveness of the proposed algorithm as a real-time capable de-blurring method. Further developments for this work comprise direct application on the RF signal, local estimation of the PSF through adaptive techniques and processing of signals distorted with non-minimum phase impulses.

Table 1. Image enhancement evaluation metrics computed for in-vivo prostatic gland images and synthetic phantom images.

Image-algorithm	RG-L	RG-A	CG	PSNR	IQ
In-vivo – MVA 64	**3.82**	**4.96**	**6.17**	**22.5**	**0.91**
In-vivo – MVA 32	3.81	4.93	6.10	**22.5**	**0.91**
In-vivo – FWRD	1.03	1.00	1.02	11.6	0.52
In-vivo – WLSD	1.27	1.85	1.20	11.5	0.52
Phantom – MVA 64	**1.64**	**1.81**	**6.51**	**35.3**	**0.91**
Phantom – MVA 32	1.62	1.79	6.46	35.2	**0.91**
Phantom – FWRD	1.04	1.00	1.12	11.8	0.37
Phantom – WLSD	1.37	1.67	1.31	11.6	0.40
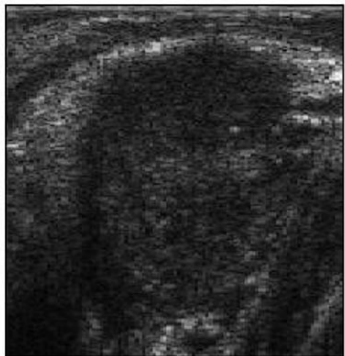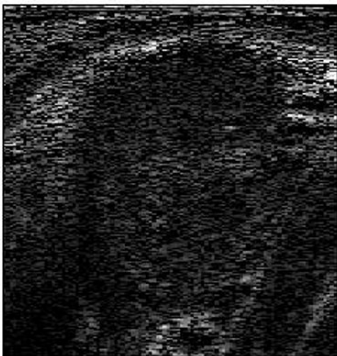
(a) (b)
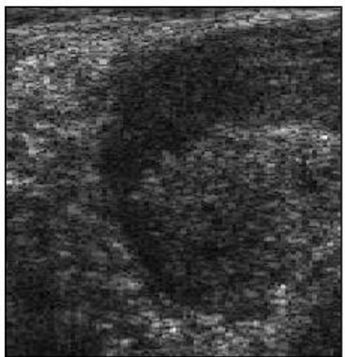
(c) (d)

Figure 1. Comparison between B-Mode images of an in-vivo prostatic gland acquisition before (**a, c**) and after proposed algorithm processing (**b, d**).

ACKNOWLEDGEMENTS

REFERENCES

1. D. Kundur and D. Hatzinakos, "Blind image deconvolution", IEEE Sig. Process. Mag., vol. 13, no. 3, pp. 43–64, May 1996.
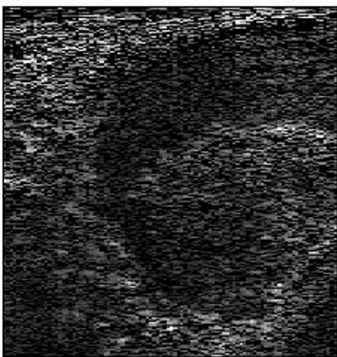2. V. Michailovich and D. Adam, "A novel approach to the 2-D blind de-convolution problem in medical ultrasound", IEEE Trans. Med. Imaging, vol. 23, no. 1, pp. 86–104, Jan. 2005.
3. G. Forney, "The Viterbi algorithm", Proc. IEEE, vol. 61, pp. 263–268, Mar. 1973.
4. U. Abeyratne, A. Petropulu, and J. Reid, "Higher order spectra based de-convolution of ultrasound images", IEEE Trans. Ultrason. Ferroelec. Freq. Contr., vol. 42, no. 6, pp. 1064–1075, Nov. 1995.
5. C. Loizou, et al., "Comparative evaluation of despeckle filtering in ultrasound imaging of the carotid artery images", IEEE Trans. Ultrason. Ferroelec. Freq. Contr., vol. 42, no. 6, pp. 1563–1669, Oct. 2005.
6. J. Tang, E. Peli, and S. Acton, "Image enhancement using a contrast measure in the compressed domain", IEEE Sig. Proc. Lett., vol. 10, no. 10, pp. 289– 292, Oct. 2005.
7. M. Izzetoglu, B. Onaral, and B. Bilgutay, "Forward: Fourier-wavelet regularized deconvolution for ill-conditioned systems", IEEE Trans. Sig. Proc., vol. 52, no. 2, pp. 418–433, Feb. 2004.
8. R. Neelamani, H. Choi, and R. Baraniuk, "Wavelet domain least squares de-convolution for ultrasonic backscattered signals", Proc. EMBS IEEE, vol. I, pp. 321–324, 2000.

THREE-DIMENSIONAL IMAGING
BY USING SINGULARITY-SPREADING
PHASE UNWRAPPING METHOD

T. Nishino, R. Yamaki, A. Hirose
Department of Electronic Engineering, The University of Tokyo, Tokyo, Japan

Abstract: When ultrasound is used to measure a three-dimensional (3D) object's shape, the interference often results in amplitude reduction of the backscattered wave so that its arrival time cannot be calculated properly. This leads to inaccurate measurement of the distance between the ultrasonic transmitter/receiver and the object. To resolve this problem, we propose a novel method. We assume that the problem of irregular distance is the same problem as the cancellation of singular points in the so-called phase-unwrapping process. The technique that we propose cancels singular points by spreading the singularity. In this paper, we compare experimental results of our technique, the singular-spreading phase unwrapping method, and a conventional technique, the minimum cost network flow method. The experiments demonstrate that our technique performs imaging better than the conventional technique.

Key words: Three-dimensional imaging, Phase unwrapping, Singularity-spreading phase unwrapping

1.   INTRODUCTION

When we measure a three-dimensional (3D) object's shape using ultrasound, interference often causes amplitude reduction so that we cannot determine the distance between the ultrasound transmitter/receiver and the object at many measurement points. As a result, we observe a 3D shape that differs from the actual one. In this paper, we report successful, precise 3D imaging

using ultrasound by considering the consistency between the value at a measurement point and the surrounding values.

2.   BASIC CONCEPT

Our method is based on the Markov-Random-Field model. It incorporates the following two important features.

1) We deal with phase information instead of pulse arrival time.

The problem in the pulse-arrival-time method is that the amplitude reduction makes the distance indeterminable. Correspondingly, the problem in the continuous wave method is observed as singular points (SPs) where the phase values have $\pm 2\pi$ rotation. We deal with the SPs.

2) We propose the singularity-spreading phase-unwrapping (SSPU) method [1] to remove the SPs.

The minimum-cost network flow (MCNF) method [2], which resolves SPs, is well known in the field of interferometric synthetic aperture radars. The MCNF method draws lines that connect positive and negative SPs. We can determine the distance to construct digital elevation maps without crossing over the lines. However, the MCNF method generates nonexistent cliffs. We solve this problem and improve the distance accuracy by using the SSPU method [1].

3.   SSPU METHOD

Figure 1 schematically illustrates the SSPU method. We remove an SP with compensation by spreading the singularity. For a positive SP in Fig. 1a, we add a counter phase rotation around it as distributed compensators as depicted in Fig. 1b. The singularity is then spread around. We repeat this process until the phase inconsistencies become negligible over the entire image.
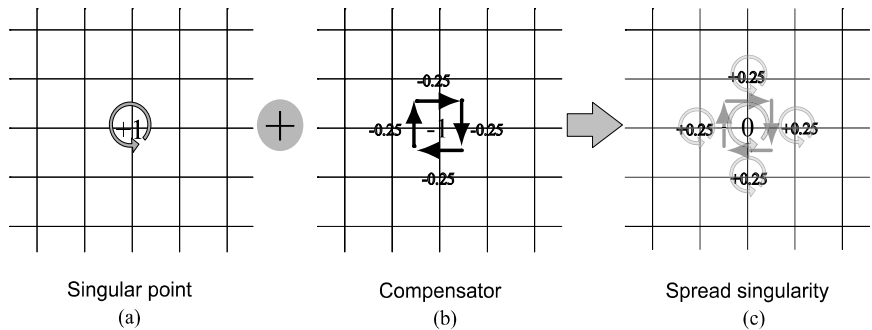
Figure 1. Spreading singularity.

4. EXPERIMENTAL RESULTS

Figure 2 depicts the shape of a cardboard section suspended in air. Figure 3 plots the measurement result when we use the pulse-arrival-time method. The transmitter/receiver moves horizontally about 20 cm over the cardboard with a 1 mm interval in the x–y plane. We can find many points of indeterminable distance as a result of interference.
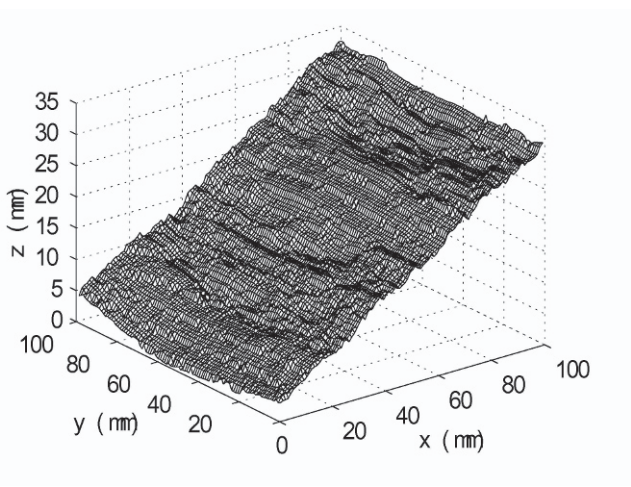
Figure 2. Cardboard section measured with a contact-type sensor.
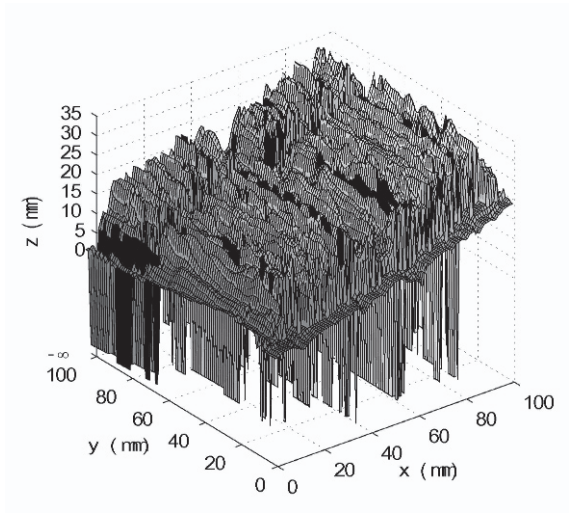
Figure 3. Measurement result using pulse-arrival-time method.

Figure 4 depicts the measurement result of phase value using a continuous signal on a gray scale (white, $+\pi$; black, $-\pi$). Figure 5 depicts singular points in the area. White (black) indicates positive (negative) singular points. There are many singular points in an area of rapid phase changes. In contrast, there are only a few singular points in an area of gradual phase changes.
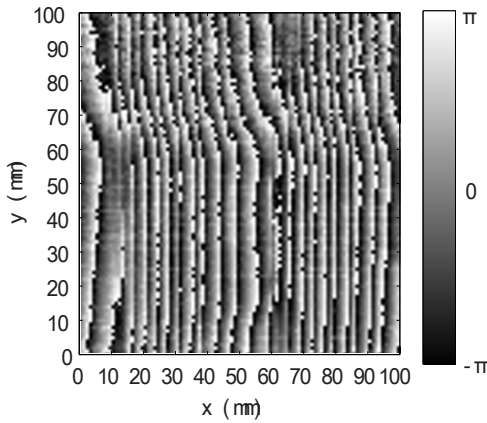
Figure 4. Phase map.
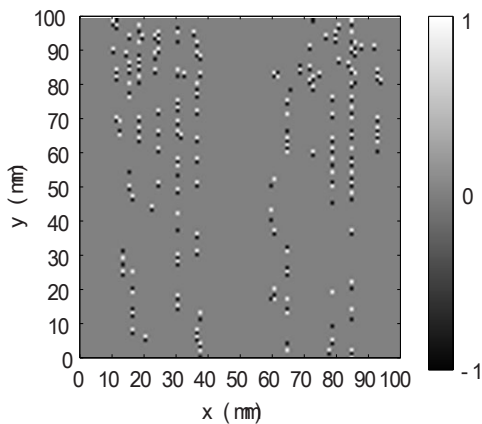
Figure 5. Singular point map.

Figures 6 and 7 presents the results of 3D imaging using the MCNF (SSPU) method. Table 1 lists the peak-noise SN ratios *PNSNR* (= (squared height of object shape)/(peak squared error)) and the mean SN ratios *MSNR* (= (squared height of object shape)/(mean squared error)). We find that the SSPU result is closer to the actual cardboard shape.
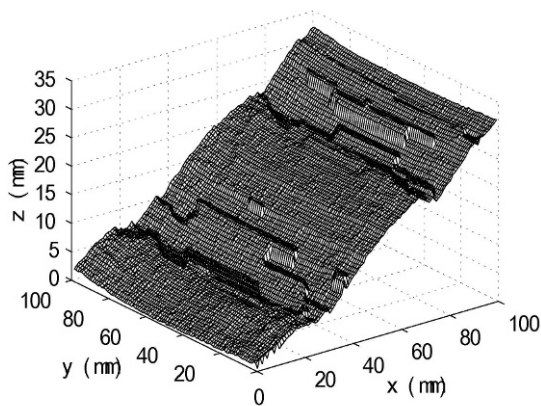
Figure 6. Measurement result using MCNF method.
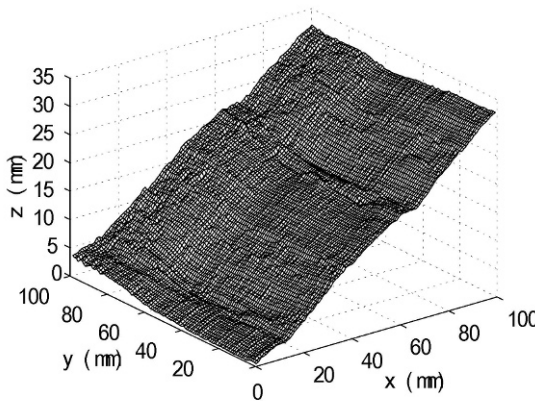
Figure 7. Measurement result using SSPU method.

Table 1. SN ratios

	PNSNR	MSNR
MCNF	14.76 dB	25.18 dB
SSPU	16.05 dB	26.89 dB

5.   CONCLUSION

Experimental results have demonstrated that the problem of indeterminable object shape due to amplitude reduction is solvable using the continuous wave method. We have proposed a novel phase-unwrapping method, SSPU. This method eliminates singular points, as well as the distortion in neighboring points, by spreading the singularity. SSPU has been found to have a better SN ratio than the MCNF method.

ACKNOWLEDGEMENTS

REFERENCES

1. R. Yamaki, and A. Hirose, Singularity-spreading phase unwrapping, *IEEE Transactions on Geoscience and Remote Sensing*, **45**(10), 3240–3251 (2007).
2. M. Costantini, A novel phase unwrapping method based on neural programming, *IEEE Transactions Geoscience and Remote Sensing* **36**(3), 813–821 (1998).

INDICATION OF PROBE-AXIS ANGLE BY EXTRACTING WALL MOTION OF HEART TO ASSIST IN OBTAINING LONG- AND SHORT-AXIS VIEWS ON ECHOCARDIOGRAPHY

K. Masuda, H. Matsuura, R. Takahashi
Graduate School of Bio-Applications and Systems Engineering, Tokyo Univ. A&T, Japan

Abstract: We have developed an algorithm to find standard cross sections of the heart from successive echograms. We first divided an echogram into small spatial regions to detect the typical motion of the mitral valve by analyzing the brightness variation and correlation coefficient among the regions. Furthermore, combining this technique with the optical flow method, we elucidated the region velocity of the left ventricle after centering the valve on echogram. By analyzing symmetry among specified regions, we distinguished the short-axis view of heart from the others.

Key words: Mitral valve, Long-axis, Short-axis, Correlation coefficient, Optical flow

1.   INTRODUCTION

Examination with echography greatly depends on the expertise and experience of an operator because of its blurriness and low spatial resolution. Normally, it is said to take at least one year to obtain the desired echogram for diagnoses. To visualize the velocity of organ motion, not only the tissue Doppler imaging (TDI) technique but also detection of the organ outline [1] is available and already integrated with echography. We have even developed software to measure the instantaneous velocity of the ventricular wall and to visualize it as a motion vector on the original echogram [2]. However, those researches are considered precise measurements for a skilled physician, not a training tool for unskilled operators to assist in finding the optimum position and angle of the ultrasound probe. If standard cross

sections of internal organs are automatically recognized from the echogram, it is possible to guide it to better images as a position feedback function for the operator. Furthermore, if the quantitative index is calculated, it may also act as a training or navigation system for an inexperienced operator. In this paper, we describe recognition software for cross sections of heart, which has been developed in our laboratory.

2.   RECOGNITION OF THE MITRAL VALVE AND LEFT VENTRICLE WALL MOTION

2.1   Mitral Valve and its Optical Flow

There are some standard cross sections of the heart called the long-axis view, short-axis view, four-chamber view, and so on. The most frequently used cross section is the long-axis view, which is determined by the line that runs from the apex of the heart to a midpoint at the base of heart. The short-axis view, on the other hand, is a plane perpendicular to the long-axis view. Figure 1 shows their comparison.
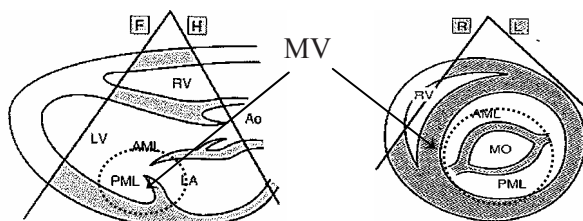
Figure 1. Standard cross sections to diagnose the heart, the long-axis view (*left*) and the short-axis view (*right*) on echocardiography.

To determine the standard cross section of heart, we have found that the mitral valve (MV) is located in the center in both views as shown in Fig. 1. MV is a dual flap valve between the left atrium and the left ventricle. During left ventricular diastole, the mitral valve opens and blood travels from the left atrium to the left ventricle. When most of the blood passes across the mitral valve during the early diastolic phase of the left ventricle, the mitral valve shows its fastest motion, which is said faster than ventricular wall motion. To verify local motion of heart on echography, we have introduced optical flow [3] and visualized it as a motion vector on the original

echogram. Optical flow is a method to calculate the motion vector of moving objects. Calculation time is much faster than the block matching method.

The left of Fig. 2 shows a result of the optical flow calculation of the left ventricle in the long-axis view during the diastolic phase by 10 [fps]. The motion vector was superimposed onto the original echogram. Despite the many vectors drawn on the posterior wall (PW), few vectors are seen on the mitral valve, where the motion of the mitral valve is faster than the posterior wall as mentioned above. The right of Fig. 2 shows the brightness distribution on the line A-P. Displacement of the mitral valve is longer than the posterior wall. The reason why few optical flows are calculated in the mitral valve is the limitation of the method, which requires that the brightness gradient of the moving object preserves between two frames. In the mitral valve, the brightness distribution is completely separated. Thus, another method to detect the mitral valve motion has to be developed.
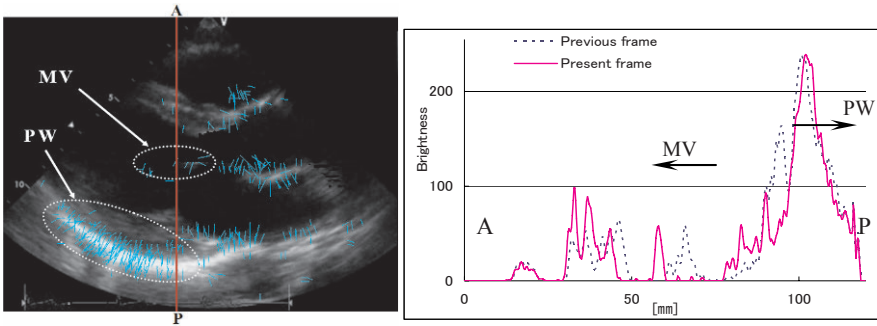
Figure 2. Echogram of left ventricle in the long-axis view during the diastolic phase with optical flow (*left*) and brightness distribution on the line A-P (*right*)

2.2　　Recognition of the Mitral Valve Motion [4]

To detect the motion of the mitral valve, we first divided an echogram into small spatial regions as shown in the left of Fig. 3, and calculated the brightness average of all the regions. The size of the region is defined as 40×20 [pixel] because the mitral valve is long sideways and almost 10 [pixel] of thickness when observing a heart as wide as possible in 640×480 [pixel] of frame size. The time variation of the brightness average of the regions is shown in the right of Fig. 3, which consists of the mitral valve, interventricular septum (IVS) and posterior wall respectively, through 4 periods of heart beats of normal volunteers age 23 years old. Brightness of

the posterior wall remains high, but with less variation. On the other hand, the brightness of the mitral valve shows a higher derivative according to its open and close. Because the circumference of mitral valve is blood, which is not revealed as brightness, the mitral valve seems to appear and disappear suddenly when it moves across the regions.

To distinguish the motion of the mitral valve from other parts, we have introduced two kinds of recognition indices, which are brightness variation rate and correlation coefficient between two neighbor regions. The brightness variation rate, the former, is calculated as the time derivative of the brightness variation shown in Fig. 5. Defining the brightness average of the region location (x,y) in the n-th frame as $I_{x,y}(n)$, the brightness variation rate $G_{x,y}(n)$ is expressed as the following equation. As mentioned above, the brightness variation rate is higher where the mitral valve passes through.
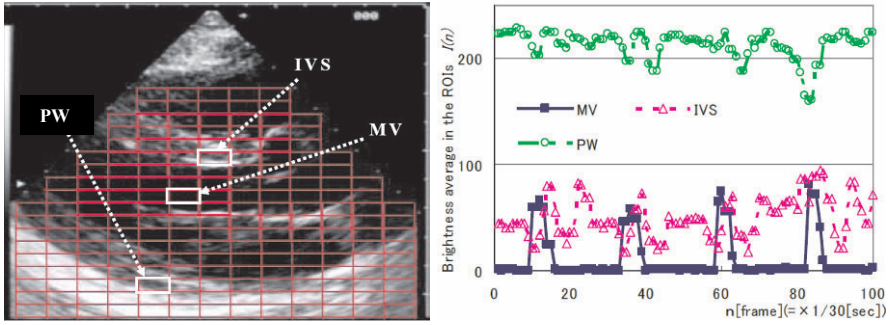
Figure 3. Division of echogram into small regions (left) and the time variation of brightness average, which includes the mitral valve, interventricular septum and posterior wall (right).

$$G_{x,y}(n) = \begin{cases} \dfrac{I_{x,y}(n) - I_{x,y}(n-1)}{I_{x,y}(n)} & \Big| \quad I_{x,y}(n) > I_{x,y}(n-1) \\[2ex] 0 & \Big| \quad I_{x,y}(n) \le I_{x,y}(n-1) \end{cases} \tag{1}$$

The correlation coefficient, the latter, is calculated as the degree of similarity of time variation of the brightness average between two neighboring regions, and is defined as Eq. (2). If the waveform of two regions $I_{x,y}(n)$ and $I_{x,y+1}(n)$ are similar with phase difference τ, the correlation coefficient $R_{x,y}(\tau)$ should be a maximum. Here, two regions are neighbored in the y-direction because the mitral valve shows a kick motion in the y-direction in both the long- and short-axis view.

$$R_{x,y}(\tau) = \frac{\sum_{n=0}^{N-1} I_{x,y}(n) I_{x,y+1}(n+\tau)}{\sqrt{\sum_{n=0}^{N-1} |I_{x,y}(n)|^2} \sqrt{\sum_{n=0}^{N-1} |I_{x,y+1}(n)|^2}} \qquad (2)$$

We have constructed software to indicate the candidate regions where both of $G_{x,y}(n)$ and $R_{x,y}(\tau)$ are higher than others. Fig. 4 shows the indicated areas where the mitral valve is by marking 80 crosses on the echogram of normal heart in the long-axis view during 8 [sec] (10 [fps]). Almost crosses are plotted on the area where the mitral valve exists. Applying the time series echocardiogram of 25 normal volunteers, we have confirmed the reliability of the recognition of the mitral valve with 95% accuracy.
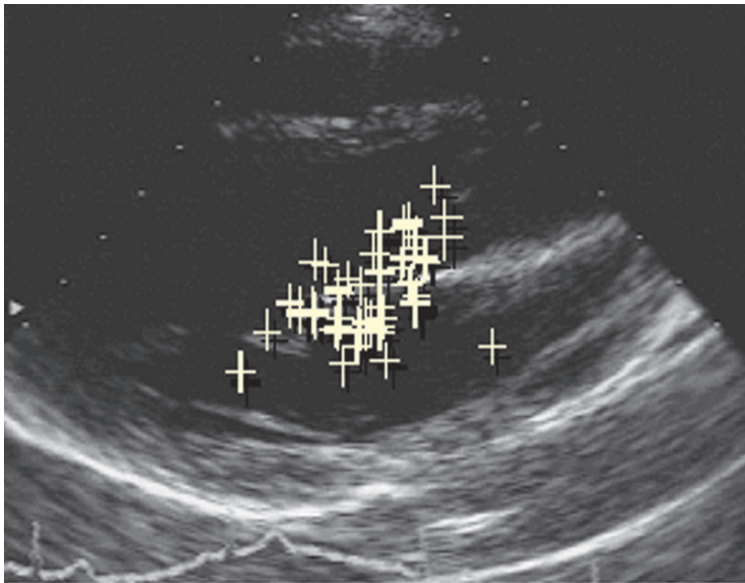
Figure 4. Recognized positions as the mitral valve.
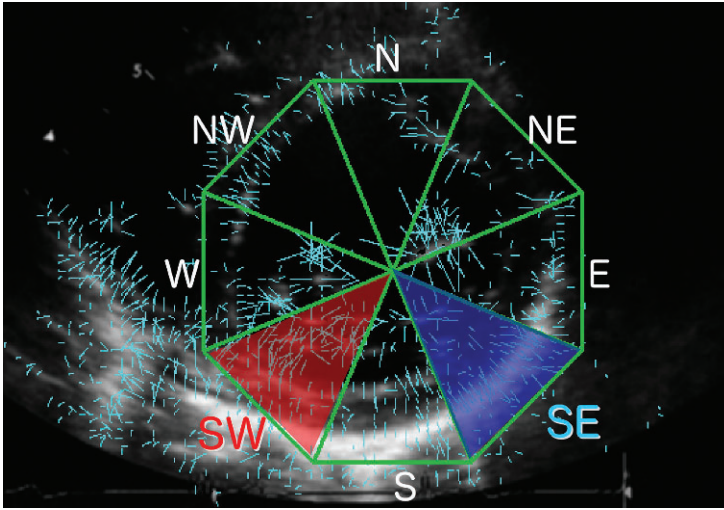
Figure 5. Radial regions of echogram.

2.3 Extraction of Surrounding Wall Motion

In the next step, we divided the echogram into 8 radial sub-regions by centering the mitral valve to calculate the optical flow as the motion vector of the surrounding wall of the left ventricle. The regions were named as N, NE, E, SE, S, SW, W, NW clockwise as shown in Fig. 5. We also defined the region velocity as the macro motion of the sub-region by averaging all vectors in the region. The absolute value and direction (angle) of each region velocity are calculated. Then we have also defined the contract velocity to elucidate the contraction vector toward the center point from the region velocity. In the long-axis view, only the regions of SW and S show high amplitude toward and apart from the center point. In the short-axis view, on the other hand, variations among S, SW and SE show a similar motion because the left ventricle wall contracts and expands concentrically. Thus, we have noticed the similarity of the contract velocity between SE and SW to distinguish the short-axis view from other cross sections.

3. ORIENTATION FOR THE SHORT-AXIS VIEW

From the above results, we analyzed the correlation of contract velocities in the regions of SW and SE. By introducing the correlation coefficient to time variation, the coefficient should be greater when the contract velocity in SE and SW are well synchronized. If the position and the angle for the short-

axis view are determined, the long-axis view is easily obtained by rotating the axis of the probe 90 [deg] in counterclockwise. Defining probe-axis angle θ as shown in Fig. 6, we have calculated region velocities in SE and SW from 0 to 150 [deg] in every 2 [sec] for 10 normal subjects.
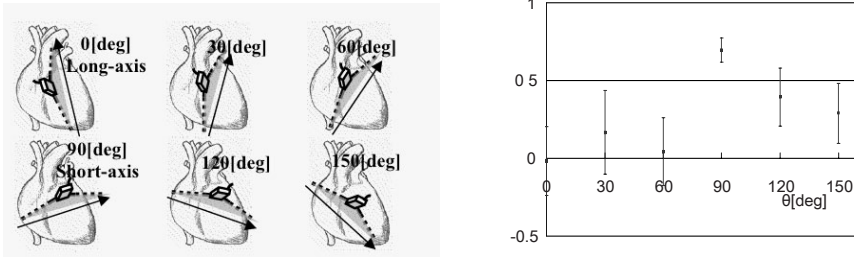
Figure 6. Definition of probe-axis angle θ (*left*) and distribution of correlation coefficient between SE and SW to probe-axis angle θ (*right*).

Making use of the Eq. (2), we have calculated the correlation coefficient between SE and SW as $R_{SE,SW}(0)$ and averaged the results for 10 subjects. Distribution of the coefficient according to the angle θ is shown in the right of Fig. 6. As anticipated, $R_{SE,SW}(0)$ showed typical difference with the maximum value when θ =90 [deg] and almost two times greater than the second maximum value when θ=120 [deg].

To find the standard cross section of heart, the software can indicate whether the position of the mitral valve is included in the frame, and the orientation for the short-axis view is correct. After finding the valve, the axis of the probe should be rotated until the short-axis view is indicated by keeping the position of the valve in the center of the frame.

The above results are derived from the normal hearts of healthy volunteers. In case of myocardial infarction, for example, the motion amplitude of region velocity should be smaller if the infarction part is included in the sub-region. In case of arrhythmic, the maximum correlation coefficient $R_{SE,SW}(\tau)$ might be obtained where τ is not 0 because wall motions among specified regions are not synchronized. We are going to analyze our method by processing more clinical video streams of various kinds of heart disease to enhance the precision of recognition.

4. CONCLUSIONS

We proposed software to support finding standard cross sections of heart by extracting motion of the mitral valve and deciding the angle of probe for an unskilled or inexperienced operator as the training or navigation system of

echocardiography. The algorism should be applied for training and education of diagnosis by expanding the software for automatic recognition.

REFERENCES

1. G.E. Mailloux, et al., IEEE Trans. Med. Imaging, vol. 8, no. 2, pp. 143–153, 1989.
2. K. Masuda, et al., Proc. of 11th International Symposium on Computer Assisted Radiology and Surgery (CAR' 97), BElsevier Science B.V., pp. 173–179, 1997.
3. K. Althoff, et al., IEEE Computers in Cardiology, vol. 27, p2000.
4. K. Masuda, et al., World Cong. Med. Phys Biomed. Eng., CD-ROM, 2006

DETECTION OF RIGHT ATRIUM MOVEMENT IN THROMBI FLOW MEASUREMENT

M. Aoki, T. Yamaguchi, H. Hachiya

Graduate School of Science and Technology, Chiba University, 1-33 Yayoi-cho Inage-ku, Chiba, 263-8522, Japan; Graduate School of Advanced Integrated Science, Chiba University, Chiba, Japan, Research Center for Frontier Medical Eng., Chiba University, Chiba, Japan

Abstract: In the medical field, a method that measures the amount of thrombi in the blood is desired. In our earlier research, we reported about a tool for measuring the ratio of thrombi in the blood at the right atrium of the heart by using transesophageal echocardiography (TEE) movies. However, it is difficult to track the motion of the contour of the atrium wall from a TEE image sequence using the previous extraction method. In this research, we propose a new method for improving the previous extraction method by adding correlation processing. The position of the processing points of each image is related mutually in serial frames in the processed TEE image sequence. We are able to continuously understand the movement of the atrium wall and accurately assess the amount of the thrombi with this improvement.

1.   INTRODUCTION

In recent years, the number of patients who undergo total knee replacement (TKR) operations is increasing. In this operation, a tourniquet is placed around the patient's legs, and thrombi are easily formed there. After this operation, the thrombi flow from the legs to the lungs through the blood stream and cause pulmonary thromboembolism (PTE). In order to cure and prevent PTE, it is important to know the amount of thrombi flowing in the blood. However, we have never had a method for rapidly and precisely determining the amount of thrombi in the blood.

In the orthopedic field, transesophageal echocardiography (TEE) is generally used to check for thrombi during a TKR operation. In earlier research, we reported a tool for measuring the ratio of flowing thrombi in the blood at the right atrium of the heart by using a TEE movie. In this tool, we applied the contour-extraction technique and speckle-reduction processing to the TEE movies to extract the thrombi information. However, we cannot track the wall of the atrium accurately with this contour extraction method since processing points in each image frame that express the shape of the atrium wall were decided independently from other frames. In this research, we tried to improve the previous contour extraction method by adding correlation processing and analyzing the movement of the atrium's wall with clinical TEE movies. In addition, we applied the optical flow to the same TEE movie to confirm the efficacy of the new contour extraction method.

2.   DATA ACQUISITION

Transesophageal echocardiography (TEE) data for the heart were acquired by ultrasonic diagnostic equipment (Hewlett Packard SONOS5500) during a TKR operation at Chiba University hospital. The center frequency of transmitted ultrasound was 4 MHz. TEE datasets were saved as DV-AVI (digital video-audio, video, still image) movies with a frame rate of 30 fps. In this research, we converted the AVI movie to still images. Figure 1a presents an example of a TEE image. The TEE images were 480×720 pixels, and each pixel had an 8-bit brightness value. In the movie, the area surrounded by the white wall is the right atrium. We can see the movement of the atrium wall, which expands and contracts repeatedly with the heart beat, and thrombi appear as high echo dots inside this wall.

3.   PREVIOUS STUDY OF THE EXTRACTION OF THROMBI IN TEE IMAGES

We applied the modified brain extraction tool [1] (mod-BET) to the original image (Fig. 1a) to determine the contour of the right atrium chamber of the heart in our previous research [2]. Figure 1b depicts an example of contour extraction. The fiber structure extraction technique [3] (FSET) was applied to extract the thrombi information as illustrated in Fig. 1c. In our processing result, thrombi information in the right atrium is extracted and presented in Fig. 1d.

The mod-BET method uses many processing points that are placed on the initial circle in the right atrium. These points expand to the outside with

repeated calculation and stop in front of the atrium wall. This method can extract the contour from an image with simple calculation, but it does not consider the relation between next (or previous) image frames. Since the relation of each processing point in two consecutive frames is uncertain, we cannot precisely know the local movement of the atrium wall.

(a) original TEE image (b) result of mod-BET method

(c) result of FSET method (d) thrombi information
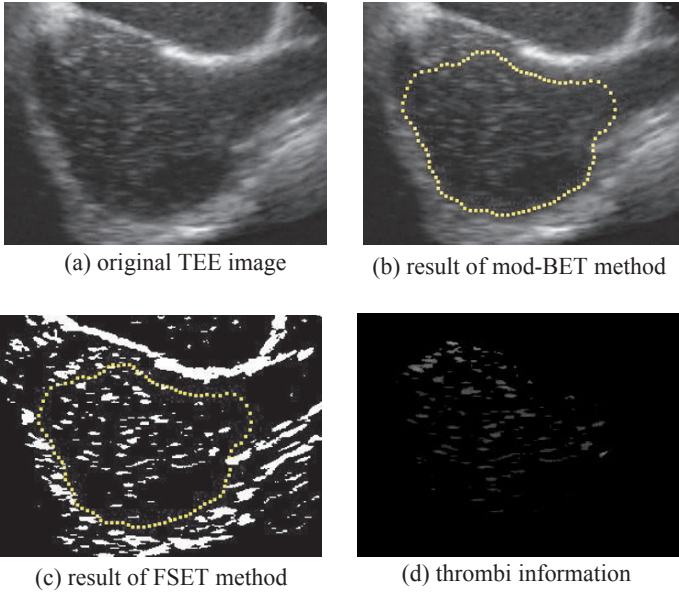
Figure 1. Example of the result of previous processing applied to TEE images. (**b–d**) display part of the right atrium.

4. CORRELATION-BASED CONTOUR EXTRACTION METHOD

To improve the accuracy of extracting the right atrium boundary, we added a new process to the mod-BET method. In the mod-BET method, the processing points expanded to the outside repeatedly under some rules. Each point had a sequence number, and the number remained constant when the point expanded to the outside. The final position of a certain processing point was decided considering the brightness of the image and the relation to two points that adjoin it.

In the new method, we establish a region of interest (ROI) around the final positions of each processing point and capture the brightness distribution in the ROI. The brightness distribution includes the information of the shape and brightness of the atrium wall; the position of the wall is then judged based on this distribution. We also applied the mod-BET method in

the next frame and set up the ROI to capture the brightness distribution. The correlation coefficient between the distribution in the previous frame's ROI and in the next frame's ROI at each processing point that has the same sequence number is then calculated. In the calculation result, each processing point in the post-frame moves to the position where the correlation is the highest. Figure 2 presents pattern diagrams of this method. In the next frame, processing points correct their positions to the same area of the wall as in the previous frame based on the calculated correlation coefficient. The ROI covers 20 × 20 pixels around each processing point, and the area of search for the highest correlation coefficient is 30 × 30 pixels. These sizes were decided by considering the resolution of the ultrasonic beam and the distance of adjoining processing points.
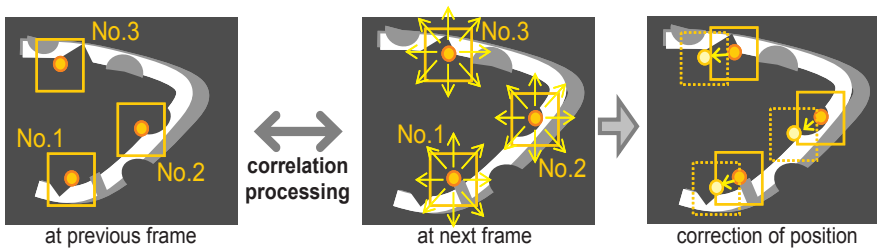
Figure 2. Proposed method for contour extraction (correlation-based contour extraction).

5.   MOVEMENT OF THE RIGHT ATRIUM WALL

The movement of the right atrium wall can be discerned using the correlation-based contour extraction method. However, the optical flow method is generally used to estimate the movement of objects in movies. We applied the optical flow method to the same TEE image sequence and compared the results of the correlation contour extraction method and the result of the optical flow method to confirm the movement of the atrium wall.

In optical-flow processing, the motion of objects is represented as vectors from originating to terminating pixels in a digital image sequence. In this research, the block-gradient, constraint-based registration method [4] was applied. This method can extract the movement of small objects and is resistant to noise. Flows were calculated based on a grid width of 15 pixels, and the ROI was set to 30 × 30 pixels around the calculation points.

For comparison, we apply correlation-based contour extraction, the optical flow, and the mod-BET method to the 110 frames (about four heart beats) of TEE images. Figure 3 presents example results calculated for each

process. Figure 3a depicts the two consecutive original images, Fig. 3b presents the mod-BET method results, Fig. 3c illustrates the correlation contour extraction results, and Fig. 3d shows the optical flow results. The red vectors represent movement to the right, and the blue vectors, movement to the left. Comparing Fig. 3c and d demonstrates the similarity of the directions of the flow vectors of the wall in both correlation-based contour extraction and optical-flow processing. In order to analyze these results, two-dimensional components of the averaged movement are estimated from every two consecutive frames. Figure 4 illustrates the movement components of the left side wall of the right atrium acquired by the mod-BET method (Fig. 4a), correlation contour extraction (Fig. 4b), and optical flow (Fig. 4a, b) for each direction in the 110 frames. In these graphs, the solid lines represent the result of mod-BET or correlation contour extraction, and the dotted lines represent those of optical flow. Comparing Fig. 4(a,b), we see that the vectors acquired by correlation-based contour extraction fit the optical flow better than those acquired by the mod-BET method. In particular, the cycles of the atrium's movement with the heart beat in correlation-based extraction and optical flow agree well as indicated in Fig. 4b. The contour extraction is thus improved by the proposed method and will be able to measure the amount of thrombi more accurately.

previous frame   next frame

(a) Two consecutive original images

(b) result of mod-BET   (c) result of correlation-based extraction   (d) result of optical flow

Figure 3. Results of mod-BET method, correlation method, and optical-flow processing.
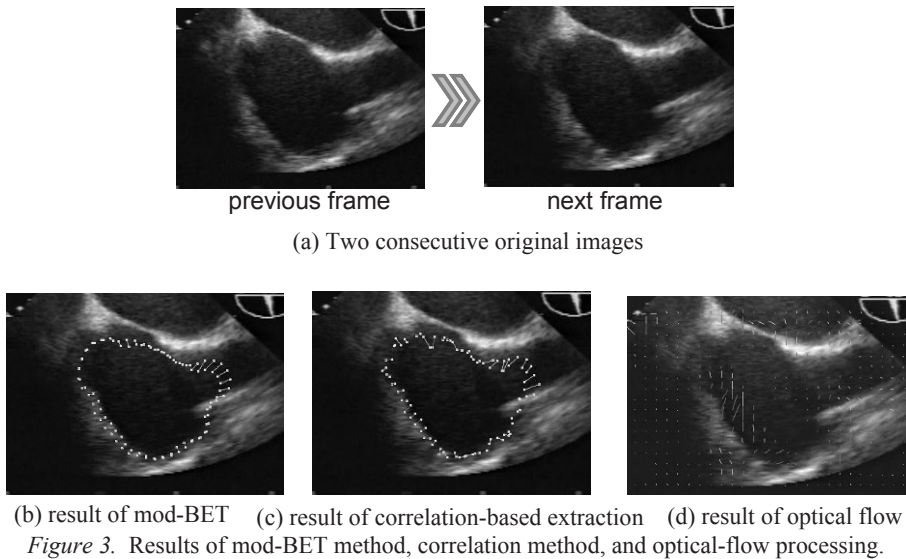
6.   CONCLUSION

We tried to improve contour extraction by adding correlation processing to the earlier extraction method in order to determine the movement of the atrium wall. We confirmed that the correlation contour extraction method can trace the wall of the right atrium more precisely than the earlier method. This method is expected to measure the amount of thrombi in the blood in the right atrium of the heart more accurately. In future work, we will apply these processes to many other cases and improve processing speed for real-time processing.

(i) Horizontal movement   (ii) Vertical movement
(a) Result of applying mod-BET method and optical flow

(i) Horizontal movement   (ii) Vertical movement
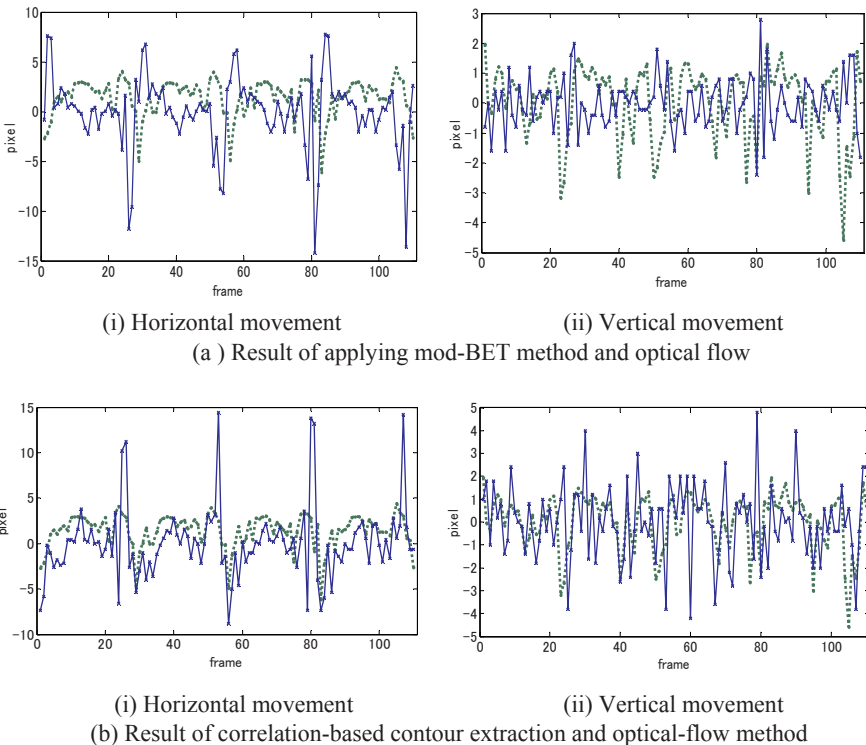(b) Result of correlation-based contour extraction and optical-flow method
Figure 4. Movement of the left side wall of the right atrium for 110 frames.

REFERENCES

1. S. M. Smith: Hum. Brain Mapp. **17** (2003) 17.
2. T. Yamaguchi, M. Aoki et al.: Jpn. J. Appl. Phys. **45** (2006) 4749.
3. T. Yamaguchi, K. Hirai et al.: Jpn. J. Appl. Phys. **44** (2005) 4615.
4. N. Ohta: IEICE Trans. **E74** (10) (1991) 3379–3388.

STUDY OF PROBE NAVIGATION ALGORITHM FOR ECHOCARDIOGRAPHY TO ACQUIRE STANDARD CROSS SECTION

T. Imai, H. Inoue, T. Sakai, K. Masuda

Graduate School of BASE, Tokyo University of A&T, 2-24-16 Naka-cho, Koganei-shi, Tokyo, 184-8588, Japan

Abstract: Examination by echography greatly depends on the expertise and experience of the operator. However, there has been no research to date to assist in finding an optimum position and angle for the ultrasound probe on a patient's body surface. In this study, we propose a system that feeds back probe navigation information to an operator to facilitate acquiring a standard cross section of the heart.

Key words: Recognition, Mitral valve, Posterior wall, Brightness variation, Optical flow, Labeling, Binarization, Correlation coefficient

1.   INTRODUCTION

Echography is highly regarded and has been applied extensively at hospitals and other sites. When conducting an echography examination, the examiner handles a long, thin probe. It is too difficult for an unskilled or inexperienced technician to scan the intended organ and to estimate its function because the spatial resolution of echograms is low. We propose a system that feeds extracted information back to the handler from a cross section by image processing as directions for handling the probe, which assists in searching for the intended organ. We applied this system to the echogram of a heart and report the results and conclusion of our experiment. Figure 1 presents a schematic view of the proposed system.
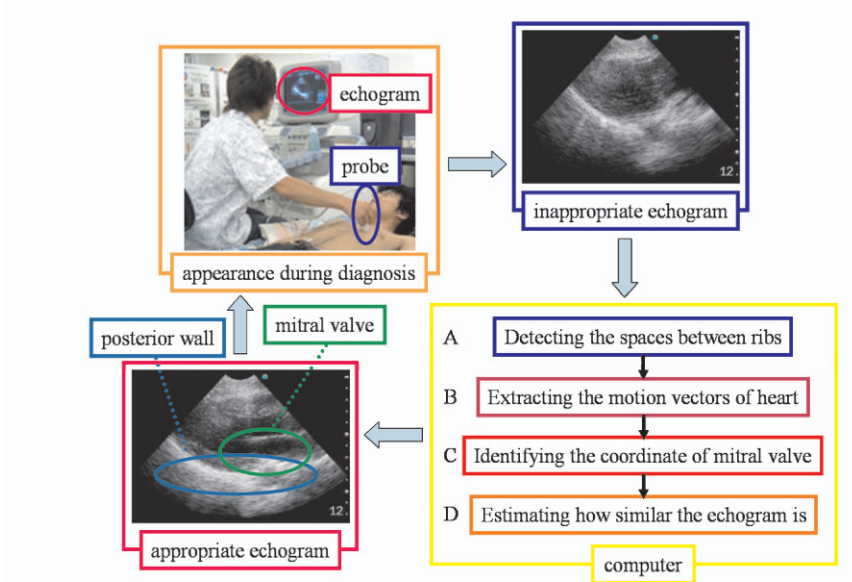
Figure 1. Block diagram of the system.

First, the imaged echogram is input into a PC. Next, the spaces between the ribs are detected by Algorithm A, and the positions are memorized by the PC. The probe is placed on those positions, and a motion vector is estimated by Algorithm B for extracting the heart motion. The probe is then moved to the position recognized as being the most appropriate. Following this, the mitral valve is placed in the center of the echogram by Algorithm C. Finally, Algorithm D (for recognizing the cross-section) determines the most appropriate probe-axis angle, which is fed back to the operator. In this paper, we report the result of experimentation and examination for considering Algorithms A and B.

2. ALGORITHMS

2.1 Algorithm for Detecting the Spaces Between the Ribs (Algorithm A)

When a probe is placed above the patient's ribs, the resolution of the echogram obtained from the probe is much too low. In order to avoid this, the probe needs to be placed above the spaces between the patient's ribs. The posterior wall is generally observed as a wide region having high resolution in the echogram of the heart when the probe is placed above the spaces between the patient's ribs. Therefore, we can gauge whether the probe was

placed above the patient's ribs or spaces between the ribs by recognizing whether or not the posterior wall region was observable based on the result of image processing. First, the imaged echogram is binarized for recognizing the region of the posterior wall. Next, the binarized image is adapted for the process of labeling, and every region consisting of highly resolute pixels adjacent to each other is numbered. The largest region among those is recognized as being the posterior wall.

2.2 Algorithm for Extracting Motion Vector (Algorithm B)

After the positions for placing the probe to obtain an echogram of the existing posterior wall are determined, the most appropriate position for obtaining a standard cross section, such as short- or long-axis, should be determined. We consider the kind of echogram for the obtained image extracted from the probe placed at the most appropriate position; we think it is an echogram in which the movement of each part is the most active. This algorithm is for extracting the motion vector of each pixel in an echogram based on the optical-flow method. By these means, we can determine the position for placing the probe. Furthermore, the mitral valve must exist in the most active cut plane because of the structure of the heart.

3. VERIFICATION OF ALGORITHMS BY ECHOGRAM EXPERIMENT OF HEART PHANTOM

3.1 Experiment for Verifying Algorithm A

In order to verify the validity of this algorithm, we applied it to an echogram imaging phantom that is an imitation of the human heart. The experimental system is depicted in Fig. 2(a), in which the rubber hemisphere imitates the posterior wall of the human heart. The radius of the hemisphere is approximately 90 mm. The experimental system includes both a heart and aluminum plates representing ribs, and these elements are placed in an aquarium filled with deaerated water. We distributed those objects in two ways.

In the first distribution, five aluminum plates are used, and the x-axial position of the center of the third plate corresponds to the position at the center of the phantom. In the second distribution, six aluminum plates are used, and the x-axial position of the center space between the third plate and fourth plate corresponds to the position of the center of the phantom. The

space between the plates is 20 mm, and all plates are arranged parallel to the *y*-axis. The *x*-axis position of the center of the phantom is 130 mm. While the *x*-, *y*-, and *z*-axis rotation and *y*- and *z*-axis position of the probe are maintained, we obtain the echogram of the phantom from the probe in each x-axial position.

We applied the algorithm to the echogram of the phantom for detecting the spaces between ribs. Figures 3 (a) and (b) present the results of measuring lengths of the posterior wall; (a) indicates how five plates are used, and (b) indicates how six plates are used. The lengths of the posterior wall are represented as the rate of width of the echogram (210 pixels). Figure 3 demonstrates that the algorithm can distinguish whether the probe is on a rib or between ribs.
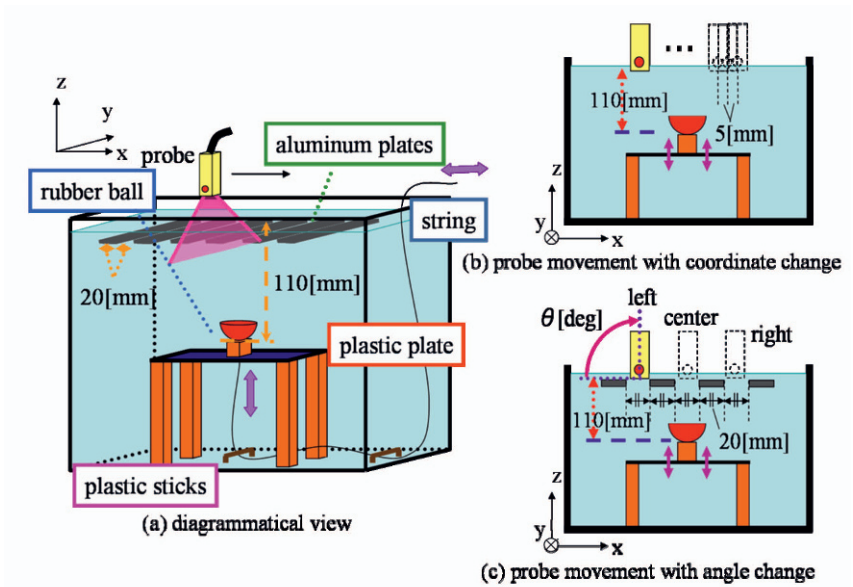

Figure 2. Experimental setup of the phantom to mimic the shape and motion of heart.
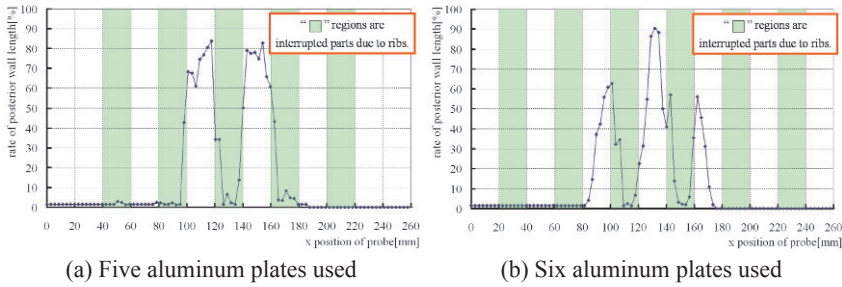
(a) Five aluminum plates used   (b) Six aluminum plates used

Figure 3. Calculated lengths of posterior wall by using the algorithm.

3.2   Experiment for Verifying Algorithm B

We subsequently conducted an experiment for estimating the motion vectors of echogram imaging the phantom of the heart in order to confirm the validity of our hypothesis. We used the experiment system illustrated in Fig. 2a, but with some modification.

    All aluminum plates were replaced, and one end of the string was bound to an actuator so that the string could be periodically tightened or slackened. This was done to imitate the periodic up-and-down movement like a real posterior wall. We decided that the amplitude of the rubber ball movement should be 12 mm, and we set three cycles of the phantom movement (1.00 Hz, 1.17 Hz, and 1.33 Hz) enabling the phantom to move 60, 70, or 80 times every minute. An echogram of the phantom during periodic up-and-down movement is obtained at 30 frames/sec for 2.0 sec after the probe is completely at rest. Next, 21 stop-motion pictures extracted every 0.1 sec were obtained in each echogram, and the motion vector between every adjacent frame was calculated. The diagrammatic view is presented in Fig. 2b.

    The motion vector can be calculated as follows with integral number n ($1 \leqq n \leqq 20$). The sum of the absolute value of the vector obtained between the nth and n+1th frame is divided by the total number of pixels within the target region during the vector extraction process. We define this value as f(x,r,n). Parameter x in f(x,r,n) stands for the *x*-axis position of the probe at that time, and r stands for the frequency of the phantom heart movement. Next, x is held constant while n is varied in the range of $1 \leqq n \leqq 20$. The maximal value is defined as flow_max. The value of flow_max is shown in Fig. 4a.

    As you can see, $f_{max}(x,r)$ becomes high when the cut plane of the echogram is near the center of the phantom. Furthermore, the motion vector remains constant even if the heart rate is varied from 60 to 80 beats per minute.

Next, four aluminum plates are arranged so the experiment can be conducted at a different angle and under different conditions. The head of the probe is fixed at three positions (left, center, and right), and the *y*-axis rotation angle θ is changed. The probe is held motionless, and an echogram is obtained. The phantom is operated so that the heart rate is 60 beats per minute. Figure 2(c) presents the diagrammatic view, and Fig. 4(b) presents the result of flow_max. As you can see, maximum flow_max is obtained when the probe is heading toward the center of the phantom, analogous to the results in the former experiment. These results indicate that the cut plane passing through the center of the heart can be selectively imaged.

(a) Probe position variation   (b) Probe angle variation
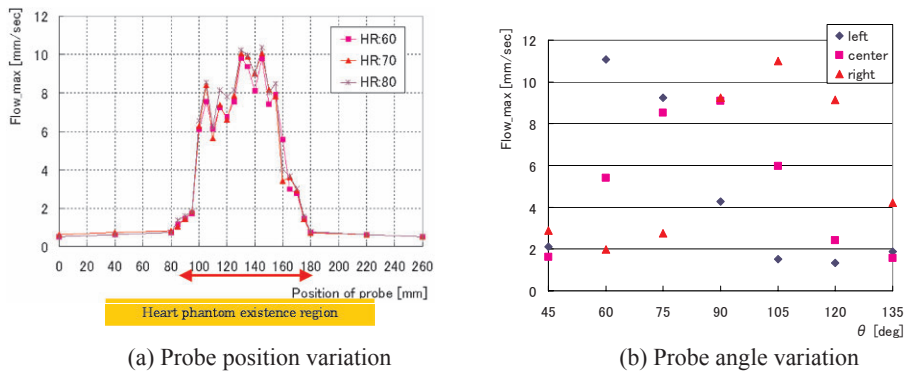
Figure 4. Variations of flow_max versus the position and angle of the probe.

4.   CONCLUSION

In this paper, we discussed image recognition methods in order to support echography imaging. There is a demand for such research, but little has been conducted. The results acquired through this study are as follows. First, we developed and studied an algorithm for detecting spaces between ribs. We also developed and studied an algorithm for determining an appropriate heart cut plane. Subsequently, experiments were performed using an echogram of a phantom heart. We confirmed that the algorithms work correctly. In future work, we will conduct an experiment of an application to an actual human heart.

DEVELOPMENT OF CAD SYSTEM FOR DIFFUSE DISEASE BASED ON ULTRASOUND ELASTICITY IMAGES

M. Yamazaki, T. Shiina, M. Yamakawa, H. Takizawa, A. Tonomura, T. Mitake

Graduate School of System and Information Engineering, University of Tsukuba, Tsukuba 305-8573, Japan; Research & Development Center, Hitachi Medical Corporation, Kashiwa 277-0804, Japan

Abstract: It is well known that as hepatic cirrhosis progresses, hepatocyte fibrosis spreads and nodule increases. However, it is not easy to diagnosis its early stage by conventional B-mode image because we have to read subtle change of speckle pattern which is not sensitive to the stage of fibrosis. Ultrasonic tissue elasticity imaging can provide us novel diagnostic information based on tissue hardness. We recently developed commercial-based equipment for tissue elasticity imaging. In this work, we investigated to develop the CAD system based on elasticity image for diagnosing defused type diseases such as hepatic cirrhosis. The results of clinical data analysis indicate that the CAD system is promising as means for diagnosis of diffuse disease with simple criterion.

Key words: Hepatic cirrhosis, Elasticity imaging, CAD, Texture analysis

1.   INTRODUCTION

It is well known that as hepatic cirrhosis progresses, fibrosis area spreads and nodule increases, consequently, liver tissues become hard. Hepatic cirrhosis often causes other diseases such as liver cancer. So diagnosing hepatic cirrhosis in early stage is necessary to treat liver disease. Biopsy and image diagnosis using B-mode image have been conventionally applied for diagnosis of hepatic cirrhosis. However, it is not easy to diagnosis its early

stage by conventional B-mode image because is not sensitive to the stage of fibrosis.

On the other hand, ultrasonic tissue elasticity imaging can provide us novel diagnostic information based on tissue hardness and consequently it is expected to detect tumor with high contrast and also discriminate benign and malignant disease.

We recently developed commercial-based equipment for tissue elasticity imaging. In terms of cancer diagnosis, by investigating the relation between tissue elasticity images and types of breast diseases for more than one hundred cases, Dr. Ito et al. constituted scores of malignancy for breast tumor [1], which is referred to as elasticity score and categorizes patterns of elasticity images into five classes from malignancy to benign. As a result, it was revealed that elasticity image enables non-experienced doctor to attain high precision of diagnosis with simple criterion based on elasticity image as well as an expert, while conventional ultrasonogram requires the skill for recognizing many and complicated characteristics of images. This fact implies that elasticity image is suit to be implemented computer-aided diagnosis (CAD) system. Therefore, we previously constituted the CAD for breast cancer diagnosis. Results categorized by the CAD system for 86 cases of breast tumor showed the high coincidence, about 90%, with those by experts.

In this work, we investigated to develop the CAD system based on elasticity image for diagnosing defused type diseases such as hepatic cirrhosis.

2.   ULTRASONIC ELASTICITY IMAGING SYSTEM

One of dominant approaches of ultrasound tissue elasticity imaging is based on the static method which measures the strain distribution inside a body produced by compressing or relaxing a tissue [2]. Until recently the equipment to be applicable to clinical use has not been appeared although many methods have been proposed for tissue elasticity imaging. Advantages of ultrasonic examination, such as real-time and simple (freehand) operation, must be preserved in the elasticity imaging system. In a freehand compression, it is necessary to suppress the influence of lateral slip. It is also necessary to have a large dynamic range of strain for stable measurement that does not depend on a compression speed and quantity. To satisfy these conditions, we developed the combined autocorrelation method (CAM) [3,4] as an approach suited for clinical application.

Recently, we developed equipment of real-time tissue elasticity imaging by integration of our method into a commercial ultrasound scanner, i.e., HITACHI EUB-8500. Results of clinical examination of breast confirmed

that real-tine tissue elasticity imaging is useful, especially for the detection of carcinoma.

On the other hand, in the case of diffuse diseases like hepatic cirrhosis, it is expected that change of tissue elasticity is widespread unlike tumor where produce locally hard area. Accordingly, it is considered to be difficult to describe relative strain images. However, it is recently reported that texture of elasticity image changes as cirrhosis progresses. Considering the process of fibrosis, it is expected that fibrosis cause the inhomogeneous distribution of tissue hardness, which produces nonuniform texture pattern of strain images. Then, we have investigated to quantify the variance of strain texture and use the result for diagnosis of the stage of cirrhosis based on degree of fibrosis and develop the CAD system.

3.   METHODS

It is well known that as hepatic cirrhosis progresses, hepatocyte fibrosis spreads and nodule increases, which cause more complicated texture of elasticity images. Cirrhosis can be categorized as 4 stage based on the extent of spreading fibrosis. However, it is not easy to diagnosis its early stage by conventional B-mode image because we have to read subtle change of speckle pattern which is not sensitive to the stage of fibrosis.

Dr. Fujimoto reported that texture of elasticity image (strain) of cirrhotic liver reflected the stage of fibrosis and constituted scores for staging, which categorizes texture patterns of elasticity images into four stages classes as shown in Fig. 1.

In order to evaluate the change of texture, two features were extracted from elasticity images. One is a shape of histogram about strain values. Figure 2 shows B-mode, the strain image and the histogram of strain distribution within ROI for normal liver and cirrhosis. The value of strain is normalized with 32 levels to constitute its histogram. The elasticity image of normal liver is relatively uniform as shown in the left of Fig. 2, which reflects homogeneous distribution of hepatocyte. As a result, the shape of histogram shows a peak around middle of strain values. On the other hand, the elasticity image becomes patchy pattern as disease progresses since hepatocyte fibrosis spreads and nodule increases. Consequently, the shape of
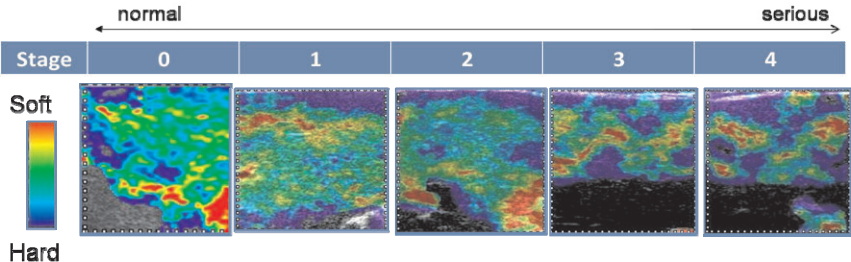

Figure 1. Elasticity images of normal liver and hepatic cirrhosis.

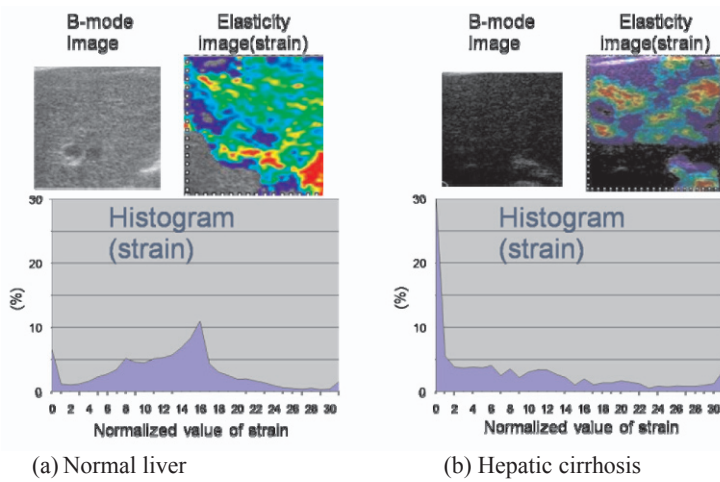(a) Normal liver   (b) Hepatic cirrhosis

Figure 2. Examples of strain distribution.

histogram becomes flat except for a peak around parts of low strain which corresponds to hard fibrous area as shown in the right of Fig. 2.

In order to quantitatively evaluate the difference of the histogram, an index defined as Eq. (1) was introduced.

$$F1 = \frac{\sum_{i=0}^{2} strain\_value\_of(i)}{\sum_{i=14}^{16} strain\_value\_of(i)} \tag{1}$$

This represents the ratio of area of histogram between low strain (0–2) and median strain (14–16). It is expected that $F1$ of cirrhosis is larger than that of normal liver.

The size of nodules may enlarge as disease progresses. It is expected that the run length, that is, a number of continuous pixels for each strain values increases for large nodules. Therefore, as a feature to detect the difference of size of nodules, run length of strain image is used.

First, the run length matrix is constituted, where the row and column of the matrix correspond to the value of strain and the run length for each strain values, respectively. Next, an index F2 which represents of the run percentage of matrix was introduced as follows,

$$F2 = \sum_{i=0}^{n-1} \sum_{j=1}^{L} P(i,j) \Big/ S \tag{2}$$

where, S means the area of ROI.

The CAD system for cirrhosis was constituted based on these two features. At learning process, the CAD extracts feature of strain histogram and run
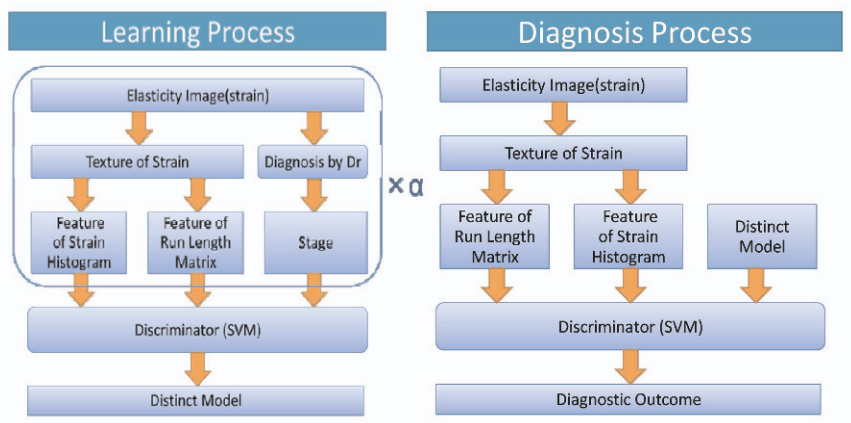

Figure 3. Learning process and diagnosis process of CAD.

length matrix from texture of strain, and these feature and the result of staging by Dr are inputted into discriminator. Distinction model is made by repeating these processes with some elasticity image samples. The distinction model is used to diagnosis test image, the stage of which is unknown, with combination of features extracted as keys to diagnosis.

4.   EXPERIMENT AND RESULT

The performance of the CAD system for discriminate "Normal" or "Cirrhosis" was evaluated using clinical data. We used 36 samples which consist of 18 normal livers and 18 cirrhoses as shown in Table 1. Leaving-one-out method was applied: a sample for test case was picked up from 36 samples and rest 35 samples were used to constitute the distinction model for CAD. Each sample as test case was diagnosed by CAD. The result is shown in the right of Table 1.

Table 1. The result of experiment. Samples are constituted by 18 elasticity images of normal liver and 18 images of hepatic cirrhosis staged 0–4 by diseases progression.

Samples			Result		
Stage	**Total**		**Stage**	**Right Diagnosis**	**Wrong Diagnosis**
0(Normal)	18	normal	0	17	1
1(Early stage)	3	cirrhosis	1	0	3
2	3		2	0	3
3	8		3	5	3
4(Serious stage)	4		4	4	0

The result implies that it is useful to diagnose normal liver and cirrhosis in serious stage with simple criterion based on two strain features. However, the CAD failed to correctly diagnosis of cirrhosis in early stage. Although a number of samples are too small to reach a definitive conclusion, this is attributed to the fact that fibrosis tissues are scarce in early stage so that their texture is similar to normal liver.

5.   CONCLUSION

We have investigated to quantify the texture pattern of elasticity image and constitute the CAD system for diagnosis of hepatic cirrhosis. The results of clinical data analysis indicate that the CAD system based on elasticity images is promising as means for diagnosis of diffuse disease with simple criterion.

For further investigation, it is necessary to improve the performance for diagnosing hepatic cirrhosis in early stage and staging of cirrhosis with the CAD system. In addition, it is expected that in the future technology for tissue elasticity imaging will be more sophisticated such as quantitative elasticity images based on elastic modulus.

ACKNOWLEDGEMENTS

REFERENCES

1. A. Itoh, E. Ueno, E. Tohno, H. Kamma, H. Takahashi, T. Shiina, M. Yamakawa and T. Matsumura: Breast Disease: Clinical Application of Ultrasound Elastography for Diagnosis, *Radiology*, Vol. 231, No. 2, pp. 341–350, 2006.
2. J. Ophir, I. Cespedes, H. Ponnekanti et al.: A Quantitative Method for Imaging the elasticity of Biological Tissues, *Ultrasonic Imaging*, Vol. 13, pp. 111–134, 1991.
3. T. Shiina, N. Nitta, E. Ueno and J. C. Bamber: Real Time Tissue Elasticity Imaging Using the Combined Autocorrelation Method, *J. Med. Ultrasonics,* Vol. 29, Autumn, pp. 119–128, 2002.
4. M. Yamakawa, N. Nitta, T. Shiina, T. Matsumura, S. Tamano, T. Mitake and E. Ueno: High-speed Freehand Tissue Elasticity Imaging for Breast Diagnosis, *Japanese Journal of Applied Physics,* Vol. 42, No. 5B, pp. 3265–3270, 2003.

FDTD METHOD AND OTHER NUMERICAL SIMULATIONS

FDTD CALCULATION OF LINEAR ACOUSTIC PHENOMENA AND ITS APPLICATION TO ARCHITECTURAL ACOUSTICS AND ENVIRONMENTAL NOISE PREDICTION

S. Sakamoto

Institute of Industrial Science, The University of Tokyo, 4-6-1, Komaba, Meguro-ku, Tokyo 153-8505, Japan

Abstract: The finite difference time domain (FDTD) method is widely used as an effective and powerful tool for analyzing acoustic problems. In architectural acoustics, impulse response is the most important quantity and therefore the FDTD method, by which the physical quantities are obtained in time domain, is more advantageous than other wave-based analysis methods, by many of which the calculation is performed in frequency domain. This paper reports application of the FDTD method to room acoustics and outdoor noise assessment.

Key words: FDTD method, Linear acoustic phenomena, Architectural acoustics, Outdoor noise propagation, Room impulse response, Noise barrier

1. INTRODUCTION

To examine and understand complicated acoustic phenomena such as reflection, diffraction and interference, visualization of sound fields is very effective not only from an educational viewpoint but also from a practical engineering viewpoint in building acoustics and noise control engineering. Recently, such numerical analysis techniques as finite element method (FEM) and boundary element method (BEM) have become popular in acoustics and they are often applied to the visualization of sound fields. Among these numerical methods, the authors have been investigating the application of the finite difference time domain (FDTD) method [1–3] to various problems in architectural acoustics and noise control engineering. In

the FDTD algorithm, the sound pressure and particle velocity in a sound field are directly computed in discrete time steps and therefore transient acoustic phenomena can be easily visualized by animation. As an application of this numerical technique, some examples of visualization of outdoor/indoor sound propagation are introduced in this report.

2.   THEORY

Wave motion in a three-dimensional sound field is described by following Euler's equations (1–3) and the equation of continuity (4).

$$\rho \cdot (\partial u/\partial t) + \partial p/\partial x = 0 \tag{1}$$

$$\rho \cdot (\partial v/\partial t) + \partial p/\partial y = 0 \tag{2}$$

$$\rho \cdot (\partial w/\partial t) + \partial p/\partial z = 0 \tag{3}$$

$$\partial p/\partial t + \kappa(\partial u/\partial x + \partial v/\partial y + \partial w/\partial z) = 0 \tag{4}$$

where, p: sound pressure, u, v, and w: particle velocity in x-, y- and z-directions, respectively, ρ: density of air, κ: volume elastic modulus of air.

    Sound field is divided into staggered grid system as shown in Fig. 1 and spatial differential terms in Eqs. (1–4) are approximated by finite difference with $2(M+1)$ points. For example, a spatial differential term of sound pressure at $x=a$ can be approximated by values of sound pressure at $2(M+1)$ points as follows.

$$\frac{\partial p(a)}{\partial x} = \sum_{m=0}^{M} D_m \left\{ \frac{p(a + (m+1/2)\Delta h) - p(a - (m+1/2)\Delta h)}{\Delta h} \right\} \tag{5}$$

$$D_m = \frac{C_m}{\sum_{n=0}^{M} (2n+1)C_n} \tag{6}$$

$$C_m = (-1)^{m+1} \frac{(2M-1)^2 (2M+1)^2}{\{2(M-m)+1\}^2} \frac{(2M+1)!}{m!(2M-m+1)!} \qquad (7)$$

Here, it should be noted that the approximation order is $O(\Delta h^{2(M+1)})$ and therefore the accuracy of the approximation becomes enough high when number of reference points, M, is made a large number.
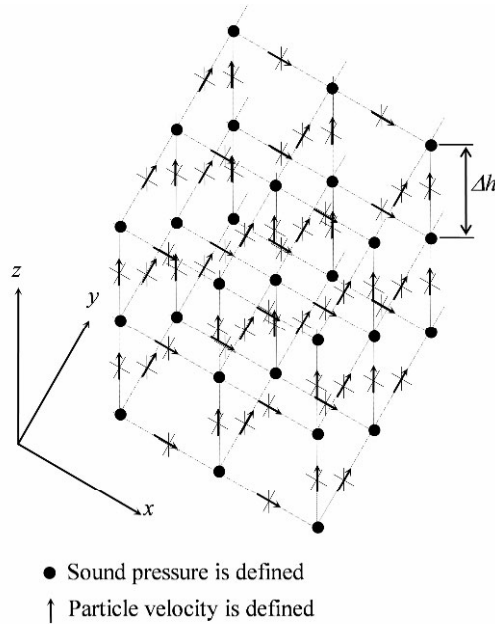

● Sound pressure is defined
↑ Particle velocity is defined

Figure 1. Definition point of p, u and v on a staggered grid system coordination.

Adopting the above finite difference approximation into the differential Eqs. (1–4) leads following FDTD schemes.

$$u^{n+1}\left(i+\frac{1}{2},j,k\right) = u^n\left(i+\frac{1}{2},j,k\right) - \frac{\Delta t}{\rho\Delta h}\sum_{m=0}^{M} D_m\left\{p^{n+\frac{1}{2}}(i+m+1,j,k) - p^{n+\frac{1}{2}}(i-m,j,k)\right\} \qquad (8)$$

$$v^{n+1}\left(i,j+\frac{1}{2},k\right) = v^n\left(i,j+\frac{1}{2},k\right) - \frac{\Delta t}{\rho\Delta h}\sum_{m=0}^{M} D_m\left\{p^{n+\frac{1}{2}}(i,j+m+1,k) - p^{n+\frac{1}{2}}(i,j-m,k)\right\} \qquad (9)$$

$$w^{n+1}\left(i,j,k+\frac{1}{2}\right) = w^n\left(i,j,k+\frac{1}{2}\right) - \frac{\Delta t}{\rho\Delta h}\sum_{m=0}^{M} D_m\left\{p^{n+\frac{1}{2}}(i,j,k+m+1) - p^{n+\frac{1}{2}}(i,j,k-m)\right\} \qquad (10)$$

$$p^{n+\frac{1}{2}}(i,j,k)=p^{n-\frac{1}{2}}(i,j,k)-\frac{\kappa\Delta t}{\Delta h}\left[\sum_{m=0}^{M}D_m\left\{u^n\left(i+m+\frac{1}{2},j,k\right)-u^n\left(i-m-\frac{1}{2},j,k\right)\right\}\right.$$

$$+\sum_{m=0}^{M}D_m\left\{v^n\left(i,j+m+\frac{1}{2},k\right)-v^n\left(i,j-m-\frac{1}{2},k\right)\right\}$$

$$\left.+\sum_{m=0}^{M}D_m\left\{w^n\left(i,j,k+m+\frac{1}{2}\right)-w^n\left(i,j,k-m-\frac{1}{2}\right)\right\}\right] \tag{11}$$

As an initial condition, sound pressure distribution with smooth profile is given. The transient responses at all discrete grid points are calculated according to the above FDTD scheme. Here, as a profile of initial condition of sound pressure, the following exponential function is adopted.

$$p(x,y,z)=\exp\left\{-\frac{x^2+y^2+z^2}{(A\Delta h)^2}\right\} \tag{12}$$

where, (x,y,z) is relative coordinates of a grid point in which a sound source point is made to be origin, A is a coefficient which prescribes the width of the initial pulse source and is made to be 2.5 in this study. Figure 2 shows the shape of the sound pressure distribution and the spectral characteristics of the source, respectively. As shown in Fig. 2, this type of the sound source has major spectral component in the frequency range below $0.5\times c/(A\Delta h)$ Hz (c is the sound velocity).
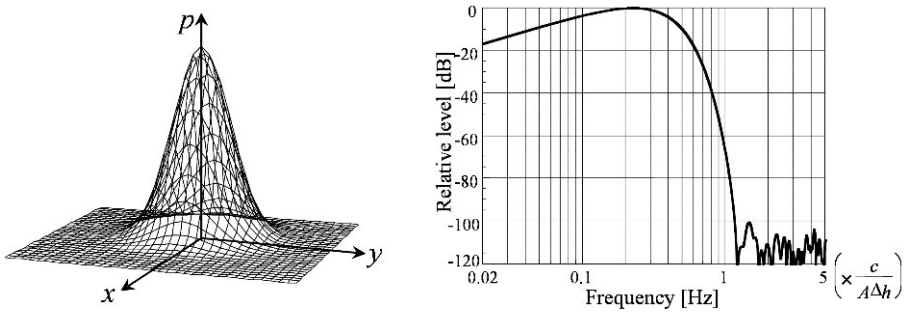

Figure 2. Sound source condition. Distribution of sound pressure around source point (*left* figure) and its spectral characteristics (*right* figure).

3. VISUALIZATION OF INDOOR/OUTDOOR SOUND PROPAGATION

In room acoustics, an impulse response of a room is the most important quantity for assessment and evaluation of acoustical quality of the room. In design stage of a hall or a theater, therefore, prediction of the response should be carefully conducted. The FDTD method described in this report can be directly applied to prediction of room impulse responses and the author's research group has made investigation on its applicability [4]. Here, an example of the application to room acoustic design is introduced. Figure 3 shows an example of auditorium under investigation. In our research, impulse responses at receiving points M1 to M6 were calculated and compared with measured data to validate the calculation method. Figure 4 shows examples of comparison results between calculation and measurement. From these figures, we confirmed basic applicability of the FDTD method to prediction of room impulse responses. Figure 5 shows an example of visualization of sound propagation in the room. In room acoustic design, such visualization of sound wave propagation seems to be useful to judge sound diffusivity in the room. From such visualization results, both effective and harmful reflections can be found visually and the information is effectively utilized to acoustic design procedure of the room shape.
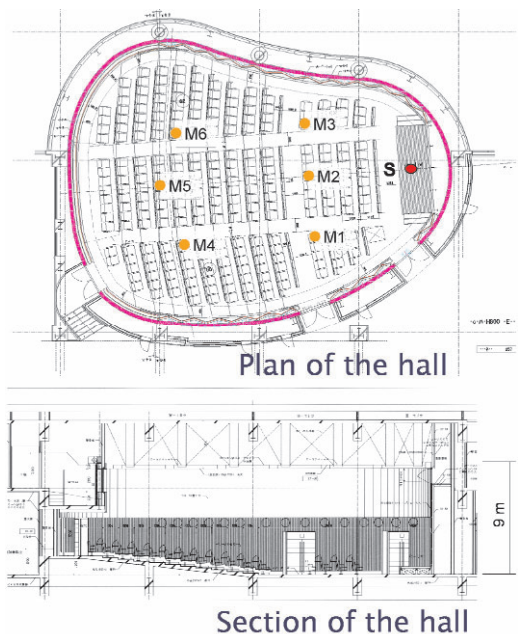

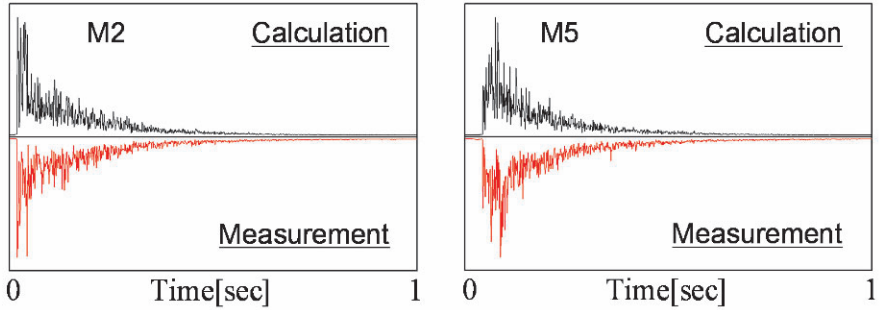*Figure 3.* Plan and section of the hall under investigation.

Figure 4. Comparison of impulse responses at M2 and M5. The wave forms were arranged in averaged root mean squared forms.
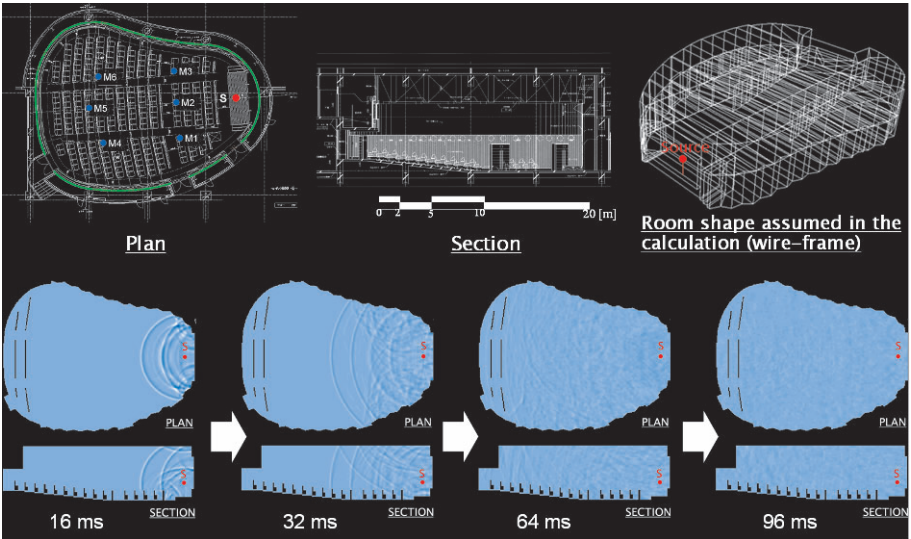

Figure 5. Visualization of sound wave propagation in a room.

As another example of application of the FDTD method, visualization of outdoor sound propagation is introduced. Environmental noise problems have been spreading in worldwide and its solution is essentially important for improvement of our quality of life. Against road traffic noise, which is one of major environmental noise sources, many kinds of strategies and methods of countermeasures have been developed. Focusing on such countermeasures and strategies, the author has been analyzed noise attenuation effects of noise barriers with several kinds of top shapes, embankments, depressed or semi-underground road structures and so on [5–7]. In this

section, an application of the FDTD to visualization of sound diffraction over several kinds of noise barriers is introduced. For barriers shown in Fig. 6, instantaneous sound pressure distribution calculated by the FDTD method in each time step was visualized. Snap shots of the sound pressure distribution for Types 1–3 at every 16 ms are shown in Fig. 7(a)–(c), respectively. In these figures, the amplitude of sound pressure is shown by monochrome shade. In Fig. 7(a) for Type 1 simplest straight barrier, a simple pattern of sound diffraction at the top of the barrier is clearly seen. On the other hand, in the cases of Type 2 and Type 3 barriers, the sound propagation becomes more complicated and multiple diffractions can be seen. The sound diffraction and interference effects seen in the visualization results affect to the attenuation efficiencies of each kind of noise barrier.
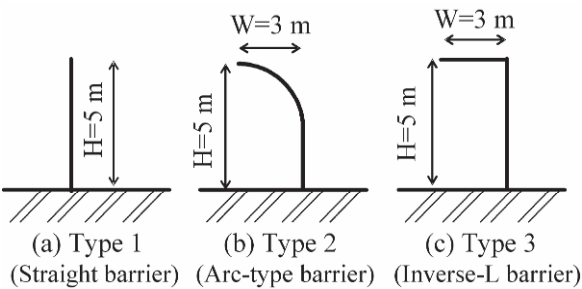
Figure 6. Sectional shapes of barriers under investigation.
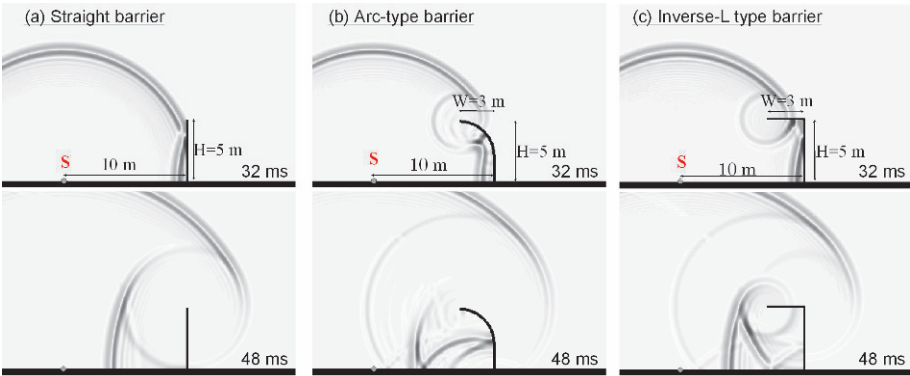
Figure 7. Sound diffraction over various types of noise barriers.

4.   SUMMARY

Basic theory of the FDTD method for linear acoustic phenomena was described and its application to architectural acoustics and outdoor noise propagation was introduced in this paper. Since transient sound wave propagation is observed in detail, visualization results obtained by the FDTD method can be effectively used for acoustical design of a room and planning of a countermeasure for mitigation of outdoor noise.

REFERENCES

1. T. Yokota, S. Sakamoto, H. Tachibana, Sound field simulation method by combining finite difference time domain calculation and multi-channel reproduction technique, *Acoust. Sci. & Tech.*, **25**, (1) 15–23 (2004)
2. T. Yokota, S. Sakamoto, H. Tachibana, Visualization of sound propagation and scattering in rooms, *Acoust. Sci. & Tech.*, **23**, (1) 40–46 (2002)
3. S. Sakamoto, T. Seimiya, H. Tachibana, Visualization of sound reflection and diffraction using finite difference time domain method, *Acoust. Sci. & Tech.*, **23**, (1) 34–39 (2002)
4. S. Sakamoto, A. Ushiyama, H. Nagatomo, The FDTD calculation of impulse responses of a small hall and their correspondence with measurement results, Proceedings of WESPAC 9, paper No. 550 (in CD-ROM) (2006)
5. S. Sakamoto, H. Tachibana, FDTD analysis of diffraction over various types of noise barriers, Proceedings of ICA 2004, I, 525–526 (2004.4)
6. S. Sakamoto, H. Tachibana, Numerical analysis on noise attenuation performance of embankment, Proceedings of Inter-noise 2003, paper No. N918 (in CD-ROM) (2003.8)
7. S. Sakamoto, H. Tachibana, Study on simplified calculation model for prediction of noise radiation from semi-underground roads, Proceedings of inter-noise 2002, paper No. N634 (in CD-ROM) (2002.8)

QUANTITATIVE ASSESSMENT OF TUBES AND RODS: COMPARISON OF EMPIRICAL AND COMPUTATIONAL RESULTS

J.J. Kaufman, G.M. Luo, B. Blazy, R.S. Siffert
CyberLogic, Inc., New York, NY; The Mount Sinai School of Medicine, New York, NY

Abstract: The primary objectives of this study were to establish an understanding of how ultrasound propagates through cylindrical rods and tubes. Another objective was to provide validation data for a computational ultrasonics software package. The long range objective of our work is to develop an ultrasound method to quantitatively assess the radial bone (the forearm) as a means for assessing osteoporosis.

Key words: Computational ultrasonics, Bone mineral density, Cortical bone, Net time delay, Ultrasound velocity, Osteoporosis

1.   INTRODUCTION

The long range objective of this research is to develop an ultrasonic method for estimating bone mineral density (BMD) at the forearm. Estimation of BMD is an important component in diagnosing and managing osteoporosis. The use of BMD is based on the well-established thesis that bone strength is strongly related to the amount of bone material present and that a stronger bone in a given individual is associated generally with a lower fracture risk [1]. Radiological densitometry (e.g., DXA), which measures the BMD at a given site is currently the accepted indicator of fracture risk. Because of its expense, inconvenience, and associated x-ray exposure, ultrasound has been proposed as an alternative to DXA [2]. As part of this project, a study of ultrasound propagation through rods and tubes was carried out.

2.   MATERIALS AND METHODS

This study used both empirical ultrasound measurements and data generated in computer simulations. Bench-top measurements were conducted on a set of 6 plastic rods and 7 plastic tubes. A 3.5 MHz 12.7 mm diameter source and 1.5 mm diameter receiver in a through-transmission configuration were used within a water tank, between which the plastic samples were placed. The received waveform was stored for subsequent processing. This configuration, as shown in Fig. 1, is similar to the one described by [3]. A set of 2D ultrasound simulations of analogous models was also carried out using a finite difference time domain method (*Wave2000 Pro*, CyberLogic, Inc., NY).
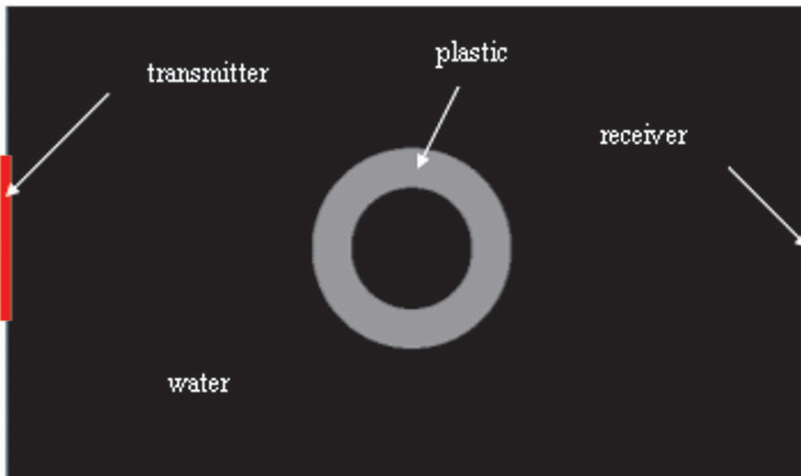

Figure 1. A typical image associated with an ultrasound simulation of propagation through a tube.

The ultrasound data obtained from both the bench-top experiments and the computer simulations were processed to obtain an ultrasound parameter known as *net time delay* (NTD), associated with each sample. The NTD is the difference between the times of travel of waveforms with and without the rod or tube in the path, *i.e.*, with water only or with water and sample [4].

3.   RESULTS

Results obtained show extremely close correspondence between the simulated and empirical results. Moreover, both the empirical and simulated results demonstrate correlations of NTD with overall rod diameter or tube

wall thickness greater than 0.99. The simulated and empirical data demonstrate two primary paths of propagation for the tubes. The first is termed the circumferential wave (CW) and travels largely within the wall of the tube. The second is termed the direct wave (DW) and travels through the wall of the tube, into the water within the tube, and then through the wall of the tube as it travels to the receiver (Fig. 2). The estimation of plastic thickness using the NTD is based on the arrival time of the direct wave.
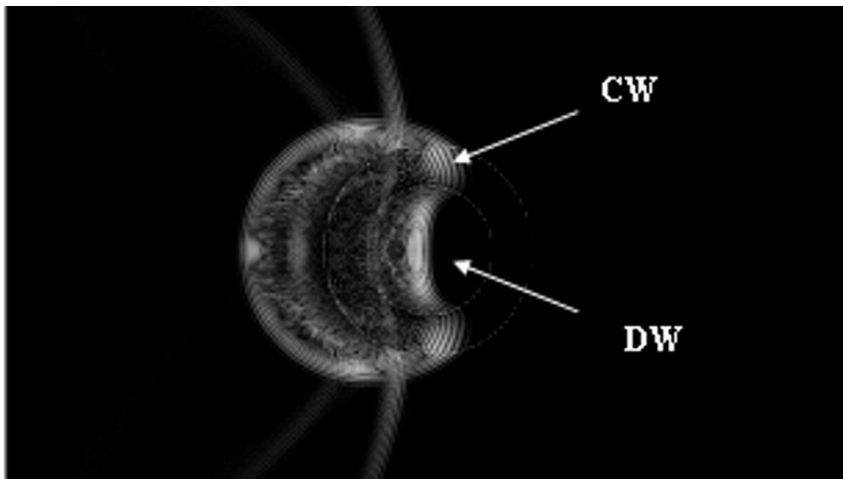
Figure 2. The ultrasound wave propagating through a simple tube showing a snapshot of the displacement magnitude at t=30.9 microseconds.

Figure 3 displays the NTD for all the rods and tubes (for the direct wave only) as a function of total plastic thickness. In this case, the total plastic thickness is the diameter for the rods and twice the wall thickness for the tubes. As may be seen, the correspondence between the empirical ("scope") and simulated ("wave2000") data is nothing short of remarkable. Note also the linear relationship between plastic thickness and NTD.
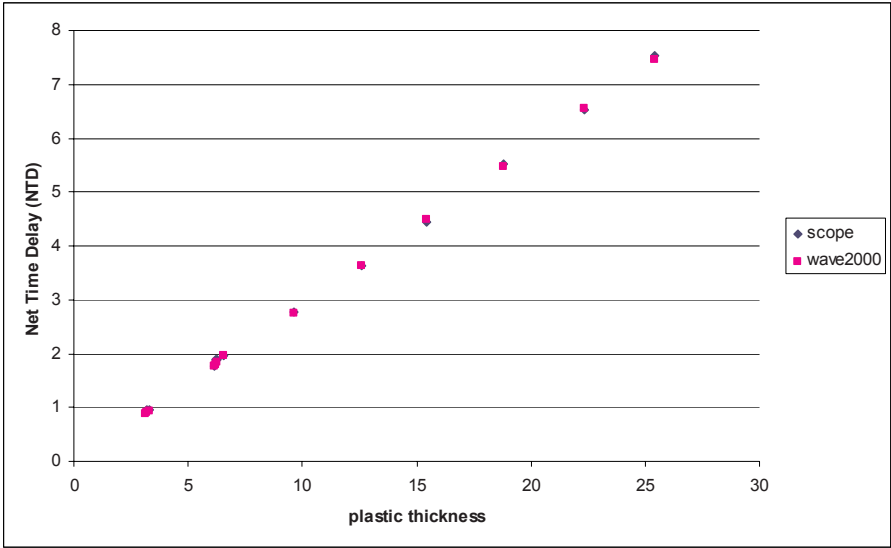
Figure 3. Comparison of the NTD vs. plastic thickness for the simulated ("Wave2000")
and empirical ("Scope") data.

4.   CONCLUSION

This study demonstrates that the net time delay parameter can be used to
estimate the thickness of plastic rods and tubes in a through-transmission
configuration. It also shows that 2D ultrasound simulation can be a useful
tool for modeling ultrasound propagation in tubular structures. Subsequent
research on human radial bone, including simulation, *in vitro* and clinical
studies, will be carried out to develop a simple non-invasive radiation-free
method for diagnosis and management of osteoporosis.

ACKNOWLEDGEMENTS

REFERENCES

1. Kaufman JJ, Siffert RS, 2001, "Non-invasive Assessment of Bone Integrity," in *Bone Mechanics Handbook*, Cowin S, Ed., CRC Press, Boca Raton.
2. Siffert RS, Kaufman JJ, 2007, Ultrasonic Bone Assessment: 'The Time Has Come', *Bone, 40*(1):5–8.
3. Robinson BS, Greenleaf JF, 1984, Measurement and Simulation of the Scattering of Ultrasound by Penetrable Cylinders, in *Acoustical Imaging*, Kaveh M, Mueller RK, Greenleaf JF, Eds., Plenum Press, New York, Vol. 13, pp. 163–178.
4. Kaufman JJ, Luo GM, Siffert RS, 2007, "A Portable Real-Time Bone Densitometer," *Ultrasound in Medicine and Biology*, *33*(9): 1445–1452.

HEATED TEMPERATURE IMAGING BY ABSORPTION OF ULTRASOUND

C. Yamaya, H. Inoue

Faculty of Engineering and Resource Science, Akita University, Akita 010-8502, Japan

Abstract: Recently, therapy using heating of a living body by ultrasound has been applied. The temperature rise of the medium depends on absorption of ultrasound. We performed basic experiments and finite-difference time-domain (FDTD) simulation that combined ultrasonic propagation and heat analysis. The temperature image can be obtained from the simulation that modeled an object to be analyzed. This paper presents temperature images generated at any time by absorption of ultrasound.

Key words: Absorption of ultrasound, Heat analysis, Finite-difference time-domain (FDTD) method, 3-D simulation

1. INTRODUCTION

The finite-difference time-domain (FDTD) method has become widely used because it provides the transient response and the space distribution. It is difficult in experiments to immediately obtain temperature information in a medium with a high spatial resolution. However, the internal temperature distribution can be understood by visualizing the temperature distribution in a simulation. This paper describes a basic experiment and simulation method. The simulation depicts the temperature distribution of the time series and visually illustrates the temperature change.

2.   MEASUREMENT SYSTEM

Figure 1 presents the temperature measurement system. The resonance frequency of a PZT transducer with a 9.6 mm radius is 1.05 MHz. In Fig. 1, the amplitude of sinusoidal wave of 1.05 MHz from the function generator (Tektronix AFG2020) is modulated by an oscillator (HP 33120A). The signal of the oscillator is a square wave of 40 MHz, and the duty ratio is 20%. A sinusoidal signal of 1.05 MHz is thus output for 5 s and 0 V for 20 s. The transducer is driven by the amplified signal to 1 W by a power amplifier (40 dB, R&K A30-10-R). An E-type thermocouple (+ Chromel, – Constantan) is covered with a glass capillary, and the head diameter (ϕ) for temperature measurement is about 60 μm. This thermocouple is scanned by six-axis control equipment, and the observation point is on a center axis of the sound source. The thermocouple output voltage is amplified by a DC amplifier and converted to a digital signal by an A/D converter (YOKOGAWA WE7000, sampling interval 1 ms, resolution 16 bits). The digital signal is input into a PC through a LAN cable. Glycerine is poured into a container with dimensions of $280 \times 80 \times 80$ mm^3. The temperature of glycerine in the container is maintained at 25℃ by a thermo-controller.

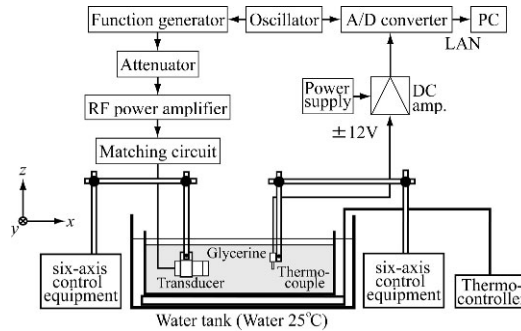*Figure 1*. Temperature measurement system.

3.   FDTD SIMULATION

Table 1 and Fig. 2 give the analysis conditions and analytic region in the FDTD simulation. The analytic region is modeled as glycerine liquid. A sinusoidal wave of 1 MHz is excited from the circular plane sound source of 9.6 mm in radius. Heating (cooling) time is 5 s (10 s). The Westervelt equation using this simulation is as follows [1–4].

$$\nabla^2 p - \frac{1}{c^2}\frac{\partial^2 p}{\partial t^2} + \frac{\delta}{\rho c^4}\frac{\partial^3 p}{\partial t^3} + \frac{\beta}{\rho c^4}\frac{\partial^2 p^2}{\partial t^2} = 0 \tag{1}$$

Here, p is the sound pressure, ρ is the density, c is the sound velocity, $c = (K/\rho)^{1/2}$, K is the bulk modulus, δ is the acoustic diffusivity, $\delta = 2c^3\alpha/\omega^2$, ω is the angular frequency, and α is the absorption coefficient. $\beta = 1+B/2A$ is the coefficient of nonlinearity with B/A being the nonlinearity parameter of the medium. In Eq. (1), the first and second terms describe linear lossless wave propagation, the third and fourth terms are the loss and nonlinear terms. In this simulation, the nonlinear term is ignored in the Westervelt equation because the maximum sound pressure in space is one hundred and several tens of kPa.

The heat conduction equation [HCE; Eq. (2)] and connection equation [Eq. (3)] are as follows.

$$\frac{\partial T}{\partial t} = \kappa\nabla^2 T + \frac{H}{\rho C} \tag{2}$$

$$H = 2\alpha I \tag{3}$$

In HCE [Eq. (2)], T is the temperature, H is the internal heat generated by the source, C is the specific heat, κ is the thermal diffusivity, and $\kappa = \lambda/\rho C$, λ is the thermal conductivity. In Eq. (3), I is the ultrasound intensity.

$$I = \frac{1}{T_p}\int_0^{T_p}\frac{p^2(t)}{\rho c}dt \tag{4}$$

Here, T_p is an integral multiple of one cycle of an ultrasound or time sufficiently longer than a cycle.

Table 2 lists the medium constants of glycerine. First, in this simulation, the ultrasonic field is analyzed by the FDTD method for acoustics (acoustic-FDTD), and the ultrasound intensity is calculated. Second, the internal heat generation is calculated from the ultrasound intensity, and heat analysis (FDTD-HCE) is executed.

Table 1. Analysis conditions in FDTD simulation.

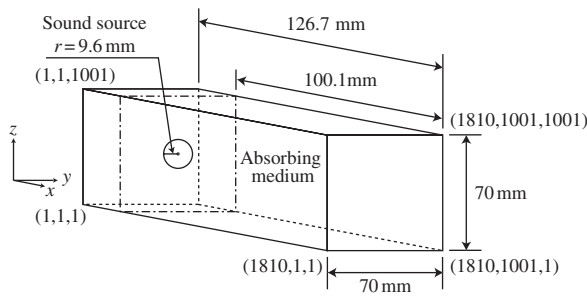|	Acoustic-FDTD	FDTD-HCE
Cell size	$\Delta x = \Delta y = \Delta z = 70$ [μm]	
Number of cells	$1810 \times 1001 \times 1001$ [cell]	
Time step	$\Delta t = 10$ [ns]	$\Delta t_h = 50000\ \Delta t$ [s]
Boundary condition	Mur's second-order absorbing boundary condition	Adiabatic boundary

Figure 2. Analytic region for FDTD simulation.

Table 2. Medium constants of glycerine [5,6].

Bulk modulus K	4.76 [10^9 N/m^2]
Density ρ	1263 [kg/m^3]
Absorption coefficient α	2700 [10^{-15} s^2/m]
Specific heat C	2460 [J/kg·K]
Thermal conductivity λ	0.287 [W/m·K]
Thermal diffusivity κ	0.924 [10^{-7} m^2/s]

4.   RESULTS AND DISCUSSION

Figure 3 depicts the temperature distribution on the center axis of the sound source at 5 s after ultrasonic irradiation. These temperature distributions are normalized by each temperature at a near field length (46.5 mm). The normalized temperature distribution of the simulation corresponds to that of the experiment over the far field. Figure 4 plots the *x-y* plane temperature distribution at each time and the one-dimensional distributions. The temperature increases where the sound pressure is high. Additionally, a moving image of heat conduction is made from numerical data for the temperature field at each time obtained by FDTD simulation.
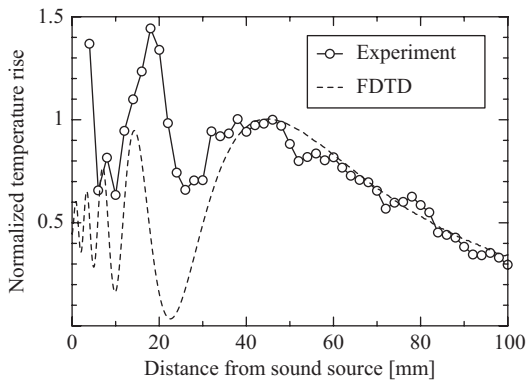
Figure 3. Temperature distributions on center axis of sound source at 5 s after ultrasonic irradiation.
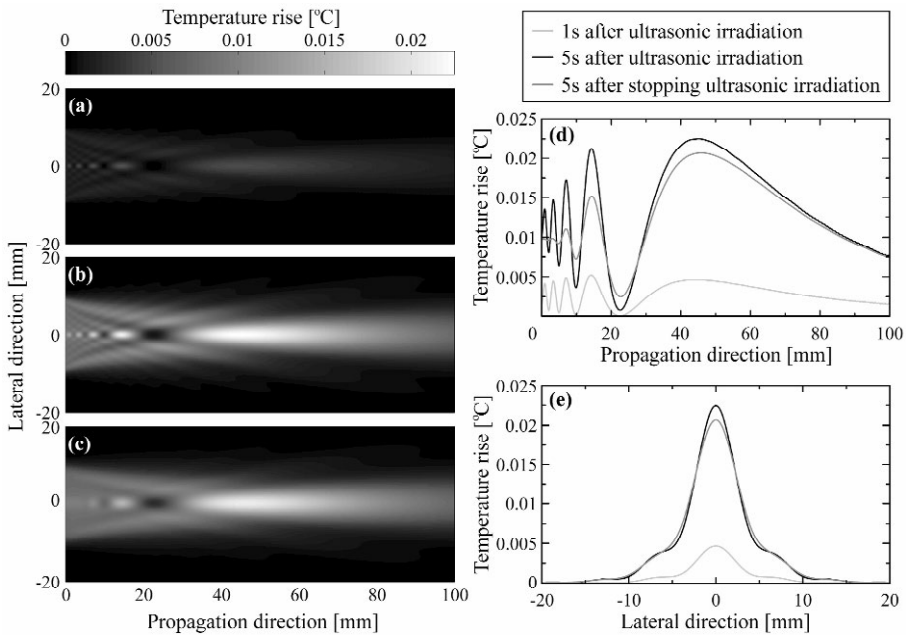

Figure 4. Simulation results of temperature distributions at *x-y* plane containing the center of sound source. (**a**) 1 s, (**b**) 5 s after ultrasonic irradiation (heating time). (**c**) 5 s after stopping ultrasonic irradiation (cooling time). (**d**) Distributions at lateral direction 0 mm. (**e**) Distribution at propagation direction 46.5 mm.

5.   CONCLUSION

In the normalized temperature distribution, the simulation result corresponds to the experiment result. The *x*-*y* plane temperature distributions obtained by simulation are also shown. It is possible to describe the temperature image from the numerical data obtained by the FDTD simulation for more complex models as further work; the simplest model was presented in this paper. Moreover, it seems that a more practical temperature distribution is obtained from the simulation of biological medium model with a lot of media having different characteristics because there are cases in which the biological medium is inhomogeneous. Consequently, therapeutic technique is expected to progress further.

ACKNOWLEDGEMENTS

REFERENCES

1.   C. Yamaya, H. Inoue, Behavior of propagation and heating due to absorption of ultrasound in medium, Jpn. J. Appl. Phys. **45**, 4429–4434 (2006).
2.   I. M. Hallaj and R. O. Cleveland, FDTD simulation of finite-amplitude pressure and temperature fields for biomedical ultrasound, J. Acoust. Soc. Am. **105**, 7–12 (1999).
3.   I. M. Hallaj, R. O. Cleveland and K. Hynynen, Simulations of the thermo-acoustic lens effect during focused ultrasound surgery, J. Acoust. Soc. Am. **109**, 2245–2253 (2001).
4.   J. Huang, R. G. Holt, R. O. Cleveland and R. A. Roy, Experimental validation of a tractable numerical model for focused ultrasound heating in flow-through tissue phantoms, J. Acoust. Soc. Am. **116**, 2451–2458 (2004).
5.   The Japan Society of Thermophysical Properties, *Thermophysical Properties Handbook* (Yokendo Co., Ltd., Tokyo, 1990) p. 448 [in Japanese].
6.   Physics Dictionary Edit Committee, *Physics dictionary* (Baifukan Co., Ltd., Tokyo, 1986) p. 2321 [in Japanese].

TIME DOMAIN ANALYSIS OF SOUND PROPAGATION IN SHALLOW WATER WITH TRANSITIONAL LAYER

T. Tsuchiya, S. Matsumoto, N. Endoh

Faculty of Engineering, Kanagawa University, High-Tech Research Center, Yokohama 221-8686, Japan; The Port and Airport Research Institute, Yokosuka 239-0826, Japan

Abstract: The characteristics of sound propagation in shallow water are influenced by the bottom media because sound propagation is affected by acoustic boundary conditions of the water-sediment interface. In order to investigate the characteristics of sound propagating in shallow water, it is necessary to develop an accurate numerical method of sound propagation. The elastic finite difference time domain (FDTD) method is very accurate and is comparatively useful for range-dependent models in shallow water. There is a transition layer of porous media on the sea bottom in shallow water. Therefore, we investigated the characteristics of sound propagation in shallow water to clarify the fluctuation of the amplitude of waveform reflected from the sea bottom with a transition layer. As a result, we found that the amplitude of the sound pulse reflected from the sea bottom is influenced by the transition layer in shallow water when the transition layer thickness exceeds one wavelength.

Key words: Numerical analysis method, Sound propagation, Shallow water, Elastic finite difference time domain method, Transition layer

1.   INTRODUCTION

Ocean Acoustic Tomography (OAT) using sound propagation times in the ocean is useful for determining the actual temperature, salinity concentration of water, and oceanic current [1]. Recently, acoustic thermometry of the ocean is being planned in shallow water because it is important to acquire observation data of the environment in shallow water for any research of

fisheries societies, geology and aerologic. OAT requires an appropriate numerical method of sound propagation to obtain the prior information of the ocean. The characteristics of sound propagation in shallow water are influenced by the bottom media because sound propagation is affected by acoustic boundary conditions of the water-sediment interface. In order to investigate the characteristics of sound propagation in shallow water, it is necessary to develop an accurate numerical method of sound propagation.

Numerical analysis of sound propagation has developed in the ultrasonic field because the computational power of personal computers has increased very rapidly. The finite difference time domain (FDTD) method [2] is very useful for calculating sound propagation in the field, although it requires a very large memory and long calculation time.

A transition layer of porous media exists on the sea bottom surface in shallow water [3]. The stress of grains in porous media is proportional to sediment depth because of the balance of gravitational attraction and buoyancy of water. Therefore, the porosity of porous media varies with depth. The density in the transition layer may be approximated by an exponential function if the porosity of the porous media is inversely proportional to the layer depth. Therefore, we investigated the characteristics of sound propagation in shallow water to clarify the amplitude fluctuation of the waveform reflected from the sea bottom with a transition layer.

2.   FORMULATION OF ELASTIC FINITE DIFFERENCE TIME DOMAIN METHOD

The basic equations considering two dimensions in coordinates (x,y) are given by Newton's motion equation and equation of continuity, where x and y are the horizontal propagation direction and depth direction below the ocean surface [4].

$$\rho \frac{\partial v_x}{\partial t} = \frac{\partial T_{xx}}{\partial x} + \frac{\partial T_{xy}}{\partial y} \qquad (1),$$

$$\rho \frac{\partial v_y}{\partial t} = \frac{\partial T_{yy}}{\partial y} + \frac{\partial T_{xy}}{\partial x} \qquad (2),$$

$$\frac{\partial T_{xx}}{\partial t} = (\lambda + 2\mu) \frac{\partial v_x}{\partial x} + \lambda \frac{\partial v_y}{\partial y} \quad (3),$$

$$\frac{\partial T_{yy}}{\partial t} = \lambda \frac{\partial v_x}{\partial x} + (\lambda + 2\mu) \frac{\partial v_y}{\partial y} \quad (4),$$

$$\frac{\partial T_{xy}}{\partial t} = \mu \left(\frac{\partial v_y}{\partial x} + \frac{\partial v_x}{\partial y} \right) \quad\quad (5).$$

Here, T_{xx} *and* T_{yy} are compression stress and T_{xy} is shear stress of each point. V_x and V_y are the particle velocities of the x and y directions. λ and μ are Lame constants that are given by density ρ, speed of longitudinal sound c_p, and speed of shear sound c_s. The finite differential equations are obtained as a function of discrete position x, y in space and discrete time t. These equations are quantized in space as $x = i \cdot \Delta x$ and $y = j \cdot \Delta y$ and in time as $t = n \cdot \Delta t$.

3.   CALCULATION OF SOUND PROPAGATION IN SHALLOW WATER WITH TRANSITION LAYER

Figure 1 depicts the model for calculating sound propagation in shallow water with a transition layer. The model dimensions are 80 m in depth and 100 m in propagation range. We assume that the speed of sound in water is 1500 m/s, the density is 1.0 g/cm^3 and the sediment is composed of silty sand. We further assume that the longitudinal speed of sound in silty sand is 1700 m/s and that silty sand density is 1.9 g/cm^3. The speed of sound in the shear direction is 200 m/s. The sediment layer covers the sediment's surface. In this figure, *wd* is the transition layer thickness.
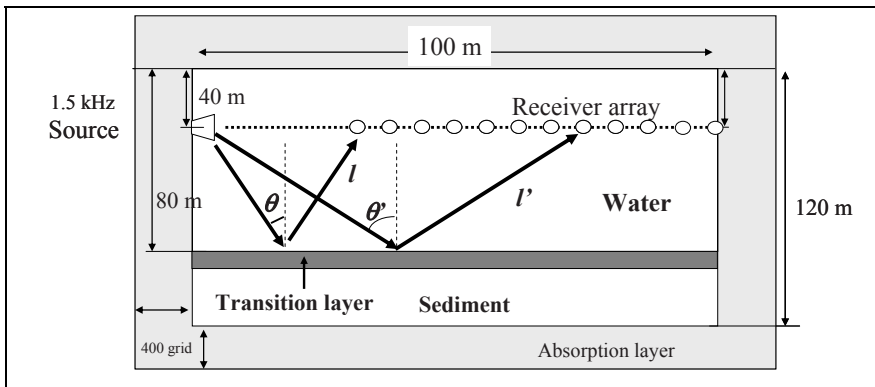

Figure 1. Schematic of model for calculating sound propagation in shallow water with a transitional layer using elastic FDTD.
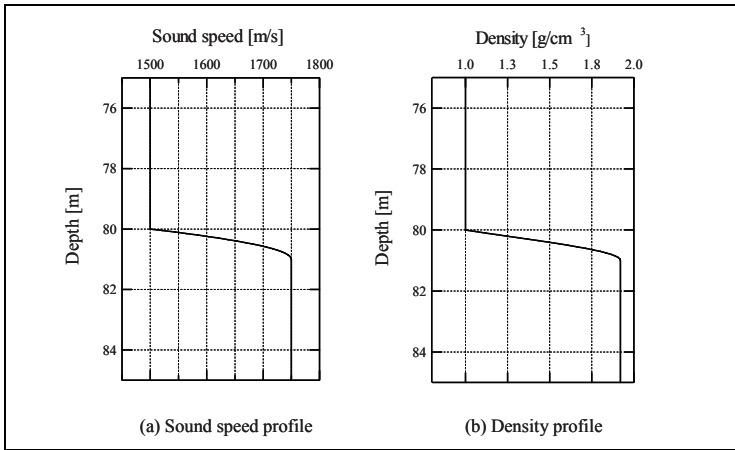
Figure 2. Sound speed and density profiles of transitional layer on bottom surface.

The sound speed and density profiles were assumed to be exponential profiles based on Ref. [5]. We used Higdon's second-order absorption boundary conditions. The grid size of absorption layers is 400 points in this model. The attenuation coefficient in the absorption layer is assumed to be a hyperbolic function because the sound pulse is reduced in the absorption layer. The point source and the receiver are both placed at 50 m in depth. The sound frequency is 1.5 kHz. The pulse amplitude is modulated by a Gaussian function, and the pulse length is 8 wavelengths. Generally, there is a transition layer of porous media on the sea bottom in shallow water [5]. The stress of grains in a porous media is proportional to the sediment depth because of the balance of gravitational attraction and buoyancy of water. Therefore, the porosity of porous media varies in the depth direction. The function of density in the transition layer may be approximated by an exponential function, if the porosity of porous media is inversely proportional to the layer depth. Figure 2 plots the sound speed and density profiles in the depth direction. In this figure, *wd* is the thickness of the transition layer. The density depth profile of the transition layer can be obtained from ρ_1, ρ_2 and *w*. In order to determine the influence of the transition layer on sound propagation, we calculated the amplitude of the waveform reflected from a sea bottom with a transition layer.

4. RESULTS AND DISCUSSIONS

Figure 3(a) plots received waveforms estimated by the elastic FDTD method. The solid line represents the waveform estimated by the elastic FDTD method; the dotted line represents the waveform derived by fluid FDTD. As shown in Fig. 3, the pulse passing directly through water arrived at 70 ms, and the second pulse reflected from the transition layer arrived at 86 ms.When we examine the amplitude of the estimated second pulse in Fig. 3, the amplitude of the pulse reflected from an elastic bottom without a transition layer is identical to the pulse reflected from a fluid bottom without a transition layer because the speed of sound for shear propagation is very low. Figure 3(b) depicts the received waveforms estimated by the elastic FDTD method. The solid line represents the pulse waveform reflected from the sea bottom with a transition layer as determined by the elastic FDTD method. The dotted line represents the pulse waveform reflected from the sea bottom without a transition layer.
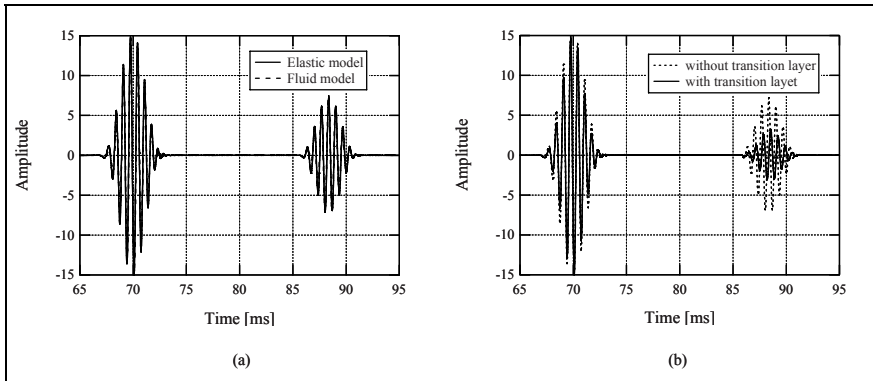
Figure 3. Receiving pulse waveforms calculated by the elastic FDTD method.

Figure 4 plots the relationship between the amplitude of the received waveform and the transition layer thickness. As depicted in Fig. 4(a) and (b), these results indicate that the pulse amplitude depends on the transition layer thickness when the thickness exceeds half a wavelength. It is shown that the amplitude of the pulse reflected by an elastic bottom may differ from that reflected by a fluid bottom. For example, the amplitude of the pulse reflected from an elastic bottom becomes 2.2 times that of a pulse reflected by a fluid bottom when the layer thickness is 0.8 m. As a result, the amplitude of the sound pulse reflected from the sea bottom is influenced by the transition layer in shallow water and must be considered as a shear wave to propagate in an elastic bottom. Figure 4 plots the amplitude of the second pulse as a function of incident angle of bottom-reflection pulse, when the

shear speed of transition layer is varied from 0 to 400 m/s. The difference of amplitude appears at around 40 degrees.

(a) Calculated by elastic FDTD method   (b) Calculated by fluid FDTD method
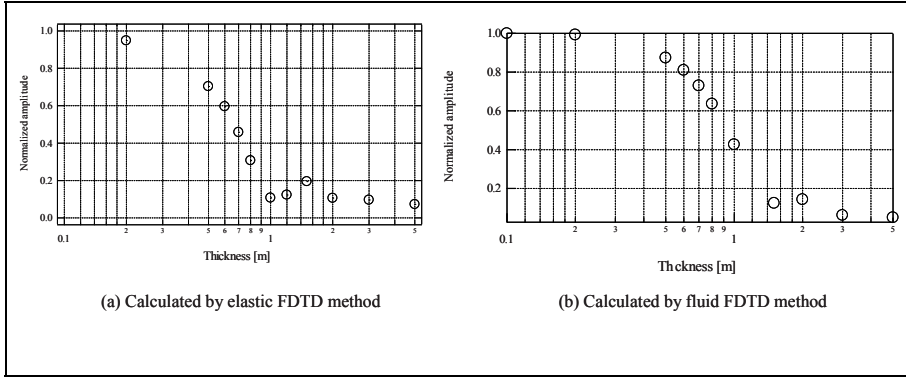
Figure 4. Relationship between the amplitude of the received waveform and the transition layer thickness.

5.   CONCLUSIONS

In order to determine the characteristics of sound propagating in shallow water, we estimated pulses reflected from a sea bottom with a transition layer using the elastic FDTD method. The porosity of porous media varies in the depth direction and is approximated as an exponential function. The amplitude of a sound pulse reflected from the sea bottom was found to be influenced by the transition layer in shallow water. It is clear that the sea bottom with a transition layer affects the sound propagation in shallow water.

REFERENCES

1. Munk, W., Worcester, P. and Wunsch, C., 1995, The tomography problem *in Ocean Acoustic Tomography*, G. K. Batchelor ed. Cambridge University Press, Cambridge, pp. 1–28.
2. Yee, K. S., Shlager, K. and Chang, A. H., 1966, Numerical solution of initial boundary value problems involving Maxwell equations in isotropic media, *IEEE Trans. Ant. Propagat.*, **14**:302–307.
3. Kimura, M., 2006, Frame bulk modulus of porous granular marine sediments, *J. Acoust. Soc. Am.* **120**:699–710.
4. Iijima, F., Tsuchiya, T. and Endoh, N. 2000, Analysis of characteristics of underwater sound propagation in the ocean by a finite difference time domain method, *Jpn. J. Appl. Phys.* **39**:3200–3204.
5. Robins, A. J., 1990, Reflection of plane acoustic waves from a layer of varying density, *J. Acoust. Soc. Am.* **87**:1546–1552.

VISUALIZATION OF TEMPERATURE DISTRIBUTION IN CYLINDRICAL CAVITY USING SOUNDS REFLECTED FROM INTERNAL SURFACE

A. Minamide, K. Mizutani, N. Wakatsuki

Graduate School of Systems and Information Engineering, University of Tsukuba, Tsukuba 305-8573, Japan

Abstract: In this paper, we propose a new acoustic computerized tomography (A-CT) method using sounds reflected once from an internal surface together with direct sounds to estimate the temperature distribution in a cylindrical cavity. By employing numerical simulations, we confirm that the use of the times of flight (TOFs) of once-reflected sounds as well as those of the direct sounds improves the precision of the temperature distribution reconstructed with the A-CT method when the distribution is symmetrical about the center of the cavity. This technique can reduce the number of transducers required to obtain the same precision.

Key words: Computerized tomography, A-CT method, Temperature distribution, Temperature measurement, Reflected sounds, Cylindrical cavity

1.   INTRODUCTION

Temperature distribution measurement is used in various fields, such as, air-conditioning control in offices, temperature control in greenhouses [1,2], and temperature management in oil plants. Acoustical means of temperature distribution measurements are thus researched and published [3–6]. Using acoustical transducers for temperature distribution measurements has several advantages, including non-contact measurement, effective use of space, and large-scale space measurement.

Acoustic computerized tomography (A-CT) method and other methods have been proposed. The A-CT method reconstructs temperature distribution from times of flight (TOFs) between acoustic transducers. However, many transducers are required in order to obtain the distribution in large-scale space. This means that measurement cost increases, and measurement system reliability deteriorates. Thus, a measurement method that uses few transducers is desired.

In this research, we deal with temperature distributions in a cylindrical cavity. We tried to reduce the number of transducers by using the TOFs of sounds reflected from an internal surface of the cavity as well as the TOFs of direct sounds.

2. PRINCIPLES

2.1 Temperature Measurement by A-CT Method

A-CT is an acoustical measurement method based on the CT method [7]. Acoustic transducers are located at equal intervals around the measurement space. Measuring the TOFs of direct sounds between transducers, reciprocals of sound velocity, which are projection data, are calculated. Since TOF measurement requires at least a pair of acoustic transducers, both sides of the projection data could not be measured. Thus, exact data are given to both sides of projection data. Because transducers are located at some intervals, sparse projection data are obtained. However, close projection data are required for back projection. Close projection data is therefore obtained by interpolating sparse projection data.

The distribution of the reciprocal of sound velocity is calculated by back projection. In order to reconstruct the temperature distribution, the reciprocals are converted into temperatures.

Some methods to reconstruct distribution from the Radon transform have been proposed. In this research, we use the filtered back-projection (FBP) method because this method is simpler than other methods.

2.2 A-CT Method Using Direct Sounds and Reflected Sounds

Figure 1 illustrates a cylindrical cavity, locations of transducers, and direct and reflected sound paths in this simulation. Eight transducers are located at equal intervals on the internal surface. The directivity of a transducer
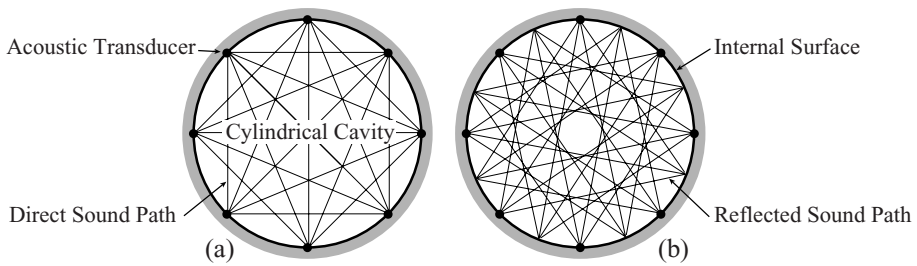
Figure 1. Sound paths formed by the 8-acoustic transducers. (**a**) 20-direct sound paths, (**b**) 16-reflected sound paths.

is assumed to be 100 degrees because it is difficult to separate direct and reflected sounds.

The thin lines in Fig. 1(a) indicate direct sound paths; there are 20 direct sound paths. The thin lines in Fig. 1(b) indicate reflected sound paths; there are 16 reflected sound paths. In Fig. 1, the direct sound paths are sparse near the internal surface, whereas reflected sound paths are not so sparse. Therefore, relatively dense data can be measured near the internal surface by using reflected sound paths.

The A-CT method using reflected sounds as well as direct sounds is similar to the A-CT method using direct sounds only. However, by using one-time reflection points, the rotation angle of the Radon transform becomes half of that of the A-CT method using direct sounds only. Therefore, the number of back projections doubles.

In reflected sound paths, the TOFs of pre- and post-reflections are required. In this paper, the TOF of pre-reflection means the TOF between a transmitter and a reflection point, and the TOF of post-reflection means the TOF between the reflection point and a receiver. The locations of primary reflection points on the internal surface of the cylindrical cavity are determined from the locations and directivity of transducers. The TOFs of both pre- and post-reflection are required. However, only the sum of the two TOFs, which are the TOFs of pre- and post-reflections, is measured. Estimating the TOFs of pre- and post-reflections from the TOF of the reflected sound path is an inverse problem. In this research, these two TOFs are regarded as equal for primary approximation because propagation distance between transducers and primary reflection points is equal.

Specifically, a point of the A-CT method using the TOFs of reflected sound paths is calculating two inverse problems, back projection and calculating the TOFs of pre- and post-reflections.

3.   VISUALIZATION OF TEMPERATURE DISTRIBUTION

Figure 2 presents the given and reconstructed temperature distributions in the simulations. The temperatures are calculated at points on the 20×20 grid. The grid size is $\Delta l \times \Delta l$. In these simulations, the TOFs are calculated to obtain the average temperature of the propagation paths.
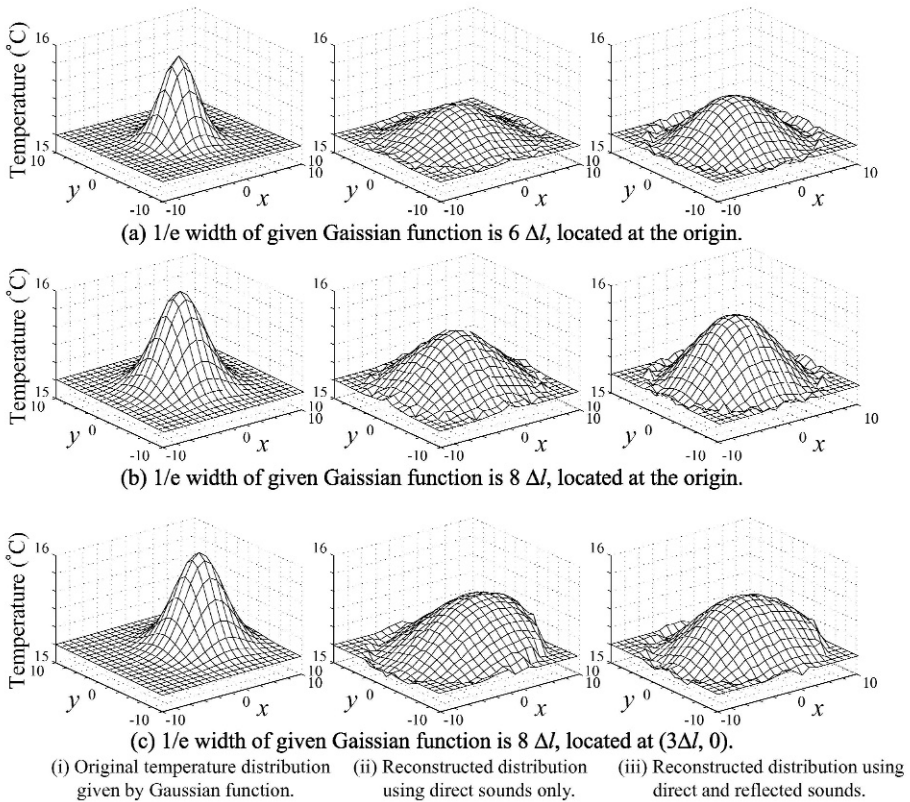

(a) 1/e width of given Gaissian function is 6 Δl, located at the origin.

(b) 1/e width of given Gaissian function is 8 Δl, located at the origin.

(c) 1/e width of given Gaissian function is 8 Δl, located at (3Δl, 0).

(i) Original temperature distribution given by Gaussian function.   (ii) Reconstructed distribution using direct sounds only.   (iii) Reconstructed distribution using direct and reflected sounds.

Figure 2. Temperature distributions.

The figures marked with (i) are the original distributions, given by a Gaussian function. The base value of the temperature distribution is 15.00 degrees centigrade, and the peak value of the temperature distribution is 16.00 degrees centigrade. The figures marked with (ii) are reconstructed distributions using the TOFs of direct sounds only. The figures marked with (iii) are reconstructed distributions using the TOFs of direct and reflected sounds.

In these simulations, the 1/e width and location of the Gaussian function are changed. In Fig. 2(a), the 1/e width of the Gaussian function is 6 Δl, and located around the origin. Figure 2(a) depicts the case of a narrow width Gaussian function. The Fig. 2(c) simulation differs from Fig. 2(b) in the location of the Gaussian function. The Gaussian function is located at (3 Δl, 0), and the 1/e width is 8 Δl.

4.   DISCUSSION OF RECONSTRUCTED DISTRIBUTIONS

Figure 3 compares the reconstructed distributions of Fig. 2. Figure 3(a) displays comparisons of Fig. 2(a) on the *x*-axis. While the peak value of the original distribution is 16.00 degrees centigrade, the peak value of the reconstructed distribution using direct sounds is 15.40 degrees centigrade. Using the reflected sounds improves the peak value up to 15.49 degrees centigrade. Moreover, the distribution reconstructed by using the direct sounds together with the reflected sounds becomes narrower than that reconstructed by using the direct sounds only.

Figure 3(b) presents comparisons of Fig. 2(b) on the *x*-axis. The Gaussian function's width of the original distribution is greater than that of Fig. 3(a). The peak value of the reconstructed distribution using direct sounds is 15.57 degrees centigrade. However, using the reflected sounds improves the peak value to 15.71 degrees centigrade. Moreover, the distribution reconstructed using direct and reflected sounds is narrower than that reconstructed by direct sounds.

Figure 3(c) depicts a comparison of Fig. 2(c) on the *x*-axis. Peak values of the reconstructed distribution using only direct sounds and using direct and reflected sounds are 15.56 degrees centigrade. Moreover, the location of the peak value shifts from the original location. Thus, utilizing the reflected sounds does not improve the result in this case.

The peak shift is caused by calculating the TOFs of pre and post-reflections. In this case, these TOFs are regarded as equal because the propagation distance between transducers and primary reflection points is equal. However, this does not consider the temperature distribution of
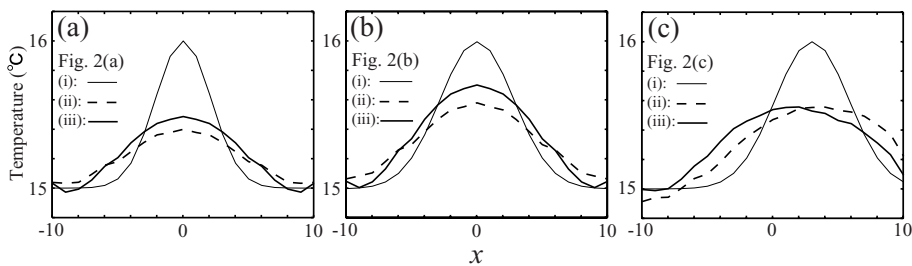
Figure 3. Comparison of reconstructed distributions on *x*-axis. (i), (ii) and (iii) correspond to those of Fig. 2, respectively.

propagation paths. Although the propagation distances are equal, the TOFs of pre- and post-reflections differ slightly because the temperature is not uniform in the cavity. Therefore, the temperature distribution should be considered by some other means.

5.   CONCLUSION

Through numerical simulation, we confirmed that using the TOFs of once-reflected sounds as well as the direct sounds improves the precision of the temperature distribution reconstructed with the A-CT method. At least for the case when the Gaussian function is located around the center of the cylindrical cavity, the reconstructed results using this technique approach the original distributions. Using this technique can thus reduce the number of transducers required while maintaining the same quality in these cases.

As future work, the reconstruction algorithm will be improved to resolve the peak shift.

REFERENCES

1. F. L. K. Kempkes, J. C. Bakker and N. J. van de Braak: Acta Hort. **456**, 363–370 (1998).
2. L. D. Albright: Acta Hort. **578**, 47–54 (2002).
3. G. Hofelmann, H. O. Luck and P. Becker: J. Aerosol Soc. **23**, 51–54 (1992).
4. K. Mizutani, A. Funakoshi, K. Nagai and K. Harakawa: Jpn. J. Appl. Phys. **38**, 3131–3143 (1999).
5. A. Funakoshi, K. Mizutani, K. Nagai, K Harakawa, T. Yokoura: Jpn. J. Appl. Phys. **39**, 3107–3111 (2000).
6. E. Ishikawa, K. Mizutani, K. Nagai: Jpn. J. Appl. Phys. **40**, 5446–5449 (2001).
7. G. N. Hounsfield: Part I. Description of System, Br. J. Radiol. **46**, 1016–1022 (1973).

REAL TIME SOUND FIELD SIMULATOR USING FIELD PROGRAMMABLE GATE ARRAY DEVICE

T. Tsuchiya, E. Sugawara, Y. Inoguchi
Department of Information Systems Design, Doshisha Uniersity, Kyotanabe 610-0321, Japan
Japan Advanced Institute of Science and Technology, Nomi 923-1292, Japan

Abstract: Possibility of real time simulator of three-dimensional acoustic field in the time domain is discussed. Based on the discrete Huygens' model (DHM), a digital equivalent circuit is developed. DHM elements are described by hardware description language (HDL) in the fixed-point arithmetic. It is estimated that the real time simulation of 1 m^3 sound field is possible using ten-odd FPGA chips, while the CPU speed of 52 TFLOPS is required using the high performance computer. It is shown that data length of 28 bits is required for the practical accuracy. Based on FPGA-DHM, the real time simulator named "Silicon Concert Hall" may come true in the near future.

Key words: FPGA, Discrete Huygens' model (DHM), Real time simulator, HDL

1. INTRODUCTION

There are latent demands of the real time simulation of sound field in the time domain. However, it is difficult to realize the real time simulation because enormous amount of computer resources are required. To achieve the real time simulation, a hardware simulator specially designed for sound field simulation is required.

In this paper, a field programmable gate array (FPGA) device is applied to the numerical simulation of sound wave propagation. FPGA is a semiconductor device containing programmable logic components and programmable interconnects. A digital equivalent circuit of sound field for FPGA device is developed based on the digital Huygens' model (DHM) [1–3]

491

or the transmission line matrix method (TLM) [4]. DHM is a numerical model in which propagation and scattering of waves are simulated as the sequences of impulses scattering on the transmission line network as Huygens' principle states.

DHM elements are described in hardware description language (HDL) and configured on a FPGA chip. The number of FPGA logic cells required for a DHM element is estimated. To reduce circuit scale of a DHM element, the fixed-point arithmetic is taken in the DHM calculations. Numerical accuracy of FPGA based DHM using the fixed-point arithmetic is then discussed. The data length required for sound field simulation in practical precision is estimated. Using the FPGA technique, the real time simulator named ``Silicon Concert Hall'' will be created in which sound field of a concert hall is fabricated on a silicon wafer.

2. DIGITAL HUYGENS' MODEL (DHM) AND DIGITAL EQUIVALENT CIRCUIT

In DHM, a three-dimensional minute acoustic field can be described by a cubic element consisting of six transmission lines as shown in Fig. 1. Each transmission line has a characteristic impedance of $Z_0 = \rho_0 c_0$, where ρ_0 is the medium density and c_0 is the propagation velocity of medium. The particular feature of DHM is that the sequences of impulses are traced in the time domain. When an input pulse P is applied to line 1 at the time $t = n\Delta t$ where $n = 1, 2, \cdots$ and $\Delta t = \Delta \ell / c_0$ as shown in Fig. 1(a), the pulse is scattered at the node because of the impedance discontinuity at the connecting node. Thus, the impulse of amplitude $-2P/3$ is reflected back to the incident line 1 and the impulses of amplitude $P/3$ are scattered to the other five lines. The scattering pulses are thus given as
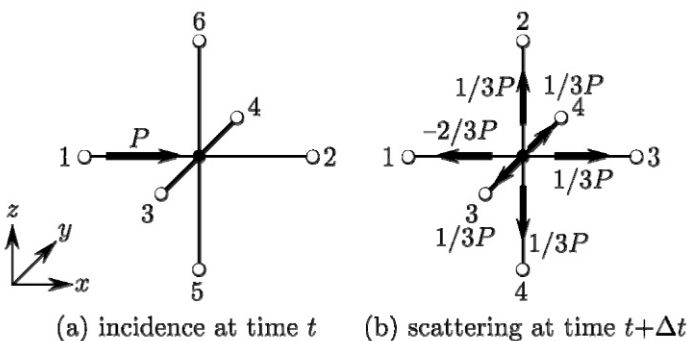

(a) incidence at time t (b) scattering at time $t + \Delta t$

Figure 1. Three dimensional DHM element and impulse scattering at element node.

$$\begin{cases} S_1^{n+1}(i,j,k) = \phi^n(i,j,k) - P_1^n(i,j,k) \\ S_2^{n+1}(i,j,k) = \phi^n(i,j,k) - P_2^n(i,j,k) \\ S_3^{n+1}(i,j,k) = \phi^n(i,j,k) - P_3^n(i,j,k) \\ S_4^{n+1}(i,j,k) = \phi^n(i,j,k) - P_4^n(i,j,k) \\ S_5^{n+1}(i,j,k) = \phi^n(i,j,k) - P_5^n(i,j,k) \\ S_6^{n+1}(i,j,k) = \phi^n(i,j,k) - P_6^n(i,j,k) \end{cases} \tag{1}$$

$$\phi^n(i,j,k) = \frac{1}{3}\sum_{m=1}^{6} P_m^n(i,j,k) \tag{2}$$
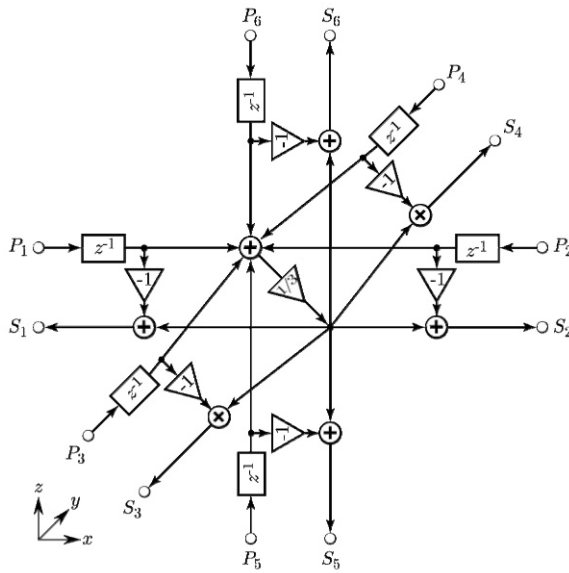

Figure 2. Digital equivalent circuit for 3D DHM element.

where P and S are incident and scattered pulses, subscripts indicate the number of the line, i, j, k denote the number of discrete points in the x-, y- and z-directions, n is the time step and ϕ is the sound pressure at the connecting node.   This process creates the propagation of waves corresponding to Huygens' principle, as the field consists of a connection of the elements forming a network. The impulse responses described in Eq. (1) can be expressed by a multi-port digital filter as shown in Fig. 2. It is easy to

implement the DHM circuits into FPGA device because DHM is essentially expressed as the digital circuit.

3.   PERFORMANCE ESTIMATION REQUIRED FOR REAL TIME SIMULATION

The typical basic architecture of FPGA device consists of an array of configurable logic cells.   When ℓ logic cells are required for the configuration of a two-dimensional DHM element, number of FPGA chips required for 1 m^2 sound space simulation is given as

$$\sqrt{2}\,\frac{\ell}{L}\,\frac{(Nf_m)^3}{Fc_0^2} \tag{3}$$

where N is the number of elements per wavelength, f_m is the maximum frequency to be simulated, L is the number of logic cells in a FPGA chip and F is the clock rate of the chip.   In this case, iterative operation is assumed. For the three-dimensional case, the number of FPGA chip is estimated as

$$\sqrt{3}\,\frac{\ell}{L}\,\frac{(Nf_m)^4}{Fc_0^3} \tag{4}$$

Table 1 shows the number of logic cells required for the two-dimensional DHM network. A Xilinx XC2V6000 FPGA chip which consists of L=76,032 logic cells [5] is used in the experiment.   The data length is assumed to be 32 bits and the fixed-point arithmetic is assumed. It is found in the two-dimensional case that one DHM element can be configured with $\ell = 263$ logic cells.   Taking into account of the fact that the 1.5 times number of cells are required to configure a three-dimensional element, the number of logic cells is estimated at about 400 for the three-dimensional case.

Table 1. Relation between number of DHM elements and number of logic cells.

Number of DHM elements	Number of logic cells	Number of logic cells per element
17	4475	263.2
65	17082	262.8
101	26530	262.7
145	38077	262.6
197	51752	262.7

Figure 3 shows the relation between the frequency of wave f_m to be simulated and the number of FPGA chips in the case of L=200,000 and F=500 MHz. For an example, only one chip is required to calculate a square

space for the frequency of f_m=10 KHz, while 18 chips are required for the cubic space. When the cubic space of 1 m³ is calculated by one chip, the specification required for FPGA chip will be $L=1.2\times10^6$ and F=1.5 GHz. A FPGA chip satisfying this specification will appear in several years.
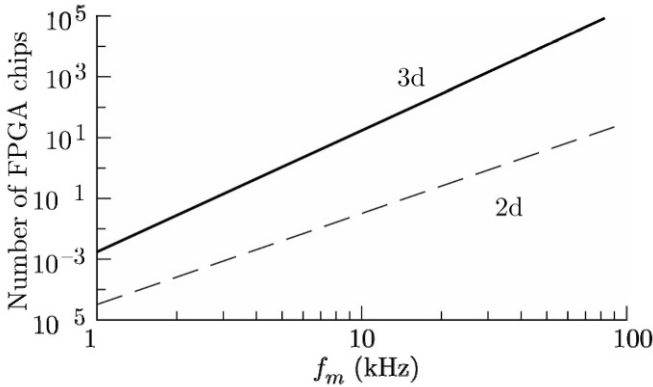

Figure 3. Relation between frequency and number of FPGA chips.

4.   ERROR ESTIMATIONS BASED ON FIXED-POINT ARITHMETIC

To reduce the circuit scale of a DHM element, the fixed-point arithmetic is taken in the DHM calculations. The fixed-point arithmetic is possible based on DHM algorithm because only one division appears in the algorithm. To estimate the numerical error in the fixed-point arithmetic, the numerical examinations are made for one-dimensional case. A thin acoustic pipe of 500 m in length is considered for a one-dimensional model. The pipe is divided into 10^5 DHM elements whose element length is $\Delta\ell=5$ mm. The time step Δt is chosen to be $8.4\,\mu$s where the sound speed c_0 is 340 m/s. One end of the pipe is driven by the velocity with a Gaussian shaped waveform and another is terminated by a sound absorber with a surface acoustic impedance of air.

Figure 4 shows the frequency characteristics of calculation error in the case of the floating-point arithmetic at x=350 m. In the figure, dashed line indicates the attenuation caused by the sound absorption of air. When data length is 28 bits or longer, the practical accuracy can be achieved because the numerical error is small enough than the attenuation caused by the sound absorption of air.
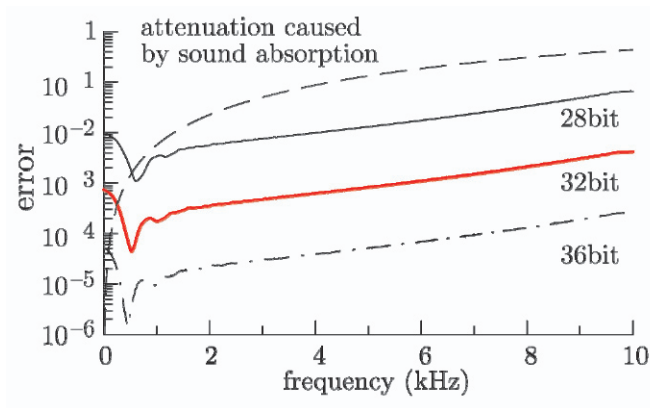
Figure 4. Frequency characteristic of numerical error for various data length at *x*=350 m.

REFERENCES

1. Y. Kagawa, T. Tsuchiya, B. Fujii and K. Fujioka, Discrete Huygens' Model Approach to Sound Wave Propagation", J. Sound Vib., **218**, 3, 419–444 (1998).
2. Y. Kagawa, N. Yoshida, T. Tsuchiya and M. Sato, Introduction to Equivalent Circuit Network Modeling, Morikita-Shuppan, Tokyo (2000) (in Japanese).
3. T. Tsuchiya and Y. Kagawa, Digital Equivalent Circuits for Acoustic Field Based on Discrete Huygens' Modeling, Jpn. J. Appl. Phys., **44**, 6B, 4297–4300 (2005).
4. P. B. Johns and R. L. Beurle, Numerical Solution of Two-dimensional Scattering Problems Using Transmission-line Matrix, Proc. IEEE, **119**, 9, 1203–1208 (1971).
5. Xilinx, Virtex-II Platform FPGAs: Complete Data Sheet, DS031 (v3.5), Nov. 5, Xilinx (2007).

TWO-DIMENSIONAL NUMERICAL ANALYSIS OF ACOUSTIC FIELD USING THE CONSTRAINED INTERPOLATION PROFILE METHOD

S. Oh, K. Okubo, T. Tsuchiya, N. Takeuchi

Faculty of Systems Science and Technology, Akita Prefectural University, 84-4 Tsuchiya-Ebinokuchi, Yurihonjo-shi, 015-0055 Japan; Faculty of System Design, Tokyo Metropolitan University, 6-6, Asahigaoka, Hino City, Tokyo, 191-0065 Japan; Faculty of Enginnering, Doshisha University, 1-3, Tatara Miyakodani, Kyotanabe, Kyoto, 612-0321 Japan

Abstract: The authors investigated acoustic field analysis using the Constrained Interpolation Profile (CIP) Method. This study examined the calculation accuracy of the two-dimensional (2-D) acoustic field analysis using the Type-M CIP Method. The results obtained using finite difference time domain (FDTD) analysis and CIP analysis are compared for two-dimensional acoustic fields. The comparison revealed that CIP analysis provides higher accuracy using the same discretization.

Key words: CIP method, FDTD method, Type-M CIP method, Acoustic field analysis

1. INTRODUCTION

Recently, numerical analyses of acoustic fields in the time domain have been investigated widely as a result of computer development. Development of accurate schemes is an important technical issue for acoustic field calculation. In this study, we examine the analysis of acoustic fields using the constrained interpolation profile (CIP) method [1–5], which is a novel method proposed by Yabe. Results obtained using finite difference time domain (FDTD) analysis [6–8] and CIP analysis are compared for a two-dimensional acoustic field.

Through comparison of results, we report the accuracy of CIP acoustic field analyses.

2.   CALCULATION

Linearized governing equations of acoustic fields are given in Eqs. (1) and (2).

$$\rho \frac{\partial \vec{v}}{\partial t} = -\nabla p \qquad (1)$$

$$\nabla \cdot \vec{v} = -\frac{1}{K} \frac{\partial p}{\partial t} \qquad (2)$$

In these equations, ρ denotes the density of the medium, K is the bulk modulus, p is sound pressure, and v is the particle velocity. Here, we assume that the calculation is for a lossless and homogeneous medium.

Moreover, assuming $\vec{v} = (v_x, 0, 0)$ in order to analyze one-dimensional (1-D) acoustic field propagation in the x-direction, we can obtain the following equations from Eqs. (1) and (2).

$$\frac{\partial p}{\partial t} + K \frac{\partial v_x}{\partial x} = 0, \qquad (3)$$

$$\frac{\partial v_x}{\partial t} + \frac{1}{\rho} \frac{\partial p}{\partial x} = 0. \qquad (4)$$

By adding and subtracting these two equations, we obtain

$$\frac{\partial (p \pm Z v_x)}{\partial t} \pm c \frac{\partial (p \pm Z v_x)}{\partial x} = 0. \qquad (5)$$

Here, Z indicates the characteristic impedance (i.e. $Z = \sqrt{\rho K}$) and c represents the sound velocity in the medium (i.e. $c = \sqrt{K/\rho}$). In addition, through simple spatial differentiation of the equations, the equations of the derivatives are given as

$$\frac{\partial(\partial_x p \pm Z\partial_x v_x)}{\partial t} \pm c \frac{\partial(\partial_x p \pm Z\partial_x v_x)}{\partial x} = 0. \quad (6)$$

Therein, $\partial_x = \dfrac{\partial}{\partial x}$. One can observe that Eqs. (5) and (6) are advection equations of $p \pm Zv_x$, $\partial_x p \pm Z\partial_x v_x$. Therefore, applying the CIP method to these equations enables solving the acoustic field propagation in the x-direction. Moreover, considering advection of $p \pm Zv_y$ and $\partial_y p \pm Z\partial_y v_y$, propagation in the y-direction as well as in the x-direction can be calculated by applying the CIP method.

We summarize the equations of 2-D acoustic field calculation as follows:

$$\frac{\partial}{\partial t} F_{x\pm} \pm c \frac{\partial}{\partial x} F_{x\pm} = 0, \quad (7)$$

$$\frac{\partial}{\partial t} G_{x\pm} \pm c \frac{\partial}{\partial x} G_{x\pm} = 0, \quad (8)$$

$$\frac{\partial}{\partial t} F_{y\pm} \pm c \frac{\partial}{\partial x} F_{y\pm} = 0, \quad (9)$$

$$\frac{\partial}{\partial t} G_{y\pm} \pm c \frac{\partial}{\partial x} G_{y\pm} = 0, \quad (10)$$

here,

$$F_{x\pm} = p \pm Zv_x, \quad (11)$$

$$G_{x\pm} = \partial_x p \pm Z\partial_x v_x, \quad (12)$$

$$F_{y\pm} = p \pm Zv_y, \quad (13)$$

$$G_{y\pm} = \partial_y p \pm Z\partial_y v_y. \quad (14)$$

It is readily apparent that Eqs. (7) to (10) are advection equations of $F_{x\pm}$, $G_{x\pm}$, $F_{y\pm}$ and $G_{y\pm}$. Therefore, application of the CIP method to these equations enables solving the 2-D sound propagation in the x-direction and y-direction.

Here, multi-dimensional analysis using the CIP method requires additional modification of the means shown in Eqs. (7) to (10). In other words, calculation of a 2-D acoustic field requires treatment of derivatives of the perpendicular to each direction. In order to completely calculate the x-direction, we also need to calculate $\partial_y p$ in the x-direction. For that reason, we apply a first-order upwind scheme to calculate these variables and obtain those propagating in the x-direction. This modified CIP method is called the "Type-M CIP method."

3.   NUMERICAL RESULTS AND DISCUSSION

We implement 2-D analysis of the acoustic field using the CIP method. Figure 1 illustrates the numerical model. In that model, it is assumed that a sound source exists on the grid point $O(x, y) = (0,0)$, as depicted in Fig. 1. Equation (15) shows the driving pressure waveform of $p_i(t)$:

$$p_i(t) = \beta(12\alpha^2 (t-\tau) - 8\alpha^3 (t-\tau)^3)e^{-\alpha(t-\tau)^2}, \qquad (15)$$

where $\tau = 50\Delta t$, $\alpha = 1.5 \times \dfrac{1}{(10\Delta t)^2}$ and $\beta = 5.4 \times 10^{-10}$. Here, Δt is the time step in numerical analyses and is listed in Table 1. $Q(x, y)$ is the observation point in Fig. 1, assuming that x and y indicate distance [m] from the origin O. We define the azimuthal angle θ as the angle between the x-axis and OQ. Table 1 lists the analytical parameters of calculations.

First, Fig. 2(a) plots the sound pressure waveform versus time that is calculated using CIP analysis at points $Q_1(5,0)$ $(\theta = 0°)$ and $Q_2(3.55, 3.55)$ $(\theta = 45°)$. The FDTD method [6,7] is illustrated in Fig. 2(b). All parameters of the FDTD calculation (grid size, Δt, medium, and so on) are identical to those of the CIP calculation. These figures indicate that the waveform of the FDTD was deformed more than that of CIP, suggesting that the numerical dispersion causes the deformation of the FDTD waveforms.

Figure 3 presents phase differences between calculated results and the exact solution. The results of FDTD analysis are also illustrated in Fig. 3. Here, calculations using the FDTD method are performed with $\Delta = 0.05\,\text{m}$ and $\Delta = 0.025\,\text{m}$ (half size of CIP grids), where Δ is the length of one side of the cell. The calculations indicate that there is only a slight phase error in the CIP result.
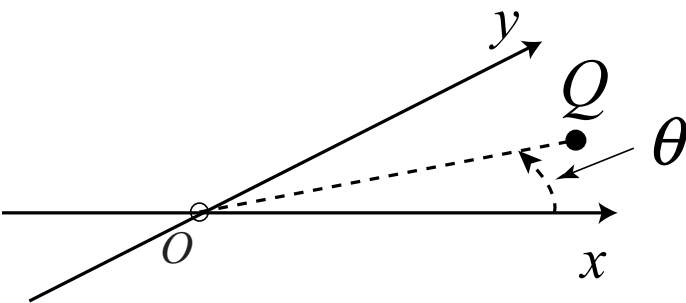
Figure 1. Numerical model.

Table 1. Analytical parameters.

grid size	$\Delta x = \Delta y = \Delta = 0.05\,\mathrm{m}$
time step	$\Delta t = 8.25 \times 10^{-5}\mathrm{s}$
θ(azimuthal angle)	$0° \leq \theta \leq 90°$
ρ	1.21
K	1.4235529×10^5
medium	air

Figure 4 graphs the normalized phase velocity versus azimuthal angle θ at 1024 Hz (point per wavelength; ppw = 6.7). This figure depicts the CIP ($\Delta = 0.05$) and the FDTD ($\Delta = 0.05$ and $\Delta = 0.025$) results. These illustrate that CIP analysis provides higher accuracy when identical discretization is used. It is noteworthy that the pressure wave front remains uniform as it propagates. CIP analysis thus provides higher phase accuracy than conventional analysis.
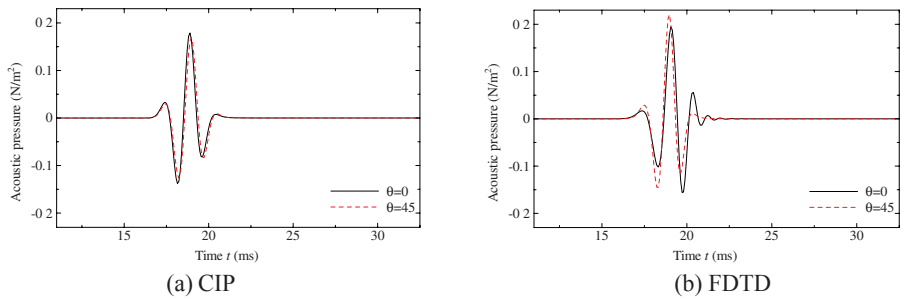

(a) CIP　　　　　　　　　　　　　　　(b) FDTD

Figure 2. Calculated waveforms of sound pressure.

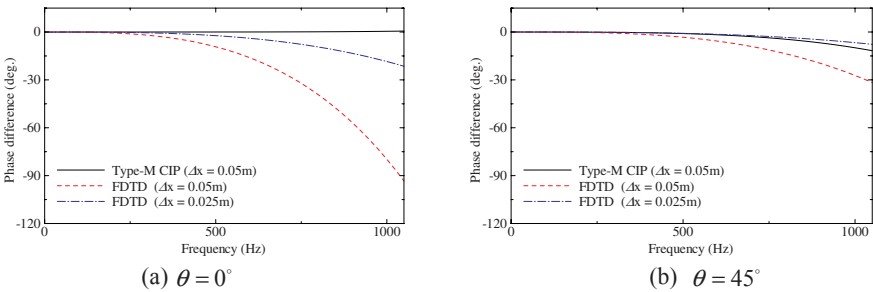(a) $\theta = 0°$ (b) $\theta = 45°$

Figure 3. Phase difference between calculated results and the exact solution.
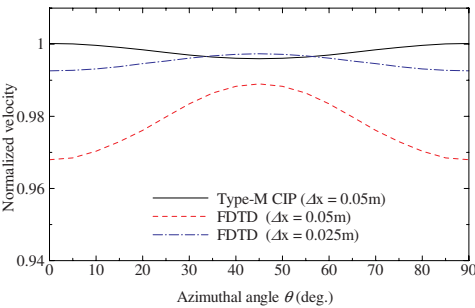
Figure 4. Normalized velocity versus azimuthal angle (at 1024 Hz, ppw = 6.7).

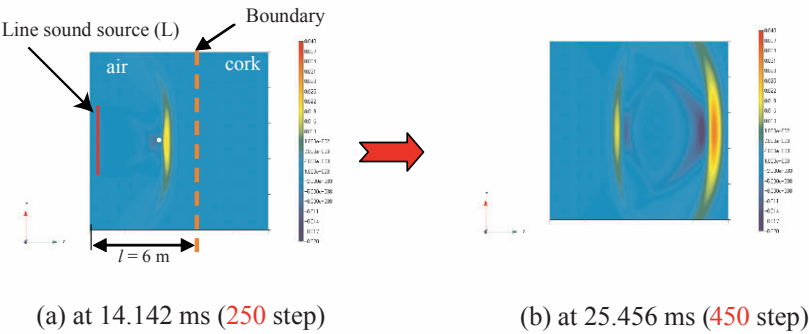(a) at 14.142 ms (250 step)   (b) at 25.456 ms (450 step)

Figure 5. Distribution of sound pressure with the boundary calculated using CIP method.

Figure 5 presents a realistic model of the distribution with the boundary calculated using the CIP method. This figure validates application of the 2-D acoustic CIP calculation for a heterogeneous analysis domain.

4.   CONCLUSION

This study examines the accuracy of acoustic field analysis using the Type-M CIP method, as well as the influence of the propagation and phase properties. As a result, this study demonstrates that the CIP method can analyze acoustic field propagation with high accuracy.

In this paper, a comparatively simple analytical model is used as an introduction of the research on acoustic field analysis by the CIP method. We intend to investigate treatment of a more realistic model in the near future.

REFERENCES

1. H. Takewaki, et al., *J. Comput. Phys.*, vol. 61, pp. 261–265, 1985.
2. T. Yabe, et al., *J. Comput. Phys.*, vol. 169, pp. 556–593, 2001.
3. T. Yabe, et al., The constrained interpolation profile method, Morikita Pub. Co., 2003.
4. K. Okubo and N. Takeuchi, *IEEE Trans. Antennas Propag.*, Jan 2007.
5. K. Okubo, et al., *Proc. Inter. IEEE Int'l. Symp. A. P.*, July, 2006.
6. K. S. Yee, *IEEE Trans. Antennas Propag.*, vol. AP-14, no. 4, pp. 302–307, May 1966.
7. K. S. Kunz and R. J. Luebbers, The finite difference time domain method for electromagnetics, electromagnetics, CRC Press, 1993.
8. D. Botteldooren, *J. Acoust. Soc. Am.*, vol. 98, no. 6, pp. 3302–3308, 1995.